Author:
Staddon, Leanne G

Title:
Vestiges of earliest crust

crustal evolution in the Narryer Terrane, Yilgarn Craton

Vestiges of earliest crust: crustal evolution in the Narryer Terrane, Yilgarn Craton.

Leanne Staddon

A dissertation submitted to the University of Bristol in accordance with the requirements for award of the degree of Doctor of Philosophy in the Faculty of Science.

School of Earth Sciences

May 2019

Word count: 56,183

Abstract

Provenance studies and our understanding of the early Earth are dominated by the mineral zircon. However, zircons are derived dominantly from felsic lithologies, which are thought to be a volumetrically minor component of Hadean and Archean crust. This thesis focuses on detrital chromites, derived solely from mafic and ultramafic protoliths, within metasediments at Jack Hills, in the Narryer Terrane, Yilgarn Craton, Western Australia. Detrital zircons found within the same metasedimentary rocks pre-date the rock record by up to 350 Myr, but their petrogenesis remains controversial, with conflicting hypotheses on the generation, evolution and destruction of Hadean and Archean crust, and the geodynamic regime under which these processes operated. Detrital chromites show significant evidence of metamorphism, including elevated ZnO and MnO and lowered Mg#s of ≤30. The correlation of ZnO content with chromite modal proportions and the fit of most heavily modified chromites to the shape of an Fe-Mg exchange isopleth provides strong evidence chromites underwent metamorphic re-equilibration in the host metasediments. This event, likely at ca. 2650 Ma, also replaced primary mineral assemblages, which are now dominated by the same metamorphic assemblages as the host metasediments. However, despite meter-scale variability Mg#, and wt. % ZnO and MnO, Cr# are consistent across all samples and regardless of rounding shape, indicating a single, magmatically dynamic igneous source of detrital chromites from Jack Hills. When compared to chromites from known tectonic settings a komatiitic origin can be excluded: the source of detrital chromites is inferred to a layered intrusion. Bulk chromite samples yield unradiogenic $^{187}Os/^{188}Os$ isotopic compositions of 0.10412 to 0.11443, resulting in rhenium-depletion ages (TRDs) of 1849 Ma to 3323 Ma. Three analyses possessed 'true' TRDs (Re analytically indistinguishable from 0), indicating Re loss of chromites in both the Archean and Proterozoic. When filtered for magmatic chromite compositions ($^{187}Re/^{188}Os < 0.1$) five Re-Os model ages (TMAs) yield a weighted mean of 3528±34 Ma (2se, MSWD=1.3). Two younger model ages at ~3000 Ma are also present, likely representing Re-loss from ~3530 Ma chromites, or metamorphic re-equilibration. The 3730 Ma Manfred Complex yields a chondritic γOs_i, indicating it may not represent the source of detrital chromites. Zircons yield typical Jack Hills ^{207}Pb-^{206}Pb age distributions, with a dominant peak at ca. 3380 Ma and more minor peaks at ~3440 Ma, ~3490 Ma, ~3520 Ma to 3540 Ma, and ~4000-4100 Ma. Oscillatory zoned zircons possess subchondritic $\varepsilon Hf(t)_{CHUR}$, and plot on a shallow array indicative reworking of crust with a $^{176}Lu/^{177}hf$ ratio of >0.02. These values are indicative of crust with a mafic composition: this study observes no evidence to suggest zircons are derived from reworking of felsic crust, as has been suggested in numerous recent publications. Detrital chromite Re-Os TMAs of ~3530 Ma overlap with two minor ^{207}Pb-^{206}Pb age distribution peaks, that are composed of zircons that possess subchondritic $\varepsilon Hf(t)_{CHUR}$ compositions, indicating a temporal link between the mafic and felsic components of the Jack Hills detrital records. This is a hallmark of a stagnant lid regime rather than modern-style plate tectonics. However, uncertainties on aspects of Re-Os TMAs, such as the potential interaction of the chromite protolith with reservoirs of super- or sub-chondritic compositions, suggests geodynamic conclusions should be taken tentatively.

Acknowledgements

This thesis would not have been possible without a long list of people who have put up with me over the last few years. The highlight of this PhD was undoubtably getting to spend a significant chunk of time exploring the Narryer Terrane and visiting the hallowed Jack Hills W-74 site. I'm extremely grateful to Tony Kemp, Chris Gray, and Matthew Rowe for the opportunity, and for only laughing a little bit when I realised on the first night that I had no cutlery. Tony Kemp is also thanked for the large supply of the Manfred Complex samples. 14WA zircons were separated and beautifully mounted by Bruno Dhuime and Ben Brennan before my arrival, saving me significant pain and panic on the approach to analysis time at the BGS. This study also benefited from the picking expertise of Lyra Sanchez, who picked the last three Jack Hills chromite samples while I stressfully wrote this thesis. Ben Buse and Stu Kearns are gratefully acknowledged for their help with the SEM and microprobe, and some of the most rapid weekend email replies I've experienced. Jeremy Rushton is also thanked for his help with CL imaging of the zircons at the BGS. I've also benefited massively throughout my PhD from the mass spectrometry wisdom bestowed by Chris Coath and Jamie Lewis. Finally, Vanessa Pashley is also thanked for her help with mass spectrometry at the BGS.

The last 3 and a half years would have been far harder without the support and guidance of my friends. I've been lucky enough to share various offices with various marvellous people, who have listened to me ramble on about chromites and zircons for nearly 4 years without complaint. These people have supported me and encouraged me solidly throughout the last few years. A big thankyou particularly goes to Holly Welsby, Lotta Kemppinen and Tim Gregory. My best friends Shanon Nicholson and Jasmin Elliott (who've had to put up with this for far longer) have kept me sane throughout the entire process. A BIG thankyou goes to the Bristol isotope group (pun intended), for the support and numerous laughs over the years. A shout out also to the department band: playing with you guys has honestly been one of the best things about my time in Bristol, even if it has meant having Christmas songs stuck in my head since October.

This thesis would never have happened without my supervisors; Ian Parkinson, Tim Elliott and Matt Horstwood. Thankyou to you all, for not only the opportunity to do this fantastic project, but also providing me with a solid understanding of isotope geochemistry. Ian particularly has borne the brunt of numerous stupid questions and decisions (who uses acetone to get chromite out of a plastic beaker!?) and has somehow still managed to mould me into (I like to think) a well-rounded and confident geochemist. Thank you for supporting me for the last few years, and the amount of time and effort you have put into my PhD.

My family have also continually supported me throughout both my undergraduate and postgraduate degrees, particularly my Mum, Dad and my sister, Robs. Sorry for the growing rock collection that always seems to end up being stored at home and pointing out the exciting rocks on holiday. Thankyou Steve Sykes for being my rock for the last year and half. I'll make a geologist out of you yet, particularly now I know you can spell komatiite.

Finally, I am eternally grateful to Mick Donnelly, without whom I would not be a geologist. Your pure enthusiasm for the subject is the reason I'm here today, and I cannot thank you enough.

For

My Family

&

For Nan

I declare that the work in this dissertation was carried out in accordance with the requirements of the University's *Regulations and Code of Practice for Research Degree Programmes* and that it has not been submitted for any other academic award. Except where indicated by specific reference in the text, the work is the candidate's own work. Work done in collaboration with, or with the assistance of, others, is indicated as such. Any views expressed in the dissertation are those of the author.

SIGNED: ..... DATE:.....

CONTENTS

LIST OF FIGURES

LIST OF TABLES

Chapter One:

Introduction

1.1. The Earliest Crust: a preamble

Our understanding of crustal evolution in the early Earth is severely inhibited by the absence of a rock record greater than 4020 million years old (Mojzsis et al., 2014; Reimink et al., 2014; 2016; *cf*. O'Neil et al., 2008), and paucity of preserved Eoarchean (≥3600 Ma) crust. The formation, composition and subsequent destruction of Hadean (>4000 Ma) and Archean (4000-2500 Ma) crust, coupled with the evolution of the mantle reservoir from which it was extracted, is one of the greatest outstanding questions within Earth sciences. Central to this debate is the geodynamic regime under which these processes operated. Disparate geodynamic hypotheses include modern-style plate tectonics (Harrison et al., 2008; Hopkins et al., 2008; 2010; Arndt, 2013; Polat et al., 2015), some form of proto-subduction (e.g. van Hunen and Moyen, 2012; Turner et al., 2014) stagnant lid regime (Kamber et al., 2005; Kemp et al., 2010; O'Neill and Debaille, 2014), sagduction and delamination (Johnson et al., 2014; Francois et al., 2014), drip tectonics (e.g. Nebel et al., 2018), and impact derived melting (Hansen, 2007; Johnson et al., 2018). This period is postulated to coincide with several of Earth's most important milestones, including the initiation of mobile lid plate tectonics and the beginnings of life. It is therefore crucial to understand crustal generation and evolution, and the geodynamic regime within which these processes operated, from the fragmentary record of Earth's most ancient crustal vestiges.

Many geodynamic hypotheses are centred on data garnered from felsic intrusives composed of tonalite, trondhjemite and granodiorite (TTG), which are the archetypal lithology of Archean cratons (e.g. Moyen and Martin, 2012): nuclei of ancient crust with deep, cold lithospheric roots that have remained stable for billions of years, forming the cores of modern-day continents. TTGs, coupled with komatiites, extrusive ultramafics emplaced at liquidus temperatures in excess of 1400 °C (e.g. Arndt, 2008), are important components of Archean cratons that are lithologically distinct the modern Earth. While a broad consensus on the origin of komatiites from relatively dry, hot mantle plumes is agreed (e.g. Arndt, 2008), the origins of TTGs are more heavily debated (e.g. Moyen and Martin, 2012). TTGs have numerous chemical affinities to modern day adakites including arc-like major and trace elements (Moyen and Martin, 2012; Moyen and Laurent, 2018), and their petrogenesis has therefore been heavily, yet controversially, linked to their generation within subduction zones (Moyen and Martin, 2012). The presence of subduction zones requires bimodality of crust, painting a picture of the Archean not dissimilar from the Earth today, with significant quantities of continental crust stabilised. However, recent studies have instead suggested TTGs are derived from protracted reworking of thickened mafic crust (Johnson et al, 2017; O'Neil and Carlson, 2017). This is more indicative of a stagnant lid regime, where a rigid crustal shell is periodically punctuated by large scale melting events, inducing lower melting of the lower crust to form evolved (continental?) lithologies (e.g. Kamber, 2005).

While the rock record yields valuable insights Archean geodynamic regimes, it is inherently incomplete. Polyphase, high grade metamorphism often distorts and clouds primary compositions and geochronological data, and certain lithologies are preferentially preserved. Detrital records may therefore provide additional constraints on crustal evolution within ancient terranes, and their use has increased significantly since the development of analytical techniques that allow rapid, in-situ analysis (e.g. Gehrels, 2014). Chief amongst analysed detrital phases is the mineral zircon, long lauded as the premier geochronometer of evolved rocks (e.g. Schoene, 2014). Nowhere is this more apparent than within the Narryer Terrane, in the Yilgarn Craton, Western Australia (Figure 1.1). Here, detrital zircons within metasediments at Jack Hills (Figure 1.2) and Mount Narryer (Figure 1.3) yield ages that not only overlap with known rock units within the Narryer Terrane, but pre-date the terrestrial rock record by up to ~350 Myr (Froude et al., 1983; Compston and Pidgeon, 1986; Wilde et al., 2001; Valley et al., 2014), providing a unique window in the Hadean Earth.

Detrital zircons from Jack Hills, and subsequently from lithological units within the Narryer Terrane, are central in geodynamic arguments for the early Earth. In stark contrast to previous interpretations of this period of Earth's history, Hadean zircons have been postulated to confirm the operation of modern-style plate tectonics and the stabilisation of significant quantities of continental crust in the Hadean (Harrison et al., 2005; 2008; 2017; Bell et al., 2011; 2014). However, this is intensely debated, and the isotopic integrity of many Hadean zircons questioned (Kemp et al., 2010; Nebel et al., 2014). Filtering for definitively magmatic Hadean zircons instead appears to suggest they are derived from reworking of mafic crust, akin to a stagnant lid regime (Amelin et al., 1999; Kemp et al., 2010; Whitehouse et al., 2017). However, despite decades of research, no clear consensus on the origin, evolution and destruction of the protolith to the Jack Hills zircons and lithologies within the wider Narryer Terrane is present.

This thesis focuses on two detrital phases from Jack Hills: zircon and chromite. While the former phase has been intensely studied (e.g. Nebel et al., 2014; Harrison et al., 2017), the latter has received little attention. Detrital chromites, however, represent the erosional products of mafic and ultramafic crust, which is suggested to represent the dominant lithology within the early Earth (e.g. Hawkesworth et al., 2017). Study of this phase will therefore allow a more complete picture of crustal evolution, and potentially aid in elucidating the geodynamic regime both chromites and zircons were crystallised under. This introductory chapter details the various lithologies of the Narryer Terrane, and charts the previous work undertaken on detrital zircons from Jack Hills. Other well described detrital phases at Jack Hills, such as xenotime and monazite, are also briefly discussed. Finally, the aims of this project are presented, and a hypothesis developed that demonstrates the geodynamic implications of an idealised coupled zircon-chromite detrital record.

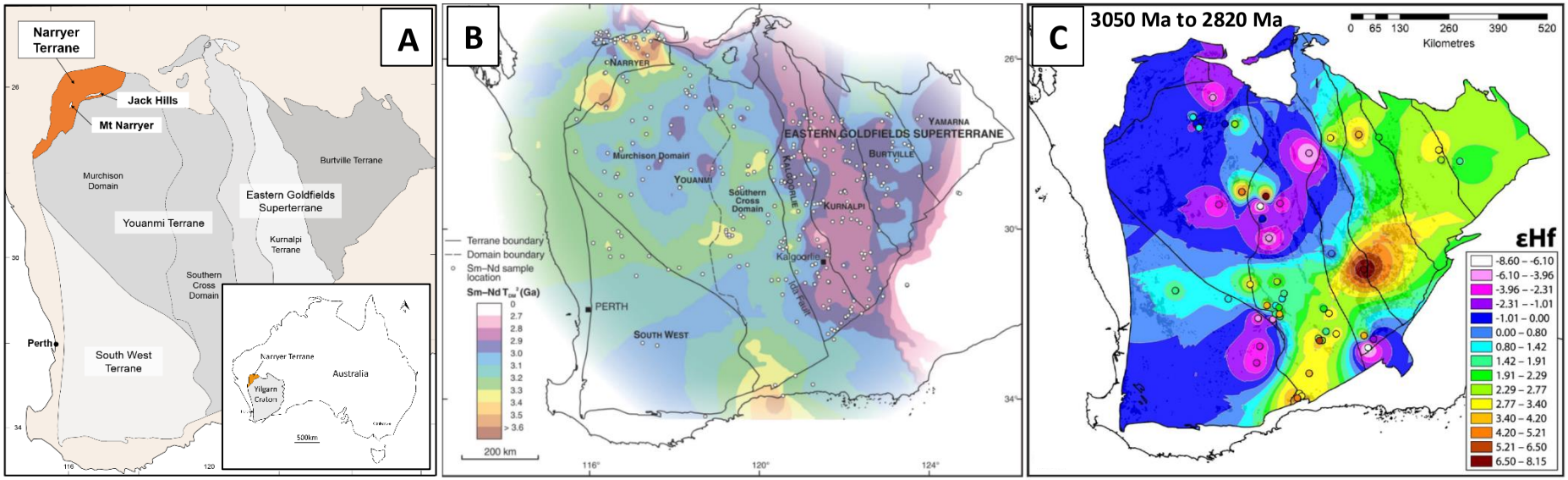

Figure 1.1: A) The position of the Narryer Terrane within the Yilgarn Craton. Terrane boundaries after Cassidy et al. (2006). Positions of the Jack Hills greenstone belt and Mt Narryer supracrustal association are also marked. Inset of the Yilgarn's position within Australia shown for reference. **B)** Figure from Wyche et al. (2012) showing Sm-Nd DM model ages. Clear division of Eastern Goldfields Superterrane and the rest of the Yilgarn craton, alongside ancient Sm-Nd TDMs for the Narryer Terrane. **C)** Figure modified from Mole et al. (2019) showing the $\varepsilon Hf(t)_{CHUR}$ composition of crust within the Yilgarn craton at 3050 Ma to 2820 Ma. This is an atypical age of crust within the Narryer Terrane hence the absence of samples. A clear division of the west and east Yilgarn is again obvious, with minor incursion of more juvenile crust in the SE of the Youanmi Terrane.

Figure 1.2: The Jack Hills belt with simplified stratigraphy, modified from Pidgeon and Wilde. (1998) and Spaggiari (2007). The W-74 site of Froude et al. (1996) and Wilde et al. (2001) is shown for reference, as is a 2654 Ma granitoid known as 'The Blob' that cross cuts metasediments ~2 km to the SW of the W-74 site. Associations defined by Spaggiari (2007) and explained in-text.

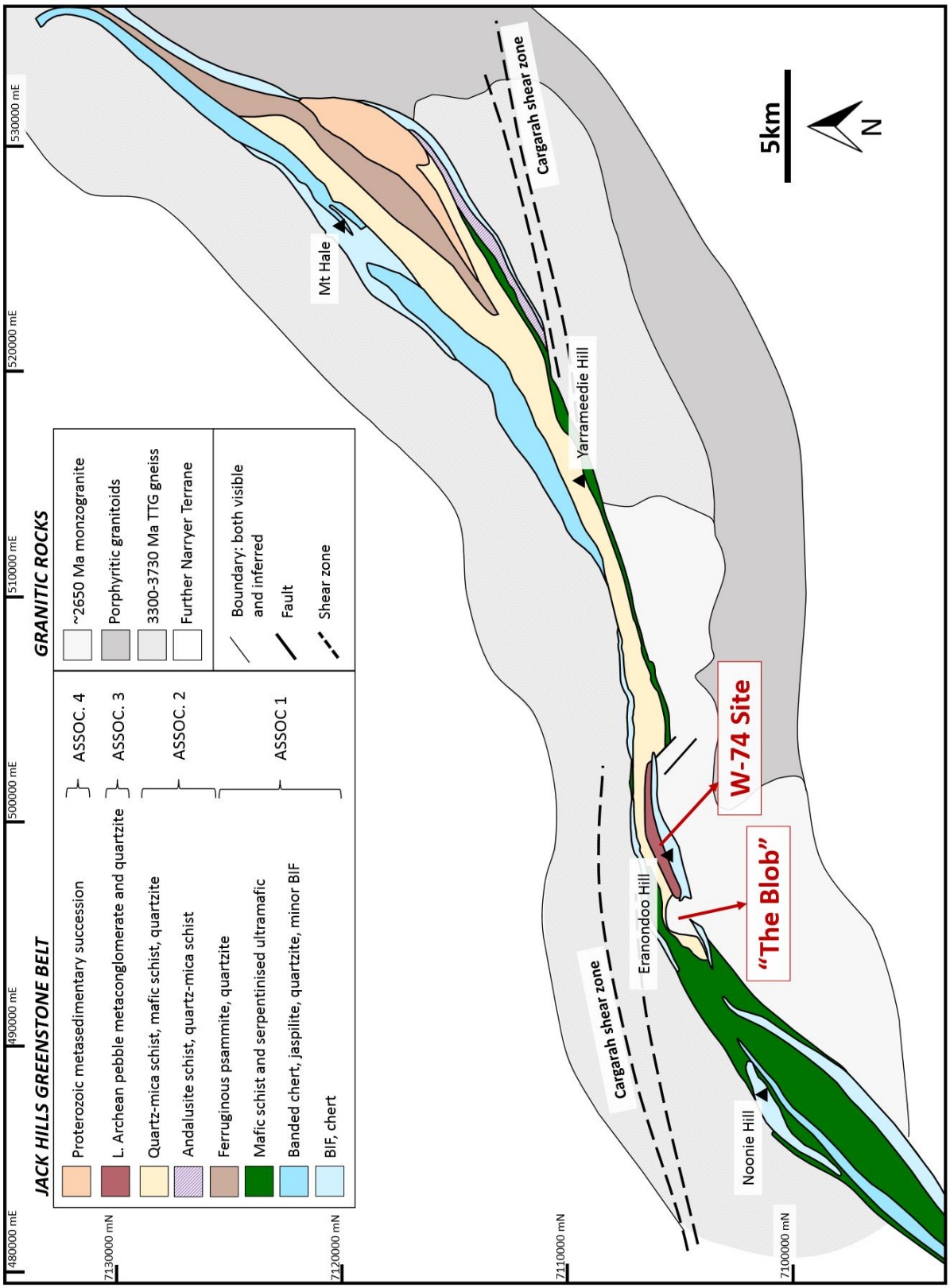

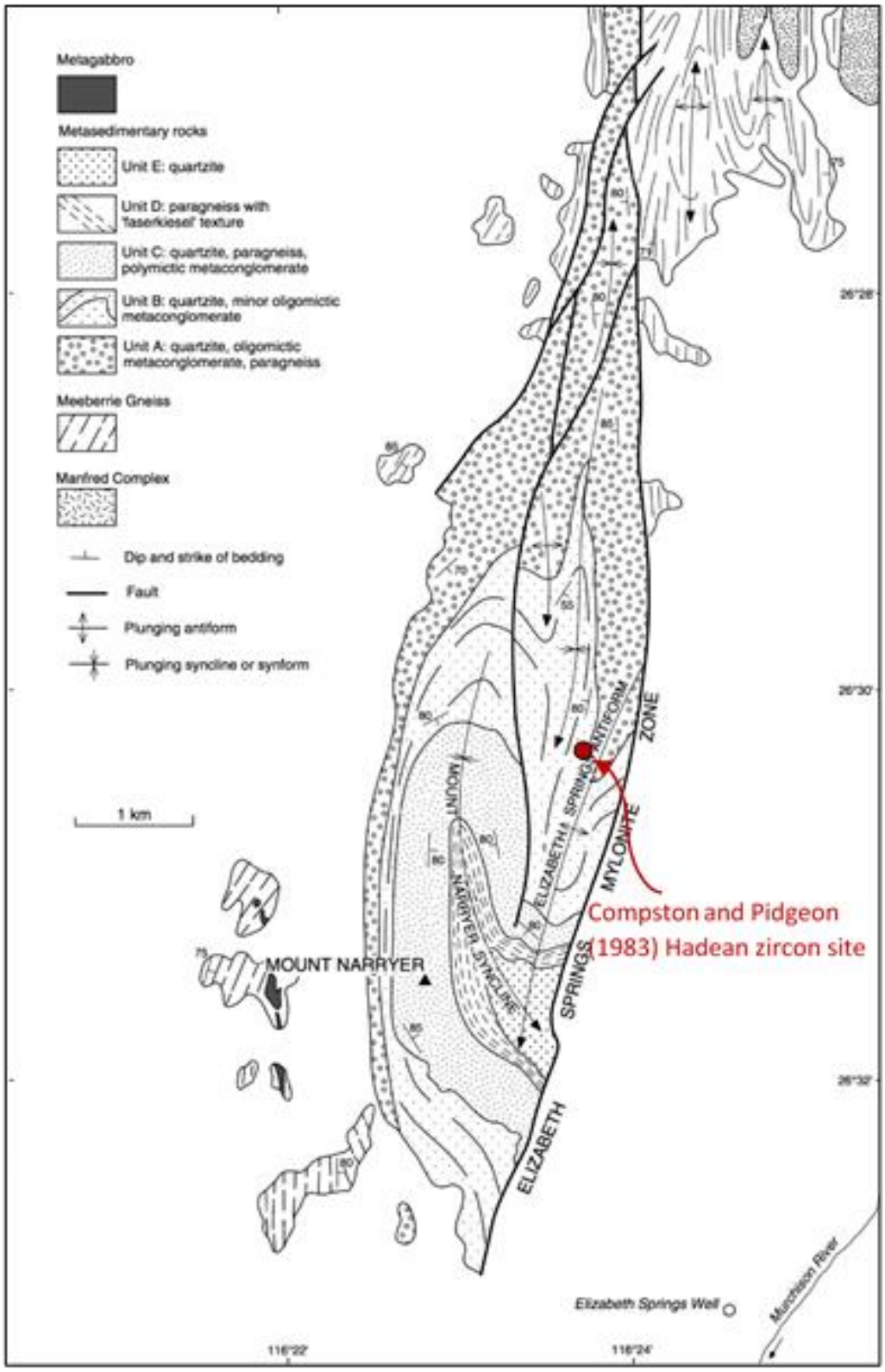

Figure 1.3: The southern sector of the Mount Narryer supracrustal succession, taken from Occipinti et al. (2001). Refolding of the ~2700 Ma Mount Narryer syncline by the ~2650 Ma Elizabeth springs antiform is clearly observed in units D and E. Folds are truncated by the Elizabeth springs mylonite zone, which also defines the eastern boundary of the belt. The original Mount Narryer Hadean zircon site is also shown.

1.2 Geological Setting

1.2.1. The Narryer Terrane, Yilgarn Craton

The Yilgarn Craton, situated in Western Australia, is the largest and most ancient of Australia's three cratons (Yilgarn, Pilbara and Gawler). The craton is sub-divided into largely N-S bounded terranes defined by both age and lithological variation (Cassidy et al., 2006; Figure 1.1), which were fully combined into a single cratonic unit by ca. 2650 Ma, contemporaneous with ubiquitous, craton-wide granitoid intrusion. A decrease in Sm-Nd model ages corresponds with increasingly juvenile εNd_{CHUR} from the western Youanmi Terrane to the Eastern Goldfields Superterrane at the easternmost edge of the craton (Wyche et al, 2012; Figure 1.1b). This, coupled with the more subchondritic Lu-Hf isotopic composition of the Youanmi, Southern Cross and Narryer Terranes (Mole et al., 2014; Figure 1.1c), suggests that the western and northern portions of Yilgarn Craton originated from reworking of older crust, while the eastern areas of the Yilgarn Craton are derived from <3000 Ma juvenile addition (Wyche et al, 2012).

This work focuses on the Narryer Terrane, the most north-westerly and ancient terrane in the Yilgarn Craton (Figure 1.1). The terrane covers an area of ~30,000km² (Myers, 1988a), and is inferred to represent a deep crustal allochthon thrust above the Youanmi terrane prior to or coincident with cratonic amalgamation (Kemp et al., 2019). The Narryer Terrane is composed of Eo to Palaeoarchean quartzofeldspathic gneisses with minor ultramafics, mafic intrusives, and metasediments (Myers and Williams, 1985; Williams and Myers, 1987; Myers, 1988a; Kemp et al., 2019), which were tectonically interleaved and heavily deformed during amphibolite to granulite facies metamorphism between 2700 Ma and 2650 Ma (Myers, 1988a; Kinny et al., 1990; Nutman et al., 1991). Late Archean granitoids (~2650 Ma to ~2700 Ma) are ubiquitous throughout the Narryer Terrane and the wider Yilgarn Craton (Kemp et al., 2019), but are not discussed further here.

The Narryer Terrane differs from the wider Yilgarn Craton not only by age, but with the absence of the widespread and economically significant ultramafic and mafic extrusives (komatiites and komatiitic basalts) of the Youanmi, Kalgoorlie and Eastern Goldfields Terranes (Williams and Myers, 1987; Barnes & Fiorentini, 2012; Arndt, 2013). The Narryer Terrane is dominantly composed of granitic gneisses, which are grouped into the 'Narryer Gneiss Complex' (NGC) of Myers and Williams (1985) by virtue of their >3000 Ma magmatic ages. While less deformed rocks (i.e. non-gneissic) that yield ages >3000 Ma are present within the terrane, this terminology is retained here for all lithologies of this age. Though zircon U-Pb ages are complex due to prolonged magmatic and metamorphic histories (e.g. Pidgeon and Wilde, 1998), the NGC has been further divided into four main units; the Meeberrie gneiss, the Eurada gneiss, the Dugel gneiss and the Manfred Complex (Myers and Williams, 1985; Williams and

Myers, 1987; Fletcher et al., 1988; Kinny et al, 1988; Myers, 1988; Nutman et al, 1991; Kinny and Nutman, 1996).

1.2.2. Granitic Gneisses of the NGC

The 3730-3600 Ma Meeberrie Gneiss

The Meeberrie gneiss is a biotite rich, quartzofeldspathic migmatite (Figure 1.4 a/b; Williams and Myers, 1987; Kinny and Nutman, 1996), formed from compositionally diverse protoliths that may yield cm-scale age variability (Williams and Myers, 1985; Myers, 1988a; Kinny and Nutman, 1996; Pidgeon and Wilde, 1998; Kemp et al., 2019). A wide range of protolith emplacement ages and compositions have been determined for the Meeberrie gneiss. These include 3731±4 Ma juvenile tonalities (Nutman et al, 1991; Hiess and Bennett, 2016), 3680 Ma-3620 Ma monzogranites with purported distinct age distributions at ~3670 Ma, ~3620 Ma and ~3600 Ma (Myers and Williams, 1985; Kinny et al, 1988; Kinny and Nutman, 1996; cf. Pidgeon and Wilde, 1998), and a putative 3300 Ma component of unknown igneous or metamorphic origin (Nutman et al, 1991; Kinny and Nutman, 1996). The bulk monzogranitic composition of the Meeberrie gneiss is deceptive, as this composition likely derived from intrusion of younger granitoids and pegmatite into protoliths with distinct TTG compositions (Pidgeon and Wilde, 1998; Kemp et al., 2019).

The 3480 Ma Eurada Gneiss

The Eurada gneiss is a series of ~3480 Ma quartzofeldspathic gneisses found at the Eurada Bore, a low strain feature ~20 km northwest of Mount Narryer (Kinny, 1987; Nutman et al, 1991). The complex is tonalitic in composition and is preserved at a lower metamorphic grade than the surrounding granulite Narryer terrane (Kemp et al., 2019). Nutman et al. (1991) reported broader age populations of 3440 Ma to 3490 Ma and a population of ~3050 Ma zircons within lower grade gneisses to the south of the Eurada Bore. Though not discussed further within their contribution, they also noted the presence of an older, inherited population of ca. 3550 Ma zircons within a single sample. No ~3300 Ma zircon metamorphic rims ubiquitously found within older gneisses (Nutman et al, 1991) have been observed within the Eurada Gneiss, suggesting this unit may have been tectonically collated with the Meeberrie and Dugel gneisses at ~3300 Ma (Occhipinti et al, 2001) or at ~2700 Ma (Nutman et al, 1993). However, the exact relationship between the Eurada gneiss and the Meeberrie and the Dugel gneisses is unclear due to the Eurada's preservation within fault bound slices (Nutman et al, 1991). Further outcrops of the Eurada gneiss are also likely preserved to the west of Jack Hills (Kemp et al., 2019).

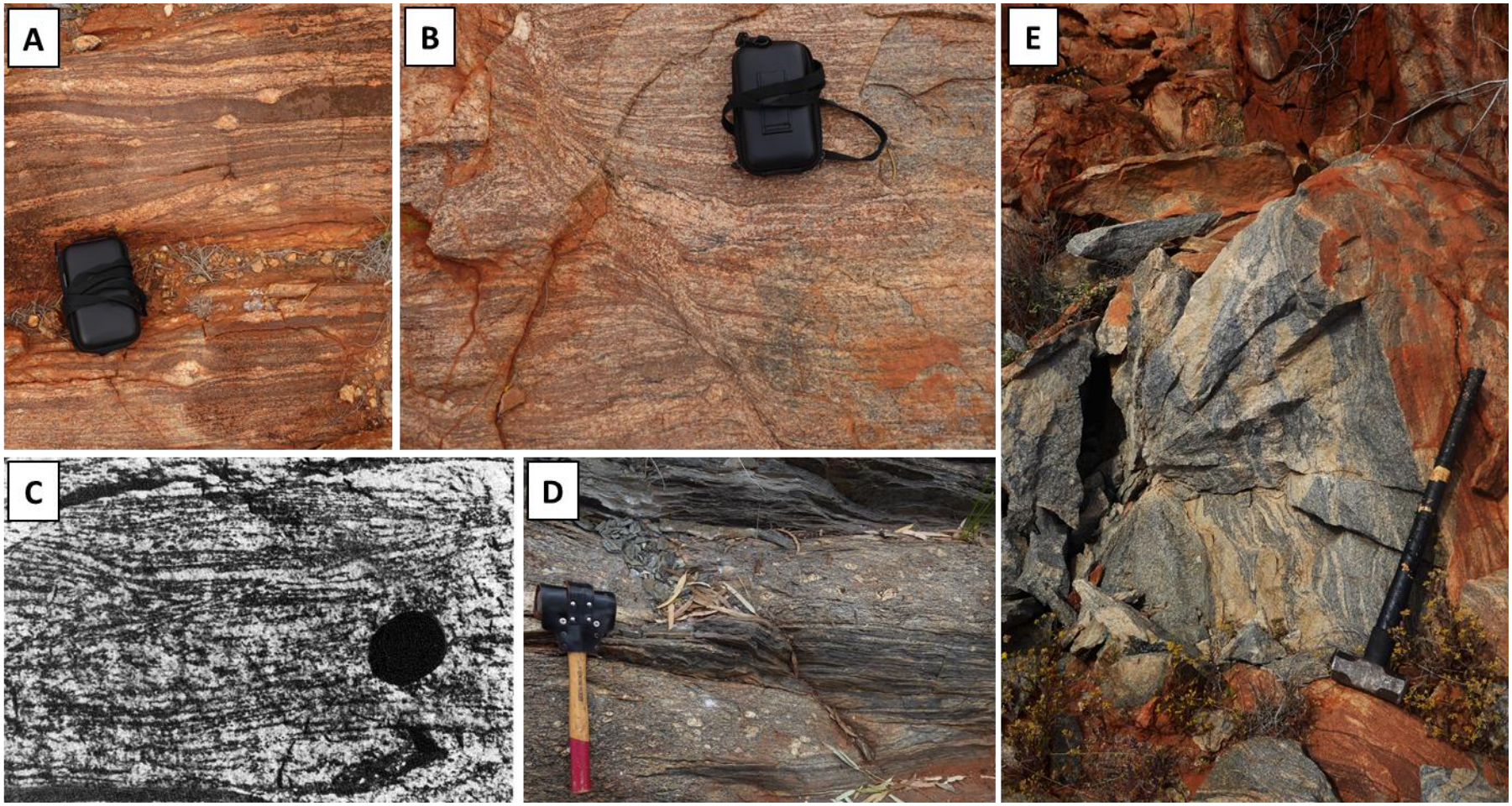

Figure 1.4: Different lithological units from the Narryer Terrane. **A)** Meeberrie gneiss with thick S_2 foliation and sigmoidal augen (less deformed?) to the SW of Mt Narryer. **B)** Migmatitic Meeberrie gneiss to the SW of Mount Narryer. This was imaged near A and highlights the heterogeneity of preservation. Shear structure also present cutting across S_2 banding. **C)** Dugel gneiss from the east of Mount Narryer: image from Myers and Williams, 1987. **D)** Foliated 3300 Ma porphyritic metagranite hosting xenoliths of ~3730 Ma banded gneiss. Image taken to the SE of the NE portion of Jack Hills. Small hammer approximately 30 cm long. **E)** Milga gneiss at the GSWA geochronology blast site. Note the less defined gneissic foliation in comparison to the Meeberrie and Dugel gneisses. Granulite sledgehammer for scale.

The 3380 Ma Dugel Gneiss

The Dugel gneiss is petrographically distinct from the Meeberrie Gneiss, with less migmatitic banding (Figure 1.4c) and a dominantly syenogranitic composition (Myers and Williams, 1985; Myers, 1988a), though locally this ranges to monzogranitic (Kemp et al., 2019). The Dugel Gneiss yields zircons that possess a high degree of discordance, but yield consistent ^{207}Pb-^{206}Pb ages of 3381 ± 22 Ma (Kinny et al, 1988), 3385±8 Ma (Kinny and Nutman, 1990) and 3375 ± 26 Ma (Nutman et al, 1991), indicating emplacement of the Dugel gneiss protolith at ca. 3380 Ma. Younger ca. 3300 Ma rims are also present within these zircons, inferred to represent either metamorphic or magmatic growth at this time (Kinny et al., 1988). The Dugel Gneiss precursors are thought to have intruded the protolith of the Meeberrie Gneiss as sheets and veins, though this relationship is now complex and tectonised due to polyphase high grade deformation (William and Myers, 1985; Myers, 1988a).

Other granitic gneisses within the Narryer Terrane

While the Meeberrie, Eurada and Dugel gneisses appear to be the most voluminous components of the NGC, numerous other metagranitoids and granitic gneisses are also present. A porphyritic granitoid cropping out to the south of Mount Narryer yields zircons with ages of 3300±6 Ma (Kinny et al., 1990), and lithologically similar ~3300 Ma granitoids have also been observed west of Mount Dugel and to the SE of Jack Hills (e.g. Figure 1.4d; Pidgeon and Wilde, 1998; Kemp, 2018; Kemp et al., 2019). Zircons within ~3300 Ma trondhjemitic metagranitoids near Jack Hills may yield zircons with cores up to 3756±6 Ma (Pidgeon and Wilde, 1998), currently the oldest zircons identified within TTGs within the Narryer terrane (Kemp et al., 2019). Finally, the Milga gneiss is a titanite-bearing granodioritic gneiss (Figure 1.4e) that crops out within the west of the terrane (Myers, 1997). Zircons within the Milga gneiss are complex, with the dominant age population at ~3000 Ma inferred to represent the age of crystallisation. Older zircon populations at 3315 Ma and ~3500 Ma likely represent inherited material, while a younger, high U zircon population at ~2630 Ma indicates metamorphic disturbance or localised pegmatite intrusion (Nelson, 1996).

1.2.3. Mafics and Ultramafics

The 3730 Ma Manfred Complex

The Manfred Complex is a series of tectonically dismembered and heavily deformed mafic and ultramafic lenses entrained within the Dugel gneiss to the NE of Mt Narryer (Williams and Myers, 1985), and less abundantly within the Meeberrie gneiss (Rowe, 2016; Kemp, 2018). The complex is dominantly amphibolitic (after leucogabbro), with more minor metaperidotite, pyroxenite, and anorthosite, and represents the disseminated fragments of a large, layered intrusive body (Williams

and Myers, 1987, Myers, 1988a/b). Remnant igneous textures are preserved locally (Myers, 1988b), especially cumulate textures, and putative igneous layering is observed in many examples (Kemp et al., 2019). Accessory spinel, allanite, apatite, pyrite, titanite and zircon have been reported within a range of lithologies (Fletcher, 1988; Kinny et al, 1988; Myers, 1998b; Rowe, 2016; Kemp, 2018).

Geochronology indicates the Manfred Complex is Eoarchean, with whole rock (WR) ^{147}Sm-^{143}Nd and ^{207}Pb-^{206}Pb analyses yielding complex isochrons that have been interpreted to represent crystallisation ages of 3680±70 Ma and 3689 ± 146 Ma, respectively (Fletcher et al, 1988). Higher resolution zircon geochronology on anorthosites yielded more robust ^{207}Pb-^{206}Pb ages of 3730 ± 6 Ma (Kinny et al., 1988), with more recent work on leucogabbros yielding zircon U-Pb ages in good agreement of this age (Kemp et al., 2019). The Manfred Complex also possesses a high Pb μ ($^{238}U/^{204}Pb$) signature of ~10 that exceeds predicted Archean mantle μ values of 7.5-8, and is coupled with a putative slightly lowered initial εNd_{CHUR} of -0.2±0.7 (Fletcher et al., 1988). This suggests the complex assimilated long lived, high μ crust during its formation, postulated to be quartz-rich sediments by Fletcher et al, (1988), owing to the low Sr and REE contents of the complex.

Other Mafic/Ultramafic Intrusives

Other mafics and ultramafics are reasonably abundant within the Narryer Terrane (e.g. Myers, 1997), but are generally observed as poorly preserved lenses within granitic gneisses. This, coupled with the general absence of zircon within mafic and ultramafic lithologies, makes geochronology challenging. As such, mafic and ultramafic crust is poorly described in comparison to granitic gneisses in the NGC. In a conference abstract, Sylvester et al. (2011) reported the presence of ~3500 Ma anorthosites and ~3300 Ga leucogabbros to the NW and NE of Mt Dugel, respectively, which had previously been mapped as part of the Manfred Complex (Myers, 1997). Lenses of leucogabbro and ultramafics (also previously reported as the Manfred Complex) near Mount Dugel and Jack Hills (Myers, 1997) have been shown to yield ages more akin to the 3380 Ma protoliths of the Dugel gneiss (Kemp et al., 2019). Gravity surveys by Athena Resources Ltd in the far north of the Narryer Terrane have also highlighted significant quantities of mafic and ultramafic intrusives. These include a Cu-Ni-PGE-rich dunitic body at Milly-Milly, the mineralised gabbroic and pyroxenitic Moonborough layered intrusion, and chromitite seams at Imagi Well. However, chromitite seams at Imagi Well appear to be Proterozoic (T. Kemp. Pers. Comm.).

1.2.4. Metamorphic History of the NGC

Like most ancient terranes, the geological history of the Narryer terrane has been clouded by polyphase, high-grade metamorphism. The current dominant metamorphic signature is believed to be derived from metamorphism at ~2700 Ma to 2650 Ma, consisting of granulite facies metamorphism

at ~2700 Ma (D_2) and retrogression at ~2650 Ma to amphibolite facies (D_3) (Kemp et al., 2019). Peak metamorphism between ~2700 Ma and ~2650 Ma produced the main foliation observed within the terrane and formed a flaser fabric parallel to previous banding of granitic gneisses (Williams and Myers, 1987). Folding from these events are observable at Mount Narryer (Figure 1.3; Williams and Myers, 1987), where the E-W trending Mount Narryer syncline (F_2) has been refolded by the NNE-SSW trending Elizabeth Springs anticline (F_3).

While ~3300 Ma has often been cited as the timing of a granulite facies event (D_1?) due to disturbance of Rb-Sr systems (Fletcher et al., 1988) and the presence of ubiquitous low Th/U 3300 Ma rims measured within zircons from the Meeberrie and Dugel gneisses, and the Manfred Complex (Kinny et al., 1988; Nutman et al., 1991; cf. Kinny and Nutman, 1996), no folding has been observed in association with this event (Kemp et al., 2019). Scant evidence of an event prior to ~2700 Ma, possibly representing the 3300 Ma event, is directly observed on the hinges of F_2 folds, where a subtle S_1 foliation is present (Williams and Myers, 1987). The apparent preservation of variable deformation between Manfred Complex and Meeberrie gneiss, and the Meeberrie and Dugel gneisses (Myers and Williams, 1985), indicates metamorphic events between the emplacement of each unit, hinting that high-grade metamorphic events also occurred at ~3700 Ma and ~3500 Ma. Another event at ca. 3000 Ma to ca. 3050 Ma has also been postulated (Nutman et al., 1991; Spaggiari, 2007). Nutman et al. (1991) suggested that while the 2650-2750 Ma event destroyed overprinted previous metamorphic events, the Narryer Terrane likely underwent multiple episodes of high-grade metamorphism, deformation and anatexis during the Archean.

1.2.5. Metasedimentary Belts

The Narryer Terrane also hosts several heavily deformed supracrustal belts. The two most voluminous and well-studied sequences crop out at Jack Hills and Mount Narryer (Figure 1.2 and 1.3). Both belts are enclosed by mylonite zones (Williams and Myers, 1987; Spaggiari, 2007), and so the original relationships of these units with the wider NGC are unknown. As this study focuses on detrital phases derived from metasediments at Jack Hills, metasediments at Mount Narryer are only briefly described.

Mount Narryer supracrustal belt

The Mount Narryer supracrustal belt is dominantly composed of high-grade metasediments and has a well-defined stratigraphy that is >2 km in thickness (Myers and Williams, 1985). Quartzites are the dominant rock type, and along with lenses of oligo to polymict metaconglomerates and pelitic metasediments, were likely deposited in a fluiviodeltaic regime (Williams and Myers, 1987; Kinny et al., 1990). Units at Mount Narryer appear to be less mature than sediments at Jack Hills, commonly containing Al-rich metamorphic phases such as cordierite, garnet and sillimanite. While

metasediments are variously described as fuchsitic (Cr-muscovite) (e.g. Williams and Myers, 1987), detrital chromites are apparently absent at Mount Narryer (Kemp et al., 2019). The age of deposition of sediments is constrained by the age of the youngest definitively magmatic (*i.e.* oscillatory zoned) detrital zircon (^{207}Pb-^{206}Pb 3281±38 Ma), and the first metamorphic growth of monazite (^{207}Pb-^{206}Pb 3291±38 Ma) at ~3300 Ma (Crowley et al., 2005; Pidgeon and Nemchin, 2006; Rasmussen et al, 2010). Although there is not a clear consensus on the exact P-T conditions of the Mount Narryer supracrustal sequence, it is widely accepted that the whole metasedimentary belt has undergone at least upper amphibolite facies metamorphism (Blight and Barley, 1981; Kinny et al, 1990), although granulite facies metamorphism is suggested by localised partial melting (Kemp et al., 2019) and the dual growth of orthopyroxene and clinopyroxene in some metasediments (Myers and Williams, 1985).

The Jack Hills greenstone/supracrustal belt

Jack Hills is located at the southern margin of the Narryer Terrane (Figure 1.1) and is a thin ~70 km long belt with a distinctly curvilinear morphology produced by dextral shearing (Spaggiari, 2007). The Jack Hills belt is preserved tectonically juxtaposed in fault-bound contact with the surrounding NGC, except for localised intrusion of a 2654 Ma monzogranite, also known as 'The Blob' (Pidgeon & Wilde, 1998; Spaggiari, 2007; Figure 1.2). Jack Hills may be interchangeably referred to as a greenstone (e.g. Spaggiari, 2007) or metasedimentary belt (e.g. Wang & Wilde, 2018), and consists largely of siliciclastics, including metaconglomerate, quartzite and quartz-mica schist, with intercalated mafic and ultramafics, banded iron formation (BIF) and chert. The presence of grunerite within BIF and hornblende within mafic schist indicates at least portions of the belt reached amphibolite facies metamorphism: hornblende within mafic schist is commonly overprinted by actinolite, showing the later retrogression to greenschist facies that defines the current dominant metamorphic signature of the belt (Spaggiari, 2007). Deformation has tectonically disturbed and juxtaposed lithological associations, making an original stratigraphy difficult to discern.

Spaggiari (2007) divided the belt into four associations determined by lithological variability. Briefly, unit 1 consists of interbedded BIF, chert and quartzite, mafic and ultramafics, and black and white banded quartzites (Figure 1.5a-d). Unit 2 contains pelitic to semi-pelitic associations, now present as quartz-mica and andalusite schists, with accompanying mafic schist and quartzite. The presence of an earlier cleavage (JH S_1) and recumbent folding (JH F_1; Figure 1.5a) absent from other lithological units suggests units 1 and 2 were deformed prior to the deposition of units 3 and 4, postulated by Spaggiari (2007) to have occurred ca. 3000 Ma. Unit 3 is restricted to the central region of the belt at Eranondoo Hill (Figure 2), and contains mature, siliciclastic sediments interpreted to have been deposited within a deltaic alluvial fan (Spaggiari, 2007) between ~3050 Ma and 2650 Ma (Crowley et al, 2005;

Rasmussen et al, 2010). The discovery of Proterozoic detrital zircon (Cavosie et al., 2004; Dunn et al., 2005; Wang and Wilde, 2018) within the Jack Hills belt led to the recognition of Unit 4, which hosts metasediments deposited during the Proterozoic. Wang & Wilde (2018) observed interbedded siliciclastics at the same apparent metamorphic grade (JH D_2) but with both Archean and Proterozoic depositional ages, highlighting that the depositional and/or tectonic relationships of units 3 and 4 may be more complex than previously postulated. Unit 3 metasediments are renowned for hosting detrital Hadean zircons (Compston and Pidgeon, 1986; Wilde et al., 2001; Valley et al., 2014), particularly at the W-74 site on Eranondoo Hill (Figure 1.2; Wilde et al., 2001), and are discussed in detail in the next section.

All lithologies from Jack Hills show clear indications of deformation and shearing: deformation is particularly striking within metaconglomerates due to strong flattening (Figure 1.5f) and recrystallisation of quartzite cobbles (Spaggiari, 2007a). Ultramafic rocks within the NE of the belt have also been subjected to intense shearing (Figure 1.5b), coincident with the main foliation of the belt (JH S_2). Earlier foliations (JH S_1) are best observed within structurally incompetent BIF (Spaggiari, 2007). Thermal or fluid events within the Jack Hills belt occurred at ~3080 Ma, 2650 Ma, ~1850-1800 Ma and 800 Ma (Spaggiari, et al., 2007b; Rasmussen et al., 2010; 2011). Monazite-xenotime thermometry of secondary inclusions within detrital zircons yield temperatures of 420°C-475°C (Rasmussen et al., 2011), indicative of upper greenschist to lower amphibolite facies metamorphism coincident with peak metamorphic conditions within unit 3 metasediments, likely at 2650 Ma. The event at ~1800 Ma (Spaggiari et al., 2007b; Rasmussen et al, 2010) and a discrete event at 800 Ma (Rasmussen et al., 2010; 2011) are of unknown magnitude, but coincide with formation of authigenic monazite and xenotime (Rasmussen et al., 2010; 2011).

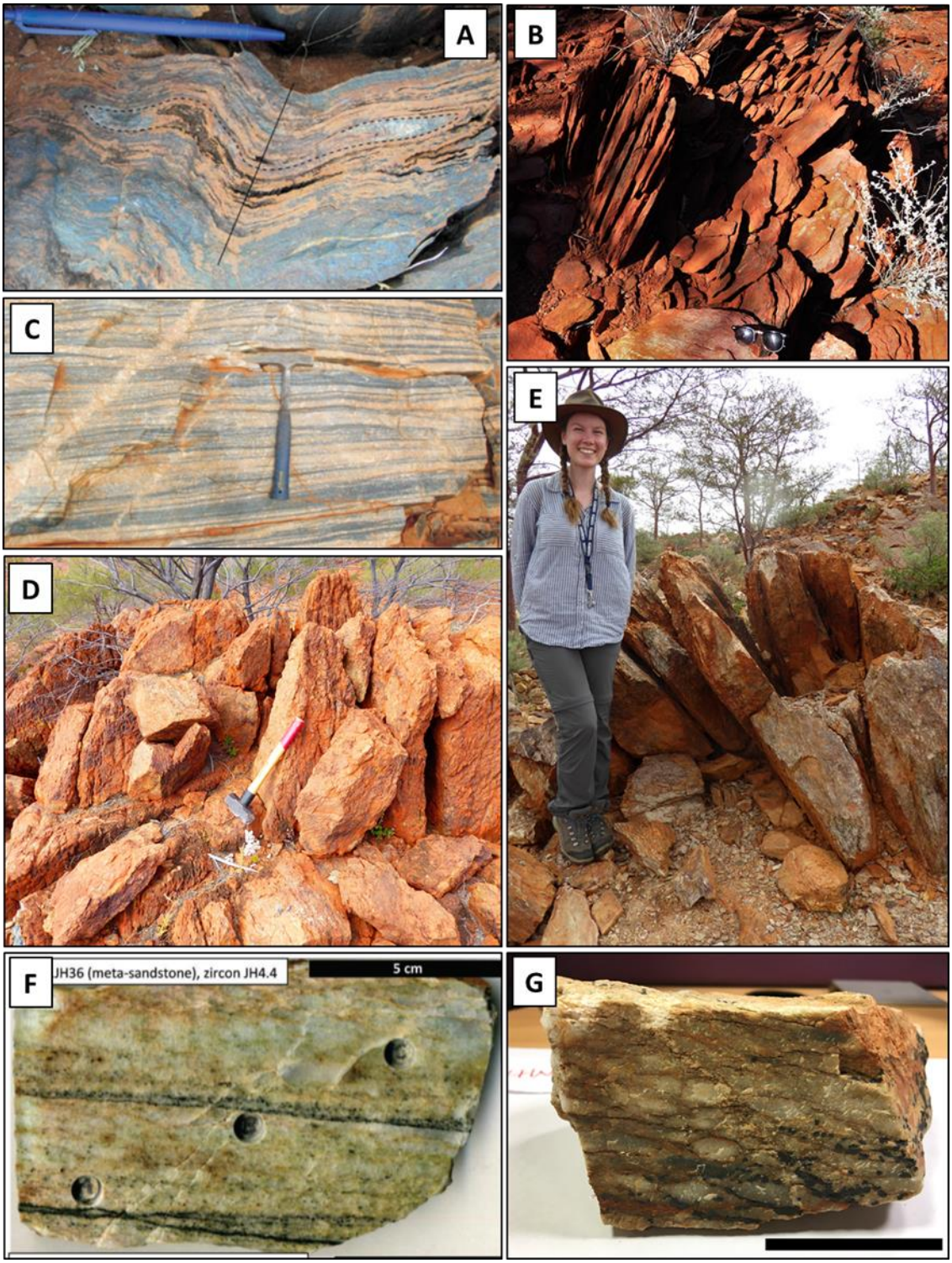

Figure 1.5: Jack Hills greenstone belt lithologies and examples of deformation. **A)** Recumbent folding (JH F_1) within association 1 BIF refolded into JH F_2 by JH D_2 event. Image from Spaggiari (2007). **B)** Heavily foliated (S_2) association 1 ultramafics within the NE of the belt. Note the variable strike and dip of the foliation. **C)** Black and white banded quartzites within association 1. Image from Spaggiari (2007). **D)** Less heavily foliated, but still heavily weathered, association 1 ultramafics from the SW of the belt. **E)** A very happy author at the W-74 site (Wilde et al., 2001) composed of association 3 metasediments. Steeply dipping, but variable, JH S_2 foliation still apparent. **F)** Chromite layers within association 3 metasandstone. Note the green colouration of this sample from the abundance of fuchsite. Image from Valley et al. (2015). **G)** Flattened and recrystallised quartzite cobbles within fuchsitic metaconglomerate from near the W-74 site of E. Scale bar is 5 cm.

1.3. Detrital zircons at Jack Hills and Mount Narryer

Mount Narryer and Jack Hills metasedimentary successions are geologically renowned as the only known places on Earth that host abundant fragments of Hadean crust. Jack Hills metaconglomerates have yielded the oldest known terrestrial zircon, a magmatically zoned grain with a concordant ^{207}Pb-^{206}Pb crystallisation age of 4374±6 Ma (Figure 1.7a; Compston and Pidgeon, 1986; Wilde et al, 2001; Valley et al, 2014). Mount Narryer quartzites yield detrital zircon up to ~4280 Ma (Froude et al, 1983; Pidgeon and Nemchin, 2006). These two sites therefore provide a unique window into the Hadean, and host zircon pre-dating the oldest known rock, the 4020 Ma Idiwhaa unit of the Acasta Gneiss (Reimink et al, 2014; 2016), by up to 350 million years. Zircons from these localities have therefore been intensely studied using a variety of geochemical and isotopic techniques to elucidate crustal formation and evolution within the Hadean and the Archean.

1.3.1. An introduction to zircon U-Pb geochronology

Zircon, $ZrSiO_4$ is a common accessory mineral within evolved magmas. Zircon holds title of the unsurpassed absolute geochronometer of crustal rocks, exploiting the three U/Th-Pb decay chain systems (^{238}U → ^{206}Pb $t_{1/2}$= 4470 My, ^{235}U → ^{207}Pb $t_{1/2}$= 700 My, ^{232}Th → ^{208}Pb $t_{1/2}$= 14 Gy). Parent nuclides U and Th strongly partition into zircon, while daughter product Pb remains highly incompatible. Pb within zircon is therefore almost wholly derived from radioactive decay (Schoene, 2014) with only minor or no correction required for "common Pb", or the initial Pb isotopic composition. Measurement of the sole stable Pb isotope ^{204}Pb (for common Pb correction), daughter nuclides ^{206}Pb, ^{207}Pb, ± ^{208}Pb, and radiogenic parent nuclides ^{235}U and ^{238}U enables the ^{206}Pb-^{238}Pb age and ^{207}Pb-^{235}U age of zircon to be determined. As ^{235}U/^{238}U is effectively consistent across terrestrial and most meteoritic samples (e.g. Hiess et al., 2012), the ^{207}Pb-^{206}Pb age can also be calculated by direct measurement of the ^{207}Pb/^{206}Pb isotopic composition of zircon (Gehrels, 2014; Schoene, 2014). The ^{207}Pb-^{206}Pb age is most typically used for older samples (>1200 Ma; Gehrels, 2014) owing to greater ingrowth of ^{206}Pb and ^{207}Pb, and larger variability of ^{207}Pb-^{235}U resulting in greater curvature of the concordia.

Critically, while isotope dilution (ID) thermal ionisation mass spectrometry (TIMS) measurements remain the highest precision method, typical concentrations of U at µg/g within zircons allows for in-situ analysis using microbeam techniques, such as secondary ion mass spectrometry (SIMS) and laser-ablation inductively coupled mass spectrometry (LA-ICP-MS). Thus, in-situ techniques enable the determination of the absolute age of zircons at a high spatial resolution, with ablation spots typically on the order of ~20 µm. This is critical, as zircon is not only resistant to physical and chemical abrasion but can survive and recrystallise, without diffusing U or Pb, during multiple cycles of magmatism

and/or metamorphism. Zircons, particularly ancient grains, may therefore retain billions of years of reprocessing within different domains of a single crystal (e.g. Hawkesworth and Kemp, 2006).

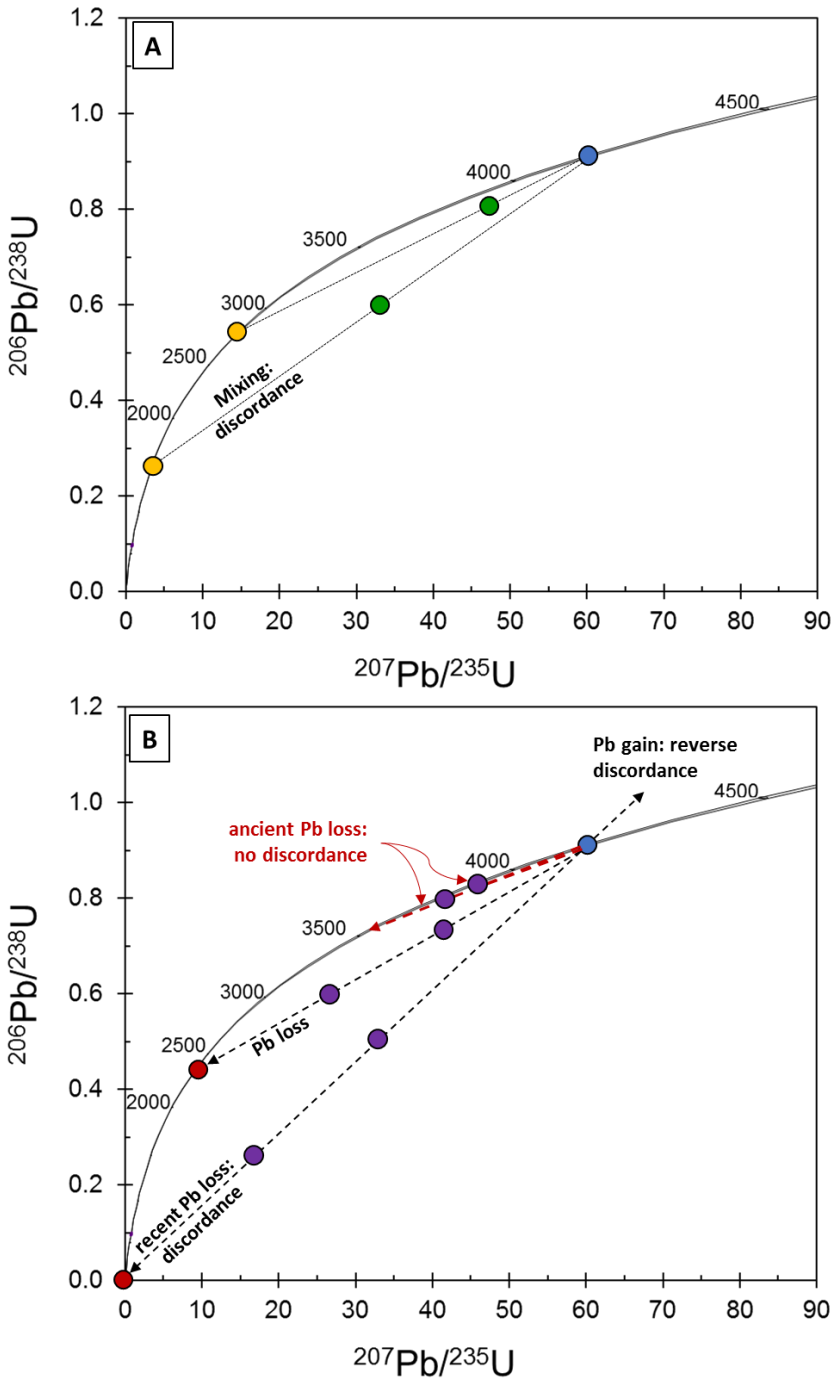

Figure 1.6: Examples of Wetherill concordia plot for U-Pb analyses and the challenges of zircon analysis. **A) Analytical discordance:** mixing between a ~4200 Ma concordant core (blue) and ~2700 Ma and ~1500 Ma concordant rims (yellow). Variable degrees of mixing during analysis result in discordant analyses (green). This is particularly problematic for TIMS measurements where the entire grain is dissolved but can be minimised during in-situ analysis by careful point placement. **B) Sample discordance**: due to Pb mobility within zircon. Recent Pb-loss (zero intercept) results in highly discordant grains. Younger events (e.g. at t= 2400 Ma within B) also induce significant discordance within zircon grains. However, ancient Pb loss (shown in red) results in arrays sub-parallel to the concordia and therefore concordant analyses. Pb gain may result in reversely discordant analyses, though Pb gain is observed far more rarely.

Furthermore, the use of two U-Pb decay systems means the concordance, or the agreement of derived ages between the different decay systems, can be measured. Concordant analyses, i.e. those that have not undergone open system behaviour, will sit on the concordia line on a Wetherill Concordia plot, where $^{207}Pb/^{235}U$ is plotted against $^{206}Pb/^{238}U$ (Figure 1.6). Discordance, or plotting off the line of concordance, may be achieved through multiple methods. This may firstly occur by mixing of two or more age domains during analysis (Figure 1.6a), which can be particularly problematic for bulk measurements. Secondly, discordance may result from Pb loss (normal discordance) or Pb gain (reverse discordance) (Figure 1.6b): this is discussed further in section 1.3.3 with relation to Hf isotopic composition. While the ^{207}Pb-^{206}Pb concordia age may be calculated by linearly regressing the analysis through 0, this becomes progressively inaccurate with increased discordance (Gehrels, 2014). Therefore, an arbitrary <10 % discordance parameter is often applied to analyses, particularly of detrital zircon (Gehrels, 2014; Vervoort and Kemp, 2016). However, grains that have undergone ancient Pb loss will fall sub-parallel to the concordia (Figure 1.6b), providing further challenges to the determination of the true crystallisation ages of ancient grains (Kemp et al., 2010; Vervoort and Kemp, 2016).

1.3.2. ^{207}Pb-^{206}Pb zircon age distributions

Mt Narryer detrital zircon U-Pb systematics

Detrital zircons have been sampled for U-Pb geochronology from all units of southern sector of the Mt Narryer supracrustal succession (Figure 1.3; Froude et al., 1983; Kinny et al., 1990; Crowley et al., 2005; Pidgeon and Nemchin, 2006; Nebel-Jacobsen et al., 2010). Zircons yield ^{207}Pb-^{206}Pb ages from 4281±11 Ma (Pidgeon and Nemchin, 2006) to 3280 Ma (Kinny et al., 1990), with distinct age distribution peaks at ~4200 Ma, from ~3700 Ma to 3600 Ma, and more minor peaks at ~3500 Ma and ~3300 Ma (Crowley et al., 2005; Pidgeon and Nemchin, 2006). These correlate with zircon age distributions of the Narryer Terrane and suggests that metasediments at Mt Narryer were derived from protoliths of granitic gneisses (Kemp et al., 2019).

Jack Hills detrital zircon U-Pb systematics

Detrital zircon at Jack Hills yield a broader range of ^{207}Pb-^{206}Pb ages than Mt Narryer, possessing concordant ^{207}Pb-^{206}Pb ages from 4376 Ma to ~3050 Ma (Figure 1.7 and Figure 1.8; e.g. Cavosie et al., 2004; Crowley et al, 2005; Nemchin et al., 2006; Holden et al, 2009; Valley et al., 2014 etc). Detrital zircons from the W-74 discovery site are dominantly aged between 3380 Ma to 3400 Ma, with this age distribution peak tailing towards 3600 Ma (Crowley et al., 2005; Holden et al., 2009; Wang and Wilde, 2018). Hadean zircons show apparent continual magmatic crystallisation between 4000 Ma and ~4380 Ma, though the highest abundance of Hadean grains are observed at 4000 Ma to ~4100

Ma (Holden et al., 2009; Whitehouse et al., 2017). Hadean zircons with ages above ~4300 Ma (Figure 1.7) are exceedingly rare, accounting for just ~0.03% of analyses within the Holden et al. (2009) dataset. Detrital zircons from Jack Hills lack the distinct ~3700 Ma to 3600 Ma age distribution peak observed at Mount Narryer (Crowley et al., 2005; Pidgeon and Nemchin, 2006), with very few zircons yielding ages between ~3600 Ma and ~3900 Ma (e.g. Crowley et al., 2005; Bell et al., 2014). However, age distributions vary across the Jack Hills belt, with ^{207}Pb-^{206}Pb age distribution peaks at ~3700 Ma reported in the NE of the belt (Crowley et al, 2005; Dunn et al., 2005), though detrital zircons were less abundant and poorer in quality than those observed at the W-74 site.

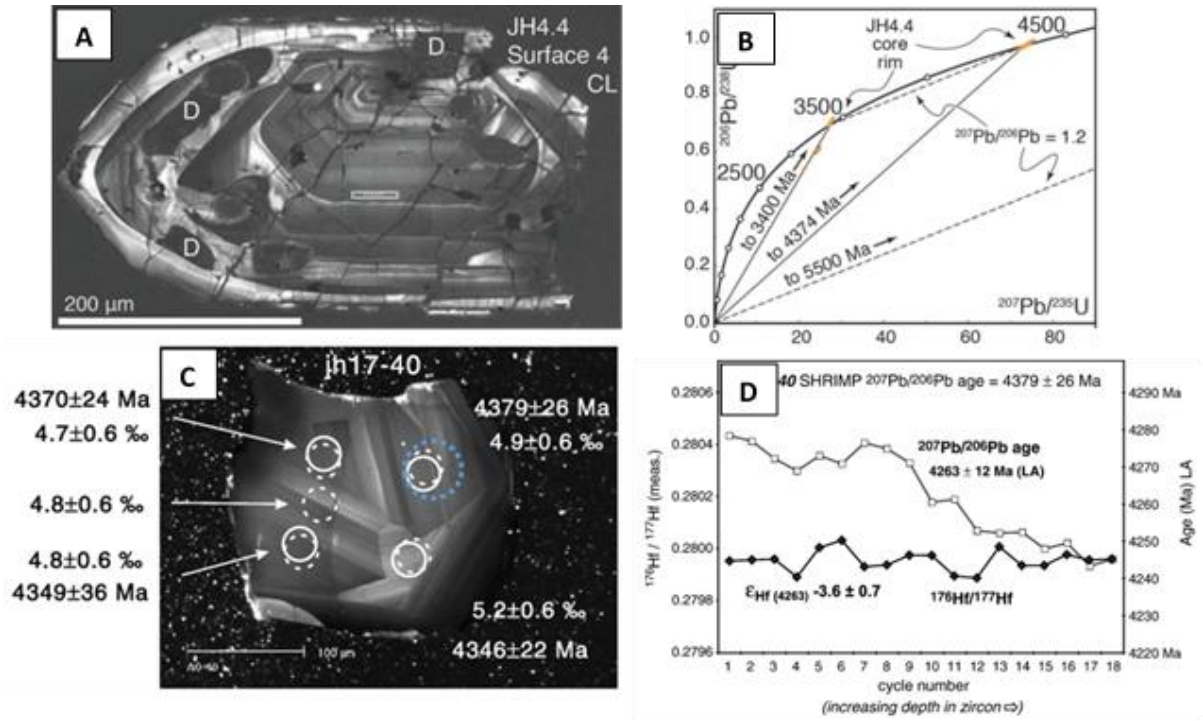

Figure 1.7: Two examples of >4350 Ma zircons found from the W-74 site within Jack Hills metaconglomerates. **A)** CL image of the fourth polished surface of JH4.4, a ~4370 Ma zircon derived from the metasandstone within Figure 1.6f, and **B)** An example Wetherill concordia plot from SIMS analysis of this zircon. Image and data modified from Valley et al. (2015). **C)** CL image of an uncracked, oscillatory zoned Hadean grain modified from Nemchin et al. (2006), with ^{207}Pb-^{206}Pb ages and oxygen isotopic composition. Corresponding Pb-Hf analysis shown in **D)** is from Kemp et al. (2010). Note the significantly younger ^{207}Pb-^{206}Pb age from LA-ICP-MS in comparison to SIMS data, highlighting the analytical challenges of such ancient grains. Hf pit position shown by blue dashed line.

Similar to detrital zircons found within the Mount Narryer supracrustal belt, zircon age distributions at Jack Hills are contemporaneous with the ages of the protoliths of the granitic gneisses within the Narryer Terrane (Cavosie et al., 2004; Crowley et al., 2005; Dunn et al., 2005; Wang and Wilde, 2018). The dominant age distribution peak at ~3380 Ma corresponds well with the age of the syenogranitic precursors of the Dugel gneiss (Kinny et al., 1988; Kinny and Nutman, 1990; Nutman et al., 1991).

More minor distribution peaks, particularly between 3400 Ma and 3500 Ma, indicate zircons of this age are derived from the Eurada gneiss (Nutman et al., 1991). The presence of 3600 Ma to ~3700 Ma within metasediments in the NE of Jack Hills (Crowley et al., 2005; Dunn et al., 2005) and at Mt Narryer (Crowley et al., 2005; Pidgeon and Nemchin, 2006) corresponds with the TTG protoliths of the Meeberrie gneiss. The scarcity of detrital zircons of this age at the W-74 site suggests the Meeberrie was not a major component within the source of the host metasediments. However, this may simply be a product of localisation within the sedimentary sources, despite the mature, quartz-rich nature of metasediments at the W-74 site. The origin of the 4000 Ma- 4100 Ma zircon age distribution peak is unknown, and thus far the source of these zircons has not been sampled within the Narryer Terrane, or indeed anywhere in the world.

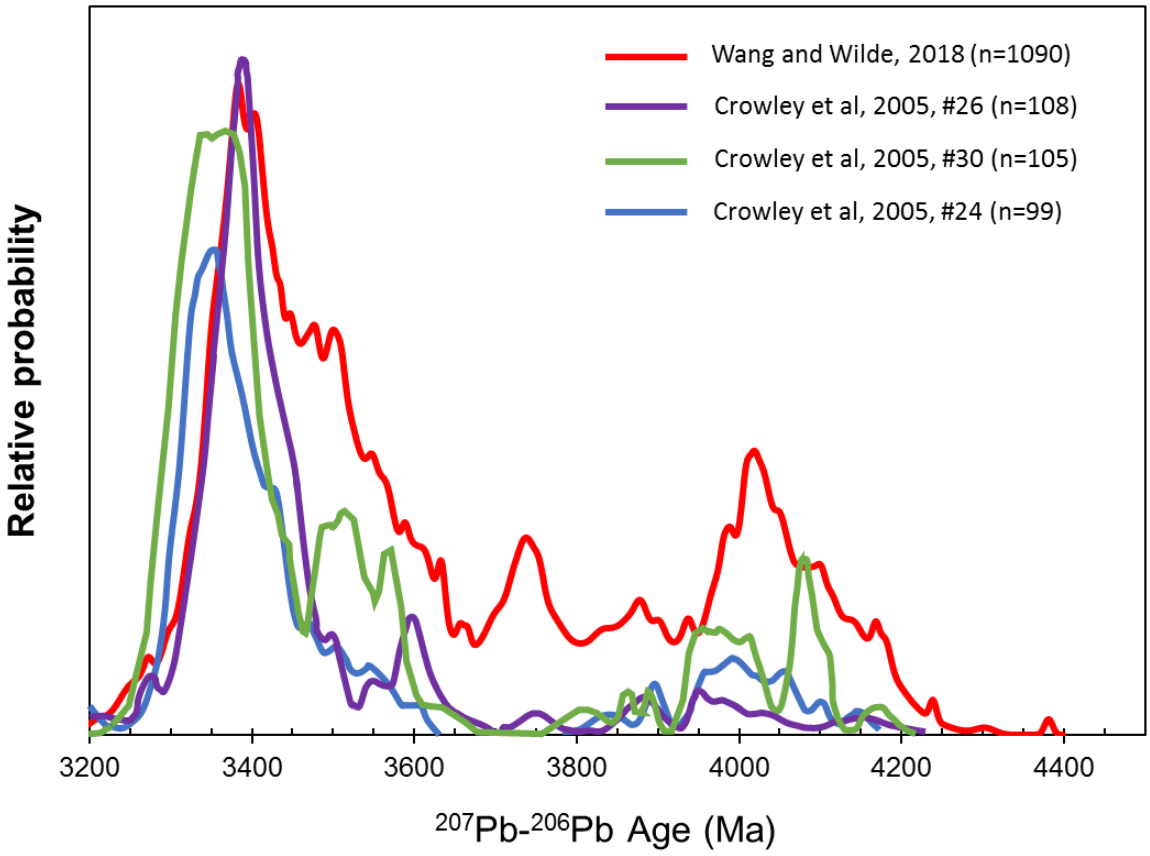

Figure 1.8: Typical ^{207}Pb-^{206}Pb age distributions for Jack Hills zircon. This is shown using probability density plots, which shows the likelihood of a random variable (zircon) to yield an age. Crowley et al. (2005) data only includes those from oscillatory zoned zircon, so is likely more indicative of Jack Hills distributions than Wang and Wilde (2018) due to the lower possibility of Pb mobility. The dominant peak at 3380-3400 Ma trails until ~3600 Ma, with more minor age distribution peaks also observed between 3400 Ma and 3600 Ma. There is a dearth of zircons between ~3650 Ma till ~3900 Ma. The Hadean age distribution peaks shown in the Wang and Wilde data are typical of Jack Hills zircon, with Hadean grains dominantly yielding ages between 4000 Ma and 4200 Ma, but particularly between 4000 Ma and 4100 Ma.

1.3.3. The Lutetium-Hafnium Decay System

Arguably the most powerful tool in the study of crustal evolution is found in another long-lived decay system: Lutetium-Hafnium, where ^{176}Lu decays to ^{176}Hf via β^- decay, with a half-life of 37.1 Gyr (Scherer et al., 2001; Soderlund et al., 2004). This system is a powerful crustal tracer (e.g. Figure 1.9), and it can be rooted in a strong temporal framework using a previously determined U-Pb age derived from the same domain or bulk zircon. Owing to limited variability of $^{176}Hf/^{177}Hf$ between natural samples, time-integrated $^{176}Hf/^{177}Hf$ is commonly expressed in parts per ten thousand, using the epsilon notation:

$$\varepsilon Hf(t)_{CHUR} = ((^{176}Hf/^{177}Hf(t)_{SAMPLE}/(^{176}Hf/^{177}Hf(t)_{CHUR})-1) \times 10{,}000 \quad \textbf{(1)}$$

CHUR represents the Lu and Hf composition of the chondritic uniform reservoir at the time of zircon crystallisation (Bouvier et al., 2008). The use of the Lu-Hf system is possible due to the variable behaviour of parent and daughter nuclides during mantle partial melting. Lu has a greater compatibility than Hf, particularly in the presence of garnet, leaving melt residue more enriched in Lu than the resultant melt (e.g. Kemp and Hawkesworth, 2014). The residue, termed depleted mantle (DM), has elevated $^{176}Lu/^{177}Hf$ in comparison to CHUR and will subsequently evolve to an increasingly radiogenic and superchondritic Hf isotopic composition (Figure 1.9). The partial melt, with significantly lower $^{176}Lu/^{177}Hf$, undergoes less ^{176}Hf ingrowth than CHUR, and thus develops to unradiogenic and progressively subchondritic Hf compositions. The slope of this evolution is controlled by $^{176}Lu/^{177}Hf$ ratio, which, if known, can be used to calculate the model age of crustal extraction from either a chondritic mantle (T_{CH}) or DM (T_{DM}) reservoir. The $^{176}Lu/^{177}Hf$ ratio of crust is also directly linked to its composition (cf. Boehnke et al., 2018). Mafic rocks, the product of greater amounts of partial melt or lower degress of fractionatal crystallisation, yield $^{176}Lu/^{177}Hf$ values of ≥0.02 (Kemp et al., 2010; Vervoort and Kemp, 2016). Felsic crust, derived from extensive fractional crystallisation of mantle-derived melts (e.g. juvenile crust) or reworking of mafic sources (e.g. crustal melts), possesses lower $^{176}Lu/^{177}Hf$ values. While a $^{176}Lu/^{177}Hf$ of 0.015 is used for bulk continental crust (e.g. Griffin et al., 2002), Archean TTG typically yield $^{176}Lu/^{177}Hf$ of ≤0.01 (Vervoort and Patchet, 1998). Felsic crust consequently evolves along a more subchondritic evolution path than mafic crust (Figure 1.9).

Within zircon, Hf is highly compatible, partitioning alongside its geochemical twin Zr (Hawkesworth and Kemp, 2006). While Lu is the most compatible of the rare earth elements (REE) within zircon (e.g. Cavosie et al., 2006), it is far more incompatible than Hf, which is typically present at wt.% within zircons (Kemp and Hawkesworth, 2014). This dichotomy of partitioning behaviour results in near negligible $^{176}Lu/^{177}Hf$ (Hawkesworth and Kemp, 2006), which inhibits subsequent radiogenic ingrowth of ^{176}Hf. Furthermore, diffusion of Hf within zircon is extremely sluggish (Cherniak et al., 1997), and so the ^{176}Lu-corrected $^{176}Hf/^{177}Hf$ ratio represents the isotopic composition of the parental melt at the

time of crystallisation. As diffusion of U and Pb in zircon is also limited, multiple generations of magmatic growth with distinct $^{176}Hf/^{177}Hf$ values may be analysed within a single crystal.

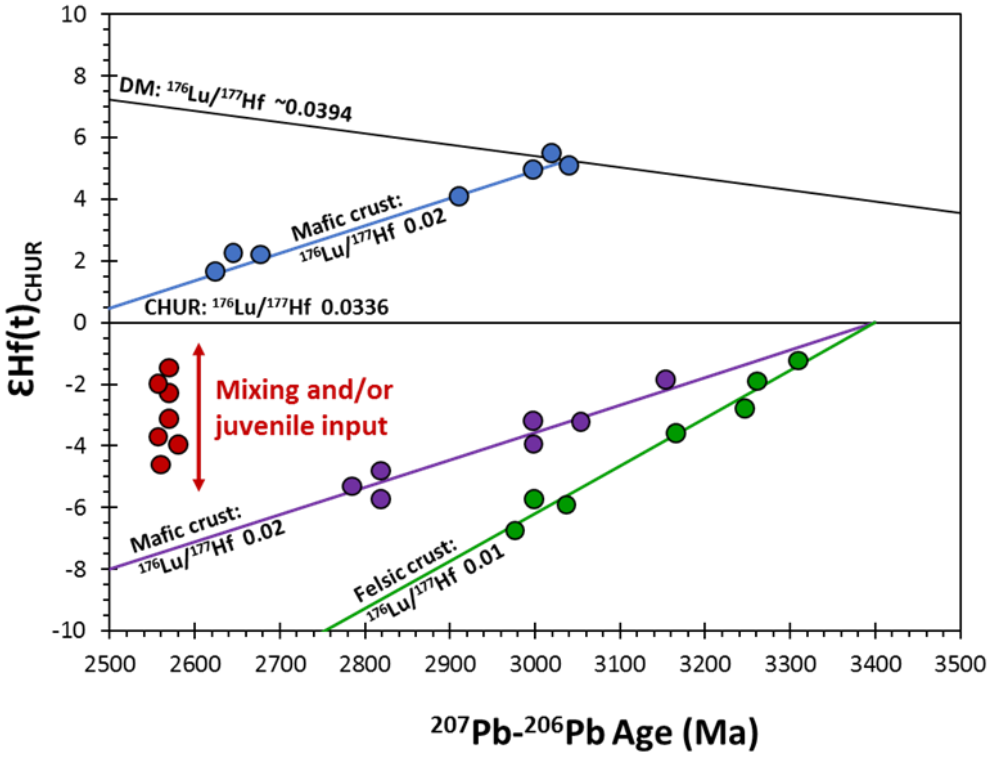

Figure 1.9: An example of zircon Pb-Hf arrays. Arrays denote the evolution paths of felsic crust ($^{176}Lu/^{177}Hf$ 0.01; green) and mafic crust ($^{176}Lu/^{177}Hf$ ~0.02; purple) extracted from chondritic mantle at 3400 Ma, and mafic crust extracted from DM (blue) at 3020 Ma. Potentially mixing between two sources, one distinctly more juvenile, is shown by red analyses that plot along a vertical mixing array. However, this mixing array highlights the complexities of Pb-Hf analyses, as the sources contributing to this mixing array cannot be determined by Pb-Hf analyses alone

Coupled Pb-Hf analysis within zircon is heavily used in the early Earth to trace the contribution of Hadean and juvenile crust in the formation of Archean TTGs (e.g. Canada: Reimink et al., 2016; Bauer et al., 2017, Vezinet et al., 2018, Greenland: Fisher and Vervoort, 2018, Pilbara: Petersson et al., 2019, Singhbhum: Chaudhuri et al., 2018) and detrital zircons (e.g. Zimbabwe: Bolhar et al., 2017, Pilbara: Kemp et al., 2015, Yilgarn: Mole et al., 2014; Kemp et al., 2019). Zircons, however, carry the caveat that they do not represent the $^{176}Lu/^{177}Hf$ ratio of their protolith. This therefore requires, in all samples bar those with juvenile compositions, a two-stage model calculation to extrapolate back to a mantle curve. This is done by inherent assumptions of the composition and the $^{176}Lu/^{177}Hf$ ratio of the protolith, which is particularly problematic within the detrital record where the $^{176}Lu/^{177}Hf$ of the protolith is unknown (Vervoort and Kemp, 2016). Where variable zircon ages are present, however, an array within ^{207}Pb-^{206}Pb vs $^{176}Hf/^{177}Hf$ space may be present (Figure 1.9). The slope of this array

would therefore likely represent the $^{176}Lu/^{177}Hf$ of parental crust, enabling both the broad composition and time of mantle extraction for the protolith to be resolved.

Two other large caveats are implicit in the determination of $\varepsilon Hf(t)_{CHUR}$ and model ages of zircon. The first is that the U-Pb age derived is the true crystallisation age of the zircon analysed. While U is considered largely immobile within zircon (Cherniak et al., 1997), diffusion of Pb is well documented (e.g. Vervoort and Kemp, 2016). Diffusive Pb loss or migration into Pb nano-clusters may be caused by high temperature processes such as metamorphism (Valley et al., 2014; Ge et al., 2018), or low temperature processes such as weathering (Schoene, 2010), the latter of which results in a zero-age intercept (Figure 1.6b). While recent Pb loss may not heavily impact ^{207}Pb-^{206}Pb ages, and therefore the initial Hf isotopic compositions subsequently determined, ancient Pb loss provides greater challenges. Owing to low $^{176}Lu/^{177}Hf$ in comparison to CHUR, zircon are very sensitive to incorrect age assignments, and ancient Pb loss has been shown to produce dramatic shifts in $\varepsilon Hf(t)_{CHUR}$ (Vervoort and Kemp, 2016), resulting in younger model ages or artificially steep $\varepsilon Hf(t)_{CHUR}$ vs. ^{207}Pb-^{206}Pb age arrays. The effects of ancient Pb loss are hard to constrain as Pb loss falls sub-parallel to the concordia, resulting in grains with apparently concordant ages (Figure 1.6b). Further to this, while these processes typically produce younger U-Pb ages as a product of Pb-loss, spuriously old, but, critically, concordant, ^{207}Pb-^{206}Pb age domains for zircons have also been reported (e.g. Ge et al., 2018). Incorrect age assignment due to ancient Pb loss within Hadean and Archean zircon may therefore result in geologically meaningless information on the protolith of the analysed grain.

The second caveat is that $\varepsilon Hf(t)_{CHUR}$ compositions may reflect mixed sources. Firstly this may be geological, with the incorporation of mixed sources with different crustal residence times resulting in mixed $^{176}Hf/^{177}Hf$ which do not yield meaningful 2-stage ages (Kemp and Hawkesworth, 2014; Vervoort and Kemp, 2016). Such events may produce mixing arrays on plots of $\varepsilon Hf(t)_{CHUR}$ vs age (Figure 1.9), but can be discrete, and therefore produce spurious zircon T_{DM}. Secondly, this may be analytical due to sampling of different growth domains within a single zircon. Ancient zircons are particularly challenging for mixed analyses: individual zircons may have undergone multiple magmatic recycling events or numerous phases of ancient Pb loss (Valley et al., 2006; Vervoort and Kemp, 2016), resulting in complex intra-grain geochronology. While this may be partially circumnavigated by careful point selection, sampling of mixed domains has been shown to produce significantly spurious data (e.g. at Jack Hills; Harrison et al., 2005; 2008; Kemp et al., 2010) in isotope-time arrays.

1.3.4. The two Jack Hills hypotheses: coupled Pb-Hf and other geochemical tools

Coupled Pb-Hf measurements have been applied to both Hadean and Archean zircon from Jack Hills and Mt Narryer (Amelin et al, 1999; Harrison et al, 2005; 2008; Blichert-Toft and Albarède, 2008;

Nebel-Jacobsen et al, 2010; Kemp et al, 2010; Bell et al, 2011; 2014; Wang and Wilde, 2018). >3800 Ma zircon display a broadly coherent array that crosses CHUR within ~100 Myr of accretion, with no evidence of juvenile mantle input until the appearance of zircon with more chondritic compositions from 3800 Ma (Figure 1.10). Previously reported superchondritic $\varepsilon Hf(t)_{CHUR}$ values initially interpreted to represent a complementary depleted reservoir (Harrison et al, 2005; Blichert-Toft and Albarède, 2008) are likely the result of incorrect age corrections from sampling of younger overgrowths (Kemp et al, 2010), and have not been replicated by other studies. The scattered, but broadly linear Pb-Hf array shows zircon was derived from reworking of an enriched (Hf>Lu) protolith that was largely homogeneous in both $^{176}Lu/^{177}Hf$ ratio and composition for ≥~400 My (e.g. Kemp et al., 2010).

However, the composition and longevity of the protolith from which zircon formed is intensely debated. Numerous authors suggest Hadean and Archean zircon plot along steep arrays (Figure 1.10a), indicative of crystallisation from reworking of a felsic protolith ($^{176}Lu/^{177}Hf$ of ≤0.01) (Harrison et al, 2005; 2008; Blichert-Toft and Albarède, 2008; Nebel-Jacobsen et al., 2010; Bell et al, 2011; 2014). Felsic crust was formed during three generation events; at ~4500-4400, ~4100 and ~3800 Ma (Bell et al, 2014). Importantly, this hypothesis requires that ~4500 Ma protocrust has no contribution to zircon Hf compositions after ~3800 Ma, and thus was destroyed by the end of the Hadean. It is postulated that, due to contemporaneous juvenile input at this time (Nebel-Jacobsen et al, 2010; Fletcher et al, 1988; Kinny et al, 1988), this change tracks the loss of Hadean crust at destructive plate margins (Bell et al, 2014). Following this, these crustal arrays are extensively used to argue for the early, voluminous formation of continental crust, and the operation of plate tectonics within the Hadean and Archean (Harrison et al., 2017).

Further indications that Jack Hills zircons crystallised from felsic melts with a strong continental affinity has been suggested from multiple lines of evidence. Zircons yield unaltered (Cavosie et al, 2006; Trail et al, 2007), fractionated REE patterns with large positive Ce and negative Eu anomalies typical of zircon from continental crust (Maas et al, 1992; Peck et al, 2001; Cavosie et al., 2006; Trail et al., 2007; 2011). U/Yb vs. Y ratios of zircons fit well with those derived from modern, continental granitoids (Grimes et al, 2007; Harrison, 2009). Ti-in-zircon thermometry demonstrates that zircons crystallised at ~700 °C, analogous to water-saturated, minimum-melt granitoids (Watson and Harrison, 2005; Harrison and Schmitt, 2008; Harrison et al, 2008). However, Ti-in-zircon thermometry at Jack Hills relies on the assumption that rutile inclusions are primary, which is debated (Rasmussen et al, 2011; Cavosie et al., 2019), and that zircons represent liquidus conditions. Zircon saturation is only induced in zircon-infertile TTG melts during late-stage cooling via fractional crystallisation (Glikson, 2006; Nutman, 2006), and so Ti-in-zircon temperatures should be interpreted with care.

Inclusions assemblages within zircon are dominated by quartz and muscovite (Figure 1.11), typical of peraluminous, dominantly S-type granitoids (Hopkins et 2008; 2010; 2012; Bell et al, 2015b). The application of muscovite geobarometry (based on Si^{4+} concentration) of inclusions were used to argue muscovites possessed a high phengite component, and therefore crystallised at pressures of > 4kbar (Hopkins et al, 2008; 2010; 2012). Subsequent application of muscovite geobarometry alongside Ti-in-zircon temperatures produces a crustal geotherm of ≤60 °C/km, far lower than predicted Hadean temperatures (Hopkins et al., 2008; 2010). This, coupled with a purported high proportion of sediment within the source of zircons, has been used to propose that Jack Hills zircons represent the eroded remnants of reworked and volumetrically significant continental crust derived from subduction zones (e.g. Harrison, 2009; 2017).

However, this geodynamic interpretation of Jack Hills zircons is controversial. Two studies have proposed zircons form shallower Pb-Hf arrays (Figure 1.10b), akin to repeated reworking of enriched mafic crust ($^{176}Lu/^{177}Hf$ of ≥0.02) that possessed a narrow compositional range and was extracted from the mantle at ~4500-4400 Ma and ~4100 Ma (Amelin et al, 1999; Kemp et al, 2010). Kemp et al (2010) further argued that steep crustal evolution arrays, interpreted as reworking of ~4500 Ma felsic crust, are a consequence of Pb-loss within Hadean zircons (Figure 1.10b; *cf.* Bell et al, 2014). Notably, these authors used strict criteria to create a heavily screened dataset, rejecting zircons that did not display magmatic (oscillatory) zoning, concordant U/Pb ages, Th/U ratios of ≥0.3, and $\delta^{18}O$ of >4.5‰. ~4500-4400 Ma mafic crust is further inferred to be the source of some ~3380 Ma detrital zircon and ~2700 Ma granitoids within the wider Narryer terrane (Kemp et al, 2010). A long-lived mafic protocrust is not consistent with early plate tectonics, where it would be rapidly destroyed or recycled at convergent plate margins. Instead, this is consistent with the presence of an enriched, mafic protocrust, perhaps from solidification of a terrestrial magma ocean, that was repeatedly recycled throughout the Hadean and Archean. This invokes a tectonic setting more akin to a stagnant lid regime, where voluminous mantle extraction events cause reworking of an altered, mafic protocrust to form TTG-like partial melts (Kamber et al, 2005; Kemp et al, 2010; Nebel et al, 2014; Johnson et al, 2017; O'Neil and Carlson, 2017).

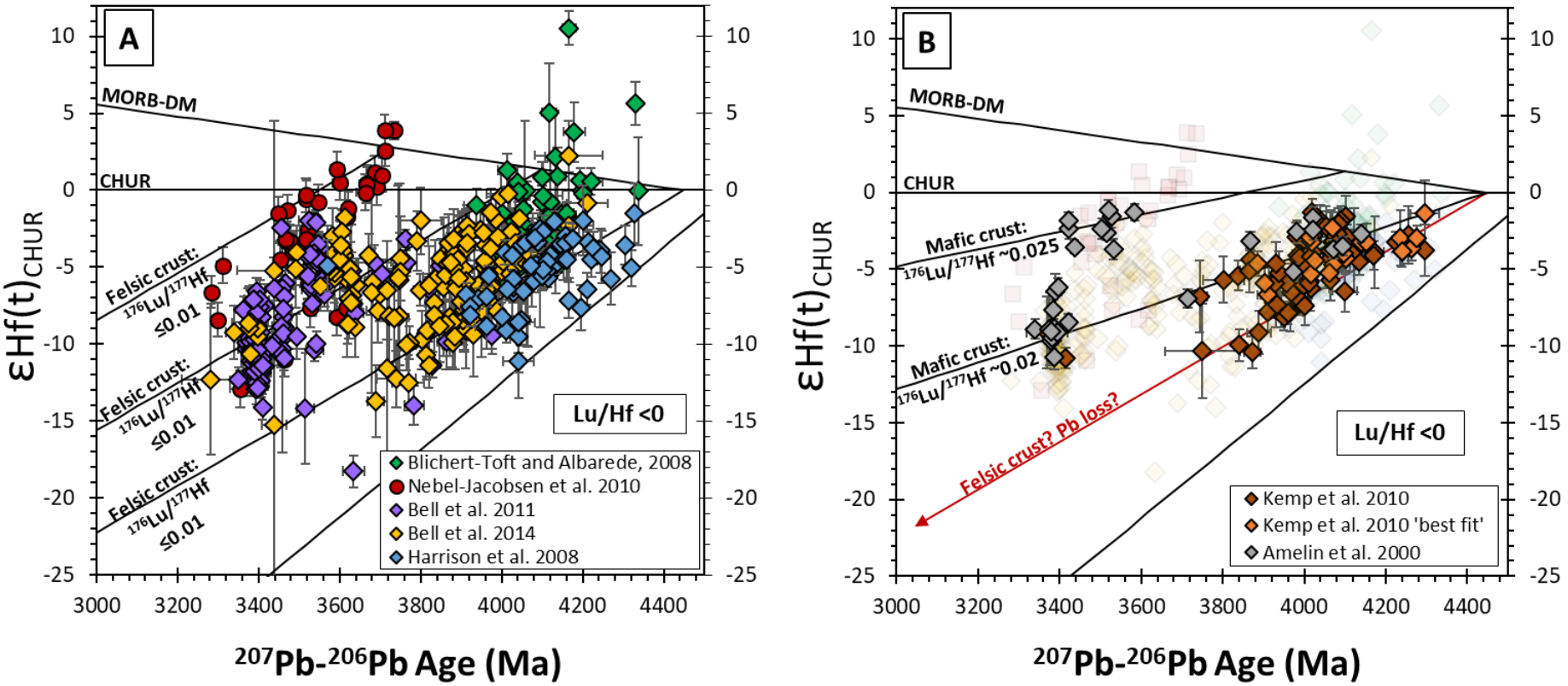

Figure 1.10: Zircon Pb-Hf data derived from Jack Hills. **A)** Data from those that argue for recycling of felsic protoliths ($^{176}Lu/^{177}Hf$ ≤0.01). Harrison et al. (2005) excluded. Nebel-Jacobsen et al. (2010) data points are from Mount Narryer but were used to define crustal evolution arrays by Bell et al. (2011) and (2014). Zircons are derived from reworking and mixing of felsic crust extracted from CHUR at ~4400 Ma, and DM at ~4200 Ma and 3730 Ma. While most points possess subchondritic Hf compositions, some Hadean zircons from Blichert-Toft and Albarede (2008) and Bell et al. (2014) yield superchondritic values. **B)** Data from those that argue for recycling of mafic protoliths ($^{176}Lu/^{177}Hf$ ~0.02). The Kemp et al. (2010) 'best fit' are zircons used to calculate the regression of a ~4450 Ma protolith, and have been stringently filtered for oscillatory zoning, U/Th ratios and oxygen isotopic composition. Zircons plot along a simpler evolution array, with mafic protoliths extracted from CHUR at ~4400 Ma and DM at ~4100 Ma. Kemp et al. (2010) also postulated that Hadean zircons that plot along felsic crustal evolution arrays are instead indicative of ancient Pb loss

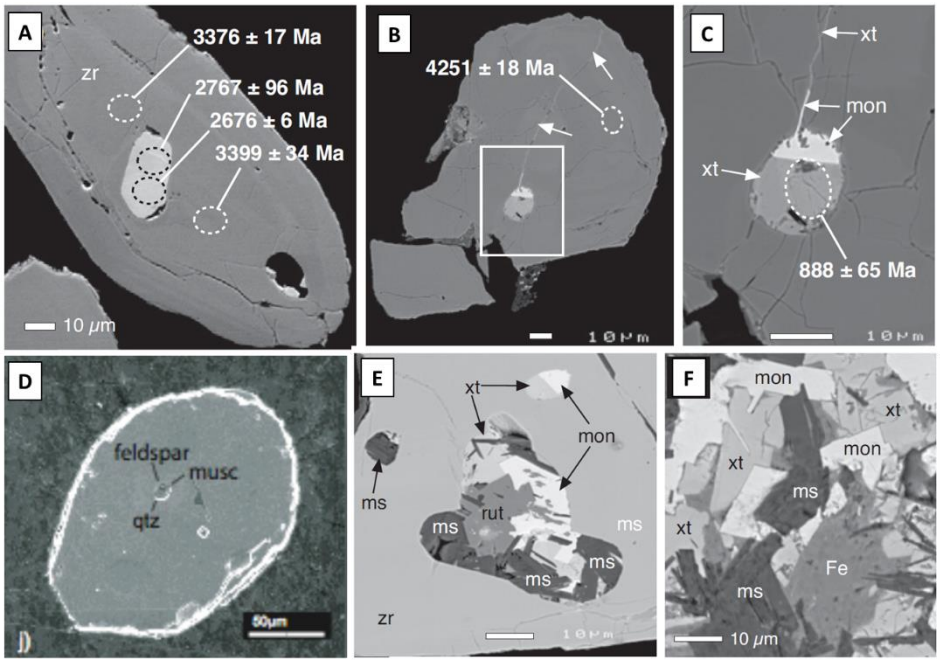

Figure 1.11: BSE images of inclusion assemblages of Jack Hills zircon. **A)** ~2650 Ma apparently isolated monazite inclusion within ~3400 Ma zircon. **B) and C)** Clearly secondary monazite and xenotime polyphase inclusion formed from fluids infiltrating racked Hadean host at ~850 Ma. **D)** Isolated inclusion assemblages of quartz, feldspar and muscovite within a ~4000 Ma zircon. **E)** polyphase inclusions within Jack Hills zircon of xenotime, monazite, rutile and muscovite. Texturally very similar to similar assemblages within the matrix of W-74 metaconglomerates, as shown in **F).** Images A-C and E-F are from Rasmussen et al. (2011), while image D is from Hopkins et al. (2010), who unfortunately did not present high resolution images within their contribution.

Though this hypothesis explains the granitoid nature of zircon REEs and Ti-in-zircon temperatures, it cannot reconcile peraluminous inclusion assemblages (Hopkins et al., 2008; 2010; 2012; Bell et al, 2015b). However, Rasmussen et al (2011) showed many inclusions in Jack Hills zircons are secondary in nature: monazite and xenotime inclusions cluster at metamorphic ^{207}Pb-^{206}Pb ages of ~2650 Ma and ~800 Ma (Figure 1.11). Monazite and xenotime of these ages are found within the matrix of the host metaconglomerates (Iizuka et al, 2010; Rasmussen et al, 2010), which is itself dominated by quartz and metamorphic muscovite (Spaggiari, 2007). Furthermore, the small size (average ~4 μm) of muscovite inclusions studied by Hopkins et al. (2008) mean they are liable to secondary fluorescence from surrounding zircon during EPMA analysis, casting doubt on this study's interpretation (Rasmussen et al., 2011; Cavosie et al., 2019). Rasmussen et al (2011) therefore suggested that quartz, muscovite, rutile, monazite and xenotime inclusions within zircon (Figure 1.11) are largely secondary in origin, likely replacing primary apatite, and so precluding a peraluminous origin of Jack Hills zircon. The absence of peraluminous zircon at Jack Hills has also been recently demonstrated by P contents matching those of I-type granitoids (Burnham and Berry, 2017), and metaluminous Al contents of all but one ≥3700 Ma zircon (Trail et al, 2017). The latter study suggested a peraluminous origin of some

Palaeoarchean zircons but did not replicate these data in a study of Si isotopes on the same zircons (Trail et al., 2018).

1.3.5. Concluding remarks

This chapter details only a minor component of the literature undertaken on these fascinating zircons. For example, early studies of the $\delta^{18}O_{SMOW}$ composition of zircon observed values from 5.4 to 15, postulated to represent significant continental weathering, incorporation of sediments with elevated $\delta^{18}O_{SMOW}$ into the source of zircons, and therefore an extensive hydrosphere within the Hadean (Mojzsis et al., 2001). Subsequent work, however, found most concordant zircons yield $\delta^{18}O_{SMOW}$ compositions of 5.4 to 7.6 (Peck et al., 2001; Cavosie et al., 2005; Bell et al., 2011). These values are still elevated in comparison to mantle values of 5.3±0.6 (2sd; e.g. Cavosie et al., 2005) requiring interaction of zircon protoliths with liquid water, and unexpected insight into the Hadean Earth. Also not discussed are other avenues of research including lithium isotopes (e.g. Ushikubo et al., 2008), purportedly primary graphitic inclusions (Bell et al., 2015a; cf. Menneken et al., 2017), the rather intensely debated palaeomagnetic qualities of zircons (Weiss et al., 2018 and references therein), and the search for shock deformation (Cox et al., 2017).

It is likely that, due to the paucity of Hadean zircons elsewhere, the Jack Hills site will remain heavily studied for decades to come, and the debate as to their formation and evolution has looks set to continue until a definitive line of evidence is found. As the susceptibility of zircon to ancient Pb loss can be partially circumnavigated by careful sample selection, data derived from these definitively magmatic, 'least altered' grains remain the benchmark for studies on Jack Hills zircon. Further analysis at Jack Hills should therefore focus on the most pristine grains (e.g. Vervoort and Kemp, 2016; Whitehouse et al., 2017) in order to gain further understanding of crustal evolution within the Narryer terrane, and the wider Archean and Hadean Earth. However, the detrital nature of Jack Hills zircon means that until Hadean crust is found within the terrane, arguments as to their formation may not be conclusively resolved.

1.4. Other phases within Jack Hills sediments

1.4.1. Monazite and xenotime

The ages and geochemistry of Jack Hills and Mt Narryer monazites were reported in two papers published in 2010. Iizuka et al. (2010) recorded the presence of monazite at Mount Narryer, and a smaller population from Jack Hills, while Rasmussen et al. (2010), in a higher resolution study, concentrated on monazites from numerous localities and lithologies at Jack Hills. Like zircon, monazite

contains abundant U and Th whilst largely excluding Pb, making it a viable mineral for isotopic and absolute U-Th-Pb dating. The U-Th-Pb closure temperature within monazite is 900 °C, making it much less liable to metamorphic Pb loss than zircon (Iizuka et al., 2010). However, monazite also crystallises during low grade (~greenschist) to granulite facies metamorphism (Iizuka et al., 2010; Rasmussen et al., 2010). Despite this, primary monazite has been shown to be stable during regional metamorphism in rocks with low concentrations of Ca, particularly within metasediments (Iizuka et al., 2010 and references therein).

Iizuka et al. (2010) observed that Jack Hills metaconglomerates host predominantly metamorphic monazites that formed at ~2700 Ma, with rarer examples of >3000 Ma detrital grains. Rasmussen et al. (2010) observed a wider range of monazite ages, from 3259±5 Ma to ~800 Ma. Similarly, they found that metamorphic ages peak at ~2650 Ma, in line with craton-wide metamorphism and granitoid intrusion (Kemp et al., 2019). Unlike Iizuka et al. (2010), Rasmussen et al. (2010) found that a large proportion of monazites yielded ages of ~1800 Ma, which is the purported age of the main foliation trend at Jack Hills (Spaggiari, 2007; 2008; Rasmussen et al., 2010). The ~2650 Ma age of metamorphic monazites therefore defines the younger depositional age of unit 3 metasediments at the W-74 site (Rasmussen et al., 2010; Cavosie et al., 2019). Interestingly, these authors also observed ~3080 Ma metamorphic monazite enclosed in magnetite within association 1 BIF, indicating a minimum age of association 1 of ~3100 Ma. Detrital monazites (>3000 Ma) are also observed at Jack Hills and are thought to have survived due to the comparatively low metamorphic grade of the belt (Iizuka et al., 2010; Rasmussen et al., 2010).

Limited data exists for xenotime within Jack Hills metasediments, with Rasmussen et al. (2010) discussing their provenance alongside monazites. They found that the xenotime population was dominantly metamorphic, with samples yielding similar ages to monazite; late Archean (~2650 Ma), Neoproterozoic (~800 Ma) ages, and a ~1800 Ma component at Mt Hale. However, all localities sampled within this study also yielded detrital grains of xenotime, with most ages grouping around ~3100 Ma. Eranondoo Hill yields a slightly older detrital population, with ages up to 3266±3 Ma. However, xenotime, like monazite, yields more information on the metamorphic history of the Jack Hills greenstone belt than the broader crustal evolution of the Narryer Terrane.

1.4.2. Rutile

In an abstract, Harrison et al. (2007) reported ^{207}Pb-^{206}Pb ages and Zr-in-rutile thermometry derived temperatures of rutiles within Jack Hills metasediments. Harrison et al. (2007) found rutiles yielded an average ^{207}Pb-^{206}Pb age of 2300±200 Ma, with a distinct age peak at 2500 Ma. This suggests rutile were detrital and subsequently reset by late Archean metamorphism, or are metamorphic in origin. Rutiles

yield distinctly younger ^{207}Pb-^{206}Pb age distribution peaks (~2500 Ma) than monazite and xenotime (~2700 Ma to ~2650 Ma). This may be a consequence of the lower U-Pb closure temperature (typically 400 °C to 600 °C) within rutile (Harrison et al., 2007), shedding light on the cooling history of the belt after potential peak metamorphism at ca. 2650 Ma (e.g. Fletcher et al., 1997).

1.4.3. Chromite

The ubiquitous presence of chromites within Jack Hills metasediments is highlighted by the presence of fuchsite (Cr-muscovite) and heavy mineral layers within many quartzites (Figure 1.5f). However, despite the concerted interest in Jack Hills zircons, chromites have remained largely unstudied. In an abstract, Cavosie et al (2002) presented XRF and EPMA data for chromites from two transects of Jack Hills, with a western transect including the 'discovery site' W-74, and an eastern transect sampling mature clastics 0.9km to the east (Cavosie et al, 2004). They observed two populations of compositionally homogeneous chromite grains; one euhedral, indicating this population had not undergone significant sedimentary transport and one well rounded, suggesting a source more distal from the Jack Hills. Both populations contain elevated, though variable, ZnO and MnO. This was attributed by the authors to a source within a mineralised greenstone belt, analogous to high ZnO chromites reported by Groves et al (1977). Dare et al (2016) also studied the chemical properties of chromites within quartzite pebbles (Figure 1.12) ~1 km away from the W-74 site. They suggested that low MgO (<1 wt.%) precluded a komatiitic source, as such high degree mantle melts should be enriched in MgO. They further inferred that detrital chromites from Jack Hills are derived from a layered intrusion, though they noted that the variable rounding present means there must be multiple sources (Dare et al, 2016).

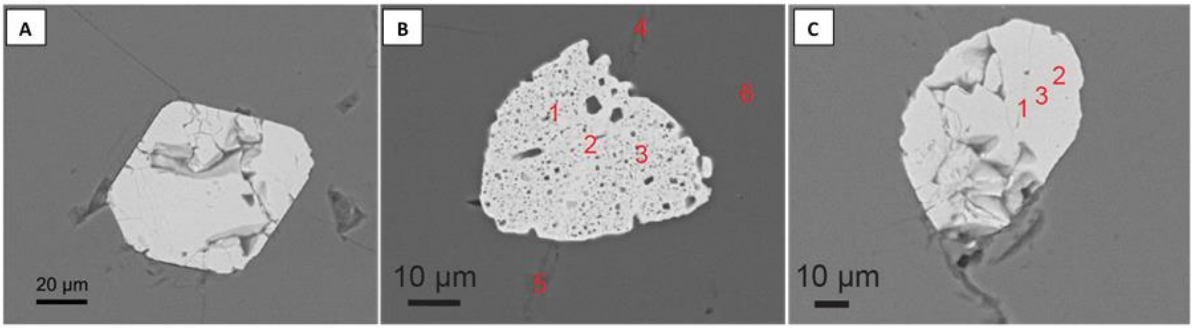

Figure 1.12: Detrital chromites from Dare et al. (2016). **A)** Euhedral example within quartzite cobble. **B)** Modified chromite within quartzite cobble showing an extensive spongy texture. **C)** More rounded(?) and heavily cracked chromite within quartzite cobble. All BSE images, red numbers are EPMA(?) analysis sites from Dare et al. (2016).

Also in an abstract, Valley et al (2005) reported the Re-Os isotopic composition of the same populations of detrital chromite as described by Cavosie et al (2002). They derived $^{187}Re/^{188}Os$ ratios of 0.0060 to 0.517 and unradiogenic $^{187}Os/^{188}Os$ ratios of 0.1057 to 0.1081 from ~50 mg aliquots of

unleached chromite. These data correspond to Re-Os model ages (TMAs) of 3500 Ma to 3200 Ma (Valley et al., 2005) indicative of mantle extraction at 3400 Ma to 3500 Ma (S. Shirey pers. com. In Dare et al., 2016). However, more detailed documentation of these interesting results has not been published. Furthermore, the elevated ZnO and MnO, coupled with lowered Mg# may be indicative of significant metamorphic exchange rather than primary elemental features of detrital chromites (e.g. Barnes, 2000; Colas et al., 2014). Jack Hills detrital chromites therefore warrant further investigation.

1.5. Understanding crustal evolution in the Narryer Terrane

1.5.1. Aims and hypotheses

This project aims to contribute to our understanding of Archean crustal evolution in the Narryer Terrane using two detrital phases from Jack Hills: detrital chromites and detrital zircons. Chromites from Jack Hills have thus far remained largely unstudied, and this body of work will represent the first systematic provenance analysis of chromites within Archean sediments. Furthermore, as chromite is a petrogenetic indicator (e.g. Barnes and Roeder, 2001), Jack Hills chromites will provide valuable insights into the composition and tectonic setting of their protoliths. Owing to the high concentration of PGEs (platinum group elements) within chromite, Re-Os geochronology of detrital grains will also provide constraints on the timing of mafic and ultramafic crustal generation. The formation of >3100 Ma crust within the Narryer Terrane is poorly understood, with only the Eoarchean Manfred Complex described in any detail (e.g. Kemp et al., 2019). The ubiquitous presence of detrital chromites within Jack Hills sediments suggests that mafic and ultramafic rocks were a large component of the Jack Hills sedimentary source catchment, and these grains likely represent the sole eroded remnants of these lithologies. Detrital chromites will therefore particularly add to our understanding of crustal evolution within the Narryer Terrane by providing compositional and temporal constraints on the generation of poorly understood Archean mafic and ultramafic crust. The aims of this study are:

- To characterise detrital spinels present within metasediments at Jack Hills, known to host detrital chromites, and, if observed, within the higher-grade Mount Narryer supracrustal sequence. This will involve scanning electron microscopy (SEM) to determine the inclusion assemblages of detrital chromites from Jack Hills and observe any features that may perturb geochemical and isotopic analyses of grains.
- To undertake electron probe microanalysis (EPMA) to determine the major and minor elemental composition of detrital grains. This will be undertaken to highlight the effects of

metamorphism, both prior to and after deposition, on Jack Hills detrital chromites. Primary signatures of chromites will also be identified to elucidate the magmatic provenance of grains.

- To determine the Re-Os model ages (TMAs) of Jack Hills detrital chromites. This is to perceive if chromites are contemporaneous with detrital zircons and to produce a temporal framework for the generation of Archean mafic and ultramafic crust within the Narryer Terrane.
- Provide additional geodynamic constraints on the generation of bulk Archean and potentially Hadean crust within the Narryer Terrane by reconciling the magmatic relationships between detrital chromites and detrital zircons.

1.5.2. Broader geodynamic connotations

Chromites and zircon have similar resistance to mechanical abrasion during sedimentary processing (Morton and Hallsworth, 1994), indicating a similar potential transport distance, and therefore making direct comparison of these two phases a viable prospect. To understand the geodynamic regime under which both chromite and zircon crystallised, a hypothesis is presented here generated from the expected relationships between chromite and zircon in an idealised detrital sample (Figure 1.13). This hypothesis should be able to distinguish between the two dominant geodynamic regimes (modern-style plate tectonics vs. stagnant lid) postulated to be operating during the time of crystallisation of Jack Hills zircons. This will involve a multi-component approach including; detrital chromite major and minor element compositions, bulk chromite Re-Os TMAs, and coupled Pb-Hf of detrital zircons.

Within a modern-style plate tectonics scenario, zircon peaks within detrital records likely represent preservation rather the generation of new crust (e.g. Hawkesworth et al., 2009). While continental collisions represent only a minor component of modern-day continental crust, zircons derived from these settings have a higher preservation potential than those derived from arcs, thus zircon peaks often correlate with the supercontinent cycle. Furthermore, chromites will crystallise during the extensional phase of collision, which possesses the lowest preservation potential for zircons (Hawkesworth et al., 2009). Thus, there should therefore be a decoupling, or an absence of a strong temporal link between zircon age distribution peaks and chromite Re-Os model ages. Further to this, where arc-magmas dominate, distinctly juvenile Pb-Hf isotopic compositions of zircons should be observed and coupled with minor proportions of chromites with corresponding Re-Os model ages. Chromites would also possess elemental compositions characterising rock units derived from this scenario: oxidised, arc-derived chromites, ophiolitic chromites, and potentially high Cr# boninites produced from a highly depleted mantle source. In particular, ophiolites (not shown on Figure 1.13), fragments of oceanic lithosphere and upper mantle obducted onto continental margins at collisional plate margins (e.g. Dilek and Furnes, 2011; González-Jiménez et al., 2014), are a fingerprint of modern-

style plate tectonics, requiring the presence of oceanic lithosphere and subduction as an obduction mechanism. If chromites derived from this tectonic setting are present within the Jack Hills record, this would be hard to reconcile with a regime other than plate tectonics. Critically, selective erosion of the diverse suite of rocks expected in this geodynamic regime will result in diverse, but distinct sedimentary sources. While there will be a dependence on the variability of exposure, this should translate into geochemical and Re-Os isotopic heterogeneity of the chromite detrital record.

Within a stagnant lid regime, there should be a strong temporal link between zircon age distribution peaks and chromite Re-Os TMAs. This is because plume-derived komatiites and their plutonic equivalents are required to thicken crust, inducing partial melting within the lower crust to form the felsic melts parental to detrital zircons (Kamber et al., 2005; Kemp et al., 2010). Zircon age distribution peaks would therefore represent episodic crustal generation events (e.g. Condie et al., 2018), rather than preferential preservation. Zircon age distribution peaks and chromite Re-Os model ages should further correspond with subchondritic Hf compositions, as zircons are derived from recycling of older crust. Finally, chromites crystallising within a stagnant lid regime will also possess a more uniform detrital chemistry due to the voluminous nature of large scale, plume-derived mantle melting events. Chromites would yield consistent, high Cr# chromites when derived from komatiites, or would be chemically similar to layered intrusions produced by high degrees of mantle melting.

These hypotheses depend strongly on the petrogenesis of detrital chromites: the variability in Cr#, Mg#, Fe^{3+}# and TiO_2 contents within chromites derived from the settings listed above are distinguishable using previously determined compositional fields (Barnes and Roeder, 2001). However, chromites will have undoubtably been modified by upper greenschist metamorphism at Jack Hills, requiring careful consideration of the metamorphic effects on grains, particularly for metamorphism sensitive parameters such as Mg#. However, detrital chromites will still preserve multiple primary geochemical signatures at the upper greenschist facies metamorphic grade suggested for metasediments within association 3 at Jack Hills (Barnes, 2000; Spaggiari, 2007; Rasmussen et al., 2010; Colás et al., 2014). The use of chromite as a petrogenetic indicator marks a movement away from traditional provenance studies and may aid in not only elucidating the generation and composition of poorly understood mafic and ultramafic crust within the Narryer Terrane, but also in clarifying the complex zircon record at Jack Hills. A dual chromite-zircon detrital record will therefore significantly add to our understanding of crustal evolution and geodynamics within the Archean, and potentially within the Hadean.

Figure 1.13 (next page): Idealised relationships between detrital chromite and detrital zircon in the two postulated geodynamic regimes for Jack Hills zircons. **A)** Modern-style plate tectonics. Minor, oxidised chromites should correlate with zircon age distribution peaks that possess dominantly juvenile Hf compositions when both detrital phases are derived from arc settings. Within continental convergent margins there should be an absence of mafic magmatic activity, and so a decoupling of the chromite-zircon detrital record. Detrital chromites should also show significant diversity between samples, due to derivation from heterogeneous sources. Detrital minerals from orogens should consist of zircons with U-Pb age distribution peaks that are a production of preservation, rather than episodic crustal generation. Zircon should possess subchondritic Hf compositions, and there should be no associated detrital chromite. **B)** Stagnant lid/sagduction tectonics. Felsic crust is derived from partial melting of altered, lower crustal mafic protoliths, zircon age distribution peaks should possess subchondritic Hf compositions. As thickening of the crust is facilitated by eruption and intrusion of plume-derived mafic and ultramafic rocks, there should also be a strong correlation between zircon U-Pb and chromite Re-Os model ages. Chromites should also possess a geochemistry akin to komatiites or komatiitic layered intrusions and possess homogenous chemistry across samples due to the expected lack of lithological diversity.

Horizontal Tectonics

Modern Plate tectonics

Convergent plate margins with cold slab subduction and continental orogenesis

Juvenile zircon (εHf >0)

Magmatic fractionation to form continental crust

Minor, oxidised chromite

Mantle wedge partial melting

Slab dehydration… slab melting in Archean?

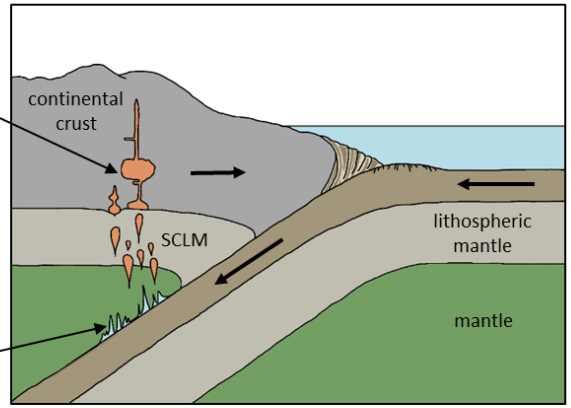

Recycled zircon (εHf <0)

Melting of mafic crust to form I- or A-type granites

No mantle input ≠ chromite

Thick, cold SCLM

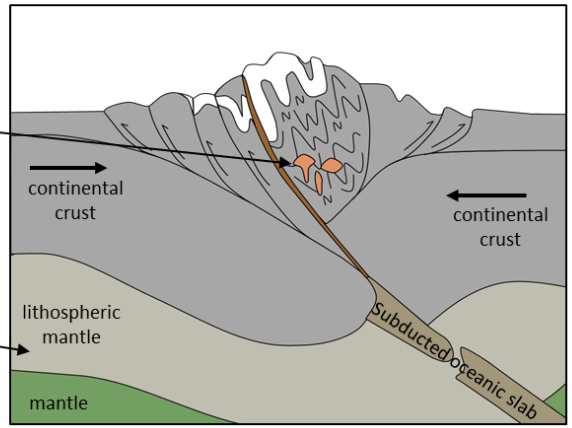

Vertical Tectonics

Stagnant Lid

Crustal thickening via mantle output causes partial melting of lower crust

Komatiitic and plutonic equivalent chromite

Plume-derived komatiitic pile and intrusives

Rapid burial and thickening of altered mafic crust

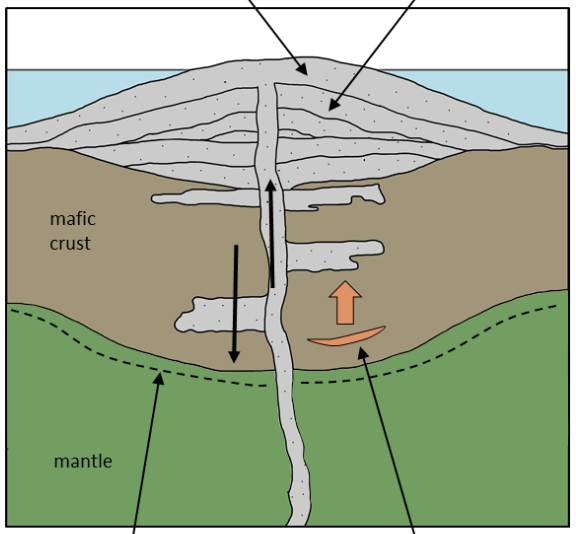

None to minor SCLM

Partial melting of altered crust to form buoyant felsic melts

Recycled zircon (εHf <0)

1.6: References

Amelin, Y., Lee, D. C., Halliday, A. N. & Pidgeon, R. T. (1999). Nature of the Earth's earliest crust from hafnium isotopes in single detrital zircons. *Nature* **399**, 252-255.

Arndt, N. T. (2013). The formation and evolution of the continental crust. *Geochemical Perspectives* **2**, 405-533.

Arndt, N. T., Lesher, C. & Barnes, S. J. (2008). Brief descriptions of six classic komatiite occurrences. *Komatiite*. Cambridge: Cambridge University Press, 16-52, and The hydrous komatiite hypothesis. *Komatiite.* Cambridge: Cambridge University Press, 328-351.

Barnes, S. J. & Fiorentini, M. L. (2012). Komatiite Magmas and Sulfide Nickel Deposits: A Comparison of Variably Endowed Archean Terranes. *Economic Geology* **107**, 755-780.

Barnes, S. J. & Roeder, P. L. (2001). The range of spinel compositions in terrestrial mafic and ultramafic rocks. *Journal of Petrology* **42**, 2279-2302.

Barnes, S. J. (2000). Chromite in komatiites, II. modification during greenschist to mid-amphibolite facies metamorphism. *Journal of Petrology* **41**, 387-409.

Bauer, A. M., Fisher, C. M., Vervoort, J. D. & Bowring, S. A. (2017). Coupled zircon Lu-Hf and U-Pb isotopic analyses of the oldest terrestrial crust, the > 4.03 Ga Acasta Gneiss Complex. *Earth and Planetary Science Letters* **458**, 37-48.

Bell, E. A., Boehnke, P., Harrison, T. M. & Mao, W. L. (2015a). Potentially biogenic carbon preserved in a 4.1 billion-year-old zircon. *Proceedings of the National Academy of Sciences of the United States of America* **112**, 14518-14521.

Bell, E. A., Boehnke, P., Hopkins-Wielicki, M. D. & Harrison, T. M. (2015b). Distinguishing primary and secondary inclusion assemblages in Jack Hills zircons. *Lithos* **234**, 15-26.

Bell, E. A., Harrison, T. M., Kohl, I. E. & Young, E. D. (2014). Eoarchean crustal evolution of the Jack Hills zircon source and loss of Hadean crust. *Geochimica Et Cosmochimica Acta* **146**, 27-42.

Bell, E. A., Harrison, T. M., McCulloch, M. T. & Young, E. D. (2011). Early Archean crustal evolution of the Jack Hills Zircon source terrane inferred from Lu-Hf, Pb-207/Pb-206, and delta O-18 systematics of Jack Hills zircons. *Geochimica Et Cosmochimica Acta* **75**, 4816-4829.

Blichert-Toft, J. & Albarede, F. (2008). Hafnium isotopes in Jack Hills zircons and the formation of the Hadean crust. *Earth and Planetary Science Letters* **265**, 686-702.

Boehnke, P., Bell, E., Stephan, T., Trappitsch, R., Keller, C., Pardo, O., Davis, A., Harrison, T. & Pellin, M. (2018). Potassic, high-silica Hadean crust. *Proceedings of the National Academy of Sciences of the United States of America* **115**, 6353-6356.

Bolhar, R., Hofmann, A., Kemp, A. I. S., Whitehouse, M. J., Wind, S. & Kamber, B. S. (2017). Juvenile crust formation in the Zimbabwe Craton deduced from the O-Hf isotopic record of 3.8-3.1 Ga detrital zircons. *Geochimica Et Cosmochimica Acta* **215**, 432-446.

Bouvier, A., Vervoort, J. D. & Patchett, P. J. (2008). The Lu-Hf and Sm-Nd isotopic composition of CHUR: Constraints from unequilibrated chondrites and implications for the bulk composition of terrestrial planets. *Earth and Planetary Science Letters* **273**, 48-57.

Burnham, A. D. & Berry, A. J. (2017). Formation of Hadean granites by melting of igneous crust. *Nature Geoscience* **10**, 457-+.

Cassidy, K. F., Champion, D.C., Krapez, B., Barley, M.E., Brown, S.J.A., Blewett, R.S., Groenewald, N.B., Tyler, I.M. (2006). A Revised Geological Framework for the Yilgarn Craton. *Geological Survey of Western Australia* **(Record 2006/8)**.

Cawood, P., Hawkesworth, C., Pisarevsky, S., Dhuime, B., Capitanio, F. & Nebel, O. (2018). Geological archive of the onset of plate tectonics. *Philosophical Transactions of the Royal Society a-Mathematical Physical and Engineering Sciences* **376**.

Cavosie, A. J., Valley., J. W., and Wilde., S. A. (2019). The Oldest Terrestrial Mineral Record: Thirty Years of Research on Hadean Zircon from Jack Hills, Western Australia. In: van Kranendonk, M. J., Bennett, V. C., and Hoffmann, J. E., (ed.) *Earth's Oldest Rocks*: Elsevier, 255-273.

Cavosie, A. J., Valley, J. W., Wilde, S. A. & Edinburgh Ion Microprobe, F. (2006). Correlated microanalysis of zircon: Trace element, delta O-18, and U-Th-Pb isotopic constraints on the igneous origin of complex > 3900 Ma detrital grains. *Geochimica Et Cosmochimica Acta* **70**, 5601-5616.

Cavosie, A. J., Valley, J. W. & Wilde, S. A. (2005). Magmatic delta O-18 in 4400-3900 Ma detrital zircons: A record of the alteration and recycling of crust in the Early Archean. *Earth and Planetary Science Letters* **235**, 663-681.

Cavosie, A. J., Wilde, S. A., Liu, D. Y., Weiblen, P. W. & Valley, J. W. (2004). Internal zoning and U-Th-Pb chemistry of Jack Hills detrital zircons: a mineral record of early Archean to Mesoproterozoic (4348-1576 Ma) magmatism. *Precambrian Research* **135**, 251-279.

Cavosie, A. J., Valley, J. W., Fournelle, J. & Wilde, S. A. (2002). Implications for sources of Jack Hills metasediments: detrital chromite. *Goldschmidt 2002*, 125.

Chaudhuri, T., Wan, Y., Mazumder, R., Ma, M. & Liu, D. (2018). Evidence of Enriched, Hadean Mantle Reservoir from 4.2-4.0 Ga zircon xenocrysts from Paleoarchean TTGs of the Singhbhum Craton, Eastern India. *Scientific Reports* **8**.

Cherniak, D., Hanchar, J. & Watson, E. (1997). Diffusion of tetravalent cations in zircon. *Contributions to Mineralogy and Petrology* **127**, 383-390.

Colas, V., Gonzalez-Jimenez, J. M., Griffin, W. L., Fanlo, I., Gervilla, F., O'Reilly, S. Y., Pearson, N. J., Kerestedjian, T. & Proenza, J. A. (2014). Fingerprints of metamorphism in chromite: New insights from minor and trace elements. *Chemical Geology* **389**, 137-152.

Compston, W. & Pidgeon, R. T. (1986). Jack Hills, evidence of more very old detrital zircons in Western Australia. *Nature* **321**, 766-769.

Condie, K., Puetz, S. & Davaille, A. (2018). Episodic crustal production before 2.7 Ga. *Precambrian Research* **312**, 16-22.

Crowley, J. L., Myers, J. S., Sylvester, P. J. & Cox, R. A. (2005). Detrital zircon from the Jack Hills and Mount Narryer, Western Australia: Evidence for diverse > 4.0 Ga source rocks. *Journal of Geology* **113**, 239-263.

Cox, M. A., Cavosie, A. J., Reddy, S. M., Bland, P. A., Valley, J. W. (2017). The hunt for schocked zircon in the Jack Hills: 21,000 and counting... *Lunar and Planetary Science Conference*.

Dare, M. S., Tarduno, J. A., Bono, R. K., Cottrell, R. D., Beard, J. S. & Kodama, K. P. (2016). Detrital magnetite and chromite in Jack Hills quartzite cobbles: Further evidence for the preservation of primary magnetizations and new insights into sediment provenance. *Earth and Planetary Science Letters* **451**, 298-314.

Dilek, Y. & Furnes, H. (2011). Ophiolite genesis and global tectonics: Geochemical and tectonic fingerprinting of ancient oceanic lithosphere. *Geological Society of America Bulletin* **123**, 387-411.

Dunn, S. J., Nemchin, A. A., Cawood, P. A. & Pidgeon, R. T. (2005). Provenance record of the Jack Hills metasedimentary belt: Source of the Earth's oldest zircons. *Precambrian Research* **138**, 235-254.

Fisher, C. M. & Vervoort, J. D. (2018). Using the magmatic record to constrain the growth of continental crust-The Eoarchean zircon Hf record of Greenland. *Earth and Planetary Science Letters* **488**, 79-91.

Fletcher, I., McNaughton, N., Pidgeon, R. & Rosman, K. (1997). Sequential closure of K-Ca and Rb-Sr isotopic systems in Archaean micas. *Chemical Geology* **138**, 289-301.

Fletcher, I. R., Rosman, K. J. R. & Libby, W. G. (1988). Sm-Nd, Pb-Pb and Rb-Sr geochronology of the Manfred Complex, Mount Narryer, Western Australia. *Precambrian Research* **38**, 343-354.

Francois, C., Philippot, P., Rey, P. & Rubatto, D. (2014). Burial and exhumation during Archean sagduction in the East Pilbara Granite-Greenstone Terrane. *Earth and Planetary Science Letters* **396**, 235-251.

Froude, D. O., Ireland, T. R., Kinny, P. D., Williams, I. S., Compston, W., Williams, I. R. & Myers, J. S. (1983). Ion microprobe identification of 4,100-4,200 myr-old terrestrial zircons. *Nature* **304**, 616-618.

Ge, R., Wilde, S., Nemchin, A., Whitehouse, M., Bellucci, J., Erickson, T., Frew, A. & Thern, E. (2018). A 4463 Ma apparent zircon age from the Jack Hills (Western Australia) resulting from ancient Pb mobilization. *Geology* **46**, 303-306.

Gehrels, G. (2014). Detrital Zircon U-Pb Geochronology Applied to Tectonics. *Annual Review of Earth and Planetary Sciences, Vol 42* **42**, 127-149.

Gerdes, A. & Zeh, A. (2006). Combined U-Pb and Hf isotope LA-(MC-)ICP-MS analyses of detrital zircons: Comparison with SHRIMP and new constraints for the provenance and age of an Annorican metasediment in Central Germany. *Earth and Planetary Science Letters* **249**, 47-61.

Gonzalez-Jimenez, J., Griffin, W., Proenza, J., Gervilla, F., O'Reilly, S., Akbulut, M., Pearson, N. & Arai, S. (2014). Chromitites in ophiolites: How, where, when, why? Part II. The crystallization of chromitites. *Lithos* **189**, 140-158.

Griffin, W., Wang, X., Jackson, S., Pearson, N., O'Reilly, S., Xu, X. & Zhou, X. (2002). Zircon chemistry and magma mixing, SE China: In-situ analysis of Hf isotopes, Tonglu and Pingtan igneous complexes. *Lithos* **61**, 237-269.

Grimes, C. B., John, B. E., Kelemen, P. B., Mazdab, F. K., Wooden, J. L., Cheadle, M. J., Hanghoj, K. & Schwartz, J. J. (2007). Trace element chemistry of zircons from oceanic crust: A method for distinguishing detrital zircon provenance. *Geology* **35**, 643-646.

Groves, D. I., Barrett, F. M., Binns, R. A. & McQueen, K. G. (1977). Spinel phases associated with metamorphosed volcanic-type iron-nickel sulfide ores from Western Australia. *Economic Geology* **72**, 1224-1244.

Hansen, V. L. (2007). Subduction origin on early Earth: A hypothesis. *Geology* **35**, 1059-1062.

Harrison, T. M., Bell, E. A. & Boehnke, P. (2017). Hadean Zircon Petrochronology. *Petrochronology: Methods and Applications* **83**, 329-+.

Harrison, T. M. (2009). The Hadean Crust: Evidence from > 4 Ga Zircons. *Annual Review of Earth and Planetary Sciences*, 479-505.

Harrison, T. M., Schmitt, A. K., McCulloch, M. T. & Lovera, O. M. (2008). Early (>= 4.5 Ga) formation of terrestrial crust: Lu-Hf, delta O-18, and Ti thermometry results for Hadean zircons. *Earth and Planetary Science Letters* **268**, 476-486.

Harrison, T. M. & Schmitt, A. K. (2007). High sensitivity mapping of Ti distributions in Hadean zircons. *Earth and Planetary Science Letters* **261**, 9-19.

Harrison, T. M., Trail, D., Schmitt, A. K. & Watson, E. B. (2007). Rutile 207Pb-206Pb ages in the Jack Hills quartzite, Western Australia. *Geochimica Et Cosmochimica Acta* **71**, A383-A383.

Harrison, T. M., Blichert-Toft, J., Muller, W., Albarede, F., Holden, P. & Mojzsis, S. J. (2005). Heterogeneous Hadean hafnium: Evidence of continental crust at 4.4 to 4.5 Ga. *Science* **310**, 1947-1950.

Hawkesworth, C., Cawood, P., Dhuime, B., Kemp, T., Jeanloz, R. & Freeman, K. (2017). Earth's Continental Lithosphere Through Time. *Annual Review of Earth and Planetary Sciences, Vol 45* **45**, 169-198.

Hawkesworth, C., Cawood, P., Kemp, T., Storey, C. & Dhuime, B. (2009). Geochemistry: A Matter of Preservation. *Science* **323**, 49-50.

Hawkesworth, C. J. & Kemp, A. I. S. (2006). Using hafnium and oxygen isotopes in zircons to unravel the record of crustal evolution. *Chemical Geology* **226**, 144-162.

Hiess, J. & Bennett, V. C. (2016). Chondritic Lu/Hf in the early crust-mantle system as recorded by zircon populations from the oldest Eoarchean rocks of Yilgarn Craton, West Australia and Enderby Land, Antarctica. *Chemical Geology* **427**, 125-143.

Hiess, J., Condon, D. J., McLean, N. & Noble, S. R. (2012). U-238/U-235 Systematics in Terrestrial Uranium-Bearing Minerals. *Science* **335**, 1610-1614.

Holden, P., Lanc, P., Ireland, T. R., Harrison, T. M., Foster, J. J. & Bruce, Z. (2009). Mass-spectrometric mining of Hadean zircons by automated SHRIMP multi-collector and single-collector U/Pb zircon age dating: The first 100,000 grains. *International Journal of Mass Spectrometry* **286**, 53-63.

Hopkins, M., Harrison, T. M. & Manning, C. E. (2012). Metamorphic replacement of mineral inclusions in detrital zircon from Jack Hills, Australia: Implications for the Hadean Earth. *Geology* **40**, E281-E281.

Hopkins, M. D., Harrison, T. M. & Manning, C. E. (2010). Constraints on Hadean geodynamics from mineral inclusions in > 4 Ga zircons. *Earth and Planetary Science Letters* **298**, 367-376.

Hopkins, M., Harrison, T. M. & Manning, C. E. (2008). Low heat flow inferred from > 4 Gyr zircons suggests Hadean plate boundary interactions. *Nature* **456**, 493-496.

Iizuka, T., McCulloch, M. T., Komiya, T., Shibuya, T., Ohta, K., Ozawa, H., Sugimura, E. & Collerson, K. D. (2010). Monazite geochronology and geochemistry of meta-sediments in the Narryer Gneiss Complex, Western Australia: constraints on the tectonothermal history and provenance. *Contributions to Mineralogy and Petrology* **160**, 803-823.

Johnson, T., Gardiner, N., Miljkovic, K., Spencer, C., Kirkland, C., Bland, P. & Smithies, H. (2018). An impact melt origin for Earth's oldest known evolved rocks. *Nature Geoscience* **11**, 795-+.

Johnson, T., Brown, M., Gardiner, N., Kirkland, C. & Smithies, R. (2017). Earth's first stable continents did not form by subduction. *Nature* **543**, 239-+.

Johnson, T., Brown, M., Kaus, B. & VanTongeren, J. (2014). Delamination and recycling of Archaean crust caused by gravitational instabilities. *Nature Geoscience* **7**, 47-52.

Kamber, B. S., Whitehouse, M. J., Bolhar, R. & Moorbath, S. (2005). Volcanic resurfacing and the early terrestrial crust: Zircon U-Pb and REE constraints from the Isua Greenstone Belt, southern West Greenland. *Earth and Planetary Science Letters* **240**, 276-290.

Kemp, A. I. S., Wilde, S. A., and Spaggiari, C. (2019). The Narryer Terrane, Yilgarn Craton, Western Australia: Review and Recent Developments. In: van Kranendonk, M. J., Bennett, V. C., and Hoffmann, J. E., (ed.) *Earth's Oldest Rocks*: Elsevier, 401-429.

Kemp, A. I. S. (2018). Early earth geodynamics: cross examining the geological testimony. *Philosophical Transactions of the Royal Society A* **376**.

Kemp, A. I. S., Hickman, A. H., Kirkland, C. L. & Vervoort, J. D. (2015). Hf isotopes in detrital and inherited zircons of the Pilbara Craton provide no evidence for Hadean continents. *Precambrian Research* **261**, 112-126.

Kemp, A. I. S. and Hawkesworth., C. J. (2014). Growth and Differentiation of the Continental Crust from Isotope Studies of Accessory Minerals. In: Rudnick, R. L. (ed.) *Treatise on Geochemistry (Second Volume)*, 379-415.

Kemp, A. I. S., Wilde, S. A., Hawkesworth, C. J., Coath, C. D., Nemchin, A., Pidgeon, R. T., Vervoort, J. D. & DuFrane, S. A. (2010). Hadean crustal evolution revisited: New constraints from Pb-Hf isotope systematics of the Jack Hills zircons. *Earth and Planetary Science Letters* **296**, 45-56.

Kinny, P. D. & Nutman, A. P. (1996). Zirconology of the Meeberrie Gneiss, Yilgarn Craton, Western Australia: An early Archaean migmatite. *Precambrian Research* **78**, 165-178.

Kinny, P. D., Wijbrans, J. R., Froude, D. O., Williams, I. S. & Compston, W. (1990). Age constraints on the geological evolution of the Narryer Gneiss Complex, Western Australia. *Australian Journal of Earth Sciences* **37**, 51-69.

Kinny, P. D., Williams, I. S., Froude, D. O., Ireland, T. R. & Compston, W. (1988). Early Archean zircon ages from orthogneisses and anorthosites at Mount Narryer, Western Australia. *Precambrian Research* **38**, 325-341.

Maas, R., Kinny, P. D., Williams, I. S., Froude, D. O. & Compston, W. (1992). The Earths oldest known crust - a geochronological and geochemical study of 3900-4200 ma old detrital zircons from Mt Narryer and Jack Hills, Western-Australia. *Geochimica Et Cosmochimica Acta* **56**, 1281-1300.

Menneken, M., Geisler, T., Nemchin, A. A., Whitehouse, M. J., Wilde, S. A., Gasharova, B. & Pidgeon, R. T. (2017). CO2 fluid inclusions in Jack Hills zircons. *Contributions to Mineralogy and Petrology* **172**.

Mojzsis, S. J., Cates, N. L., Caro, G., Trail, D., Abramov, O., Guitreau, M., Blichert-Toft, J., Hopkins, M. D. & Bleeker, W. (2014). Component geochronology in the polyphase ca. 3920 Ma Acasta Gneiss. *Geochimica Et Cosmochimica Acta* **133**, 68-96.

Mojzsis, S. J., Harrison, T. M. & Pidgeon, R. T. (2001). Oxygen-isotope evidence from ancient zircons for liquid water at the Earth's surface 4,300 Myr ago. *Nature* **409**, 178-181.

Mole, D. R., Kirkland, C. L., Fiorentini, M. L., Barnes, S. J., Cassidy, K. F., Issac, C., Belousova, E. A., Hartnady, M., and Thebaud, N. (2019). Time-space evolution of an archean craton: A Hf-isotope window into continent formation. *Earth Science Reviews* **in press**.

Morton, A. & Hallsworth, C. (1994). Identifying provenance-specific features of detrital heavy mineral assemblages in sandstones. *Sedimentary Geology* **90**, 241-256.

Moyen, J. & Laurent, O. (2018). Archaean tectonic systems: A view from igneous rocks. *Lithos* **302**, 99-125.Moyen, J. F. & Martin, H. (2012). Forty years of TTG research. *Lithos* **148**, 312-336.

Myers, J. S. (1997). Byro, W.A., Sheet SG 50 10 (2nd Edition). Western Australia Geological Survey.

Myers, J. S. (1988a). Early Archean Narryer Gneiss Complex, Yilgarn Craton, Western-Australia. *Precambrian Research* **38**, 297-307.

Myers, J. S. (1988b). Oldest known terrestrial anorthosite at Mount Narryer, Western Australia. *Precambrian Research* **38**, 309-323.

Myers, J. S. & Williams, I. R. (1985). Early precambrian crustal evolution at Mount Narryer, Western Australia. *Precambrian Research* **27**, 153-163.

Nebel, O., Capitanio, F., Moyen, J., Weinberg, R., Clos, F., Nebel-Jacobsen, Y. & Cawood, P. (2018). When crust comes of age: on the chemical evolution of Archaean, felsic continental crust by crustal drip tectonics. *Philosophical Transactions of the Royal Society a-Mathematical Physical and Engineering Sciences* **376**.

Nebel, O., Rapp, R. P. & Yaxley, G. M. (2014). The role of detrital zircons in Hadean crustal research. *Lithos* **190**, 313-327.

Nebel-Jacobsen, Y., Munker, C., Nebel, O., Gerdes, A., Mezger, K. & Nelson, D. R. (2010). Reworking of Earth's first crust: Constraints from Hf isotopes in Archean zircons from Mt. Narryer, Australia. *Precambrian Research* **182**, 175-186.

Nelson, D. R., 1996, 105002: dark inclusion phase in orthogneiss, east of Cargarra Well; Geochronology dataset 7; in Compilation ofgeochronology data, June 2006 update: Western Australia Geological Survey.

Nutman, A. P. (2006). Comment on "Zircon thermometer reveals minimum melting conditions on earliest Earth" II. *Science* **311**.

Nutman, A. P., Kinny, P. D., Compston, W. & Williams, I. S. (1991). SHRIMP U-Pb zircon geochronology of the Narryer Gneiss Complex, Western Australia. *Precambrian Research* **52**, 275-300.

O'Neil, J. & Carlson, R. W. (2017). Building Archean cratons from Hadean mafic crust. *Science* **355**, 1199-1202.

O'Neill, C. & Debaille, V. (2014). The evolution of Hadean-Eoarchaean geodynamics. *Earth and Planetary Science Letters* **406**, 49-58.

O'Neil, J., Carlson, R. W., Francis, D. & Stevenson, R. K. (2008). Neodymium-142 evidence for Hadean mafic crust. *Science* **321**, 1828-1831.

Occhipinti, S. A., Sheppard, S., Myers, J. S., Tyler, I. M., and Nelson, D. R., 2001, Archaean and Palaeoproterozoic geology of the Narryer Terrane (Yilgarn Craton) and the southern Gascoyne Complex (Capricorn Orogen), Western Australia — a field guide: Western Australia Geological Survey,Record 2001/8, 70p.

Pearson, D. & Wittig, N. (2008). Formation of Archaean continental lithosphere and its diamonds: the root of the problem. *Journal of the Geological Society* **165**, 895-914.

Peck, W. H., Valley, J. W., Wilde, S. A. & Graham, C. M. (2001). Oxygen isotope ratios and rare earth elements in 3.3 to 4.4 Ga zircons: Ion microprobe evidence for high delta O-18 continental crust and oceans in the Early Archean. *Geochimica Et Cosmochimica Acta* **65**, 4215-4229.

Petersson, A., Kemp, A. I. S., Hickman, A. H., Whitehouse, M. J., Martin, L. & Gray, C. M. (2019). A new 3.59 Ga magmatic suite and a chondritic source to the east Pilbara Craton. *Chemical Geology* **511**, 51-70.

Pidgeon, R. T. & Nemchin, A. A. (2006). High abundance of early Archaean grains and the age distribution of detrital zircons in a sillimanite-bearing quartzite from Mt Narryer, Western Australia. *Precambrian Research* **150**, 201-220.

Pidgeon, R. T. & Wilde, S. A. (1998). The interpretation of complex zircon U-Pb systems in Archaean granitoids and gneisses from the Jack Hills, Narryer gneiss Terrane, Western Australia. *Precambrian Research* **91**, 309-332.

Polat, A., Wang, L. & Appel, P. (2015). A review of structural patterns and melting processes in the Archean craton of West Greenland: Evidence for crustal growth at convergent plate margins as opposed to non-uniformitarian models. *Tectonophysics* **662**, 67-94.

Rasmussen, B., Fletcher, I. R., Muhling, J. R., Gregory, C. J. & Wilde, S. A. (2012). Metamorphic replacement of mineral inclusions in detrital zircon from Jack Hills, Australia: Implications for the Hadean Earth. *Geology* **40**, E282-E283.

Rasmussen, B., Fletcher, I. R., Muhling, J. R., Gregory, C. J. & Wilde, S. A. (2011). Metamorphic replacement of mineral inclusions in detrital zircon from Jack Hills, Australia: Implications for the Hadean Earth. *Geology* **39**, 1143-1146.

Rasmussen, B., Fletcher, I. R., Muhling, J. R. & Wilde, S. A. (2010). In situ U-Th-Pb geochronology of monazite and xenotime from the Jack Hills belt: Implications for the age of deposition and metamorphism of Hadean zircons. *Precambrian Research* **180**, 26-46.

Reimink, J. R., Davies, J., Chacko, T., Stern, R. A., Heaman, L. M., Sarkar, C., Schaltegger, U., Creaser, R. A. & Pearson, D. G. (2016). No evidence for Hadean continental crust within Earth's oldest evolved rock unit. *Nature Geoscience* **9**, 777.

Reimink, J. R., Chacko, T., Stern, R. A. & Heaman, L. M. (2014). Earth's earliest evolved crust generated in an Iceland-like setting. *Nature Geoscience* **7**, 529-533.

Rowe, ML 2016, Petrology and geochemistry of the Eoarchaean Manfred Complex: origin and components: Geological Survey of Western Australia, Record 2016/22, 150p.

Scherer, E., Munker, C. & Mezger, K. (2001). Calibration of the lutetium-hafnium clock. *Science* **293**, 683-687.

Schoene, B. (2014). U-Yh-Pb Geochronology. In: Rudnick, R. L. (ed.) *Treatise of Geochemistry (Second Edition)*, 341-370.

Soderlund, U., Patchett, J. P., Vervoort, J. D. & Isachsen, C. E. (2004). The Lu-^{176} decay constant determined by Lu-Hf and U-Pb isotope systematics of Precambrian mafic intrusions. *Earth and Planetary Science Letters* **219**, 311-324.

Spaggiari, C. V., Wartho, J. A. & Wilde, S. A. (2008). Proterozoic deformation in the northwest of the Archean Yilgarn Craton, Western Australia. *Precambrian Research* **162**, 354-384.

Spaggiari, C. V. (2007). Structural and lithological evolution of the Jack Hills greenstone belt, Narryer Terrane, Yilgarn Craton, Western Australia. *Western Australia Geological Survey* **Record 2007/3**, 49.

Sylvester, P., Souders, A. K., Crowley, J. L., and Myers, J. S. (2011). The Archean anorthosite monzogranite magmatic association of the Narryer Gneiss Terrane, Western Australia. *Goldschmidt 2011*, 1975.

Trail, D., Boehnke, P., Savage, P. S., Liu, M. C., Miller, M. L. & Bindeman, I. (2018). Origin and significance of Si and O isotope heterogeneities in Phanerozoic, Archean, and Hadean zircon. *Proceedings of the National Academy of Sciences of the United States of America* **115**, 10287-10292.

Trail, D., Tailby, N., Wang, Y. L., Harrison, T. M. & Boehnke, P. (2017). Aluminum in zircon as evidence for peraluminous and metaluminous melts from the Hadean to present. *Geochemistry Geophysics Geosystems* **18**, 1580-1593.

Trail, D., Watson, E. B. & Tailby, N. D. (2011). The oxidation state of Hadean magmas and implications for early Earth's atmosphere. *Nature* **480**, 79-U238.

Trail, D., Mojzsis, S. J., Harrison, T. M., Schmitt, A. K., Watson, E. B. & Young, E. D. (2007). Constraints on Hadean zircon protoliths from oxygen isotopes, Ti-thermometry, and rare earth elements. *Geochemistry Geophysics Geosystems* **8**.

Turner, S., Rushmer, T., Reagan, M. & Moyen, J. (2014). Heading down early on? Start of subduction on Earth. *Geology* **42**, 139-142.

Ushikubo, T., Kita, N. T., Cavosie, A. J., Wilde, S. A., Rudnick, R. L. & Valley, J. W. (2008). Lithium in Jack Hills zircons: Evidence for extensive weathering of Earth's earliest crust. *Earth and Planetary Science Letters* **272**, 666-676.

Valley, J. W., Reinhard, D. A., Cavosie, A. J., Ushikubo, T., Lawrence, D. F., Larson, D. J., Kelly, T. F., Snoeyenbos, D. R. & Strickland, A. (2015). Nano- and micro-geochronology in Hadean and Archean zircons by atom-probe tomography and SIMS: New tools for old minerals. *American Mineralogist* **100**, 1355-1377.

Valley, J. W., Cavosie, A. J., Ushikubo, T., Reinhard, D. A., Lawrence, D. F., Larson, D. J., Clifton, P. H., Kelly, T. F., Wilde, S. A., Moser, D. E. & Spicuzza, M. J. (2014). Hadean age for a post-magma-ocean zircon confirmed by atom-probe tomography. *Nature Geoscience* **7**, 219-223.

Valley, J. W., Cavosie, A. J., Fu, B., Peck, W. H. & Wilde, S. A. (2006). Comment on "Heterogeneous hadean nafnium: Evidence of continental crust at 4.4 to 4.5 Ga". *Science* **312**.

Valley, J. W., Cavosie, A. J., Shirey, S. & Wilde, S. A. (2005). 3.2 to 3.5 Ga Re-Os Model Ages for Detrital Chromite from Jack Hills, Western Australia: Implications for Pilbara and Yilgarn Craton Evolution. *American Geophysical Union, Fall Meeting 2005, abstract #V21F-08*.

van Hunen, J., Moyen, J. & Jeanloz, R. (2012). Archean Subduction: Fact or Fiction? *Annual Review of Earth and Planetary Sciences, Vol 40* **40**, 195-219.

Vervoort, J. D. & Kemp, A. I. S. (2016). Clarifying the zircon Hf isotope record of crust-mantle evolution. *Chemical Geology* **425**, 65-75.

Vervoort, J. & Patchett, P. (1996). Behavior of hafnium and neodymium isotopes in the crust: Constraints from Precambrian crustally derived granites. *Geochimica Et Cosmochimica Acta* **60**, 3717-3733.

Vezinet, A., Pearson, D. G., Thomassot, E., Stern, R. A., Sarkar, C., Luo, Y. & Fisher, C. M. (2018). Hydrothermally-altered mafic crust as source for early Earth TTG: Pb/Hf/O isotope and trace element evidence in zircon from TTG of the Eoarchean Saglek Block, N. Labrador. *Earth and Planetary Science Letters* **503**, 95-107.

Wang, Q. & Wilde, S. A. (2018). New constraints on the Hadean to Proterozoic history of the Jack Hills belt, Western Australia. *Gondwana Research* **55**, 74-91.

Watson, E. B. & Harrison, T. M. (2005). Zircon thermometer reveals minimum melting conditions on earliest Earth. *Science* **308**, 841-844.

Weiss, B. P., Fu, R. R., Einsle, J. F., Glenn, D. R., Kehayias, P., Bell, E. A., Gelb, J., Araujo, J., Lima, E. A., Borlina, C. S., Boehnke, P., Johnstone, D. N., Harrison, T. M., Harrison, R. J. & Walsworth, R. L. (2018). Secondary magnetic inclusions in detrital zircons from the Jack Hills, Western Australia, and implications for the origin of the geodynamo. Geology 46, 427-430.

Whitehouse, M. J., Nemchin, A. A. & Pidgeon, R. T. (2017). What can Hadean detrital zircon really tell us? A critical evaluation of their geochronology with implications for the interpretation of oxygen and hafnium isotopes. *Gondwana Research* **51**, 78-91.

Wilde, S. A., Valley, J. W., Peck, W. H. & Graham, C. M. (2001). Evidence from detrital zircons for the existence of continental crust and oceans on the Earth 4.4 Gyr ago. *Nature* **409**, 175-178.

Williams, I. R. & Myers, J. S. (1987). Archaean geology of the Mount Narryer region Western Australia. Geological Survey of Western Australia: Report 22, 1-32.

Wyche, S., Kirkland, C. L., Riganti, A., Pawley, M. J., Belousova, E. & Wingate, M. T. D. (2012). Isotopic constraints on stratigraphy in the central and eastern Yilgarn Craton, Western Australia. *Australian Journal of Earth Sciences* **59**, 657-670.

Chapter Two:

Materials and Methods

2.1: Introduction

This chapter describes the samples studied within this thesis and details the analytical techniques used. Despite intentional sampling of fuchsitic lithologies (Myers and Williams, 1985) and a concerted search within heavy mineral separates, no chromites or Cr-Al spinels were observed within the metasedimentary sequences at Mount Narryer. This may be a function of the amphibolite to granulite facies metamorphism that the Mount Narryer sequence underwent at ca. 2700 Ma to 2650 Ma (Kemp et al., 2019): chromite is not stable at such high P-T conditions (e.g. Barnes, 2000), as it is replaced by magnetite in an oxidising reaction. This does not mean chromite has never been present within the Mount Narryer succession. Heavily altered Cr-bearing magnetites are present within quartzites and sillimanite-, cordierite-, and garnet- bearing metaconglomerates, and while it cannot be proven, these may represent the relicts of replaced detrital chromites. Oxide phases at Mount Narryer are therefore not discussed within this thesis, which instead focuses on detrital oxides from Jack Hills.

2.2. Fieldwork and sample collection

2.2.1. Jack Hills metasediments

In order to study detrital chromites and zircons from Jack Hills, ten samples of metasediment were taken from at or near the W-74 'discovery site' of Wilde et al. (2001) (Figure 2.1). All metasediment samples were from previous hammer sights or as loose pebbles: no in-situ outcrop was hammered at this site. Two metaconglomerate samples (16WA9 and 10) collected from across the valley were deemed of sufficient distance from the W-74 site to hammer from outcrop. Metasediment samples that both possessed and lacked the characteristic fuchsitic green colouration were collected. 14WA samples were obtained by Tim Elliott in 2014, whilst 16WA samples were collected by Leanne Staddon in a 2016 field season. Sampling localities and approximate distance from the W-74 site are shown in Figure 2.1.

While it may seem beneficial to sample from a wide range of metasediment lithologies and localities, sedimentary depositional ages and lithological relationships at Jack Hills are complex (Cavosie et al., 2004; Dunn et al., 2005; Spaggiari, 2007; Wang and Wilde, 2018), with strong evidence for discrete intercalation of metasediments with both Archean and Proterozoic depositional ages across the belt (Wang and Wilde, 2018). However, the W-74 site has a broad, but reasonably well constrained depositional age of 3050 Ma to 2650 Ma (Crowley et al., 2005; Rasmussen et al., 2010). It was therefore deemed sensible to undertake this study on well characterised sediments so that more robust interpretations on the validity of chromite chronological data could be attained. Any future

comparative analysis away from the W-74 would therefore require stringent characterisation of the age of deposition of metasediments before analysis of chromites is undertaken.

2.2.2. Jack Hills ultramafics

In addition to metasediments, metamorphosed mafics and ultramafics were also taken from the Jack Hills supracrustal belt (Figure 2.2). The mafic and ultramafic successions of Jack Hills have garnered very little attention, with only a single, brief description in Spaggiari (2007). This is unsurprising, as lithologies are typically heavily recrystallised and deformed (e.g. Figure 1.5b and 1.5d), with metamorphic assemblages of hornblende and garnet present in many of the mafic schists, and talc and amphibole in ultramafics (Spaggiari, 2007). Mafics and ultramafics are also part of association 1 (Spaggiari, 2007). This indicates they were metamorphosed during JH D_1, though it is apparent they have been heavily overprinted by the dominant subvertical S_2 foliation of the belt. Rare examples, however, yield good ultramafic erosional textures, suggesting they would yield a more primary mineral assemblage than their heavily sheared counterparts. Mafic and ultramafic rocks were collected from various locations across the Jack Hills belt (Figure 2.2), and were distinctive as high-relief, dark brown mounds above the surrounding granitoids and metasediments. Samples that yielded good ultramafic weathering textures and coarse grained, less heavily recrystallised textures were preferentially sampled.

2.2.3. Manfred Complex mafics and ultramafics

A selection of Manfred Complex mafic and ultramafic rocks were also analysed during this study. Whilst none of these were collected by the author during fieldwork, there is a good representation of the Manfred Complex within 14WA samples and extra lithologies (TKN samples) supplied by Tony Kemp (University of Western Australia). 13TKN22 was shipped as a single large stone, while the remaining TKN samples were shipped partially crushed. The largest and most abundant outcrops of the Manfred Complex are observed to the NE of Mount Narryer (Figure 2.3), where leucogabbro, anorthosite, metaperidotite, metaharzburgite and metapyroxenite are observed (Williams and Myers, 1987; Myers, 1997; Kemp et al., 2019) as disseminated pods and rafts up to 2 km in length within the Dugel and Meeberrie Gneisses. Whilst it is likely that all lithologies to the NE of Mount Narryer are derived from the Manfred Complex (Fletcher et al., 1988; Kinny et al., 1988; Myers, 1988; Kemp et al., 2019) it is important to recognise that only leucogabbros and anorthosite have been precisely dated using zircon U-Pb geochronology (Kinny et al., 1988; Kemp et al., 2019), producing some uncertainties of the ages of ultramafic samples. Finally, this is highlighted by unpublished analyses of mafic and ultramafic crust elsewhere within the Narryer Terrane that yield significantly younger ages than the 3730 Ma Manfred Complex (Kemp et al., 2019), despite being labelled as part of this intrusion.

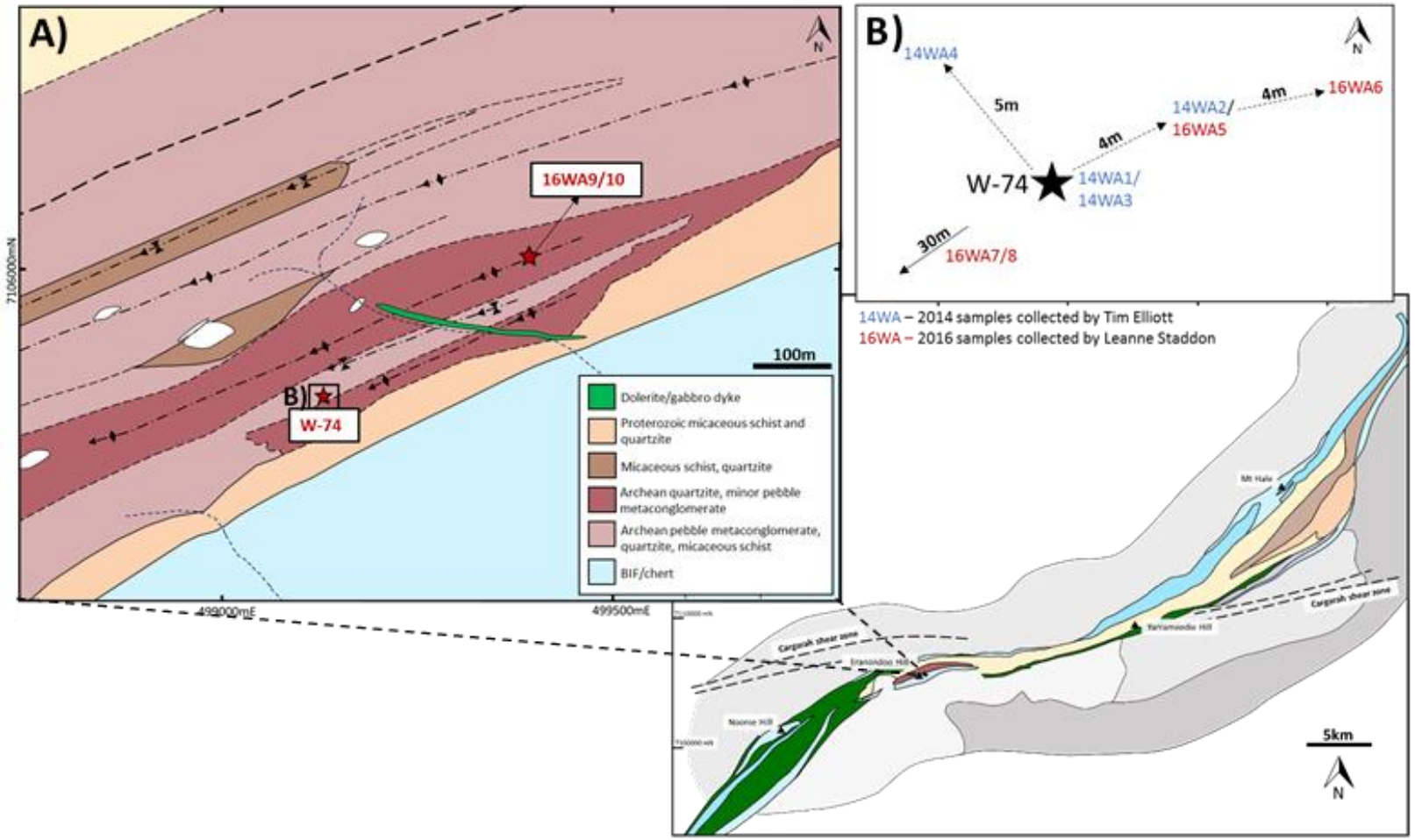

Figure 2.1: **A)** Sampling locations of Jack Hills metasediments on a simplified geological map of Eranondoo Hill, modified after Spaggiari (2007). The position of the W-74 site is shown in relation to the geology of Jack Hills, also modified after Spaggiari (2007). Refer to Figure 1.2 for colours of lithological units. **B)** Inset of sampling locations around the W-74 'discovery site' (Wilde et al., 2001). 16WA7 and 16WA8 collected approximately 30m to the SW of the W-74 site.

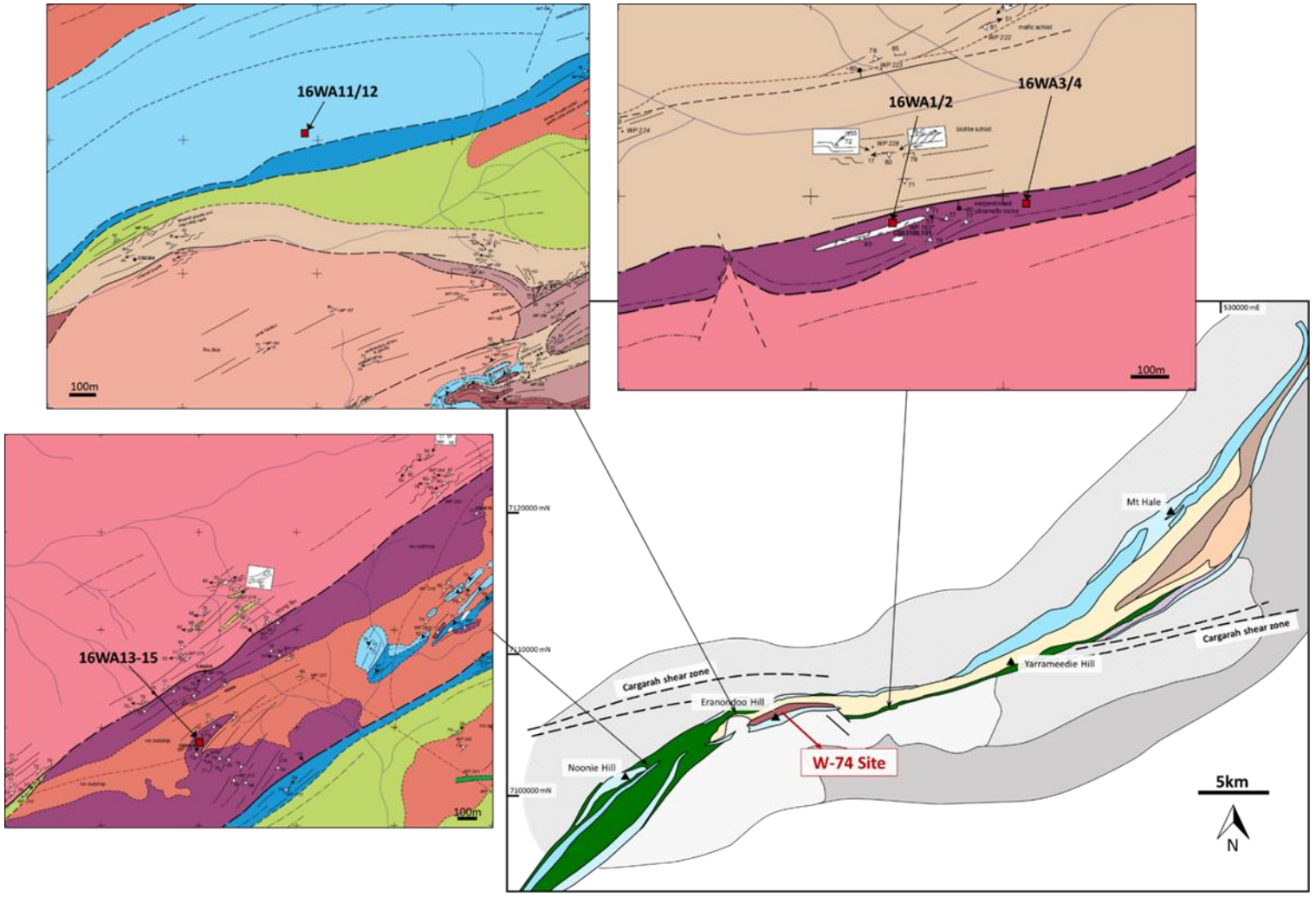

Figure 2.2: Sampling locations of metamorphosed ultramafic rocks sampled during the 2016 field season, modified from Spaggiari, 2007. Please see this publication for a more detailed explanation of colour coding: blue= BIF, pinks= granitoids and granitic gneisses, browns= metasediments, green= mafic schists and ultramafics

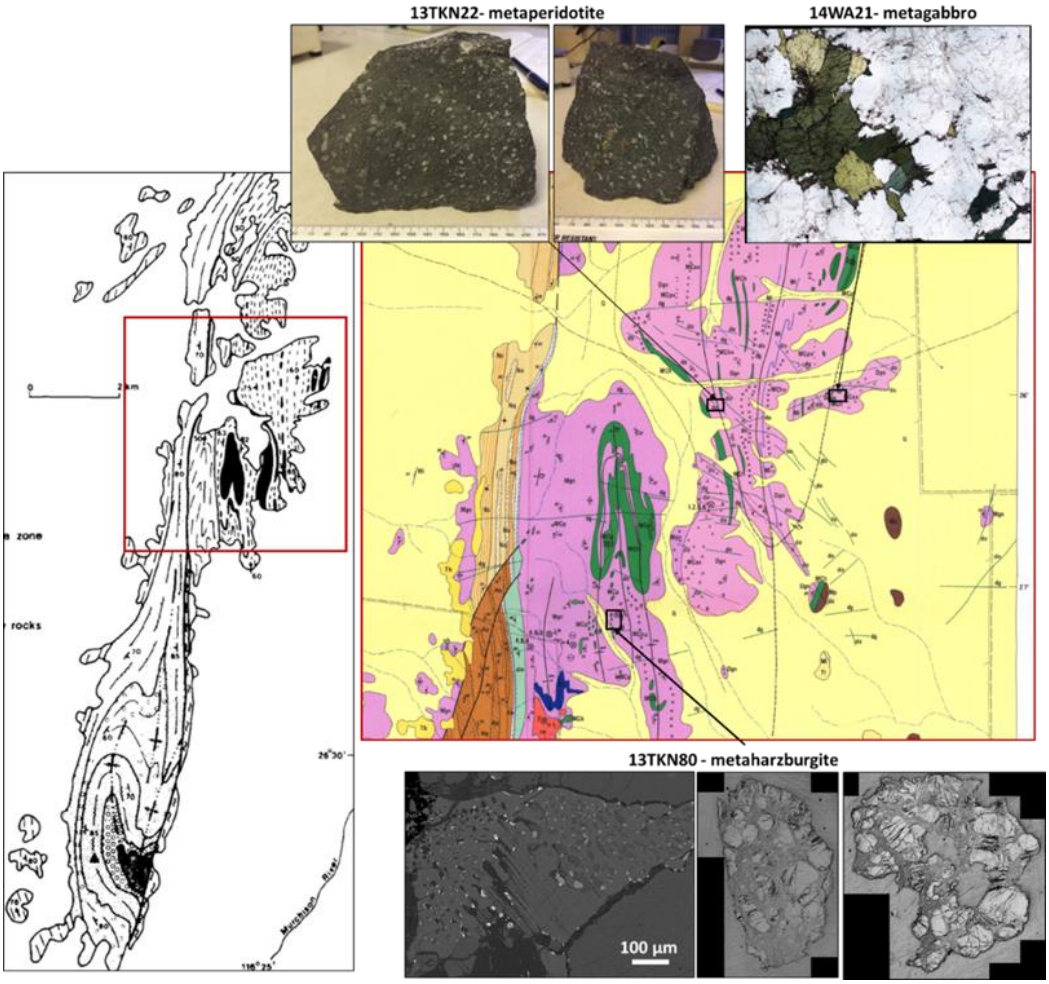

Figure 2.3: Sampling locations of mafic and ultramafic lithologies sampled from the 3730 Ma Manfred Complex. Greyscale map modified from Williams and Myers (1985), while coloured map is modified from Williams and Myers, 1987. Pinks= granitic gneisses, green= Manfred Complex, browns= metasediments and yellow= drift cover. 14WA21 metagabbro XPL image supplied by Danny Stubbs.

2.3 Sample descriptions

2.3.1 Jack Hills metasediment samples

This section details samples of metasedimentary rocks that were collected from at or near the W-74 site during fieldwork at Jack Hills in 2014 and 2016. Broad descriptions, including details of detrital and authigenic phases within sediments, are given in this section and a summary of data is shown in Table 2.1. Thin sections were available for 14WA1-4: as such *in-situ* descriptions were undertaken in greater detail. Modal proportions of chromites in these samples were calculated by area of total thin section. Descriptions of 16WA metasediments were undertaken by studying *ex-situ* heavy mineral separates, and so quantitative modal proportions could not be determined.

Detrital chromites derived from metasediment at the W-74 site show a spectrum of rounding shapes, and are classified here as euhedral octahedra (EO), rounded octahedra (RO) or rounded grains (RC–

rounded chromite). EO yield minimal rounding on two or fewer faces, with many euhedral grains showing little or no evidence of sedimentary transport. RC grains demonstrate limited indication of original octahedral habit on two or less faces and are often present as highly spherical morphologies. RO are grains with morphologies between rounded and euhedral chromite. RO are the most abundant morphology of grains within Jack Hills metasediments, with highly spherical and highly euhedral grains least the abundant. Within 14WA2, RO are further split into a scale of 1-4, with 1 representing the most rounded RO, and 4 representing the most euhedral RO.

14WA1- pebble metaconglomerate

14WA1 was sampled as a loose boulder sat directly on the original W-74 outcrop (Figure 1.2e/Figure 2.1). It consists of strongly elongated quartzite pebbles within an anastomosing matrix of finer (≤100 µm) quartz and fuchsite. Accessory phases include chromite, zircon, anhedral iron oxides, cubic crystals of layered quartz and iron oxide, rutile, and rare monazite. Rare, finer grained iron oxide-quartz banded pebbles are also present, which host ~1 wt. % Fe-Ni sulphide. Thin section analysis of this sample indicates chromites are dominantly <200 µm and account for 0.05% of the total thin section, or 0.25-0.5% of the matrix. Detrital chromites display the full range of chromite rounding shapes, from RC to EO. Detrital zircons occur as brown to lilac crystals that typically range in size from ~100 µm to ~200 µm. Most zircons appear have undergone some form of rounding, though many preserve more euhedral prismatic and pyramid morphologies (e.g. Corfu et al., 2003). Zircons in 14WA1 are generally stubby in morphology, with needle-like zircons commonly observed within rapidly crystallised granitoids and gabbros absent. Approximately 140 zircons were picked from this sample: 14WA zircon mounts were created by Ben Brennan and Bruno Dhuime during a Masters project at the University of Bristol, and so it is unclear if this lower number of grains in comparison to other samples is truly indicative of a lower zircon modal abundance.

14WA2- pebble to cobble metaconglomerate

14WA2 is a pebble-cobble metaconglomerate sampled downhill from less prominent metasediments than at the W-74 site. While it yields flattened quartzite pebbles with often sigmoidal morphologies, the height-length aspect ratio appears to be greater than in other samples (Figure 2.5), indicating this metasediment has undergone less strain or quartzite recrystallisation during deformation. 14WA2 yields the same accessory phases as 14WA1, but with the addition of rare pyrite and a dramatic increase in the proportion of cubic iron oxides: the reddish-brown colour of some cubic phases within this sample suggests they are composed of hematite, though many black examples are present that are likely magnetite. The layered internal morphologies of these cubic iron oxides indicates they may represent the replacement of cubic pyrite. All chromite morphologies are present, but there is a slight

decrease in the proportion of euhedral octahedral compared to other, finer-grained samples. 14WA2 represents the sample with the coarsest and highest modal abundance chromite, with thin section analysis suggesting chromite account for 0.24% of the WR, or ~2.5% of matrix. Approximately 300 zircons were picked from 14WA2, which are slightly coarser in grain size, suggesting the higher modal proportion of detrital chromites is mirrored by detrital zircons. Zircons are again largely stubby in morphology, though a few grains possess significantly higher length-to-width ratios, indicating more elongate morphologies are present within this sample (e.g. Supplementary Material 11; grains 14WA2-137, 221 and 256). Well rounded zircons are again present, with clear truncation of oscillatory zoning indicating an origin of rounding by sedimentary reworking, rather than metamorphic disequilibrium, which typically produces "soccer ball" zircons (e.g. Corfu et al., 2003).

14WA3- pebble metaconglomerate

14WA3 yields heavily flattened quartzite pebbles and is distinctly less fuchsite rich than other samples from the W-74 outcrop. It consists of accessory chromite, zircon, iron oxide, rutile and monazite. Chromite within this sample show a dramatic drop in the proportion of euhedral morphologies, even compared to coarser-grained 14WA2, with rounded chromite becoming the dominant rounding shape. There is also a large increase in detrital zircons with inclusions and rims of xenotime, monazite and amorphous iron, with the density of such inclusions likely retaining zircon in heavy fractions during processing. The two thin sections analysed of 14WA3 yield very similar modal proportions of chromite in both the WR and matrix, averaging at 0.025% and ~0.24-0.26%, respectively. This is the lowest modal proportion of chromite within Jack Hills 14WA1-4 metasediments. A slightly higher number of zircons was picked from 14WA3 than 14WA1, though grains from this sample appear darker brown in transmitted light, and generally are darker in cathodoluminescence (CL) images. A detailed study of inclusion assemblages within these zircons was also undertaken during the Masters thesis by Ben Brennan at the University of Bristol, who found inclusion assemblages dominated by quartz, with more minor feldspar, Fe-Ti oxides, and apatite.

14WA4- Granular quartzite to pebble metaconglomerate

14WA4 represents the finest grained of the 14WA4 samples, and in places is clearly a granular quartzite rather than metaconglomerate (Figure 2.5). Variation in clast support means that the matrix is more heterogeneous than in metaconglomerates: the matrix also contains appreciable K-feldspar, which appears to have modified largely to muscovite and fuchsite. Chromite and zircon dominate the budget of accessory minerals. Monazite is also coarser and more abundant than in other 14WA samples. Cubic reddish-brown crystals remain abundant, as do cubic and anhedral magnetite, and monazite-xenotime-Fe bearing zircon. As with quartzite 16WA7, chromites within 14WA4 are finer

grained and more euhedral than other samples, though the proportion of EO is less than 16WA7 and more similar in proportion to 14WA1. Analysis of a single thin section suggests that 14WA4 chromites are present at 0.026% of the WR, and ~0.4-0.5% of the matrix, which is more heterogeneously distributed than other samples. Zircons are present as lilac-brown crystals with a range of rounding shapes.

Figure 2.4: Sampling locations of 16WA metasediment samples. Red outlined closer pictures of 16WA5, which was taken from shrapnel of a previous hammer site (note the fresh interior surface of metaconglomerate) and 16WA9 also provided. 16WA9 inset also provides a clear view of the typically green, fuchsite-rich colouration of many metasedimentary units at Jack Hills. 16WA6, 7 and 8 were collected as loose boulders: boulders were deemed of sufficient size to have not travelled far from their original location.

Sample Location	Lithology	Fuch-rich?	Access. phases	Trace phases	Chromite morphology	Chromite grain size	Zircon morphology	Zircon grain size
14WA1	Pebble metaconglomerate	Y	Chr, zrc, FeOx	Qtz/FeOx intergrowths, rut, mon, sulph	RC-RO-EO. RO most abundant	<200 µm	Stubby prismatic, some rounded	100-200 µm
14WA2	Pebble to cobble metaconglomerate	Y	Chr, Zrc, FeOx, Qtz/FeOx intergrowths	Rut, mon, sulph, pyr	RC-RO-EO. RO most abundant.	~200 µm	Stubby prismatic, often rounded. Trace elongate.	~200 µm
14WA3	Pebble metaconglomerate	Y	Chr, zrc, FeOx, Qtz/FeOx intergrowths	Rut, mon	RC-RO-EO. >abundance EO	<200 µm	Stubby prismatic, often rounded. Trace elongate	<200 µm
14WA4	Granular quartzite to pebble metaconglomerate	Y	Chr, zrc, FeOx, Qtz/FeOx intergrowths, mon	rut	RC-RO-EO	<180 µm	Stubby prismatic, often rounded. Higher prop. elongate	<180 µm
16WA5	Pebble metaconglomerate	Y	Chr, zrc, FeOx	Qtz/FeOx intergrowths, sulph	RC-RO-EO	~200 µm	Stubby prismatic, often rounded. Minor elongate	~200 µm
16WA6	Pebble metaconglomerate	N	Chr, zrc, FeOx	Qtz/FeOx intergrowths	RC-RO-EO	<200 µm	Stubby prismatic and >proportion elongate. Often rounded.	<200 µm
16WA7	v.coarse to granular quartzite	Y	Chr, zrc, FeOx	-	RC-RO-EO	≤150 µm	Elongate prismatic, some needle like. Often rounded.	≤150 µm
16WA8	Pebble metaconglomerate	Y	Chr, zrc, FeOx	Qtz/FeOx intergrowths	RC-RO-EO	~200 µm	Stubby prismatic, often rounded. Higher prop. elongate	~200 µm
16WA9	Pebble metaconglomerate	Y	Chr, zrc, FeOx	Qtz/FeOx intergrowths, sulph	RC-EO dominant, minor RO	~150µm (EO) ~200µm (RC)	Stubby prismatic, often well rounded. Some elongate.	≥200 µm
16WA10	Pebble metaconglomerate	N	-	Chr, zrc, FeOx, sulph	RC-EO dominant, minor RO	~150µm (EO) ~200µm (RC)	Stubby prismatic, often well rounded. V. minor elongate.	≥200 µm

Table 2.1: Summary of sample descriptions for metasediment samples 14WA1-4 and 16WA5-10. Fuch = fuchsite (Cr-mica). Grain size of both chromite and zircons refer to the average diameter of either phase within the sample.
Mineral abbreviations: chr=chromite, zrc=zircon, FeOx=iron oxide (magnetite/hematite), Qtz/FeOx intergrowths= Layered quartz and iron oxide intergrowths, rut=rutile, mon=monazite, sulph= sulphide of unknown composition, pyr=pyrite.
Chromite morphologies: RC=rounded chromite, RO=rounded octahedral, EO= euhedral octahedral. See main text for further details.

16WA5- pebble metaconglomerate

16WA5 represents ~1.5 kg of sample taken from the remnants of a freshly fallen/hammered section of metaconglomerate. This samples was taken close to 14WA2, slightly below and to the NE of the W-74 site (Figure 2.1; 2.4). 16WA5 yields variably recrystallised and flattened quartzite clasts within a strongly aligned, sugary white-brown matrix with abundant fuchsite (Figure 2.5). Similar to 14WA2, many quartzite pebbles retain high height: length aspect ratios. Chromite and zircon are the most abundant accessory phases, and chromites are present as the full range of morphologies, from RC to EO. Chromites are similar in grain size to 14WA2, though 500-250 µm grains are less abundant. Zircons are abundant within 16WA5 and present as optically clear, lilac crystals with diverse rounding morphologies (see Supplementary Material 11). Zircons are typically 200 µm to 250 µm in size, though many are 100 µm to 200 µm.

16WA6- pebble metaconglomerate

16WA6 was collected as a 2.5kg of loose pebble metaconglomerate, slightly downhill from and to the NE of 14WA2 and 16WA5 (Figure 2.1 and 2.4). It is strongly foliated with variably flattened and recrystallised quartzite clasts, and is poorer in fuchsite than surrounding metaconglomerates. Rather than lesser influence of hydrothermal fluids, the scarcity of fuchsite appears to represent a low abundance of chromite, which is not as pervasive within 16WA6 as high modal proportion samples such as 14WA2 and 16WA5. Chromites are again present as all rounding morphologies, from RC to EO. Detrital zircons were also not particularly abundant within 16WA6, despite significantly more metasediment being crushed for this sample than 16WA5, and zircons were typically slightly finer in size than 14WA2 and 16WA5, with most ≤200 µm.

16WA7- very coarse to granular quartzite

16WA7 is finer grained than all other samples, and represents a quartzite with a typically sugary texture, or a very fine metaconglomerate (Figure 2.4 and 2.5). 16WA7 was the first sample taken a distance from the traditional W-74 site (Figure 2.1), being sampled as a loose pebble ~35m to the WNW. Quartzite clasts are fine grained in comparison to other Jack Hills metasediments (≤ 2 mm) or rarely present as granular (2-4 mm) to pebble grain-sized clusters. Low abundance clasts of chert are granular in size. Prevalent bright green, Cr-rich fuchsite veins are readily observed cross-cutting the metasediment sample (Figure 2.5), likely correlating with areas of greater modal proportions of chromite. Chromite and zircon are typically much finer (≤150 µm) and possess more euhedral habits, with EO morphologies dominating chromites. Within zircon this manifests as dominantly optically clear lilac crystals with very high length:width aspect ratios. These zircons are typically dark in CL images with disturbed internal zoning.

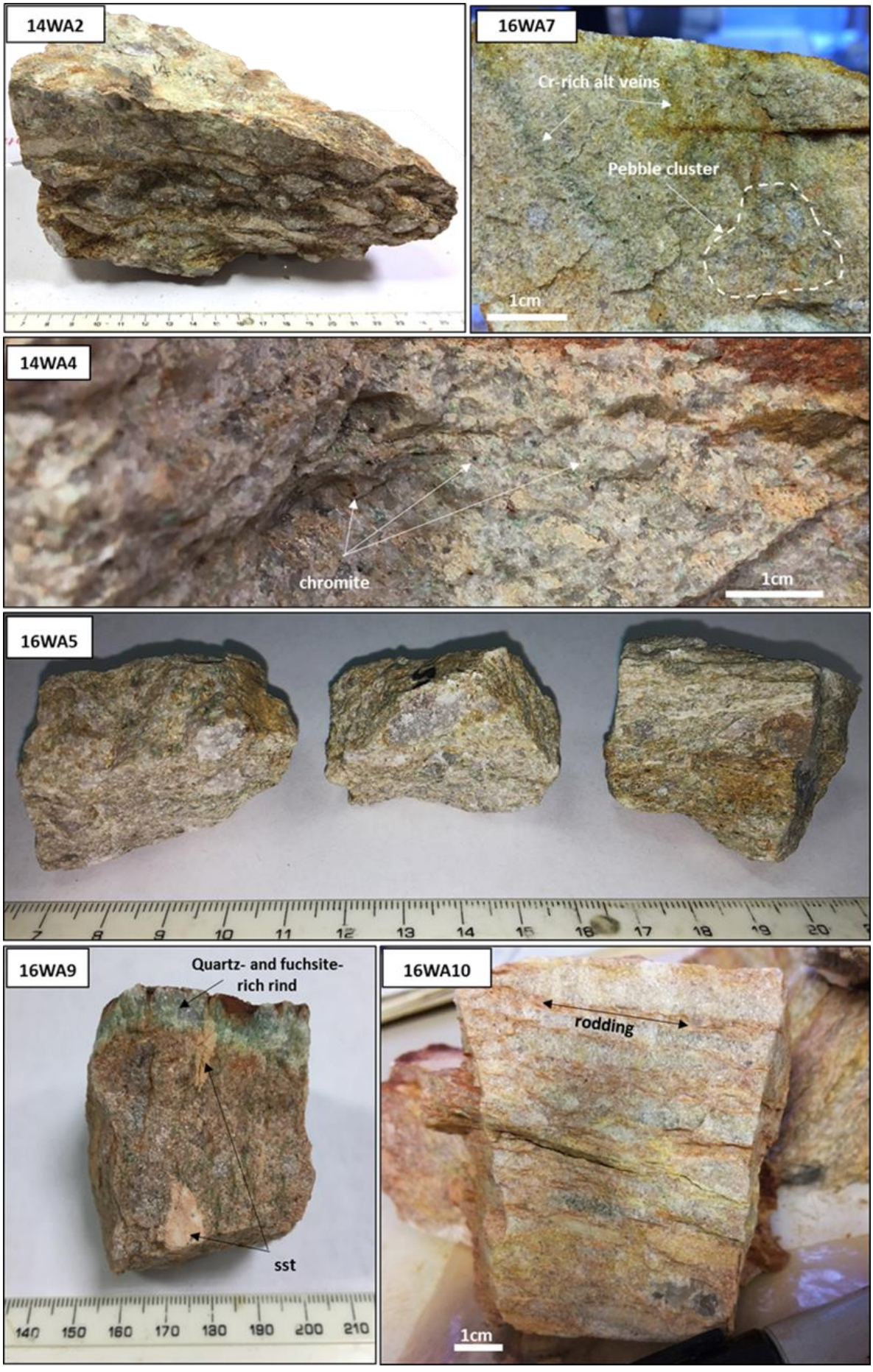
14WA2
16WA7
Cr-rich alt veins
Pebble cluster
1cm
14WA4
chromite
1cm
16WA5
16WA9
Quartz- and fuchsite-rich rind
sst
16WA10
rodding
1cm

Figure 2.5 (previous page): Close up images of 14WA and 16WA metasediments samples from at or near the W-74 site. **Sst**= sandstone. 14WA4 and 16WA5 are pebble metaconglomerates. 14WA4 and 16WA7 are more quartzitic. A fuchsite rich band (coincident with increased proportion of chromite?) is also shown for reference. 16WA9 and 16WA10 were sampled away from the W-74 site. Note deformation-derived rodding of quartzite pebbles within 16WA10.

16WA8 – pebble metaconglomerate

16WA8, sampled to the SW of the W-74 site (Figure 2.1), is a pebble metaconglomerate, with a slightly finer clast size than 14WA2 and 16WA5. It yields strongly aligned, flattened and recrystallised quartzite pebbles set in a finer grained, anastomosing matrix of quartz and muscovite. Coarse chromites within surrounding fuchsite are easily discernible within 16WA8 without the use of a hand lens. Chromites and zircons within 16WA8 are coarser (200 µm-250 µm dominant) than finer grained metasediment samples such as 14WA4 and 16WA7, and more similar in size to detrital phases within 14WA2 and 16WA5, although at slightly lower modal proportions. Zircons are lilac to brown in colour, and of a similar grain size to 14WA2. However, unlike zircons within 14WA2, detrital zircons within 16WA8 possess abundant and large inclusions. Inclusions are dominantly composed of quartz and muscovite (e.g. Hopkins et al., 2010; Rasmussen et al., 2011; Bell et al., 2015), with minor apatite, monazite, xenotime and iron oxide.

16WA9 and 16WA10- pebble metaconglomerate

16WA9 and 16WA10 are two samples taken from across the valley to the NE of the W-74 site (Figure 2.1 and Figure 2.4). Both 16WA9 and 16WA10 yield clear discrepancies from W-74 samples. Both samples are distinctly reddish in colour, punctuated by green fuchsite (Figure 2.5). While such colouration is less pronounced in the interior of 16WA9-10, it is distinctly different to W-74 metaconglomerates. There is also a pronounced increase in clasts of sugary, fine-grained sandstone or chert clasts, which yield apparent reduction spots. These are present with clasts of quartzite, darker polycrystalline quartz, and banded iron formation (BIF). This indicates 16WA9 and 16WA10 are less mature than those sampled at the W-74 site. Despite being sampled within three meters of one another, 16WA9 and 16WA10 also yield subtle differences.

16WA9 has an exterior rind rich in quartz and fuchsite, within which coarse grained chromites are easily discernible. 16WA10 yields distinctly rodded clasts of quartzite, indicating higher strain (Figure 2.5). Such features are absent within 16WA9, indicating meter-scale variability in strain. 16WA10 is also far less fuchsitic that 16WA9 and is resultingly poorer in detrital chromite. Chromites from these two samples are also different from those at the W-74 site, yielding heavily bimodal morphologies: RO is far rarer within both 16WA9 and 16WA10, whilst RC and EO dominate. At ≥200 µm, zircons from 16WA9 and 16WA10 are generally coarser grained than zircons from the W-74 site, and often possess

a distinctly reddish-brown appearance. This colouration correlates with darker CL grains, indicating it is likely a result of higher U concentration. Also unlike grains from the W-74 site, both samples yield appreciable proportions of grains with near-spherical morphologies, suggesting extensive transport. Such morphologies are only very rarely observed at the W-74 site.

2.3.2. Jack Hills ultramafics

16WA13

16WA13 was sampled from the southwest limb of the Jack Hills supracrustal belt (Figure 2.2), and is a heavily recrystallised ultramafic with no retained primary silicate assemblage. Minor chlorite is present, and the predominance of serpentine indicates this sample was once olivine-rich. Relict crystals are outlined by serpentinisation-derived magnetites, and indicates this sample possessed a ≥1 mm grain size (Figure 2.6c). Despite complete loss of primary silicates, 16WA13ii retains significant quantities (modal proportion approximately 1 %) of chromite. However, chromites have coarse ferritchromit and magnetite rims (Figure 2.6 a-b), with strongly embayed primary cores. This may indicate the trivalent cation compositions of cores has also been compromised. Such strong textural development of secondary rims is generally only present in chromites that have undergone amphibolite facies metamorphism (Barnes, 2000), suggesting at least ultramafics within the SW limb of Jack Hills have reached this metamorphic grade. The texture of relict chromites within 16WA13ii is however very interesting, with 'stringers' of aligned chromites (Figure 2.6c). The preservation of relict silicate grain boundaries within this sample suggests relict chromite stringers are unlikely to be an effect of deformation: such features would have been lost or severely flattened. Chromite stringers may therefore represent relict magmatic textures.

2.3.3. Manfred Complex mafics and ultramafics

13TKN80

Metaharzburgite 13TKN80 was sampled to the NE of Mount Narryer, just south of the largest, folded component of the disseminated Manfred Complex (Figure 2.3). 13TKN80 is medium to coarse grained, with a magmatic mineralogy consisting dominantly of Cr-rich orthopyroxene, with more minor olivine (Fo84-Fo85; Rowe, 2016), poikilitic clinopyroxene and spinel. This sample has been partially recrystallised to serpentine, with preferential replacement of olivine (often producing pseudomorphs), and along the margins and exsolution planes of pyroxenes. The modification of some spinels to magnetite also shows this. The distribution of serpentinisation is heterogeneous, but typically accounts for greater than 20% of the sample. Metamorphic phases are absent. Spinel is present as both spinel *sensu-stricto* and Cr-spinel (or picotite). Coarser crystals (>40 μm) within olivine

and pyroxenes (Figure 2.7a-c) are likely primary magmatic (i.e. crystallised on the liquidus) in origin, though spinel is more commonly observed as an exsolution product of both orthopyroxene and clinopyroxene (Figure 2.7c). Coarser spinels also show evidence of late-magmatic or sub-solidus growth (Figure 2.7c), indicating their elemental compositions will have equilibrated with surrounding silicates. Mantling of olivine also suggests that at least some spinel formed after the crystallisation of this phase (Figure 2.7d). Abundant exsolution textures within both pyroxene of spinel indicate pyroxenes were Al-rich when crystallising. This may indicate mid to deep crustal emplacement depths, with stalling of plagioclase crystallisation allowing Al to partition into pyroxenes. However, this may also be a consequence of increased volatile content. Evidence of sub-solidus growth (Figure 2.7c) and the coarse grain size of 13TKN80 also indicate slow cooling of this sample.

13TKN22

Metaperidotite 13TKN22 was also sampled from the NE of Mount Narryer (Figure 2.3). This sample is heavily recrystallised to a serpentinite, though still possess a relict porphyritic texture. Magmatic pyroxene has been modified to Na- and K- poor amphibole, with clear 120:60˚ cleavages (Figure 2.8a). While amphiboles were only analysed using EDS, the Mg- and Ca- rich compositions of 13TKN22 amphiboles indicate they belong to the calcic amphibole group, with Al- bearing and Mg- rich hornblende likely to represent the dominant amphibole type. The presence of tremolite rims on hornblende (Figure 2.8b) indicates that 13TKN22 reached amphibolite facies, before retrogressing to greenschist facies. The presence of relict clinopyroxene and replacement amphibole indicates the now recrystallised phenocrysts were originally pyroxene-group minerals, perhaps orthopyroxene due to this minerals higher susceptibility to serpentinisation. Spinel group minerals are present as chromites within 13TKN22: coarser grains are observed within hornblende or serpentine pseudomorphs (Figure 2.8c-d), while finer, Cr-rich chromites are observed within phenocryst pseudomorphs. A single olivine inclusion within chromite (Figure 2.8c) yielded a composition of Fo84, in good agreement with harzburgite 13TKN80 (Rowe, 2016). Olivine-spinel geothermometry (using the equations of Ballhaus et al., 1991) yield an equilibrium temperature of ~460 °C, indicative of upper greenschist to lower amphibolite facies metamorphism, rather than magmatic equilibration. Finally, this sample again indicates strong evidence of sub-solidus chromite growth (Figure 2.8d), and this, coupled with the medium grain size of serpentine pseudomorphs, slow cooling.

14WA21

14WA21 is also sampled from the NE of Mount Narryer (Figure 2.3) and is a medium to coarse-grained metagabbro composed of hornblende and plagioclase. Minor apatite is also present. While retaining a magmatic crystallisation texture, primary pyroxene within this sample has undergone static

recrystallisation to hornblende (Figure 2.3). The presence of hornblende also suggests that 14WA21 has reached amphibolite facies, though it can be definitively stated this sample reached at least greenschist facies. Spinel group minerals are apparently absent from this sample, though no detailed SEM investigations have been undertaken within this study.

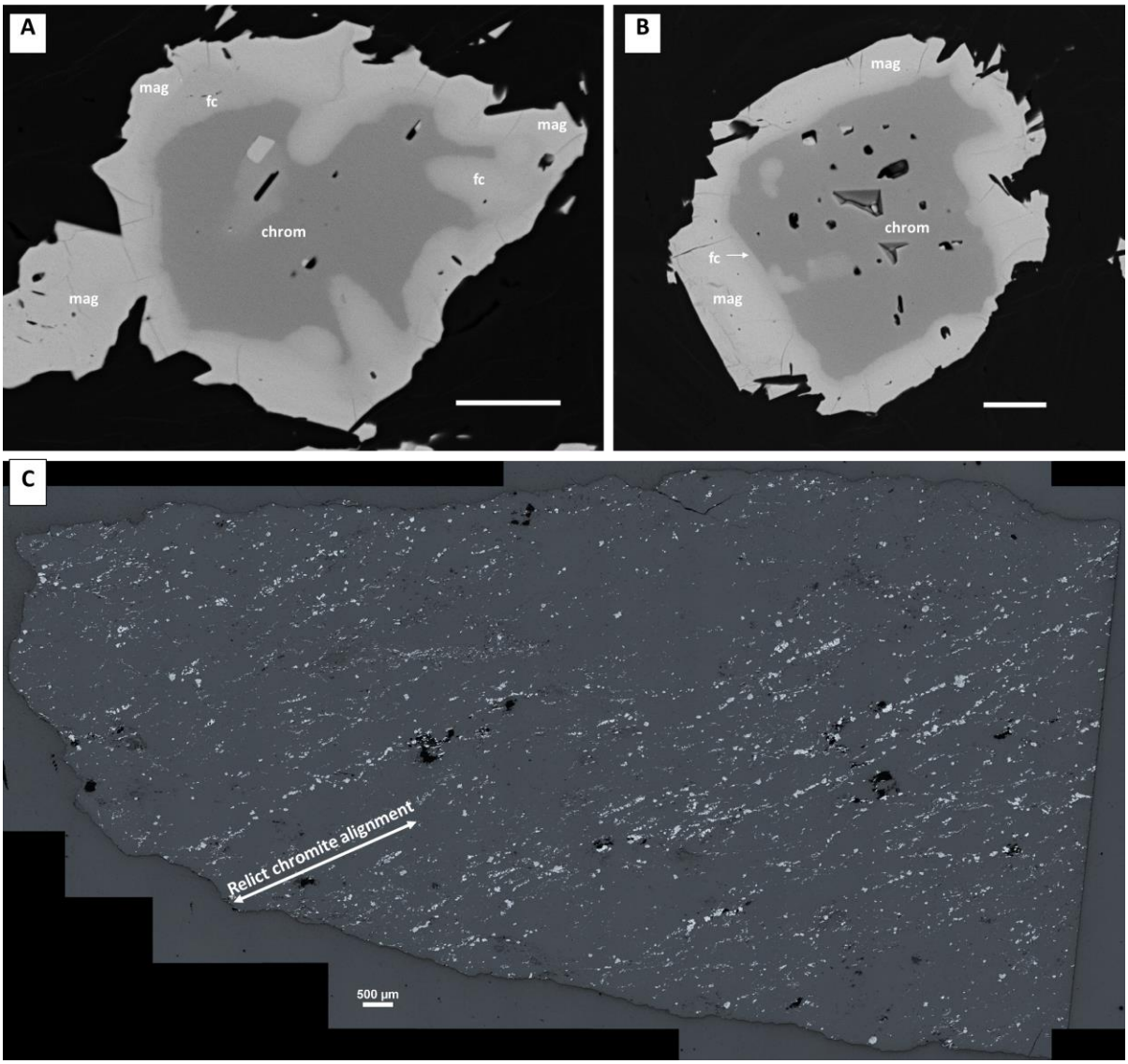

Figure 2.6: 16WA13. **A)** BSE image of heavily embayed chromite (chrom) core with thick ferritchromit (fc) and magnetite rims. Scale bar 20 µm. **B)** BSE image of another relict chromite core, but with a substantially thinner ferritchromit rim. Scale bar 20 µm. **C)** Reflected light mosaic of texturally unusual chromite 'stringers' in serpentine and chlorite matrix. Every >50 µm light grey crystal in this image is a relict chromite.

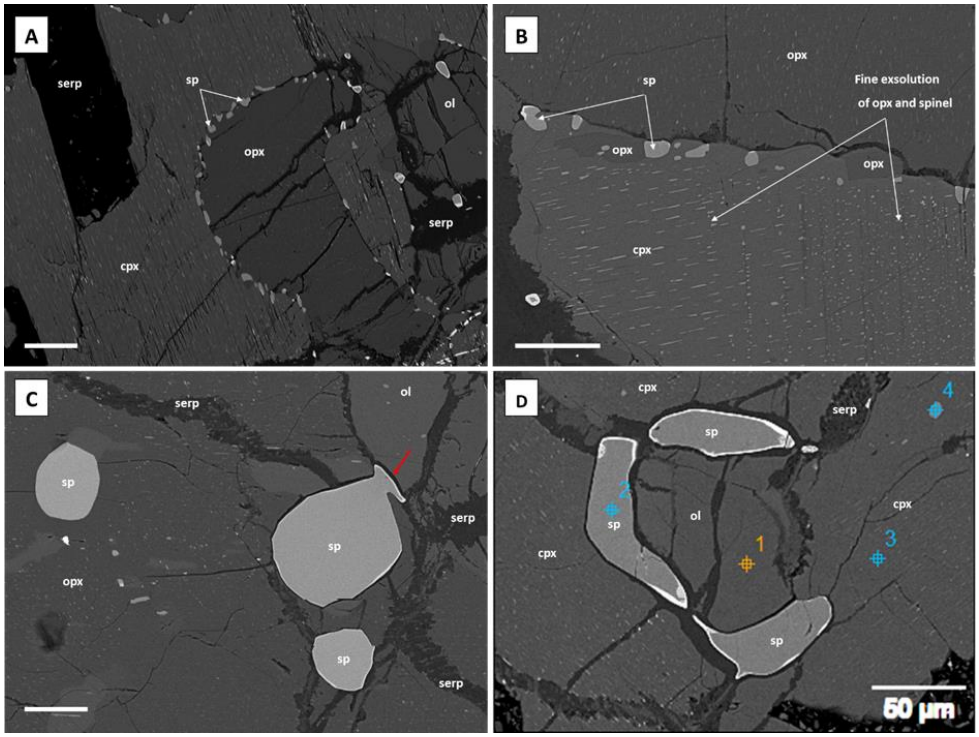

Figure 2.7 (above): BSE images of 13TKN80. **A)** Typical mineralogy of 13TKN80, including orthopyroxene (opx), clinopyroxene (cpx), olivine (ol), serpentine (serp) and spinel (sp). Both pyroxenes show abundant exsolution of one another and spinel, indicating an originally Al-rich composition. **B)** Spinel and opx (darker grey) exsolution within cpx (lighter grey). Exterior spinels are still likely exsolution products as finer exsolution is absent around them. **C)** Coarser, likely liquidus spinels within opx and bordering olivine. Overgrowth on coarsest spinel marked with red arrow. **D)** Poikilitic spinel encapsulating olivine. Note the fine magnetite rims where spinel is in contact with serpentine. All scale bars 50 µm.

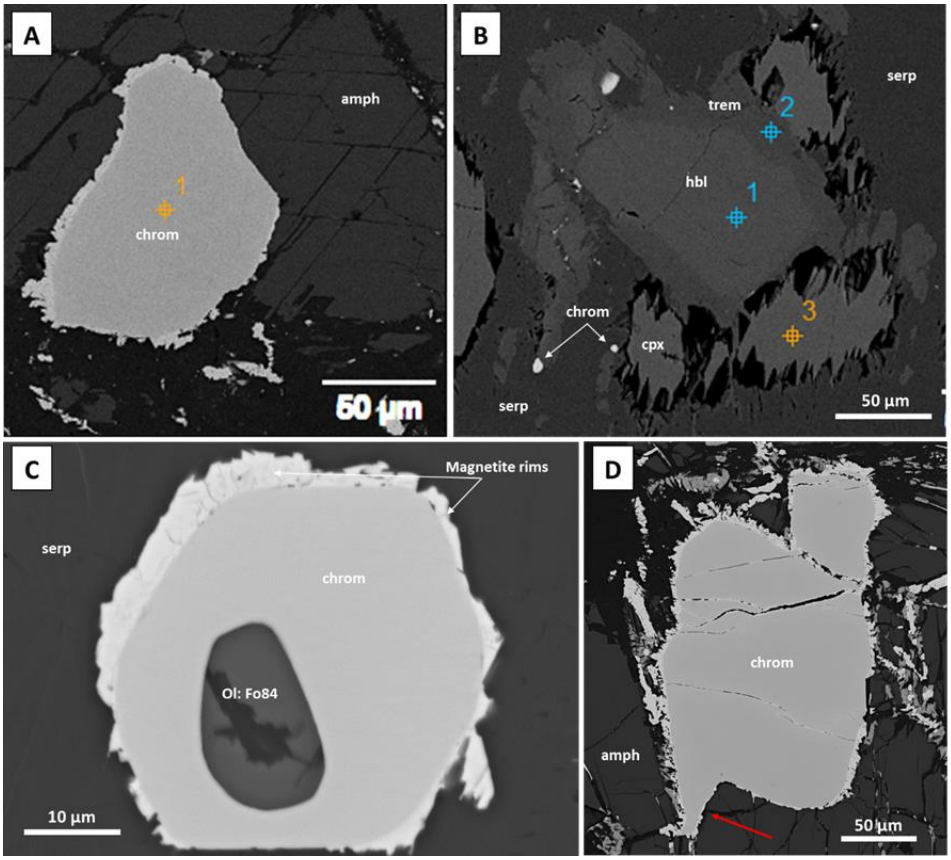

Figure 2.8 (previous page): BSE images of 13TKN22**. A)** Chromite (chrom) with minor magnetite rim in unanalysed amphibole (amph). Note the well defined 120/60 cleavage of the amphibole. **B)** Hornblende (hbl) and with suspected tremolite (trem) rims within a relict phenocryst now replaced by serpentine (serp). Ragged edged clinopyroxene (cpx) also present, indicating a soft phase has perhaps been lost during polishing. Very fine (<10 µm) chromites are also present. **C)** Olivine (ol) inclusion within chromite. Note the well-developed magnetite rims of this chromite in comparison to A), likely due to its smaller grain size and position within serpentine rather than amphibole. **D)** Coarse chromite within amphibole and serpentine. Clear overgrowth texture noted by the red arrow, indicative of sub solidus or late magmatic growth.

2.4. Sample Processing

2.4.1. Initial Processing

14WA1-4: Jack Hills metasediments

Processing of 14WA metasediments was undertaken by Ben Brennan and Bruno Dhuime at the University of Bristol, during a Masters project undertaken prior to this study. 14WA1-4 metasediments were split, crushed using a tungsten carbide jaw crusher, and then sieved into 500-250 µm, 250-120 µm and 120-50 µm size fractions. Density separation of metasediments was performed using a Wilfley table to separate out heavy mineral phases, namely zircon and chromite, and remove the light phases such as quartz and muscovite, which dominate the modal mineralogy of metasediments. Magnetic separation was undertaken at this time to remove the bulk of iron oxides. Final purification of heavy separates was achieved using heavy liquid separation, enabling greater separation of zircon and chromite.

16WA5-10: Jack Hills metasediments

16WA5-10 metasediments were split using a plastic wrapped splitter, or manually broken apart using a plastic-wrapped hammer to avoid metal contamination. Metasediments were then crushed using a tungsten carbide jaw crusher, and rinsed to remove fine organics and clays. Crushed samples were then hand-sieved into 500-250 µm and <250 µm size fractions. As the Wilfley table was not available for use, heavy mineral separates were collected by panning. This process was repeated twice to produce higher yields of heavy minerals. Magnetic or heavy liquid separation was not undertaken, and so chromites, zircon and iron oxides were present within the same heavy mineral separates.

16WA whole rock (WR) and Manfred Complex samples

16WA samples collected during 2016 fieldwork were sawn to remove weathering rinds and increase transportability prior to shipping. Manfred Complex samples were shipped at the same time: 13TKN22 and 14WA21 consisted of single large samples from which weathering rinds had been removed. 13TKN80 was shipped coarsely crushed, with fragments approximately 2 cm in size. Samples for SEM and EPMA analysis were then partially broken using a plastic wrapped hammer until fragments of a

suitable size for epoxy mounts were recovered. 16WA lithologies that were used for WR isotopic analysis were manually split, before being crushed in a tungsten carbide jaw crusher. Once crushed to a uniform size, samples were milled to powder using a metal-free agate ball mill. The ball mill was cleaned with ethanol and low-Fe sand prior to milling of individual samples. As Manfred Complex ultramafics were observed to be medium to coarse grained, approximately 150 grams of 13TKN80 and 14WA21 were milled to achieve powder homogenisation.

2.4.2. Pre-analytical procedures for zircon

Zircons for Pb-Hf analysis were hand-picked under a binocular microscope from heavy mineral separates. Care was taken, in both this study and for those picked for the masters project, to pick grains of different sizes and morphologies to yield the most complete spectrum of data. Approximately 200-250 zircons were picked per sample, with the assumption that approximately half of the grains would be suitable for analysis. Zircons were mounted in ~20 x ~10 grids and covered with an ideal mixture of EpoFix low viscosity resin and EpoFix hardener, which was then left for ~24 hours to dry. Once removed from mounting tape, the epoxy mount was placed under a binocular microscope to check for bubbles, which if present were infilled with fresh epoxy and again left for approximately 24 hours. Bubbles were in-filled for maximum stability during later isotopic analysis via laser ablation.

Owing to the fine size and geological value of samples, a slow polishing procedure was developed for 16WA zircon mounts. Polishing began manually with 2000 and 4000 grade (~10 µm and ~5 µm grit size respectively) sand paper, and then samples were manually polished with 3 µm diamond paste, before a final 1 µm polish using the Buehler automated polisher. This was undertaken for ~2.5 to 3 minutes to produce a final polish on grains while not inducing any polishing topography on grains. New polishing pads were used for polishing of zircons to remove any potential sources of contamination. Further contamination risks were minimised by sonic bathing zircon mounts in isopropanol for ~5 mins between each polishing phase.

Zircon mounts were then imaged in transmitted light to characterise internal structures such as cracks and cloudiness prior to analytical point selection. Imaging for 14WA zircon mounts was undertaken using a transmitted light microscope at the NERC Isotope Geosciences Laboratories (NIGL) at the British Geological Survey (BGS), while 16WA zircon mounts were imaged using a transmitted light microscope within the Bristol Isotope Group (BIG) at the University of Bristol. Zircons that were clearly metamict, and therefore opaque within transmitted light, were avoided. Sub-surface cracks and inclusions that may perturb analysis could also be detected and avoided by imaging of zircons in transmitted light. Zircon mounts were then carbon coated and imaged using scanning electron microscope (SEM) techniques. Electron imaging was undertaken using a FEI Quanta 600 SEM at the

BGS and a Hitatchi S-3500N SEM at the University of Bristol. Electron imaging of mounts used cathode luminescence (CL) and back scattered electrons (BSE). BSE imaging allows careful characterisation of the 2D polished surface of grains, and can be used to avoid cracks and inclusions visible at the surface, as well as highlight clearly metamict domains. CL imaging measures the intensity of light, or luminescence, emitted from by trace elements within a phase: Dy^{3+} is the principal emitter within zircons (Corfu et al., 2003). CL imaging is used within zircons to show internal growth structures and estimate relative concentrations of U and REE. High U zircons appear dark in CL: U^{4+} is not only a CL inhibitor but where present in high concentrations may also cause radiation damage that inhibits luminesnce and results in low CL intensities (e.g. Corfu et al., 2003). These two imaging techniques are regularly used in conjunction when determining the best domains within zircons for in-situ analytical work (e.g. Hanchar and Miller, 1993; Schoene, 2014).

In this study, the three imaging techniques- transmitted, CL and BSE, were used in combination to determine the best analytical sites for analysis of Jack Hills zircons. Numerous studies have suggested that preferential sampling of the most definitively magmatic grains leads to the most robust isotopic analyses (Kemp et al., 2010; Whitehouse et al., 2017), particularly in ancient zircons such as those at Jack Hills. To emulate this, points were selected in the most optically clear portions of zircons, i.e. areas free of cracks and cloudiness. Those with clearly disturbed growth zoning (e.g. Corfu et al., 2003) were avoided in all sampled except 14WA2. Further to this, a further subset of grains was selected that retained oscillatory zoning, a definitively magmatic texture, with the presence of unblurred fine lamellae indicating limited diffusion of key elements. Points were also chosen on zircon domains ≥~40 µm across in order to fit the ~35 µm spot size required for Hf analyses. All spots chosen for in-situ isotopic analysis are shown in Supplementary Material 11, for both preliminary analytical work and the data presented in Chapter 5 of this thesis.

2.4.3. Pre-analytical procedures for chromite

Chromites were also hand-picked under a binocular microscope. For EPMA work, chromites were split by sample, grain size, and rounding shapes, so that any chemical variation observed could be correlated with any physical variability of grains. Chromites are often heavily associated with fuchsite and iron oxide: such chromites were also analysed via EPMA to determine if the crystallisation of fuchsite had significantly modified chromite chemistry. Furthermore, to observe any major and minor elemental differences between ex-situ chromites, likely derived from the matrix of metasediments, and those present within quartzite cobbles (Dare et al., 2016), cobbles were dissolved using concentrated SpA HF. This process left chromites (±zircon, sulphide, monazite) untouched but heavily leached. While chromites are significantly rarer within cobbles than in the matrix of metasediments,

13 chromite grains were successfully leached from quartzite cobbles, set within epoxy mounts, and their chemical compositions determined by EPMA ("leach HF" within Supplementary Material 1). A single chromite was observed within quartzite cobbles in a thin section of 14WA2: probe data is not reported for this grain owing to a low analytical total (97.16 %), likely as a result of surrounding fuchsite that had infiltrated the quartzite cobble.

Chromites were mounted into grids and set within epoxy, before being slowly polished using a similar methodology to the one described for zircons in Section 2.4.2. However, chromites proved much more challenging to polish than zircons, requiring significantly longer on a 3 µm diamond polishing pad to produce the required polish. As such, a Buehler automated polisher was used, with individual samples requiring between 10 minutes and 30 minutes at a pressure of 15 N to 20 N. Typically, those that were more heavily cracked proved harder to polish, though grains that possessed high Cr#s polish much more easily and to a smoother, less cracked appearance (Figure 2.9). Fuchsite also proved challenging to polish, often requiring extra stabilisation by in-filling with epoxy. Once polished, chromite epoxy mounts were imaged using reflected light microscopy and/or carbon coated and imaged microbeam techniques. Examples of these are provided in Figure 2.9.

2.5. Scanning electron microscopy and microprobe analysis

Chromite SEM Analysis

Electron imaging of detrital chromites was undertaken using the Hitatchi S-3500N variable pressure SEM at the University of Bristol. This was undertaken to observe any features such as cracks and inclusions that may perturb future analyses and highlight areas of further interest. Chromites were imaged using back scattered electrons (BSE). As the electron beam interacts atomic nuclei, some electrons are elastically scattered. Greater scattering of electrons is induced by nuclei of higher atomic number, resulting in a higher intensity recorded by the BSE detector. Phases that contain elements with higher atomic nuclei are denser, and therefore brighter within BSE images. BSE imaging is particularly effective at highlighting domains of high and low Cr# (see chapter 3). Where observed, inclusion assemblages within chromites were documented and analysed using a ThermoNoran energy dispersive spectrometer, allowing semi-quantitative analysis via energy dispersive spectrometry (EDS). An accelerating voltage of 20 kV was used in order to fully encapsulate the Kα and Kβ x-ray emissions for Zn, with a typical emission current of ~60 nA. EDS spectra were reduced and interpreted using Thermo Scientific NSS EDS software.

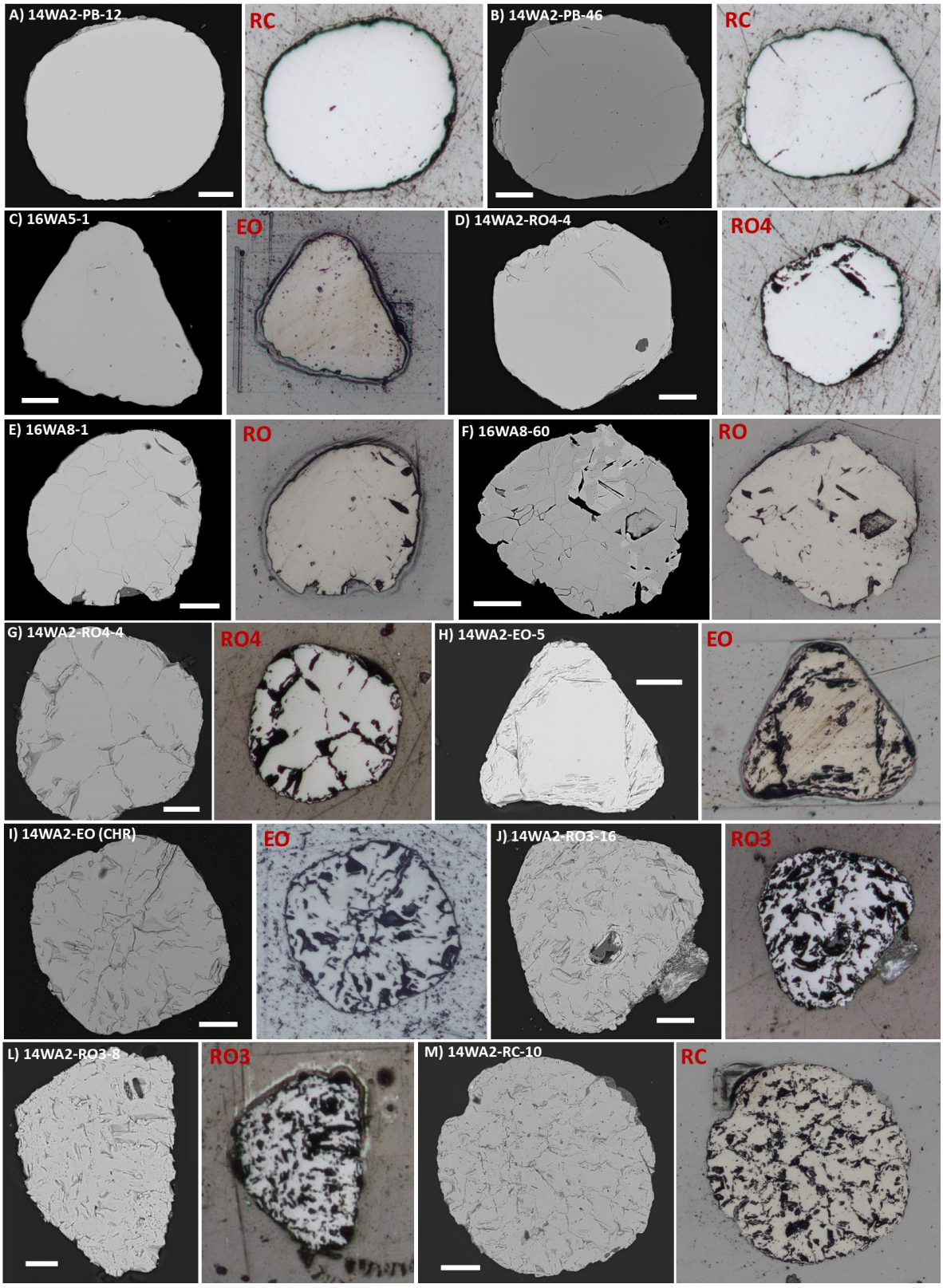

Figure 2.9: Examples of ex-situ chromites in both BSE (left) and the same grain in reflected light (right). A-D shows smoothly textured grains, with minimal to no cracks and inclusions. Note the apparently isolated fuchsite inclusions with (A) and (D). E-H shows progressively more texturally modified grains, with polygonal fracturing, minor embayment structures from recrystallisation during fuchsite growth (E) and high Cr# domains (F). I-M shows significantly more fractured and inclusion bearing grains. RC, RO (in 14WA2 1-4 to show variable rounding) and EO signifies the rounding shape of grains. All scale bars 50 µm.

Chromite EPMA

Chromite major and minor elements were quantified using the Cameca SX100 microprobe at the University of Bristol, which is equipped with 5 wave dispersive spectrometers (WDS). Cr, Al, Fe, Mg, Zn, Mn, Ti, V, Ni of chromites were analysed as oxides using a 20kV accelerating voltage and a 10nA faraday current. Emission currents were 60-100µA, while counting times consisted of 30 seconds for major elements (>~3 wt.%) and 60 seconds for minor elements. Si, Na and Ca were included within the set up to observe any silicate contamination, with analysis with >0.15 wt.% of these elements leading to the analysis being omitted. Na was not part of the analysis in samples with high Zn contents, owing to significant overlap of the Na Kα with the Zn Kβ. The overlap of Ti Kβ on V Kα was corrected online via analysis of V-free $SrTiO_3$, or via the use of high-resolution slits to separate Ti Kβ and V Kα wavelengths. Mineral and synthetic standards used for calibration are listed in Table 2.2. Secondary standards of known composition and that encapsulated the range of elements analysed, typically amphibole KK1 and a chromite mineral standard, were analysed prior to analysis of unknowns. The method of Droop (1987) was employed to stoichiometrically calculate the ferric iron content of chromite. The robustness of this calculation was monitored by measurement of four spinel standards (8316, 8311, 79-1 and 8315) from Wood and Virgo (1989) every ~20 analyses, which are well characterised for $Fe^{3+}/\sum Fe$ using both stoichiometry and Mossbauer analysis. While Cr-spinels 8316 and 8311 were generally well determined, spinels 79-1 and 8315 proved more challenging to derive consistent $Fe^{3+}/\sum Fe$ data for. Some Jack Hills samples yielded chromites with systematically low totals: the potential mechanisms of this feature are discussed in more detail in chapter 3. As such, only chromite with totals of 97.5-102 % are discussed in the forthcoming chapters.

EPMA line scans were also undertaken to assess the role of fuchsite crystallisation on chromite major and minor element chemistry. Initial analyses using the same set up conditions as chromite resulted in significantly lower alkali concentrations than expected (Zane and Rizzo, 1999). To circumnavigate this, a separate fuchsite set up was generated and run using a defocused electron beam. This was achieved using a spot size set to 10 µm, though this typically resulted in a ~6 µm beam diameter. Furthermore, as alkalis are less stable under an electron beam, these were analysed first to minimise their loss via migration. This was found to increase the alkalis within fuchsite to acceptable proportions (Zane and Rizzo, 1999; Rasmussen et al., 2012). A full fuchsite EPMA set up is also available in Table 2.2.

Table 2.2: Electron Microprobe conditions and calibration standards							
Element	**Oxide**	**Standard**	**Beam size (µm)**	**Spectrometer**	**Crystal**	**Count Time (s)**	**Background (s)**
CHROMITE							
Cr	Cr_2O_3	Cr_2O_3	1	1	LPET	30	15
Ti	TiO_2	Ilmenite[b]	1	1	LPET	60	30
Ca	CaO	Wollastonite	1	1	LPET	60	30
Mg	MgO	SJO	1	2	TAP	60	30
Fe	FeO	Ilmenite[b]	1	3	LLIF	30	15
V	V_2O_3	V metal	1	3	LLIF	60	30
Mn	MnO	Mn metal	1	3	LLIF	60	30
Si	SiO_2	SJO	1	4	TAP	60	30
Al	Al_2O_3	Albite[b]	1	4	TAP	30	15
Zn	ZnO	Zn metal	1	5	LLIF	30/60	15/30
Ni	NiO	Ni metal	1	5	LLIF	60	30
FUCHSITE							
Cr	Cr_2O_3	Cr_2O_3	5	1	LPET	60	30
Ti	TiO_2	Ilmenite[b]	5	1	LPET	60	30
Ca[a]	CaO	Wollastonite	5	1	LPET	10	5
K[a]	K_2O	Eifel Sanidine[b]	5	1	LPET	10	5
Mg	MgO	SJO	5	2	TAP	60	30
Fe	FeO	Ilmenite[b]	5	3	LLIF	30	15
V	V_2O_3	V metal	5	3	LLIF	60	30
Mn	MnO	Mn metal	5	3	LLIF	60	30
Si	SiO_2	SJO	5	4	TAP	30	15
Al	Al_2O_3	Albite[b]	5	4	TAP	30	15
Zn	ZnO	Zn metal	5	5	LLIF	60	30
Ni	NiO	Ni metal	5	5	LLIF	30	15
Na[a]	Na_2O	Albite[b]	5	2	TAP	10	5

Table 2.2: EPMA set up and calibration standards. [a]Elements analysed first in sequence due to migration of alkalis away from electron beam. [b]Standards calibrated with a 5 µm beam. SJO= St John's olivine

2.6. Re-Os geochronology methodology

2.6.1. Sample size and preparation

Jack Hills detrital chromites

While previous Re-Os analysis of chromites is well documented (e.g. Bennet et al., 2002; Rollinson et al., 2002; Frei et al., 2003; Coggon et al., 2016), such studies have typically focused on chromitites, from which grams of sample can be dissolved to yield Re-Os measurements. However, the detrital nature of grains from Jack Hills and the presence of Re-bearing iron oxides within the same metasediment samples means such chromite separates must be picked individually. This places significant limits on the sample mass that can be dissolved: picking of 1000 grains equates to approximately 25 mg of chromites. To dissolve a gram of detrital chromites would therefore require approximately 40,000 grains, which is unworkable. As such, individual samples of unleached detrital chromites for Re-Os isotopic analysis ranged between ~3 mg and ~30 mg. While chromites typically possess Os concentrations of tens to hundreds of ppb, Re is typically present at sub ppb concentrations (Shirey and Walker, 1998). For a ~10 mg sample, assuming a 30 ppb Os concentration, this equates to approximately ~300 pg of Os. Even assuming a yield of ~50 %, this results in an Os load ideal for the thermal ionisation mass spectrometer (TIMS). However, assuming a 0.3 ppb Re concentration, this same sample would yield just 3 pg of Re. Re blanks are often higher in concentration than this (e.g. ~10 pg Shirey and Walker, 1995), and samples are therefore extremely sensitive to blank correction and blank heterogeneity.

Leaching of chromites within session 5 was undertaken, with a more detailed discussion as to why presented in Chapter 4. Chromites were first leached at ~120 °C in 4 ml of concentrated SpA HF for ~48 hours. Leaching acid was then removed, and chromites rinsed several times in 18.2 MΩ Milli-Q water to remove all traces of HF. A second leaching step was then conducted by adding 4 ml 6M 1Δ HCl to chromites, which was heated to ~120 °C for another 48 hours. The 6M 1Δ HCl was then removed, and chromites rinsed. Chromites were carefully dried down to near dryness in Milli-Q: it was found completely dry chromites within savillex beakers would behave very statically, to the point where they would swiftly evacuate the beakers. Leaching was undertaken to remove any silicates (particularly fuchsite), sulphides, and potentially iron oxides that may perturb analyses.

Manfred Complex WR and spinel separates

Spinel separates from 13TKN80 and chromites from 13TKN22 were also analysed for Re-Os. Approximately 100 grams of sample was crushed using a tungsten carbide jaw crusher, and then sieved into <500 µm separates. Initial attempts to separate spinels using hand panning failed, owing

to the small grain size of this phase and their location within coarser olivines and pyroxenes (Figure 2.7 and Figure 2.8). To circumnavigate this, the silicate portion of Manfred Complex samples was dissolved and separates concentrated using progressive acid leaching. As with chromite samples in session 5, leaching acids were removed and samples rinsed with Milli-Q ~5 times between each acid step. Samples were first leached in ~6 ml of concentrated SpA HF for ~48 hours at 120°C. HF was then removed, and the spinel-bearing beaker filled with ~6 mls of 2:1 1ΔHNO3 and SpA HF for ~48 hours at 130 °C. While these two steps successfully removed pyroxenes within 13TKN80 and amphibole in 13TKN22, an olivine (± serpentine?) gel was observed for both samples. To dissolve this gel, approximately 2 ml of 1Δ HNO3 was added at 120 °C for 24 hours, followed by ~4 mls of 1Δ HCl at 120 °C for a shorter period of ~4 hours. This protocol successfully removed silicate gel in both samples without dissolving spinels and enabled enough concentrate of this phase to be successfully weighed and analysed isotopically.

2.6.2. Blank reduction

Owing to the small sample sizes analysed, achieving the lowest possible blanks was critical within this study. Os blanks are largely controlled by HNO_3 (Birck et al., 1997). Nitric is therefore typically sparged, such that dissolved Os is removed by bubbling of HEPA filtered air through 1Δ HNO_3. This step has been shown to significantly reduce the Os concentration of 1Δ HNO_3, and therefore the whole total procedural blank (TPB). Sparging to reduce Os blanks may also be aided by using low volumes during carius tube digestion: while unsuitable for WR analysis, 4 ml total inverse aqua regia (3 ml 1Δ HNO_3 and 1 ml 1Δ HCl) perfectly dissolves low mass samples during carius tube digestion. As the Os concentration of chromites is typically tens to hundreds of ppb (Shirey and Walker, 1998; Carlson, 2005), this results in Os TPBs of <1 % of sample Os, which is ideal.

While these procedures regularly produce sub pg Os blanks, Re blanks in this study were found to remain unacceptably high. Initially, it was suspected that the blank may be present within reagents, and so reagents were cleaned and blank tested. Isoamylol, or 3-methyl-1-butanol, is used in the solvent extraction of Re and was found to possess a slightly elevated Re blank. However, cleaning of isoamylol, using Milli-Q water, and other reagents was found to make little difference to the overall TPB. Further analyses suggested two sources for elevated Re blanks; carius tubes and the TIMS itself.

Previously, carius tubes were cleaned in ~1/3 analar HNO3, 2/3 Milli-Q (Cohen and Waters, 1996). However, this study observed this procedure produced heterogeneous Re blanks that ranged from 5.6 pg to >38 pg, dependant on the amount of time tubes spent cleaning. Such blank contributions dwarf the amount of Re analysed, and so an aggressive carius tube cleaning method was developed (Figure 2.10). Carius tubes are rinsed with Milli-Q and placed within a 2L Savillex Teflon beaker. Carius tubes

are then filled with concentrated, reagent-grade HCl: ideally 1Δ HCl would be used, but this would require >500 ml of 1Δ HCl for a sample run. Once tubes are filled with HCl, the inside of the 2L Savillex Teflon beaker is filled with cold Milli-Q water. This is then placed within a large Pyrex borosilicate beaker, and boiled RO water is added. Teflon lids for 15 ml or 30 ml beakers are used to separate the 2L Teflon beaker and the ~5L Pyrex beaker. It was found that without these Teflon lids, the large surface area at the base of the 2L Savillex beaker induced melting at the contact with the Pyrex beaker. The whole set up is placed on a hotplate, which is heated to ~200 °C, ideally bringing the RO water within the Pyrex beaker to a rolling boil. While the Milli-Q within the 2L Teflon beaker may be added hot, it was found the heat within the 2L Teflon beaker was easier to control if Milli-Q was added cold.

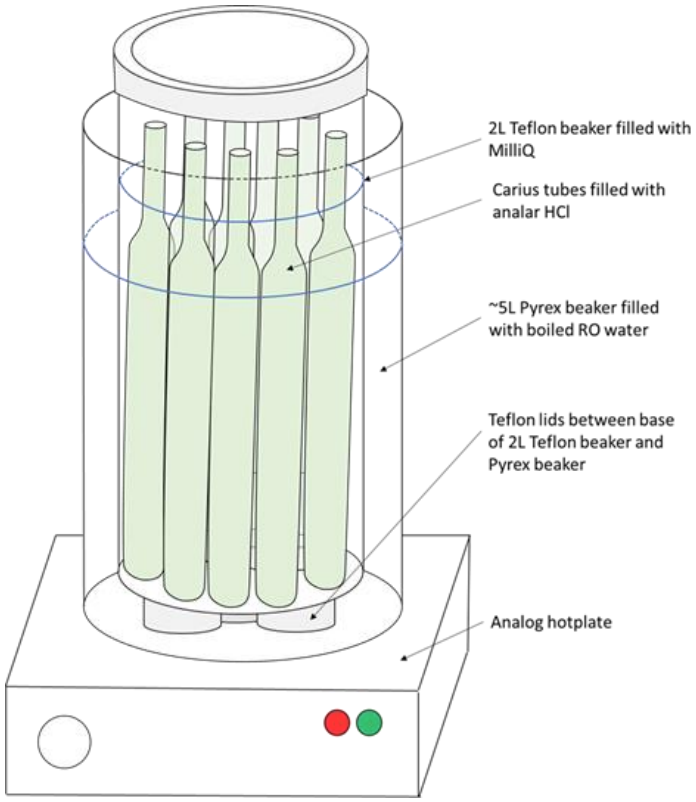

Figure 2.10: Schematic representation of aggressive carius tube cleaning procedure developed during this study. Approximate fill heights for Milli-Q water within the 2L Teflon beaker and RO water within the pyrex beaker are shown by blue lines.

The second step taken to reduce and homogenise Re blanks was switching the measurement of Re from the TIMS to a ThermoFisher Neptune multi-collector inductively coupled plasma mass spectrometer (MC-ICP-MS). Much of the Re blank heterogeneity observed may have resulted from variable background Re from within the TIMS. All other isotopic analyses conducted on the TIMS within BIG (Sr, Cr, Ca, Pb) are run using Re filaments, which results in small but resolvable amounts of Re liberated from the filament. Switching to the MC-ICP-MS also provides the advantage that samples

can be doped with Ir (Zhu et al., 2017) to more accurately determine mass bias: Re only possesses two isotopes, making instrumental fractionation of Re isotopes difficult to determine on the TIMS (Reisberg and Meisel, 2002).

2.6.3. Digestion and chemical separation of Re and Os

Once bulk samples were picked, uncrushed chromites and WR powders were weighed and transferred into aggressively cleaned borosilicate carius tubes, and digested in a method modified from Shirey and Walker (1995). Enriched ^{190}Os and ^{185}Re isotopic spikes were also weighed for addition prior to digestion. An ideal amount of enriched ^{190}Os spike was weighed to produce optimal spike-sample mixtures (Figure 2.11), producing minimal error magnification (F) while enabling spike-sample mixtures to be run on the secondary electron multiplier (SEM) on the TIMS. Samples, spikes and acids were added to carius tubes using a cut disposable pipette, enabling the disposable pipette to act as a funnel for powdered and unpowdered samples. While some powder and very fine samples inevitably became statically charged to the inside of the disposable pipettes, these were washed down by subsequent addition of ^{190}Os and ^{185}Re spikes and acid. Spikes and chilled acids were added to carius tubes frozen in dry ice, so that volatile Os tetroxide (OsO_4) did not escape during the sealing procedure. Inverse aqua regia was used for digestion: inverse aqua is more oxidising than traditional aqua regia, and therefore more adept at oxidising Os to its highest valency state for complete spike equilibrium (Reisberg and Meisel, 2002). 8 ml and 12 ml of inverse aqua regia were used for chromite separates and rock powders, respectively. Due to the small sample sizes, a total of 4 ml inverse aqua regia was added to session 5 samples.

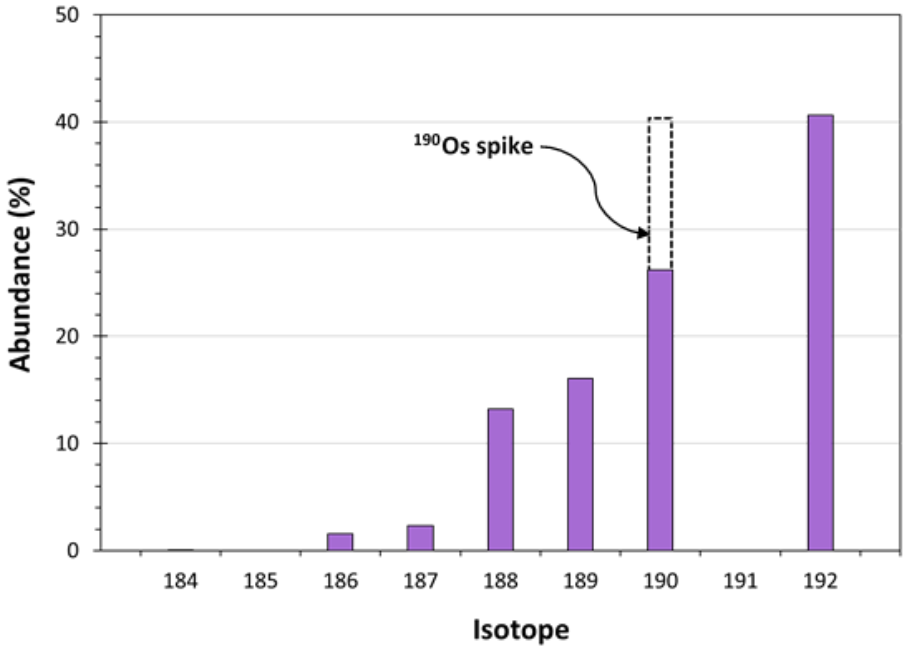

Figure 2.11 (Previous Page): Natural isotopic abundances (%) of Os, and the approximate additional ^{190}Os spike required for ideal spike-sample mixtures whilst running on the SE-M on the TIMS. This results in a $^{190}Os/^{192}Os$ ratio of ~1 when spiked.

Once sample, isotopic spikes and appropriate amounts of inverse aqua regia had been added, carius tubes were sealed using an oxy-propane torch, wrapped in Al foil, placed in steel tubes (Figure 2.12) and heated to 230 °C for 48-58 hours to enable spike equilibration and complete sample dissolution. Once cooled to room temperature, carius tubes were placed in a freezer overnight so that acids were cold and gas pressure low when opening. Carius tubes were then opened by use of a hot oxy-propane torch to propagate a scored crack through the thickened glass. Despite adding chromites uncrushed, incomplete sample dissolution was never encountered, likely due to the heavily cracked nature of Jack Hills grains. Owing to their high silicate proportion, WR powders never completely dissolved. This is a common feature of carius tube digestion of WR samples, where HF cannot be used. Post-digestion HF desilicification may be used to dissolve remnant powder (e.g. Ishikawa et al., 2014), yet this method has been shown to yield no observable increase in Re or Os concentrations (Day et al., 2015), suggesting sufficient attack of the silicate phase to liberate its Re and Os budget. As such, remnant powders were simply avoided when removing inverse aqua regia.

Os was subsequently purified by multiple solvent extractions. Firstly, Os is partitioned into ~6 ml of carbon tetrachloride (CCl_4), from inverse aqua regia. Re remains within the inverse aqua regia, successfully separating parent and daughter isotopes. Secondly, Os is partitioned from the CCl_4 to ~6 ml of UpA HBr, which is left to equilibrate for ~24 hours before the CCl_4 is removed and the UpA HBr dried down. This set of solvent extractions follows the modified method of Cohen and Waters (1996). The second step of this procedure reduces Os from Os tetroxide to $OsBr_6^{2-}$, reducing Os to a non-volatile valency state. Os was then further purified using the micro-distillation technique of Birck et al. (1997). The Os bearing drydown was redissolved in 10 µL of UpA HBr and dried down on the lid of a conical 7ml Savillex beaker. 20 µL of UpA HBr was placed in the apex of the beaker, while 50 µL of highly oxidising CrO_3-H_2SO_4 was placed directly over the Os-bearing drydown. Once the CrO_3-H_2SO_4 was added to beaker was rapidly and securely tightened upside down (Figure 2.13), to minimise the loss of volatile OsO_4 (Birck et al., 1997; Bragagni et al., 2018). For increased thermal distribution, the microdistillation unit was wrapped in Al foil with the HBr-bearing apex protruding and placed on a hotplate at 90 °C for 3 hours. During microdistillation, $OsBr_6^{2-}$ is oxidised to volatile OsO_4, which was transferred in gas phase to UpA HBr, where it was reduced to $OsBr_6^{2-}$. This procedure typically produces Os yields of 70% to 90% (Birck et al., 1997).

Re was also purified using solvent extraction. Re-bearing inverse aqua regia was dried down, and then was re-dissolved in 2 ml of 2M 1Δ HNO_3 for solvent extraction using isoamylol (3-methyl-1-butanol) in

a method modified from Birck et al. (1997). Re was first back extracted into pre-cleaned isoamylol: Re-bearing 2M 1Δ HNO_3 was added to 2 ml of isoamylol, shaken for two minutes, and centrifuged for a further 4 minutes at 4000 rpm. This results in 2M 1Δ HNO_3 and isoamylol forming immiscible layers. An additional clean up step was performed by removal of isoamylol into a further 2 ml of 2M 1Δ HNO_3. This mixture was again shaken and centrifuged, and the 2M 1Δ HNO_3 removed. For WR samples, a gram of sample was regularly dissolved, resulting in a significantly higher matrix than chromite and spinel separates. As such, an additional 2 ml of 2M 1Δ HNO_3 clean up step was performed for WR samples. Finally, Re was back extracted from isoamylol into 2.5 ml of Milli-Q water. Approximately 2 ml of Milli-Q water was removed for analysis: as Milli-Q forms the bottom layer of the two immiscible liquids, the outside of the pipette was rinsed with Milli-Q after collection of Re-bearing Milli-Q. While this does not completely remove all isoamylol from the outside of the pipette tip, it significantly reduces the proportion of isoamylol that is included in the final Re-bearing liquid. Re-bearing Milli-Q water was then dried down and redissolved in 2% 1Δ HNO_3 for MC-ICP-MS analysis. Birck et al. (1997) suggested yields were 50 % for this procedure, though semi-quantitative tests performed in this study suggests they may be lower (Resiberg and Meisel, 2002).

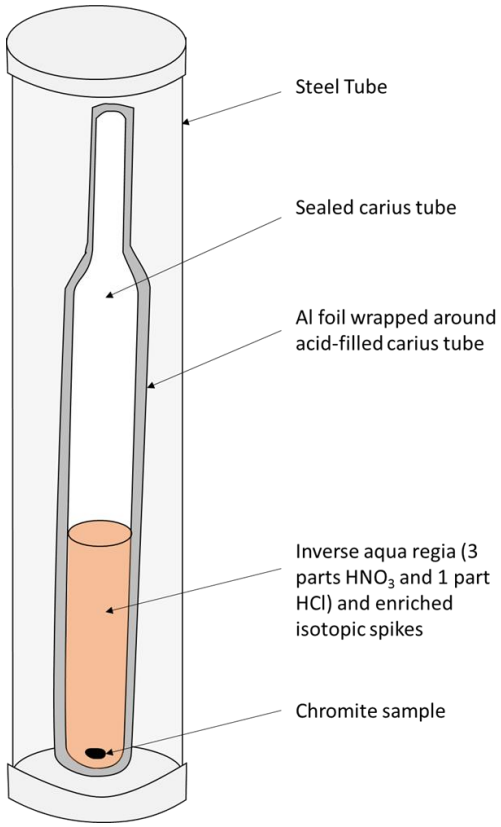

Figure 2.12: Schematic representation of carius tube digestion. HCl 1D and 1D HNO_3 sparged prior to use.

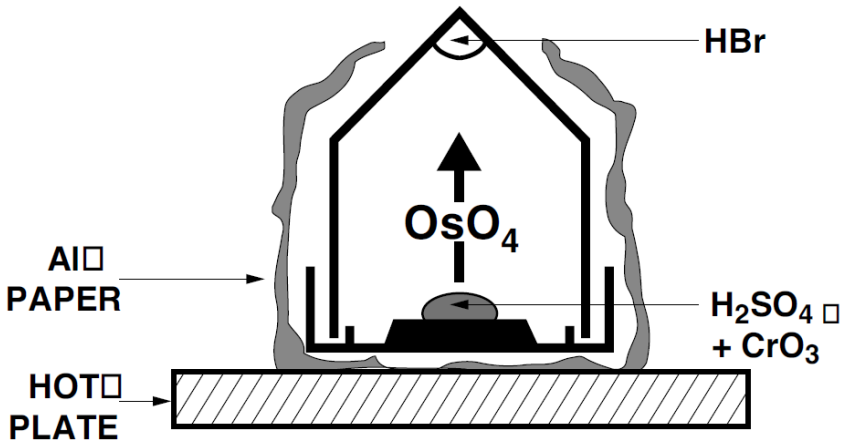

Figure 2.13: Schematic representation of microdistillation from Birck et al. (1997). Os is oxidised using a H_2SO_4-CrO_3 mixture to OsO4, which volatilises and is transported as a gas phase to the apex of the beaker. Here, HBr reduces OsO4 to $OsBr_6^{2-}$, enabling quantitative separation of Os from any matrix at the base of the beaker.

Re-Os mass spectrometry

The Os-bearing HBr drydown was redissolved in 0.75 µL UpA HBr and loaded onto a Pt filament, which had been previously lightly outgassed to a dull red glow at atmospheric pressure. 1µL of $Ba(OH)_2$/NaOH activator was added on top of the sample. Both HBr and activator were loaded under a binocular miSrscope to achieve a small and central load onto the Pt wire. The Os isotopic composition and concentration of samples were then determined using ion-counting on the secondary electron multiplier (SEM) of a ThermoFisher thermal ionisation mass spectrometer in negative mode (N-TIMS) at the University of Bristol (Creaser et al., 1991; Völkening et al., 1991). Analyses were conducted using a Re-free source, to minimise isobaric interferences on ^{187}Os. Approximately $0.3x10^{-7}$ millibars of oxygen were bled into the source chamber to encourage the ionisation of Os as OsO_3^-. All isotopes of Os were measured as OsO_3^- in a dynamic SE-M method with a 4.1945 second integration time and a 3 second idle time. $^{185}ReO_3^-$ at mass 233 was additionally monitored for the isobaric interference of $^{187}ReO_3^-$ on $^{187}OsO_3^-$. However, Re is typically emitted as ReO_4^- (Reisberg and Meisel, 2002) and should be quantitively separated during wet chemistry, so this correction is largely minimal. $^{198}PtO_2^-$ was also monitored throughout the sample run, as if significant quantities of filament-derived Pt are ionised this may cause interferences (Luguet et al., 2008).

A ~100 pg Os DTM standard (Table 2.3) was run prior to analyses as validation for samples: data for this standard are available in Supplementary Material 3. Both standard and sample filaments were heated and tuned using automated procedures on the TIMS software, until a steady or slightly growing beam of ~100,000 counts on the SEM was achieved. Individual samples were run for 100 cycles, which

provided sufficiently precise counting statistics for $^{187}Os/^{188}Os$ ratios. Raw Os isotopic ratios were taken forward to data reduction, which consisted of an oxygen isotopic correction, an iterative calculation to determine spike/sample ratios, corrections for instrumental mass bias (using a $^{192}Os/^{188}Os$ ratio of 3.08271) and the isobaric interference of ^{187}Re on ^{187}Os. Finally, the Os isotopic composition and concentration of the sample were determined using spike-stripping and the isotope dilution equation. A 2sd rejection criteria was further applied to $^{187}Os/^{188}Os$ ratios and Os concentrations. A ^{188}Os correction was also necessary within some samples, because some rogue ^{188}Os spike was detected occasionally: excess ^{188}Os was corrected via normalisation to $^{189}Os/^{188}Os$ of 1.219708. While this largely resulted in little change in the $^{187}Os/^{188}Os$, this normalisation produced significant changes in $^{187}Os/^{188}Os$ in some low mass samples.

Determination of Re concentrations was undertaken on a ThermoFisher Neptune multi-collector inductively coupled plasma mass spectrometer (MC-ICP-MS) at the University of Bristol, using ion counting on the SEM. A multidynamic method with a 2 mass jump between two cup configurations was employed to measure the Re isotopic composition and concentration of standards and samples, details of which are provided in Table 2.4. Sample was desolvated into the mass spectrometer using an Aridus II, significantly increasing sensitivity. Sensitivity, though not beam stability, was also increased by the use of a Ni X skimmer cone. Gas flows were typically ~5.7 to ~5.9 L min-1 for Ar and ~0.05 L min-1 for N: both Re and Ir were very sensitive to the small changes in N. By using low-Re cones, and a single Aridus and nebuliser tip, Re blanks (measured within clean 2% 1Δ HNO_3) were typically less than 3000 cps at the beginning of analysis.

As mass bias cannot be internally corrected for Re, samples were doped with 20 ppb Ir, and a nominal $^{191}Ir/^{193}Ir$ ratio of 0.5929 (Zhu et al., 2017) used to correct for instrumental mass bias using the exponential fractionation law:

$$Rtrue = Rmeas \,.\, \left(\frac{M1}{M2}\right)^{\beta} \quad \textbf{(1)}$$

Where R_{true} is the mass bias corrected ratio, R_{meas} is the measured ratio, M_1 and M_2 are the atomic weights of the two ratioed isotopes. β is fractionation factor calculated by the following equation:

$$\beta = \frac{\ln\left(\frac{Rtrue}{Rmeas}\right)}{\ln\left(\frac{M1}{M2}\right)} \quad (\mathbf{2})$$

Table 2.3: Isotope standards

Osmium												
Standard	$^{184}Os/^{188}Os$	2se	$^{186}Os/^{188}Os$	2se	$^{187}Os/^{188}Os$	2se	$^{189}Os/^{188}Os$	2se	$^{190}Os/^{188}Os$	2se	$^{192}Os/^{188}Os$	2se
Os DTM	0.001306	0.000006	0.119965	0.000037	0.173927	0.000005	1.219708	0.000009	1.983803	0.000017	3.08271*	-
Os DROsS	0.001305	0.000005	0.119929	0.000058	0.160924	0.000004	1.219705	0.000015	1.983803	0.000015	3.08271*	-
Rhenium												
Standard	$^{185}Re/^{187}Re$	2se	$^{187}Re/^{185}Re$	2se								
NIST 3143	0.597198	-	1.674485	0.00117								
U-Pb												
Standard	$^{207}Pb/^{206}Pb$	2se%	$^{207}Pb/^{235}U$	2se%	$^{206}Pb/^{238}U$	2se%	^{207}Pb-^{206}Pb	2se	^{207}Pb-^{235}U	2se	^{206}Pb-^{238}U	2se
GJ1	0.060139	0.031	0.81117	0.065	0.097860	0.065	607.70	0.67	603.11	0.30	601.86	0.37
91500	0.074941	0.030	1.8525	0.066	0.179365	0.040	1066.01	0.61	1064.32	0.44	1063.51	0.39
Plešovice	0.053244	0.027	0.39396	0.057	0.053694	0.034	337.96	0.61	337.26	0.16	337.16	0.11
OG1	0.29907	0.037					3465.40	0.60			3440.70	3.2
Lu-Hf												
Standard	$^{176}Hf/^{177}Hf$	2se	$^{176}Lu/^{177}Hf$	2se	$^{176}Yb/^{177}Hf$	2se						
91500	0.282303	3	0.000311	136	0.0106–0.0168							
Mudtank	0.282506	13	<0.0003									
Plešovice	0.282481	13	0.0004–0.0015		0.0038–0.0245							
OG1	0.280633	34	0.00121	86	0.007-0.075							

Table 2.3: Isotope standards used throughout this study with known isotopic ratios from literature. Os DTM and DROsS isotopic ratios characterised by Luguet et al. (2008). *Os isotopic ratio used in mass bias corrections. Re NIST 3143 values derived from Miller et al. (2011). U-Pb standards from Horstwood et al. (2016) and Stern et al. (2009). Lu-Hf standards from a variety of sources. 91500 values are derived from Blichert-Toft (2008) and Slama et al. (2009), Mudtank from Woodhead and Hergt (2005), Plešovice from Slama et al. (2009), and OG1 from Kemp et al. (2017). All uncertainties are 2se absolute apart from U-Pb ratio uncertainties, which are 2se%.

Table 2.4 Neptune II cup configuration for Re									
Line 1	L4	L3	L2	L1	IC1	H1	H2	H3	H4
	-	^{181}Ta	^{182}W	^{184}W	^{185}Re	^{186}W	^{187}Re	^{191}Ir	^{193}Ir
Line 2	L4	L3	L2	L1	IC1	H1	H2	H3	H4
	-	^{183}W	^{184}W	^{186}W	^{187}Re	^{188}Os	^{189}Os	^{193}Ir	-

Table 2.4: Cup configurations for Re collection on Neptune II MC-ICP-MS. ^{185}Re and ^{187}Re are run on ion counters, with a 2 mass jump between line 1 and 2.

Tuning using a 9 ppt NIST SRM 3143 standard (Table 2.3) doped with 20 ppb Ir typically resulted in between 80,000 and ~100,000 cps on ^{185}Re (~250,000 total cps Re), and ~3 V of ^{191}Ir. Samples were typically analysed in 1 ml of 2 % 1Δ HNO_3 to achieve acceptable counting statistics. An Ir-doped blank was analysed for 20 cycles prior to standards or samples to blank correct ^{185}Re and ^{187}Re intensities. Samples were run for 40 cycles, which near exhausted the 1 ml of Re-bearing 2 % 1Δ HNO_3. Integration times were 4.194 seconds, with a 6 second idle time to allow the magnet to settle. Samples were blank subtracted and corrected for mass bias, and then spike-sample mixtures unmixed and the Re concentration determined using the isotope dilution equation:

$$Conc_{\mathrm{smp}}\,(\mathrm{ppm}) = \frac{\left(\frac{(spW * Conc_{\mathrm{sp}}) * W_{\mathrm{nat}}}{W_{\mathrm{sp}}}\right) * \left[\frac{AbA_{\mathrm{sp}} - (R_{\mathrm{meas}} * AbB_{\mathrm{sp}})}{(R_{\mathrm{meas}} * AbB_{\mathrm{smp}}) - AbA_{\mathrm{smp}}}\right]}{smpW} \quad \textbf{(3)}$$

Where conc is the concentration of the spike or sample in ppm, spW is the spike weight in grams, and W_{nat} and W_{sp} represent the summed natural mass of the natural sample and spike, respectively. AbA and AbB represent the known abundance of the numerator and denominator of the measured ratio, respectively. This calculation is then divided by the weighed sample mass (in grams) to determine the sample concentration.

2.6.4. Re-Os terminology

Once Re and Os concentration and the ^{187}Os/^{188}Os isotopic composition of samples had been determined, rhenium depletion ages (TRDs; Re/Os=0) and model ages (TMAs; Re/Os= >0) were then calculated using the following equations:

$$\textbf{Re-Os } \boldsymbol{TRD} = \frac{1}{\lambda} * \ln\left[\frac{\left(\frac{^{187}Os}{^{188}Os}\right)CHONDRITE - \left(\frac{^{187}Os}{^{188}Os}\right)SAMPLE}{\left(\frac{^{187}Re}{^{188}Os}\right)CHONDRITE} + 1\right] \quad \textbf{(4)}$$

$$\textbf{Re-Os } \boldsymbol{TMA} = \frac{1}{\lambda} * ln\left[\frac{\left(\frac{^{187}Os}{^{188}Os}\right)CHONDRITE - \left(\frac{^{187}Os}{^{188}Os}\right)SAMPLE}{\left(\frac{^{187}Re}{^{188}Os}\right)CHONDRITE - \left(\frac{^{187}Re}{^{188}Os}\right)SAMPLE} + 1\right] \quad \textbf{(5)}$$

Where λ is the decay constant of ^{187}Re (1.666×10^{-11} yr^{-1}; Smoliar et al., 1996), and chondritic isotopic compositions are taken from the mixed chondrite values of Shirey and Walker (1998), where the ^{187}Os/^{188}Os ratio is 0.127 and the ^{187}Re/^{188}Os ratio is 0.40186. It is important to note that the Re and

Os isotopic composition varies between chondrite groups (e,g, Walker et al., 2002a; Day et al., 2016), and these values are the lower limits of non-carbonaceous groups. The effects of chondrite values used on Re-Os model ages is discussed in detail in Chapter 4. Uncertainties for TRDs and TMAs were calculated using a model age covariance matrix (Albarède, 1995), with $^{187}Os/^{188}Os$ 2se and a 1% uncertainty on the decay constant of ^{187}Re the greatest contributions to age uncertainty. Initial Os compositions (γOs_i) for Manfred Complex samples were also calculated using the equation:

$$\gamma Os_i = \left[\frac{\left(\frac{187Os}{188Os}\right) SAMPLE(t)}{\left(\frac{187Os}{188Os}\right) CHONDRITE(t)} - 1 \right] * 100 \quad \textbf{(6)}$$

Where γOs_i represents the difference between time-integrated sample and chondritic reservoirs in parts per hundred (%). For the Manfred Complex both reservoirs are time integrated to 3730 Ma, the U-Pb zircon age of anorthosites (Kinny et al., 1988) and leucogabbro (Kemp, 2018).

2.7. Zircon U-Pb and Lu-Hf analysis

2.7.1. Zircon U-Pb analyses

Zircon were analysed for U-Pb using the Nu instruments Nu Plasma HR Nu MC-ICP-MS at the Natural Environment Research Council Isotope Geosciences Laboratory (NIGL) of the BGS, coupled with an ESI ArF excimer 193 nm laser. Zircon were analysed using a method slightly modified from Bauer and Horstwood (2018), resulting in a coupled Pb-Hf analysis with the total ablation depth kept to <20 µm. This is ideal for analysis of ancient, complexly zoned zircons that yield significant intra-grain U-Pb variability, as is commonly noted in Hadean grains at Jack Hills (Nemchin et al.., 2006; Whitehouse et al., 2017a; Cavosie et al., 2019). U-Pb measurements were conducted using a 20 µm spot size, 10 Hz repetition rate and a ~2.7 Jcm^{-2} fluence, with a 10 second total ablation time, resulting in an ablation depth of ~5 µm for the U-Pb measurement. A longer sample line was also employed to reduce the noise of the ablation. Each integration run of standards and samples measured an electronic and instrumental baseline for 30 seconds each prior to ablations. The gains of faradays and ion counters were measured daily. The initial cup configuration for preliminary analyses included measurement of ^{206}Pb isotopes on faraday cups, anticipating significant radiogenic ingrowth and subsequent high Pb concentrations due to the >3000 Ma age of zircons (Bauer and Horstwood, 2018). However, the low U concentration of Jack Hills zircon (Crowley et al., 2005) meant this resulted in small signals and therefore unacceptable uncertainties. As such, subsequent analysis measured both ^{207}Pb and ^{206}Pb using ion counters. Both cup and ion counter configurations are shown in Table 2.5.

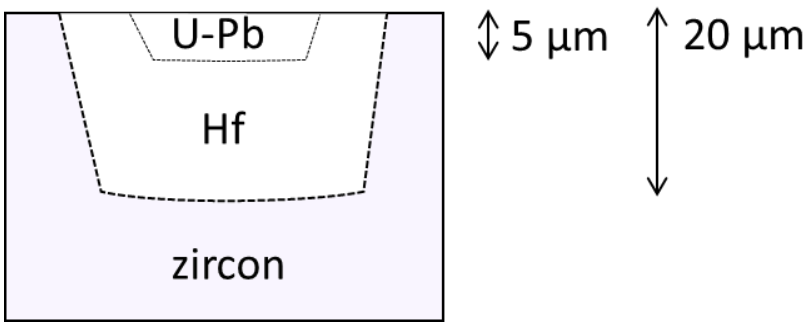

Figure 2.14: Schematic representation of Pb-Hf ablation pits. U-Pb ablation creates a pit 5 µm in depth, while the Lu-Hf ablation forms a pit ~15 µm in depth. This creates a total ablation depth of approximately 20 µm.

Sample unknowns were bracketed by reference materials to correct for laser and instrument induced fractionation effects, and determine the U concentrations of unknowns. Zircon standard GJ1 was used as the primary reference material (PRM), while Plešovice, 91500 and OG1 were used as further validation materials to assess the robustness of U-Pb measurements (Table 2.3; Stern et al., 2009; Horstwood et al., 2016). While 91500 and OG1 have U concentrations, and therefore Pb concentrations, more comparable to most sample unknowns (~100 ppm to ~200 ppm), GJ1 (~280 ppm to ~300 ppm U) was found to yield the most consistent isotopic ratios across multiple sessions, suggesting it represents the most homogeneous standard. Apparent inter-crystal heterogeneity was observed during ablation of OG1 (see Chapter 5), though it is unclear if this represents true sample heterogeneity or analytical imprecision. All data was reduced using Iolite (Paton et al., 2010), and a common Pb correction was not applied. Despite the small ablation volumes, uncertainties for individual measurements were kept below 1% (2s%) for ^{207}Pb-^{206}Pb ages, and below 2% (2s%) for ^{206}Pb-^{238}U ages so that the age uncertainty contribution to Hf uncertainties was minimal.

In-session uncertainties including excess variance of the PRM were propagated into sample measurements using Iolite (Paton et al., 2010). Long-term systematic variability, that is the variability of the validation reference materials (VRM) between sessions, was propagated following the methods of Horstwood et al. (2016). This incorporated the reference ratio uncertainties of the PRM, long-term excess variance on the VRM, and decay constant uncertainties. Plesovice was used to characterise the long-term, inter-session excess variance required to bring the MSWDs of VRMs to 1. While OG1 is more comparable to sample unknowns in both U concentration and age, minor suspected inter-grain heterogeneity meant that Plesovice was determined the more robust VRM. For October 2017 to September 2018 sessions (14WA2, 14WA3, 16WA5, and 16WA6), Plesovice possessed a 1se % excess variance of 0.65 % for $^{206}Pb/^{238}U$, 0.71 % for $^{207}Pb/^{235}U$ and 0.275 % for $^{207}Pb/^{206}Pb$. PRM reference ratio uncertainties were 0.0325, 0.0315, and 0.0255 (all 1se %) for $^{206}Pb/^{238}U$, $^{207}Pb/^{235}U$ and

$^{207}Pb/^{206}Pb$, respectively. Decay constant uncertainties were again propagated into age uncertainties at 1s % level, and were 0.05, 0.1, and 0.112 for $^{206}Pb/^{238}U$, $^{207}Pb/^{235}U$ and $^{207}Pb/^{206}Pb$. Poorer analytical uncertainties in May 2017 (14WA4) meant that Plesovice already possessed an MSWD of 1, meaning that the propagation of excess variance of VRM was not required, as uncertainties already captured any inter-session variability. As such, systematic uncertainties have not been propagated into 14WA4 age uncertainties.

Table 2.5: Nu Instruments Nu Plasma HR MC-ICP-MS cup configuration for U-Pb										
Preliminary	ExH	H6	H4	C	ICO	IC1	L3	IC2	L4	L5
	^{238}U	^{235}U	-	-	^{208}Pb	^{207}Pb	^{206}Pb	^{205}Tl	^{204}Pb	^{203}Tl
Normal	ExH	H6	H4	C	IC0	IC1	L3	IC2	L4	L5
	^{238}U	^{235}U	-	-	^{207}Pb	^{206}Pb	^{205}Tl	^{204}Pb	^{203}Tl	^{202}Hg

Table 2.5: Preliminary and subsequently used (normal) cup confiurations for on the Nu Instruments HR NU MC-ICP-Ms at the NIGL, BGS. Within the preliminary analysis set up, ^{206}Pb was placed on a faraday cup due to anticipated high intensities. However, the low U concentrations of Jack Hills zircons meant this was not the case, and so this study reverted to the normal BGS set up for zircon analysis. Within this set up both ^{206}Pb and ^{207}Pb are analysed on ion counters.

2.7.2. Zircon Lu-Hf analyses

Zircons that possess concordant (<10 %) U-Pb ages were further analysed for Lu-Hf, with analyses particularly focusing on oscillatory zoned grains. Hf measurements were undertaken using the Thermo Scientific Neptune Plus MC-ICP-MS, also at the NIGL, using an ESI UP193FX laser. Cup configurations for these analyses are shown in Table 2.6. Spot sizes for Lu-Hf measurements were 35 µm and placed over the previous U-Pb ablation pit (Figure 2.14) to ensure the best chances of sampling of the same zircon domain. Lu-Hf ablations were conducted using a 10 Hz repetition rate and a ~7 Jcm^{-2} fluence, with a 10 second total ablation time. This results in an ablation depth of ~15 µm, bringing the total ablation depth for coupled both U-Pb and Lu-Hf analyses to ~20 µm. Blocks of 10-15 unknowns were bracketed by well characterised Hf standards (Table 2.3): 91500 (Blichert-Toft, 2008) was used as the PRM, while Mud Tank (Woodhead and Hergt, 2005), Plešovice (Sláma et al., 2009) and OG1 (Kemp et al., 2017) were used as validation materials to determine the robustness of the Hf measurement. Although 91500 typically possesses lower $^{176}Yb/^{177}Hf$ ratios than Jack Hills zircons, it is apparent from the reproducibility of $^{176}Hf/^{177}Hf$ of validation standards within the study that the use of 91500 as a PRM is robust. Further to this, OG1 has comparable $^{176}Yb/^{177}Hf$ (Supplementary Material 8; Kemp et al., 2017), enabling direct determination of the rigour of correction on mass 176.

Table 2.6: Neptune MC-ICP-MS cup configuration for Lu-Hf									
Cup Configuration	L4	L3	L2	L1	C	H1	H2	H3	H4
	^{172}Yb	^{173}Yb	^{175}Lu	^{176}Hf/Lu/Yb	^{177}Hf	^{178}Hf	^{179}Hf	^{180}Hf	-

Table 2.6: Lu-Hf analysis cup configuration on the Neptune MC-ICP-MS at the NIGL, BGS.

Prior to Hf measurements, the ICP-MS was tuned for maximum sensitivity at the lowest oxide production rate. An Yb-doped Hf solution was analysed prior to ablation to check the robustness of the isobaric interference correction of ^{176}Yb. This is undertaken to allow calibration of the Yb and Hf mass bias relationship so that a ^{176}Yb/^{173}Yb modified for this calibration can be used in the correction of the ^{176}Yb interference on ^{176}Hf using measured ^{172}Yb and ^{173}Yb, based on the measured Hf mass bias at the time of analysis. The resultant ^{176}Hf/^{177}Hf ratio was observed to be slightly higher than expected in doped solutions with elevated ^{176}Yb/^{177}Hf, indicating increased oxide generation. This required a slightly higher nominal ratio of ^{176}Yb/^{173}Yb of 0.7962 (c.f. 0.79435) to correct for ^{176}Yb and could increase inaccuracy at higher Yb/Hf (e.g. at ^{176}Yb/^{177}Hf >>0.2). However, no sample unknown possessed a ^{176}Yb/^{177}Hf ratio of greater than 0.1, and so data were not filtered for this ratio. It should be noted that alibration of Yb and Hf mass bias relationships by solution infers the same fractionation behaviour as laser ablation, which has been shown to not always be the case (e.g. Gu et al., 2019 and references therein). However, discrepencies in mass bias and resultant mass 176 isobaric interference should be observable within reference material ^{176}Hf/^{177}Hf values.

Hf data was processed offline using Iolite (Paton et al., 2010). Beam intensities were tuned for >4 V on ^{180}Hf (total Hf ~12 V) for 91500, which resulted in sample 180Hf intensities of between 4.7 V to 8.6 V. As with U-Pb measurements, in-session PRM uncertainties and excess variance were propagated into Hf measurements of the unknowns and validation materials. No propagation for long-term excess variance of the VRM was required.

Data are presented as ƐHf(t), which represents the deviation of zircon initial ^{176}Hf/^{177}Hf ratio in parts per 10,000 from a time-integrated chondritic uniform reservoir (CHUR):

$$\text{ƐHf(t)}_{\text{CHUR}} = ((^{176}\text{Hf}/^{177}\text{Hf(t)}_{\text{SAMPLE}}/(^{176}\text{Hf}/^{177}\text{Hf(t)}_{\text{CHUR}})\text{-1}) \text{ x } 10{,}000 \quad \textbf{(7)}$$

Back calculations were undertaken using a CHUR ^{176}Hf/^{177}Hf ratio of 0.282785 and a CHUR ^{176}Lu/^{177}Hf ratio of 0.0336 (Bouvier et al., 2008), and a decay constant (λ) of 1.867x10^{-11} (Soderlund et al., 2004). A complementary depleted mantle (DM) evolution curve is also calculated by extrapolation of modern MORB ƐHf(t)$_{CHUR}$ compositions (+16) back to 4450 Ma, the purported first crustal generation event (Kemp et al., 2010; Vervoort and Kemp, 2016). Individual Pb-Hf model ages (T_{CH} or T_{DM}) were not calculated for oscillatory zoned zircons within Chapter 5 owing to the significant uncertainties surrounding such two-stage calculations within detrital records (see Vervoort and Kemp, 2016).

However, the presence of arrays within plots of $\varepsilon Hf(t)_{CHUR}$ vs. ^{207}Pb-^{206}Pb age meant that these features could be used to determine broad mantle extraction ages from the $\varepsilon Hf(t)_{CHUR}$ compositions of Jack Hills zircons. Zircon Pb-Hf model ages (T_{CH} or T_{DM}) are shown briefly in Figure 6.2 to show their dependence on modelling parameters and their comparison to chromite Re-Os model ages.

Uncertainties for $\varepsilon Hf(t)_{CHUR}$ values were propagated using the methods of Ickert, 2013, which incorporates uncertainties associated with measured ratios, decay constants, sample age and CHUR. It is apparent that, particularly within old grains, that the propagation of systematic uncertainties into ^{207}Pb-^{206}Pb ages, resulting in larger age uncertainties, can induce significantly elevated uncertainties for $\varepsilon Hf(t)_{CHUR}$ when propagated through this measurement (Figure 2.15). Systematic ^{207}Pb-^{206}Pb uncertainties of >2 2σ% will result in additional uncertainty on $\varepsilon Hf(t)_{CHUR}$ measurements of 1-2, particularly within Hadean grains (Figure 2.15). This has large implications for the robustness of $\varepsilon Hf(t)_{CHUR}$ arrays, as regressions of such arrays are weighted by uncertainties. However, many studies do not propagate analytical or systematic uncertainties from reference materials through their data, therefore significantly under estimating the $\varepsilon Hf(t)_{CHUR}$ uncertainties. Coupled Pb-Hf plots of published literature shown within this thesis possess uncertainties recalculated using the Ickert (2013) uncertainty propagation methodology, and thus include decay uncertainties, but assume propagation of just analytical ^{207}Pb-^{206}Pb uncertainties, i.e. no excess variance of standards. The variable 2σ uncertainties reported for ^{207}Pb-^{206}Pb ages (e.g. Whitehouse et al., 2017a) in all previous literature, bar Wilde and Wang (2018), indicates reference material uncertainties and systematic uncertainty have not been propagated into final age uncertainties. This therefore suggests that the $\varepsilon Hf(t)_{CHUR}$ uncertainties provided for previous Jack Hills data should therefore be considered as a minimum.

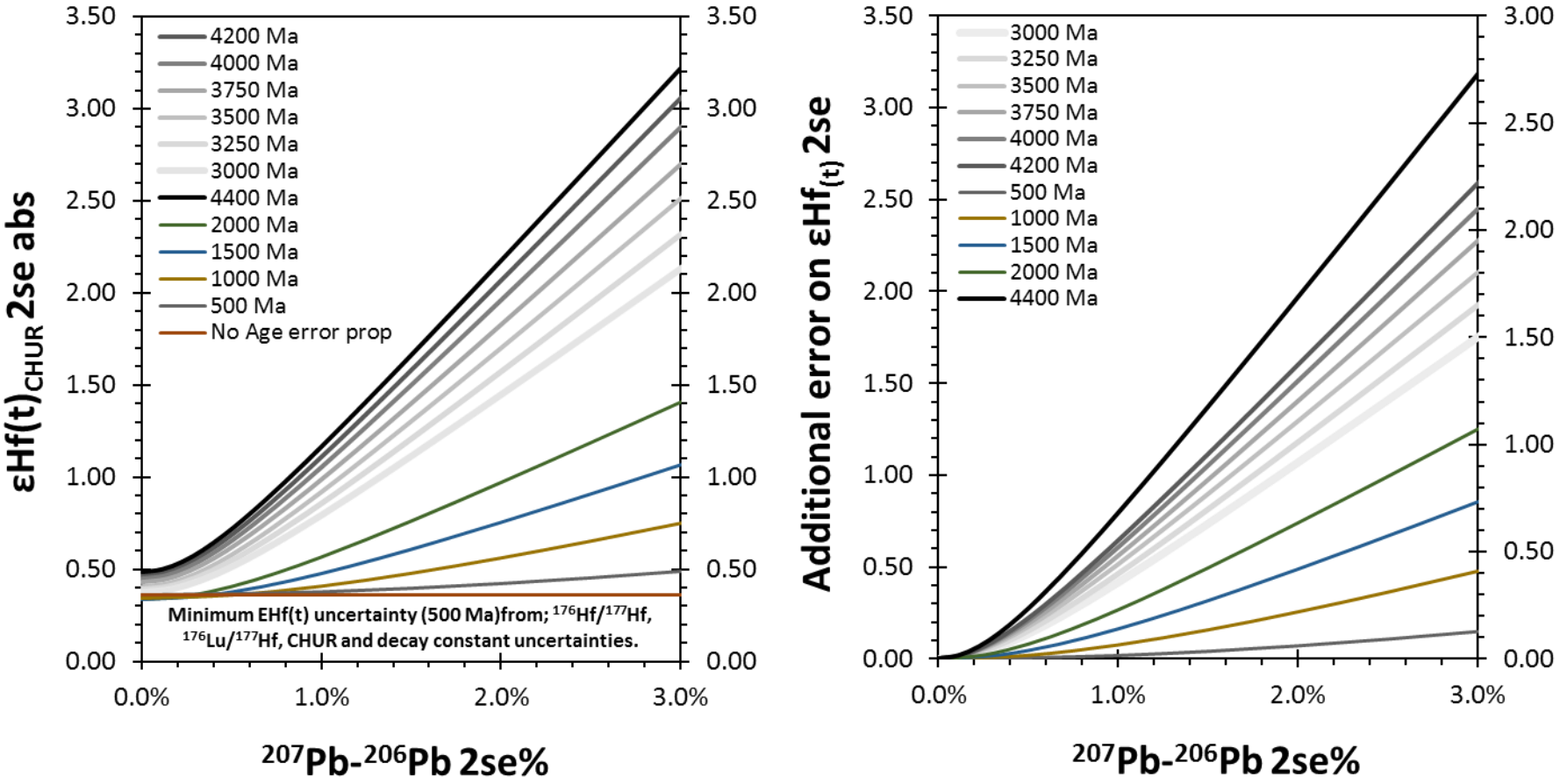

Figure 2.15: Hf uncertainties propagated using the method of Ickert et al. (2013). **A)** The absolute ƐHf(t)$_{CHUR}$ uncertainty (2se) for zircons of a set ages, with increasing ^{207}Pb-^{206}Pb ratio uncertainty. Note that a Hadean grain with an expected 1% 2se% uncertainty should never have a Hf uncertainty of less than 1 ƐHf(t) **B)** Additional uncertainty expected on ƐHf(t) values with increasing ^{207}Pb-^{206}Pb uncertainties

2.8 References

Ballhaus, C., Berry, R.F., and Green, D.H. (1991). High pressure experimental calibration of the olivine-orthopyroxene-spinel oxygen geobarometer: implications for the oxidation state of the upper mantle. *Contributions to Mineralogy and Petrology* **107**, 27-40.

Bauer, A. M. & Horstwood, M. S. A. (2018). Small-volume Lu-Hf and U-Pb isotope determination of complex zircons by solution and laser ablation MC-ICP-MS. *Chemical Geology* **476**, 85-99.

Bennett, V. C., Nutman, A. P. & Esat, T. M. (2002). Constraints on mantle evolution from Os-187/Os-188 isotopic compositions of Archean ultramafic rocks from southern West Greenland (3.8 Ga) and Western Australia (3.46 Ga). *Geochimica Et Cosmochimica Acta* **66**, 2615-2630.

Birck, J. L., RoyBarman, M. & Capmas, F. (1997). Re-Os isotopic measurements at the femtomole level in natural samples. *Geostandards Newsletter-the Journal of Geostandards and Geoanalysis* **21**, 19-27.

Blichert-Toft, J. (2008). The Hf isotopic composition of zircon reference material 91500. *Chemical Geology* **253**, 252-257.

Bouvier, A., Vervoort, J. D. & Patchett, P. J. (2008). The Lu-Hf and Sm-Nd isotopic composition of CHUR: Constraints from unequilibrated chondrites and implications for the bulk composition of terrestrial planets. *Earth and Planetary Science Letters* **273**, 48-57.

Bragagni, A., van Acken, D., Fonseca, R., Speelmanns, I., Wainwright, A., Heuser, A., Nowell, G. & Luguet, A. (2018). Re-Os and HSE in individual base metal sulfide grains: Evaluating micro-analytical procedures using a sulfide reference material. *Chemical Geology* **493**, 426-440.

Carlson, R. W. (2005). Application of the Pt-Re-Os isotopic systems to mantle geochemistry and geochronology. *Lithos* **82**, 249-272.

Cavosie, A. J., Wilde, S. A., Liu, D. Y., Weiblen, P. W. & Valley, J. W. (2004). Internal zoning and U-Th-Pb chemistry of Jack Hills detrital zircons: a mineral record of early Archean to Mesoproterozoic (4348-1576 Ma) magmatism. *Precambrian Research* **135**, 251-279.

Cavosie, A. J., Valley., J. W., and Wilde., S. A. (2019). The Oldest Terrestrial Mineral Record: Thirty Years of Research on Hadean Zircon from Jack Hills, Western Australia. In: van Kranendonk, M. J., Bennett, V. C., and Hoffmann, J. E., (ed.) *Earth's Oldest Rocks*: Elsevier, 255-273.

Coggon, J. A., Luguet, A., Fonseca, R. O. C., Lorand, J. P., Heuser, A. & Appel, P. W. U. (2015). Understanding Re-Os systematics and model ages in metamorphosed Archean ultramafic rocks: A single mineral to whole-rock investigation. *Geochimica Et Cosmochimica Acta* **167**, 205-240.

Cohen, A. S. & Waters, F. G. (1996). Separation of osmium from geological materials by solvent extraction for analysis by thermal ionisation mass spectrometry. *Analytica Chimica Acta* **332**, 269-275.

Creaser, R., Papanastassiou, D. & Wasserburg, G. (1991). Negative thermal ion mass-spectrometry of Osmium, Rhenium, and Iridium. *Geochimica Et Cosmochimica Acta* **55**, 397-401.

Crowley, J. L., Myers, J. S., Sylvester, P. J. & Cox, R. A. (2005). Detrital zircon from the Jack Hills and Mount Narryer, Western Australia: Evidence for diverse > 4.0 Ga source rocks. *Journal of Geology* **113**, 239-263.

Dare, M. S., Tarduno, J. A., Bono, R. K., Cottrell, R. D., Beard, J. S. & Kodama, K. P. (2016). Detrital magnetite and chromite in Jack Hills quartzite cobbles: Further evidence for the preservation of primary magnetizations and new insights into sediment provenance. *Earth and Planetary Science Letters* **451**, 298-314.

Day, J., Waters, C., Schaefer, B., Walker, R. & Turner, S. (2016). Use of Hydrofluoric Acid Desilicification in the Determination of Highly Siderophile Element Abundances and Re-Pt-Os Isotope Systematics in Mafic-Ultramafic Rocks. *Geostandards and Geoanalytical Research* **40**, 49-65.

Day, J. M. D., Brandon, A. D. & Walker, R. J. (2016). Highly Siderophile Elements in Earth, Mars, the Moon, and Asteroids. *Highly Siderophile and Strongly Chalcophile Elements in High-Temperature Geochemistry and Cosmochemistry* **81**, 161-238.

Dunn, S. J., Nemchin, A. A., Cawood, P. A. & Pidgeon, R. T. (2005). Provenance record of the Jack Hills metasedimentary belt: Source of the Earth's oldest zircons. *Precambrian Research* **138**, 235-254.

Fletcher, I. R., Rosman, K. J. R. & Libby, W. G. (1988). Sm-Nd, Pb-Pb and Rb-Sr geochronology of the Manfred Complex, Mount Narryer, Western Australia. *Precambrian Research* **38**, 343-354.

Frei, R. & Jensen, B. K. (2003). Re-Os, Sm-Nd isotope- and REE systematics on ultramafic rocks and pillow basalts from the Earth's oldest oceanic crustal fragments (Isua Supracrustal Belt and Ujaragssuit nunat area, W Greenland). *Chemical Geology* **196**, 163-191.

Gu, H., Sun, H., Wang, F., Ge, C. & Zhou, T. (2019). A new practical isobaric interference correction model for the in situ Hf isotopic analysis using laser ablation-multi-collector-ICP-mass spectrometry of zircons with high Yb/Hf ratios. *Journal of Analytical Atomic Spectrometry* **34**, 1223-1232.

Hanchar, J. & Miller, C. (1993). Zircon zonation patterns as revealed by cathodoluminescence and backscattered electron images - implications for interpretation of complex crustal histories. *Chemical Geology* **110**, 1-13.

Hiess, J., Condon, D. J., McLean, N. & Noble, S. R. (2012). U-238/U-235 Systematics in Terrestrial Uranium-Bearing Minerals. *Science* **335**, 1610-1614.

Horstwood, M. S. A., Kosler, J., Gehrels, G., Jackson, S. E., McLean, N. M., Paton, C., Pearson, N. J., Sircombe, K., Sylvester, P., Vermeesch, P., Bowring, J. F., Condon, D. J. & Schoene, B. (2016). Community-Derived Standards for LA-ICP-MS U-(Th-)Pb Geochronology - Uncertainty Propagation, Age Interpretation and Data Reporting. *Geostandards and Geoanalytical Research* **40**, 311-332.

Ickert, R. B. (2013). Algorithms for estimating uncertainties in initial radiogenic isotope ratios and model ages. *Chemical Geology* **340**, 131-138.

Ishikawa, A., Senda, R., Suzuki, K., Dale, C. & Meisel, T. (2014). Re-evaluating digestion methods for highly siderophile element and Os-187 isotope analysis: Evidence from geological reference materials. *Chemical Geology* **384**, 27-46.

Kemp, A., Vervoort, J., Bjorkman, K. & Iaccheri, L. (2017). Hafnium Isotope Characteristics of Palaeoarchaean Zircon OG1/OGC from the Owens Gully Diorite, Pilbara Craton, Western Australia. *Geostandards and Geoanalytical Research* **41**, 659-673.

Kemp, A. I. S. (2018). Early earth geodynamics: cross examining the geological testimony. *Philosophical Transactions of the Royal Society a-Mathematical Physical and Engineering Sciences* **376**.

Kemp, A. I. S., Wilde, S. A., Hawkesworth, C. J., Coath, C. D., Nemchin, A., Pidgeon, R. T., Vervoort, J. D. & DuFrane, S. A. (2010). Hadean crustal evolution revisited: New constraints from Pb-Hf isotope systematics of the Jack Hills zircons. *Earth and Planetary Science Letters* **296**, 45-56.

Kemp, A. I. S., Wilde, S. A., and Spaggiari, C. (2019). The Narryer Terrane, Yilgarn Craton, Western Australia: Review and Recent Developments. In: van Kranendonk, M. J., Bennett, V. C., and Hoffmann, J. E., (ed.) *Earth's Oldest Rocks*: Elsevier, 401-429.

Kinny, P. D., Williams, I. S., Froude, D. O., Ireland, T. R. & Compston, W. (1988). Early Archean zircon ages from orthogneisses and anorthosites at Mount Narryer, Western Australia. *Precambrian Research* **38**, 325-341.

Luguet, A., Nowell, G. M. & Pearson, D. G. (2008). (184)Os/(188)Os and (186)Os/(188)Os measurements by Negative Thermal Ionisation Mass Spectrometry (N-TIMS): Effects of interfering element and mass fractionation corrections on data accuracy and precision. *Chemical Geology* **248**, 342-362.

Miller, C., Peucker-Ehrenbrink, B. & Ball, L. (2009). Precise determination of rhenium isotope composition by multi-collector inductively coupled plasma mass spectrometry. *Journal of Analytical Atomic Spectrometry* **24**, 1069-1078.

Myers, J. S. (1988). Oldest known terrestrial anorthosite at Mount Narryer, Western Australia. *Precambrian Research* **38**, 309-323.

Myers, J. S. (1997). Byro, W.A., Sheet SG 50 10 (2nd Edition). Western Australia Geological Survey.

Myers, J. S. & Williams, I. R. (1985). Early Precambrian crustal evolution at Mount Narryer, Western Australia. *Precambrian Research* **27**, 153-163.

Nemchin, A. A., Pidgeon, R. T. & Whitehouse, M. J. (2006). Re-evaluation of the origin and evolution of > 4.2 Ga zircons from the Jack Hills metasedimentary rocks. *Earth and Planetary Science Letters* **244**, 218-233.

Paton, C., Woodhead, J., Hellstrom, J., Hergt, J., Greig, A. & Maas, R. (2010). Improved laser ablation U-Pb zircon geochronology through robust downhole fractionation correction. *Geochemistry Geophysics Geosystems* **11**.

Rasmussen, B., Fletcher, I. R., Muhling, J. R., Gregory, C. J. & Wilde, S. A. (2011). Metamorphic replacement of mineral inclusions in detrital zircon from Jack Hills, Australia: Implications for the Hadean Earth. *Geology* **39**, 1143-1146.

Rasmussen, B., Fletcher, I. R., Muhling, J. R., Gregory, C. J. & Wilde, S. A. (2012). Metamorphic replacement of mineral inclusions in detrital zircon from Jack Hills, Australia: Implications for the Hadean Earth. *Geology* **40**, E282-E283.

Rasmussen, B., Fletcher, I. R., Muhling, J. R. & Wilde, S. A. (2010). In situ U-Th-Pb geochronology of monazite and xenotime from the Jack Hills belt: Implications for the age of deposition and metamorphism of Hadean zircons. *Precambrian Research* **180**, 26-46.

Reisberg, L. & Meisel, T. (2002). The Re-Os isotopic system: A review of analytical techniques. *Geostandards Newsletter-the Journal of Geostandards and Geoanalysis* **26**, 249-267.

Rollinson, H., Appel, P. W. U. & Frei, R. (2002). A metamorphosed, early Archaean chromitite from west Greenland: Implications for the genesis of Archaean anorthositic chromitites. *Journal of Petrology* **43**, 2143-2170.

Rowe, ML 2016, Petrology and geochemistry of the Eoarchaean Manfred Complex: origin and components: Geological Survey of Western Australia, Record 2016/22, 150p.

Shirey, S. B. & Walker, R. J. (1995). Carius tube digestion for low-blank Rhenium-Osmium analysis. *Analytical Chemistry* **67**, 2136-2141.

Shirey, S. B. & Walker, R. J. (1998). The Re-Os isotope system in cosmochemistry and high-temperature geochemistry. *Annual Review of Earth and Planetary Sciences* **26**, 423-500.

Schoene, B. (2014). U-Yh-Pb Geochronology. In: Rudnick, R. L. (ed.) *Treatise of Geochemistry (Second Edition)*, 341-370.

Slama, J., Kosler, J., Condon, D., Crowley, J., Gerdes, A., Hanchar, J., Horstwood, M., Morris, G., Nasdala, L., Norberg, N., Schaltegger, U., Schoene, B., Tubrett, M. & Whitehouse, M. (2008). Plesovice zircon - A new natural reference material for U-Pb and Hf isotopic microanalysis. *Chemical Geology* **249**, 1-35.

Smoliar, M. I., Walker, R. J. & Morgan, J. W. (1996). Re-Os ages of group IIA, IIIA, IVA, and IVB iron meteorites. *Science* **271**, 1099-1102.

Soderlund, U., Patchett, J. P., Vervoort, J. D. & Isachsen, C. E. (2004). The Lu-176 decay constant determined by Lu-Hf and U-Pb isotope systematics of Precambrian mafic intrusions. *Earth and Planetary Science Letters* **219**, 311-324.

Spaggiari, C. V. (2007). Structural and lithological evolution of the Jack Hills greenstone belt, Narryer Terrane, Yilgarn Craton, Western Australia. *Western Australia Geological Survey* **Record 2007/3**, 49.

Stern, R., Bodorkos, S., Kamo, S., Hickman, A. & Corfu, F. (2009). Measurement of SIMS Instrumental Mass Fractionation of Pb Isotopes During Zircon Dating. *Geostandards and Geoanalytical Research* **33**, 145-168.

Volkening, J., Walczyk, T. & Heumann, K. (1991). Osmium isotope ratio determinations by negative thermal ionization mass-spectrometry. *International Journal of Mass Spectrometry and Ion Processes* **105**, 147-159.

Walker, R. J., Horan, M. F., Morgan, J. W., Becker, H., Grossman, J. N. & Rubin, A. E. (2002). Comparative Re-187-Os-187 systematics of chondrites: Implications regarding early solar system processes. *Geochimica Et Cosmochimica Acta* **66**, 4187-4201.

Wang, Q. & Wilde, S. A. (2018). New constraints on the Hadean to Proterozoic history of the Jack Hills belt, Western Australia. *Gondwana Research* **55**, 74-91.

Whitehouse, M. J., Nemchin, A. A. & Pidgeon, R. T. (2017). What can Hadean detrital zircon really tell us? A critical evaluation of their geochronology with implications for the interpretation of oxygen and hafnium isotopes. *Gondwana Research* **51**, 78-91.

Wilde, S. A., Valley, J. W., Peck, W. H. & Graham, C. M. (2001). Evidence from detrital zircons for the existence of continental crust and oceans on the Earth 4.4 Gyr ago. *Nature* **409**, 175-178.

Williams, I. R. & Myers, J. S. (1987). Archaean geology of the Mount Narryer region Western Australia. Geological Survey of Western Australia: Report 22, 1-32.

Wood, B. J. & Virgo, D. (1989). Upper mantle oxidation-state: ferric iron contents of lherzolite spinels by Fe-57 Mossbauer-spectroscopy and resultant oxygen fugacities. *Geochimica Et Cosmochimica Acta* **53**, 1277-1291.

Woodhead, J. & Hergt, J. (2005). A preliminary appraisal of seven natural zircon reference materials for in situ Hf isotope determination. *Geostandards and Geoanalytical Research* **29**, 183-195.

Zane, A. & Rizzo, G. (1999). The compositional space of muscovite in granitic rocks. *Canadian Mineralogist* **37**, 1229-1238.

Zhu, Z. H., Meija, J., Zheng, A. R., Mester, Z. & Yang, L. (2017). Determination of the Isotopic Composition of Iridium Using Multicollector-ICPMS. *Analytical Chemistry* **89**, 9375-9382.

Chapter Three:

Detrital chromites: physical and chemical compositions

This chapter is modified from a paper currently drafted for submission to the Journal of Petrology.

Headings and figures have been changed for consistent formatting, and other thesis chapters referenced where appropriate.

Data analysis and interpretation were conducted by the author (LS), as was drafting of the manuscript. IP formulated olivine-spinel geothermometry calculations and aided in interpretation of EPMA data. TE provided 14WA samples. TK provided samples of the Manfred Complex and aided in fieldwork collection of 14WA and 16WA samples. All supervisors (IP and TE) and co-authors (TK) provided minor feedback and edits on the manuscript**.**

Detrital chromite from Jack Hills: implications for the petrogenesis of mafic and ultramafic crust within the Narryer Terrane, Western Australia

Staddon L. G.,*[1,2], Parkinson I. J.,[1], Elliott T.,[1] and Kemp A. I. S.[3]

[1]School of Earth Sciences, Wills Memorial Building, Queens Road, University of Bristol, Bristol, UK, BS8 1RJ.

[2]NIGL, British Geological Survey, Nicker Hill, Keyworth, Nottinghamshire, UK, NG12 5GG

[3]School of Earth Sciences, University of Western Australia, 35 Stirling Highway, Perth 6009, Australia

*Corresponding author: leanne.staddon@bristol.ac.uk

KEYWORDS: Jack Hills, chromite, Narryer Terrane, Archean, Hadean

ABSTRACT

Detrital chromite is found within Hadean zircon bearing metasedimentary rocks at Jack Hills, which is situated within the Narryer Terrane, Yilgarn Craton, Western Australia. Systematic variations in mineral chemistry with changing tectonic setting means spinel is commonly used as a petrogenetic indicator, and so chromites represent good candidates to understand the petrogenesis of poorly understood mafic and ultramafic crust within the Narryer Terrane. Jack Hills detrital chromites are observed as a range of rounded shapes, indicating variable and protracted sedimentary reworking, although mineral chemistry does not covary with grain morphology. Chromites exhibit strong secondary modification signatures of lowered Mg# with highly elevated ZnO and MnO compared to magmatic chromite. Further evidence of extensive alteration is shown by the presence of internal pitted domains, and the replacement of primary inclusions by low temperature phases, that are also abundant as secondary metamorphic assemblages within the metasediment matrix. We propose modification of chromite occurred within the host metasediment by interaction of grains with a metamorphic fluid during deformation of the belt at ~2650 Ma. Despite significant modification of divalent cations and the formation of fuchsite (Cr-rich muscovite) we find only localised variability in Cr#. Compositional variability of chromite cores is consistent across all samples, signifying a primary origin of Cr#. While other key petrogenetic tools, such as Fe_2O_3 and TiO_2, are complicated by mineral non-stoichiometry and secondary mobility within the Jack Hills metasedimentary rocks, Cr# represents a robust provenance indicator. The variable Cr# of detrital chromites preclude a komatiitic origin but fit well with chromite compositions derived from layered intrusions, where spinel liquidus compositions are readily changed by magmatic fractionation and interaction with intercumulus liquids. The Manfred Complex, a 3730 Ma dismembered layered intrusion within the Narryer Terrane, is discussed as a potential source for Jack Hills detrital chromite.

3.1. Introduction

The detrital record of crustal evolution within the early Earth is dominated by analysis of the mineral zircon. This is particularly evident in the Narryer Terrane, within the Yilgarn Craton, in Western Australia (Figure 3.1). Here, Proterozoic to late Archean (Cavosie et al., 2004; Crowley et al., 2005; Rasmussen et al., 2010; Wang and Wilde, 2018) metasedimentary rocks at Jack Hills (Figure 3.2) yield the oldest known fragments of terrestrial crust; individual grains of detrital zircon with magmatic ^{207}Pb-^{206}Pb ages of up to 4374±6 Ma (Compston & Pidgeon, 1986; Wilde et al., 2001; Valley et al., 2014). Despite isolated occurrences of Hadean detrital zircon elsewhere (e.g. Byerly et al., 2018 and references therein), including Mt Narryer to the SW (Figure 3.1; Froude et al., 1983; Pidgeon & Nemchin, 2006), and rare examples of Hadean xenocrystic zircon (Nelson et al., 2000; Wyche et al., 2004; Iizuka et al., 2006; Chaudhuri et al., 2018), Jack Hills detrital zircons thus far represent the most abundant remnants of Hadean (>4030 Ma; Reimink et al., 2014) crust. These important grains therefore provide a unique window into Hadean crustal evolution and have subsequently been rigorously interrogated using numerous geochemical and isotopic techniques (*e.g.* Nebel et al., 2014; Harrison et al., 2017). Despite this, what Jack Hills zircon tell us about the composition, evolution and subsequent destruction of their igneous protoliths is controversial, with conflicting hypotheses inferring vastly disparate geodynamic conditions within the early Earth. Such hypotheses include a 'cool early Earth', with the putative operation of plate tectonics (e.g. Harrison et al., 2008; 2017; Bell et al., 2014), production of zircon-bearing crust by internal reworking of mafic protocrust (e.g. Amelin et al.,1999; Kemp et al., 2010), or compositionally diverse Hadean protoliths (Wang & Wilde, 2018).

While the Jack Hills zircon record yields valuable, if controversial, constraints on the evolution of felsic crust within the Narryer Terrane, the zircon record provides little information on the evolution of contemporaneous mafic and ultramafic crust. While the wider Yilgarn Craton is renowned for the presence of economically significant komatiites (Arndt et al., 2008), extensively exploited for Ni-Cu-PGE (Barnes & Fiorentini, 2012), the generation and evolution of mafic and ultramafic crust within the Narryer Terrane is poorly constrained. Indeed, the only >3100 Ma mafic and ultramafic crust described within the entire Yilgarn Craton is the Eoarchean Manfred Complex (Myers, 1988b; Wyche, 2007), a 3730 Ma disseminated layered intrusion within the Narryer Terrane (Fletcher et al., 1988; Kinny et al., 1988; Kemp et al., 2018). Petrological and isotopic analysis of ancient mafic and ultramafic crust can be challenging. This includes disturbance of typically robust isotopic geochronometers during high grade metamorphism, the loss of mineral assemblages during recrystallisation, and the scarcity of reliable geochronometers such as zircon within mafic and ultramafic lithologies. It is therefore understandable that the strongly deformed fragments of mafic and ultramafic crust within the Narryer Terrane have received less consideration than surrounding quartzofeldspathic gneisses and granitoids.

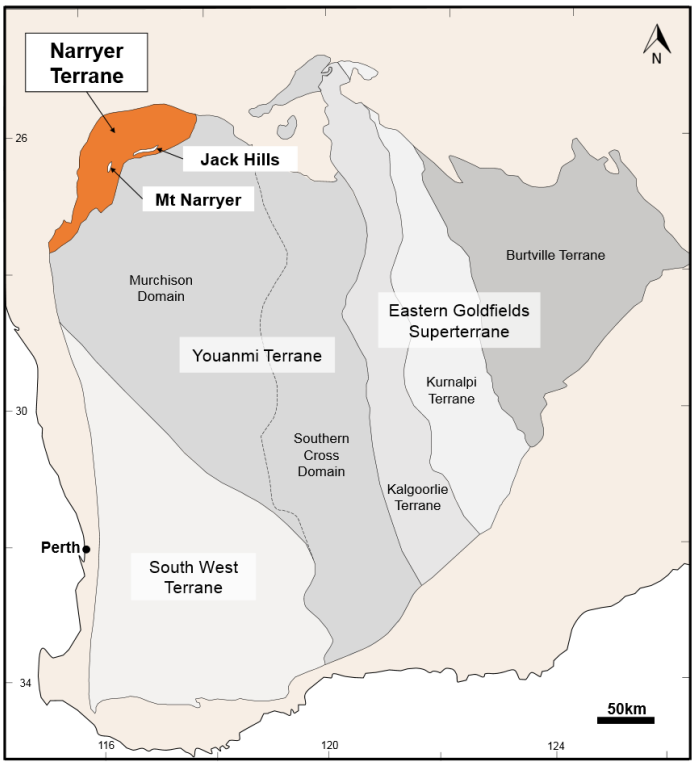

Figure 3.1: Map of the Yilgarn Craton, in Western Australia, showing the position of the Narryer Terrane, Jack Hills and Mount Narryer. Modified from Wilde and Spaggiari, (2007), with terrane boundaries after Cassidy et al, (2006).

However, the eroded remnants of mafic and ultramafic crust are ubiquitous within Jack Hills metasedimentary rocks, in the form of detrital chromite. Unlike zircon and other detrital phases observed at Jack Hills, including minor monazite and xenotime (Rasmussen et al., 2010; Iizuka et al., 2010), chromite has a magmatic provenance restricted solely to mafic and ultramafic crust (Barnes & Roeder, 2001). Furthermore, chromite is frequently used as a petrogenetic indicator, owing to the presence of systematic chemical variations in chromite formed under different tectonic conditions (Irvine, 1967; Dick & Bullen., 1984; Roeder, 1994; Barnes & Roeder, 2001; Kamenetsky et al., 2001). Critically, the sequestration of platinum group elements (PGEs) into spinel means that chromite is amenable to geochronology using Re-Os and Pt-Os decay systems (Shirey & Walker, 1998), potentially allowing a temporal framework of the generation of mafic and ultramafic crust within the Narryer Terrane to be constrained. The value of detrital chromite to elucidate the provenance of grains magmatic protolith has previously been demonstrated (Barnes & Roeder, 2001; Lenaz & Princivalle, 2005; Barkov et al., 2013), though additional care will be required to quantify the effects of metamorphism on grains found within ancient terranes (Barnes, 2000; Colás et al., 2014). Understanding how and when detrital chromite formed will therefore expand on the Jack Hills zircon record and provide valuable information on the composition and petrogenesis of poorly described

mafic and ultramafic crust that was potentially exposed in the Narryer Terrane at the time the sedimentary rocks were deposited.

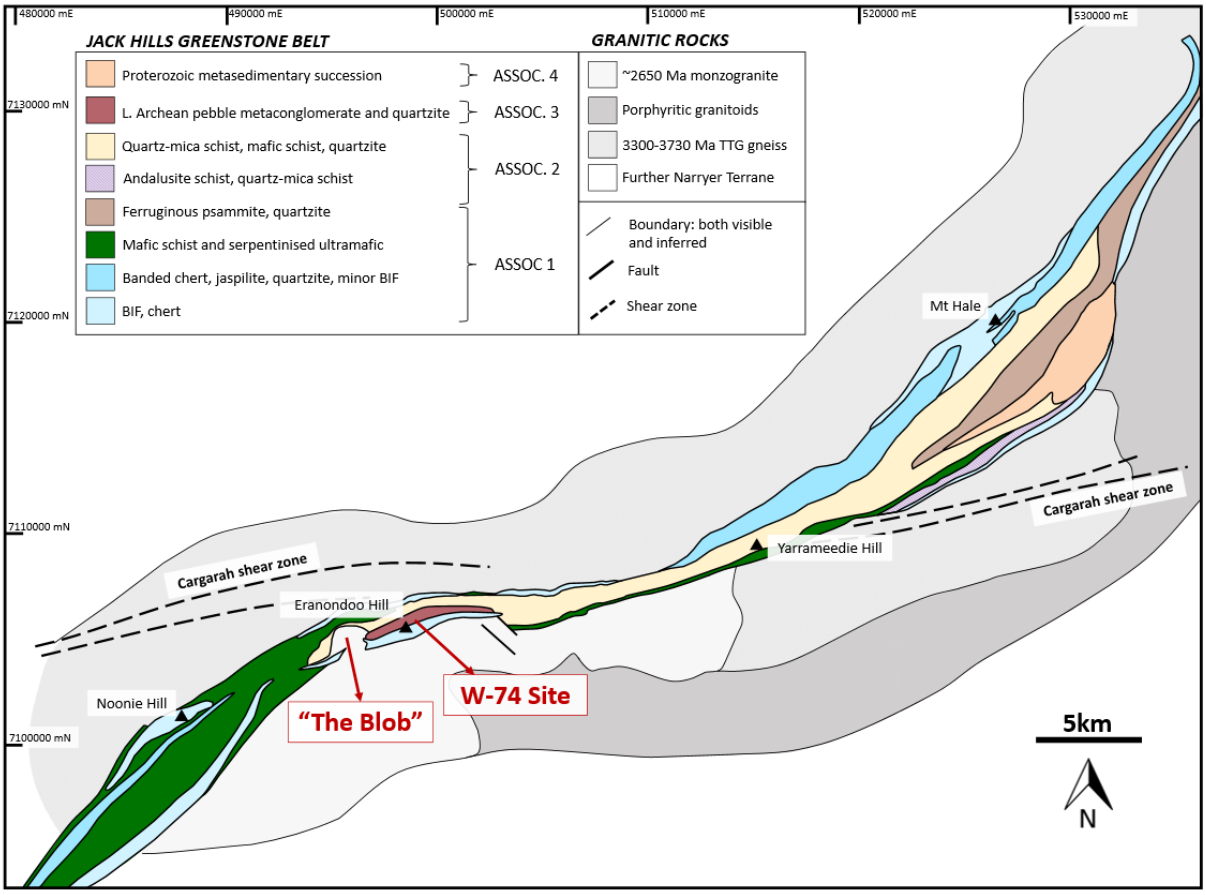

Figure 3.2: Simplified geological map of Jack Hills and surrounding quartzo-feldspathic gneiss and granitoids, after Spaggiari (2007b), and Pidgeon and Wilde (1998). The original W-74 discovery site (Wilde, 2001) at Eranondoo Hill and monzogranitic 'the Blob' intruding metasediments shown for reference.

Despite concerted interest in zircon at Jack Hills, detrital chromites observed within the same metasediments have remained largely unstudied. In an abstract, Cavosie *et al.* (2002) observed two populations of chemically homogeneous chromite from two transects of Jack Hills; rounded grains and euhedral octahedra, that yielded low Mg# ((Mg/Mg+Fe)x100), and elevated, but variable, wt. % ZnO and MnO. Also in an abstract, Valley *et al.* (2005) reported Re-Os model ages (TMAs, see discussion in section Chapter 4) of 3500 Ma to 3200 Ma for the same collection of detrital chromites. This major element chemistry was also confirmed by Dare *et al.* (2016) in analyses of chromites within quartzite cobbles to the NW of the W-74 site. This study proposed that low MgO contents of chromites precluded derivation from komatiites, and that both chromite and Fe-Ni-sulphides observed within quartzite clasts are the erosional products of at least one layered intrusion. However, lowered Mg#, particularly when coupled with elevated ZnO and MnO, is also a fingerprint of secondary metamorphic

modification of chromite (Barnes, 2000; Colás et al., 2014), making this interpretation uncertain and warranting further investigation of such grains.

Here we report major element geochemistry of Jack Hills detrital chromites from 10 metasedimentary samples collected from at or near the W-74 site (Wilde et al., 2001). This study represents the first systematic study of detrital chromite from Archean sediments, and signifies a new direction compared to traditional provenance studies undertaken by analysis of detrital zircon. We highlight the effects of metamorphism on chromite major element compositions, discuss the retention of primary signatures, and propose a plausible provenance for detrital chromites. Finally, we highlight the significance of these grains in enhancing our understanding of the genesis of Jack Hills metasediments and the evolution of mafic and ultramafic crust within the Narryer Terrane.

3.2. Geological Setting

3.2.1. The Narryer Terrane

The Narryer Terrane is the most north-westerly terrane within the Yilgarn Craton, in Western Australia (Myers, 1988a; Kemp et al., 2019; Figure 3.1), and has been interpreted as a deep crustal allochthon thrust above the Youanmi Terrane (Nutman et al., 1993), prior to or coincident with cratonic amalgamation (Kemp et al., 2019). The terrane is dominantly composed of granitic lithologies, now largely preserved as quartzofelsdspathic orthogneiss, with minor ultramafic and mafic intrusives, and metasediments (Myers & Williams, 1985; Williams & Myers, 1987; Myers, 1988a). These units are commonly grouped into the Narryer Gneiss Complex (NGC) (Myers, 1988a) by their virtue of >3000 Ma protolith ages. Late Archean (~2650-2700 Ma) granitoids are abundant within the Narryer Terrane but omitted from the NGC given their younger magmatic ages (Kemp et al., 2019). The Narryer Terrane has undergone high-grade, polyphase deformation, with amphibolite to granulite facies events at ~2700-2650 Ma forming the dominantly observed gneissic fabric (Myers, 1988a; Kinny, 1990; Nutman et al., 1991). There is evidence for previous high-grade thermal events, particularly at ca. 3300 Ma (Nutman et al., 1991; Kinny & Nutman, 1996) and it is likely the Narryer Terrane underwent multiple episodes of deformation and anatexis during the Archean (Kinny & Nutman, 1996).

Despite complicated zircon geochronology (Pidgeon & Wilde, 1998), three dominant quartzofeldspathic orthogneiss units are identified within the NGC. The oldest, the Meeberrie gneiss, is a biotite-rich migmatite that consists of 3670-3600 Ma monzogranitic and 3730 Ma tonalitic protoliths, though age variability is complex and often present at grain scale (Nutman et al., 1991; Kinny & Nutman, 1996; Pidgeon and Wilde, 1998). The Eurada gneiss is a series of ~3480 Ma tonalitic

gneisses observed at the Eurada Bore, a fault-bound, low strain feature situated in the south of the Narryer Terrane (Nutman et al., 1991). The Dugel gneiss yields a well constrained age of 3375 ± 26 Ma (Nutman et al., 1991) and it is thought its syenogranitic protoliths intruded the Meeberrie Gneiss as a series of sheet-like and pegmatitic bodies (Myers, 1988a; Kemp et al., 2019).

The Meeberrie and Dugel gneiss host dispersed fragments of the Manfred Complex, a magmatically and tectonically dismembered and variably metamorphosed layered intrusion. The complex is dominantly amphibolitic (after gabbro and leucogabbro), with pyroxenite, metaperidotite and anorthosite (Williams & Myers, 1987; Fletcher et al., 1988; Myers, 1988b). Relict igneous textures and layering are locally preserved (Kemp et al., 2019). Zircon within Manfred Complex anorthosite and leucogabbro yield ^{207}Pb-^{206}Pb ages of 3730±6 Ma (Kinny et al., 1988; Kemp, 2018), with other lithologies yielding Sm-Nd and Pb-Pb WR ages of 3680 ± 70 Ma and 3689 ± 146 Ma, respectively (Fletcher et al., 1988). The Complex also retains a Pb high μ signature of ~10, suggesting incorporation of a long-lived, high U-Pb reservoir into the parental magma, likely via assimilation of older crust (Fletcher et al., 1988).

3.2.2. Jack Hills

The Jack Hills are located at the southern margin of Narryer Terrane (Figure 3.1 & 3.2) and compromise a thin, ~70km long belt, with a distinctly curvilinear morphology produced by dextral shearing (Spaggiari, 2007a). The Jack Hills belt is preserved tectonically juxtaposed in fault-bound contact with the surrounding NGC, except for localised intrusion of 2654 Ma monzogranite, also known as 'The Blob' (Figure 3.2; Pidgeon & Wilde, 1998; Spaggiari et al., 2007b). Jack Hills may be interchangeably referred to as a greenstone (e.g. Spaggiari, 2007a/b) or metasedimentary belt (e.g. Wang & Wilde, 2018), and consists largely of siliciclastics, including metaconglomerate, quartzite and quartz-mica schist, with intercalated mafic and ultramafic rocks, banded iron formation (BIF) and chert. The presence of grunerite within BIF and hornblende within mafic schist indicates at least portions of the belt reached amphibolite facies metamorphism: hornblende within mafic schist is commonly overprinted by actinolite, showing the later retrogression to greenschist facies that defines the current dominant metamorphic signature (Spaggiari, 2007a). Deformation has tectonically disturbed and juxtaposed lithological associations, making an original stratigraphy difficult to discern.

Spaggiari (2007a) divided the belt into four associations determined by lithological variability (Figure 3.2). Briefly, unit 1 consists of interbedded BIF, chert and quartzite, mafic and ultramafics, and black and white banded quartzites. Unit 2 yields pelitic to semi-pelitic associations, now present as quartz-mica and andalusite schists, with accompanying mafic schist and quartzite. The presence of an S1 cleavage and recumbent folding absent from other lithological units suggests units 1 and 2 were

deformed prior to the deposition of units 3 and 4 (Spaggiari, 2007a). Unit 3 is restricted to the central region of the belt at Eranondoo Hill (Figure 3.2), and contains mature, siliciclastic sediments interpreted to have been deposited within a deltaic alluvial fan (Spaggiari, 2007a/b) between ~3050 Ma and 2650 Ma (Crowley et al, 2005; Rasmussen et al, 2010). The discovery of Proterozoic detrital zircons (Cavosie et al., 2004; Dunn et al., 2005) within the Jack Hills belt led to the recognition of Unit 4, which hosts metasediments deposited during the Proterozoic. Wang & Wilde (2018) observed interbedded siliciclastics at the same apparent metamorphic grade but with both Archean and Proterozoic depositional ages, highlighting that the depositional and/or tectonic relationships of units 3 and 4 may be more complex than previously postulated.

Metasedimentary rocks from Eranondoo Hill, chiefly oligomict pebble to cobble metaconglomerate and quartzite, are renowned for hosting Hadean detrital zircon (Compston & Pidgeon, 1986; Wilde et al., 2001). The best characterised and most heavily sampled metasediments for analysis of detrital zircon crop out at the W-74 'discovery site' (Figure 3.3). Unsurprisingly, Jack Hills detrital zircon have been the subject of numerous publications and reviews (*e.g.* Nebel et al., 2014; Harrison et al., 2017). While a detailed description of the zircons is beyond the remit of this publication, it is critical to note that the ^{207}Pb-^{206}Pb age distribution peaks of Archean detrital zircon correspond well with the known major units of the NGC and granitic lithologies surrounding Jack Hills (Nutman et al., 1991; Pidgeon & Wilde, 1998). This strongly suggests Jack Hills metasediments were derived from units within the Narryer Terrane. Detrital zircon from the W-74 site dominantly yield ^{207}Pb-^{206}Pb ages of 3380-3600 Ma, with ~12% of zircon yielding Hadean ^{207}Pb-^{206}Pb ages (Crowley et al., 2005; Holden et al., 2009). The dominant age distribution peak of ~3380-3400 Ma is contemporaneous with protoliths of the Dugel gneiss, with a peak tail of ^{207}Pb-^{206}Pb ages towards 3600 Ma likely composed of zircon derived from protoliths of the Eurada and Meeberrie gneisses. While zircon derived from the protoliths of the Meeberrie gneiss appear to be underrepresented at the W-74 site in comparison to their abundance within the Narryer Terrane, detrital zircons with analogous ^{207}Pb-^{206}Pb ages are more abundant within sediments in the NE of the belt, and at Mount Narryer to the SW (Crowley et al, 2005; Dunn et al, 2005). The source of >3800 Ma detrital zircons remains unknown as no lithologies of this age are observed within the Narryer Terrane. This indicates the source of these zircons are thus far undiscovered, have been recycled (note the presence of younger rims; Chapter 5), or that detrital zircons were sourced from outside the Narryer Terrane.

Metasediment from the W-74 site shows clear indications of deformation; intense shearing is particularly evident with an anastomosing micaceous matrix, where a strong foliation is coincident with flattening and recrystallisation of quartzite cobbles (Spaggiari, 2007a). Thermal or fluid events within the Jack Hills belt occurred at ~3080 Ma, 2650 Ma, ~1850-1800 Ma and 800 Ma (Spaggiari, et

al., 2007b; Rasmussen et al., 2010; 2011). Monazite-xenotime thermometry of secondary inclusions within detrital zircon yield temperatures of 420°C-475°C (Rasmussen et al., 2011), indicative of upper greenschist to lower amphibolite facies metamorphism coincident with peak metamorphic conditions within unit 3 metasediments, likely at 2650 Ma. The event at ~1800 Ma (Spaggiari et al., 2007b; Rasmussen et al, 2010) and a discrete event at 800 Ma (Rasmussen et al., 2010; 2011) are of unknown magnitude, but coincide with formation of authigenic monazite and xenotime (Rasmussen et al., 2010; 2011).

3.3. Methods and Materials

3.3.1. Sample collection and preparation

Six samples of 3050 Ma to 2650 Ma (Crowley et al., 2005; Rasmussen et al., 2010) pebble metaconglomerate (14WA1-4, 16WA5-6) were collected from or near to the W-74 site (Wilde et al., 2001) at Jack Hills (Figure 3.3). A further sample of pebble metaconglomerate (16WA8) and a quartzite (16WA7) were collected along strike approximately 35m to the WNW of the W-74 site. Finally, two pebble metaconglomerates (16WA9-10) were sampled from a prominent ridge across the valley to the NE. As these metasedimentary units were sampled away from the W-74 site it is important to note that their depositional ages are unknown (e.g. Wang & Wilde, 2018). Individual sample descriptions of 14WA1-4 and 16WA5-10 metasedimentary rocks and their detrital mineral distributions are provided in Chapter 2. Metasediments were collected as loose slabs; the large size of individual metasedimentary samples (>30 cm) collected suggests they are likely derived from at or near their original position. Distinctly green, fuchsite-rich (muscovite with >1 wt. % Cr_2O_3 (Challis et al., 1995)) samples were collected with the aim of yielding the highest concentrations of chromite grains. Chromites were separated using standard crushing and separation procedures, then sieved to yield size fractions of ≤500 μm for analysis. 14WA1-4 heavy minerals were concentrated using a Wilfey table, followed by magnetic and heavy liquid separation. 16WA5-10 was separated into heavy fractions via panning. Chromites were picked by hand, separated per sample location, grain size and rounding shape (see Section 3.4.1), mounted in epoxy resin and polished to approximately equatorial planes. Detrital grains within a thin section of 14WA2 were also analysed, as were chromites liberated via HF leaching of quartzite cobbles from 14WA2 and 16WA5. No chemical differences between *in-situ* and bulk chromites were observed, so they are discussed together herein.

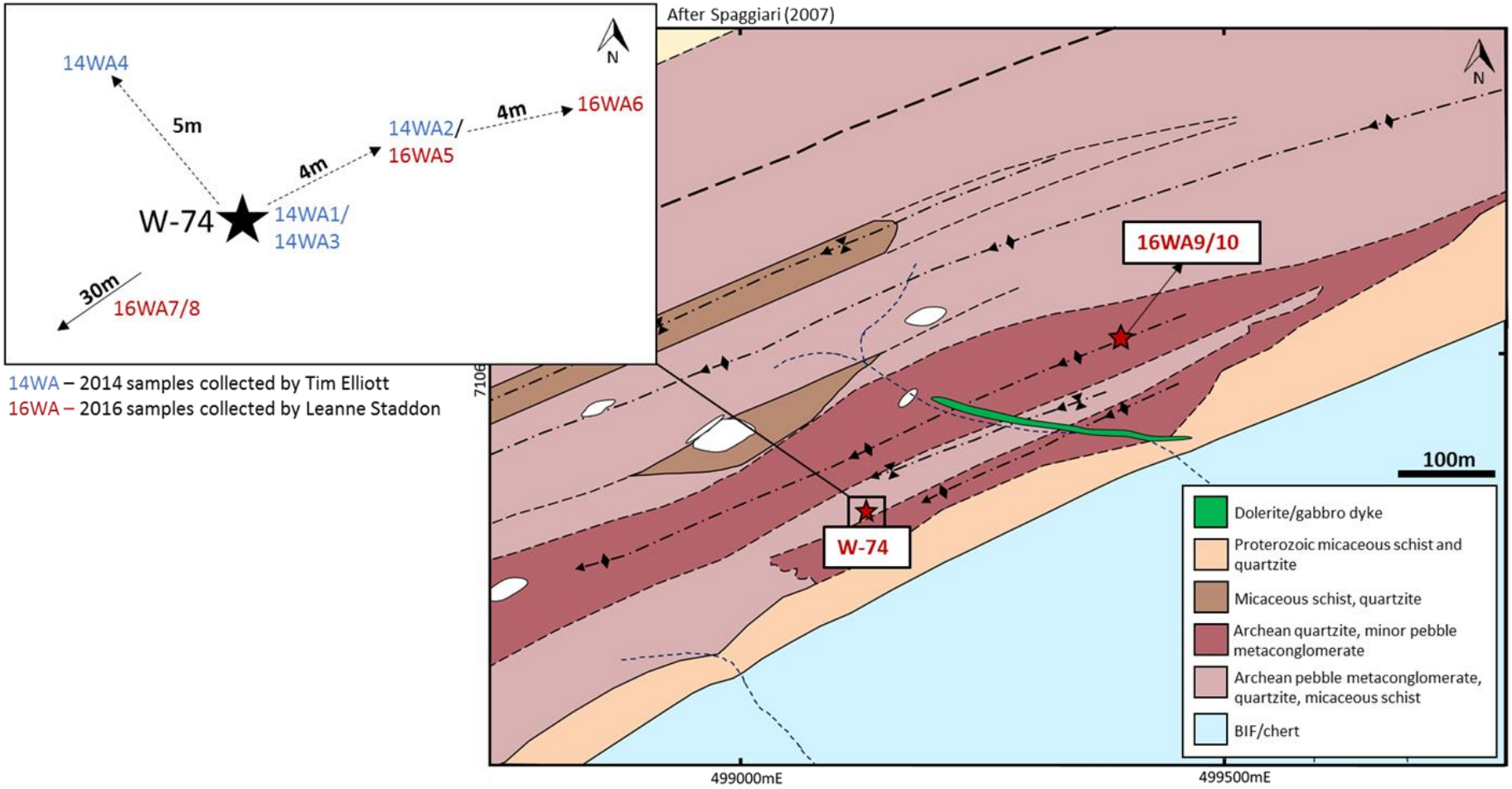

Figure 3.3: Higher resolution geological map of sampling locations at and around the W-74 discovery site (see Figure 1.2).

3.3.2. Chromite analysis

Chromites were imaged using reflected light microscopy and/or back scattered electron imaging using the Hitatchi S-3500N scanning electron microscope at the University of Bristol. Imaging was undertaken to observe any features such as cracks and inclusions that may perturb analyses, and to identify areas of interest within chromite grains. Chromite major elements were determined from individual spots and line scans using the Cameca SX100 microprobe at the University of Bristol. Cr, Al, Fe, Mg, Zn, Mn, Ti, V, and Ni abundances of chromite were determined using a 20kV accelerating voltage, a 10nA beam current, and appropriate peak counting and background times. Si, Na and Ca were included within the set up to monitor any silicate contamination; analyses with >0.15 wt. % oxide of these elements were omitted. Na was not included in later analysis of high Zn chromite, owing to significant overlap of the Na Kα with the Zn Kβ. As such, only Si and Ca were used to trace any contamination in high Zn samples. The overlap of Ti Kβ on V Kα was corrected either online via analysis of V-free $SrTiO_3$ or using high-resolution slits. No resolvable variability in the V_2O_3 contents of chromite or chromite secondary standards was observed between the two set ups.

The method of Droop (1987) was employed to stoichiometrically calculate the ferric iron content of chromite, with the robustness of this calculation monitored in-run by regular measurement of four spinel standards (8316, 8311, 79-1 and 8315) well characterised for $Fe^{3+}/\sum Fe$ using both stoichiometry and Mössbauer analysis from Wood & Virgo (1991). 14WA4, 16WA6 and 16WA9-10 yielded chromite with systematically low totals, typically between 97% and 98%. Both EDS and WDS analysis of these grains revealed no additional detectable elements present within chromite, and standards and other samples analysed within the same run yielded good totals. The cause of low totals within these samples is unknown but may reflect non-stoichiometry, though there is no correlation between totals and Fe^{3+} concentrations (Supplementary Material 2.1). Non-stoichiometry is well known from other analyses of natural spinel (Kamperman et al., 1996; Rollinson et al., 2012), but in the absence of direct oxygen or Mössbauer measurements, this remains unresolved and Fe_2O_3 contents of chromite should be considered minimum concentrations. While other analyses are restricted to those that yield totals of 98-102, chromites with totals of 97.5-102 from 14WA4, 16WA6 and 16WA9-10 are included in this contribution. All EPMA analyses of detrital chromites are provided in Supplementary Material 1.

3.4. Results

3.4.1. Chromite morphology and inclusion assemblages

Jack Hills detrital chromites are observed as variably rounded, ≤500 µm grains that are enclosed by or closely associated with fuchsite within quartzite or metaconglomerate matrix (Figure 3.4a). Finer (≤100 µm) chromite has previously been reported within metaconglomerate quartzite cobbles (Dare et al., 2016). Such grains were observed only rarely *in-situ* during this study (Figure 4b), though HF leaching of quartzite cobbles liberated a small number of grains (n = 12). Chromite derived from metasediment at the W-74 site are present as euhedral octahedra (EO), rounded octahedra (RO) or rounded grains (RC– rounded chromite) (Figure 4a). Euhedral octahedra yield minimal rounding on two or fewer faces, with many euhedral grains showing little or no evidence of transport. RC grains demonstrate limited indication of original octahedral habit on two or less faces and are often present as highly spherical morphologies. Rounded octahedra are grains with morphologies between rounded and euhedral chromite. Many chromites show textural evidence of sedimentary transport, including

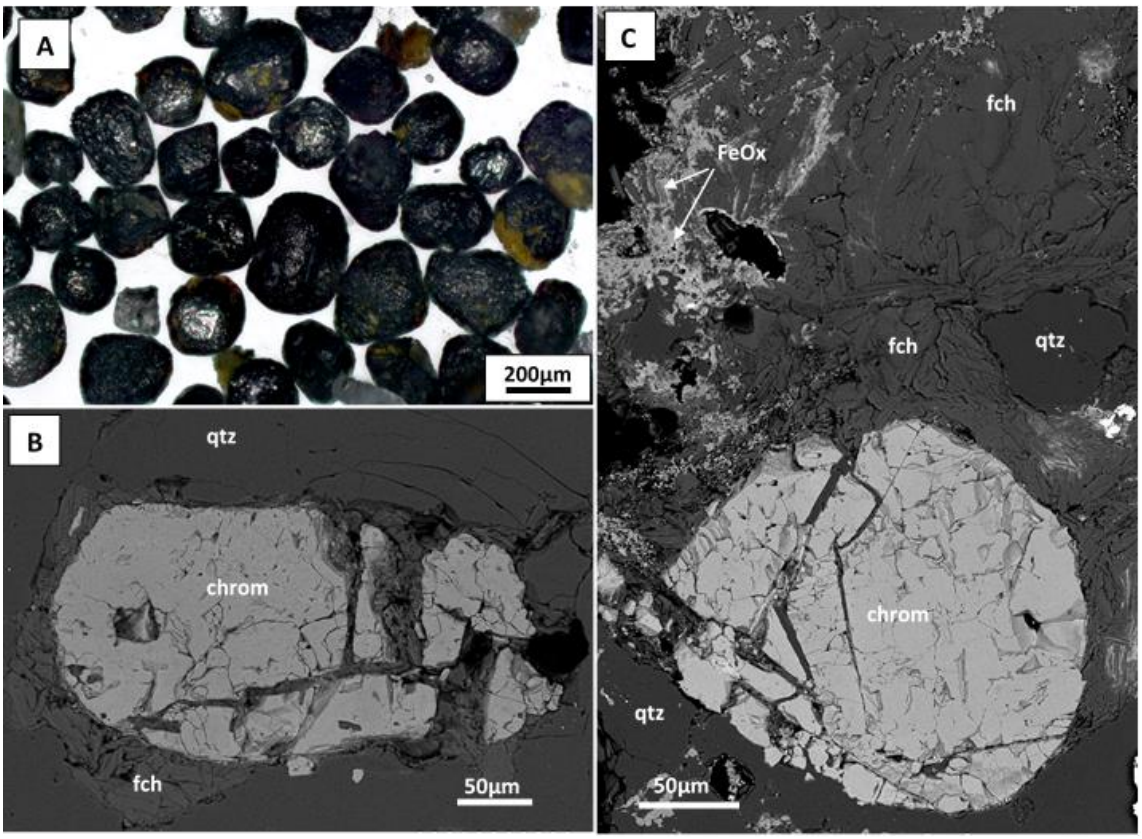

Figure 3.4: Jack Hills detrital chromite A) Optical microscope image illustrating e*x-situ* variably rounded morphologies of chromite grains. Note the green-brown fuchsite on some chromites. B) BSE image of chromite observed *in-situ* with quartzite cobble. Despite being isolated from metaconglomerate matrix the cobble has been infiltrated by secondary muscovite. C) BSE image of complex and ragged boundaries between chromite and Cr-muscovite within metaconglomerate matrix. Grain heavily fractured on its southern margin. Chrom – chromite, qtz – quartz, fch – fuchsite, FeOx – iron oxide (likely magnetite).

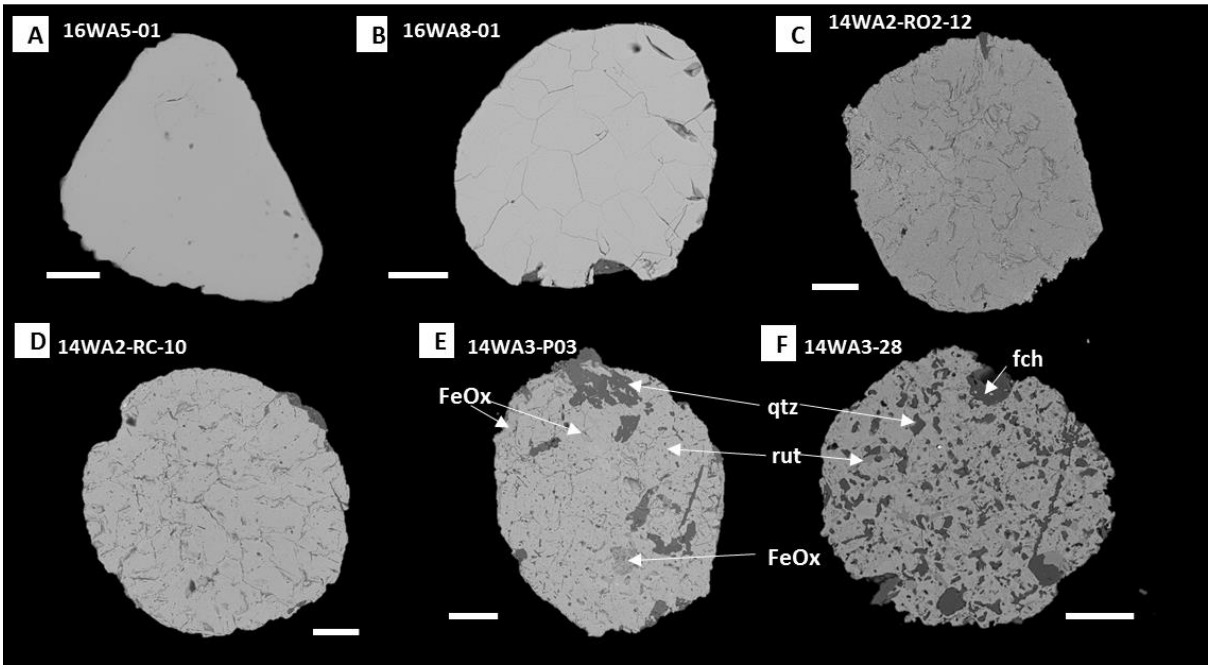

Figure 3.5: BSE images showing chromite textural variation. All scale bars 50 µm. A) Smooth with minimal fracturing, commonly associated with high Cr#. B) Polygonal fracturing, no pitted domains. C) Fractured with very fine pitted domains. No coarser pores, with pitted domains localised to edges and near fractures. D) Fractured with increasingly pitted textures, often away from obvious fractures. E) and F) porous chromite, fractures apparently lost or in-filled by secondary material. Secondary material often aligned to crystallographic axes. Qtz – quartz, fch – fuchsite, FeOx – iron oxide (likely magnetite), and rut- rutile.

grain pitting and rounding of broken surfaces. 16WA9 and 16WA10 (sampled to the NE of W-74) yield a more bimodal distribution than other sample sites, with chromite dominantly RC and minor EO (Section 2.3.1).

A range of internal textures are present (Figure 3.5a-f), with grains often heavily cracked and displaying ragged boundaries with surrounding fuchsite (Figure 3.4c). Fractures occasionally displaying distinct polygonal morphologies (Figure 3.5b). Cracks are at times filled with quartz, fuchsite, and Fe-oxide. Furthermore, distinct 'pitted' textural domains within chromites reveal the presence of ≤10 µm inclusions of dominantly quartz and fuchsite (Figure 3.5/3.6). Rarer porous textures with ≥30 µm inclusion assemblages also observed (Figure 3.5e/f). Both pitted and porous domains are particularly observed at chromite rims or adjacent to cracks, and where chromite is enclosed by fuchsite (Figure 3.5c). In rare cases, porous domains account for the entire chromite grain (Figure 3.5e-f). Fine laths of rutile, dominantly aligned to chromite crystallographic axes, are also frequently observed within and associated with pitted and porous domains (Figure 3.5e-f and 3.6a). Isolated monomineralic and polyphase silicate and oxide inclusions are also present within grains (Figure 3.6). Such inclusions typically lack euhedral morphologies, with globular or anhedral habits largely observed (e.g. Figure 3.6b), though some rarely show more distinct, subhedral to euhedral morphologies (Figure 3.6a). Chromite inclusion and crack filling assemblages of quartz, fuchsite and rutile (Figure 3.6a-b, e) are

often accompanied by other fine-grained (typically ≤10 µm) phases, including Fe-oxide (Figure 3.6b), Fe-sulphide (Figure 3.6c/f), and very fine (<5 µm), rarer monazite (Figure 3.6d).

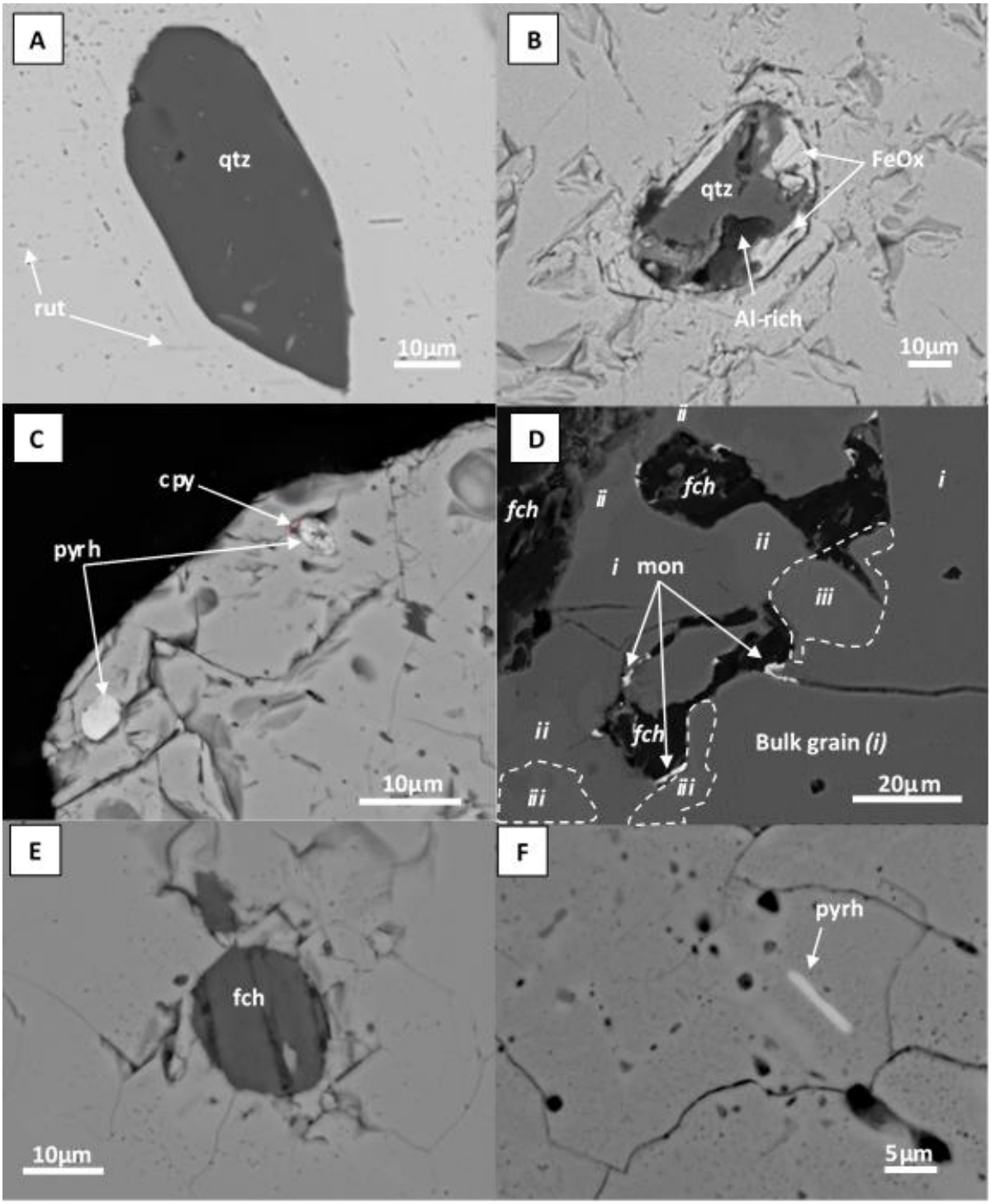

Figure 3.6 (previous page): BSE images of inclusion assemblages **A)** Eu/subhedral quartz which contains rutile, a Mg- silicate, and apatite? Note the surrounding pitted domain but absence of cracks, showing apparent isolation of this inclusion from fractures. **B)** Polyphase assemblage of quartz, iron oxide, muscovite, and an Al-rich phase. **C)** Subhedral Fe-sulphide within pitted domain of chromite. Pyrh- pyrrhotite and cpy- chalcopyrite. **D)** Monazite (mon) associated with muscovite within fractures of altered grain. Brighter portions of chromite have higher Cr# than the rest of the grain. *(i)* Cr# of bulk grain, *(ii)* mildly elevated Cr# shown by slight increase in BSE brightness, and *(iii)* highly elevated Cr# shown by bright BSE domain **E)** Anhedral inclusion of fuchsite (fch) with surrounding fractures and pitted domain. **F)** Pyrrhotite exploiting crystallographic axes of chromite. Associated with pitted domain and areas of higher Cr#.

3.4.2. Chromite Major Element Abundances

Representative analyses of detrital chromite from each metasediment sample location are presented in Table 3.1, and the full EPMA data set is available in Supplementary Material 1. Chromite from all sample locations yield elevated ZnO (up to 13 wt.%) and MnO (up to 2.8 wt.%), coupled with low Mg# (Mg/(Mg+Fe^{2+}) x100) of ≤ 30 (Figure 3.7a-b). Chromites yield high, but variable Cr# (Cr/(Cr+Al) x100) of 48-82, with the bulk of chromites displaying Cr# of 54-66 (Figure 3.8), resulting in an average Cr# of 62. Chromite major element abundances show no variation with grain size or rounding shape (Supplementary 2.2 and 2.3) but differ systematically between sampling location of metasediments (Figure 3.7 and 3.8).

Sample variability (Ti^{4+} and divalent cations; Fe^{2+}, Mg^{2+}, Zn^{2+}, Mn^{2+}, and Ni^{2+})

14WA1 chromites yield Mg# of 5-18, 2-4 wt.% ZnO and the highest MnO contents of all samples at 1.6-2.8 wt.%. 14WA2 chromites have the most variable Mg# of all samples, ranging from 5-22, the lowest ZnO contents at 0.5-2 wt.%, and MnO of 0.7-1.4 wt.%. 14WA3 chromites yield scattered Mg# of 2-17: most grains have Mg# of ≤8. Grains also yield very high ZnO contents largely of 5-9 wt.%, and variable, but high MnO of 1-2.5 wt.%. 14WA4 chromite have MnO contents indistinguishable from 14WA3 but are more homogeneous in Mg# and ZnO content, containing 3-6 wt.% and dominantly 5-7 wt.%, respectively. Owing to the proximity of the sampling locations of 16WA5 to 14WA2 (see Figure 3.3) it was anticipated that grains would be geochemically identical, but 16WA5 are found to yield systematically higher ZnO contents than 14WA2, at 1.5-3 wt.%, though MnO contents and Mg# are indistinguishable. TiO_2 is typically <1 wt.%. Individual analyses where TiO_2 is above 1 wt.% correlate with areas where laths of rutile are present, and are omitted from consideration. As the typical TiO_2 concentration of detrital chromite is < ~0.3 wt.% (Figure 3.7c and 3.8c), this suggests grains with TiO_2 >0.3 wt.% may also be a product of overlap with rutile laths. Lower Cr# grains also more commonly contain rutile, suggesting overlap as a viable mechanism for higher TiO_2. Despite this, many chromites with ~0.3-0.8 wt.% TiO_2 show no evidence of rutile laths in BSE images, although though interaction of the electron beam with sub-surface rutile inclusions cannot be discounted. NiO within grains is largely below the detection limit of ~0.03 wt.% (Supplementary Material 2.4).

Sample	14WA1	14WA2	14WA2	14WA3	14WA4	14WA4	16WA5	16WA5	16WA6	16WA7	16WA8	16WA9	16WA10
Size fraction (µm)	250-120	250-120	250-120	120-50	250-120	250-120	<500	<500	<500	<500	<500	<500	<500
Grain #	4	3	17	44	28	36	19	20	12	7	5 core	2	20
Morphology	RO	RO (4)	RO (2)	RO	RO/RC	EO	RO	RO	EO	RO/EO	RO/RC	EO	RC
SiO_2	0.02	0.00	0.08	0.00	0.00	0.08	0.01	0.11	0.01	0.00	0.01	0.03	0.03
TiO_2	0.18	0.12	0.32	0.27	0.09	0.22	0.12	0.16	0.19	0.28	0.08	0.22	0.04
Al_2O_3	18.52	17.98	11.89	18.13	18.53	9.87	20.28	9.53	18.26	22.43	19.02	19.48	20.35
Cr_2O3	46.20	48.43	51.52	42.43	44.42	55.60	44.18	50.12	45.82	38.52	44.69	45.26	44.11
V_2O_3	0.12	0.14	0.19	0.16	0.11	0.06	n/a	n/a	n/a	n/a	n/a	0.14	0.13
Fe_2O_3	0.00	0.00	3.97	4.37	0.82	0.00	0.00	7.09	0.00	1.81	0.05	0.00	0.00
FeO	27.66	28.57	28.26	24.39	26.17	25.36	28.76	28.68	27.50	23.79	28.63	29.19	26.65
MgO	1.20	1.83	2.40	1.39	0.62	0.46	2.18	1.51	1.67	0.49	0.91	0.76	0.42
MnO	2.13	0.83	1.46	2.03	1.84	2.27	0.71	1.39	0.33	0.73	0.95	1.80	1.28
CaO	0.00	0.00	0.01	0.00	0.01	0.01	0.00	0.01	0.01	0.01	0.00	0.00	0.00
Na_2O	0.00	0.05	0.10	0.00	0.00	0.00	n/a	n/a	n/a	n/a	n/a	n/a	n/a
NiO	0.00	0.00	0.00	0.00	0.01	0.00	0.02	0.00	0.00	0.00	0.01	0.00	0.00
ZnO	3.08	1.29	0.84	7.29	6.19	4.55	2.11	1.51	4.32	11.24	3.95	1.39	5.50
Total	**99.10**	**99.24**	**101.03**	**100.46**	**98.80**	**98.49**	**98.38**	**100.11**	**98.11**	**99.31**	**98.31**	**98.27**	**98.52**
Mg#	7.20	10.23	11.83	8.03	3.95	3.13	11.90	7.15	9.77	3.30	5.36	4.44	2.76
Cr#	62.60	64.37	74.41	61.09	61.66	79.07	59.37	77.91	62.74	53.53	61.19	60.92	59.25
$Fe^{3+}/\Sigma Fe$	0.00	0.00	0.11	0.14	0.03	0.00	0.00	0.18	0.00	0.06	0.00	0.00	0.00

Table 3.1: Representative EPMA analysis of chromite from each sample location. V_2O_3 not measured for 16WA5-7 and partial 16WA8. Fe_2O_3 calculated from AB_2O_4 stoichiometry using the equations of Droop (1987).

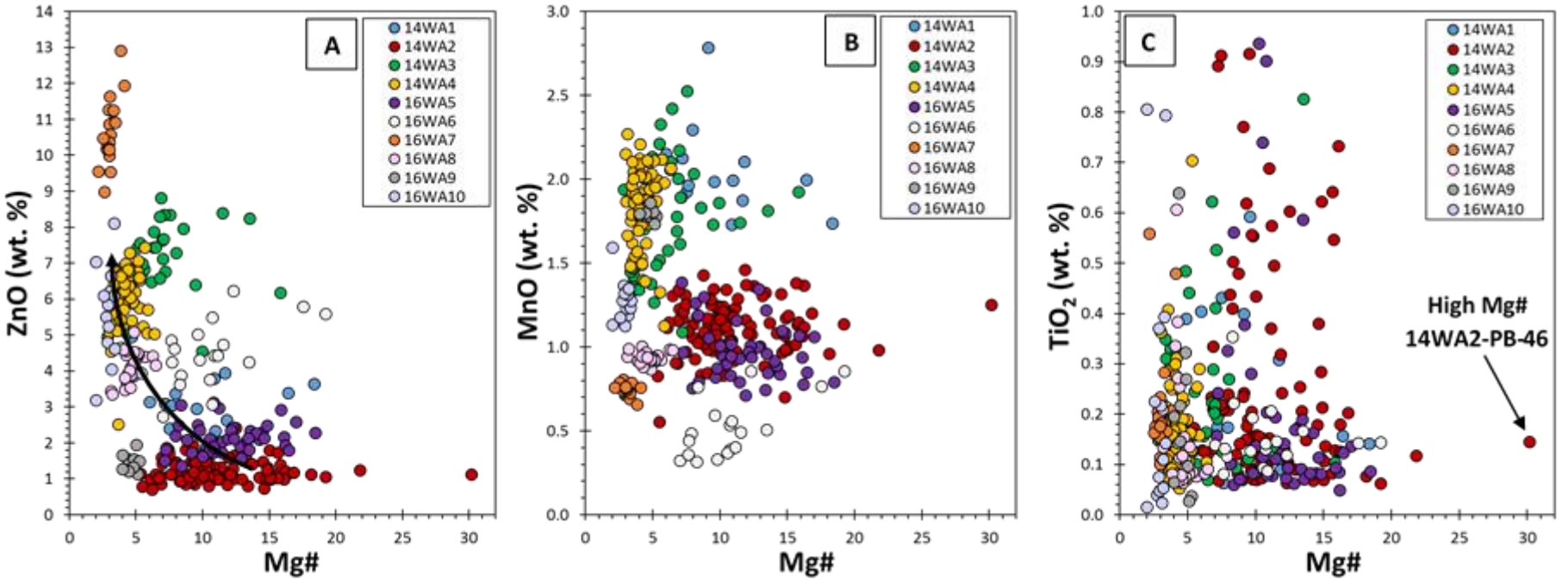

Figure 3.7: Divalent cation plots: each data point is separated by sample and represents a core or near-core composition of chromite. **A)** ZnO vs Mg#. Apparent increasing metamorphic or metasomatic grade shown by arrow. **B)** MnO vs Mg#, no distinct variation with sample location. **C)** TiO_2 vs Mg#. Most grains yield low TiO_2 of <0.25 wt.%. It is likely that some analyses above this value overlapped with subsurface rutile laths, though some grains with >0.25 wt.% TiO_2 show no evidence of rutile laths. TiO_2 >1 wt. % clearly represents overlap with rutile laths, so are omitted.

Within 16WA6 chromites, ZnO is found to be intermediate between 14WA1 and 16WA8 at 2.8-6.2 wt.%. Grains from this sample yield distinctly lower MnO contents than all other samples (<0.6 wt.%), and Mg# between 7-20. 16WA7 chromites yield the highest ZnO contents of all samples at 9-13 wt.%, coupled with homogeneous MnO of 0.6-0.8 wt.%, and very low Mg# of ≤5. 16WA8 was sampled within 5m of 16WA7, but chromites yield vastly different mineral chemistry, with ZnO of 3-5 wt.%, very homogeneous MnO of ~0.9 wt.%, and Mg#s of ≤8. 16WA9 and 16WA10 were sampled from outcrop NE of the W-74 site, from a prominent ridge across the valley. 16WA9 yields grains with low ZnO (1-2 wt.%), similar to 14WA2, but at lower and more homogeneous Mg# of 4-5. 16WA9 yield homogeneous MnO of 1.6-1.8 wt.%. Despite being sampled less than 2m apart, 16WA10 chromites contain considerably higher and more heterogeneous ZnO than 16WA9, at 3-8 wt.%. It also yields slightly lower, but similarly homogeneous Mg#s of 2-4. 16WA10 MnO contents are also resolvably lower at 1.1-1.6 wt.%.

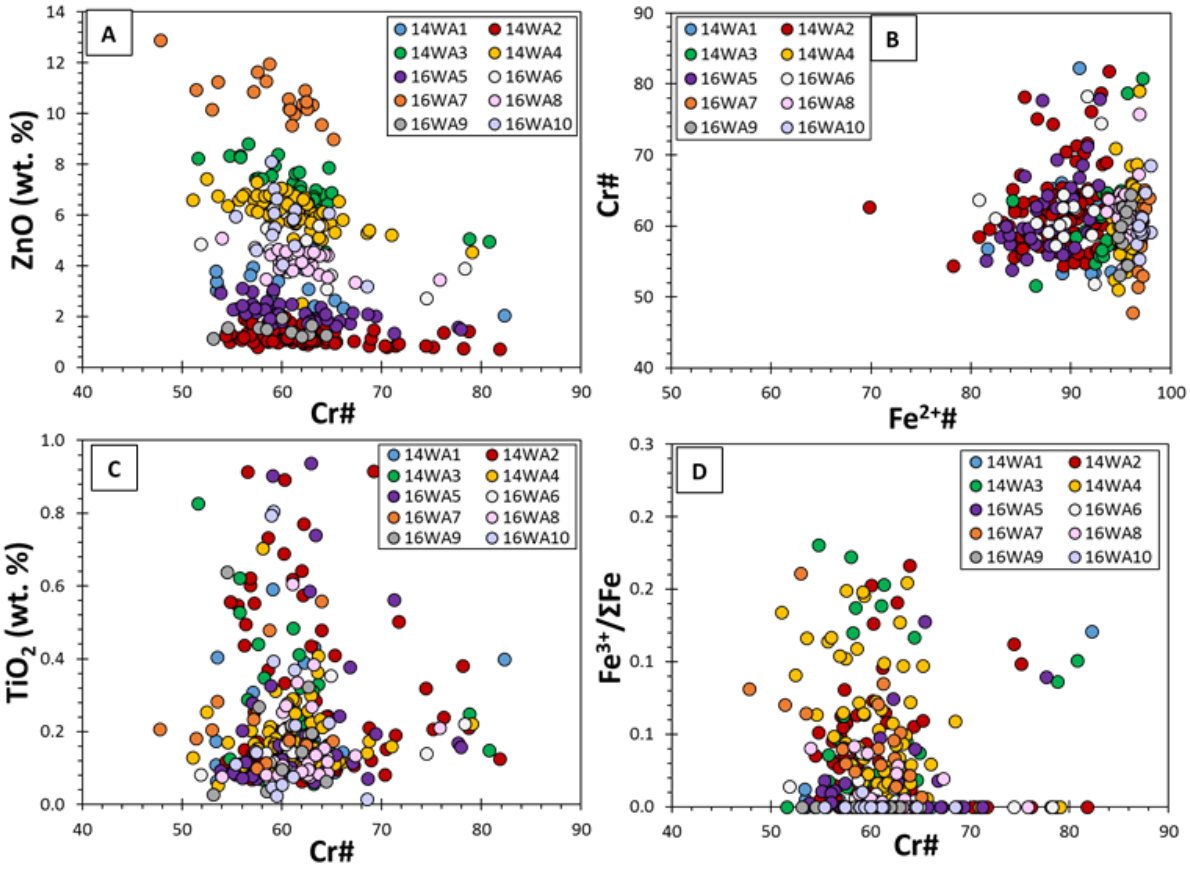

Figure 3.8: Trivalent cation plots. **A)** ZnO vs Cr#. No variation in Cr# shown despite apparent increasing ZnO. Increased equilibration of grain with modifying medium shown by arrow. **B)** Cr# vs Fe^{2+}# ($Fe^{2+}/(Fe^{2+}+Mg^{2+})x100$), fit of numerous samples to an isopleth shape (see Figure 3.12), shown more clearly in Figure 3.11. **C)** TiO_2 concentrations vs Cr#. Scatter towards 1 wt.% a mixture of high TiO_2 grains and likely overlap of rutile laths. High Cr# grains appear to be slightly elevated in TiO_2 in comparison to bulk lower Cr# grains. **D)** $Fe^{3+}/\Sigma Fe$ (total Fe) vs Cr#, no distinct variation with Cr#, but all grains <0.25.

Sample variability (trivalent cations: Cr^{3+}, Al^{3+}, Fe^{3+}, V^{3+})

Despite considerable variability of divalent cations between sampling locations, Cr# of detrital chromites largely show a consistent range across all samples (Figure 3.8). There is a faint trend of increasingly Al-rich grains with greater ZnO content of samples; it is particularly apparent that 16WA7 chromites yield slightly lower Cr# than other samples (Figure 3.8a). Lowered ZnO with increasing Cr# is also observed within individual samples (Figure 3.8a), though this is an effect of the lower Mg# these grains have equilibrated at. Chromites yield low Fe_2O_3 calculated contents, with the bulk of the detrital population containing ≤2 wt.% Fe_2O_3, though sporadic outliers with up to 8 wt.% Fe_2O_3 are present. The low Fe_2O_3 contents of grains result in highly variable $Fe^{3+}/\Sigma Fe$ ratios of 0-0.2, with chromites yielding Fe3+/ΣFe of dominantly <0.1 (Figure 3.8d). Interestingly many chromites, particularly grains with elevated Cr#, yield consistent, non-stoichiometric cation totals of less than 3 when normalised to 4 oxygens (Figure 3.9). This requires the absence of Fe_2O_3, and a decrease in the proportion of anions to cations (e.g. Cr_2O_3 to CrO) to charge balance. While V_2O_3 was not measured for 16WA5-7, it is consistently present at 0.05 wt.%, to 0.3 wt.% within chromites, and yields no inter-sample variability. There is a hint of two trends of decreasing V_2O_3 within increasing Cr# within chromite (Supplementary Material 2.5), but as V_2O_3 variability within chromite is not well understood, this is not discussed further.

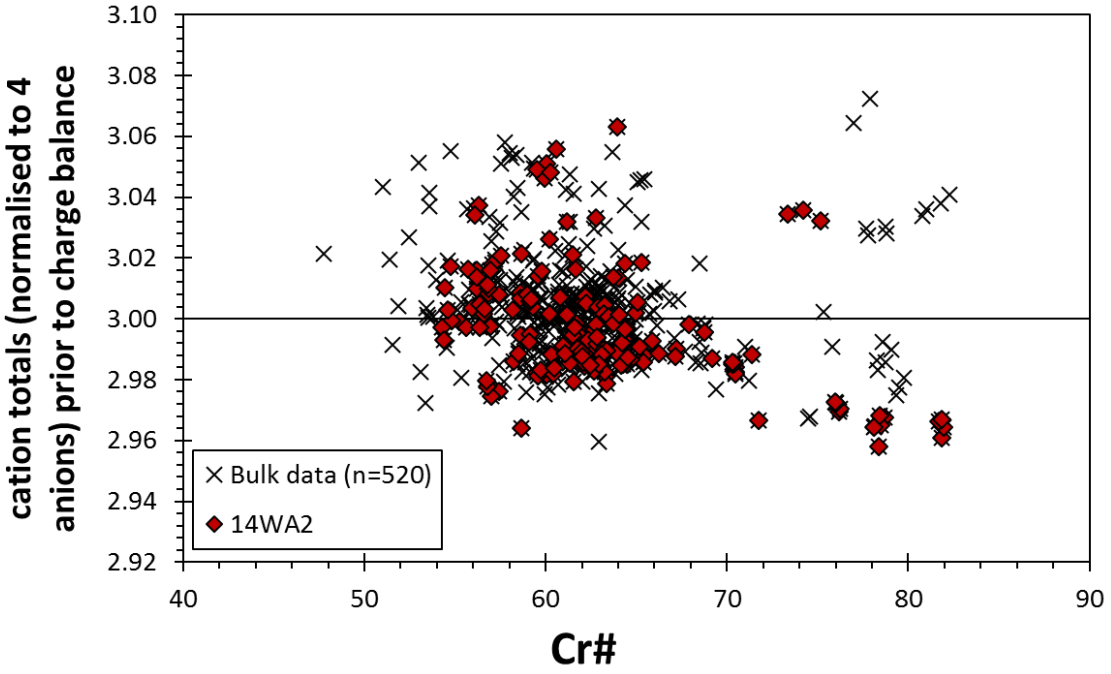

Figure 3.9: Cation totals normalised to 4 anions prior to charge balancing to determine Fe_2O_3 content of grains: spinels with greater than 3 cations are charge balanced to determine Fe_2O_3 using the equations of Droop (1987), which spinels that yield cation totals less than 3 are non-stoichiometric. Bulk data plotted to show the consistent non-stoichiometry of multiple intra-grain points, strongly indicating non-stoichiometry is not an analytical artefact. Most data cluster between 2.98 and 3.02 cations normalised to 4 anions at Cr# 55-70. High Cr# grains within 14WA2 tend to yield definitively non-stoichiometric compositions (~2.97) or >3.02 cations in proportion to 4 anions.

Within grain variability

Zoning; While the largest systematic variations in chromite mineral chemistry are with varying sample location, Jack Hills detrital chromites do show distinct internal zonation trends. Line scans of grains often reveal variability of divalent cation abundances, particularly Mg# (Figure 3.10). While chromites do not exhibit morphologically or microstructurally distinct cores and rims, these terms are used here to describe the centre and outer edges of grains. Most chromites have slightly lowered wt. % ZnO towards rims (Figure 3.10a) or else homogeneous ZnO compositions. MnO is largely homogeneous across chromite, although lower concentrations at the rim relative to core are observed (Figure 3.10a-b). Homogeneous Mg# appears to be restricted to some chromites within high ZnO 16WA7 (Figure 3.10c): all other samples yield chromites that display distinct variability in Mg#. Low ZnO samples 14WA2 and 16WA5 yield clear decreases in Mg# from the core to rim of the grain (Figure 3.10a). High ZnO samples, such as 14WA3 and 14WA4, often yield rims with higher Mg# (Figure 3.10b) though lowering of Mg# from core to rim is also observed. Grains with elevated Mg# at the rims show increases in both MgO and FeO from core to rim, compensated by decreases in ZnO and MnO.

While grains yield zoning profiles of divalent cations, intra-grain changes in Cr# are largely absent (Figure 3.10). Core to rim trends of marginally higher or lower Cr# (e.g. ±2) are sometimes observed (Figure 3.10 a/c), but there is no systematic behaviour observed. Like Cr#, Fe_2O_3 contents are generally homogeneous across chromite grains, with non-systematic variability likely reflecting major and minor element error propagated through stoichiometry measurements. As previously observed by spot analysis, many grains purportedly yield no Fe_2O_3 across the entire grain (Figure 3.10b). Individual grains do yield distinct variations in Fe_2O_3 that are clearly not related to stoichiometry calculations and are systematic in origin. This is present as both decreases and enrichments in Fe_2O_3 from core to rim: increases in Fe_2O_3 may be coupled with an increase in Cr# (Figure 10a; Supplementary Material 2.6).

Coupled elemental and textural variation; Distinct zones of elevated Cr# within detrital chromite are also rarely observed (Figure 3.11). These features are closely associated with pitted domains and fractures, and exhibit both diffuse (e.g. Figure 3.11a; Supplementary Material 2.7) and sharp (Figure 3.11d-f) boundaries with surrounding chromite. High Cr# domains are distinguished by their smooth texture in comparison to surrounding chromite, with a distinctive absence of pits or small-scale fractures. High Cr# domains are mostly observed at the edge of grains adjacent to enclosing fuchsite or as smooth domains within fractures (Figure 3.6d; 3.11a-c). These domains may also be localised along chromite crystallographic axes or be observed as distinct polygonal areas bound by crystallographic axes (Figure 10d-f).

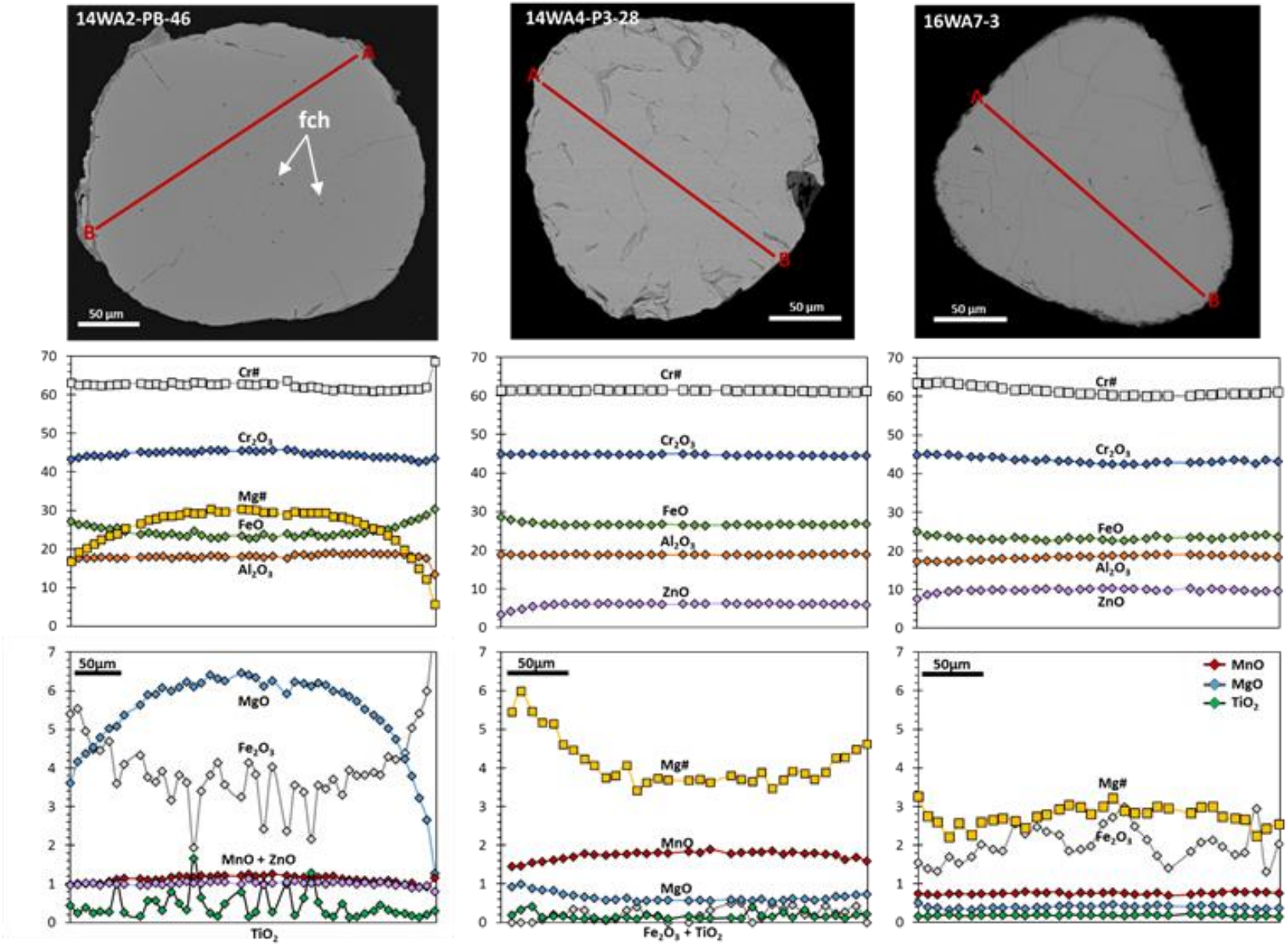
14WA2-PB-46
A
B
fch
50 µm
14WA4-P3-28
A
B
50 µm
16WA7-3
A
B
50 µm
Cr#
Cr_2O_3
Mg#
FeO
Al_2O_3
ZnO
50µm
MgO
Fe_2O_3
MnO + ZnO
TiO_2
MnO
Fe_2O_3 + TiO_2
MgO
TiO_2

Figure 3.10 (previoust page): Examples of zonation patterns observed within Jack Hills detrital chromites, including BSE images of line path taken. Isolated, globular inclusions of fuchsite (fch) also shown 14WA2-PB-46. **A)** Decreasing Mg# towards rims: most commonly shown by low ZnO samples 14WA2 and 16WA5. 14WA2-PB-46 yields the most variable zoning patterns observed in all Jack Hills grains and is likely the least altered grain analysed. This example also includes elevated Fe_2O_3 at its rims, resulting in an area of mildly elevated Cr# **B)** Elevated Mg# towards rims: commonly observed in high ZnO samples such as 14WA3 and 4 and 16WA7. ZnO and Mn are lost from chromite at the expense of FeO and MgO, increasing the Mg# of rims relative to the core of the grain. **C)** Homogeneous Mg#. No change in mineral chemistry across the grain in divalent or trivalent cations. This example has a slight elevation in Mg# on one edge after a minor decrease from the core, as is often observed in 16WA7.

These domains are characterised by high Cr# (70+), low totals (<98 %), the apparent absence of Fe_2O_3, lower ZnO and V_2O_3 and occasionally slightly elevated MnO (Supplementary Material 2.6). High Cr# zones within detrital chromite are chemically indistinguishable from low Fe_2O_3, high Cr# grains within the same samples. Only a single domain of low Cr# has been observed within chromite, bounding a, monomineralic quartz inclusion alongside iron oxide (Supplementary Material 2.7).

3.5. Discussion

3.5.1. Chromite morphology and the origin of inclusion assemblages

The variably rounded morphologies of chromite, from RC to EO, and external pitting of grains attests to their detrital nature and their variable and often protracted reworking history. While metamorphic disequilibrium will often result in chemical rounding of phases (e.g. zircon; Corfu et al., 2003), the presence of fuchsite around variably rounded chromites indicates variable crystal shape was present prior to fuchsite growth. Further to this, the presence of chromite within quartzite cobbles of metaconglomerate (Figure 3.4b; Dare et al., 2016) suggests cycling of some grains in at least two sedimentation events. Categorisation of grains by rounding shape suggests multiple geographical provenance sources, with at least one very proximal to permit the presence of EO. This extensive erosional reworking history of some chromites are at odds with the highly fractured nature of many grains (Figure 3.5b-e), which, though dependent on distance travelled, would likely not survive extensive sedimentary transport. This strongly suggests that fracturing of grains occurred *in-situ*, likely alongside deformation of metasediments (Spaggiari, 2007a; Rasmussen et al., 2010; 2011).

Jack Hills detrital chromites yield apparent inclusion assemblages of quartz, fuchsite, rutile, Fe-oxide, and Fe-sulphide (Figure 3.6). These phases, particularly low temperature silicates such as quartz and fuchsite, form under distinctly different magmatic conditions to chromite, which is a commonly an early liquidus phase (Barnes & Roeder, 2001). However, these low temperature silicates are present within the matrix of Jack Hills metasediments, alongside authigenic rutile, monazite and xenotime (Harrison et al., 2007; Rasmussen et al., 2010; Iizuka et al., 2010). Furthermore, the growth of muscovite and fuchsite around variably rounded chromite clearly attests to a secondary origin.

Inclusions of quartz and Cr-poor muscovite have also been reported within detrital zircon (Hopkins et al., 2008; 2010; Rasmussen et al., 2011; Bell et al., 2015), both as monomineralic and polyphase inclusions alongside monazite and xenotime (Rasmussen et al., 2011). Monazite and xenotime inclusions within detrital zircon have been shown to yield demonstrably younger ^{207}Pb-^{206}Pb ages than the host grain of ~2650 Ma and 800 Ma (Rasmussen et al., 2011). Furthermore, Ti-in-quartz and monazite-xenotime Gd-exchange geothermometry of zircon inclusions yielded distinctly metamorphic temperatures of ≤487 °C (Rasmussen et al., 2011). Rasmussen *et al.* (2011) therefore hypothesised that quartz, muscovite, rutile, monazite and xenotime inclusions within zircon were precipitated from post-depositional fluids, filling the voids left from the dissolution of primary apatite (Rasmussen et al., 2012; Bell et al., 2015; c.f. Hopkins et al., 2010; 2012), likely coincident with metamorphism at ~2650 Ma (Rasmussen et al., 2010; 2011).

The occurrence of demonstrably secondary assemblages of the same phases as observed within detrital zircon, coupled with the starkly different magmatic compositions required to crystallise refractory chromite and low temperature quartz and muscovite, provides robust evidence that inclusion assemblages within chromite are secondary in origin. Interestingly, many secondary inclusions of quartz and fuchsite are observed isolated from fractures within chromites (e.g. Figure 3.6a; 3.10a). Isolation of inclusions has been used as a line of evidence for a primary origin of many quartz and muscovite inclusions within detrital zircon (e.g. Bell et al., 2015). The detection of clearly secondary, apparently isolated inclusion assemblages within detrital chromite suggests caution should be applied when using this as a line of evidence for the presence of primary inclusions, and instead points to the presence of sub-micron or annealed fractures within grains, or fracturing below the polished surface.

The close association of secondary inclusions, fractures, and texturally distinct pitted zones may be explained by assessing the microstructures chromites commonly display during deformation and recrystallisation of their host protolith. Secondary, generally metamorphic, modification of chromite typically results in the formation of porous or spongy textures (Gervilla et al., 2012; Colás et al., 2014). It has been postulated this is a direct result of equilibration at lower metamorphic temperatures: chromite undergoes mass loss as it exchanges Mg for Fe during equilibration with surrounding silicates (Gervilla et al., 2012). However, chromites retain their initial crystal size during this process, creating internal pores and resulting in porous or spongy textures (Gervilla et al., 2012; Colás et al., 2014), which are subsequently infiltrated by fluids that precipitate the same metamorphic assemblage as the host rock. This process would explain the anhedral nature of very fine inclusions within pitted domains of detrital chromite, and the presence of coarser, porous textures present within heavily altered chromite (Figure 3.5e/f).

However, many grains that exhibit microstructures attributed to secondary processes yield the same mineral chemistry as chromite without pitted or porous domains. While it is challenging to analyse pitted domains via EPMA due to the presence of micron-scale silicates, the expected significant changes in mineral chemistry should be evident from brighter BSE images. Such features are not always observed. In pitted domains with recognised mineral chemistry variations (e.g Figure 3.6f), changes in mineral chemistry are rather manifested as elevated Cr# (Figure 3.11; Supplementary Material 7). The partitioning of Mg and Fe between an equilibrating phase and chromite is related to the activity, and therefore the proportions, of Cr, Al and Fe^{3+} within chromite (Dick & Bullen, 1984; Kamenetsky et al., 2001). Grains with higher Cr# yield lowered Mg# in comparison to chromite with low or intermediate Cr#, despite being equilibrated under the same conditions (Kamenetsky et al., 2001), producing a characteristic sloped or curved isopleth (Irvine, 1965; Dick & Bullen, 1984; Kamentsky et al., 2001). This exchange would therefore also aid in the volume reduction of chromite, creating fine pores for secondary fluids to exploit. However, this process cannot account for the presence of all pitted domains within chromite, suggesting that fluid mediated changes in mineral chemistry are not always the driving force in the formation of such domains.

This apparent absence of changes in mineral chemistry associated with many pitted domains indicates they may therefore represent the product of direct recrystallisation or sub-micron fracturing of chromites during fluid infiltration. This interpretation fits particularly well with the predominance of pitted and porous domains at the edge of grains and along fractures (Figure 3.5c; 11). However, the mechanism as to how either of these processes often occur without changing the mineral chemistry of affected areas compared to the rest of the crystal remains elusive. It signifies either complete equilibration of grains with the same secondary fluid, or suggests that the metamorphic event was too low temperature to induce significant and consistent trivalent elemental mobility (≤ upper greenschist facies; Barnes, 2000; Colás et al., 2014). The presence of coarser sub to euhedral secondary inclusions within chromite is likely the result of direct dissolution of a primary inclusion phase (e.g. Figure 3.6a), akin to the replacement of apatite within zircon (Rasmussen et al., 2011). More anhedral secondary inclusion assemblages may show the replacement of previous melt inclusions or anhedral inclusions (Figure 3.6e; Supplementary Material 2.8).

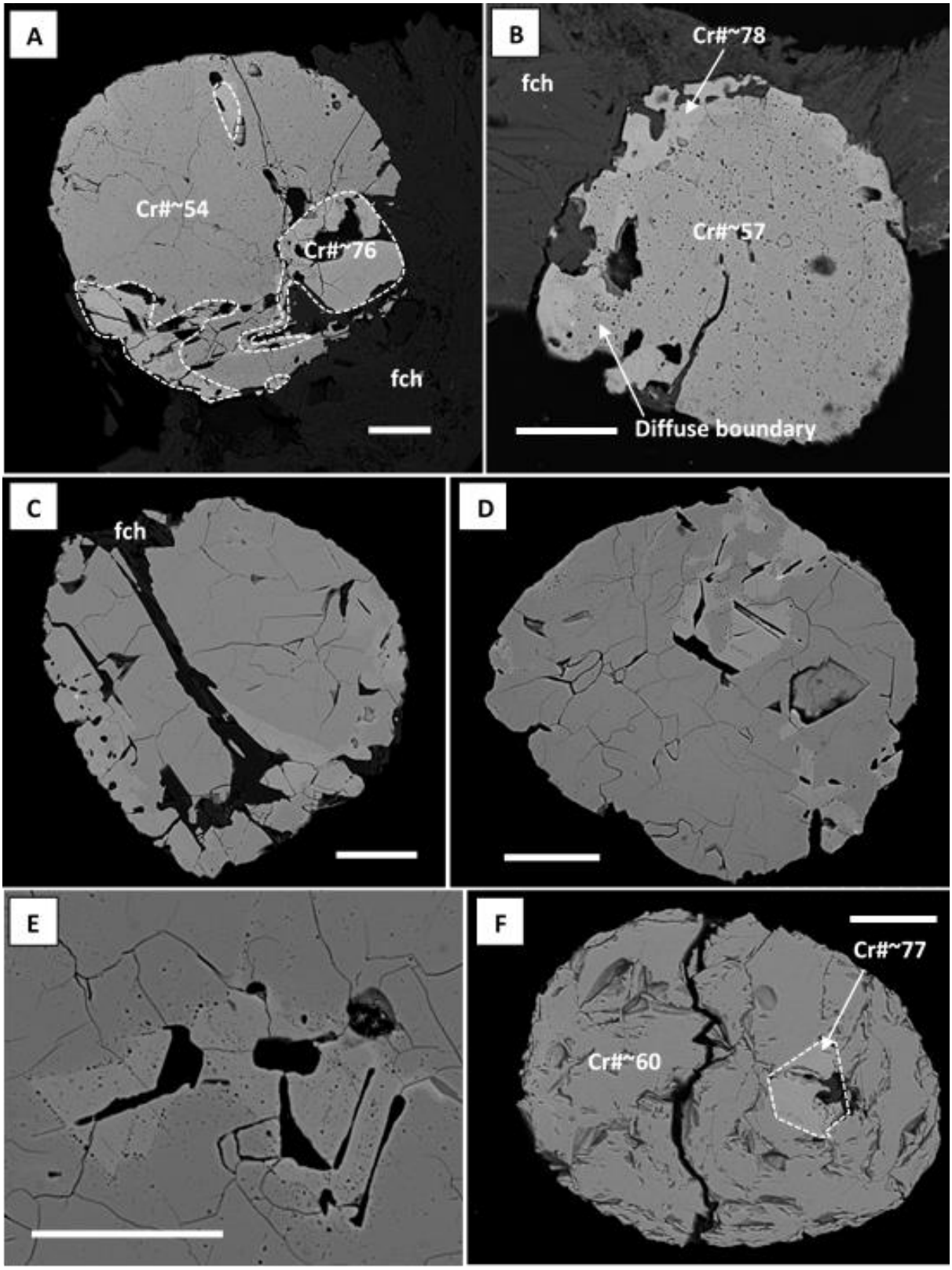

Figure 3.11: Variation in mineral chemistry: BSE images with elevated contrast to show high Cr# domains. **A)** and **B)** High Cr#, pit-free domains at the edge of grains, and **C)** along or associated with cracks. **D)**, **E)**, and **F)** High Cr# domains bound by chromite crystallographic axes, closely associated with laths of fuchsite and anhedral quartz along margins of high Cr# zones. All scale bars are 50 µm.

Observed alignment of alteration phases with chromite crystallographic axes (Figure 3.5e/6a and f) is noted elsewhere, including by chlorite (Fleet et al., 1993; Gervilla et al., 2012) and phlogopite (Rollinson et al., 2002). This textural feature is likely produced by exploitation of the lowest energy interface within chromite (Fleet et al., 1993). Whether rutile was precipitated from metamorphic fluids, or was exsolved from chromite, perhaps via reduction or oxidisation of grains (e.g. Cameron et al., 1979), is unclear. High Ti domains associated with cracks within zircon (Harrison & Schmitt, 2007), and the secondary growth of rutile within metasediment matrix (Harrison et al., 2007) attest to Ti mobility within Jack Hills metasediments. Despite this, direct exsolution from chromite that previously yielded higher TiO_2 contents cannot be discounted. The presence of Ti mobility may provide insights into the physiochemical conditions of metamorphic fluids: while Ti was once largely considered immobile, it has been shown to migrate along cm to meter length scales in highly alkaline or acidic (van Baalen, 1993) and briny fluids (Rapp et al., 2011).

It is more problematic to prescribe an origin to inclusions of Fe-sulphide, as magmatic sulphide and chromite are commonly co-liquidus phases under sulphur saturated magmatic conditions. Authigenic pyrite, easily distinguished by cubic habits, are present within Jack Hills metasediments (e.g. Cavosie et al., 2004). Fe-sulphide (typically ≤40 µm pyrite, pyrrhotite, intergrowths of pyrite and pyrrhotite, and rarer pentlandite) are also ubiquitous within isolated quartzite cobbles (Dare et al., 2016, Supplementary Material 2.9), although pyrrhotite and pentlandite appear to be rarely present or completely absent within the metasediment matrix. Fe-sulphide (pyrrhotite and pyrite) and rare chalcopyrite observed as inclusions within Jack Hills chromites appear to be closely linked to pitted domains (Figure 3.6a) and have been observed exploiting crystallographic axes of chromite (Figure 3.6f). Crystallographically aligned inclusions of sulphide cannot be the result of primary exsolution from chromite: this highlights the requirement of later infiltration of sulphur saturated fluids that may have replaced primary exsolved phases. This, coupled with the presence of authigenic pyrite, indicates a secondary origin for many Fe-sulphide inclusions within chromite.

To conclude, the presence of secondary inclusion assemblages and texturally pitted domains indicates detrital chromite underwent significant fluid mediated secondary modification within the host metasediment, or a metasedimentary precursor. Individual or multiple episodes of deformation and fluid mobility resulted in the dissolution of primary inclusions, recrystallisation along fractures and at the rims of chromite, and the precipitation of secondary, low temperature phases that are also found as authigenic minerals within the matrix of metasediments. Secondary phases, silicates quartz and fuchsite, also filled voids produced by volume loss within chromite and by dissolution of previous phases. The effects of secondary fluids on the mineral chemistry of grains are discussed in the next section.

3.5.2. Mineral chemistry

Secondary modification of chromite

Jack Hills detrital chromites yield high ZnO and MnO coupled with low Mg# of <30 (Figure 3.7). Chromites with such chemical compositions are rare, and therefore where observed commonly noted (*e.g.* Wylie et al., 1987; Santti et al., 2010; Fanlo et al., 2015). Elevated ZnO and MnO with low Mg# is now largely attributed to secondary processes (e.g. Barnes, 2000), and although poorly constrained in comparison to magmatic chromite variations, a developing body of literature investigating the effects of secondary modification of chromite major, minor and trace elements has emerged (e.g. Barnes, 2000; González-Jiménez et al., 2009; Gervilla et al., 2012; Colás et al., 2014). Hypotheses as to the various processes that modify chromite are disparate, but largely allude to interaction of magmatic chromite with hydrothermal or metamorphic fluids. These include: elemental mobility via interaction with aqueous fluids during the breakdown of surrounding Mg-Fe silicates via serpentinisation (Marques et al., 2007; Hodel et al., 2017) and/or metamorphism (Barnes, 2000; González-Jiménez et al., 2009; Gervilla et al., 2012; Colás et al., 2014; Fanlo et al., 2015; Ahmed & Surour, 2016), Cu-Zn-Ni-(Co) sulphide mineralisation of the host rock (Wylie, 1987; Marques et al., 2007; Fanlo et al., 2015), often strongly associated with gahnite (Heimann et al., 2005), and magmatic sulphide mineralisation (Groves et al., 1977). The effects of these processes on chromite mineral chemistry are dependent on the temperature and longevity of alteration, the nature and fO_2 of the aqueous medium, the composition of the host rock and its subsequent chromite/silicate ratio, and the fluid/rock ratio during modification (Colás et al., 2014; Ahmed & Surour, 2016).

Divalent cations of chromite undergo significant mobility during subsolidus processes, both magmatic and metamorphic, with evidence of metamorphism-induced exchange of divalent cations from at least lower greenschist facies (Barnes, 2000; González-Jiménez et al., 2009). The most commonly observed divalent cation mobility during thermal events is a decrease in Mg#: Fe^{2+} diffusively enters the chromite lattice at the expense of Mg^{2+}, reducing the Mg# of grains and often introducing strong zonation profiles (Barnes, 2000; Colás et al., 2014). The exchange of Mg and Fe is highly dependent on temperature, and the lowering of Mg# is the direct result of re-equilibration of chromite with surrounding Mg-Fe silicates with decreasing magmatic or metamorphic temperatures (Barnes, 2000). This equilibration is the basis of the commonly used olivine-spinel geothermometer (Irvine, 1965; 1967; Ballhaus et al., 1991; Sack & Ghiriso, 1991). ZnO, MnO and to a lesser extent CoO, which has not been observed within Jack Hills grains, also diffusively enter the chromite lattice in exchange for MgO, NiO and often TiO_2 (Barnes, 2000; Colás et al., 2014).

Trivalent cations appear largely immobile during low temperature alteration (Barnes, 2000), though rarely the interaction of chromite with acidic fluids during sea-floor hydrothermal metasomatism has been shown to induce extensive trivalent and divalent cation exchange (Wylie et al., 1987; Marques et al., 2007; Hodel et al., 2017). Under oxidising conditions, the transition of chromite to ferritchromit ($Fe^{3+}{}_2CrO_4$), generally in the form of ferritchromit rims, is most commonly reported (e.g. Kimball et al., 1990). The formation of ferritchromit represents the loss of Al_2O_3 to Fe_2O_3 either diffusively (Wylie et al., 1987; Gervilla et al., 2012; Colás et al., 2014) or via reaction with magnetite rims (Evans & Frost., 1975; Barnes, 2000). This reaction has been reported at greenschist facies (Kimball et al., 1990; González-Jiménez et al., 2009), but becomes particularly pervasive at and above amphibolite facies metamorphism (Barnes, 2000; González-Jiménez et al., 2009; Colás et al., 2014; Ahmed & Surour, 2016). Further significant mobility of trivalent cations, such as high Cr# relict cores transitional to ferritchromit, extensive alteration to ferritchromit and Cr-magnetite, appears to be restricted to grains that have undergone amphibolite facies metamorphism and above (Barnes, 2000).

Signatures of metamorphism within Jack Hills chromite

Jack Hills detrital chromite yield elevated, but variable ZnO and MnO, with lowered and increasingly homogenised Mg#, which attest to variable degrees of modification of grains via secondary alteration. The coupled growth in ZnO content with increasingly homogenised and lowered Mg# likely signifies increased alteration by the modifying medium, and can be interpreted to represent an increase in metamorphic grade or greater equilibration of samples (Figure 3.7a). As such, 14WA2 and 16WA5 characterise the least modified compositions of detrital chromites, yielding the highest and most variable Mg# at the lowest ZnO wt. %. Chromites from 16WA7 yield the most altered grain chemistry, with up to 13 wt.% ZnO and Mg# <5.

We propose the observed signatures of secondary modification occurred after deposition of detrital chromite, during metamorphism of the Jack Hills metasediments. Firstly, as previously discussed, interaction of chromite with metamorphic fluids is shown by secondary inclusion assemblages (Figure 3.6). These assemblages are identical to authigenic phases observed within metasediment matrix and secondary inclusions within detrital zircons (Iizuka et al, 2010; Rasmussen et al, 2010; 2011). Secondly, the only variation of very homogeneous mineral chemistry (particularly in samples such as 14WA4, and 16WA9 and 10) does not relate to physical characteristics of grains, such as rounding shape or grain size (Supplementary Material 2.2 and 2.3), but only changing sample location. Further to this, chromites yield significant inter-sample chemical variability despite the proximity (often <5 m) of sampling locations (Figure 3.2). Finally, when chromites are plotted for Cr# vs Fe^{2+}# (inverse Mg#), samples with the highest apparent modification (i.e. > Zn, < Mg#) plot along a trend that yields a

distinct curvilinear shape of an isopleth. This relationship becomes less pronounced with decreasing ZnO content (Figure 3.12), indicating less equilibration of chromite from these samples. For grains from individual samples to fit along definitive and distinct isopleths requires modification under the same physiochemical conditions, including temperature, fO_2 and Mg# of modifying medium, despite apparent significant variation in source proximity shown by grain rounding. However, we stress the composition (Mg# and $Fe^{3+}/totR^{3+}$) of the secondary equilibrating medium, and the temperature of equilibration are unknown.

For example, 16WA9 and 16WA10 metasediments were sampled approximately 2m apart in the same lithological unit, yet yield chromites with staggeringly different grain chemistry, particularly for wt. % ZnO and MnO (Figure 3.7). If the observed modification signatures occurred whilst chromites were still within their original igneous protoliths the presence of laterally extensive, homogenised secondary fluids of hydrothermal or metamorphic origin would be required. For different morphologies of grains to exhibit the same mineral chemistry would have further required the same protolith compositions and fluid/rock ratio, again homogenised on a multi kilometre scale. Finally, complete isolation of grains during post-erosional sedimentary processing, potentially during multiple cycling events, is needed to account for the variable rounding shape of grains and consistency of chromite chemistry both within the matrix and cobbles of host metasediments. This series of events is extremely unlikely and strongly suggests instead post-depositional modification of chromites within metasediments.

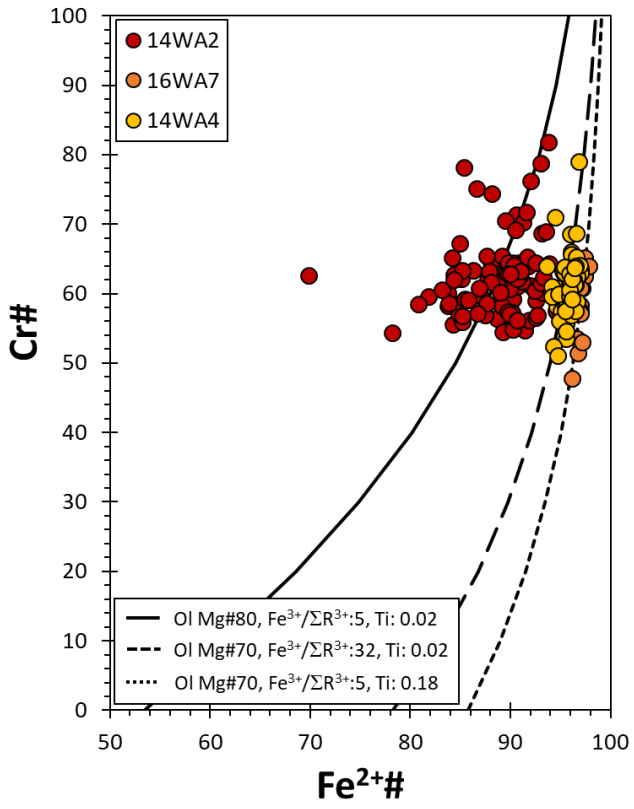

Figure 3.12: Cr# vs Fe^{2+}#. This diagram clearly shows the fit of high ZnO samples (particularly 16WA7) to the shape of an isopleth. All isopleths calculated for 450 °C, typical of upper greenschist facies metamorphism. This figure shows a clear greater fit of detrital chromites with high ZnO to an isopleth. Highest ZnO 16WA7 clearly yields the best fit to an isopleth, with increasing scatter with decreasing ZnO content of grains. This figure also indicates that the composition of high ZnO samples cannot explained by equilibration with olivine. The solid line represents the fit of an isopleth calculated using $Fe^{3+}/\Sigma R^{3+}$ and TiO_2 contents observed within detrital chromites, equilibrating at olivine Mg#80 at 450 °C. A thought experiment to derive the compositions of 14WA4 and 16WA7 chromites whilst equilibrating with olivine is shown by the dashed lines. To equilibrate with olivine (even at lower Mg#70) within high ZnO samples requires either high $Fe^{3+}/\Sigma R^{3}$ of >30 or high Ti cations proportions of >0.18 (total 3 cations). Neither of these compositions represent Jack Hills detrital chromites, suggesting that the equilibrating medium is not olivine.

The metre scale variability of ZnO and Mg# of detrital chromites at Jack Hills can be reconciled by changes in grain size and modal proportions of grains within metasediment. Chromites are the sole ZnO bearing phase within sediments but are present at low modal proportions of <1 % (see Chapter 2). As such, small changes in the modal proportion of chromite can account for large variations of wt.% ZnO within detrital chromites during interaction and equilibration with secondary fluids. Mass balance calculations show that infiltrating fluids containing ≤50 ppm Zn can account for the observed variability of ZnO within detrital chromites (Figure 3.13). While chromites are abundant in quartzite 16WA7 and finer metaconglomerate 14WA4, chromites typically possess a finer grain size, resulting in overall lower modal proportions of chromite and subsequently higher wt.% ZnO. Chromite is coarser within high ZnO 14WA3, but grains are present at lower concentrations than other metaconglomerate samples. Low ZnO samples 14WA2 and 16WA5 possess the highest modal abundance of coarser detrital chromite (Figure 3.13). The correlation between grain size and Mg# is not as robust. For example, 16WA9 is a metaconglomerate with comparable grain size and apparent modal abundance to 14WA2 and 16WA5, yet yields lower and more homogeneous Mg#. This may instead suggest that another factor, such as a higher fluid/rock ratio, controls the exchange of Mg and Fe during metamorphism. Alternatively, this may reflect a greater number of sources for Mg and Fe than Zn. Significantly, chromites from 16WA10, sampled within 2m of 16WA9 possesses a similar Mg# to 16WA9 chromite, but has a lower modal proportion of chromite, which may explain the higher ZnO content (Figure 3.7a).

One difficulty in explaining the lowering of Mg# of chromites during re-equilibration within the host metasediment is the apparent absence of a high MgO phase within sediments. This is particularly evident for increasingly modified samples, such as 16WA7. Hypothetical isopleths are presented in Figure 3.12 to show that in high ZnO samples it is impossible to achieve the low Mg# of chromite while equilibrating with olivine. Chromites would require $Fe^{3+}/\Sigma R^{3+}$ (R^{3+}: total $^{3+}$ cations) of 30 or extremely high Ti to produce the metamorphic signatures observed (Figure 3.12). As would be expected from a mature sedimentary succession such as is present in the Jack Hills belt, magmatic Mg-Fe silicates such

olivine and pyroxene are absent. The sole Mg-Fe silicate phase observed within samples is secondary fuchsite, which yields high Mg# of ~40-60 (Supplementary Material 2.10; Hopkins et al., 2010), but at low concentrations (MgO < 2 wt.%, often <1 wt.%, and FeO < 2 wt.%) heterogeneously distributed within fuchsite.

Owing to the low concentration of detrital chromite within metasediments, it is not unreasonable that scavenging of MgO from chromite by fuchsite during metamorphism could modify the Mg# of chromite. Mass balance calculations confirm this: MgO loss to fuchsite can account for the lowered Mg# of chromite (Mg#10 used in Figure 3.14) at chromite:fuchsite proportions >0.2; below this value original Mg# of chromite become impossible. Interestingly, calculations at the observed ~1:1 proportion of chromite and fuchsite, and recorded fuchsite MgO contents of 0.8-1.8 wt.%, suggest Mg# of chromite must have been low (< 40) prior to modification (Figure 3.14). This indicates magmatic sub-solidus or metamorphic exchange of major elements within chromite prior to in-situ metamorphism, or conceivably prior to deposition within Jack Hills sediments. Mass balance and the fit of highly modified chromite to an isopleth therefore likely represents equilibration of chromite and fuchsite within metasediments, rather than olivine within a magmatic protolith (Figure 3.12).

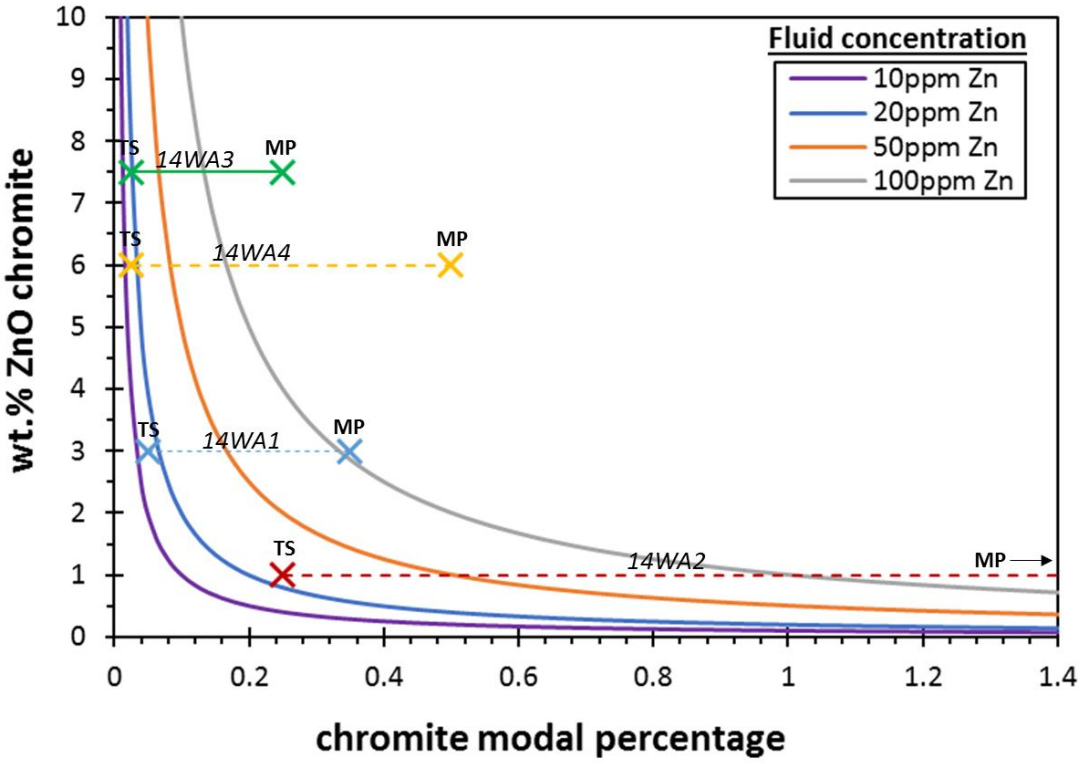

Figure 3.13: Potential ZnO content of detrital chromites when interacting with a Zn-bearing fluid as function of modal percentage of chromite. 4 fluid concentrations (10, 20, 50 and 100 ppm) shown also shown. Small changes in modal proportion at low modal percentages cause significant differences in the ZnO content of chromite. **TS**= proportion of chromite within the entire thin section (including quartzite cobbles), **MP**= matrix proportion: proportion of chromites within the matrix (not including quartzite cobbles). Only four samples have thin sections, but chromite modal proportions show a good correlation with equilibrium lines.

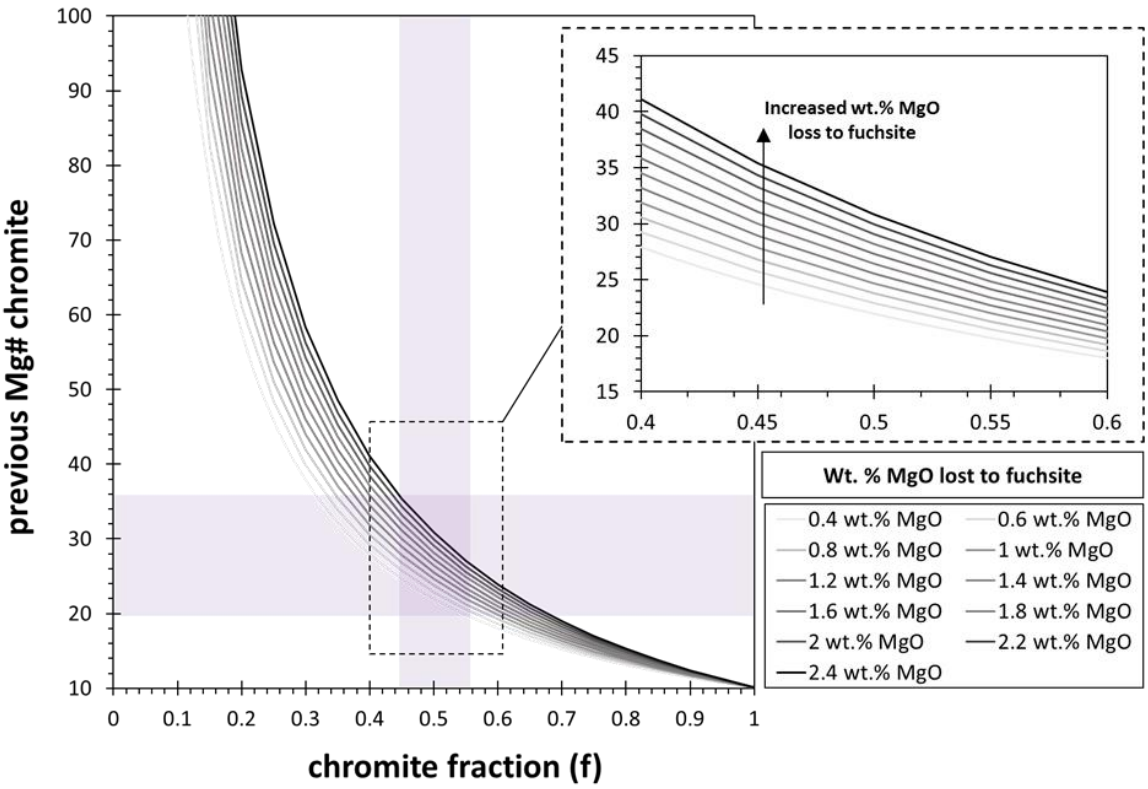

Figure 3.14: Mg# mass balance calculations between detrital chromites and fuchsite. This calculation assumes the current wt.% MgO within fuchsite is derived solely from chromite (i.e. closed system behaviour), and subsequently model backwards to determine the Mg# of detrital chromites prior to MgO loss to fuchsite. A current Mg# of 10 for chromite is used. The purple rectangles show the most commonly observed proportion of chromite:fuchsite (0.45-0.55), and the corresponding anticipated previous Mg# of detrital chromite. Mass balance calculations therefore suggest that at chromite:fuchsite proportions >0.2, scavenging of MgO by fuchsite can account for the Mg# and MgO concentrations observed within both detrital chromite and fuchsite. This further suggests that at the observed modal proportions and fuchsite MgO contents, chromites already possessed lowered Mg# (<40) prior to precipitation of fuchsite.

3.5.3. Trivalent cations: retained primary signatures?

Regardless of the degree of secondary modification of divalent cations within chromite, Cr# are broadly consistent across all metasediment sample locations (Figure 3.8), with only a slight trend towards lower Cr# in the highest wt. % ZnO samples (Figure 3.8a). The consistent range of Cr# across all samples can be explained by either the absence of significant trivalent mobility, or the partial equilibration of chromite during secondary modification with a lower Cr# equilibrant. If secondary equilibration was significant for trivalent cations, the latter scenario should be manifested as homogenisation to lower or higher Cr# in increasingly Zn-rich samples. This is not observed, and the slight trend towards lower Cr# is not statistically significant as it is controlled by a single point of Cr# 47 (Figure 3.8a). Furthermore, for low ZnO chromite retaining substantial Mg# zonation, this would suggest faster diffusion of trivalent cations than divalent cations. This scenario would contrast with all

previous studies of metamorphic diffusion within chromite (e.g. Barnes, 2000; González-Jiménez et al., 2009; Gervilla et al., 2012; Colás et al., 2014), and is rejected as implausible.

The retention of the consistent range in Cr# of the cores of chromites across all sample locations therefore suggests that metamorphic fluids were of insufficient temperature to induce significant trivalent cation mobility. This advocates limitation of maximum metamorphic grade to upper greenschist facies, or at most lower amphibolite facies, to restrict significant exchange of trivalent cations (Barnes, 2000). This is supported by previous studies of Jack Hills, where peak metamorphic conditions ascribed to unit 3 metasediments is upper greenschist to lower amphibolite facies (Spaggiari, 2007a; Rasmussen et al., 2010; 2011). The absence of ferritchromit rims, which typically form at ~500-600 °C (Kimball et al., 1990; Barnes, 2000; González-Jiménez et al., 2009) is also another indication of metamorphic grade restriction to ca. upper greenschist facies. Alternatively, this may suggest that metamorphic fluids coincident with cation exchange were not particularly oxidising, as also suggested by the presence of secondary sulphide (Figure 3.6c/f). However, the presence of iron oxide as a secondary phase within detrital chromite and zircon (Weiss et al., 2018; Tang et al., 2018), and the metasediment matrix appears to refute this, though these may have formed during a later event, or as evolved fluids after the precipitation of sulphides.

The primary nature of Cr# within grains is apparently at odds with the presence of surrounding fuchsite, whose elevated Cr content is almost certainly derived from detrital chromites (Hopkins et al., 2010; Rasmussen et al., 2011). Fuchsite yields Cr_2O_3 concentrations of ~2-3 wt.% (Cr# <5; Supplementary Material 2.10), that decrease with increasing distance from chromite grains (Rasmussen et al., 2011, supplementary figure DR3). Such low concentrations within fuchsite require very little mobilisation of Cr from chromite, and suggests that the Cr required was scavenged from rims and heavily altered areas of chromite during metamorphic crystallisation of fuchsite (e.g. Figure 3.6d; 3.10). The loss of Cr^{3+} for Fe^{3+} is shown in some zonation patterns (Figure 9a; Supplementary Material 2.6), resulting in trends of lowered Cr#. The qualitative trend of decreasing Cr# with increasing ZnO (Figure 3.8a) content may also represent increased exchange of Cr for Al in highly equilibrated samples.

However, where the greatest changes in trivalent mineral chemistry due to alteration are observed, localised zones of high Cr# are present (Figure 3.11), rather than low Cr# domains anticipated from loss of Cr to fuchsite. The absence of Fe_2O_3 within high Cr# domains (e.g. Supplementary Material 2.6) suggests exchange of Al for Fe^{3+} cannot account for the increase in Cr#, and these domains yield no characteristics to suggest they are transitional to ferritchromit. High Cr# domains can however be reconciled via preferential loss of Al during trivalent equilibration between chromite and fuchsite

(Supplementary Material 2.11), i.e. trivalent cations lost to fuchsite at a lower Cr# from chromite. This value is typically Cr# 50-60, dependent on the Cr# of host chromite and equilibrating fuchsite (Supplementary Material 2.11). High Cr# domains therefore likely represent localised areas of trivalent mobility during metamorphism of the host metasediment, coincident with crystallisation of fuchsite and peak metamorphism of Jack Hills metasediments.

3.5.4. The timing and cause of chromite modification

It is apparent from modification of chromite major element chemistry and loss of primary mineral assemblages that alteration of chromites likely occurred coincident with the authigenic formation of fuchsite. Fuchsite has been reported globally within metamorphosed sediments (Heinrich, 1965; Martyn & Johnson., 1986; Kerrich et al., 1987; Challis et al., 1995; Randive et al., 2015), particularly those of Archean age (Martyn & Johnson., 1986), and is ubiquitously associated with detrital chromite or Cr-spinel (Heinrich, 1965; Challis et al., 1995; Randive et al., 2015). It is postulated fuchsite within metasediments forms from hydrothermal or metasomatic fluids derived from magmatic intrusions and/or regional metamorphism that have variably leached Cr from surrounding ultramafic rocks or detrital chromites (Heinrich, 1965; Challis et al., 1995; Arif & Moon, 2007; Randive et al., 2015).

Within these studies, only Challis *et al.* (1995) reported the mineral chemistry of associated chromites present within fuchsitic metasediments spatially linked to magmatic intrusions and fault zones in NW Nelson, New Zealand. The metasediments of Challis *et al.* (1995) were metamorphosed at amphibolite facies, therefore at a higher grade than upper greenschist metasediments at Jack Hills, but they also observed chromite elevated in ZnO (up to 13.7 wt. %) and MnO (up to 3.5 wt. %) coupled with lowered Mg#. Critically, the detrital grains described had a well constrained provenance, which showed the observed signatures could only have occurred within metasediments. Though there are clear differences between Jack Hills chromite and those reported in Challis *et al.* (1995), such as significant mobility of trivalent cations linked to finer grain size and higher-grade metamorphism, this study highlights that the chemical compositions of detrital chromites observed at Jack Hills can be explained through the interaction of detrital grains with metamorphic or metasomatic fluids that precipitated authigenic fuchsite.

It is important to know that while both 2650 Ma (Rasmussen et al., 2010; 2011) and ~1800 Ma (Spaggiari 2007a) have been proposed for peak metamorphism of unit 3 within the Jack Hills belt, the metamorphic and deformational history of the belt is poorly constrained (e.g. Kemp et al., 2019). In addition, recent studies have shown that metasedimentary rocks with Proterozoic depositional ages are finely intercalated with, and at the same apparent metamorphic grade, as metasedimentary units with apparent Archean depositional ages (Wang and Wilde, 2018), showing that metasediments must

have been deformed during the Proterozoic. The ~2650 Ma event also coincided with amphibolite to granulite metamorphism throughout the Narryer Terrane, and ubiquitous granitoid emplacement within the entire Yilgarn Craton (Kemp et al., 2019). The presence of contemporaneous monazite and xenotime inclusions within detrital zircons, and within the matrix of metasedimentary rocks at the W-74 site, led Rasmussen et al. (2010; 2011) to suggest that 2650 Ma represented peak metamorphism at least within metasediments with purported Archean depositional ages. This age also corresponds to the age of 'The Blob' granitoid, which intrudes the Jack Hills belt to the SW of the W-74 site (Pidgeon and Wilde, 1998). Proterozoic metamorphism has also impacted the metasediments (see Section 4.4.2), and muscovites with ~1800 Ma Ar-Ar ages define the main foliation of the belt (Spaggiari 2007a; Spaggiari et al., 2008). However, the closure temperature for Ar-Ar of muscovite is 350-420 °C (Spaggiari et al., 2008), while the closure temperature for U-Pb within monazite is ~900 °C for U-Pb (Iizuka et al., 2010). This indicates muscovite may have been reset, and suggests Proterozoic metamorphism did not represent peak metamorphism at Jack Hills. Further work is clearly required to provide additional constraints on the timing and intensity of metamorphism at the Jack Hills belt.

Despite ambiguity surrounding the age of metamorphism, it can be stated that upper greenschist to lower amphibolite facies metamorphism induced significant cation mobility and localised trivalent cation mobility within detrital chromite. This also coincided with replacement of primary mineral assemblages within chromite and zircon (Rasmussen et al., 2011; Bell et al., 2015). However, there is also evidence from zonation patterns of chromite for more than one modification event. For example, 14WA2-PB-46 retains significant core-to-rim variation in Mg# and MnO yet has homogeneous ZnO at 1 wt.% (Figure 3.10a). This would indicate either faster homogenisation of ZnO than Mg#, or that 14WA2-PB-46 had elevated wt. % ZnO prior to *in-situ* secondary modification. The loss of MnO towards rims is also indicative of previous elevation. Chromite with >1 wt.% ZnO is not observed within unaltered, magmatic grains (Barnes, 2000), and so least altered grains within 14WA2 indicate a prior secondary modification event. This suggests either a second, lower temperature event *in-situ* that again lowered Mg#, or modification of grains prior to deposition in their protolith. The second of these scenarios is preferred, owing to the high Mg# observed within 14WA2-PB-46 compared to other samples and even grains within 14WA2 (Figure 3.7c).

The elevation of Mg# towards rims within samples 14WA3, 14WA4 and 16WA7 (Figure 3.10b-c) also hints at a second modification event, this time definitively within metasediments. The increase in Mg# is also associated with a decrease in ZnO and MnO, apparently exchanged for both MgO and FeO (Figure 3.10b). The dependence of Mg# on temperature suggests that this change in zonation pattern represents equilibration of rims at a higher temperature than the cores of grains, indicating a prograde metamorphic path from core to rim. This can be reconciled by two scenarios, either a second, higher

temperature deformational event, or increasing temperatures as part of the same event. A second, high temperature event would have overprinted temperatures recorded by monazite-xenotime pairs during the first deformation of Jack Hills metasediments at ~2650 Ma (Rasmussen et al., 2011), suggesting the latter scenario is more likely. The presence of this signature in only high ZnO samples indicates variable fluid/rock ratios, and therefore fluid pathways through metasediments.

3.6. Provenance

While detrital chromites clearly exhibit protracted metamorphic histories, some fundamental interpretations on the magmatic protolith of chromite can be constrained. An extra-terrestrial origin for chromites can be instantly excluded: such spinels typically display dendritic habits (Byerly & Lowe, 1994), high Cr# (Roeder, 1994) or elevated (>0.5 wt. %) V_2O_3 (Cronholm & Schmitz, 2007). Consistent variability of Cr# across all samples regardless of rounding shape, and therefore clearly different geographical source domains, indicates that chromites likely share a common provenance and therefore a common mafic or ultramafic protolith. This suggests a single, large scale mafic or ultramafic source was present in the catchment of Jack Hills sediments. While determination of the Fe_2O_3 content of grains is challenging due to apparent non-stoichiometry of grains, the ferric iron contents of chromite can clearly be described as low, as significant non-stoichiometry would have resulted in lower totals. Zonation patterns of least altered grains suggest that only minor amounts of Fe_2O_3 entered the crystal lattice during secondary deformation (Figure 3.10a), and that low $Fe^{3+}/\sum R^{3+}$ of <10 is a primary feature of detrital chromite. As the magmatic Fe_2O_3 content of magmatic chromite is strongly reliant on the oxygen fugacity it crystallised under (e.g. Ballhaus et al., 1991), this indicates a largely reduced source for detrital chromite. The complete loss of primary inclusion assemblages within chromites means inclusion studies, like those commonly undertaken for zircons (e.g. Bell et al., 2015), are not viable for detrital chromites at Jack Hills.

Unfortunately, some of the most heavily exploited tools in understanding the petrogenesis of chromite and consequently their protolith, such as Mg# and TiO_2, also display clear evidence of secondary modification, and so should be used with extreme caution when elucidating the provenance of Jack Hills chromite. While mass balance of chromite and fuchsite compositions suggests Mg# of chromite was already low (<40) at the time of deposition, it cannot be determined if this was because of prior magmatic sub-solidus or metamorphic processes, and so Mg# is not considered further. The TiO_2 content of chromites that do not show rutile exsolution may yield primary Ti contents, but evidence of Ti mobility of unknown magnitude within Jack Hills metasediments has been previously observed (Harrison & Schmitt, 2007). Therefore, commonly used plots for the provenance of chromite (Supplementary S2.12), such as TiO_2 vs Cr_2O_3 or Al_2O_3 (Kamenetsky et al., 2001), may be

unreliable. The retention of primary Cr# within the cores of Jack Hills chromite will therefore be the most valuable tool in understanding the petrogenesis of detrital grains, alongside careful and conservative use of $Fe^{3+}/\sum R^{3+}$ and TiO_2 contents.

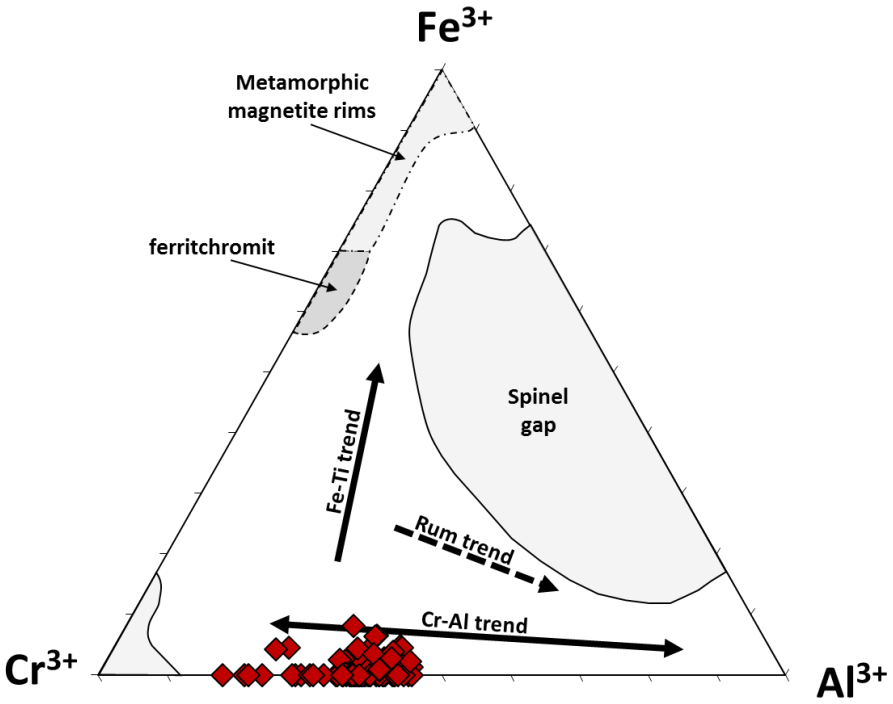

Figure 3.15: Trivalent cation triangular plot, modified from Barnes and Roeder (2001), showing three magmatic compositional pathways for spinel: Cr-Al, Fe-Ti, and Rum trends, which are explained further in text. The compositional space of ferritchromit, Cr-magnetite, and spinel miscibility gaps shown for reference. Core or near core compositions of 14WA2 chromites shown in red diamonds.

To understand the petrogenesis of Jack Hills detrital chromites, and therefore potentially of mafic and ultramafic crust within the Narryer Terrane, we use the fields of Barnes & Roeder (2001), a comparative study of over 26,000 spinels from different tectonic settings. We compare these fields to grains from 14WA2, which represents the most heavily analysed and least altered compositions of detrital chromite. As previously stated, the consistency and repetition of Cr# across all samples regardless of rounding shape and secondary elemental modification suggests that detrital chromites are likely derived from a single magmatic source. A magmatically dynamic, laterally extensive provenance is therefore required to account for the variability of Cr# and grain morphologies: while protection within quartzite cobbles may have aided in the survival of the most euhedral grains, it seems unlikely the full range of rounding shapes observed can be explained by variable protection alone. Though potentially clouded by secondary processes, particularly with reference to Fe_2O_3

contents, chromites ostensibly fit on a Cr-Al trend (Figure 15; Irvine, 1967; Barnes & Roeder, 2001), where no enrichment of Fe^{3+} and Ti is observed with changing Cr#. This trend reflects the Cr-Al composition of melt within lavas, and the interaction of chromite with Cr and Al bearing silicates such as pyroxene or magmatic fractionation within plutonic rocks (Barnes & Roeder, 2001). The apparent primary low Fe_2O_3 and TiO_2 content of grains preclude the presence of a strong Fe-Ti or Rum trend (Figure 3.15), which forms via the reaction of plutonic chromites with intercumulus liquid enriched in both Fe^{3+} and Ti.

As expected, detrital chromites from all samples plot in the field of chromite affected by metamorphism in Cr# vs. Fe^{2+}# space (Figure 3.16a), due to their low Mg#. Dare *et al.* (2016) suggested low Mg# precluded a komatiitic origin, but our study indicates this signature occurred *in-situ* within metasediments, and should not be considered to ascribe provenance. Despite this, we also propose komatiites are not the source of detrital chromite, but with this conclusion founded on the more robust signature of Cr#. As a product of high temperature and high degree mantle melts, komatiites have high Cr/Al ratios and therefore yield chromite with high Cr# (Barnes & Roeder, 2001). Komatiitic chromite Cr# remain tightly clustered due to the inhibition of magmatic fractionation or subsolidus equilibration, which is a product of their volcanic nature. This is at odds with the variable Cr# of Jack Hills detrital chromite, for both Al-undepleted (AUDK) komatiites (Figure 3.16b) and Al-depleted komatiites (ADK). ADK are not shown in Figure 16 as they yield chromite with too high Cr# to represent a source of detrital chromite. Some portions of komatiitic lavas, such as olivine-rich dunitic channels and sheets, have been shown to yield chromite with lower Cr# (60-70) than bulk ADK and AUDK (Barnes, 1998; Barnes & Roeder, 2001). However, chromites are not abundant in these reduced cumulates, and would be unlikely to dominate the detrital record over their bulk komatiitic counterparts. Detrital grains do yield low TiO_2 and $Fe^{3+}/\sum R^{3+}$, comparable to komatiites (Figure 17a), and high Cr# detrital grains from Jack Hills do fall within komatiitic fields (Figure 3.16b), attesting to a potential komatiitic affinities of at least some grains.

We propose that for the variability of Cr# observed, detrital chromite fits best with chromite derived from two tectonic settings. The first of these invokes the involvement of large degrees of mantle melting, and subsequent fractional crystallisation and/or subsolidus equilibration with Cr-Al bearing phases within a layered intrusion. The second tectonic setting where variable Cr# may be explained is that of ophiolites and associated mantle rocks. Within ophiolites, Cr# disparity is indicative of variable depletion and pressure of crystallisation of the mantle segment (Dick and Bullen, 1984; Barnes and Roeder, 2001). Detrital chromite initially seems to fit with the bulk ophiolitic chromite field, displaying a strong Cr-Al trend with consistently low TiO_2 and $Fe^{3+}/\sum R^{3+}$ contents. However, the fractionated Cr# observed would require sampling of multiple mantle domains with heterogeneous depletion. Such

extreme variability in mantle fertility is a) unlikely to be expressed in an early Earth record (chromites ≥3400-3500 Ma (Valley et al., 2005), where limited evidence for depleted mantle exists (e.g. Petersson et al., 2019 and references therein), and b) unlikely to be consistently sampled across multiple sediment samples. We also add that other, more qualitative indicators of ophiolitic chromite such as coarse, anhedral podiform grains and platinum group alloys (PGA) as both inclusions within chromite

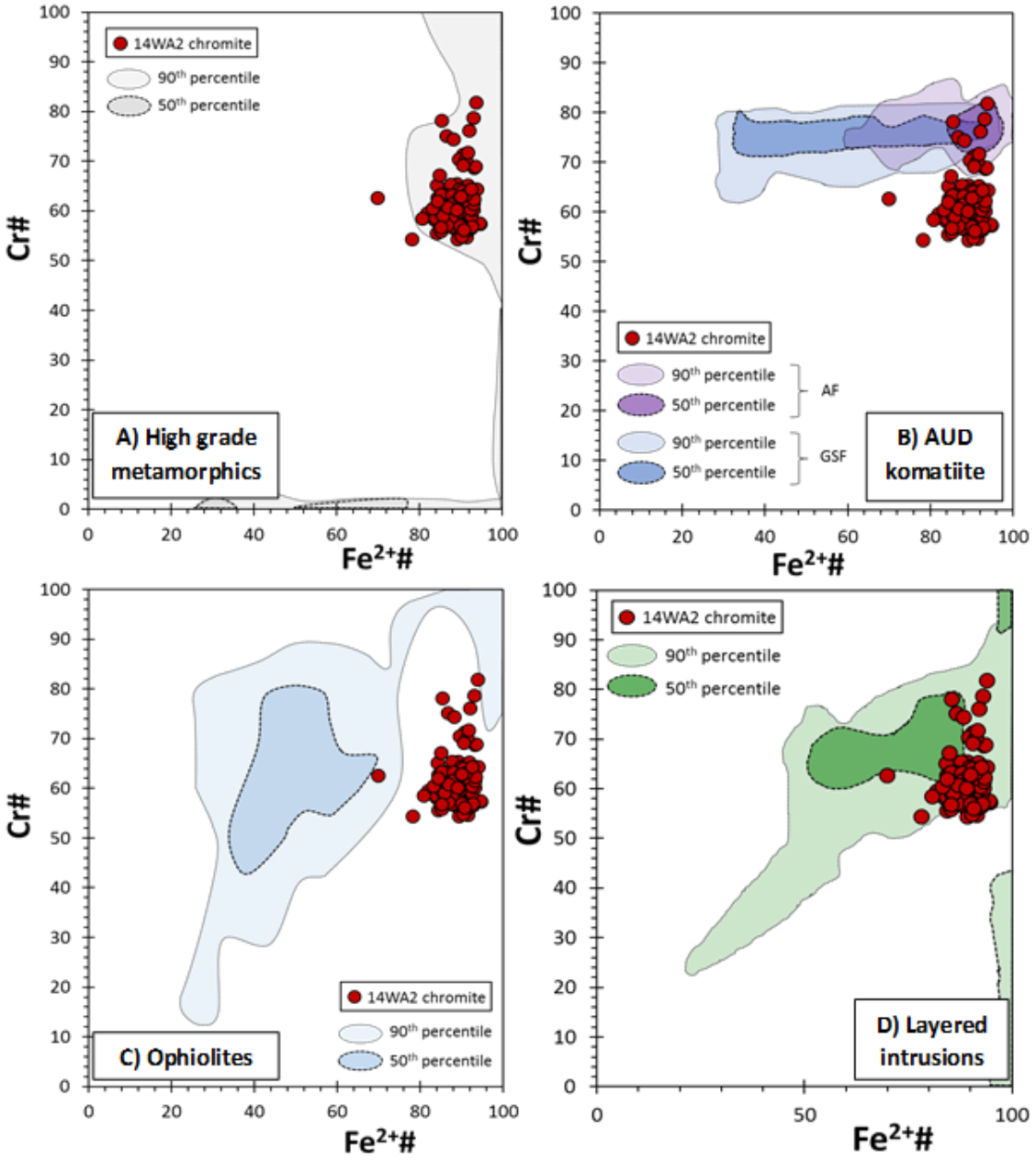

Figure 3.16: Provenance: Cr# vs Fe^{2+}#, diagrams modified from Barnes and Roeder (2001). **A)** Stong fit of 14WA2 detrital chromite with chromite that have undergone high grade metamorphism. This is due to significantly lowered Mg#: the higher Cr#, lowered Mg# field likely reflects ferritchromit. **B)** Distinct absence of fit with chromite from Al-undepleted komatiites, where the absence of magmatic fractionation results in largely homogeneous Cr#. AF- chromites from AUDK that have undergone amphibolite facies metamorphism, GSF- chromites from AUDK that have undergone greenschist facies metamorphism. **C)** Strong fit of bulk field for chromite from ophiolites, where Cr# is controlled by variable mantle depletion. **D)** Strong fit of chromite from layered intrusions: Cr# variability a function of subsolidus equilibration and changing liquidus compositions.

and as a detrital phase (e.g. Barkov et al., 2013) are notably absent at Jack Hills. It is unlikely PGAs were lost during metamorphism, as they are typically locally re-precipitated after dissolution (Gonzalez-Jimenez et al., 2009).

An origin of chromite from a layered intrusion may explain the variation in Cr# observed, although at considerably lower Mg# (Figure 16d) due to secondary alteration of detrital grains. Chromite derived from layered intrusions generally plot along a strong Fe-Ti trend owing to enrichment of Fe^{3+} and Ti^{2+} from interaction with trapped intercumulus liquid (Barnes & Roeder, 2001). Chromitites show less pronounced Fe-Ti trends, but represent a very minor proportion of layered intrusions, and as such are excluded from fields presented here (Barnes & Roeder, 2001). However, Fe-Ti trends are a feature of interaction with intercumulus liquid (Barnes & Roeder, 2001): deep-seated, high-pressure adcumulates supress the crystallisation of feldspar, resulting in partitioning of Al into silicates. These silicates readily exchange with spinel, forming a Cr-Al trend (Barnes & Roeder, 2001), while the low proportion of intercumulus liquid inhibits exchange of Fe^{3+} and Ti. The absence of a strong Fe-Ti trend therefore does not preclude a layered intrusive origin for detrital grains. While disseminated chromites from layered intrusions generally yield higher $Fe^{3+}/\sum R^{3+}$ than detrital grains, particularly at higher Cr#, Figure 3.17b shows how variable $Fe^{3+}/\sum R^{3+}$ can be within layered intrusions. Indeed, chromites from Archean layered intrusions with comparable Cr#, Fe^{3+}/R^{3+} and TiO_2 contents to Jack Hills chromites have been reported (e.g. Rollinson et al., 2002; Berger et al., 2013; Szilas et al., 2017). Intriguingly, the absence of Cr# variation with rounding shape of grains may provide qualitative evidence of a potential layered intrusion source, which yield consistent lithologies and mineral chemistry laterally for many kilometres.

Evans & Frost (1975) previously noted that care must be taken in the interpretation of metamorphosed spinel, which can serendipitously plot within the same field as layered intrusions at amphibolite facies, albeit at lower Mg#. We refute this as an origin of the observed Cr# variability within detrital grains for numerous reasons. Firstly, more recent work has highlighted the variable modification of grains at this grade, with resultant mineral chemistry strongly dependent on the variable metamorphic processes and the original tectonic location (Barnes, 2000; Colás et al., 2014). Secondly, metasediments at Jack Hills only reach upper greenschist facies or at most lower amphibolite facies metamorphism, and no significant *in-situ* exchange of Cr-Al-Fe^{3+} has occurred. The presence of metamorphism prior to deposition is harder to constrain, but the elevation in wt. % ZnO within least altered grains may indicate prior metamorphism. However, thirdly, metamorphism of chromites within their mafic/ultramafic protolith is almost always associated with the development of ferritchromit rims, which should survive sedimentary transportation, but are not observed within Jack Hills chromite.

Therefore, while the secondary mobility of important provenance indicators (particularly Mg#) means interpretation of Jack Hills detrital chromite is challenging and an ophiolitic origin cannot be fully discounted, we propose that a layered intrusion origin is the most likely provenance of detrital grains. The strong Cr-Al trend of grains potentially indicates that the protolith of Jack Hills detrital chromites was emplaced at a mid to deep crustal level. It is unclear in the absence of variable Fe^{3+} or TiO_2 the direction of fractionation but if high Cr# grains represent liquidus compositions they likely preserve evidence of extensive mantle melting, akin to komatiites. The consistent range of Cr# across all samples therefore indicates the detrital catchment of Jack Hills metasediments was dominated by a laterally extensive layered intrusion. It is important to note that the presence of both chromite and zircon within quartzite cobbles suggests Jack Hills sediments represent reworking of previous sedimentary sequences. It is therefore plausible that the source of detrital chromite had already been completely or partially reworked at the time of deposition of the Jack Hills sediments, and therefore may not represent the distribution of mafic and ultramafic crust at 3050 to 2650 Ma (Crowley et al., 2005; Rasmussen et al., 2010).

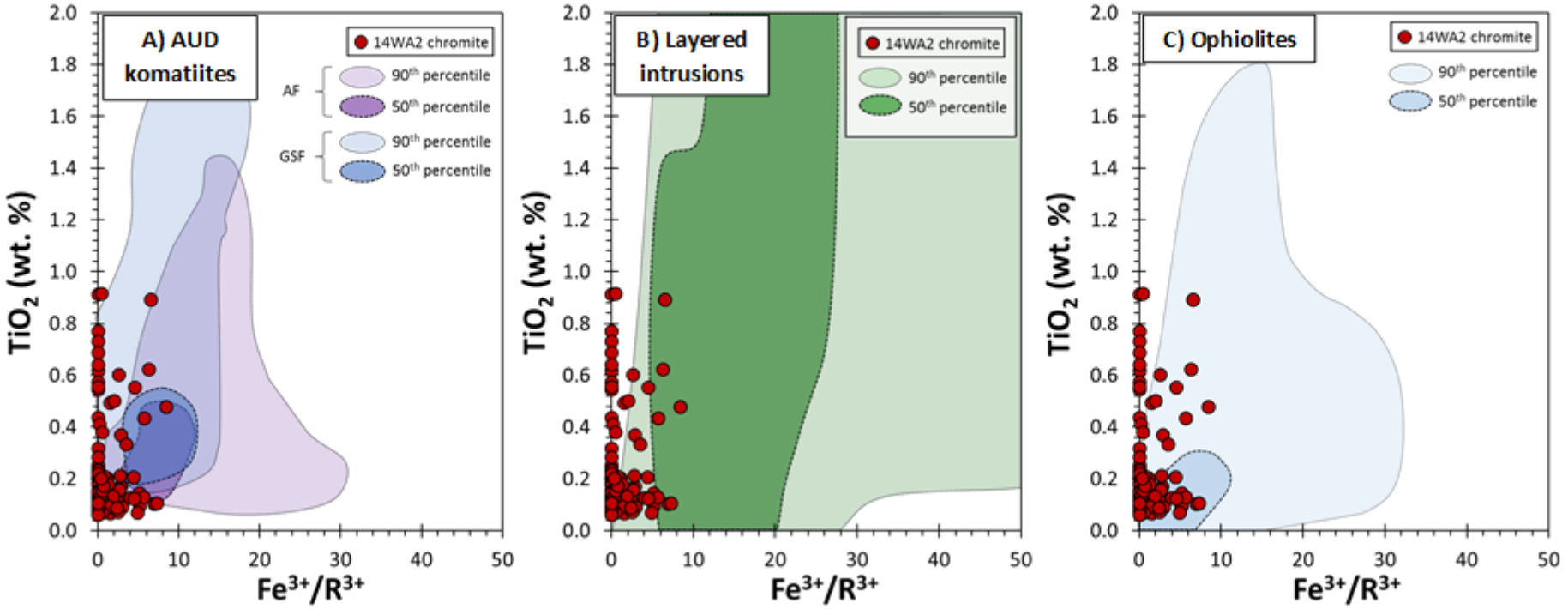

Figure 3.17: Provenance: TiO_2 vs Fe^{3+}/R^{3+}, diagrams modified from Barnes and Roeder (2001). Fit of 14WA2 chromite to all fields for **A)** AUDK, **B)** layered intrusions and **C)** ophiolites. TiO_2 concentrations of Jack Hills chromites yield good overlap with all shown fields, though they appear to be slightly lower than komatiitic chromites. Fe^{3+}/R^{3+} compositions are lower than most fields bar ophiolites, though this may be a consequence of minor non-stoichiometry.

3.7. Potential sources to chromites within the Narryer Terrane

The Manfred Complex

As major and minor element chemistry of Jack Hills detrital chromite allude to a layered intrusion origin, the sole described layered intrusion within the Narryer Terrane, the 3730 Ma Manfred Complex (Kinny et al., 1988; Fletcher et al., 1988; Myers, 1988b), must be considered as a source. Spinel within the Manfred Complex is dominantly spinel *sensu stricto* or picotite and is observed closely associated with magmatic olivine (Kemp et al., 2018) or exsolved from cumulus orthopyroxene or clinopyroxene (Figure 3.18a). However, the Manfred Complex also comprises metaperidotites that contains chromite (Fletcher, 1988; Myers, 1988b; Kemp et al., 2018). Here we compare least altered 14WA2 chromites with chromites from 13TKN22, a pyroxene-phyric peridotite metamorphosed to hornblende and serpentine (Section 2.3.2). Chromite is observed as disseminated crystals with variably formed magnetite rims (Figure 3.18). An inclusion of olivine within chromite (Figure 18b) yields a Mg# of 84 and equilibrated with surrounding chromite at a metamorphic, likely retrograde, temperature of ~460 °C (Section 2.3.2).

13TKN22 chromites (n=13) yield consistent Cr# of 76-80 (Table 3.2), coupled with low Mg# of <20, likely reflecting metamorphism of the host metaperidotite. 13TKN22 chromites also yield limited ZnO of ca. 0.6 wt.%, and heterogeneous MnO of 0.4-1.4 wt.%. The mildly elevated ZnO and MnO contents, coupled with high Cr# and Fe^{3+} contents of metaperidotite chromites may indicate metamorphic modification of grains. While NiO is present at magmatic concentrations of >0.1 wt.%, this may be a function of the high magnetite component of 13TKN22 chromites (Table 3.2; Barnes, 1998). However, the sharpness of the boundary between chromite and magnetite (Figure 3.18) does not indicate a transitional change towards ferritchromit and magnetite (Barnes, 2000), and slightly elevated ZnO contents of 0.6 wt.% have been reported in unaltered chromite derived from layered intrusions previously. This suggests there may have been only minor metamorphic contribution of ZnO to 13TKN22 chromites. While chromites clearly equilibrated with surrounding silicates at metamorphic temperatures, significant mobility of trivalent cations appears to have been restricted. This suggests that high $Fe^{3+}/\Sigma R^{3+}$ and Cr# of chromites are a primary feature: the high Fe^{3+} and TiO_2 content of 13TKN22 chromites (Figure 3.19), alongside sub-solidus growth (Figure 18c), shows clear interaction with intercumulus liquids.

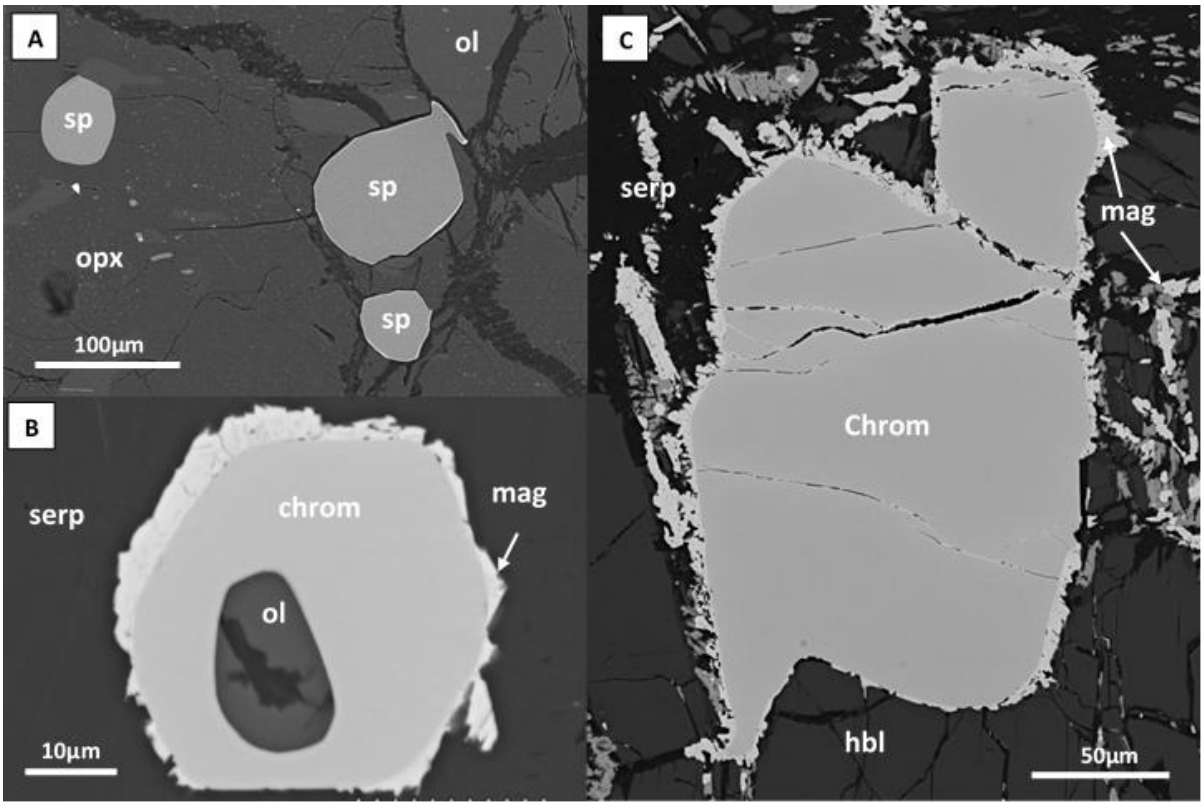

Figure 3.18: Manfred Complex spinel and chromite. A) Individual and exsolved grains of spinel (sp) within orthopyroxe (opx) in Manfred Complex metaharzburgite 13TKN80. Also closely associated with olivine (ol). B) Coarse chromite (chrom) grain within amphibole (amph) in recrystallised metaperidotite 13TKN22. C) Chromite within hornblende in 13TKN22. D) Finer chromite within 13TKN22, with a strong magnetite rim (mag) and an inclusion of olivine. This pair yields metamorphic equilibration temperatures of ~460 °C, indicative of upper greenschist facies metamorphism.

High Cr# Jack Hills detrital grains overlap well with the Cr# of 13TKN22 chromites (Figure 3.19a). This does not account for the lower Cr# detrital grains observed, but analysis of one sample does not represent the entire Manfred Complex. However, while some detrital grains yield similar Cr# to chromites from the Manfred Complex, they contain slightly lower TiO_2 and significantly lower Fe^{3+}/R^{3+} contents (Figure 3.19b). As previously stated, these two provenance indicators should be used with caution when interpreting Jack Hills chromite, and this dichotomy may simply be a result of TiO_2 mobility and underestimation of Fe^{3+}/R^{3+} from non-stoichiometry within detrital grains. The largest caveat to ascribing a provenance from the Manfred Complex is that the Complex dates to 3730 Ma, while Jack Hills detrital chromites yield, currently unpublished, Re-Os TMAs of 3400-3500 Ma (Valley et al., 2005). However, the assimilation of crust with radiogenic $^{187}Os/^{188}Os$ may account for this discrepancy, yielding artificially younger TMAs (see Chapter 4 for further discussion). Further geochemical and isotopic analysis of well-preserved chromites from other Manfred Complex metaperidotites may conclude for or against their representation as the source of Jack Hills detrital chromites. Finally, many mafic and ultramafic bodies within the Narryer Terrane, though labelled as

the Manfred Complex on geological maps, are significantly younger (Kemp et al., 2019). Further analysis of chromite-bearing lithologies within these intrusions may therefore provide further source constraints on detrital chromites from Jack Hills.

Sample Crystal # Classification	13TKN22 40 chromite	13TKN22 42 chromite	13TKN22 43 chromite	13TKN22 45 chromite	13TKN22 46 chromite	13TKN22 47 chromite
SiO_2	0.00	0.00	0.03	0.01	0.01	0.02
TiO_2	1.13	1.03	0.84	0.76	0.99	0.97
Al_2O_3	9.23	9.26	8.83	8.13	9.29	9.18
Cr_2O3	43.66	44.18	43.02	45.86	44.17	43.87
V_2O_3	n/a	n/a	n/a	n/a	0.24	0.25
Fe_2O_3	12.88	12.63	13.52	12.77	12.99	12.95
FeO	28.10	27.72	28.13	27.54	27.35	27.20
MgO	2.72	3.41	1.98	3.33	3.75	3.72
MnO	1.32	0.45	1.83	0.45	0.46	0.43
CaO	0.01	0.03	0.01	0.00	0.02	0.03
NiO	0.14	0.12	0.12	0.15	0.14	0.13
ZnO	0.60	0.59	0.67	0.53	0.60	0.58
Total	***99.80***	***99.43***	***98.99***	***99.52***	***100.00***	***99.33***
Mg #	14.73	17.99	11.15	17.71	14.63	14.59
Cr #	76.03	76.20	76.58	79.09	76.13	76.22
Fe^{3+}/ΣFe	0.29	0.29	0.30	0.29	0.30	0.30

Table 3.2: Representative EPMA analysis of chromite from 13TKN22. V_2O_3 not measured for 13TKN22 40-45. Fe_2O_3 calculated from AB_2O_4 stoichiometry using the equations of Droop (1987).

Jack Hills ultramafics

A single sample of ultramafic from Jack Hills, 16WA13, was analysed for chromite major and minor elements within this study. Chromites have clearly equilibrated at amphibolite facies (Section 2.3.2), indicating even trivalent cations may not be robust (e.g. Barnes, 2000), and so comparisons should be made tentatively. Chromite cores show a narrow range of Cr# between 68 and 72 (Figure 3.20; Table 3.3). The trend towards the Cr-Fe^{3+} apex is indicative of trivalent cation mobility: the same minor trend within cores indicates chromite cores have also experienced some mobility. Such chemical trends are expected given the thick ferritchromit and magnetite rims on 16WA13 relict chromites (Figure 2.6). As chromites trend towards high Cr#, it suggests the primary Cr# of these grains was ca. Cr#70 or lower. This suggests that this heavily recrystallised ultramafic is not a komatiite, as komatiitic chromite typically yield Cr# of >~75. While the maximum Cr# falls within the range of chromites from komatiitic dunites, the high proportion of relict chromites within 16WA13 indicates this unit does not possess this petrogenesis (Barnes & Roeder, 2001).

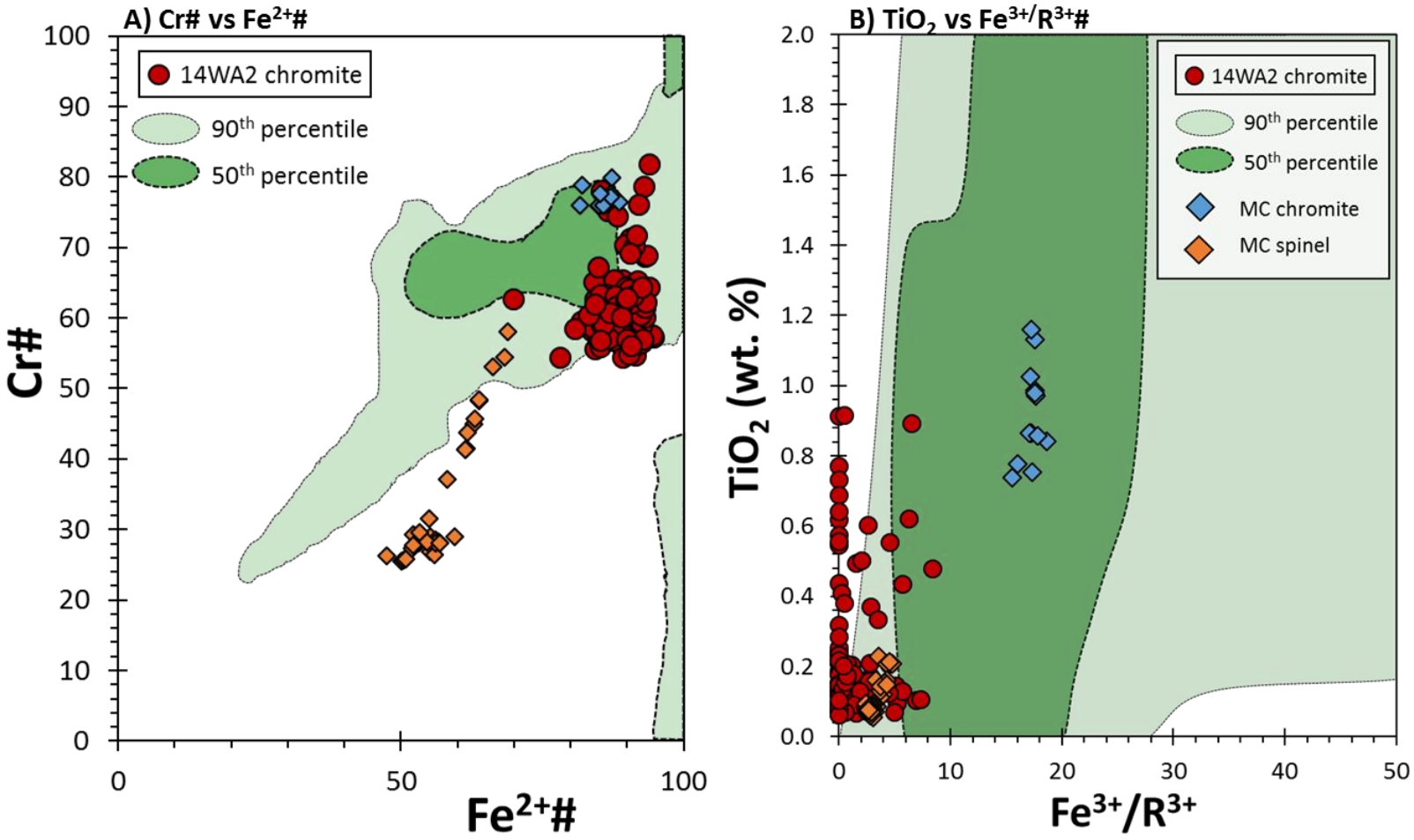

Figure 3.19: Manfred Complex chromite major element chemistry, fields derived from Barnes & Roeder (2001). **A)** Cr# vs Fe^{2+}#, Manfred Complex chromites cluster at or near compositions similar high Cr# 14WA2 grains. However, Jack Hills detrital chromites clearly do not match the dominantly spinel or picotite compositions of the Manfred Complex **B)** Fe^{3+}/R^{3+} and TiO_2 content of 14WA2 detrital grains far lower than chromite within metaperidotite, though overlap with spinel compositions.

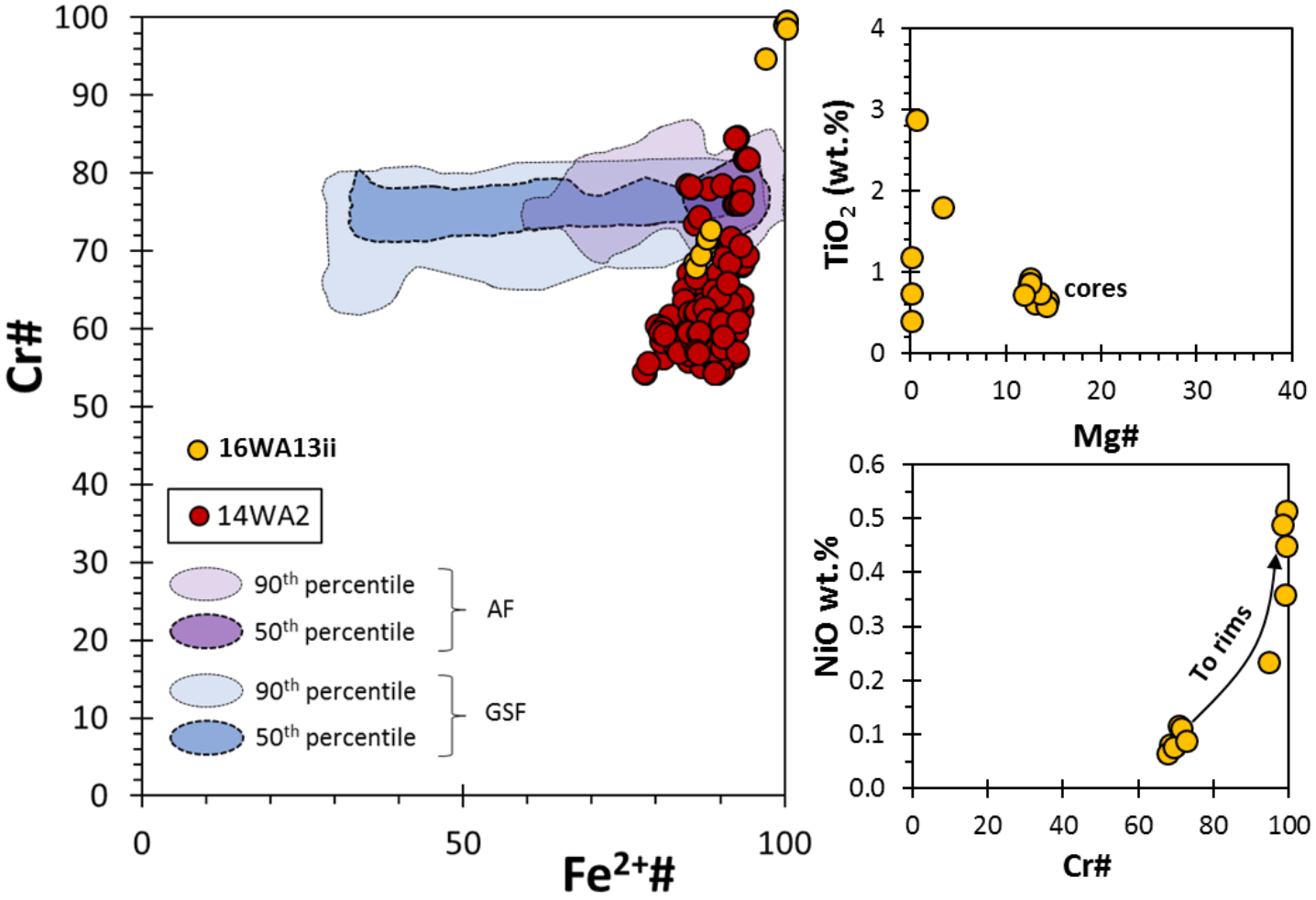

Figure 3.20: 16WA13 chromite compositions: clustered cores at Cr#70 transitioning to Fe^{3+}-rich ferritchromit and magnetite rims. Ferritchromit and magnetite rims show variable TiO_2 and increasing NiO with increasing Cr#, a result of loss of Al to Fe^{3+}. The increased NiO of rims is a product of their high magnetite component (Barnes, 1998). Cores still retain up to ~0.1 wt.% NiO, which is significantly higher than detrital chromites.

Sample	16WA13	16WA13	16WA13	16WA13	16WA13	16WA13	16WA13	16WA13
	relict core	*relict core*	*relict core*	*relict core*	*relict core*	*relict core*	*relict core*	*relict core*
SiO_2	0.03	0.00	0.02	0.02	0.03	0.02	0.04	0.02
TiO_2	0.62	0.64	0.92	0.58	0.86	0.75	0.86	0.72
Al_2O_3	13.31	14.06	12.80	14.38	12.52	13.66	12.64	11.93
Cr_2O_3	45.96	45.61	46.48	45.32	46.77	46.15	47.19	47.38
Fe_2O_3	6.47	6.06	5.76	6.04	5.87	5.98	5.55	6.31
FeO	27.89	27.62	28.25	27.68	28.17	28.02	28.35	28.20
MgO	2.83	3.12	2.68	3.09	2.65	2.94	2.67	2.55
MnO	1.21	1.10	1.20	1.09	1.19	1.16	1.20	1.23
CaO	0.01	0.01	0.00	0.00	0.03	0.01	0.00	0.01
NiO	0.08	0.08	0.12	0.06	0.10	0.08	0.11	0.09
ZnO	1.08	1.09	1.06	1.14	1.08	1.11	1.04	1.02
Total	99.48	99.40	99.28	99.42	99.27	99.87	99.64	99.47
Mg#	13.00	14.39	12.49	14.26	12.37	13.58	12.48	11.84
Cr#	69.84	68.51	70.89	67.89	71.47	69.39	71.47	72.70
$Fe^{3+}/\Sigma fe$	0.17	0.16	0.16	0.16	0.16	0.16	0.15	0.17

Table 3.3: Core compositions of relict chromites within Jack Hills ultramafic 16WA13. V_2O_3 not measured for this sample. Fe_2O_3 calculated from AB_2O_4 stoichiometry using the equations of Droop (1987).

Clear signs of metamorphic re-equilibration of relict chromite cores are also shown by elevated wt. % ZnO and MnO (Table 3.3). These samples have probably experienced amphibolite facies metamorphism, and so tectonic interpretations should be taken cautiously. However, it is apparent there is some overlap between 16WA13 chromites and Jack Hills detrital grains (Figure 3.20). It is unclear if the elevated Cr# in comparison to detrital grains is an igneous feature, or the product of metamorphic equilibration.

3.8. Conclusions

Variably rounded grains of detrital chromite are present alongside detrital Hadean zircon within fuchsitic metasediments at Jack Hills. We have conducted a detailed EPMA investigation of chromite grains in a bid to expand beyond the heavily studied zircon record, and elucidate the petrogenesis of Archean mafic and ultramafic crust within the Narryer Terrane, and potentially the wider Yilgarn Craton. Chromites have undergone significant modification during deformation of host metasediments, during which grains equilibrated with metamorphic fluids and co-precipitating fuchsite, leading to significant mobility of divalent cations and locally trivalent cations. Modification of divalent cations is shown by elevated ZnO and MnO, coupled with lowered Mg# (Barnes, 2000; Colás et al., 2014). Increasingly homogenised and lowered Mg# alongside elevated wt.% ZnO suggests greater equilibration with metamorphic fluids, likely due to lower modal proportions of chromite

and/or changing fluid/rock ratios. Higher Mg#, and therefore likely temperature, rims within high ZnO chromites attest to the presence of a second, discrete event, or prograde conditions within a single deformation event. Furthermore, metamorphic fluids precipitated secondary phases, particularly low temperature silicates such as quartz and fuchsite, within voids in chromites left by dissolution of primary inclusions and in zones of recrystallisation. We propose this deformation event coincides with peak upper greenschist to lower amphibolite facies metamorphism of Jack Hills metasediments at ~2650 Ma (Rasmussen et al., 2010; 2011). Finally, zoning profiles within low ZnO 14WA2 chromites testifies to potential previous enrichment of ZnO and MnO, likely prior to deposition.

Despite localised trivalent cation mobility, chromites yield consistent Cr# across all samples. This indicates the Cr# of chromite cores are a robust petrogenetic indicator. The repeated variability of Cr# regardless of rounding shape and sample location suggests a single protolith for detrital grains, which was both magmatically dynamic and laterally extensive to yield the multiple geographical sources required. This precludes a komatiitic source for most grains. While the absence of other indicators of an ophiolitic source are not found, this tectonic setting cannot be discounted. However, we propose that due to the observed Cr-Al trend, low Ti and Fe^{3+}, and the laterally extensive magmatic event required, Jack Hills chromites are derived from a deep-seated layered intrusion. It is currently unclear whether chromites represent the remnants of a hitherto unknown ~3400-~3500 Ma (Valley et al., 2005) layered intrusion, or rather the remnants of the 3730 Ma Manfred Complex (Kinny et al., 1988; Kemp et al., 2018). While both the Manfred Complex and detrital grains yield apparent komatiitic affinities from high degrees of mantle melting, the presence of true metavolcanics greenstone belts is notably absent within the Narryer Terrane.

This study highlights the complexities of ascribing a provenance to detrital chromites that have undergone significant metamorphic exchange of major and minor elements. However, with a careful and detailed approach and characterisation of metamorphic signatures, we also show that grains may preserve important information on igneous precursors, suggesting detrital chromites may be a powerful petrogenetic tool within Archean sediments. Further clarification of provenance may also be possible using emerging field of both bulk grain and in-situ PGE analysis of chromites (e.g. Coggon et al., 2015; Page and Barnes, 2016; Park et al., 2017), particularly in examples such as Jack Hills where Ti mobility inhibits the distinction between ophiolitic and layered intrusive sources. Finally, fuchsitic metasediments are commonly reported within Archean terranes (e.g. Randive et al., 2015). While further petrological and experimental studies of the interaction of chromites and fluid-derived fuchsite are required, well preserved detrital chromite within such sediments may present a novel tool in understanding the geodynamic conditions of the early Earth.

Funding

This work was funded by a NERC Doctoral Training Partnership PhD studentship to Leanne Staddon, alongside CASE sponsorship from the British Geological Survey.

Acknowledgements

The assistance of Stuart Kearns and Ben Buse with EPMA work is gratefully acknowledged. Matthew Rowe and Chris Gray are thanked for their help during fieldwork in the Narryer Terrane, as are Bruno Dhuime and Ben Brennan for separation of 14WA1-4 samples.

3.9. References

Ahmed, A. H. & Surour, A. A. (2016). Fluid-related modifications of Cr-spinel and olivine from ophiolitic peridotites by contact metamorphism of granitic intrusions in the Ablah area, Saudi Arabia. *Journal of Asian Earth Sciences* 122, 58-79.

Amelin, Y., Lee, D. C., Halliday, A. N. & Pidgeon, R. T. (1999). Nature of the Earth's earliest crust from hafnium isotopes in single detrital zircons. *Nature* 399, 252-255.

Arif, M. & Moon, C. J. (2007). Nickel-rich chromian muscovite from the Indus suture ophiolite, NW Pakistan: Implications for emerald genesis and exploration. *Geochemical Journal* 41, 475-482.

Arndt, N. T., Lesher, C. & Barnes, S. J. (2008). Brief descriptions of six classic komatiite occurrences. *Komatiite*. Cambridge: Cambridge University Press, 16-52.

Ballhaus, C., Berry, R.F., and Green, D.H. (1991). High pressure experimental calibration of the olivine-orthopyroxene-spinel oxygen geobarometer: implications for the oxidation state of the upper mantle. *Contributions to Mineralogy and Petrology* 107, 27-40.

Barkov, A. Y., Nixon, G. T., Levson, V. M., Martin, R. F. & Fleet, M. E. (2013). Chromian spinel from PGE-bearing placer deposits, British Colombia, Canada: Mineralogical associations and provenance. *Canadian Mineralogist* 51, 501-536.

Barnes, S. J. & Fiorentini, M. L. (2012). Komatiite Magmas and Sulfide Nickel Deposits: A Comparison of Variably Endowed Archean Terranes. *Economic Geology* 107, 755-780.

Barnes, S. J. & Roeder, P. L. (2001). The range of spinel compositions in terrestrial mafic and ultramafic rocks. *Journal of Petrology* 42, 2279-2302.

Barnes, S. J. (2000). Chromite in komatiites, II. modification during greenschist to mid-amphibolite facies metamorphism. *Journal of Petrology* 41, 387-409.

Bell, E. A., Boehnke, P., Hopkins-Wielicki, M. D. & Harrison, T. M. (2015). Distinguishing primary and secondary inclusion assemblages in Jack Hills zircons. *Lithos* 234, 15-26.

Bell, E. A., Harrison, T. M., Kohl, I. E. & Young, E. D. (2014). Eoarchean crustal evolution of the Jack Hills zircon source and loss of Hadean crust. *Geochimica Et Cosmochimica Acta* 146, 27-42.

Berger, J., Diot, H., Lo, K., Ohnenstetter, D., Femenias, O., Pivin, M., Demaiffe, D., Bernard, A. & Charlier, B. (2013). Petrogenesis of Archean PGM-bearing chromitites and associated ultramafic-mafic-anorthositic rocks from the Guelb el Azib layered complex (West African craton, Mauritania). *Precambrian Research* 224, 612-628.

Byerly, B. L., Lowe, D. R., Drabon, N., Coble, M. A., Burns, D. H. & Byerly, G. (2018). Hadean zircon from a 3.3 Ga sandstone, Barberton greenstone belt, South Africa. *Geology* 46, 1-4.

Byerly, G. & Lowe, D. (1994). Spinel from Archean impact spherules. *Geochimica Et Cosmochimica Acta* 58, 3469-3486.

Cameron, E. N. (1979). Titanium-bearing oxide minerals of the critical zone of the eastern Bushveld Complex. *American Mineralogist* 64, 140-150.

Cassidy, K. F., Champion, D.C., Krapez, B., Barley, M.E., Brown, S.J.A., Blewett, R.S., Groenewald, N.B., Tyler, I.M. (2006). A Revised Geological Framework for the Yilgarn Craton. *Geological Survey of Western Australia* (Record 2006/8).

Cavosie, A. J., Valley., J. W., and Wilde., S. A. (2019). The Oldest Terrestrial Mineral Record: Thirty Years of Research on Hadean Zircon from Jack Hills, Western Australia. In: van Kranendonk, M. J., Bennett, V. C., and Hoffmann, J. E., (ed.) *Earth's Oldest Rocks*: Elsevier, 255-273.

Cavosie, A. J., Valley, J. W., Fournelle, J. & Wilde, S. A. (2002). Implications for sources of Jack Hills metasediments: detrital chromite. *Goldschmidt 2002*, 125.

Challis, A., Grapes, R. & Palmer, K. (1995). Chromian muscovite, uvarovite, and zincian chromite: Products of regional metasomatism in northwest Nelson, New Zealand. *Canadian Mineralogist* 33, 1263-1284.

Chaudhuri, T., Wan, Y., Mazumder, R., Ma, M. & Liu, D. (2018). Evidence of Enriched, Hadean Mantle Reservoir from 4.2-4.0 Ga zircon xenocrysts from Paleoarchean TTGs of the Singhbhum Craton, Eastern India. *Scientific Reports* 8.

Coggon, J. A., Luguet, A., Fonseca, R. O. C., Lorand, J. P., Heuser, A. & Appel, P. W. U. (2015). Understanding Re-Os systematics and model ages in metamorphosed Archean ultramafic rocks: A single mineral to whole-rock investigation. *Geochimica Et Cosmochimica Acta* 167, 205-240.

Colas, V., Gonzalez-Jimenez, J. M., Griffin, W. L., Fanlo, I., Gervilla, F., O'Reilly, S. Y., Pearson, N. J., Kerestedjian, T. & Proenza, J. A. (2014). Fingerprints of metamorphism in chromite: New insights from minor and trace elements. *Chemical Geology* 389, 137-152.

Compston, W. & Pidgeon, R. T. (1986). Jack Hills, evidence of more very old detrital zircons in Western Australia. *Nature* 321, 766-769.

Corfu, F., Hanchar, J., Hoskin, P. & Kinny, P. (2003). Atlas of zircon textures. *Zircon* **53**, 469-500.

Cronholm, A. & Schmitz, B. (2007). Extraterrestrial chromite in latest Maastrichtian and Paleocene pelagic limestone at Gubbio, Italy: The flux of unmelted ordinary chondrites. *Meteoritics & Planetary Science* 42, 2099-2109.

Crowley, J. L., Myers, J. S., Sylvester, P. J. & Cox, R. A. (2005). Detrital zircon from the Jack Hills and Mount Narryer, Western Australia: Evidence for diverse > 4.0 Ga source rocks. *Journal of Geology* 113, 239-263.

Dare, M. S., Tarduno, J. A., Bono, R. K., Cottrell, R. D., Beard, J. S. & Kodama, K. P. (2016). Detrital magnetite and chromite in Jack Hills quartzite cobbles: Further evidence for the preservation of primary magnetizations and new insights into sediment provenance. *Earth and Planetary Science Letters* 451, 298-314.

Dick, H. J. B. & Bullen, T. (1984). Chromian spinel as a petrogenetic indicator in abyssal and alpine-type peridotites and spatially associated lavas. *Contributions to Mineralogy and Petrology* 86, 54-76.

Droop, G. (1987). A general equation for estimating Fe-3+ concentrations in ferromagnesian silicates and oxides from microprobe analyses, using stoichiometric criteria. *Mineralogical Magazine* 51, 431-435.

Dunn, S. J., Nemchin, A. A., Cawood, P. A. & Pidgeon, R. T. (2005). Provenance record of the Jack Hills metasedimentary belt: Source of the Earth's oldest zircons. *Precambrian Research* 138, 235-254.

Fanlo, I., Gervilla, F., Colas, V. & Subias, I. (2015). Zn-, Mn- and Co-rich chromian spinels from the Bou-Azzer mining district (Morocco): Constraints on their relationship with the mineralizing process. *Ore Geology Reviews* 71, 82-98.

Fleet, M. E., Angeli, N. & Pan, Y. M. (1993). Oriented chlorite lamellae in chromite from the Pedra-Branca mafic-ultramafic complex, Ceara, Brazil. *American Mineralogist* 78, 68-74.

Fletcher, I. R., Rosman, K. J. R. & Libby, W. G. (1988). Sm-Nd, Pb-Pb and Rb-Sr geochronology of the Manfred Complex, Mount Narryer, Western Australia. *Precambrian Research* 38, 343-354.

Froude, D. O., Ireland, T. R., Kinny, P. D., Williams, I. S., Compston, W., Williams, I. R. & Myers, J. S. (1983). Ion microprobe identification of 4,100-4,200 myr-old terrestrial zircons. *Nature* 304, 616-618.

Gervilla, F., Padron-Navarta, J. A., Kerestedjian, T., Sergeeva, I., Gonzalez-Jimenez, J. M. & Fanlo, I. (2012). Formation of ferrian chromite in podiform chromitites from the Golyamo Kamenyane serpentinite, Eastern Rhodopes, SE Bulgaria: a two-stage process. *Contributions to Mineralogy and Petrology* 164, 643-657.

Gonzalez-Jimenez, J. M., Griffin, W. L., Gervilla, F., Kerestedjian, T. N., O'Reilly, S. Y., Proenza, J. A., Pearson, N. J. & Sergeeva, I. (2012). Metamorphism disturbs the Re-Os signatures of platinum-group minerals in ophiolite chromitites. *Geology* **40**, 659-662.

Gonzalez-Jimenez, J. M., Kerestedjian, T., Proenza, J. A. & Gervilla, F. (2009). Metamorphism on Chromite Ores from the Dobromirtsi Ultramafic Massif, Rhodope Mountains (SE Bulgaria). *Geologica Acta* 7, 413-429.

Groves, D. I., Barrett, F. M., Binns, R. A. & McQueen, K. G. (1977). Spinel phases associated with metamorphosed volcanic-type iron-nickel sulfide ores from Western Australia. *Economic Geology* 72, 1224-1244.

Harrison, T. M., Bell, E. A. & Boehnke, P. (2017). Hadean Zircon Petrochronology. *Petrochronology: Methods and Applications* 83, 329.

Harrison, T. M., Schmitt, A. K., McCulloch, M. T. & Lovera, O. M. (2008). Early (>= 4.5 Ga) formation of terrestrial crust: Lu-Hf, delta O-18, and Ti thermometry results for Hadean zircons. *Earth and Planetary Science Letters* 268, 476-486.

Harrison, T. M., Trail, D., Schmitt, A. K. & Watson, E. B. (2007). Rutile ^{207}Pb-^{206}Pb ages in the Jack Hills quartzite, Western Australia. *Geochimica Et Cosmochimica Acta* 71, A383-A383.

Harrison, T. M. & Schmitt, A. K. (2007). High sensitivity mapping of Ti distributions in Hadean zircons. *Earth and Planetary Science Letters* 261, 9-19.

Heimann, A., Spry, P. G. & Teale, G. S. (2005). Zincian spinel associated with metamorphosed proterozoic base-metal sulfide occurrences, Colorado: A re-evaluation of gahnite composition as a guide in exploration. *Canadian Mineralogist* 43, 601-622.

Heinrich, E. W. (1965). Further information on the geology of chromian muscovites. *American Mineralogist* 50, 758-762.

Hodel, F., Macouin, M., Triantafyllou, A., Carlut, J., Berger, J., Rousse, S., Ennih, N. & Trindade, R. I. F. (2017). Unusual massive magnetite veins and highly altered Cr-spinels as relics of a Cl-rich acidic hydrothermal event in Neoproterozoic serpentinites (Bou Azzer ophiolite, Anti-Atlas, Morocco). *Precambrian Research* 300, 151-167.

Holden, P., Lanc, P., Ireland, T. R., Harrison, T. M., Foster, J. J. & Bruce, Z. (2009). Mass-spectrometric mining of Hadean zircons by automated SHRIMP multi-collector and single-collector U/Pb zircon age dating: The first 100,000 grains. *International Journal of Mass Spectrometry* 286, 53-63.

Hopkins, M., Harrison, T. M. & Manning, C. E. (2012). Metamorphic replacement of mineral inclusions in detrital zircon from Jack Hills, Australia: Implications for the Hadean Earth. *Geology* 40, E281-E281.

Hopkins, M. D., Harrison, T. M. & Manning, C. E. (2010). Constraints on Hadean geodynamics from mineral inclusions in > 4 Ga zircons. *Earth and Planetary Science Letters* 298, 367-376.

Hopkins, M., Harrison, T. M. & Manning, C. E. (2008). Low heat flow inferred from > 4 Gyr zircons suggests Hadean plate boundary interactions. *Nature* 456, 493-496.

Iizuka, T., McCulloch, M. T., Komiya, T., Shibuya, T., Ohta, K., Ozawa, H., Sugimura, E. & Collerson, K. D. (2010). Monazite geochronology and geochemistry of meta-sediments in the Narryer Gneiss Complex, Western Australia: constraints on the tectonothermal history and provenance. *Contributions to Mineralogy and Petrology* 160, 803-823.

Iizuka, T., Horie, K., Komiya, T., Maruyama, S., Hirata, T., Hidaka, H. & Windley, B. F. (2006). 4.2 Ga zircon xenocryst in an Acasta Gneiss from northwestern Canada: Evidence for early continental crust. *Geology* 34, 245-248.

Irvine, T. N. (1967). Chromian spinel as a petrogenetic indicator part 2: Petrologic application. *Canadian Journal of Earth Sciences* 4, 71-103.

Irvine, T. N. (1965). Chromian spinel as a petrogenetic indicator. Part 1. Theory. *Canadian Journal of Earth Sciences* 2, 648-672.

Kamenetsky, V. S., Crawford, A. J. & Meffre, S. (2001). Factors controlling chemistry of magmatic spinel: An empirical study of associated olivine, Cr-spinel and melt inclusions from primitive rocks. *Journal of Petrology* 42, 655-671.

Kamperman, M., Danyushevsky, L. V., Taylor, W. R. & Jablonski, W. (1996). Direct oxygen measurements of Cr-rich spinel: Implications for spinel stoichiometry. *American Mineralogist* 81, 1186-1194.

Kemp, A. I. S., Wilde, S. A., and Spaggiari, C. (2019). The Narryer Terrane, Yilgarn Craton, Western Australia: Review and Recent Developments. In: van Kranendonk, M. J., Bennett, V. C., and Hoffmann, J. E., (ed.) *Earth's Oldest Rocks*: Elsevier, 401-429.

Kemp, A. I. S. (2018). Early earth geodynamics: cross examining the geological testimony. *Philosophical Transactions of the Royal Society A* 376.

Kemp, A. I. S., Wilde, S. A., Hawkesworth, C. J., Coath, C. D., Nemchin, A., Pidgeon, R. T., Vervoort, J. D. & DuFrane, S. A. (2010). Hadean crustal evolution revisited: New constraints from Pb-Hf isotope systematics of the Jack Hills zircons. *Earth and Planetary Science Letters* 296, 45-56.

Kerrich, R., Fyfe, W. S., Barnett, R. L., Blair, B. B., and Willmore, L. M. (1987). Corundum, Cr-muscovite rocks at O'Briens, Zimbabwe: the conjunction of hydrothermal desilicification and LIL-element enrichment-geochemical and isotopic evidence. *Contributions to Mineralogy and Petrology* 95, 481-498.

Kimball, K. L. (1990). Effects of hydrothermal alteration on the compositions of chromian spinels. *Contributions to Mineralogy and Petrology* 105, 337-346.

Kinny, P. D. & Nutman, A. P. (1996). Zirconology of the Meeberrie Gneiss, Yilgarn Craton, Western Australia: An early Archaean migmatite. *Precambrian Research* 78, 165-178.

Kinny, P. D., Wijbrans, J. R., Froude, D. O., Williams, I. S. & Compston, W. (1990). Age constraints on the geological evolution of the Narryer Gneiss Complex, Western Australia. *Australian Journal of Earth Sciences* 37, 51-69.

Kinny, P. D., Williams, I. S., Froude, D. O., Ireland, T. R. & Compston, W. (1988). Early Archean zircon ages from orthogneisses and anorthosites at Mount Narryer, Western Australia. *Precambrian Research* 38, 325-341.

Lenaz, D. & Princivalle, F. (2005). Crystal chemistry of detrital chromian spinel from the southeastern Alps and Outer Dinarides: The discrimination of supplies from areas of similar tectonic setting? *Canadian Mineralogist* 43, 1305-1314.

Marques, A. F. A., Barriga, F. J. A. S. & Scott, S. D. (2007). Sulfide mineralization in an ultramafic-rock hosted seafloor hydrothermal system: From serpentinization to the formation of Cu-Zn-(Co)-rich massive sulfides. *Marine Geology* 245, 20-39.

Martyn, J. E. & Johnson, G. I. (1986). Geological setting and origin of fuchsite-bearing rocks near Menzies, Western Australia. *Australian Journal of Earth Sciences* 33, 373-390.

Myers, J. S. (1988a). Early Archean Narryer Gneiss Complex, Yilgarn Craton, Western-Australia. *Precambrian Research* 38, 297-307.

Myers, J. S. (1988b). Oldest known terrestrial anorthosite at Mount Narryer, Western Australia. *Precambrian Research* 38, 309-323.

Myers, J. S. & Williams, I. R. (1985). Early Precambrian crustal evolution at Mount Narryer, Western Australia. *Precambrian Research* 27, 153-163.

Nebel, O., Rapp, R. P. & Yaxley, G. M. (2014). The role of detrital zircons in Hadean crustal research. *Lithos* 190, 313-327.

Nelson, D. R., Robinson, B. W. & Myers, J. S. (2000). Complex geological histories extending for >= 4.0 Ga deciphered from xenocryst zircon microstructures. *Earth and Planetary Science Letters* 181, 89-102.

Nutman, A. P., Bennett, V. C., Kinny, P. D. & Price, R. (1993). Large-scale crustal structure of the Northwestern Yilgarn Craton, Western Australia: Evidence from Nd isotopic data and zircon geochronology. *Tectonics* 12, 971-981.

Nutman, A. P., Kinny, P. D., Compston, W. & Williams, I. S. (1991). SHRIMP U-Pb zircon geochronology of the Narryer Gneiss Complex, Western Australia. *Precambrian Research* 52, 275-300.

Page, P. & Barnes, S. J. (2016). The influence of chromite on osmium, iridium, ruthenium and rhodium distribution during early magmatic processes. *Chemical Geology* 420, 51-68.

Park, J. W., Kamenetsky, V., Campbell, I., Park, G., Hanski, E. & Pushkarev, E. (2017). Empirical constraints on partitioning of platinum group elements between Cr-spinel and primitive terrestrial magmas. *Geochimica Et Cosmochimica Acta* 216, 393-416.

Petersson, A., Kemp, A. I. S., Hickman, A. H., Whitehouse, M. J., Martin, L. & Gray, C. M. (2019). A new 3.59 Ga magmatic suite and a chondritic source to the east Pilbara Craton. *Chemical Geology* **511**, 51-70.

Pidgeon, R. T. & Nemchin, A. A. (2006). High abundance of early Archaean grains and the age distribution of detrital zircons in a sillimanite-bearing quartzite from Mt Narryer, Western Australia. *Precambrian Research* 150, 201-220.

Pidgeon, R. T. & Wilde, S. A. (1998). The interpretation of complex zircon U-Pb systems in Archaean granitoids and gneisses from the Jack Hills, Narryer gneiss Terrane, Western Australia. *Precambrian Research* 91, 309-332.

Randive, K. R., Korakoppa, M. M., Muley, S. V., Varade, A. M., Khandare, H. W., Lanjewar, S. G., Tiwari, R. R. & Aradhi, K. K. (2015). Paragenesis of Cr-rich muscovite and chlorite in green-mica quartzites of Saigaon-Palasgaon area, Western Bastar Craton, India. *Journal of Earth System Science* 124, 213-225.

Rapp, J., Klemme, S., Butler, I. & Harley, S. (2010). Extremely high solubility of rutile in chloride and fluoride-bearing metamorphic fluids: An experimental investigation. *Geology* **38**, 323-326.

Rasmussen, B., Fletcher, I. R., Muhling, J. R., Gregory, C. J. & Wilde, S. A. (2012). Metamorphic replacement of mineral inclusions in detrital zircon from Jack Hills, Australia: Implications for the Hadean Earth. *Geology* 40, 282-283.

Rasmussen, B., Fletcher, I. R., Muhling, J. R., Gregory, C. J. & Wilde, S. A. (2011). Metamorphic replacement of mineral inclusions in detrital zircon from Jack Hills, Australia: Implications for the Hadean Earth. *Geology* 39, 1143-1146.

Rasmussen, B., Fletcher, I. R., Muhling, J. R. & Wilde, S. A. (2010). In situ U-Th-Pb geochronology of monazite and xenotime from the Jack Hills belt: Implications for the age of deposition and metamorphism of Hadean zircons. *Precambrian Research* 180, 26-46.

Reimink, J. R., Chacko, T., Stern, R. A. & Heaman, L. M. (2014). Earth's earliest evolved crust generated in an Iceland-like setting. *Nature Geoscience* 7, 529-533.

Roeder, P. L. (1994). Chromite- from the fiery rain of chrondrules to the Kilauea-Iki lava lake. *Canadian Mineralogist* 32, 729-746.

Rollinson, H., Adetunji, J., Yousif, A. A. & Gismelseed, A. M. (2012). New Mossbauer measurements of Fe3+/Sigma Fe in chromites from the mantle section of the Oman ophiolite: evidence for the oxidation of the sub-oceanic mantle. *Mineralogical Magazine* 76, 579-596.

Rollinson, H., Appel, P. W. U. & Frei, R. (2002). A metamorphosed, early Archaean chromitite from west Greenland: Implications for the genesis of Archaean anorthositic chromitites. *Journal of Petrology* 43, 2143-2170.

Sack, R. O. & Ghiorso, M. S. (1991). Chromian spinels as petrogenetic indicators- thermomdynamics and petrological applications. *American Mineralogist* 76, 827-847.

Santti, J., Kontinen, A., Sorjonen-Ward, P., Johanson, B. & Pakkanen, L. (2006). Metamorphism and chromite in serpentinized and carhonate-silica-altered peridotites of the paleoproterozoic Outokumpu-Jormua ophiolite belt, eastern Finland. *International Geology Review* 48, 494-546.

Shirey, S. B. & Walker, R. J. (1998). The Re-Os isotope system in cosmochemistry and high-temperature geochemistry. *Annual Review of Earth and Planetary Sciences* 26, 423-500.

Spaggiari, C. V. (2007a). Structural and lithological evolution of the Jack Hills greenstone belt, Narryer Terrane, Yilgarn Craton, Western Australia. *Western Australia Geological Survey* Record 2007/3, 49.

Spaggiari, C. V., Pidgeon, R. T. & Wilde, S. A. (2007b). The Jack Hills greenstone belt, Western Australia - Part 2: Lithological relationships and implications for the deposition of > 4.0 Ga detrital zircons. *Precambrian Research* 155, 261-286.

Szilas, K., van Hinsberg, V., McDonald, I., Naeraa, T., Rollinson, H., Adetunji, J. & Bird, D. (2018). Highly refractory Archaean peridotite cumulates: Petrology and geochemistry of the Seqi Ultramafic Complex, SW Greenland. *Geoscience Frontiers* 9, 689-714.

Tang, F., Taylor, R. J. M., Einslie, J. F., Borlina, C. S., Fu, R. R., Weiss, B. P., Williams, H. M., Williams, W., Nagy, L., Midgley, P. A., Lima, E. A., Bell., E. A., Harrison, M. T., Alexander, E. W., and Harrison, R. J. (2019). Secondary magnetite in ancient zircon precludes analysis of a Hadean geodynamo. *Proceedings of the National Academy of Sciences of the United States of America* 116, 407-412.

Valley, J. W., Cavosie, A. J., Ushikubo, T., Reinhard, D. A., Lawrence, D. F., Larson, D. J., Clifton, P. H., Kelly, T. F., Wilde, S. A., Moser, D. E. & Spicuzza, M. J. (2014). Hadean age for a post-magma-ocean zircon confirmed by atom-probe tomography. *Nature Geoscience* 7, 219-223.

Valley, J. W., Cavosie, A. J., Shirey, S. & Wilde, S. A. (2005). 3.2 to 3.5 Ga Re-Os Model Ages for Detrital Chromite from Jack Hills, Western Australia: Implications for Pilbara and Yilgarn Craton Evolution. *American Geophysical Union, Fall Meeting 2005, abstract #V21F-08*.

Van Baalen, M. (1993). Titanium mobility in metamorphic systems - a review. *Chemical Geology* **110**, 233-249.

Wang, Q. & Wilde, S. A. (2018). New constraints on the Hadean to Proterozoic history of the Jack Hills belt, Western Australia. *Gondwana Research* 55, 74-91.

Weiss, B. P., Fu, R. R., Einsle, J. F., Glenn, D. R., Kehayias, P., Bell, E. A., Gelb, J., Araujo, J., Lima, E. A., Borlina, C. S., Boehnke, P., Johnstone, D. N., Harrison, T. M., Harrison, R. J. & Walsworth, R. L. (2018). Secondary magnetic inclusions in detrital zircons from the Jack Hills, Western Australia, and implications for the origin of the geodynamo. *Geology* 46, 427-430.

Wilde, S. A., Valley, J. W., Peck, W. H. & Graham, C. M. (2001). Evidence from detrital zircons for the existence of continental crust and oceans on the Earth 4.4 Gyr ago. *Nature* 409, 175-178.

Williams, I. R. & Myers, J. S. (1987). Archaean geology of the Mount Narryer region Western Australia. Geological Survey of Western Australia: Report 22, 1-32.

Wood, B. J. & Virgo, D. (1989). Upper mantle oxidation-state: ferric iron contents of lherzolite spinels by Fe-57 Mossbauer-spectroscopy and resultant oxygen fugacities. *Geochimica Et Cosmochimica Acta* 53, 1277-1291.

Wyche, S. (2007). Evidence of Pre-3100 Ma Crust in the Youanmi and South West Terranes, and Eastern Goldfields Superterrane, of the Yilgarn Craton. In: van Kranendonk, M. J., Smithies, R. H. & Bennett, V. C. (eds.) *Earth's Oldest Rocks*: Elsevier, 113-124.

Wyche, S., Nelson, D. R. & Riganti, A. (2004). 4350-3130 Ma detrital zircons in the Southern Cross Granite-Greenstone Terrane, Western Australia: Implications for the early evolution of the Yilgarn Craton. *Australian Journal of Earth Sciences* 51, 31-45.

Wylie, A. G., Candela, P. A. & Burke, T. M. (1987). Compositional zoning in unusual Zn-rich chromite from the Sykesville District of Maryland and its bearing on the origin of ferritchromit. *American Mineralogist* 72, 413-422.

Zane, A. & Rizzo, G. (1999). The compositional space of muscovite in granitic rocks. *Canadian Mineralogist* 37, 1229-1238.

.

.

Chapter Four:

Re-Os Geochronology

4.1 Introduction

The temporal and physiochemical constraints on the generation of >3100 Ma mafic and ultramafic crust within the Narryer Terrane and the wider Yilgarn Craton are poorly understood (Wyche, 2007). This is in direct contrast to other Archean terranes, where significant quantities of intrusive mafic and ultramafic crust and volcanic komatiites are often described. Ubiquitous detrital chromites within metasediments demonstrate the presence of large quantities of mafic and ultramafic crust within the erosional catchment of sediments at Jack Hills (e.g. Cavosie et al., 2004; Valley et al., 2015; Chapter 3). Critically, chromites are amenable to Re-Os geochronology (e.g. Shirey and Walker, 1998), which exploits the decay of long-lived ($t_{1/2}$= 42 Ga; $\lambda = 1.666 \times 10^{-11}$ yr^{-1}; Smoliar et al., 1996) ^{187}Re via β^- emission to ^{187}Os. This is because chromite typically yields several ppb of Os but sub ppb Re, resulting in low $^{187}Re/^{188}Os$ ratios of <0.1 (e.g. Shirey and Walker, 1998; Carlson, 2005). While a low Re concentration makes chromites susceptible to the influence of Re mobility, the low Re concentration results in only minor changes in the $^{187}Os/^{188}Os$ ratios of chromites, resulting in only mildly modified Re-Os model ages (e.g. Frei et al., 2003). This, coupled with the resistance of chromites to processes such as erosion, weathering and serpentinisation, means chromites are considered the best capsules of robust initial Os isotopic compositions (Bennett et al., 2002; Frei et al., 2003; Carlson, 2005). This can translate into determination of model ages from chromites or the resolution of the initial Os isotopic compositions in mafic and ultramafic crust with previously well constrained ages. Chromites are also amenable to Pt-Os geochronology, where variability in $^{186}Os/^{188}Os$ is measured as parts per ten thousand, though the large sample sizes required to undertake such studies means Pt-Os has not been analysed here.

Chapter 3 discussed the major and minor element chemical composition of detrital chromites and concluded that grains likely shared a common, layered intrusive source. This hypothesis has large implications for Re-Os analysis. Firstly, as the low concentrations of Os and Re within chromites require hundreds of grains per analysis, a shared magmatic provenance indicates bulk analysis of grains will be robust. While only approximately 100 grains are required for Os analysis, over 500 grains per sample are required to yield ~5 pg of Re, assuming a 100% yield. If chromites did not share a single source, such large numbers of chromites per analysis may result in the calculation of mixed, and therefore geologically meaningless, model ages. Second, while many examples of mafic and ultramafic crust yield chondritic initial $^{187}Os/^{188}Os$ compositions (Foster et al., 1997; Bennet et al., 2002; Putchel et al., 2004, 2009a, 2014; Connolly et al., 2011), many layered intrusions have been shown to yield elevated γOs_i compositions (deviation of initial $^{187}Os/^{188}Os$ from chondritic mantle in %) due to the assimilation of radiogenic crust (e.g. Horan et al., 2001; Schoenberg et al., 1999; 2003; Marques et al., 2003; Day et al., 2008; O'Driscoll et al., 2009; Zhong et al., 2011). The role of assimilation is more

challenging to constrain within Archean layered intrusions, where HSE delivery via the late veneer is incomplete and Re-Os systematics are often perturbed by high-grade metamorphism. Rhenium-Osmium studies of Archean mafic and ultramafic rocks often yield Re-Os model ages (TMAs) or isochrons younger than those suggested by Sm-Nd and Pb-Pb WR geochronology, postulated to represent crustal assimilation (Coggon et al., 2015; Ishikawa et al., 2017), metamorphism (Bennet et al., 2002; Rollinson et al., 2002; Frei et al., 2003; Touboul et al., 2014) or, more controversially, early enriched mantle reservoirs (Frei et al., 2003; Putchel et al., 2009b). In a bid to comprehend the effects of crustal assimilation within Jack Hills detrital chromites, this study has also analysed the Re-Os isotopic composition of the Manfred Complex (Myers, 1988; Rowe, 2016), a heavily disseminated 3730 Ma layered intrusion found within the Narryer Terrane (Fletcher et al., 1988; Kinny et al., 1988; Kemp et al., 2019).

One unpublished study has been undertaken to determine the Re-Os isotopic composition of Jack Hills chromites. Valley et al. (2005) reported chromite yielded $^{187}Os/^{188}Os$ values of 0.1057 to 0.1081 and typically low $^{187}Re/^{188}Os$ of 0.0060 to 0.0517. This corresponds to Re-Os TMAs of 3200 Ma to 3500 Ma, which they suggested represented derivation of chromites from a chondritic mantle source at 3400 Ma to 3500 Ma (S. Shirey pers. comm. in Dare et al., 2016). They also noted a strong similarity to the Re-Os composition of these chromites and the komatiitic Talga-Talga chromites in the Pilbara Craton (Bennett et al., 2002), and suggested a potential Archean association between the two terranes.

This chapter details the determination of the Re-Os isotopic composition of Jack Hills detrital chromites, using Re-depletion ages ($^{187}Re/^{188}Os$ sample = 0, TRD) and TMAs. It highlights the challenges of low sample sizes in determining accurate robust Re-Os compositions, and discusses some of the caveats of model ages, including chondrite Os isotopic heterogeneity and crustal assimilation. We also show that despite evidence of Re-Os mobility within Jack Hills chromites both prior to and after deposition within host metasediments robust Re-Os model ages are still yielded by some samples of Jack Hills chromites. Finally, we postulate the most robust Re-Os model ages and model the potential of the Manfred Complex to represent a source of detrital grains.

4.2 Materials and Methods

4.2.1. Separation techniques

Ten samples of chromite and zircon bearing fuchsitic metasediments were sampled from at or near the W-74 site at Jack Hills (Wilde, 2001). Detrital chromites and zircons were separated from metasediment matrix and concentrated using standard mineral separation techniques: samples were crushed, sieved and panned. A hand magnet was used on 14WA samples to remove coarser iron oxides, and samples were further concentrated using heavy liquid separation. Chromites and samples

of the Manfred Complex were analysed across 6 separate sessions (Table 1). Session 5 detrital chromites were aggressively leached using concentrated SpA HF and 6M once distilled (1D) HCl, but this was found to have no effect on Re-Os isotopic compositions or concentrations, and so was not undertaken in other sessions.

After major and minor element characterisation of samples, chromites were hand-picked for Re-Os analysis. Sample size were variable but picking of ~500 to 1000 chromites typically yielded sample sizes between 10 mg and 20 mg for 250-120 µm size fractions. Some bulk chromite samples were significantly smaller. For example, smaller mass samples (~6 mg) of 14WA2 in session 3 were selected intentionally to observe the degree of Os isotopic heterogeneity. In addition to this, session 5 samples were aggressively leached in concentrated HF and 6M 1D HCl. This ultimately disaggregated already heavily cracked chromites, likely putting clay- and silt-sized chromite particulates into suspension and inducing significant sample loss during removal of leaching acids. As such, samples within session 5 weighed between 2 mg and 4 mg, significantly lower than the >10 mg sample sizes ideally analysed.

Manfred Complex harzburgite 13TKN80 and metagabbro 14WA21 were hand crushed and powdered using an agate ball mill to avoid metal contamination. Due to the coarse grain size of these rocks (see Chapter 2) large bulk rock samples (>150 grams) were powdered to achieve chemical homogenisation and avoid HSE nugget effects. Chromite and Cr-bearing spinel are also present within harzburgitic 13TKN80 and metaperidotite 13TKN22, respectively, and were also separated for further Re-Os analysis. Spinels were studied for direct comparison of model ages with detrital chromites, and to reduce the possibility of Re mobility from samples with silicate materials that possess significantly higher $^{187}Re/^{188}Os$.The small size of spinels, particularly within 13TKN80 (<80 µm, Rowe, 2016), and presence within silicates made separation and concentration by panning techniques impossible. As such, spinels were separated from silicate matrix by preferential dissolution of silicates using a 1:2 mixture of SpA HF and 1D HNO_3. Samples were then fluxed in 2 ml of 1D HNO_3, dried down, and fluxed in 2 ml of 1D HCl to fully destroy olivine and serpentine that did not dissolve in the initial HF:HNO_3 dissolution. This procedure did not dissolve spinels, but completely removed the silicate matrix of the rock samples.

4.2.2 Re-Os analytical chemistry

Once bulk samples were picked, uncrushed chromites and ultramafic rock powders were weighed and transferred into aggressively cleaned borosilicate glass carius tubes and digested in a method modified from Shirey and Walker (1995). Briefly, enriched ^{190}Os and ^{185}Re isotopic spikes were weighed and added to carius tubes along with inverse aqua regia: 8 ml and 12 ml of inverse aqua regia were used for chromite separates and rock powders, respectively. Due to the small sample sizes, a total of 4 ml

inverse aqua regia was added to session 5 samples. Carius tubes were then sealed and heated to 230 °C for 48-58 hours to enable spike equilibration and complete sample dissolution. Despite adding chromites uncrushed, incomplete sample dissolution was never encountered, likely due to the heavily cracked nature of Jack Hills grains. Blank contribution of Re and Os were monitored during the process by the analysis of two total procedural blanks (TPB) per session, in all bar session 5 where TPB-1 vented during carius tubes digestion. TPBs for both Re and Os are shown in Table 1.

Table 4.1: total procedural blanks for Os and Re						
SESSION	**Date undertaken**	**TPB-1 Os blank (pg)**	**2se**	**TPB-2 Os blank (pg)**	**2se**	**Average Os blank (pg)**
1	July 2016	1.92	0.01	na	na	**1.92**
2	March 2017	1.39	0.02	2.54	0.02	**1.97**
3	July 2017	0.71	0.01	0.67	0.01	**0.69**
4	July 2018	0.43	0.01	0.47	0.01	**0.45**
5	February 2019	na	na	0.07	0.06	**0.07**
6	April 2019	1.28	0.01	1.00	0.01	**1.14**
SESSION	**Date undertaken**	**TPB-1 Re blank (pg)**	**2se**	**TPB-2 Re blank (pg)**	**2se**	**Average Re blank (pg)**
1	July 2016	45.13	0.01	32.06	0.38	**38.60**
2	March 2017	4.56	0.04	6.63	0.03	**5.60**
3	July 2017	19.83	0.05	20.11	0.08	**19.95**
4	July 2018	1.56	0.04	1.07	0.04	**1.32**
5	February 2019	na	na	0.39	0.04	**0.39**
6	April 2019	1.67	0.01	1.18	0.01	**1.43**

Table 4.1: Os and Re TPB concentrations for different sessions.

Os was subsequently purified by multiple solvent back extractions. Firstly, into carbon tetrachloride (CCl_4) from inverse aqua regia, and then from CCl_4 to UpA HBr following the method of Cohen and Waters (1996). Os-bearing UpA HBr was then further purified at 90 °C for 3 hours using the micro-distillation technique of Birck et al. (1997), where OsO_4 is oxidised using CrO_3-H_2SO_4 and transferred in the gas phase to UpA HBr, within which it is reduced to $OsBr_6^{2-}$. Re-bearing inverse aqua regia, from which the Os had been removed using CCl_4, was dried down, and re-dissolved in 2M 1D HNO_3 for solvent extraction using isoamylol (3-methyl-1-butanol) following a method modified from Birck et al. (1997). Re was first back extracted into pre-cleaned (using MilliQ water) isoamylol, the Re-bearing isoamylol then cleaned with 2M 1D HNO_3 and finally the Re back extracted into MilliQ water. A second cleaning step of 2M 1D HNO_3 was included for bulk rock samples due to the larger proportion of matrix, but this step was not included for chromite samples due to the smaller sample sizes. The Re-bearing MilliQ water was then dried down and redissolved in 2% 1D HNO_3 for MC-ICP-MS analysis.

4.2.3 Re-Os mass spectrometry

The purified Os-bearing aliquot was redissolved in 0.75 µL UpA HBr and loaded onto a lightly outgassed Pt filament. 1µL of $Ba(OH)_2$/NaOH activator was added on top of the sample. The Os isotopic composition and concentration of samples were then determined using ion-counting on the secondary electron multiplier (SEM) of the ThermoFisher Triton thermal ionisation mass spectrometer in negative mode (N-TIMS) at the University of Bristol. Approximately $0.3x10^{-7}$ bars of oxygen were bled into the source chamber to encourage the ionisation of Os as OsO^{3-}. Data reduction consisted of an oxygen isotopic correction, an iterative calculation to determine spike/sample ratios, corrections for instrumental mass bias (using a $^{192}Os/^{188}Os$ ratio of 3.08271) and the isobaric interference of ^{187}Re on ^{187}Os. Finally, the Os isotopic composition and concentration of the sample were determined by spike-stripping and the isotope dilution equation. A 2sd rejection criteria was further applied to $^{187}Os/^{188}Os$ ratios and Os concentrations. A 100 pg Os DTM standard was analysed across all sessions as validation and yielded an average $^{187}Os/^{188}Os$ ratio (n=15) of 0.173997±360 (2sd), within uncertainty of previous analyses undertaken with larger Os loads (e.g. Luguet et al., 2008). Full Os standard data is available in Supplementary Material 3.

Determination of Re concentrations was undertaken on a ThermoFisher Neptune multi-collector inductively coupled plasma mass spectrometer (MC-ICP-MS) at the University of Bristol, using ion counting on the SEM. As mass bias cannot be internally corrected for Re, samples were doped with 20 ppb Ir. A nominal $^{191}Ir/^{193}Ir$ ratio of 0.5929 (Zhu et al., 2017) was used to correct for instrumental mass bias using the exponential fractionation law. An Ir-doped blank was analysed directly prior to determination of samples to blank correct ^{185}Re and ^{187}Re intensities. Spike and sample mixtures were then unmixed and the Re concentration determined using the isotope dilution equation. An Ir-doped 9 ppt solution of NIST SRM3134 was monitored to determine the robustness of measurements throughout runs. Rhenium TPBs drastically decreased throughout analytical sessions with the development of aggressive cleaning techniques for the carius tubes and transfer to the MC-ICP-MS from the TIMS (see chapter 2) and were consistently <2 pg by session 4 (Table 1). This still results in a large blank contribution to measured Re due to small sample sizes used, though session 5 blanks are at the lower limits of blanks achieved by carius tube digestion (e.g. Birck et al., 1997; Pearson et al., 1998).

4.2.4. Re-Os terminology

Once Re and Os concentration and the $^{187}Os/^{188}Os$ isotopic composition of samples had been determined, Re-Os rhenium depletion ages (TRDs; Re/Os=0) and model ages (TMAs; Re/Os= >0) were then calculated using the following equations:

$$\textbf{Re-Os } \boldsymbol{TRD} = \frac{1}{\lambda} * \ln\left[\frac{\left(\frac{^{187}Os}{^{188}Os}\right)CHONDRITE - \left(\frac{^{187}Os}{^{188}Os}\right)SAMPLE}{\left(\frac{^{187}Re}{^{188}Os}\right)CHONDRITE} + 1\right] \quad \textbf{(1)}$$

$$\textbf{Re-Os } \boldsymbol{TMA} = \frac{1}{\lambda} * ln\left[\frac{\left(\frac{^{187}Os}{^{188}Os}\right)CHONDRITE - \left(\frac{^{187}Os}{^{188}Os}\right)SAMPLE}{\left(\frac{^{187}Re}{^{188}Os}\right)CHONDRITE - \left(\frac{^{187}Re}{^{188}Os}\right)SAMPLE} + 1\right] \quad \textbf{(2)}$$

where λ is the decay constant of ^{187}Re (1.666x10^{-11} yr^{-1}; Smoliar et al., 1996), and chondritic isotopic compositions are taken from the mixed chondrite values of Shirey and Walker (1998), where the ^{187}Os/^{188}Os ratio is 0.127 and the ^{187}Re/^{188}Os ratio is 0.40186. It is important to note that the Re and Os isotopic composition varies between chondrite groups (e,g, Shirey and Walker, 1988; Walker et al., 2002a; Day et al., 2016), and these values are the lower limits of non-carbonaceous groups. This is discussed in further detail later within this chapter. Uncertainties for TRDs and TMAs were calculated using a model age covariance matrix (Albarède, 1995), with the greatest contributions to ages being the ^{187}Os/^{188}Os 2se uncertainty and a 1% uncertainty on the decay constant of ^{187}Re. Initial Os compositions (γOs_i) for Manfred Complex samples were also calculated using the equation:

$$\boldsymbol{\gamma Os_i} = \left[\frac{\left(\frac{^{187}Os}{^{188}Os}\right)SAMPLE(t)}{\left(\frac{^{187}Os}{^{188}Os}\right)CHONDRITE(t)} - 1\right] * 100 \quad \textbf{(3)}$$

where γOs_i represents the difference between time-integrated sample and chondritic reservoirs in parts per hundred (%). For the Manfred Complex both reservoirs are time integrated to 3730 Ma, the U-Pb zircon age of anorthosites (Kinny et al., 1988) and leucogabbro (Kemp, 2018). This therefore implies that ultramafic and mafic rocks found to the NE of Mount Narryer are the remnants of the same 3730 Ma intrusive body (Fletcher, 1988; Kinny et al., 1988; Myers, 1988; Kemp et al., 2019).

The effects of crustal assimilation on the Manfred Complex γOs_i and Os concentration were modelled using mass balance, using the following equation:

$$\frac{^{187}\mathrm{Os}}{^{188}\mathrm{Os}}(i)_{\mathrm{MIX}} = \frac{\left(\frac{^{187}\mathrm{Os}}{^{188}\mathrm{Os}}(i)_{\mathrm{MC}} * Os\ conc_{\ \mathrm{MC}} * f\right) + \left(\frac{^{187}\mathrm{Os}}{^{188}\mathrm{Os}}_{3730\mathrm{Ma\ CONTAM}} * Os\ conc_{\ \mathrm{CONTAM}} * (1-f)\right)}{(\mathrm{Os\ conc}_{\ \mathrm{MC}} * f) + (\mathrm{Os\ conc}_{\ \mathrm{CONTAM}} * (1\text{-}f))} \quad \textbf{(4)}$$

where ^{187}Os/^{188}Os(i)$_{MIX}$ is the initial Os isotopic composition of 13TKN80 spinel separates at 3730 Ma, ^{187}Os/^{188}Os(i)$_{MC}$ is the initial Os isotopic composition of the Manfred Complex at 3730 Ma assuming derivation from a chondritic mantle source, and ^{187}Os/^{188}Os(i)$_{CONTAM}$ is the Os isotopic composition of the contaminating reservoir at 3730 Ma. This value is calculated by forward modelling from a chondritic source at the designated mantle extraction age (4100 Ma or 4300 Ma) using the measured ^{187}Re/^{188}Os of typical Archean lithologies (Table 2). Osmium concentrations for the Manfred Complex are taken from 13TKN80 WR samples: while these likely possess higher Os concentrations than the bulk complex as they are olivine and spinel rich, the average Os concentration of the Manfred Complex

is unknown. The Os concentrations for contaminants are taken from literature (Table 2). F is the proportion of the Manfred Complex, and equation 4 is rearranged for this value in equation 5:

$$f = \frac{Os\ conc_{\text{CONTAM}} * \frac{^{187}Os}{^{188}Os}3730\text{Ma CONTAM} - Os\ conc_{\text{CONTAM}} * \frac{^{187}Os}{^{188}Os}(i)_{\text{MIX}}}{\left[\begin{array}{l}\left(Os\ conc_{\text{MC}} * \frac{^{187}Os}{^{188}Os}(i)_{\text{MIX}} - Os\ conc_{\text{CONTAM}} * \frac{^{187}Os}{^{188}Os}(i)_{\text{MIX}}\right) - \\ \left(\frac{^{187}Os}{^{188}Os}(i)_{\text{MC}} * Os\ conc_{\text{MC}} - Os\ conc_{\text{CONTAM}} * \frac{^{187}Os}{^{188}Os}3730\text{Ma CONTAM}\right)\end{array}\right]} \quad \textbf{(5)}$$

Table 4.2: Re and Os concentrations of potential contaminants

Lithology	Os conc (ppb)	Re conc (ppb)	$^{187}Re/^{188}Os$	Reference
Isua pillow basalt	0.052	0.584	53.2	Frei et al. (2003)
Lewisian tonalite	0.0026	0.093	168	Burton et al. (2000)
Lewisian transitional	0.627	1.50	11.4	Burton et al. (2000)
Kambalda komatiite	1.33	0.48	2.35	Lambert et al. (1998)
Belingwe komatiite (TF)	1.50	1.643	1.64	Putchel et al. (2009a)
Re/Os = 5	0.80	0.85	5	-

Table 4.2: Different Archean lithologies used in crustal assimilation modelling. References for Os and Re concentrations provided. Re/Os = 5 a hypothetical intermediate lithology generated by the author. (TF) = Tony's flow.

4.3 Results

4.3.1 Chromite Re-Os composition

We present Re-Os analyses for detrital chromites from 14WA2 (n=11), 14WA4 (n=6), 14WA1 (n=3), 14WA3 (n=3) and a single analysis for 16WA6, 16WA8 and 16WA9. All bulk chromite samples yield Os concentrations of 13- 72 ppb, with subchondritic $^{187}Os/^{188}Os$ ratios of 0.10412- 0.11443. These unradiogenic compositions yield TRDs of 1849-3323 Ma, which represent a minimum age for those samples. There is a broad negative correlation between TRDs and Os concentration, with the most radiogenic samples yielding the lowest Os concentrations (Figure 1). This is particularly evident in chromites from 14WA2, which yield the most pristine major element compositions, but show a negative and broadly linear correlation (R^2=0.66, n=11) between Os concentrations and TRDs. Ostensibly, this trend is observed within all samples apart from 14WA4, which yields consistent TRDs of ca. 3200 Ma-3250 Ma regardless of Os concentration in all but 1 sample (Figure 1). High Os (>50 ppb) concentration samples consistently yield $^{187}Os/^{188}Os$ ratios of ≤0.10535, or TRDs of between ~3150 Ma and ~3300 Ma, with more radiogenic isotopic compositions restricted to samples which yield Os concentrations of < 50 ppb (Table 3).

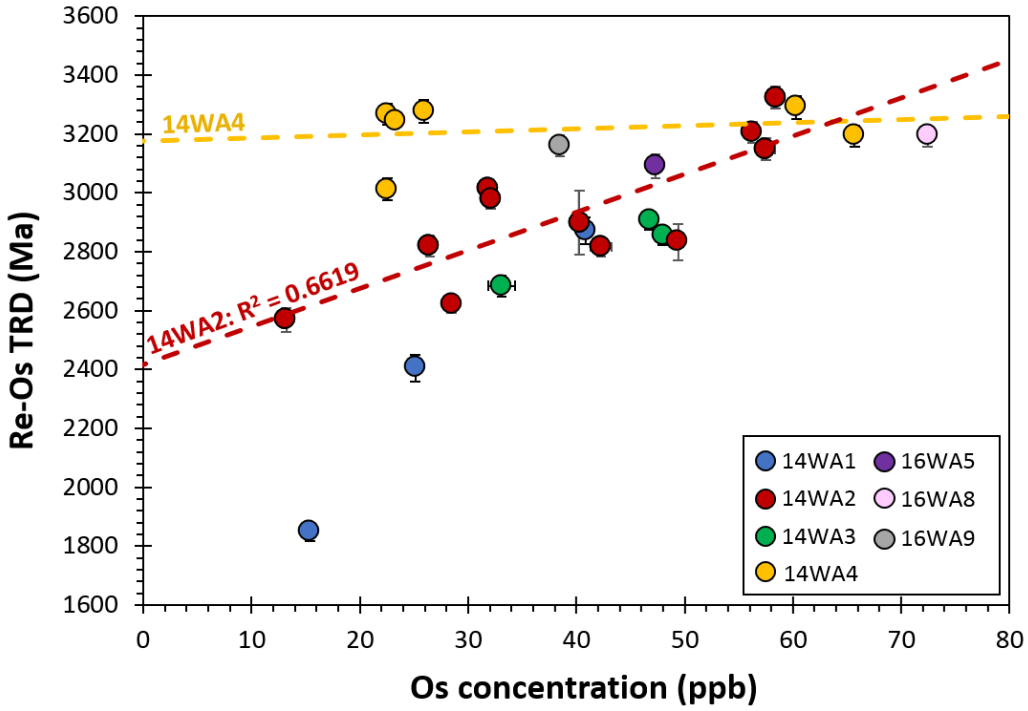

Figure 4.1: Os concentration and Re-Os TRDs of detrital chromites from Jack Hills. Data show a broad decrease in TRD with decreasing Os concentration in all samples bar 14WA4. Oldest TRDs clustered at ~3200 Ma, represented by high Os concentration samples and 14WA4. All uncertainties 2se.

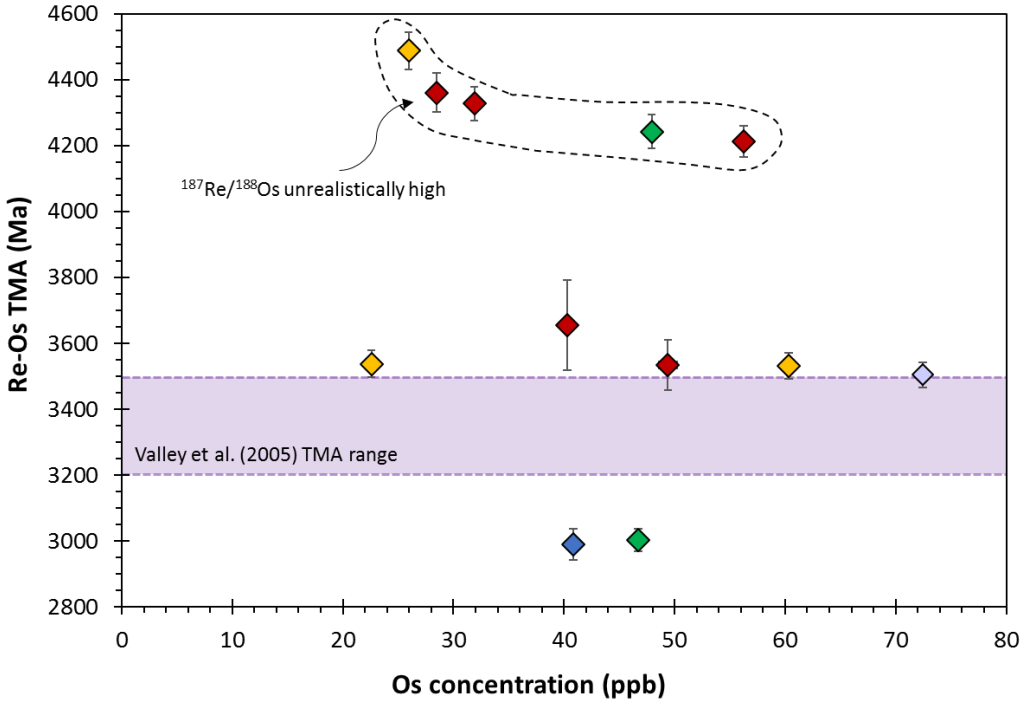

Figure 4.2: Os concentration and Re-Os TMAs of detrital chromites from Jack Hills. 5 samples from session 1 and unrealistic model ages not included in this figure. Hadean model ages are likely the product of Re addition, and so are not considered as robust Re-Os TMAs. Two populations at ~3500 Ma and 3000 Ma present, the first of which yields slightly older Re-Os TMAs than the range determined by Valley et al. (2005).

Due to high and heterogeneous Re blanks (Table 4.1), the 5 analyses undertaken during the first session are disregarded for the calculation of Re-Os model ages (TMAs), meaning 16 TMAs for detrital chromites TMAs have been determined (Table 4.3 and Figure 4.2). Three samples yield Re concentrations analytically indistinguishable from 0, resulting in $^{187}Re/^{188}Os$ ratios of 0. These 'true TRDs' yield Re-Os ages of 1849±49 Ma, 3090±40 Ma and 3192±32 Ma (uncertainties 2se). Chromites that yield non-zero yield Re concentrations possess between 0.13 and 3.35 ppb, with no apparent correlation between $^{187}Re/^{188}Os$ and $^{187}Os/^{188}Os$ isotopic composition (Figure 4.3). Many of these values result in high $^{187}Re/^{188}Os$ ratios that produce erroneous model ages, including 5 apparent Hadean Re-Os TMAs (Figure 4.2), and some geologically impossible ages (Table 4.3). In response to this, we filter chromites with sensible $^{187}Re/^{188}Os$ ratios of <0.1 or <1 ppb Re, which are typical of magmatic chromites (Shirey and Walker, 1998; Carlson, 2005). While 'sensible' model ages do not represent a large proportion of total samples analysed (n=7), five chromite analyses yield model ages that overlap within 2se (Figure 4.3), yielding a weighted mean (Figure 4.4) of 3528±34 Ma (2se; MSWD 1.3). These model ages are derived from detrital chromites from three separate metasediment samples: 14WA2, 14WA4 and 16WA8. Two detrital chromite samples from 14WA1 and 14WA3 yield significantly younger model ages that are self-consistent of 2989±48 Ma and 3003±34 Ma, respectively. There is also no relationship between major and minor elements, grain size or rounding shape and the Re-Os model ages of detrital chromites.

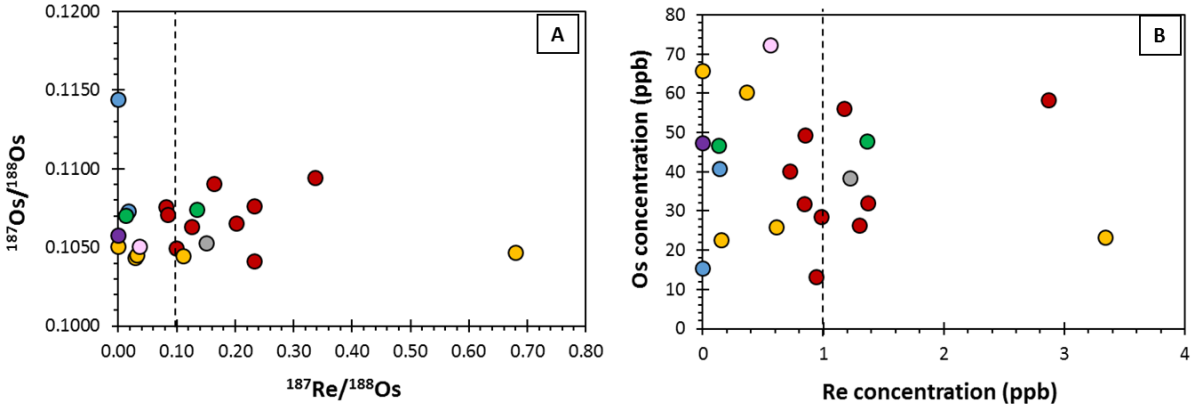

Figure 4.3: A) $^{187}Re/^{188}Os$ plotted against $^{187}Os/^{188}Os$ for detrital chromites from Jack Hills, excluding 5 samples for session 1. Linear correlation is used to produce isochrons, but no linear relationships are present within the samples. Magmatic chromites typically yield $^{187}Re/^{188}Os$ ratios of <0.1, which is also shown for reference. **B)** Os concentration plotted against Re concentration. Samples that yield both $^{187}Re/^{188}Os$ ratios of >0.1 and a Re concentration of >1 ppb are rejected.

Table 4.3: Re-Os isotopic composition of Jack Hills detrital chromites														
S*	**Sample**	**Rounding**	**Size fraction**	**Re conc. (ppb)**	**2se**	**Os conc. (ppb)**	**2se**	**$^{187}Os/^{188}Os$**	**2se**	**$^{187}Re/^{188}Os$**	**TRD (Ma)**	**2se**	**TMA (Ma)**	**2se**
1	14WA1	RO	250-120	na	na	25.13	0.27	0.11058	0.00014	na	2404	31	na	na
1	14WA2	RC	250-120	na	na	42.29	0.98	0.10770	0.00013	na	2816	34	na	na
1	14WA2	RO	250-120	na	na	57.51	0.81	0.10536	0.00013	na	3149	37	na	na
1	14WA3	RO	250-120	na	na	33.12	1.21	0.10863	0.00017	na	2684	36	na	na
1	14WA4	RO	250-120	na	na	22.57	0.24	0.10632	0.00014	na	3012	36	na	na
2	14WA1	RC	250-120	0.00	0.01	15.41	0.03	0.11443	0.00029	0.0000	1849*	45	1849*	45
2	14WA2	RC	250-120	0.72	0.00	40.28	0.14	0.10711	0.00074	0.0851	2900	109	3655	137
2	14WA2	RO	250-120	2.87	0.01	58.42	0.08	0.10412	0.00011	0.2328	3323	37	7620	na
2	14WA2	EO	250-120	0.84	0.01	31.90	0.04	0.10631	0.00010	0.1251	3013	34	4327	52
2	14WA3	RC	250-120	1.36	0.00	47.94	0.10	0.10741	0.00013	0.1344	2856	34	4243	52
2	14WA4	RC	250-120	0.00	0.00	65.69	0.16	0.10505	0.00010	0.0000	3192*	35	3192*	35
2	14WA4	EO	250-120	0.61	0.01	25.94	0.05	0.10445	0.00015	0.1114	3277	39	4488	56
2	14WA3	RO	500-250	0.13	0.00	46.70	0.09	0.10706	0.00010	0.0132	2907	32	3003	34
3	14WA1	EO	250-120	0.14	0.01	40.85	0.13	0.10731	0.00025	0.0162	2871	46	2989	48
3	14WA2	RO-1	250-120	1.37	0.02	32.09	0.03	0.10655	0.00011	0.2023	2979	34	5857	na
3	14WA2	RO-2	250-120	1.30	0.01	26.48	0.02	0.10766	0.00015	0.2327	2821	36	6495	na
3	14WA2	RO-3	250-120	0.94	0.01	13.21	0.01	0.10943	0.00023	0.3372	2569	41	14434	na
3	14WA2	RO-4	250-120	1.17	0.01	56.25	0.06	0.10495	0.00009	0.0986	3206	35	4212	47
3	14WA4	RC	500-250	0.36	0.00	60.31	0.08	0.10436	0.00010	0.0283	3289	36	3531	38
3	14WA4	RO	500-250	0.15	0.01	22.58	0.03	0.10452	0.00014	0.0315	3268	38	3537	41
4	14WA2	ALL	250-120	0.98	0.01	28.47	0.03	0.10905	0.00012	0.1636	2623	31	4361	59
5	14WA2	ALL	<250	0.85	0.01	49.40	0.21	0.10757	0.00038	0.0815	2834	62	3534	77
5	14WA4	ALL	50-250	3.34	0.01	23.31	0.02	0.10467	0.00013	0.6794	3247	37	negative	na
5	16WA5	ALL	<250	0.00	0.01	47.32	0.10	0.10577	0.00018	0.0000	3090*	40	3090*	40
5	16WA8	ALL	<250	0.56	0.01	72.44	0.18	0.10504	0.00011	0.0366	3193	35	3504	39
5	16WA9	ALL	<250	1.22	0.01	38.48	0.05	0.10527	0.00013	0.1502	3161	36	4970	na

Table 4.3: Re-Os isotopic data for all Jack Hills chromites analysed in this study. S* = session number, conc. = concentration. Model ages calculated using the mixed chondrite values ($^{187}Os/^{188}Os$ = 0.127 and $^{187}Re/^{188}Os$ = 0. 40186) from Shirey and Walker (1998). * represents 'true' TRDs, where measured sample $^{187}Re/^{188}Os$ is analytically indistinguishable from 0.

Table 4.4: Re-Os isotopic composition of samples from the Manfred Complex														
S*	**Sample**	**Re conc. (ppb)**	**2se**	**Os conc. (ppb)**	**2se**	**$^{187}Os/^{188}Os$**	**2se**	**$^{187}Re/^{188}Os$**	**TRD (Ma)**	**2se**	**TMA (Ma)**	**2se**	**γOs_i (3730 Ma)**	**2se**
4	14WA21	0.00378	0.00006	0.001631	0.00007	2.36780	0.27634	10.9839	na	na	11529	na	3.59	0.08
4	14WA21	0.00291	0.00015	0.001458	0.000003	2.42351	0.01261	9.4523	na	na	13574	na	2.59	0.13
4	13TKN80	0.02	0.00004	2.16	0.002	0.10799	0.00008	0.0486	2775	30	3147	34	1543	18
4	13TKN80	0.03	0.00004	2.12	0.005	0.10787	0.00012	0.0627	2791	33	3292	39	1695	0.94
6	13TKN80 spinel	na	na	18.61	0.041	0.10223	0.00040	na	3590	66	na	na	0.98	0.39

Table 4.4: Re-Os isotopic data for Manfred Complex rock powders thus far analysed in this study. S* = session number, conc. = concentration. 13TKN80 is a well preserved harzburgite, while 14WA2 is an ~amphibolite facies metagabbro. γOs_i represents variation from a chondritic reservoir in parts per hundred (%) at 3730 Ma, the well constrained crystallisation age of anorthosites (Kinny et al., 1988) and leucogabbros (Kemp, 2018) within the complex. Model ages (TRDs and TMAs) and γOs_i calculated using the mixed chondrite values ($^{187}Os/^{188}Os = 0.127$ and $^{187}Re/^{188}Os = 0.40186$) from Shirey and Walker (1998).

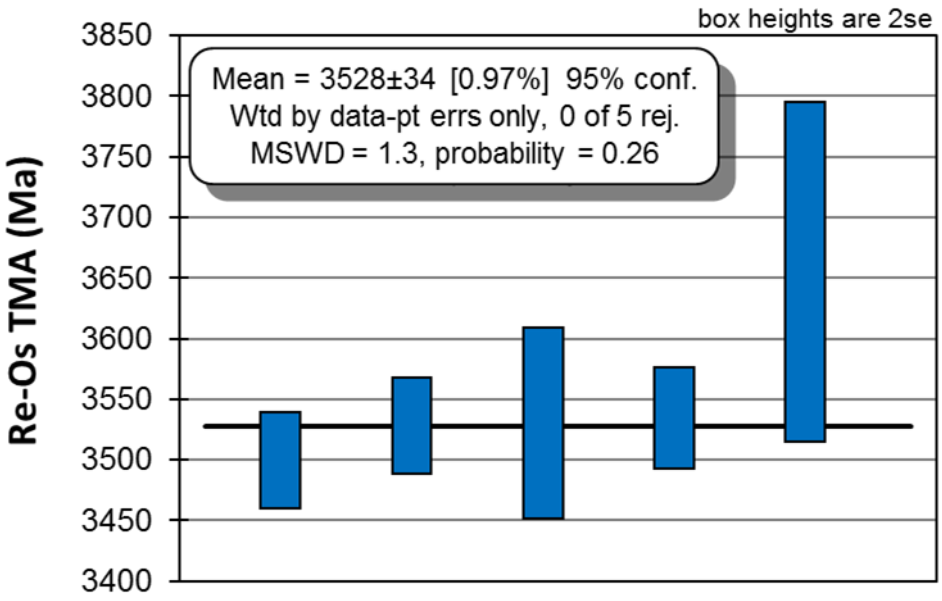

Figure 4.4: Weighted mean of the most robust Re-OS TMAs derived for Jack Hills chromites. Figure formulated using isoplot (Ludwig, 2003), with box heights representing 2se.

4.3.2 The Manfred Complex Re-Os composition

Five analyses of the Re-Os isotopic composition of the Manfred Complex are also presented here. Two 1g powder aliquots of harzburgite 13TKN80 yielded self-consistent $^{187}Os/^{188}Os$ ratios of 0.10787 and 0.10799 with $^{187}Re/^{188}Os$ ratios of 0.048 and 0.063 (Table 4). This, coupled with the high Os concentration of >2 ppb and the low Re concentrations of 0.02 ppb and 0.03 ppb, indicates the PGE budget of this sample is dominated by a low $^{187}Re/^{188}Os$ phase, likely spinel or olivine, which are ubiquitously distributed throughout the sample (Rowe, 2016). 13TKN80 Re-Os TMAs of 3147±47 Ma and 3292±39 Ma (uncertainties 2se) are significantly younger than the 3730 Ma crystallisation age constrained by ^{207}Pb-^{206}Pb zircon geochronology (Kinny et al., 1988; Kemp, 2018) and correspond to a γOs_i of 2.6 to 3.6. Two 1g powdered samples of 14WA21, a statically recrystallised metagabbro were also studied. As expected for a more evolved sample, 14WA21 yielded radiogenic $^{187}Os/^{188}Os$ ratios of 2.37 and 2.42 with high $^{187}Re/^{188}Os$ ratios of 9.45 and 10.98, respectively. Osmium concentrations were very low at 1.63 and 1.46 ppt, as were Re concentrations at 3.78 and 2.91 ppt. This ultimately resulted in geologically impossible Re-Os TMAs, though further analysis may result in an isochron for Manfred Complex bulk rock samples.

A sample of 13TKN80 spinel separates possessed a high Os concentration of 18.6 ppb. The $^{187}Os/^{188}Os$ of this sample is very low at 0.10223, producing a Re-Os TRD of 3590 Ma. However, the small size of this sample (~0.5 mg) meant that Re concentrations were extremely blank sensitive, and so spurious Re concentrations of 1.3 ppb were likely derived from blank heterogeneity. This resulted in

geologically meaningless TMAs. The small sample size for 13TKN80 spinels also required a large ^{188}Os normalisation, and meant thus sample was far more sensitive to Os blanks that detrital chromites or WR Manfred Complex powders.

4.4 Discussion

4.4.1 Chromite rhenium-depletion ages (TRDs)

The Re-Os TRDs of detrital grains can be interpreted to represent the minimum age of detrital samples. For 14WA4, as all bar one sample yields Re-Os TRDs of >3190 Ma, indicating chromites are at least Mesoarchean in age. Furthermore, 4 out of 6 analyses of 14WA4 yield consistent Re-Os TRDs ca. 3250 Ma, suggesting the minimum age of grains from 14WA4 me be ~50 Myr older. High concentration (>55 ppb) chromites from 14WA2 and 16WA8 also yield TRDs of 3190 Ma- 3300 Ma. This consistency of these data with 14WA4 indicates ~3200 Ma may represent a minimum age for chromites from 14WA2 and 16WA8 also. However, some 14WA2 chromites yield significantly more radiogenic Os isotopic compositions and therefore younger TRDs, which correlate with lowered Os concentrations. This is likely indicative of a nugget effect, with a high Os concentration phase likely dominating the Os isotopic composition of bulk samples. The variability of Os concentrations observed may therefore reflect variable mixtures between a low Os concentration and high Os concentration phase. While nugget effects are most commonly reported in silicate rock powders (e.g. Meisel et al., 2001), the presence of fine IPGE-rich (Os, Ru, Ir) phases within chromites is well known, and suggests this is a viable process to induce the relationship observed (e.g. Rehkamper et al., 1999; González-Jiménez et al., 2012; Páge and Barnes, 2016; Park et al., 2017).

Mass balance calculations show the high Os concentration phase is unlikely to be Fe-sulphide (Figure 4.5). Where observed within Jack Hills chromites, Fe-sulphides typically compose less than 0.1% of the total grain volume, requiring sulphides to possess an unrealistically high Os concentration of >50 ppm to significantly influence the overall concentration of a samples (Figure 4.5). This, coupled with the likely secondary origin of sulphides within detrital grains (Section 3.5.1) indicates the phase controlling the Os concentration of bulk samples may be discrete PGE alloys. Within plutonic samples IPGEs associated with chromite will typically form alloys or PGE-rich sulphides such as laurite, encapsulated in chromites either by 1) growth at the reduced interface between melt and chromite (Finnigan et al., 2008; Páge and Barnes, 2016) or 2) or co-crystallisation of IPGE-bearing alloys and chromites at liquidus temperatures (Brenan and Andrews, 2001). Discrete exsolution of sub-micron IPGE alloys within chromites may also represent a viable mechanism to explain the nugget effects observed here. This therefore indicates that the Os isotopic composition of low Os concentration samples may therefore be controlled by chromite, while high Os concentration analyses may sample both chromite

and potentially discrete IPGE alloys. Thus, both chromites and IPGE alloys represent the same reservoir, but the IPGE is more resilient to later mobility of PGEs. This is particularly the case for Re, which will be poorly abundant or completely absent within such IPGE phases. However, it is important to note that IPGE alloys have not been directly imaged by this study within Jack Hills chromites, and until these phases are observed their presence cannot be definitively concluded.

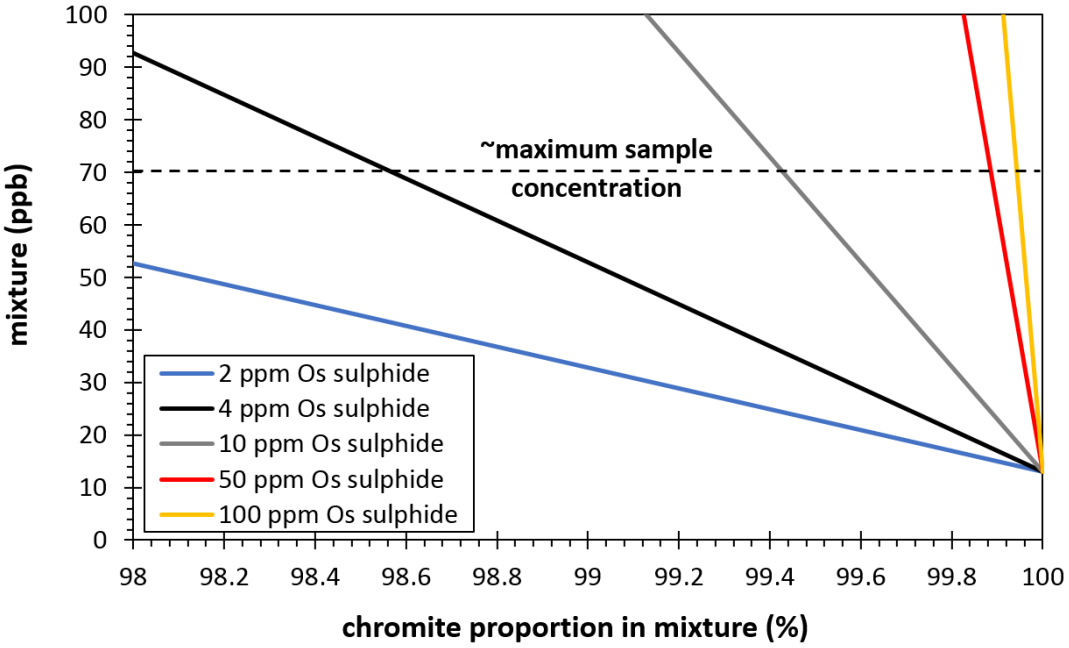

Figure 4.5: Mass balance calculation showing the effects of hypothetical sulphide inclusions with variable Os concentrations on bulk sample concentrations. Where observed, sulphides typically account for 0.1% of the grain, indicating sulphides would have to have > 50 ppm Os to significantly influence to concentration of the overall sample mixture. This is highly unlikely, as the most Os-rich known sulphides (peridotitic sulphides within diamonds) typically possess <10 ppm Os (Shirey and Walker, 1998), and suggests sulphides are not the source of the observed nugget effect.

The small sample sizes employed in this study (typically ≤20 mg) makes these samples particularly susceptible to nugget effects. Indeed, 2750 Ma to 3100 Ma TRDs attained by Valley *et al.* (2005) represent a median to our data, likely due to the significantly larger sample sizes (~50 mg) employed by the Valley *et al.* (2005) study. The more radiogenic nature of low Os concentration samples is likely indicative of elevated $^{187}Re/^{188}Os$ in comparison to samples with a greater proportion of the higher Os concentration phase, enabling greater ingrowth of ^{187}Os over time. Critically, however, this lower Os concentration makes these samples more amenable to Re-Os disturbance and suggests that some of the more radiogenic isotopic compositions may instead be those more greatly affected by Re addition. Higher Os concentrations are therefore more resilient to this secondary mobility. However, even higher Os concentration samples still show evidence of modification, with the presence of a 'true' TRD

in a 66 ppb Os sample: modification of high Os concentration laurite inclusions within ophiolitic spinel has been previously reported (Gonzalez-Jiminez et al., 2012). If lower concentration samples reflect greater proportions of chromite within the bulk mixture, this indicates that, as expected, the chromites themselves may be isotopically disturbed or possess a greater $^{187}Re/^{188}Os$ than the high Os concentration phase. This appears to have occurred in all samples bar 14WA4, where the potential chromite end member still retains the same Os isotopic composition as the high Os concentration phase.

The major and minor element composition of detrital chromites suggests they share a common source, and this may also be inferred from the Os isotopic composition of samples studied here. As previously noted by Valley et al. (2005), the consistency of TRDs in 14WA4 and samples with an Os concentration of >50 ppb is unexpected for grains with a mixed detrital heritage. This study also notes there is no relationship between rounding shape or major element geochemistry and the Os concentration or isotopic composition of grains. Grain size was not as quantitively tested for changes in model ages as 120-50 μm fractions were not picked for analysis, however no obvious relationship between grain size and Os isotopic composition is observed (Table 4.3). The consistency of high Os concentration TRDs and the absence of correlation with grain size or rounding shape is a strong indication of a shared magmatic history of Jack Hills detrital chromites.

4.4.2 The presence of 'true TRDs'

While higher Os concentration samples yield TRDs between 3200 Ma and 3300 Ma, most bulk chromite analyses yield TRDs significantly younger than ~3200 Ma. Amongst these are three 'true' TRDs, where the Re concentration of the sample is analytically indistinguishable from 0, resulting in no further ingrowth of radiogenic ^{187}Os. This is indicative of a Re loss event, the timing of which is given by chromite TRDs (e.g. as observed with high degrees of mantle melting: Pearson et al., 2007; Griffin et al., 2014). Critically, two ages returned by the samples that yield true TRDs correlate with known or postulated metamorphic events within the Narryer Terrane, while the third is slightly younger. The oldest 'true' TRD, at 3192±35 Ma is just within uncertainty of a ca. 3200-3300 Ma event at Mount Narryer purported by Iizuka et al. (2010). It is slightly too young to be coincident with D1 metamorphism within the Narryer Terrane, for which a ~3300 Ma age has been postulated by numerous authors (Kemp et al., 2019 and references therein).

The second true TRD is observed at 3090±40 Ma, which is coincident with monazite and xenotime ages of ca.3080 Ma within association 1 BIF (Rasmussen et al., 2010). Field and petrological evidence strongly indicates that association 1 underwent metamorphism prior to the deposition of W-74 sediments, postulated to have occurred at ~3000 Ma (Spaggiari, 2007 a/b). Xenotime and monazite

from Mount Hale (Rasmussen et al., 2010) and now detrital chromites may date this metamorphic event. This may indicate that the protolith of detrital chromites was proximal to Jack Hills, as is also indicated by the euhedral nature of many of the chromites, or that a ca. 3080 Ma event was more widespread within the Narryer Terrane than previously thought. The final true TRD yields an age of 1849±45 Ma, coincident with the Capricorn Orogen at 1780 Ma to 1830 Ma (Spaggiari et al., 2008). This age is recorded at Jack Hills by white mica defining the main foliation (Spaggiari, 2007), xenotime at Mount Hale (Rasmussen et al., 2010) and by K-Ar ages and Rb-Sr isochrons of the Meeberrie Gneiss near Mount Narryer (Fletcher et al., 1988; Kinny et al., 1990) This TRD also overlaps with 1858±6 Ma authigenic monazite within the centre of the belt (Rasmussen et al., 2010), which slightly predates the Capricorn Orogen.

Critically, the presence of a Proterozoic TRD strongly indicates disturbance of the Re-Os system *in-situ* after deposition of detrital chromites within host sediments. The timing of the ~1850 Ma TRD is of interest as peak metamorphic conditions of the host metasediments are believed to have occurred at 2650 Ma (Rasmussen et al., 2010). This age has also been interpreted by this study to represent the timing of major and minor element modification of chromites (see chapter 3). However, the ostensibly most robust sample for Os isotopic composition (14WA4) yields some of the most modified Mg#s and wt.% ZnO and MnO chromite contents, suggesting there is not a strong link between the modification of chromite major elements and Re-Os mobility. This can be reconciled if the fluids associated with the ~2650 Ma were not particularly oxidising: chromites do not possess significant Fe_2O_3 contents and yield minimal evidence of Fe_2O_3 mobility into grains (Figure 3.10) suggesting the fluids interacting with chromites may have been more reduced. Os and Re are most mobile under oxidising conditions (e.g. Gonzalez-Jimenez et al., 2012), indicating this metamorphic event may not have induced significant Re or Os mobility. It seems unusual that the ~1800-1850 Ma event at Jack Hills was associated with fluid oxidised enough to induce Re and possible Os mobility, but did not induce significant oxidation of chromite. This may indicate the presence of discrete IPGE phases at the edges of grains, where percolating fluids can more easily modify chromites.

What is fascinating with regards to the retention of true TRDs is that most samples are a mixture of 500+ grains derived from a single metasediment sample. It therefore seems surprising that individual samples yield true TRDs when other samples from the same sediment sample yield clearly disturbed, but distinctly different Re-Os isotopic compositions. This does not appear to be an analytical artefact: while Re blanks were higher within earlier runs and samples may therefore be impacted by heterogeneity of Re blank contribution, the 0.39 pg TPB recorded for session 5 suggests the 3090 Ma TRD is a true feature of this sample. While the slightly negative Re concentration (-28 ppt) derived for this sample suggests that blank contribution was slightly over estimated indicating blanks for this

sample were nearer 0.3 pg: the only way to produce a Re concentration analytically distinct from zero for this analysis is to assume Re blank heterogeneity is ≤0.1 pg. Requiring a blank with a ~75% lower concentration than the measured TPB seems unrealistic, even with the aggressive cleaning procedure employed here. Re blanks were considerably higher for the session yielding ca. 1850 Ma and 3090 Ma TRDs (4.56 pg and 6.63 pg, yielding an average blank of 5.6 pg). As before, the slightly negative Re concentration of the 3090 Ma sample suggests that blanks were if anything slightly over estimated. It is therefore highly likely that the 'true' TRDs discussed here are true sample features rather than analytical artefacts.

4.4.3 Chromite model ages (TMAs)

While some bulk chromite samples yield sensible Re concentrations and therefore $^{187}Re/^{188}Os$ ratios (<0.1), many analyses yield spurious Re concentrations that result in unrealistic Re-Os TMAs. There are several possibilities for the origin of elevated Re concentrations within chromites, which can broadly be defined into either analytical or sample-dependent issues. Session 5 yielded a Re blank of 0.39 pg, but still produced a single sample of chromites with unrealistic Re concentrations of >3 ppb ($^{187}Re/^{188}Os$ 0.68), yet an unradiogenic $^{187}Os/^{188}Os$ ratio of 0.10463. High Re concentrations within sessions 1 to 3 may have been derived from significant uncertainties derived from high Re blanks. However, the low TPB within this session 5 suggests an analytical origin for spurious Re concentrations is unlikely. This therefore suggests that elevated Re concentrations may be a real feature of Jack Hills chromite samples. High Re concentrations are not coupled with a more radiogenic $^{187}Os/^{188}Os$ ratios (Figure 4.3 and Table 4.3), and indeed some of the most unradiogenic $^{187}Os/^{188}Os$ compositions yield the highest Re concentrations. This indicates that any Re ingrowth was extremely limited, suggesting a recent origin for Re addition to chromites. Assuming 14WA4 chromites are all derived from the ca. 3530 Ma population, modelling indicates Re addition must have within the last 10 Myr to be within uncertainty of the $^{187}Os/^{188}Os$ ratios determined (Figure 4.6). A potential source of Re enrichment could be phases formed during the weathering of the host metasediment. Such phases, largely hematite, are abundant within Jack Hills metasediments, even in samples that have undergone magnetic separation (14WA1-4) during preparation of heavy mineral separates. Though care was taken to remove these phases during picking, it is possible rare examples have made it through into analyses.

When filtered for Re concentration (<1 ppb) and $^{187}Re/^{188}Os$ ratio (<0.1), five samples yield self-consistent (at 2se) TMAs, producing a weighted mean of 3528±34 Ma (2se, MSWD= 1.3; Figure 4). These data are present across three samples and are interpreted to represent the most robust TMAs derived of Jack Hills detrital chromites within this study (Figure 4.4). These ages are marginally older

than the 3400 Ma- 3500 Ma Re-Os TMAs determined previously (Valley et al., 2005; Dare et al., 2016), which given the older TRDs attained by this study is not unreasonable. There are two further Re-Os TMAs that are self-consistent within Jack Hills chromites: 14WA3 RO yields an age of 3003±34 Ma and 14WA1 EO yields an age of 2989±48 Ma (Figure 4.2). The significance of these grains is unclear, but they yield similar and low Re concentrations (0.13 ppb and 0.14 ppb) and therefore $^{187}Re/^{188}Os$ ratios (0.013 and 0.016) in comparison to chromites that yield ca. 3530 Ma TMAs. This may signify they represent the products of partial Re loss during ~1850 Ma metamorphism, or re-equilibration of chromites TMAs during metamorphism at ~3000 Ma. The isotopic similarity of these two samples is striking and indicates that the latter of these two scenarios may be the most likely. These two model ages are outside of error of the ~3090 Ma 'true' TRD, indicating that if they reflect metamorphic resetting, it did not occur during the same event. Finally, though Re-Os model ages are complicated by significant Re and potentially Os mobility, the most robust samples yield a weighted mean of 3528±34 Ma. This indicates this population of detrital chromite were derived from a layered intrusion extracted from chondritic mantle at ca. 3530 Ma.

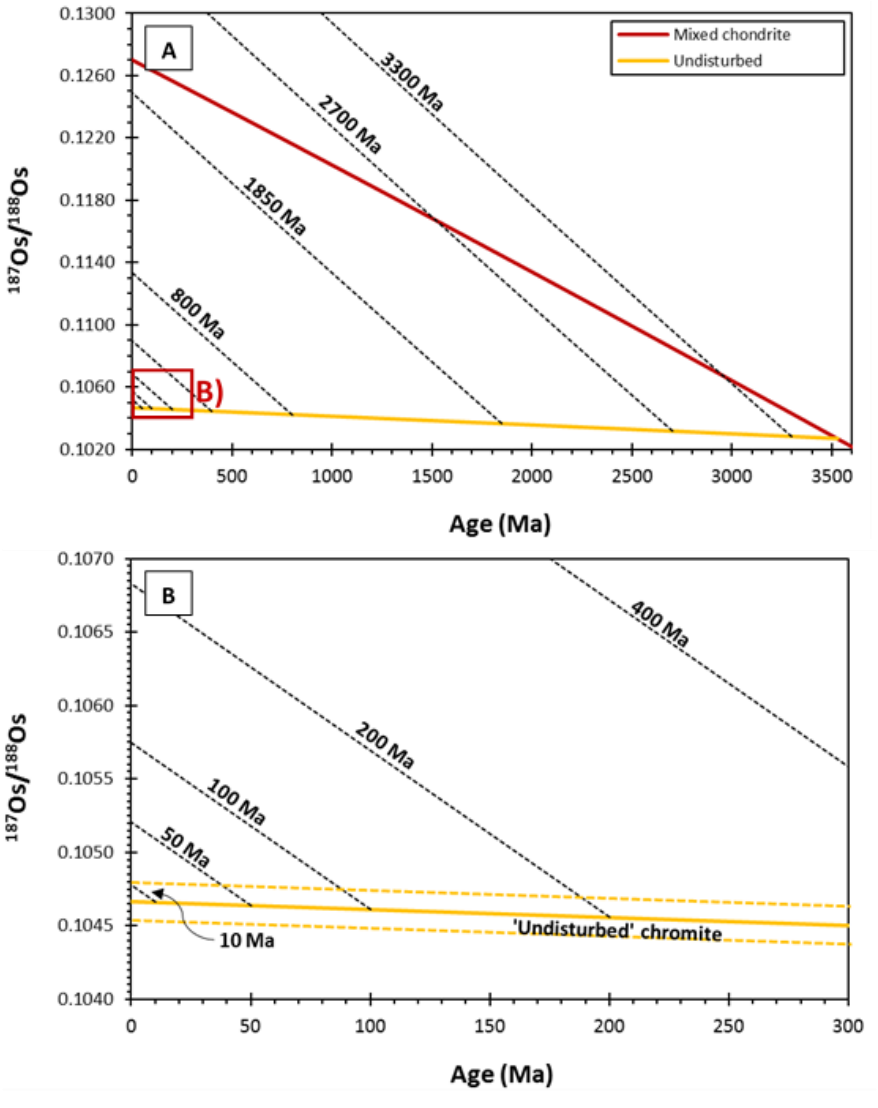

Figure 4.6 (previous page): Modelling the effects of Re addition using the sample of 14WA4 measured in session 5. This assumes the Re concentration of ca. 3.34 ppb is the result of Re addition, and models this sample as 'undisturbed' by forcing the TMA to the 3530 Ma population using the measured $^{187}Os/^{188}Os$ of 0.10467. The Re addition event is modelled at different times and the subsequent evolution of the resultant $^{187}Os/^{188}Os$ shown. This shows that to retain the $^{187}Os/^{188}Os$ of this sample (within error of 14WA4 ca. 3250 Ma TRDs) requires Re addition to have occurred within the last 10 Myr.

4.5. The caveats of chromite Re-Os model ages

4.5.1 Which chondrite group to use?

While we propose a ca. 3530 Ma crystallisation age for chromites, it is important to note there are several inherent assumptions associated with the determination of model ages. For Re-Os, the largest of these assumptions is the derivation of detrital chromites from a chondritic mantle source that has a $^{187}Os/^{188}Os$ ratio of 0.127 and a $^{187}Re/^{188}Os$ ratio of 0.40186 (Shirey and Walker, 1998). While there is evidence the mantle possessed a chondritic composition in the Archean (Foster et al., 1997; Bennet et al., 2002; Putchel et al., 2004, 2009a, 2014; Connolly et al., 2011), the Re-Os isotopic system of different chondrites vary by chondrite class (Walker et al., 2002a). Currently, compilations of modern $^{187}Os/^{188}Os$ ratios for different chondrites groups suggest they vary between 0.1258±0.0016 to 0.1284±0.002 (Day et al., 2016). For example, Coggon et al. (2015) used ordinary (O) chondrites with $^{187}Os/^{188}Os$ ratios of 0.1283 and $^{187}Re/^{188}Os$ ratios of 0.422 to determine Re-Os model ages of chromites, taken from an upper mantle composition determined by Walker et al. (2002b). Day et al. (2016) instead give $^{187}Os/^{188}Os$ ratios of 0.1280±0.0008 and a $^{187}Re/^{188}Os$ ratio of 0.4179 for O-chondrites. Enstatite (E) chondrites are reported to yield $^{187}Os/^{188}Os$ ratios of 0.1284±0.002 and $^{187}Re/^{188}Os$ ratios of 0.4206 (Day et al., 2016). Non-carbonaceous chondrites all yield $^{187}Os/^{188}Os$ compositions within error of the putative PUM composition determined by Meisel et al. (1996). Carbonaceous (C) chondrites typically yield $^{187}Os/^{188}Os$ ratios of at 0.126, which is ~2% less radiogenic than O- and E-chondrites (Day et al., 2016; Walker et al., 2016). The processes that have resulted in variable $^{187}Os/^{188}Os$ and $^{187}Re/^{188}Os$ chondritic ratios are unclear, with hypotheses including the presence of discrete and heterogeneously distributed primordial carrier phases (Horan et al., 2009; Walker et al., 2016) and aqueous and thermal alteration on the parent body (Walker et al., 2002a).

Normalisation to different non-carbonaceous chondrite groups results in TMAs within uncertainty of one another, as differing Os isotopic compositions are largely offset by variability in $^{187}Re/^{188}Os$ ratios. Using the O-chondrite values supplied by Coggon et al. (2015) results in TMAs approximately 11 Myr older, well within uncertainty of current model ages. However, normalisation to E-chondrites yields TMAs nearer 40 Myr older, though this value is still within uncertainty of the weighted mean of ca. 3530 Ma chromites. As such, differences between chondrite groups only impacts marginally on

detrital chromite Re-Os TMAs. Normalisation to PUM (Meisel et al., 1996), using the $^{187}Re/^{188}Os$ suggested by Bennett et al. (2002), does however show significant differences, with model approximately 86 Myr older. This results in an older weighted average of the five most robust Re-Os TMAs of 3612±21 Ma.

It is also important to note that normalising to different chondrite groups has a large impact on TRDs, particularly on those that are younger (Figure 4.7). Using O-chondrites results in a modest increase of ~30 Myr for the oldest two 'true' TRDs of 3090 Ma and 3192 Ma, but a substantially older (>90 Myr) increase in age for the ca. 1850 Ma TRD. This effect is mirrored when normalising to E-chondrites, with increases in TRDs of 50-55 Myr and >110 Myr for the older and youngest 'true' TRDs, respectively (Figure 4.7). As with model ages, use of PUM compositions results in increases in 'true' TRDs of ~200 Myr and ~100 Myr for the youngest TRD and oldest TRDs, respectively. This produces a ~3300 Ma TRD for the oldest 'true' TRD, in line with suspected metamorphic events within the Narryer Terrane (Kemp et al., 2019), but removes geological context from the other 'true' TRDs.

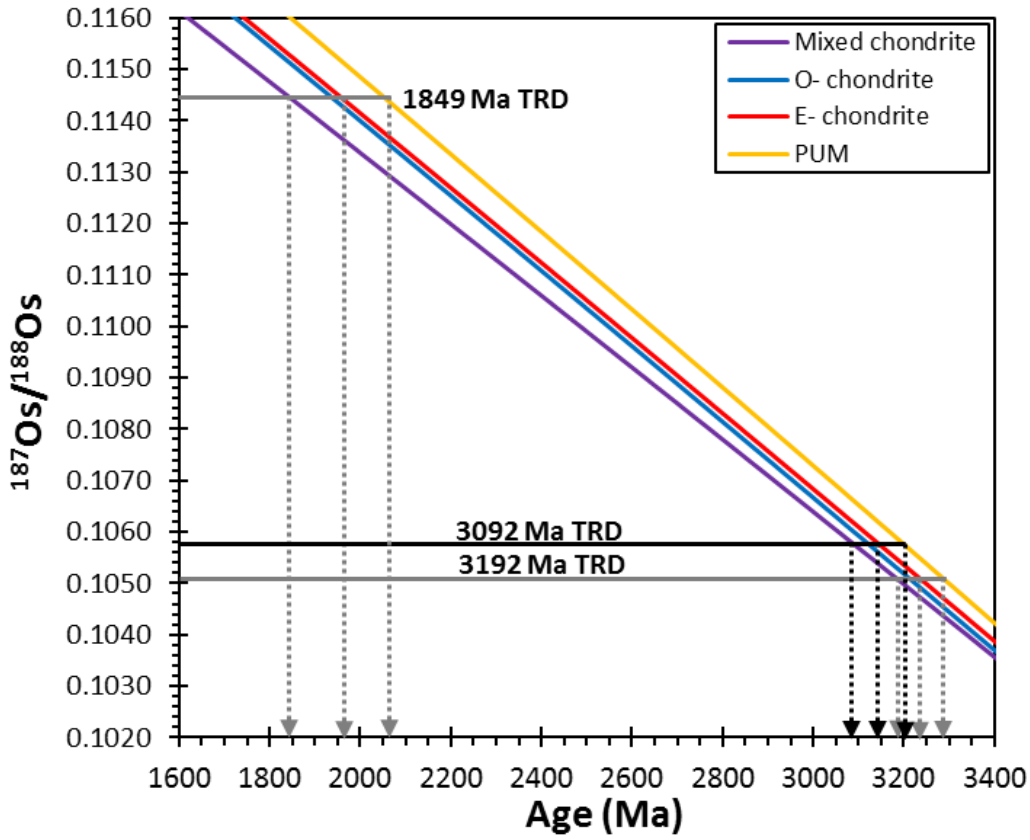

Figure 4.7: This figure highlights the differences in derived Re depletion ages between mixed chondritic source (Shirey and Walker., 1998), ordinary (O) chondrites (Walker et al., 2002a; Coggon et al., 2015), enstatite (E) chondrites (Day et al., 2016), and primitive upper mantle (PUM; Meisel et al., 1996; Bennett et al., 2002). These different chondritic evolutions affect the three 'true' TRDs observed within Jack Hills chromite samples. As the differences evolve to increasingly divergent values, the difference in age from normalising to different chondrite groups is more pronounced in younger TRDs than > 3000 Ma TRDs.

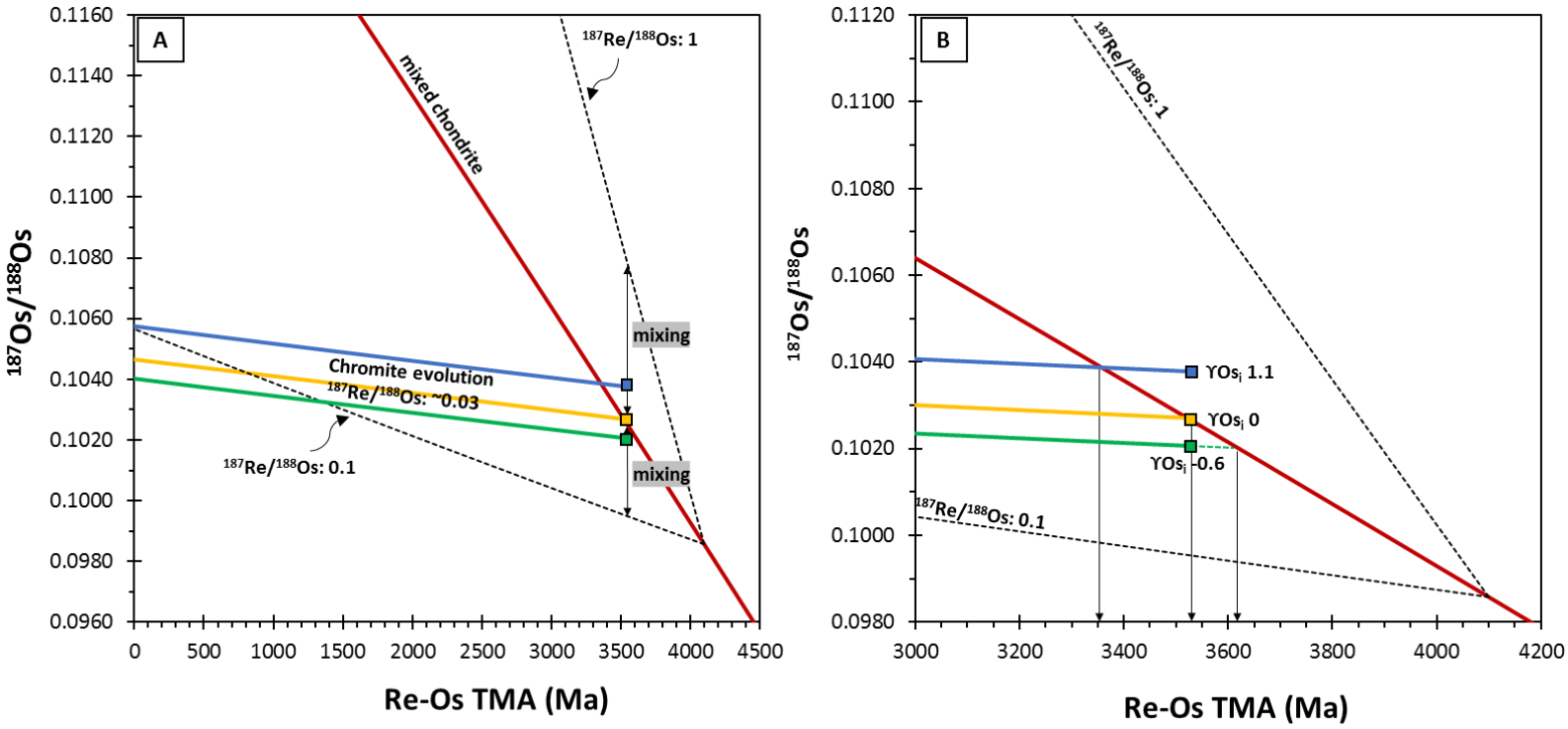

Figure 4.8: Cartoon showing the hypothetical effects of interaction with non-chondritic reservoirs on a chromite derived from a previously chondritic melt. Three scenarios are shown here; chromite from a chondritic source, chromite with an elevated initial Os isotopic composition due to assimilation of radiogenic crust extracted from chondritic mantle at 4100 Ma, and chromite with a lowered initial Os isotopic composition due to interaction with SCLM formed at 4100 Ma. **A)** The yellow line shows chromite derived from chondritic mantle (γOs_i= 0) at 3530 Ma, that evolves with a $^{187}Re/^{188}Os$ ratio of ~0.03. The blue line shows the effect of mixing of ~20% of a crustal reservoir with a $^{187}Re/^{188}Os$ ratio of 1, resulting in a radiogenic initial Os isotopic composition (γOs_i= 1.1). The chromite evolves to a more radiogenic modern $^{187}Os/^{188}Os$ due to the elevated γOs_i despite evolving with the same $^{187}Re/^{188}Os$. The green line shows interaction of the same chromite composition with a depleted reservoir ($^{187}Re/^{188}Os$ ~0.1). This results in a negative initial Os isotopic composition (γOs_i= -0.6) and a less radiogenic $^{187}Os/^{188}Os$ ratio. **B)** A closer example of A), showing the differences in model ages interaction with these reservoirs has imparted. Assimilation of crust has resulted in ca. 100 Myr younger model age, while interaction with a depleted reservoir yields ~40 Myr older model ages.

Ruthenium nucleosynthetic anomalies suggest the Earth's late veneer matches most closely with E-chondrites (Fischer-Gödde and Kleine, 2017), and this may indicate that E-chondrites are the most robust indicators of the composition of chondritic mantle (e.g. Putchel et al., 2009). However, E-chondrites yield the largest uncertainties (2σ) for the parent body $^{187}Os/^{188}Os$ isotopic composition: the uncertainty on this value overlaps with the average chondritic composition (Shirey and Walker, 1998; Day et al., 2016) used to calculate model ages in this study. Until these values can be more quantitively determined, or the processes underlying the $^{187}Os/^{188}Os$ variability of different chondrite groups resolved, the averaged chondrite or O-chondrite $^{187}Os/^{188}Os$ and $^{187}Re/^{188}Os$ isotopic compositions likely yield the most robust chondritic mantle composition, and therefore model ages.

4.5.2 A non-chondritic γOs_i?

Another large assumption is that detrital chromites crystallised from a magmatic reservoir with a chondritic $^{187}Re/^{188}Os$ composition, e.g. a chondritic melt that has not interacted with reservoirs that possess super- or sub-chondritic $^{187}Re/^{188}Os$. Due to the lower compatibility of Re during partial melting, crust typically yields superchondritic $^{187}Re/^{188}Os$, resulting in elevated $^{187}Os/^{188}Os$ over time. The residue of partial melting retains a subchondritic $^{187}Re/^{188}Os$ ratio, resulting in lowered $^{187}Os/^{188}Os$. Assimilation of crust therefore largely results in radiogenic or superchondritic γOs_i of the previously chondritic melt, and artificially younger model ages (Figure 4.8). This is particularly apparent if the assimilated crust is long-lived. Interaction with the complementary depleted reservoir to crustal extraction, sub continental lithospheric mantle (SCLM), yields lower $^{187}Re/^{188}Os$ will therefore impart a negative γOs_i on magmatic bodies, producing artificially older TMAs (Figure 4.8). Crustal assimilation is particularly apparent in many Proterozoic and Phanerozoic layered intrusions, within which chromitites have been shown to yield elevated γOs_i as a result of significant assimilation of long-lived, radiogenic crust (Figure 4.9; Horan et al., 2001; Schoenberg et al., 1999; 2003; Marques et al., 2003; Day et al., 2008; O'Driscoll et al., 2009; Zhong et al., 2011). Interaction with SCLM has also been reported (e.g. Nägler et al., 1997; Mondal et al., 2007).

In contrast to previous examples, interaction with crustal or SCLM reservoirs is impossible to determine for the protolith from the Os isotopic composition of the Jack Hills detrital chromites. The only age limitations that can be applied to detrital chromites are a >2650 Ma crystallisation age, which is constrained by the first metamorphic event of W-74 sediments (Rasmussen et al., 2010). While a layered intrusion origin of these grains does not rule out interaction with SCLM, most layered intrusions typically yielded positive γOs_i compositions (e.g. Day et al., 2008). Quantification of these processes are more complicated in Archean mafic and ultramafic lithologies, where the temporal constraints on mafic and ultramafic lithologies are challenging, and Re-Os open system behaviour may

be induced by high grade metamorphism (Bennett et al., 2002; Rollinson et al., 2002; Frei et al., 2003; Touboul et al., 2014; Coggon et al., 2015; Ishikawa et al., 2017). This therefore suggests that ca. 3530 Ma age of Jack Hills detrital chromite should be considered a minimum crystallisation age.

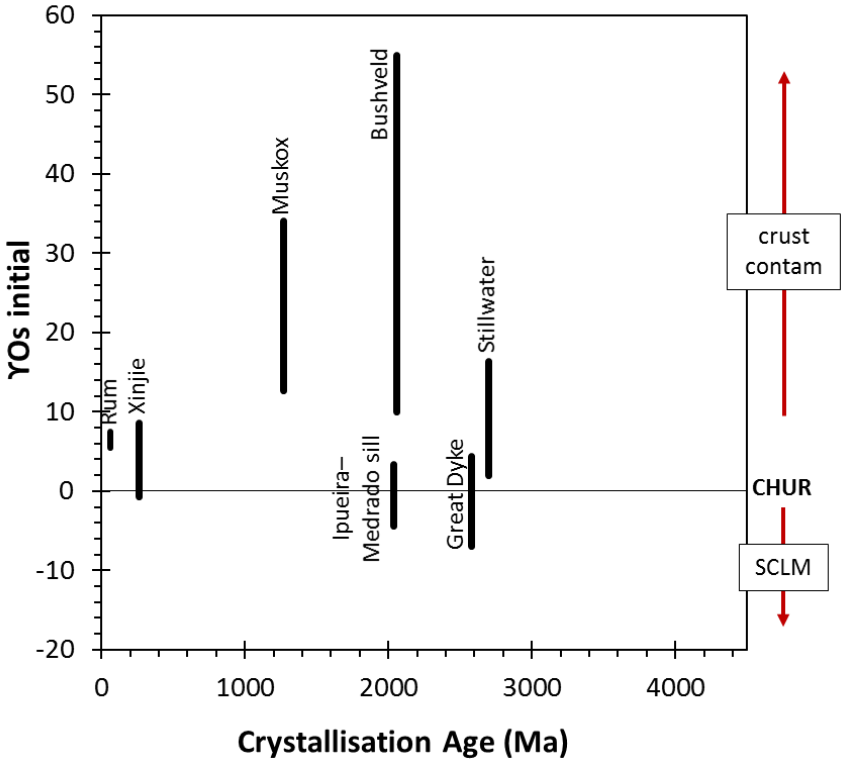

Figure 4.9: Elevated and variable γOs_i within late Archean, Proterozoic and Phanerozoic layered intrusions. *Stillwater*: Horan et al, 2001; *Great Dyke*: Schoenberg et al, 2003; *Bushveld*: Schoenberg et al, 1999; *I-M sill*; Marques et al, 2003; *Muskox*: Day et al, 2008; Xinjie: Zhong et al, 2011; *Rum*: O'Driscoll et al, 2009. γOs_i values taken straight from literature and have not been recalculated.

4.6 A possible Manfred Complex origin?

To test the veracity of Re-Os TMAs produced by crustal assimilation by an ancient layered intrusion, we also analysed well-preserved samples from the 3730 Ma Manfred Complex (Fletcher et al., 1988; Kinny et al., 1988; Myers, 1988; Kemp, 2018). The only Re-Os study of ultramafic rocks of comparable age has been undertaken in and around the Isua greenstone belt, in West Greenland. Chromitites here yield chondritic to mildly elevated γOs_i of 0-4 at ~3800 Ma (Bennett et al., 2002; Rollinson et al., 2002; Coggon et al., 2015), despite WR, low Os concentration samples yielding extremely erroneous γOs_i compositions (Frei et al., 2003). The mildly elevated γOs_i of these chromitites has been inferred to represent either assimilation of radiogenic crust (Coggon et al., 2015) or the effects of high-grade metamorphism (Rollinson et al., 2002). These studies have an advantage over the Manfred Complex as the Ujaragssuit nunât layered body hosts largely undeformed chromitites, which are conspicuously

absent within the Manfred Complex (Rowe, 2016). Low $^{187}Re/^{188}Os$ chromites within ancient mafic and ultramafic lithologies are the best candidates for Re-Os isotopic study of ancient crust (e.g. Frei et al., 2003), as the resultant ages are more resilient to Re mobility than higher $^{187}Re/^{188}Os$ silicates. While chromites have been described within metaperidotites in the Manfred Complex (Fletcher et al., 1988; Rowe, 2016), their higher silicate/oxide ratio (and therefore higher $^{187}Re/^{188}Os$ bulk rock ratio) means chromites are more liable to secondary modification than if they were derived from a chromitite.

Analysis of bulk powders from the 13TKN80 yield Re-Os model ages of 3150-3300 Ma derived from mixed CHUR values, resulting in γOs_i of between 2.6 and 3.6. These values are significantly lower than modern layered intrusions (Figure 4.9), but still elevated in comparison to chondritic mantle, and consistent with similarly aged West Greenland chromitites (Bennett et al., 2002; Frei et al., 2003). The extremely well-preserved nature of 13TKN80 (Rowe, 2016), bar minor serpentinisation, indicates elevated γOs_i is unlikely to be a secondary feature, but may indicate minor crustal assimilation. This is at odds with the Nd and Hf composition of the Manfred Complex, which are chondritic (Fletcher et al., 1988; Souders et al., 2016; Kemp. pers.comm.), though the Manfred Complex does possess a Pb high μ signature (Fletcher et al., 1988).

However, this elevated γOs_i may also represent mixed Re and Os sources within this WR sample, with higher Re/Os orthopyroxene and low Re/Os olivine and spinel contributing to the total PGE budget of the WR powder. This is not ideal for a direct comparison to detrital chromite, and so a spinel separate of this sample was also analysed. Despite only a TRD being calculated, a significantly lower γOs_i of ~1 is observed, which represents a maximum γOs_i of these separates. This indicates derivation of the Manfred from a chondritic or near chondritic source, as expected from the chondritic compositions of Hf and Nd. The mildly elevated γOs_i may represent a small proportion of crustal assimilation (Figure 4.10). Modelling highlights it is unlikely any assimilated components are from evolved lithologies: the low concentrations of such samples require significant quantities of such lithologies to be assimilated (Table 4.5), which would drastically modify the SiO_2 content of the complex. Small amounts (<6 %) of assimilation of basaltic contaminants may explain the mildly elevated signature (Table 4.5), though the long-lived nature of these reservoirs is perhaps at odds with the Nd and Hf data. Due to the high Pb μ signature of the Manfred Complex, another potential contaminant source is mafic protocrust. Evidence from the Jack Hills zircon record attests to its involvement in the generation of the NGC till at least ~3380 Ma (Amelin et al., 1999; Kemp et al., 2010). The Re and Os concentration of protocrust is unknown, as highly siderophile elements (HSEs) were still being delivered as part of the late veneer (e.g. Walker, 2009; 2016). This makes the involvement of protocrust near impossible to model.

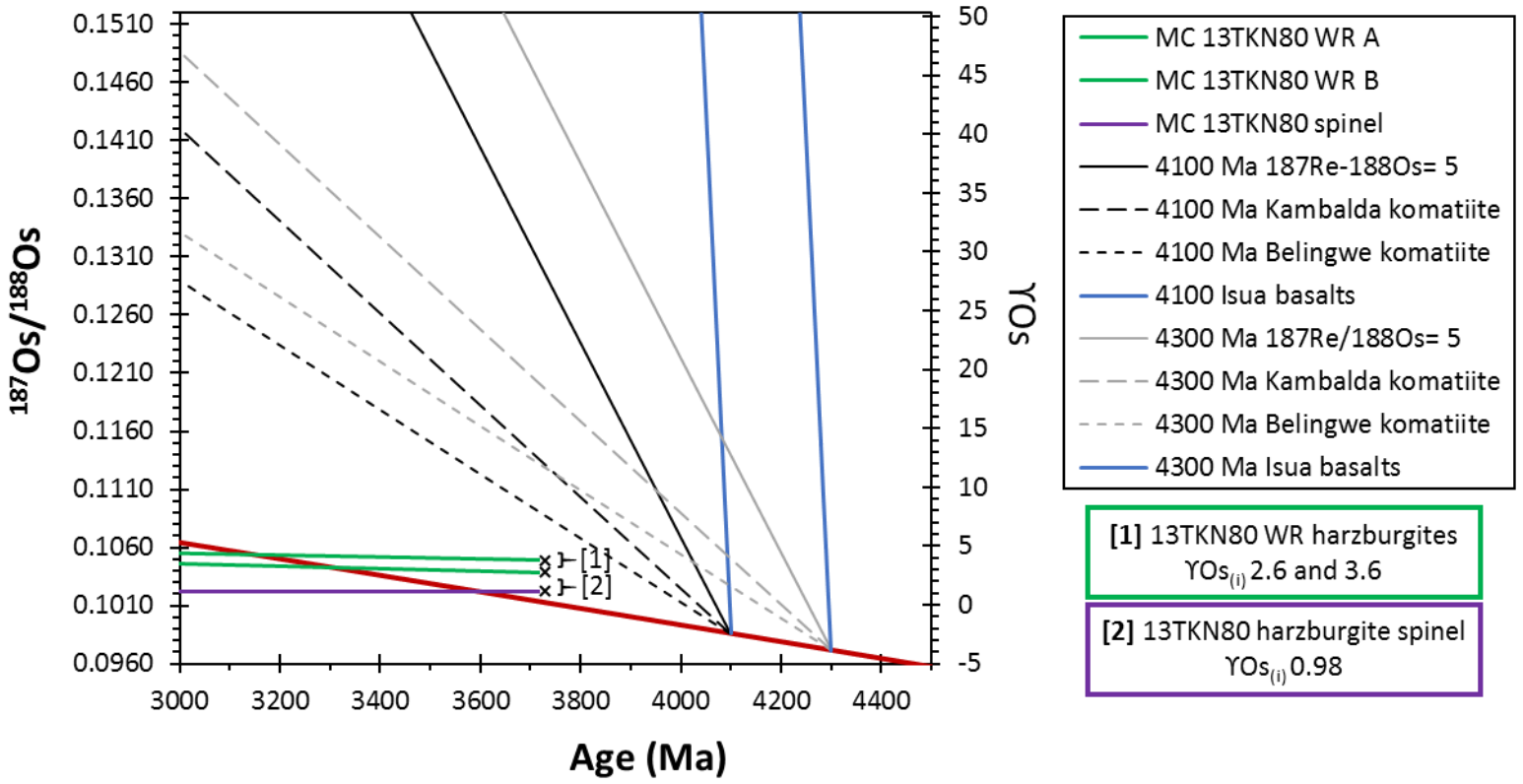

Figure 4.10: The role of crustal assimilation on 13TKN80 WR and spinel separate. Potential assimilant $^{187}Os/^{188}Os$ pathways shown for reference. [1] shows the elevated γOs_i of WR samples from 13TKN80- these values are very comparable to chromites within other layered bodies of this age (Bennett et al., 2002; Rollinson et al., 2002; Coggon et al., 2015), though it is unusual for WR to preserve such low values (e.g. Frei et al., 2003). [2] shows the spinel separates from the same sample with a near-chondritic composition. It is likely that, given the uncertainties with chondritic compositions, this shows an essentially chondritic γOs_i. Mixed chondrite values of $^{187}Os/^{188}Os$ 0.127 and $^{187}Re/^{188}Os$ 0.40186 used chondritic reservoir and calculation of γOs_i.

Table 4.5: Manfred Complex crustal assimilation modelling			
Lithology	**Age (Ma)**	**Assimilation Required (%)**	**Reference**
Isua pillow basalt	4100	11.3	Frei et al. (2003)
Isua pillow basalt	4300	7.7	Frei et al. (2003)
Lewisian tonalite	4100	44.5	Burton et al. (2000)
Lewisian transitional	4100	5.1	Burton et al. (2000)
Lewisian transitional	4300	3.3	Burton et al. (2000)
Kambalda komatiite	4100	18.3	Lambert et al. (1998)
Kambalda komatiite	4300	8.6	Lambert et al. (1998)
Belingwe komatiite (TF)	4100	13.1	Putchel et al. (2009a)
Belingwe komatiite (TF)	4300	12.1	Putchel et al. (2009a)
Re/Os = 5	4100	9.1	-
Re/Os = 5	4300	6	-

Table 4.5: Amount of assimilation of contaminating lithology (%) required to produce a γOs_i of ~1 at 3730 Ma within the Manfred Complex. Assimilation %s acquired using equation 4 and 5. TF = Tony's Flow.

Studies of Bushveld have shown the γOs_i of layered intrusions can be complex over hundreds of meters (Schoenberg et al., 1999). Congruently, the origin of chromitites within stratiform intrusions is postulated to be the result of magma mixing (e.g. Irvine, 1977; Mondal and Mathez, 2007) or assimilation of pre-existing crust (e.g. Kinnaird et al., 2002; Spandler et al., 2005), implying mixed and variable γOs_i should be an inherent feature of layered intrusion chromitites. Chromitites are thus far absent within the Manfred Complex (Rowe, 2016), though would make ideal candidates for further Re-Os study. It is therefore imperative that a wide range of samples, which have been minimally affected by metamorphism, are studied for Re-Os before robust conclusions on the Os isotopic composition of the Manfred Complex are fully constrained.

4.7. Conclusions

This chapter details the Re-Os model ages of Jack Hills detrital chromites and well-preserved mafics and ultramafics from the Manfred Complex sampled near Mount Narryer. Jack Hills detrital chromites yield high Os concentrations and typically unradiogenic $^{187}Os/^{188}Os$ isotopic ratios of ≤0.114. Two of three 'true' TRDs present correlate with known metamorphic events within the terrane, indicating Re-Os disturbance of some samples prior to and after deposition of detrital grains within metasediments. Recent Re addition is apparent within some samples, subsequently heavily modifying their measured $^{187}Re/^{188}Os$ ratios and resulting in geologically impossible TMAs. When filtered for sensible chromite Re/Os ratios of <0.1 and Re concentrations of <1 ppb, chromites yield self-consistent Re-Os TMAs that yield a weighted mean of 3528±34 Ma (2se, MSWD= 1.3). The age of this population is postulated to represent the most robust Re-Os model ages of detrital chromites from Jack Hills. Two younger, but again self-consistent, model ages date a second population of chromites to ca. 3000 Ma. The lower Re/Os ratios of these samples suggest they may represent partial Re loss of the chromites from the ca. 3528 Ma population, or metamorphic re-equilibration at ca. 3000 Ma (Spaggiari, 2007b).

The inferred layered intrusive provenance for these grains may imply that the magmatic source they are derived from assimilated radiogenic crust during emplacement, as is observed in many modern layered intrusive bodies crust (Horan et al., 2001; Schoenberg et al., 1999; 2003; Marques et al., 2003; Day et al., 2008; O'Driscoll et al., 2009; Zhong et al., 2011). This would result in the chromite protolith possessing a positive γOs_i, imparting artificially younger model ages on detrital chromites. To test this hypothesis, the γOs_i of well-preserved samples from the 3730 Ma Manfred Complex were analysed. Bulk rock powders of metaharzburgite 13TKN80 yielded model ages of 3150 to 3300 Ma, coincident with γOs_i of 2.6 to 3.6. A spinel separate however yields a near-chondritic maximum γOs_i of 0.1. This suggests a largely chondritic Os isotopic composition for the Manfred Complex, and indicates it is not the source of detrital chromites. However, further analysis and sample collection is required to fully quantify whether this intrusive body may represent the source of detrital chromites. We therefore postulate that the most robust model ages of these chromites are shown by the ca. 3530 Ma population. While this may imply that detrital chromites represent a mantle extraction event at this time, we note that to fully characterise the true crystallisation age and quantify the effects of crustal assimilation, their source must be directly sampled within the Narryer Terrane.

4.8. References

Amelin, Y., Lee, D. C., Halliday, A. N. & Pidgeon, R. T. (1999). Nature of the Earth's earliest crust from hafnium isotopes in single detrital zircons. *Nature* **399**, 252-255.

Bennett, V. C., Nutman, A. P. & Esat, T. M. (2002). Constraints on mantle evolution from Os-187/Os-188 isotopic compositions of Archean ultramafic rocks from southern West Greenland (3.8 Ga) and Western Australia (3.46 Ga). *Geochimica Et Cosmochimica Acta* **66**, 2615-2630.

Birck, J. L., RoyBarman, M. & Capmas, F. (1997). Re-Os isotopic measurements at the femtomole level in natural samples. *Geostandards Newsletter-the Journal of Geostandards and Geoanalysis* **21**, 19-27.

Brenan, J. M. & Andrews, D. (2001). High-temperature stability of laurite and Ru-Os-Ir alloy and their role in PGE fractionation in mafic magmas. *Canadian Mineralogist* **39**, 341-360.

Burton, K., Capmas, F., Birck, J., Allegre, C. & Cohen, A. (2000). Resolving crystallisation ages of Archean mafic-ultramafic rocks using the Re-Os isotope system. *Earth and Planetary Science Letters* **179**, 453-467.

Carlson, R. W. (2005). Application of the Pt-Re-Os isotopic systems to mantle geochemistry and geochronology. *Lithos* **82**, 249-272.

Cavosie, A. J., Wilde, S. A., Liu, D. Y., Weiblen, P. W. & Valley, J. W. (2004). Internal zoning and U-Th-Pb chemistry of Jack Hills detrital zircons: a mineral record of early Archean to Mesoproterozoic (4348-1576 Ma) magmatism. *Precambrian Research* **135**, 251-279.

Cavosie, A. J., Valley, J. W., Fournelle, J. & Wilde, S. A. (2002). Implications for sources of Jack Hills metasediments: detrital chromite. *Goldschmidt 2002*, 125.

Coggon, J. A., Luguet, A., Fonseca, R. O. C., Lorand, J. P., Heuser, A. & Appel, P. W. U. (2015). Understanding Re-Os systematics and model ages in metamorphosed Archean ultramafic rocks: A single mineral to whole-rock investigation. *Geochimica Et Cosmochimica Acta* **167**, 205-240.

Cohen, A. S. & Waters, F. G. (1996). Separation of osmium from geological materials by solvent extraction for analysis by thermal ionisation mass spectrometry. *Analytica Chimica Acta* **332**, 269-275.

Connolly, B. D., Puchtel, I. S., Walker, R. J., Arevalo, R., Piccoli, P. M., Byerly, G., Robin-Popieul, C. & Arndt, N. (2011). Highly siderophile element systematics of the 3.3 Ga Weltevreden komatiites, South Africa: Implications for early Earth history. *Earth and Planetary Science Letters* **311**, 253-263.

Dare, M. S., Tarduno, J. A., Bono, R. K., Cottrell, R. D., Beard, J. S. & Kodama, K. P. (2016). Detrital magnetite and chromite in Jack Hills quartzite cobbles: Further evidence for the preservation of primary magnetizations and new insights into sediment provenance. *Earth and Planetary Science Letters* **451**, 298-314.

Day, J. M. D., Brandon, A. D. & Walker, R. J. (2016). Highly Siderophile Elements in Earth, Mars, the Moon, and Asteroids. *Highly Siderophile and Strongly Chalcophile Elements in High-Temperature Geochemistry and Cosmochemistry* **81**, 161-238.

Day, J. M. D., Pearson, D. G. & Hulbert, L. J. (2008). Rhenium-osmium isotope and platinum-group element constraints on the origin and evolution of the 1.27 Ga Muskox layered intrusion. *Journal of Petrology* **49**, 1255-1295.

Finnigan, C. S., Brenan, J. M., Mungall, J. E. & McDonough, W. F. (2008). Experiments and models bearing on the role of chromite as a collector of platinum group minerals by local reduction. *Journal of Petrology* **49**, 1647-1665.

Fischer-Godde, M., Burkhardt, C., Kruijer, T. S. & Kleine, T. (2015). Ru isotope heterogeneity in the solar protoplanetary disk. *Geochimica Et Cosmochimica Acta* **168**, 151-171.

Fletcher, I. R., Rosman, K. J. R. & Libby, W. G. (1988). Sm-Nd, Pb-Pb and Rb-Sr geochronology of the Manfred Complex, Mount Narryer, Western Australia. *Precambrian Research* **38**, 343-354.

Foster, J. G., Lambert, D. D., Frick, L. R. & Maas, R. (1996). Re-Os isotopic evidence for genesis of Archaean nickel ores from uncontaminated komatiites. *Nature* **382**, 703-706.

Frei, R. & Jensen, B. K. (2003). Re-Os, Sm-Nd isotope- and REE systematics on ultramafic rocks and pillow basalts from the Earth's oldest oceanic crustal fragments (Isua Supracrustal Belt and Ujaragssuit nunat area, W Greenland). *Chemical Geology* **196**, 163-191.

Gonzalez-Jimenez, J. M., Griffin, W. L., Gervilla, F., Kerestedjian, T. N., O'Reilly, S. Y., Proenza, J. A., Pearson, N. J. & Sergeeva, I. (2012). Metamorphism disturbs the Re-Os signatures of platinum-group minerals in ophiolite chromitites. *Geology* **40**, 659-662.

Griffin, W. L., Belousova, E. A., O'Neill, C., O'Reilly, S. Y., Malkovets, V., Pearson, N. J., Spetsius, S. & Wilde, S. A. (2014). The world turns over: Hadean-Archean crust-mantle evolution. *Lithos* **189**, 2-15.

Horan, M. F., Alexander, C. M. O. & Walker, R. J. (2009). Highly siderophile element evidence for early solar system processes in components from ordinary chondrites. *Geochimica Et Cosmochimica Acta* **73**, 6984-6997.

Horan, M. F., Morgan, J. W., Walker, R. J. & Cooper, R. W. (2001). Re-Os isotopic constraints on magma mixing in the Peridotite Zone of the Stillwater Complex, Montana, USA. *Contributions to Mineralogy and Petrology* **141**, 446-457.

Iizuka, T., McCulloch, M. T., Komiya, T., Shibuya, T., Ohta, K., Ozawa, H., Sugimura, E. & Collerson, K. D. (2010). Monazite geochronology and geochemistry of meta-sediments in the Narryer Gneiss Complex, Western Australia: constraints on the tectonothermal history and provenance. *Contributions to Mineralogy and Petrology* **160**, 803-823.

Irvine, T. N. (1977). Origin of chromitite layers in the Muskox intrusion and other stratiform intrusions: A new interpretation. *Geology* **5**, 273-277.

Ishikawa, A., Suzuki, K., Collerson, K. D., Liu, J. G., Pearson, D. G. & Komiya, T. (2017). Rhenium-osmium isotopes and highly siderophile elements in ultramafic rocks from the Eoarchean Saglek Block, northern Labrador, Canada: implications for Archean mantle evolution. *Geochimica Et Cosmochimica Acta* **216**, 286-311.

Kemp, A. I. S., Wilde, S. A., and Spaggiari, C. (2019). The Narryer Terrane, Yilgarn Craton, Western Australia: Review and Recent Developments. In: van Kranendonk, M. J., Bennett, V. C., and Hoffmann, J. E., (ed.) *Earth's Oldest Rocks*: Elsevier, 401-429.

Kemp, A. I. S. (2018). Early earth geodynamics: cross examining the geological testimony. *Philosophical Transactions of the Royal Society A* **376**.

Kemp, A. I. S., Wilde, S. A., Hawkesworth, C. J., Coath, C. D., Nemchin, A., Pidgeon, R. T., Vervoort, J. D. & DuFrane, S. A. (2010). Hadean crustal evolution revisited: New constraints from Pb-Hf isotope systematics of the Jack Hills zircons. *Earth and Planetary Science Letters* **296**, 45-56.

Kinnaird, J., Kruger, F., Nex, P. & Cawthorn, R. (2002). Chromitite formation - a key to understanding processes of platinum enrichment. *Transactions of the Institution of Mining and Metallurgy Section B-Applied Earth Science* **111**, B23-B35.

Kinny, P. D., Wijbrans, J. R., Froude, D. O., Williams, I. S. & Compston, W. (1990). Age constraints on the geological evolution of the Narryer Gneiss Complex, Western Australia. *Australian Journal of Earth Sciences* **37**, 51-69.

Kinny, P. D., Williams, I. S., Froude, D. O., Ireland, T. R. & Compston, W. (1988). Early Archean zircon ages from orthogneisses and anorthosites at Mount Narryer, Western Australia. *Precambrian Research* **38**, 325-341.

Lambert, D., Foster, J., Frick, L., Hoatson, D. & Purvis, A. (1998). Application of the Re-Os isotopic system to the study of Precambrian magmatic sulfide deposits of Western Australia. *Australian Journal of Earth Sciences* **45**, 265-284.

Ludwig, K.R., 2003. Isoplot/Ex: Special Publication No. 4. Berkeley Geochronology

Luguet, A., Nowell, G. M. & Pearson, D. G. (2008). (184)Os/(188)Os and (186)Os/(188)Os measurements by Negative Thermal Ionisation Mass Spectrometry (N-TIMS): Effects of interfering element and mass fractionation corrections on data accuracy and precision. *Chemical Geology* **248**, 342-362.

Marques, J. C., Ferreira, C. F., Carlson, R. W. & Pimentel, M. M. (2003). Re-Os and Sm-Nd isotope and trace element constraints on the origin of the chromite deposit of the Ipueira-Medrado sill, Bahia, Brazil. *Journal of Petrology* **44**, 659-678.

Meisel, T., Moser, J. & Wegscheider, W. (2001). Recognizing heterogeneous distribution of platinum group elements (PGE) in geological materials by means of the Re-Os isotope system. *Fresenius Journal of Analytical Chemistry* **370**, 566-572.

Meisel, T., Walker, R. & Morgan, J. (1996). The osmium isotopic composition of the Earth's primitive upper mantle. *Nature* **383**, 517-520.

Mondal, S. & Mathez, E. (2007a). Origin of the UG2 chromitite layer, Bushveld Complex. *Journal of Petrology* **48**, 495-510.

Mondal, S. K., Frei, R. & Ripley, E. M. (2007b). Os isotope systematics of mesoarchean chromitite-PGE deposits in the Singhbhum Craton (India): Implications for the evolution of lithospheric mantle. *Chemical Geology* **244**, 391-408.

Myers, J. S. (1988). Oldest known terrestrial anorthosite at Mount Narryer, Western Australia. *Precambrian Research* **38**, 309-323.

Myers, J. S. (1997). Byro, W.A., Sheet SG 50 10 (2nd Edition). Western Australia Geological Survey.

Nagler, T. F., Kramers, J. D., Kamber, B. S., Frei, R. & Prendergast, M. D. A. (1997). Growth of subcontinental lithospheric mantle beneath Zimbabwe started at or before 3.8 Ga: Re-Os study on chromites. *Geology* **25**, 983-986.

Nutman, A. P., Kinny, P. D., Compston, W. & Williams, I. S. (1991). SHRIMP U-Pb zircon geochronology of the Narryer Gneiss Complex, Western Australia. *Precambrian Research* **52**, 275-300.

O'Driscoll, B., Day, J. M. D., Daly, J. S., Walker, R. J. & McDonough, W. F. (2009). Rhenium-osmium isotopes and platinum-group elements in the Rum Layered Suite, Scotland: Implications for Cr-spinel seam formation and the composition of the Iceland mantle anomaly. *Earth and Planetary Science Letters* **286**, 41-51.

Page, P. & Barnes, S. J. (2016). The influence of chromite on osmium, iridium, ruthenium and rhodium distribution during early magmatic processes. *Chemical Geology* **420**, 51-68.

Park, J. W., Kamenetsky, V., Campbell, I., Park, G., Hanski, E. & Pushkarev, E. (2017). Empirical constraints on partitioning of platinum group elements between Cr-spinel and primitive terrestrial magmas. *Geochimica Et Cosmochimica Acta* **216**, 393-416.

Pearson, D., Parman, S. & Nowell, G. (2007). A link between large mantle melting events and continent growth seen in osmium isotopes. *Nature* **449**, 202-205.

Pearson, D. G., Shirey, S. B., Harris, J. W. & Carlson, R. W. (1998). Sulphide inclusions in diamonds from the Koffiefontein kimberlite, S Africa: constraints on diamond ages and mantle Re-Os systematics. *Earth and Planetary Science Letters* **160**, 311-326.

Puchtel, I. S., Walker, R. J., Touboul, M., Nisbet, E. G. & Byerly, G. R. (2014). Insights into early Earth from the Pt-Re-Os isotope and highly siderophile element abundance systematics of Barberton komatiites. *Geochimica Et Cosmochimica Acta* **125**, 394-413.

Puchtel, I. S., Walker, R. J., Brandon, A. D. & Nisbet, E. G. (2009a). Pt-Re-Os and Sm-Nd isotope and HSE and REE systematics of the 2.7 Ga Belingwe and Abitibi komatiites. *Geochimica Et Cosmochimica Acta* **73**, 6367-6389.

Puchtel, I., Walker, R., Anhaeusser, C. & Gruau, G. (2009b). Re-Os isotope systematics and HSE abundances of the 3.5 Ga Schapenburg komatiites, South Africa: Hydrous melting or prolonged survival of primordial heterogeneities in the mantle? *Chemical Geology* **262**, 355-369.

Puchtel, I. S., Brandon, A. D. & Humayun, M. (2004). Precise Pt-Re-Os isotope systematics of the mantle from 2.7-Ga komatiites. *Earth and Planetary Science Letters* **224**, 157-174.

Puchtel, I. S., Brugmann, G. E., Hofmann, A. W., Kulikov, V. S. & Kulikova, V. V. (2001). Os isotope systematics of komatiitic basalts from the Vetreny belt, Baltic Shield: evidence for a chondritic source of the 2.45 Ga plume. *Contributions to Mineralogy and Petrology* **140**, 588-599.

Rehkamper, M., Halliday, A. N., Fitton, J. G., Lee, D. C., Wieneke, M. & Arndt, N. T. (1999). Ir, Ru, Pt, and Pd in basalts and komatiites: New constraints for the geochemical behavior of the platinum-group elements in the mantle. *Geochimica Et Cosmochimica Acta* **63**, 3915-3934.

Rollinson, H., Appel, P. W. U. & Frei, R. (2002). A metamorphosed, early Archaean chromitite from west Greenland: Implications for the genesis of Archaean anorthositic chromitites. *Journal of Petrology* **43**, 2143-2170.

Rowe, ML 2016, Petrology and geochemistry of the Eoarchaean Manfred Complex: origin and components: Geological Survey of Western Australia, Record 2016/22, 150p.

Schoenberg, R., Nagler, T. F., Gnos, E., Kramers, J. D. & Kamber, B. S. (2003). The source of the Great Dyke, Zimbabwe, and its tectonic significance: Evidence from Re-Os isotopes. *Journal of Geology* **111**, 565-578.

Schoenberg, R., Kruger, F. J., Nagler, T. F., Meisel, T. & Kramers, J. D. (1999). PGE enrichment in chromitite layers and the Merensky Reef of the western Bushveld Complex; a Re-Os and Rb-Sr isotope study. *Earth and Planetary Science Letters* **172**, 49-64.

Shirey, S. B. & Walker, R. J. (1998). The Re-Os isotope system in cosmochemistry and high-temperature geochemistry. *Annual Review of Earth and Planetary Sciences* **26**, 423-500.

Shirey, S. B. & Walker, R. J. (1995). Carius tube digestion for low-blank Rhenium-Osmium analysis. *Analytical Chemistry* **67**, 2136-2141.

Souders, K., and Sylvester, P. (2016). Hf Isotope Systematics of Archean Anorthosites: Manfred Complex, Yilgarn Craton, Western Australia. *American Geophysical Union, Fall Meeting 2016*.

Spaggiari, C. V. (2007a). The Jack Hills greenstone belt, Western Australia - Part 1: Structural and tectonic evolution over > 1.5 Ga. *Precambrian Research* **155**, 204-228.

Spaggiari, C. V., Pidgeon, R. T. & Wilde, S. A. (2007b). The Jack Hills greenstone belt, Western Australia - Part 2: Lithological relationships and implications for the deposition of > 4.0 Ga detrital zircons. *Precambrian Research* **155**, 261-286.

Spandler, C., Mavrogenes, J. & Arculus, R. (2005). Origin of chromitites in layered intrusions: Evidence from chromite-hosted melt inclusions from the Stillwater Complex. *Geology* **33**, 893-896.

Sylvester, P., Souders, A. K., Crowley, J. L., and Myers, J. S. (2011). The Archean anorthosite monzogranite magmatic association of the Narryer Gneiss Terrane, Western Australia. *Goldschmidt 2011*, 1975.

Touboul, M., Liu, J. G., O'Neil, J., Puchtel, I. S. & Walker, R. J. (2014). New insights into the Hadean mantle revealed by W-182 and highly siderophile element abundances of supracrustal rocks from the Nuvvuagittuq Greenstone Belt, Quebec, Canada. *Chemical Geology* **383**, 63-75.

Valley, J. W., Cavosie, A. J., Shirey, S. & Wilde, S. A. (2005). 3.2 to 3.5 Ga Re-Os Model Ages for Detrital Chromite from Jack Hills, Western Australia: Implications for Pilbara and Yilgarn Craton Evolution. *American Geophysical Union, Fall Meeting 2005, abstract #V21F-08*.

Walker, R. J. (2016). Siderophile elements in tracing planetary formation and evolution. *Geochemical Perspectives* **5**, 1-145.

Walker, R. (2009). Highly siderophile elements in the Earth, Moon and Mars: Update and implications for planetary accretion and differentiation. *Chemie Der Erde-Geochemistry* **69**, 101-125.

Walker, R. J., Horan, M. F., Morgan, J. W., Becker, H., Grossman, J. N. & Rubin, A. E. (2002). Comparative Re-187-Os-187 systematics of chondrites: Implications regarding early solar system processes. *Geochimica Et Cosmochimica Acta* **66**, 4187-4201.

Walker, R. J., Prichard, H. M., Ishiwatari, A. & Pimentel, M. (2002). The osmium isotopic composition of convecting upper mantle deduced from ophiolite chromites. *Geochimica Et Cosmochimica Acta* **66**, 329-345.

Wyche, S. (2007). Evidence of Pre-3100 Ma Crust in the Youanmi and South West Terranes, and Eastern Goldfields Superterrane, of the Yilgarn Craton. In: van Kranendonk, M. J., Smithies, R. H. & Bennett, V. C. (eds.) *Earth's Oldest Rocks*: Elsevier, 113-124.

Zhong, H., Qi, L. A., Hu, R. Z., Zhou, M. F., Gou, T. Z., Zhu, W. G., Liu, B. G. & Chu, Z. Y. (2011). Rhenium-osmium isotope and platinum-group elements in the Xinjie layered intrusion, SW China: Implications for source mantle composition, mantle evolution, PGE fractionation and mineralization. *Geochimica Et Cosmochimica Acta* **75**, 1621-1641.

Zhu, Z. H., Meija, J., Zheng, A. R., Mester, Z. & Yang, L. (2017). Determination of the Isotopic Composition of Iridium Using Multicollector-ICPMS. *Analytical Chemistry* **89**, 9375-9382.

Chapter Five:

Coupled Pb-Hf of detrital zircons

5.1. Introduction

Vestiges of the Earth's earliest crust are preserved at Jack Hills, within the Narryer Terrane, in Western Australia (Figure 5.1). Here, fuchsitic metasediments contain detrital zircons that yield concordant ^{207}Pb-^{206}Pb ages of up to 4372±6 Ma (Compston and Pidgeon, 1986; Wilde et al., 2001; Valley et al., 2014), predating the rock record by up to 350 Ma (Reimink et al., 2014; cf. O'Neil et al., 2008). Jack Hills detrital zircons have thus been interrogated using a variety of geochemical and isotopic techniques, yet how zircons formed and the geodynamic regime under which they were emplaced remains controversial. While there have been arguments for the potential crystallisation of zircon within impact melt sheets (Kenny et al., 2016; cf. Darling et al., 2009) or from diverse protoliths (Wang and Wilde, 2018), the two most compelling and highly debated hypotheses are those of horizontal tectonics (e.g. modern-style plate tectonics; Harrison et al., 2005; 2008; Hopkins et al., 2008; 2010; 2012; Bell et al., 2011; 2014) or vertical tectonics (e.g. stagnant lid regime; Amelin et al., 2000; Kemp et al., 2010; Whitehouse et al., 2017). These disparate hypotheses have large implications for the broader geodynamic regime operating in the early Earth.

Inclusions of quartz and muscovite (Hopkins et al., 2008; 2010; Bell et al., 2015), low Ti-in-zircon (Watson and Harrison, 2005; Harrison and Schmitt, 2007) and Pb-Hf arrays yielding protolith $^{176}Lu/^{177}Hf$ ratios of ≤0.01 (Harrison et al., 2008; Bell et al., 2011; 2014: Figure 5.1a) have been used to infer the presence of low geothermal gradients, sediment input, and recycling of felsic protoliths. This has been postulated to represent the formation of zircons from wet, minimum-melt granitoids, the operation of plate tectonics and an abundance of continental crust in the Hadean and Archean (Harrison et al., 2017). However, the primary origin of quartz and fuchsite inclusions within Jack Hills zircon has been questioned (Rasmussen et al., 2011; 2012), and steep Pb-Hf crustal arrays have been postulated to be systematic of ancient Pb loss, rather than recycling of felsic protoliths (Kemp et al., 2010). Both Amelin et al. (1999) and Kemp et al. (2010) instead found that zircon plot along shallower Pb-Hf trajectories (Figure 5.1b), comparable to recycling of a protolith with a $^{176}Lu/^{177}Hf$ composition of ~0.02, which is indicative of mafic crust. Critically, both studies used stricter filtering of detrital zircons: Amelin et al (1999) applied a 10% discordance criterion for ID-TIMS measurements (Nebel et al., 2014), while Kemp et al (2010) screened out Hadean zircon that did not contain magmatic (oscillatory) zoning, had concordant U/Pb ages, Th/U ratios of ≥0.3, and $\delta^{18}O_{SMOW}$ of >4.5‰. Arguments that Ti-in-zircon temperatures are too low for zircon to be derived from melting of mafic crust (e.g. Arndt, 2013) can be countered by the observation that Ti-in-zircon thermometry rarely records liquidus temperatures (Nutman, 2006). The debate surrounding the origin of Jack Hills zircon therefore continues.

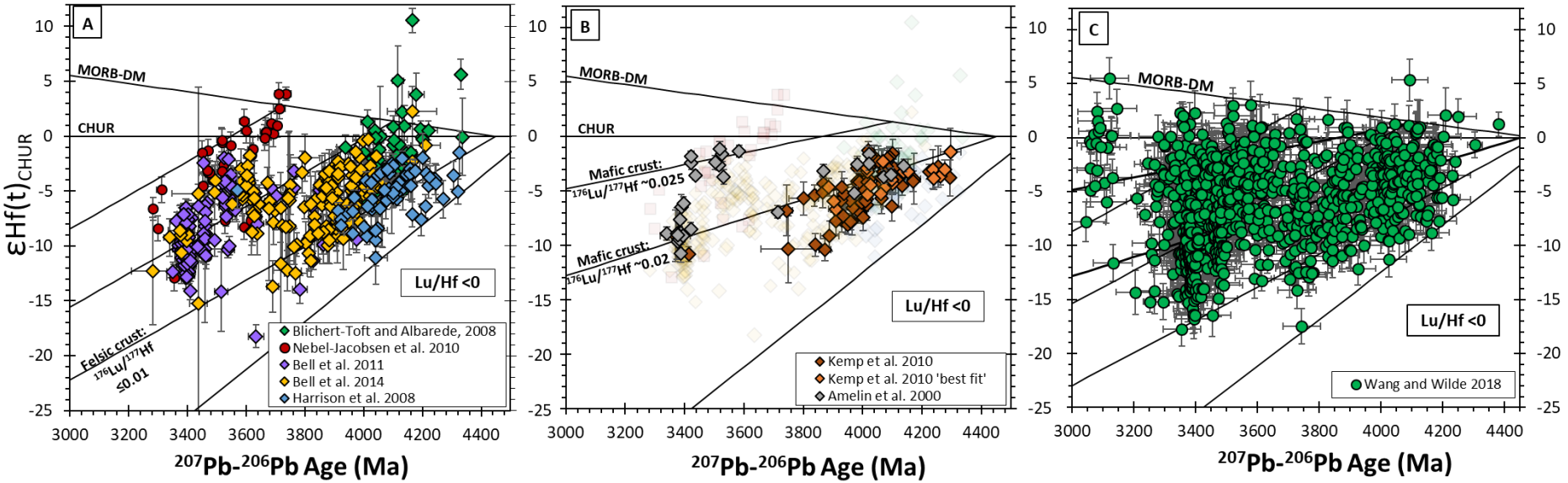

Figure 5.1: Previous Pb-Hf work undertaken on zircons from Jack Hills. All data recalculated using the ^{176}Lu decay constant of Soderlund et al. (2004) and CHUR parameters of Bouvier et al. (2008). MORB-DM back calculated to 4450 Ma from a modern day $\varepsilon Hf(t)_{CHUR}$ of +16 (Vervoort and Kemp, 2016). **A)** Those that argue for reworking of a felsic protolith to form detrital zircon Pb-Hf compositions. Crustal extraction events at ~4450 Ma, ~4100 Ma and 3730 Ma produce felsic crust that evolve along a steep crustal evolution path, coincident with a $^{176}Lu/^{177}Hf$ ratio of ≤0.01. **B)** Those that argue for reworking of mafic crust. Mafic crust is extracted from CHUR and DM at ~4450 Ma and ~4100 Ma, respectively, and evolves along shallower crustal arrays that are indicative of a $^{176}Lu/^{177}Hf$ ratio of ~0.02. **C)** Data from Wang and Wilde. (2018) who argue for reworking of compositionally diverse protoliths to generate the compositional variability observed within their data.

Naturally, much of this debate has centred on the Hadean zircons from Jack Hills, yet the Pb-Hf composition of Archean zircons may add further to these investigations. Archean zircons have been postulated to fit to several distinct crustal arrays (e.g. Kemp et al., 2010; Bell et al., 2011; 2014), yet only a single sufficiently filtered zircon dataset has been produced (Amelin et al., 1999, n=25). Two studies have thus far focused solely on Archean zircons. When filtered for magmatic zircons (those listed as oscillatory), data from Bell et al. (2011) and Bell et al. (2014) only yield 40 Pb-Hf data points, which are largely more subchondritic than data from Amelin et al. (1999) (Figure 5.2). Despite this, both studies use bulk data to infer Pb-Hf arrays, which fill quite different Pb-Hf compositional spaces (Figure 5.2) and have been interpreted to represent recycling of felsic crust. However, these studies used large spot sizes (>69 µm) and long ablation times, causing significant loss of spatial resolution, and Bell et al. (2011) did not supply data on discordance, so the robustness of ^{207}Pb-^{206}Pb ages used for calculation of initial Hf compositions cannot be verified. This casts doubt on the veracity of Pb-Hf measurements, despite apparent attempts to filter for magmatic grains. Recent work by Wang and Wilde (2018) also analysed many Archean zircons (Figure 5.1c) but filtered data solely for U/Th ratios, and so these data are not included in direct comparison.

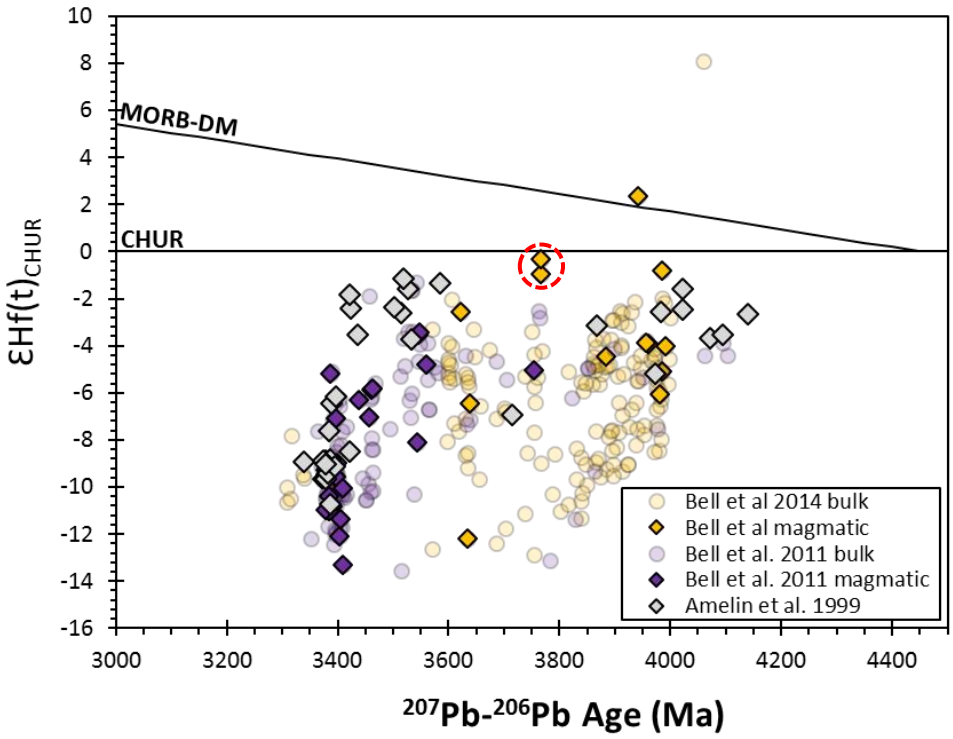

Figure 5.2: Bulk and magmatic (zircons listed as possessing oscillatory zoning) Pb-Hf data from Bell et al. (2011) and (2014) in comparison to data from Amelin et al. (1999). Error bars removed for clarification. Clear discrepancy between Bell et al. and Amelin et al. data, particularly within Archean grains aged between 3400 Ma and 3600 Ma, where the Amelin et al. (1999) data possesses more radiogenic compositions. Differences between Bell et al. bulk and magmatic data is also present, particularly within the Bell et al. (2014) data. Circles data points from the same grain.

This chapter details the U-Pb and Lu-Hf systematics for detrital zircons from 14WA2, 14WA4 and 16WA5, with full imaging and spot locations available in the supplementary material associated with this chapter. Coupled Pb-Hf of these zircons were determined using low-volume ablation methods (Bauer and Horstwood, 2018), enabling high spatial resolution analysis of zircons that may possess complex intra-grain U-Pb variability. We calculate the U-Pb ages of grains, including ^{207}Pb-^{206}Pb age distributions, and discuss the potential sources of these zircons within the Narryer Terrane. Pb-Hf analyses of bulk zircons and those filtered for oscillatory zoning are also presented, highlighting potential ancient Pb-loss arrays within bulk data and highlighting the simplification of data from oscillatory zoned data sets. Finally, the potential magmatic sources of the protoliths of detrital zircons are determined from inter-crystal evolution arrays, and the timing and composition of crustal generation events constrained. Broader implications to Hadean and Archean geodynamics are discussed alongside detrital chromites in Chapter 6.

5.2. Materials and Methods

5.2.1 Sample preparation and zircon selection

After separation from bulk metasediments, zircons were picked and mounted in epoxy, then carefully polished to roughly equatorial sections. Zircons were imaged using back scattered electron (BSE) and cathodoluminescence (CL) detectors on a FEI Quanta 600 scanning electron microscope at the British Geoloigcal Survey (BGS) and a Hitatchi S-3500N at the University of Bristol (e.g. Figure 5.3 and 5.4). Further imaging in transmitted light was also undertaken: all three imaging techniques were used to select grains for analysis. Zircons were chosen that were optically clear (in transmitted light), and therefore free of cracks, cloudiness or inclusions within the subsurface, and that possessed zonation domains large enough for Hf ablation (≥40 μm). Spot selection was also guided by BSE images to to avoid surface inclusions, cracks and metamict domains. Selection of optically clear zircons likely preferentially sampled low U concentration grains, as increased opacity is clearly linked to higher U, darker CL grains (Supplementary Material 11), though if such grains possessed oscillatory zoning they were included. These grains, and those sampled that do not possess oscillatory zoning, are included in the 'bulk zircon' data sets of 14WA2 and 14WA4: a 'bulk zircon' sample set was not undertaken for 16WA5.

Further filtering was applied to select grains with definitively magmatic zoning, with this population labelled as 'oscillatory' for the remainder of this chapter. This subset of grains included only zircons that possessed pristine oscillatory, or pristine oscillatory and sector zoning, alongside a high degree of (<10 %) concordance for both ^{206}Pb-^{238}U/^{207}Pb-^{206}Pb and ^{207}Pb-^{235}U/^{206}Pb-^{238}U. CL images of examples of Hadean and Archean zircons included in this subset are shown in Figure 5.4 and Figure 5.5,

respectively. While this is not as stringent a filtration as applied by Kemp et al. (2010) and suggested by Nemchin et al. (2006), features such as metamorphic U/Th and lowered $\delta^{18}O_{SMOW}$ should not be coupled with magmatic oscillatory zoning. Furthermore, while the presence of oscillatory zoning does not definitively preclude the presence of ancient and recent Pb loss (e.g. Nemchin et al., 2006), significant Pb-loss would destroy or distort the fine lamellae expected within definitively magmatic grains. This therefore suggests that oscillatory zoning is the most appropriate filter to apply in the analysis of ancient grains. We are therefore confident we have sampled the most pristine zircon within samples, though add that future oxygen isotopic work may be beneficial to determine the presence of grains with elevated $\delta^{18}O_{SMOW}$ (>7), and remove these from Pb-Hf analyses.

5.2.2. Zircon U-Pb analyses

Zircon were analysed for U-Pb using the Nu instruments Nu Plasma HR MC-ICP-MS at the Natural Environment Research Council Isotope Geosciences Laboratory (NIGL) of the BGS, coupled with an ESI ArF excimer 193 nm laser. Zircons were analysed using a method slightly modified from Bauer and Horstwood (2017), where sequential U-Pb and Lu-Hf analysis resulted in a total ablation depth kept to < 20 µm. This is ideal for analysis of ancient, complexly zoned zircons that yield significant intra-grain U-Pb variability, as is commonly noted in Hadean grains at Jack Hills (Nemchin et al.., 2006; Whitehouse et al., 2017a; Cavosie et al., 2019). U-Pb measurements were conducted using a 20 µm spot size, 10 Hz repetition rate and a ~2.7 Jcm^{-2} fluence, with a 10 second total ablation time. This resulted in an ablation depth of ~5 µm for the U-Pb measurement. A longer sample transport tube was used to reduce the noise of the ablation. Initial experiments included measuring ^{206}Pb on a faraday cup, anticipating significant radiogenic ingrowth and subsequent high Pb concentrations, as may be expected for >3000 Ma zircons (Bauer and Horstwood, 2018). However, the low U content of Jack Hills zircon (Crowley et al., 2005) meant this resulted in small signals and therefore unacceptable uncertainties. As such, subsequent analysis measured ^{207}Pb and ^{206}Pb using ion counters (Section 2.7.1; Table 2.4).

Sample unknowns were bracketed by reference materials to correct for laser and instrument induced fractionation effects, including downhole fractionation of U and Pb. Zircon standard GJ1 was used as the primary reference material (PRM), while Plešovice, 91500 and OG1 were used as further validation materials to assess the robustness of U-Pb measurements (Stern et al., 2009; Horstwood et al., 2016). All data was reduced using Iolite, and a common Pb correction was not applied. Full U-Pb standard data are available in Supplmentary Material 4 and 5. Despite the small ablation volumes, uncertainties for individual measurements were kept below 1% (2s%) for ^{207}Pb-^{206}Pb ages, and below 2% (2s%) for ^{206}Pb-^{238}U ages so that the age uncertainty contribution to Hf uncertainties was minimal. In-session

uncertainties including excess variance of the PRM were propagated into sample measurements using Iolite. Long-term systematic variability, that is the variability of the validation reference materials (VRM) between sessions, was propagated following the methods of Horstwood et al. (2016). This incorporated the reference ratio uncertainties of the PRM, long-term excess variance on the VRM, and decay constant uncertainties. For the values used in the propagation see Section 2.7.1.

5.2.3 Zircon Lu-Hf analyses

Zircons that yielded concordant (<10 %) U-Pb ages were analysed for Lu-Hf. Despite many not possessing definitively magmatic zoning, all zircons within 14WA2 were analysed, herein termed 'bulk zircon', as were a small number of zircons with non-oscillatory zonation in 14WA4. Lu-Hf measurements of oscillatory zoned grains was undertaken in all samples. Hf measurements were undertaken using the Thermo Scientific Neptune Plus MC-ICP-MS, also at the NIGL, using an ESI UP193FX laser. Spot sizes for Lu-Hf measurements were 35 µm and placed over the previous U-Pb ablation pit to ensure the best chances of sampling of the same zircon domain. Lu-Hf analyses were conducted using a 10 Hz repetition rate and a ~7 Jcm^{-2} fluence, with a 10 second total ablation time. This results in an ablation depth of ~15 µm, bringing the total ablation depth for coupled U-Pb and Lu-Hf analyses to ~20 µm. Blocks of 10-15 unknowns were bracketed by well characterised Hf standards to correct for laser and instrument induced fractionation: 91500 (Blichert-Toft, 2008) was used as the PRM, while Mud Tank (Woodhead and Hergt, 2005), Plešovice (Sláma et al., 2009) and OG1 (Kemp et al., 2017) were used as validation materials to determine the robustness of the Hf measurement. As with U-Pb measurements, all validation material $^{176}Hf/^{177}Hf$ ratios were within uncertainty of previously determined $^{176}Hf/^{177}Hf$ ratios, with these measurements recorded in Supplementary Material 8 and 9.

Prior to Hf measurements, the ICP-MS was tuned for maximum sensitivity at the lowest oxide production rate. An Yb-doped Hf solution was analysed prior to ablation to check the robustness of the isobaric interference correction of ^{176}Yb. This is undertaken to allow calibration of the Yb and Hf mass bias relationship so that a $^{176}Yb/^{173}Yb$ modified for this calibration can be used in the correction of the ^{176}Yb interference on ^{176}Hf using measured ^{172}Yb and ^{173}Yb, based on the measured Hf mass bias at the time of analysis. The resultant $^{176}Hf/^{177}Hf$ ratio was observed to be slightly higher than expected in doped solutions with elevated $^{176}Yb/^{177}Hf$, indicating increased oxide generation. This required a slightly higher nominal ratio of $^{176}Yb/^{173}Yb$ of 0.7962 (c.f. 0.79435) to correct for ^{176}Yb and could increase inaccuracy at higher Yb/Hf (e.g. at $^{176}Yb/^{177}Hf$ >>0.2). However, no sample unknown possessed a $^{176}Yb/^{177}Hf$ ratio of greater than 0.1, and so data were not filtered for this ratio. ^{175}Lu was also monitored to correct for the isobaric interference of ^{176}Lu on ^{176}Hf. Correlations in sample

$^{176}Hf/^{177}Hf$ and $^{176}Hf/^{177}Hf$ or $^{176}Yb/^{177}Hf$ would be expected if this interference correction was not robust: none were observed (Figure 5.5). Hf data were processed offline using Iolite (Paton et al., 2010). As with U-Pb measurements, in-session PRM uncertainties and excess variance were propagated into Hf measurements of the unknowns and validation materials. No propagation for long-term excess variance of the VRM was required.

Data are presented as ƐHf(t), which represents the deviation of zircon initial $^{176}Hf/^{177}Hf$ ratio in parts per 10,000 from a time-integrated chondritic uniform reservoir (CHUR). Back calculations were undertaken using a CHUR $^{176}Hf/^{177}Hf$ ratio of 0.282785 and a CHUR $^{176}Lu/^{177}Hf$ ratio of 0.0336 (Bouvier et al., 2008), and a decay constant (λ) of $1.867x10^{-11}$ (Soderlund et al., 2004). A complementary depleted mantle (DM) evolution curve is also calculated by extrapolation of modern MORB $ƐHf(t)_{CHUR}$ compositions (+16) back to 4450 Ma, the purported first crustal generation event (Kemp et al., 2010; Vervoort and Kemp, 2016). Individual Pb-Hf model ages (T_{CH} or T_{DM}) were not calculated for zircons in this study owing to the significant uncertainties surrounding such two-stage calculations within detrital records (see Vervoort and Kemp, 2016 and methods and materials). However, the presence of arrays within plots of $ƐHf(t)_{CHUR}$ vs. ^{207}Pb-^{206}Pb age meant that these features could be used to determine broad mantle extraction ages from the $ƐHf(t)_{CHUR}$ compositions of Jack Hills zircons.

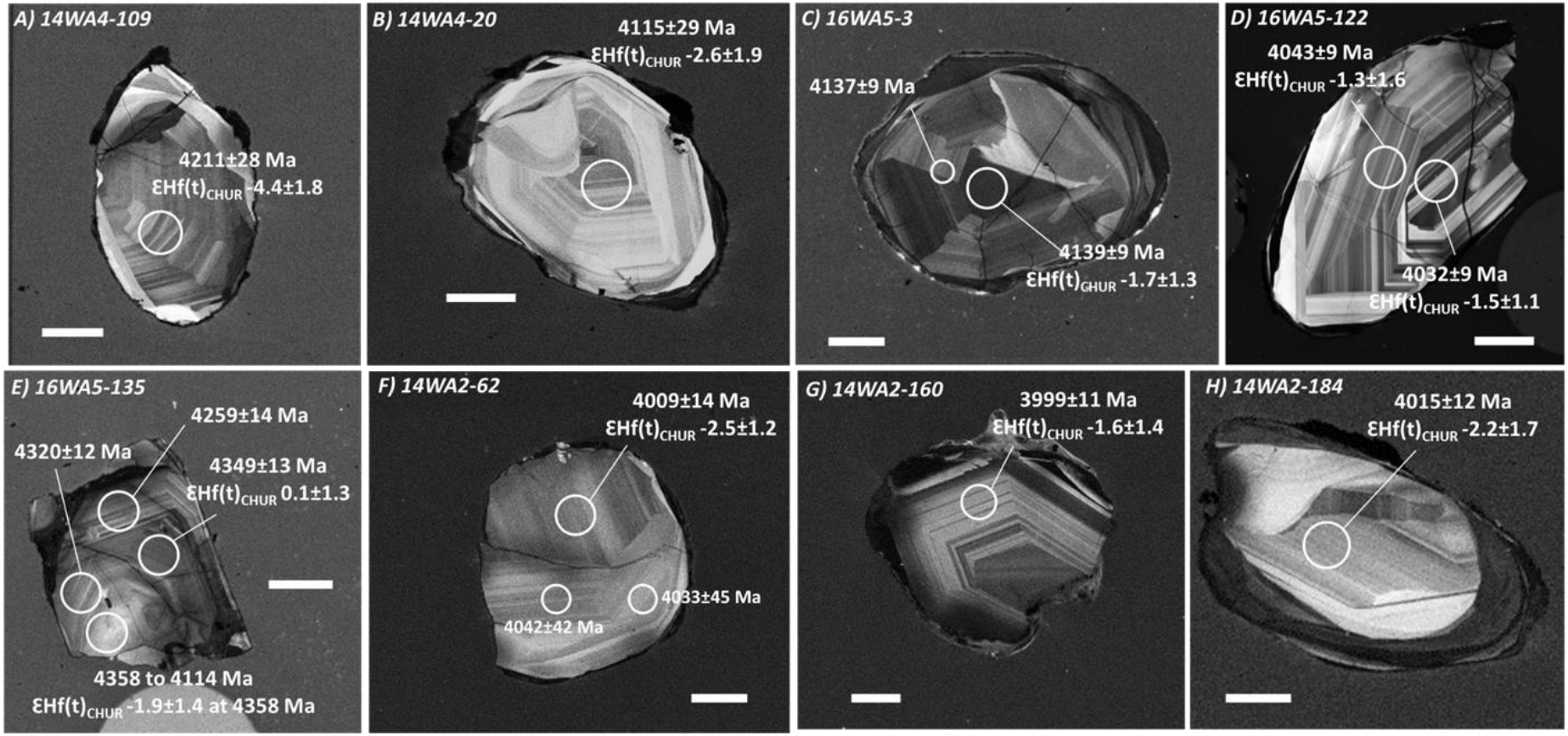

Figure 5.3: CL images of examples of Jack Hills Hadean detrital zircons from this study. These zircons have been filtered for oscillatory zoning to be included in the oscillatory zoned subset. White arrows show the magmatic or metamorphic rims that are ubiquitous on Hadean grains at Jack Hills. Grains with larger uncertainties in F) are from the preliminary session in February 2017. Scale bars 50 µm. U-Pb analysis spots 20 µm, Hf spots 35µm: where only ^{207}Pb-^{206}Pb ages are shown the 20 µm ablation pit was centred in the selected 35µm spot size.

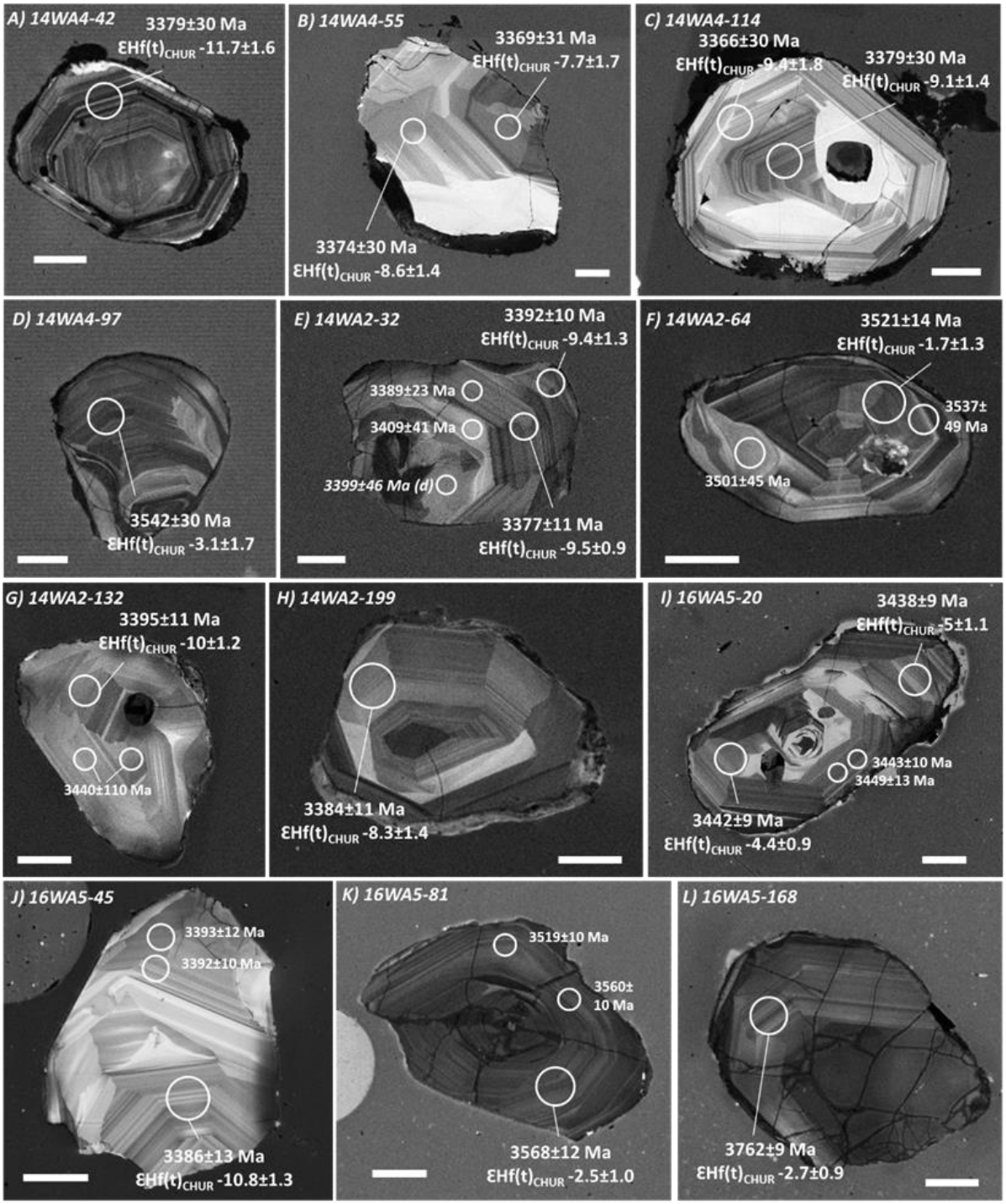

Figure 5.4: CL images of examples of oscillatory zoned Archean detrital zircons. Note the absence of ubiquitous rims observed within Hadean grains in most samples. As with Hadean grains, preliminary analyses from February 2017 are also included in E), F) and G). Scale bars 50 µm. U-Pb analysis spots 20 µm, Hf spots 35µm: where only ^{207}Pb-^{206}Pb ages are shown the 20 µm ablation pit was centred in the selected 35µm spot.

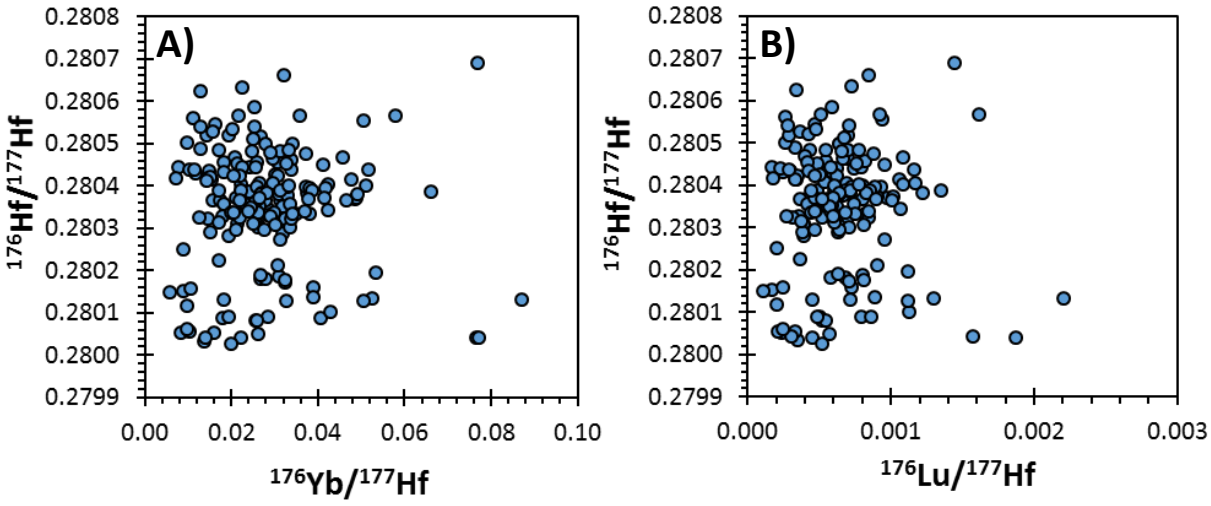

Figure 5.5: Absence of a correlation between **A)** $^{176}Yb/^{177}Hf$ and $^{176}Hf/^{177}Hf$ and **B)** $^{176}Lu/^{177}Hf$ and $^{176}Hf/^{177}Hf$, suggesting the correction for the isobaric interference on mass 176 is robust.

5.3 Results

5.3.1. Zircon U-Pb

We report 406 new LA-ICP-MS U-Pb analyses for 306 Jack Hills zircons from the W-74 'discovery site' (Wilde et al., 2001), with the full data set, including discordant grains not included in further analysis, available in Supplementary Material 6. Preliminary U-Pb analyses conducted in February 2017 with large uncertainties are included in some figures (e.g. 5.3 and 5.4) but are not discussed further in this chapter or provided within supplementary material. Sixteen zircons were rejected as they yielded greater than 10% discordance for ^{206}Pb-$^{238}U/^{207}Pb$-^{206}Pb or ^{207}Pb-$^{235}U/^{206}Pb$-^{238}U ages. Zircons with <10% discordance yield ^{207}Pb-^{206}Pb ages of between 3069±14 Ma to 4349±13 Ma (Figure 5.6), and therefore date from the Mesoarchean to early Hadean. No late Archean or Proterozoic zircons were encountered during this study, though zircons of this age have been reported from other localities at Jack Hills (Cavosie et al., 2004; Dunn et al., 2005; Wang and Wilde, 2018). Uranium concentrations range between 33 ppm and 442 ppm, and common Pb was negligible. 82% of zircons analysed in this study yielded ^{207}Pb-^{206}Pb ages between 3350 Ma and 3600 Ma.

Jack Hills zircons consistently yield a dominant age distribution peak at 3380-3400 Ma, which tails off to approximately 3600 Ma (Figure 5.7). We also observe more minor and heterogeneous age distribution peaks between different metasediment samples at ~3440 Ma, ~3470 Ma, ~3490 Ma and ~3520-3540 Ma. These age peaks are also present within kernel density estimate (KDE) plots (Supplementary Material 7). The dearth of zircon between 3700 Ma and 3900 Ma is also apparent within our data, with only 5 zircons (1.6 %) yielding ages between these two dates (Figure 5.7).

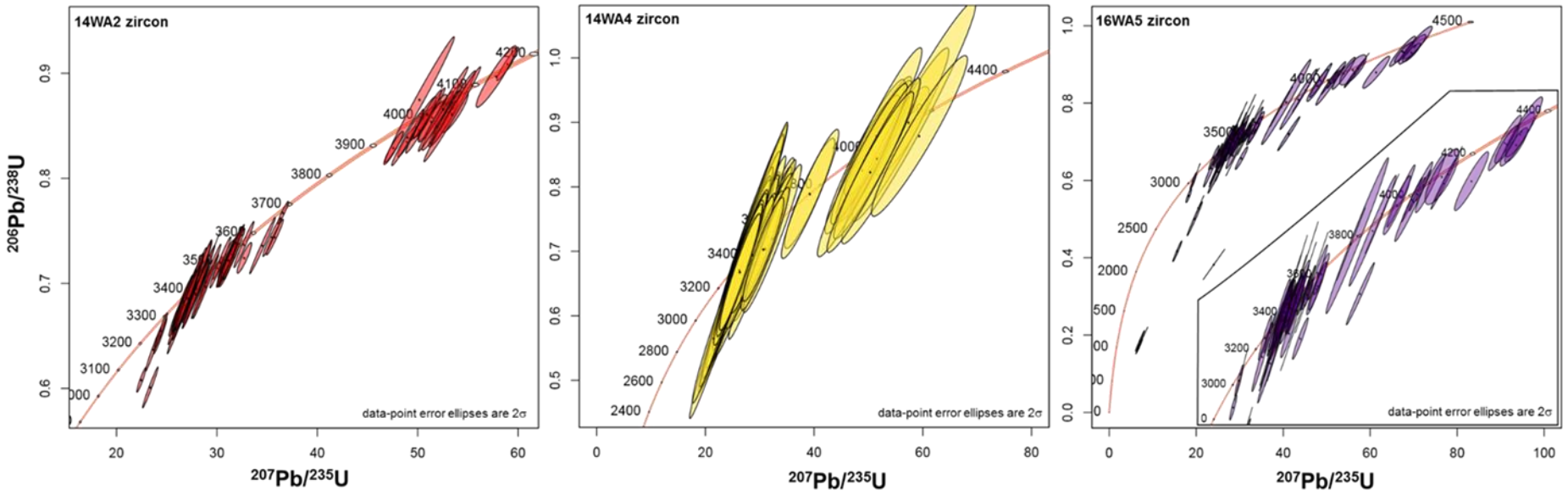

Figure 5.6: Wetherill U-Pb Concordia for detrital zircons from Jack Hills. No grains have been excluded for discordance, showing the concordant nature of analyses within this study. As 16WA5 shows the most discordant data points, an inset is provided for better observation of concordant analyses. This image also highlights that $^{206}Pb/^{238}U$ uncertainties are higher, particularly within 14WA4. This is a consequence of the measurement of ^{238}U using faraday cups rather than ion counters. Higher uncertainty of $^{206}Pb/^{238}U$ within 14WA4 reflected in the lower precision of the PRM during this analytical session (see Supplementary Material 5). Plot generated using IsoplotR (Vermeesch, 2018), all uncertainties 2se.

We also find zircons aged between 3600 Ma to 3700 Ma and 3900 Ma to 4000 Ma represent only a minor component of grains, with only 6 (2 %) and 7 (2.3 %) zircons within these age brackets, respectively. We encountered 33 Hadean zircons within this study, accounting for ~10% of total Jack Hills zircon analysed here, similar to the yield of Hadean grains in other studies from this site (e.g. Nebel et al., 2014). There is observed sample variability, with 14WA2 yielding 12%, 14WA4 11% and 16WA5 8% Hadean zircon in comparison to bulk sample zircon ages. 14WA3 and 16WA6 data, included in supplementary information, were not analysed in sufficient quantity to deduce the proportion of Hadean grains. Finally, we also observe a minor age distribution peak in Hadean zircons between 4000 and 4100 Ma, which tails off with increasing age (Figure 5.7). This peak is present in all samples and has been reported by numerous authors previously (e.g. Holden et al., 2009; Whitehouse et al., 2017a).

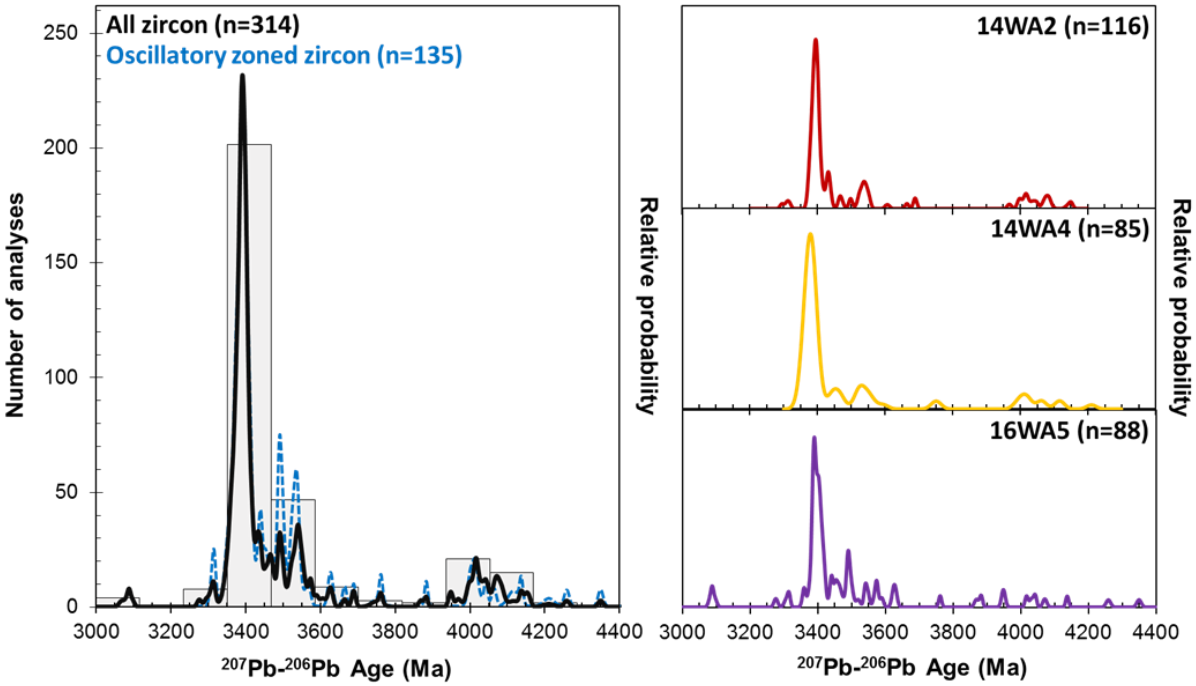

Figure 5.7: Relative probability of zircon age from **A)** All <10 % discordant analyses (including zircons from 14WA2, 14WA3, 14WA4 16WA5 and 16WA6), with 'bulk zircons' in black and those filtered for oscillatory zoning in blue. A single representative data point was used for zircons that possessed multiple ages within uncertainty of one another. 12 bins used for histogram. Relative probability for individual samples **B)** 14WA2, **C)** 14WA4, and **D)** 16WA5 also shown. Generated using Isoplot (Ludwug, 2003).

5.3.2. Zircon Lu-Hf

We also report the Lu-Hf compositions of a subset of zircon. One hundred and eighty two zircons previously analysed for U-Pb were analysed from 14WA2, 14WA4 and 16WA5, with a filtered dataset of 83 oscillatory zoned zircons also presented. The full Pb-Hf dataset for Jack Hills samples are available in Supplementary Material 10. Zircons yield $^{176}Hf/^{177}Hf$ ratios of 0.280026 to 0.280690 and low

$^{176}Lu/^{177}Hf$ ratios of 0.000108 to 0.002209, which, when integrated with ^{207}Pb-^{206}Pb ages, yield time-integrated $^{176}Hf/^{177}Hf(t)$ ratios of 0.279884 to 0.280605. This results in largely negative $\varepsilon Hf(t)_{CHUR}$ compositions of -16 to +4 for the bulk zircon dataset, and -13.5 to +0.1 for the oscillatory zoned zircon subset. Our data possess slightly higher uncertainties in comparison to some pre-existing literature due to the small ablation volumes and the propagation of analytical and systematic uncertainties. $^{176}Yb/^{177}Hf$ ratios range from 0.0058 to 0.0870, and were typically less than 0.04. These values are high in comparison to the PRM (Table 2.3), but well below the $^{176}Yb/^{177}Hf$ of doped solutions analysed prior to ablation. Furthermore, while the zircon standard commonly used for high $^{176}Yb/^{177}Hf$ correction is Temora ($^{176}Yb/^{177}Hf$ 0.032±15; Wu et al., 2006), VRM OG1 has comparable $^{176}Yb/^{177}Hf$ to sample unknowns (average $^{176}Yb/^{177}Hf$ 0.033, up to 0.075; Kemp et al., 2017). Critically, the weighted mean of $^{176}Hf/^{177}Hf$ obtained for VRM OG1 (0.280637±85) is indistinguishable from $^{176}Hf/^{177}Hf$ ratios previously determined by solution analysis (0.280633±34) and LA-ICP-MS (0.280560±20) by Kemp et al. (2017), indicating the robustness of the ^{176}Yb correction on sample unknown with similar $^{176}Yb/^{177}Hf$. Furthermore, there is no residual correlation between initial $^{176}Hf/^{177}Hf$ ratios and $^{176}Yb/^{177}Hf$ of sample unknowns (Figure 5.5a). This, coupled with the absence of a correlation between standard corrected $^{176}Hf/^{177}Hf$ and $^{176}Lu/^{177}Hf$ ratios (Figure 5.5b), again indicates the robustness of our Yb isobaric interference calculation.

Only two Jack Hills zircons analysed here yield superchondritic $\varepsilon Hf(t)$; 4142±16 Ma 14WA2-95 and 4086±11 Ma 14WA2-201. Neither yield the strong magmatic zoning required to be part of the filtered dataset. Five zircons yield chondritic or near chondritic $\varepsilon Hf(t)_{CHUR}$ values, with 3 of these included in the filtered dataset due to the presence of crisp oscillatory zoning. The remainder of zircons yield mildly to strongly subchondritic $\varepsilon Hf(t)_{CHUR}$ compositions, indicating they are derived from an enriched (Hf>Lu) crustal source. The ^{207}Pb-^{206}Pb age distribution peaks possess distinct, subchondritic Hf isotopic compositions that can differ by over 6 $\varepsilon Hf(t)_{CHUR}$ units in age distribution peaks less than 50 My apart (e.g. at 3380-3400 Ma and ~3440 Ma). This is particularly observed within oscillatory grains of 14WA2, and less strongly in 14WA4 and 16WA5. Age distributions peaks at 3380 Ma and ~3520 Ma also show variable $\varepsilon Hf(t)_{CHUR}$, with apparent vertical arrays in $\varepsilon Hf(t)_{CHUR}$ compositions present.

Table 5.1. Pb-Hf compositions of oscillatory zoned zircons

Sample		Ratios						Ages				Initial Hf		$\varepsilon Hf(t)_{CHUR}$		
Sample	Crystal #	$^{176}Yb/^{177}Hf$	2se	$^{176}Lu/^{177}Hf$	2se prop	$^{176}Hf/^{177}Hf$	2se prop	Disc %	^{207}Pb-^{206}Pb Age	2se	2se prop	$^{176}Hf/^{177}Hf$ $(t)_{SAMP}$	$^{176}Hf/^{177}Hf$ $(t)_{CHUR}$	$\varepsilon Hf(t)$	2se	2se sys
14WA2	19	0.042220	0.000330	0.001171	0.000033	0.280405	0.000035	0.2	3386	10	11	0.280329	0.280592	-9.40	1.33	1.33
14WA2	20	0.031410	0.000190	0.000798	0.000022	0.280367	0.000033	0.4	3397	10	12	0.280315	0.280585	-9.64	1.27	1.27
14WA2	21	0.015730	0.000290	0.000406	0.000014	0.280366	0.000036	0.5	3689	10	11	0.280337	0.280389	-1.87	1.37	1.38
14WA2	25	0.026790	0.000480	0.000699	0.000019	0.280518	0.000025	1.5	3523	11	12	0.280470	0.280501	-1.07	1.01	1.02
14WA2	26	0.026040	0.000330	0.000644	0.000017	0.280303	0.000030	1.2	3398	10	12	0.280261	0.280584	-11.52	1.17	1.18
14WA2	28	0.016250	0.000120	0.000469	0.000013	0.280545	0.000034	-0.1	3431	10	11	0.280514	0.280562	-1.72	1.30	1.30
14WA2	32	0.022450	0.000300	0.000617	0.000017	0.280373	0.000023	0.7	3377	11	12	0.280333	0.280598	-9.46	0.95	0.95
14WA2	39	0.018080	0.000890	0.000359	0.000010	0.280327	0.000023	1.4	3400	10	11	0.280303	0.280583	-9.96	0.94	0.95
14WA2	47	0.021320	0.000780	0.000392	0.000011	0.280310	0.000040	0.6	3497	10	11	0.280284	0.280518	-8.36	1.50	1.51
14WA2	62	0.038950	0.000170	0.000722	0.000048	0.280159	0.000031	0.5	4009	14	14	0.280103	0.280174	-2.52	1.24	1.25
14WA2	64	0.034010	0.000580	0.000638	0.000044	0.280499	0.000032	0.1	3521	14	15	0.280456	0.280502	-1.66	1.26	1.27
14WA2	85	0.014970	0.000590	0.000298	0.000020	0.280435	0.000036	1.6	3537	13	14	0.280415	0.280491	-2.73	1.39	1.39
14WA2	96	0.024100	0.000220	0.000486	0.000032	0.280387	0.000034	0.7	3399	14	15	0.280355	0.280584	-8.14	1.32	1.33
14WA2	104	0.027830	0.000590	0.000555	0.000037	0.280366	0.000036	1.8	3391	14	15	0.280330	0.280589	-9.24	1.38	1.39
14WA2	119	0.014680	0.000680	0.000315	0.000021	0.280323	0.000041	2.6	3388	14	15	0.280302	0.280591	-10.29	1.55	1.56
14WA2	125	0.026510	0.000900	0.000537	0.000036	0.280408	0.000053	2.3	3381	14	15	0.280373	0.280596	-7.93	1.96	1.96
14WA2	132	0.048500	0.001500	0.000975	0.000068	0.280369	0.000032	0.4	3395	11	12	0.280305	0.280586	-10.01	1.24	1.25
14WA2	135	0.038200	0.000490	0.000821	0.000055	0.280334	0.000034	-0.6	3400	12	13	0.280280	0.280583	-10.79	1.31	1.32
14WA2	137	0.041740	0.000510	0.000933	0.000064	0.280396	0.000044	1.7	3372	11	12	0.280335	0.280601	-9.48	1.64	1.65
14WA2	146	0.020090	0.000270	0.000474	0.000031	0.280533	0.000039	0.0	3436	11	12	0.280502	0.280559	-2.05	1.47	1.48
14WA2	149	0.025430	0.000720	0.000584	0.000040	0.280585	0.000041	2.7	3316	11	13	0.280548	0.280639	-3.24	1.54	1.55
14WA2	160	0.026610	0.000490	0.000581	0.000041	0.280181	0.000037	2.2	3999	11	12	0.280136	0.280180	-1.57	1.43	1.43
14WA2	169	0.027840	0.000410	0.000639	0.000044	0.280498	0.000042	0.6	3532	11	12	0.280454	0.280495	-1.44	1.58	1.58
14WA2	171	0.008830	0.000190	0.000168	0.000011	0.280152	0.000037	1.7	3995	11	12	0.280139	0.280183	-1.56	1.42	1.43
14WA2	174	0.037300	0.002400	0.000802	0.000063	0.280399	0.000043	1.6	3401	11	12	0.280346	0.280582	-8.40	1.61	1.61
14WA2	184	0.053300	0.001000	0.001118	0.000075	0.280196	0.000044	0.3	4015	12	12	0.280109	0.280170	-2.16	1.67	1.67
14WA2	188	0.015550	0.000160	0.000340	0.000023	0.280415	0.000043	0.6	3527	11	12	0.280392	0.280498	-3.78	1.61	1.61
14WA2	189	0.047700	0.001300	0.001060	0.000070	0.280415	0.000039	-0.1	3402	11	12	0.280345	0.280581	-8.41	1.48	1.48
14WA2	196	0.021260	0.000240	0.000485	0.000032	0.280452	0.000035	1.2	3536	11	12	0.280419	0.280492	-2.60	1.34	1.35
14WA2	197	0.018370	0.000500	0.000416	0.000028	0.280455	0.000037	0.4	3540	11	12	0.280427	0.280490	-2.25	1.41	1.41
14WA2	198	0.018340	0.000180	0.000430	0.000029	0.280433	0.000039	0.0	3388	12	13	0.280405	0.280591	-6.63	1.47	1.48
14WA2	199	0.029590	0.000620	0.000694	0.000046	0.280406	0.000036	0.8	3384	11	12	0.280361	0.280593	-8.29	1.37	1.38
14WA2	229	0.038700	0.001000	0.000853	0.000057	0.280388	0.000043	0.5	3386	11	12	0.280332	0.280593	-9.28	1.61	1.61
14WA2	237	0.021620	0.000280	0.000510	0.000034	0.280567	0.000043	0.8	3436	11	12	0.280533	0.280559	-0.91	1.61	1.61
14WA2	238	0.008996	0.000090	0.000204	0.000014	0.280251	0.000035	3.0	3665	11	12	0.280237	0.280406	-6.03	1.34	1.35

Sample	Crystal #	$^{176}Yb/^{177}Hf$	2se	$^{176}Lu/^{177}Hf$	2se prop	$^{176}Hf/^{177}Hf$	2se prop	Disc %	^{207}Pb-^{206}Pb Age	2se	2se prop	$^{176}Hf/^{177}Hf$ $(t)_{SAMP}$	$^{176}Hf/^{177}Hf$ $(t)_{CHUR}$	ƐHf(t)	2se	2se sys
14WA4	5	0.021920	0.000270	0.000521	0.000026	0.280325	0.000042	3.1	3382	30	30	0.280291	0.280595	-10.83	1.70	1.70
14WA4	11	0.026180	0.000770	0.000583	0.000027	0.280338	0.000047	8.3	3465	30	30	0.280299	0.280540	-8.58	1.86	1.86
14WA4	15	0.027880	0.000430	0.000683	0.000031	0.280181	0.000044	-0.1	4016	29	29	0.280128	0.280169	-1.46	1.77	1.77
14WA4	18	0.021900	0.001300	0.000500	0.000023	0.280425	0.000042	-2.0	3519	29	29	0.280391	0.280503	-4.01	1.70	1.70
14WA4	20	0.052490	0.000750	0.001302	0.000073	0.280134	0.000047	0.5	4115	29	29	0.280030	0.280102	-2.57	1.87	1.87
14WA4	41	0.021190	0.000410	0.000469	0.000023	0.280371	0.000050	0.1	3517	29	29	0.280339	0.280505	-5.90	1.96	1.96
14WA4	42	0.033700	0.001000	0.000841	0.000038	0.280323	0.000040	-0.2	3379	30	30	0.280268	0.280597	-11.71	1.63	1.63
14WA4	49	0.045600	0.001800	0.001081	0.000049	0.280467	0.000035	0.1	3367	30	30	0.280397	0.280605	-7.41	1.48	1.48
14WA4	51	0.034200	0.001000	0.000753	0.000033	0.280334	0.000041	-0.1	3371	30	30	0.280285	0.280602	-11.31	1.67	1.67
14WA4	55	0.041150	0.000390	0.000956	0.000051	0.280449	0.000042	0.9	3369	31	31	0.280387	0.280603	-7.71	1.71	1.71
14WA4	60	0.030760	0.000470	0.000905	0.000040	0.280212	0.000037	0.1	3753	29	29	0.280146	0.280346	-7.13	1.54	1.54
14WA4	67	0.022500	0.001700	0.000725	0.000050	0.280633	0.000041	1.6	3348	30	30	0.280586	0.280617	-1.11	1.67	1.67
14WA4	73	0.027020	0.000230	0.000832	0.000036	0.280382	0.000033	1.1	3375	30	30	0.280328	0.280600	-9.69	1.42	1.42
14WA4	75	0.025490	0.000450	0.000792	0.000034	0.280444	0.000037	1.6	3382	30	30	0.280392	0.280595	-7.23	1.54	1.54
14WA4	85	0.022120	0.000600	0.000686	0.000033	0.280388	0.000030	0.4	3372	30	30	0.280343	0.280602	-9.21	1.34	1.34
14WA4	86	0.057920	0.000420	0.001613	0.000073	0.280566	0.000033	1.6	3398	30	30	0.280460	0.280584	-4.41	1.41	1.41
14WA4	88	0.031160	0.000960	0.000953	0.000040	0.280272	0.000040	1.5	3392	29	29	0.280210	0.280588	-13.49	1.63	1.63
14WA4	89	0.042900	0.000990	0.001126	0.000041	0.280102	0.000037	1.1	4118	29	29	0.280012	0.280100	-3.13	1.55	1.55
14WA4	97	0.030640	0.000610	0.000815	0.000036	0.280457	0.000042	3.1	3542	30	30	0.280401	0.280488	-3.10	1.70	1.70
14WA4	98	0.022710	0.000810	0.000563	0.000022	0.280360	0.000035	2.7	3379	30	30	0.280323	0.280597	-9.75	1.48	1.48
14WA4	107	0.026850	0.000960	0.000638	0.000027	0.280380	0.000037	2.3	3389	31	31	0.280338	0.280591	-8.99	1.55	1.55
14WA4	108	0.031990	0.000430	0.000848	0.000039	0.280660	0.000030	3.6	3355	30	30	0.280605	0.280613	-0.27	1.33	1.33
14WA4	109	0.076500	0.001000	0.001576	0.000081	0.280043	0.000044	3.4	4211	28	28	0.279914	0.280037	-4.39	1.77	1.77
14WA4	114	0.031400	0.001100	0.000714	0.000032	0.280389	0.000033	2.4	3379	30	30	0.280342	0.280597	-9.07	1.42	1.42
14WA4	120	0.029500	0.001100	0.000668	0.000031	0.280464	0.000042	1.2	3549	29	29	0.280418	0.280483	-2.31	1.70	1.70
14WA4	122	0.020580	0.000590	0.000471	0.000028	0.280423	0.000040	-0.8	3375	30	30	0.280392	0.280600	-7.39	1.64	1.64
14WA4	124	0.031360	0.000920	0.000701	0.000032	0.280483	0.000036	2.2	3528	30	30	0.280435	0.280497	-2.21	1.52	1.52
14WA4	132	0.026470	0.000430	0.000600	0.000027	0.280371	0.000035	2.6	3383	31	31	0.280332	0.280594	-9.35	1.49	1.49
14WA4	146	0.029830	0.000810	0.000686	0.000031	0.280336	0.000048	2.9	3397	30	30	0.280291	0.280585	-10.47	1.89	1.89
16WA5	3	0.050500	0.001000	0.001117	0.000054	0.280128	0.000039	1.9	4139	9	9	0.280038	0.280086	-1.70	1.49	1.49
16WA5	11	0.037020	0.000740	0.000844	0.000038	0.280339	0.000036	0.2	3393	9	10	0.280284	0.280588	-10.83	1.36	1.37
16WA5	17	0.017020	0.000660	0.000439	0.000020	0.280388	0.000033	-0.1	3387	9	10	0.280359	0.280591	-8.27	1.26	1.27
16WA5	18	0.021860	0.000480	0.000515	0.000023	0.280367	0.000036	0.7	3456	9	10	0.280333	0.280546	-7.59	1.36	1.37
16WA5	20	0.037200	0.000510	0.000880	0.000040	0.280475	0.000034	0.1	3438	9	10	0.280417	0.280558	-5.03	1.30	1.30
16WA5	26	0.035770	0.000280	0.000924	0.000042	0.280567	0.000027	1.5	3441	8	10	0.280506	0.280555	-1.77	1.06	1.07
16WA5	31	0.011570	0.000086	0.000287	0.000013	0.280437	0.000034	0.8	3501	12	13	0.280418	0.280515	-3.49	1.31	1.32
16WA5	34	0.024990	0.000290	0.000609	0.000030	0.280311	0.000034	0.4	3412	12	13	0.280271	0.280575	-10.83	1.31	1.31
16WA5	40	0.012830	0.000350	0.000337	0.000015	0.280625	0.000034	-0.8	3359	12	13	0.280603	0.280610	-0.26	1.31	1.31

Sample	Crystal #	$^{176}Yb/^{177}Hf$	2se	$^{176}Lu/^{177}Hf$	2se prop[a]	$^{176}Hf/^{177}Hf$	2se prop[a]	Disc %	^{207}Pb-^{206}Pb Age	2se	2se prop	$^{176}Hf/^{177}Hf$ $(t)_{SAMP}$	$^{176}Hf/^{177}Hf$ $(t)_{CHUR}$	ƐHf(t)	2se	2se sys
16WA5	45	0.029050	0.000320	0.000598	0.000029	0.280327	0.000038	1.3	3393	12	13	0.280288	0.280588	-10.68	1.44	1.45
16WA5	81	0.032610	0.000470	0.000757	0.000030	0.280452	0.000030	2.1	3568	12	13	0.280400	0.280471	-2.52	1.18	1.19
16WA5	86	0.020570	0.000170	0.000471	0.000024	0.280337	0.000037	0.8	3455	12	13	0.280306	0.280547	-8.59	1.41	1.41
16WA5	122	0.032400	0.001200	0.000709	0.000033	0.280172	0.000034	0.6	4032	9	9	0.280117	0.280158	-1.48	1.31	1.31
16WA5	123	0.033260	0.000480	0.000776	0.000040	0.280401	0.000030	1.3	3488	8	10	0.280349	0.280524	-6.25	1.16	1.17
16WA5	130	0.051800	0.001100	0.001162	0.000056	0.280437	0.000039	-1.2	3490	8	10	0.280359	0.280523	-5.85	1.47	1.47
16WA5	131	0.049200	0.001400	0.001224	0.000054	0.280381	0.000041	3.2	3411	13	14	0.280301	0.280576	-9.82	1.55	1.55
16WA5	135	0.087000	0.001300	0.002209	0.000098	0.280132	0.000037	1.3	4349	13	13	0.279945	0.279943	0.08	1.46	1.46
16WA5	144	0.025040	0.000440	0.000677	0.000030	0.280512	0.000033	-0.1	3482	13	12	0.280467	0.280528	-2.19	1.28	1.28
16WA5	168	0.042400	0.000270	0.001068	0.000050	0.280343	0.000029	0.1	3762	9	10	0.280265	0.280340	-2.68	1.14	1.15

Table 5.1: Pb-Hf compsoitons of oscillatory zoned sub set of Jack Hills zircons. [a]ratios standard corrected and excess variance of PRM (91500) propagated into uncertainties. Discordance % is the discordance between ^{206}Pb-^{238}U and ^{207}Pb-^{206}Pb ages. The uncertainty on ƐHf(t) calculated using the equations of Ickert (2013) and, for 2se sys, incorporating the long-term systematic ^{207}Pb-^{206}Pb uncertainties. Initial Hf compositions of CHUR and samples calculated using the chondritic parameters of Bouvier et al. (2008) and the decay constant of Soderlund et al. (2004).

5.4. Discussion

5.4.1. Zircon U-Pb

^{207}Pb-^{206}Pb zircon age distributions

As expected, there is excellent agreement between the distribution of ^{207}Pb-^{206}Pb ages of 14WA and 16WA Jack Hills zircon and those published previously (e.g. Maas and McCulloch, 1991; Crowley et al., 2005; Holden et al., 2009), owing to their derivation from the W-74 site (Wilde et al., 2001). The dominant peak at 3380 Ma to 3400 Ma is thought to correspond with the age of the syenogranitic protoliths of the Dugel gneiss (e.g. Cavosie et al., 2004). The consistently low U concentrations (largely <250 ppm) of these samples has been suggested to instead represent the derivation of these zircon from more intermediate compositions, precluding the Dugel gneiss as a potential source (Crowley et al., 2005). However, the low U concentration of grains is likely to be an artefact of selective transport during extensive sedimentary processing: grains with higher U concentrations are likely to develop metamict textures (e.g. Corfu et al., 2003), making them easier to destroy during transport. Further arguments, such as the differences in internal zoning between Jack Hills and Dugel gneiss zircons (Crowley et al., 2005) and the predominance of the Dugel peak over Meeberrie age distributions, may be due to different metamorphic histories and variable detrital provenance, respectively. Zircons from the Dugel gneiss are particularly discordant (Kinny et al., 1988; Nutman et al., 1991), invoking significant recent Pb loss that likely modified primary igneous textures, suggesting that comparison between zonation textures are not robust. While the Meeberrie gneiss appears to be the dominant gneiss in the Narryer Terrane today, this is hard to determine without substantial geochronological analysis of granitic gneisses within the Narryer Terrane (e.g. Kemp et al., 2019). It is likely the dominance of the Dugel peak at the W-74 site may simply reflect localised sampling within the source of the Jack Hills sediments. Metasediments containing zircon with ^{207}Pb-^{206}Pb age distribution peaks more akin to the Meeberrie gneiss are reported at Mount Narryer to the SW and in the NE of the Jack Hills belt (Crowley et al., 2005; Dunn et al., 2005; Pidgeon and Nemchin, 2006). Due to these arguments, coupled with the consistency of the 3380-3400 Ma age distribution peak across all samples, this study favours the origin of 3380 Ma- 3400 Ma zircons from syenogranitic and monzogranitic protoliths of the Dugel gneiss, rather than an exotic source.

More minor and heterogeneous, but resolvable age distribution peaks at ~3440 Ma, ~3470 Ma, ~3490 Ma and ~3520 Ma to ~3540 Ma are also present (Figure 5.7), which have also been previously reported (e.g. Cavosie et al., 2004), and appear slightly under-represented when comparing oscillatory grains to bulk zircon data (Figure 5.7a). The 3440 Ma-3490 Ma age distribution peaks may correspond to protoliths of the Eurada gneiss (Nutman et al., 1991), which yields comparable, though complex, zircon

^{207}Pb-^{206}Pb ages of 3340 to 3390 Ma. A younger 3050 Ma Eurada component was also noted (Nutman et al., 1991), taken to represent pegmatite intrusion. This age component is also apparently present within detrital zircons at Jack Hills (Figure 5.7; Crowley et al., 2005): pegamtitic zircon should be easily distinguished by trace elements, so testing this suggestion is plausible. Wang and Wilde (2018) suggested these more minor age distribution peaks may represent derivation of zircon from the TTG and monzogranitic protoliths of the Meeberrie Gneiss. However, the Meeberrie gneiss yields resolvable zircon ^{207}Pb-^{206}Pb age distributions 3730 Ma, ~3670 Ma, 3620 Ma and 3600 Ma with more minor 3300 Ma components (Nutman et al., 1991; Kinny and Nutman, 1996; cf. Pidgeon and Wilde, 1998), requiring significant Pb-loss for the Meeberrie gneiss to represent the source of these grains. The consistency of peaks, particularly at 3470 Ma- 3490 Ma, suggests this is unlikely. Another suggested source for Archean Jack Hills zircons is the granitoids and granitic gneisses directly surrounding the Jack Hills belt (Pidgeon and Wilde, 1998; Kemp et al., 2010). Pidgeon and Wilde (1998) noted that a ~3500 Ma event may be present within this granitoids, suggesting a potential source for the two oldest minor peaks. However, it is important to note that apart from a single sample of the Eurada gneiss with inherited 3550 Ma zircons (Nutman et al., 1991) no currently known component of the Narryer Terrane yields a crystallisation age of ca. 3520 Ma to 3540 Ma. As such, the source of the 3520 Ma-3540 Ma distribution peak is unknown and may be exogenous to the Narryer Terrane. Further trace element analysis of such grains may also be of interest to determine if they are mafic in origin.

Like other authors, we find Hadean zircons are most abundant in a distinct ^{207}Pb-^{206}Pb age distribution peak of 4000 Ma- 4100 Ma, with the number of Hadeans zircon decreasing from ~4020 Ma towards our oldest grain at 4349±14 Ma. An age distribution peak at this time is well documented (Cavosie et al., 2004; Holden et al., 2009; Wang and Wilde, 2018; cf. Whitehouse et al., 2017a), but its source is unknown as no lithological units of this age are known to crop out within the Narryer Terrane, or indeed anywhere on Earth. An important feature of Jack Hills Hadean zircon is the presence of ubiquitous overgrowth rims which, though too fine to be studied here (Figure 5.4), have been shown to yield significantly younger ages (Holden et al., 2009; Nebel et al., 2014). Holden et al. (2009) did not find a single Hadean grain without overgrowths, indicating Hadean zircon underwent multiple igneous or metamorphic growth events. This suggests that Hadean crust may not have been directly exposed at the surface during deposition of the Jack Hills metasediments (Nebel et al., 2014; Cavosie et al., 2019), and Hadean grains studied here are rather an inherited component within eroded Archean granitoids, or grains eroded from older metasedimentary rocks. However, >3050 Ma granitoids with xenocrystic Hadean zircon remain elusive (Kemp et al., 2019).

Intragrain ^{207}Pb-^{206}Pb age variability and the effects of Pb loss

Another consequence of multiple episodes of magmatic and/or metamorphism is the observation that Hadean grains (particularly those >4100 Ma) yield complex intragrain ^{207}Pb-^{206}Pb ages (Kemp et al., 2010; Bellucci et al., 2017; Whitehouse et al., 2017a). This is exacerbated by ancient Pb loss or mobility, where Pb loss soon after the crystallisation of the zircon produces spuriously younger ^{207}Pb-^{206}Pb ages sub-parallel to the concordia. Recent work has shown that fluid- or magmatic-induced Pb mobility can also lead to spuriously old ages due to the formation of Pb nanospheres within zircons that have undergone UHT metamorphism (Kusiak et al., 2013; 2015; Whitehouse et al., 2017). Atom probe tomography (APT) analysis of grain J4.4 (Figure 1.7), arguably the best documented >4350 Ma grain, yielded Pb migration over just ~25 nm with the formation of Pb nano-clusters with $^{207}Pb/^{206}Pb$ ratios of 1.2±0.05 surrounded by homogeneous zircon with a $^{207}Pb/^{206}Pb$ ratio of 0.30± 0.05 (Valley et al., 2014; 2015). The APT needles yielded a bulk $^{207}Pb/^{206}Pb$ of 0.52±0.04, within uncertainty of the SIMS $^{207}Pb/^{206}Pb$ value, indicating that on the scale of in-situ analyses (either SIMS or LA-ICP-MS) magmatic ages of Hadean Jack Hills zircons should be robust (Valley et al., 2014; Cavosie et al., 2019). Recently, however, significant Pb mobility over large scale domains (~5 µm) was reported in a ca. 4277 Ma Jack Hills zircon (Ge et al., 2018). This zircon which yielded concordant ^{207}Pb-^{206}Pb SIMS 'ages' along recrystallisation fronts up to 200 My older than the bulk crystal, with the oldest apparent age (4486±17 Ma) predating silicate differentiation. Overlap of LA- or SIMS pits with such domains would lead to spuriously old ages. Furthermore, Ge et al. (2018) noted that ~14% of Hadean zircon within their study yielded domains enriched in Pb, suggesting Pb mobility may be abundant within Jack Hills zircon and therefore a real concern for the derivation of robust ^{207}Pb-^{206}Pb ages, particularly within lower volume SIMS pits.

We also find complex intragrain ^{207}Pb-^{206}Pb ages within 16WA5-135 (Figure 5.8), the oldest zircon analysed here (Figure 5.3e) and an exceedingly rare example of a >4300 Ma magmatically zoned Jack Hill zircon (e.g. Cavosie et al., 2019). The complexity of intragrain ages within 16WA5-135 is exemplified within a single U-Pb analysis of the texturally cloudy core (Figure 5.3e) that yields variable within-ablation, near-concordant ^{207}Pb-^{206}Pb ages between 4358±12 Ma and 4114±21 Ma. To counter such large intragrain variations in ^{207}Pb-^{206}Pb ages within Hadean grains (e.g. Holden et al., 2009), it has been suggested that only grains with multiple consistent and concordant ^{207}Pb-^{206}Pb ages should be taken forward for further analyses (Whitehouse et al., 2017a). Within zircon 16WA5-135, this study finds that 2 portions of the core analysis produce ^{207}Pb-^{206}Pb ages within uncertainty of the 'best spot' ^{207}Pb-^{206}Pb age of 4349±13 Ma, which we interpret as the crystallisation age of this grain. The outer, finely zoned domain yields a distinct <4300 Ma age, indicating 16WA5-135 formed a younger overgrowth in at least one recycling event. The 'best spot' represents the point originally chosen on

the grain for analysis due to its oscillatory zoning and optically clear nature, indicating selection for these features represents a robust mechanism of elucidating the primary crystallisation age of the zircon. This is also apparent in a growing body of literature, where oscillatory zoned Hadean examples yield the least ^{207}Pb-^{206}Pb variability (e.g. JH14-40- Nemchin et al., 2006; Kemp et al., 2010; 01JH36-69- Valley et at al., 2014; Grain A32- Bellucci et al., 2017). This study therefore agrees with Whitehouse et al. (2017a)'s recommendation for multiple U-Pb analyses of zircons prior to Hf analysis, though notes that pre-filtering for oscillatory zoned zircons improves the chance of deriving robust ^{207}Pb-^{206}Pb ages.

It is also important to note that while intra-grain variation is well documented for Hadean zircon (Cavosie et al., 2006; 2019; Nemchin et al., 2006; Whitehouse et al., 2017a), the effects of Pb mobility on the resultant ^{207}Pb-^{206}Pb ages of Jack Hills Archean zircons is unstudied. These zircons have also likely had a protracted magmatic and metamorphic history, indicating Pb mobility may also be a real and worrying aspect of <4000 Ma zircons. While detailed nano-scale analyses have not been undertaken, U-Pb analysis undertaken during this study suggests significant U-Pb intragrain variability is present in only a minor proportion of Archean zircons that yield complete or partial oscillatory zoning. This is particularly apparent within 16WA5, where large, clearly magmatic grains were chosen to test the veracity of measurements prior to continued runs of unknowns. All bar one (16WA5-81; Figure 5.4k) of these zircons yielded consistent ^{207}Pb-^{206}Pb ages across multiple days of ablation (Figure 5.9), with 16WA5-81 yielding consistent ^{207}Pb-^{206}Pb ages in 2 of 3 ablation spots (Figure 5.9e). This suggests that, while multiple U-Pb analyses are a prudent step for determining the true crystallisation age of Archean Jack Hills zircon, the U-Pb systematics do not appear to be as disturbed and heterogeneous as within Hadean grains.

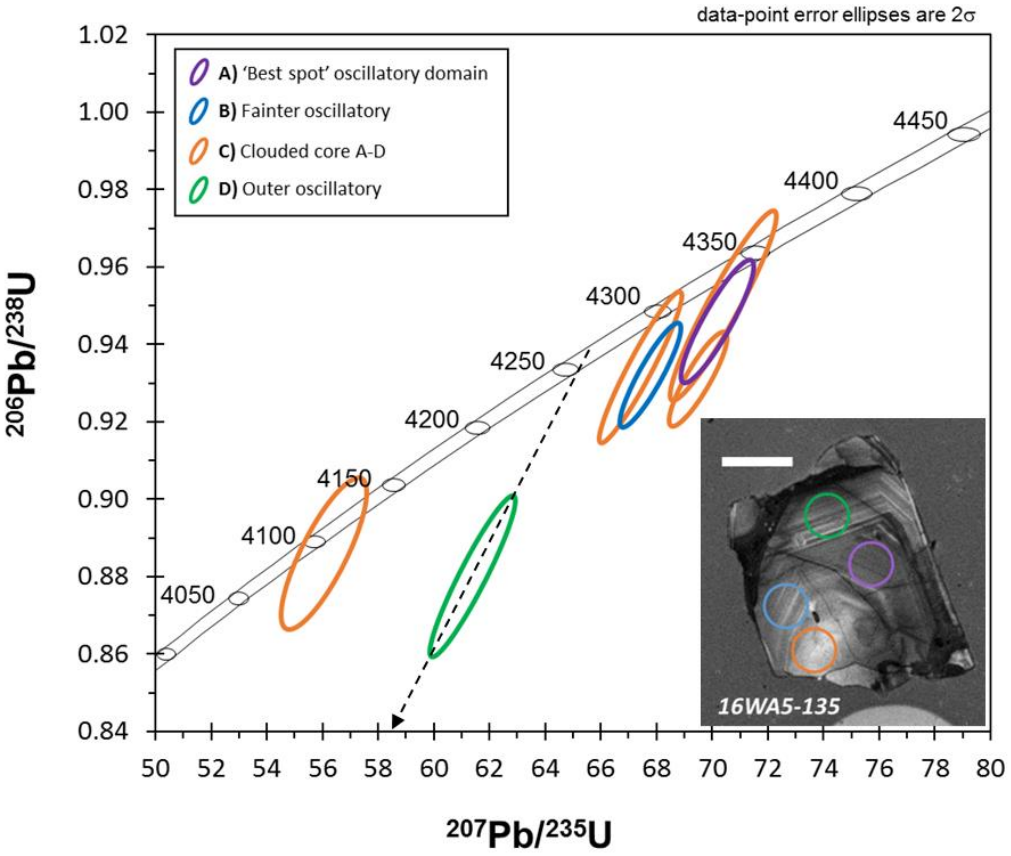

Figure 5.8: Wetherill concordia plot for grain 16WA5-135 colour coded for U-Pb spots, with locations of analyses shown in the inset CL image (scale bar 50 µm). The four orange analyses represent different portions of a single, 10 second ablation which has been split into four sections in Iolite (Paton et al., 2010). The clouded core shows apparent micron scale ^{207}Pb-^{206}Pb age variability, likely a function of ancient Pb loss due to the concordant nature of younger ages. While such data is challenging to interpret, the correlation of the 'best spot' and portions of the integration for the clouded core possess ages of ~4350 Ma, indicating this is the crystallisation age of the grain. The outer oscillatory rim shows evidence of recent Pb loss, though it is unclear if this domain represents new growth at ~4260 Ma or has undergone ancient Pb loss from ~4350 Ma. Generated using Isoplot (Ludwig, 2003).

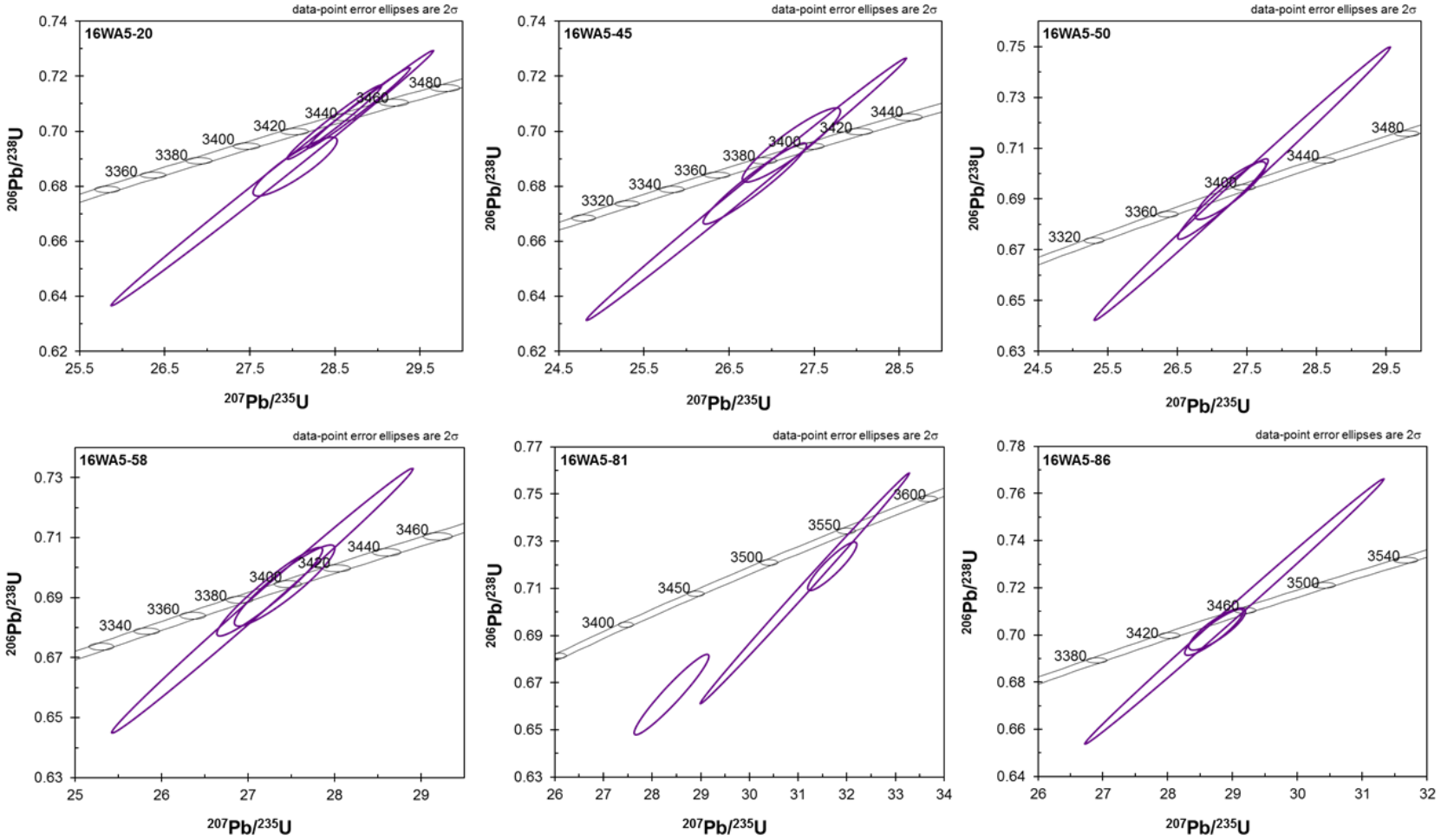

Figure 5.9: Wetherill concordia plots showing examples of some 16WA5 zircon with multiple U-Pb analyses. All examples bar 16WA5-81 (also shown in Figure 5.5k) show consistent U-Pb across multiple sessions: U uncertainties were unacceptable large on one day of measurement. Plots generated using Isoplot (Ludwig, 2003).

5.4.2. Zircon Pb-Hf

The Hf composition of Jack Hills zircons

The Jack Hills zircons studied here yield dominantly subchondritic $\varepsilon Hf(t)_{CHUR}$ compositions, indicative of the origin of the bulk of grains from an enriched (Hf>Lu), crustal reservoir. Subchondritic $\varepsilon Hf(t)_{CHUR}$ compositions of Jack Hills zircons are in good agreement with numerous other authors (Amelin et al., 1999; Harrison et al., 2008; Kemp et al., 2010; Bell et al., 2011; 2014; Wang and Wilde, 2018), and in contrast to some earlier studies (Harrison et al., 2005; Blichert-Toft and Albaréde, 2008). It is now largely accepted that Hadean superchondritic points are likely due to discrepancies between the conceived and true age of chronologically complex Hadean grains; placement of Hf ablations outside the domain measured for U-Pb (e.g. Harrison et al., 2005), drilling into younger overgrowths during ablation (Nebel et al., 2014), and incorrect age assignment due to ancient Pb loss (Valley et al., 2006; Kemp et al., 2010). We find only two data points within the 'bulk zircon' population that yield definitively superchondritic $\varepsilon Hf(t)_{CHUR}$ values, both of which are Hadean. 14WA2-95 possesses an age of 4142±16 Ma and $\varepsilon Hf(t)_{CHUR}$ +4, while 14WA2-201 yields an age of 4086±11 Ma and $\varepsilon Hf(t)_{CHUR}$ +0.6. The first of these sits well above the DM line at this time (Figure 5.10). This is clear evidence the Pb-Hf composition of this zircon is an analytical artefact, perhaps due to drilling into a younger age domain or due to ancient Pb mobility clouding the true age of the grain. This suggests that the second of these points may also represent an analytical artefact, but further U-Pb work may be useful to clarify this.

The starkly subchondritic nature of data is particularly apparent between the ages of 4400 Ma and 4100 Ma and between 3600 Ma and 3380 Ma (Figure 5.10), in agreement with almost all previous Pb-Hf studies of Jack Hills zircon (Amelin et al., 1999; Harrison et al., 2008; Kemp et al., 2010; Bell et al., 2011; 2014). This highlights the formation of these zircons without the direct involvement of a juvenile or DM reservoir. This does not preclude mantle-derived magmatic activity at these times but does suggest mantle-derived magmas were not involved as a magmatic component in the generation of the source of Jack Hills zircons (Kemp et al., 2010). However, a subtle shift towards more chondritic Hf compositions of zircons crystallised at 4000-4050 Ma has been previously noted by other studies (e.g. Kemp et al., 2010). This subtle shift towards more chondritic Hf compositions at 4000 Ma- 4100 Ma has been argued to represent juvenile input at this time by numerous authors (Kemp et al., 2010; Bell et al., 2011; 2014). Subsequent evolution of crust generated during this event can also be used to reconcile the compositions of more juvenile Archean zircons at 3500 Ma- 3600 Ma and ~3420 Ma (Figure 5.10) via reworking of mafic (Kemp et al., 2010) or felsic (Bell et al., 2011; 2014) crust extracted at this time. The possible composition and age of extraction of more juvenile Archean zircons observed within this study is discussed further in 5.4.3.

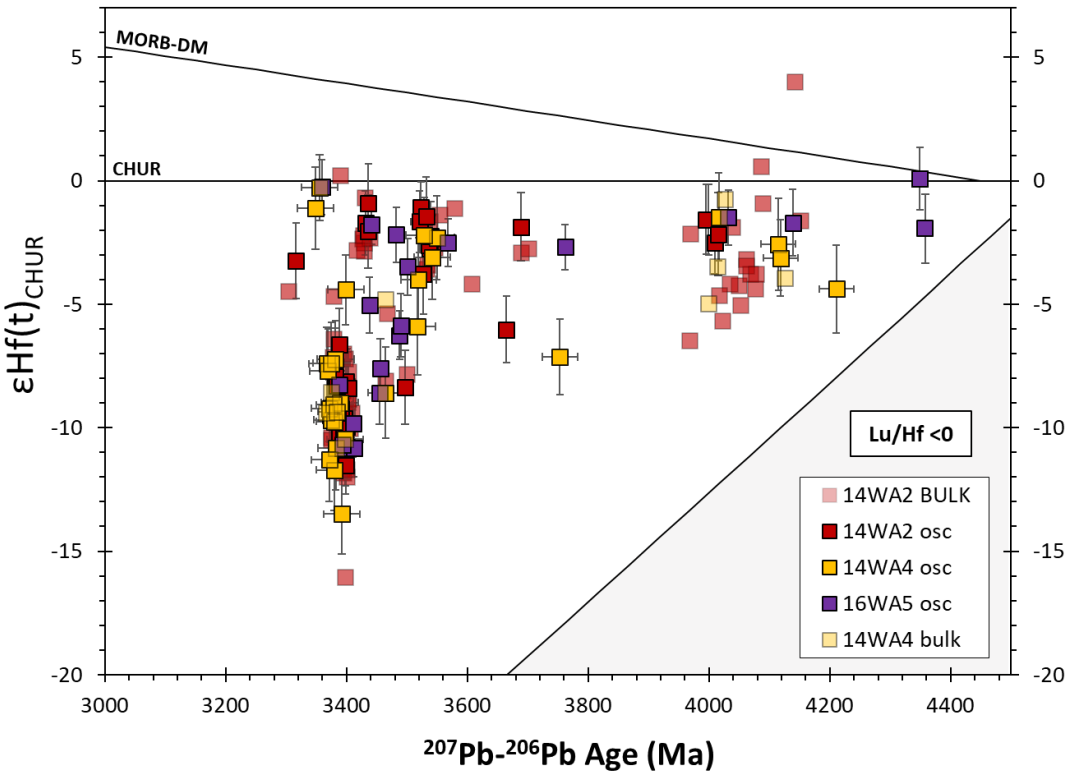

Figure 5.10: All Pb-Hf data points generated within this study. No error bars shown for bulk data, which is set as semi-transparent for easy comparison. All data calculated using the ^{176}Lu decay constant of Soderlund et al. (2004) and CHUR parameters of Bouvier et al. (2008). MORB-DM back calculated to 4450 Ma from a modern day $\varepsilon Hf(t)_{CHUR}$ of +16 (Vervoort and Kemp, 2016). Uncertainties calculated using the method of Ickert (2013).

'Bulk' zircon data is clearly more scattered than zircons with oscillatory zoning, particularly within the most heavily analysed sample, 14WA2 (Figure 5.10 and 5.11a). These analyses include crystals with patchy, altered, sector, homogeneous and faint oscillatory zonation: some of these textures may reflect either solid state recrystallisation or metamorphic induced elemental mobility, which can destroy primary oscillatory zoning (e.g. Whitehouse et al., 2017a). Despite this, bulk data from this study appears to yield far less scatter than many other studies. This is particularly apparent in comparison to large scale studies that output hundreds to thousands of datapoints, where careful characterisation of individual grains is clearly not as thorough. A recent example of this approach is Wang and Wilde (2018), who presented 1092 new Pb-Hf analyses for Jack Hills zircons (Figure 5.1c). Despite strikingly careful logging of sediments along atransect of Jack Hills, the only pre-filters these authors used was a <10 % discordance parameter and the retention of magmatic Th/U ratios of >0.1. The result are data that yield Pb-Hf compositions that fill almost all the space between DM and the impossible Lu/Hf <0 domain between the ages of 3350 Ma and 4400 Ma (Figure 5.1c). These authors suggested that zircons therefore represented derivation from diverse lithological types that were reworked with little juvenile input. However, this bulk approach is unhelpful as it clouds much of the

meaningful geological data, as is evidenced by the simpler Pb-Hf arrays determined by studies that prescribe stricter pre-screening filters (e.g. Kemp et al., 2010).

Two other more recent studies by Bell et al. (2011) and (2014) also yielded greater scattering of data in comparison to this work. These studies did report the zonation of their zircon but used large spot sizes (>60 μm) and indiscriminate ablation techniques. Indeed, Bell et al. (2014) stated that their sequence consisted of "15 cycles, or until the zircon was ablated through, with most analyses continuing for 10 or 11 cycles", which is particularly worrying in grains with multiple overgrowth domains. While these authors measured Pb-Hf concurrently (akin to Kemp et al., 2010) to monitor the ^{207}Pb-^{206}Pb age (though not discordance) during analysis, the significant decrease in spatial capability means that sampling of mixed domains, and therefore mixed ^{207}Pb-^{206}Pb ages, is a real possibility. We therefore take the decrease in scattered Pb-Hf compositions as the product of careful selection of optically clear areas, avoidance of clearly disturbed grains, and lower volume laser ablation.

The complex nature of many of these grains over small distances (<20 μm) is also evident from the most subchondritic $\varepsilon Hf(t)_{CHUR}$ point analysed. The Hf iteration for this analysis (14WA2-20), was divided into two when clear discrepancies in the ^{176}Hf/^{177}Hf ratio of the signal were observed. The splits of the iteration yielded $\varepsilon Hf(t)_{CHUR}$ compositions outside of uncertainty of one another of -9.6±1.6 and -16.1±3.2. The more subchondritic nature of the second point suggests that the laser drilled into material older than the ~3400 Ma ^{207}Pb-^{206}Pb age determined for this grain. The ^{176}Hf/^{177}Hf composition of this domain is more akin to ~3800 Ma to 4000 Ma zircon, though the age of this domain is hard to constrain without an additional U-Pb analysis. This therefore strongly suggests that the most strongly subchondritic data point is an analytical artefact, which alongside the two superchondritic points, has not been excluded from 'bulk' analysis to show the pitfalls of Pb-Hf work within these ancient, complex grains (Figure 5.10 and 5.11).

Pb-Hf of oscillatory zoned grains

While bulk zircons reveal significantly less scatter than other studies, it is still important to discuss only the most pristine, oscillatory zoned grains for Pb-Hf compositions when trying to understand crustal evolution (e.g. Kemp et al., 2019). Zircons from 14WA2 and 14WA4 yield very similar Pb-Hf compositions, though 14WA4 possesses significantly higher $\varepsilon Hf(t)_{CHUR}$ uncertainties due to propagation from the higher uncertainty ^{207}Pb-^{206}Pb ages for this sample (Figure 5.11b). 16WA5 zircons possess subtly different Pb-Hf compositions to 14WA2 and 14WA4, and at first glance appear similar to data derived by Bell et al. (2011), though at a significantly steeper angle (Figure 5.11c; 5.12a). This steep array however appears to be arbitrary, as it would plot along an impossible evolution with a ^{176}Lu/^{177}Hf ratio of <0. However, many Pb-Hf points of oscillatory zoned 16WA5 zircons do overlap

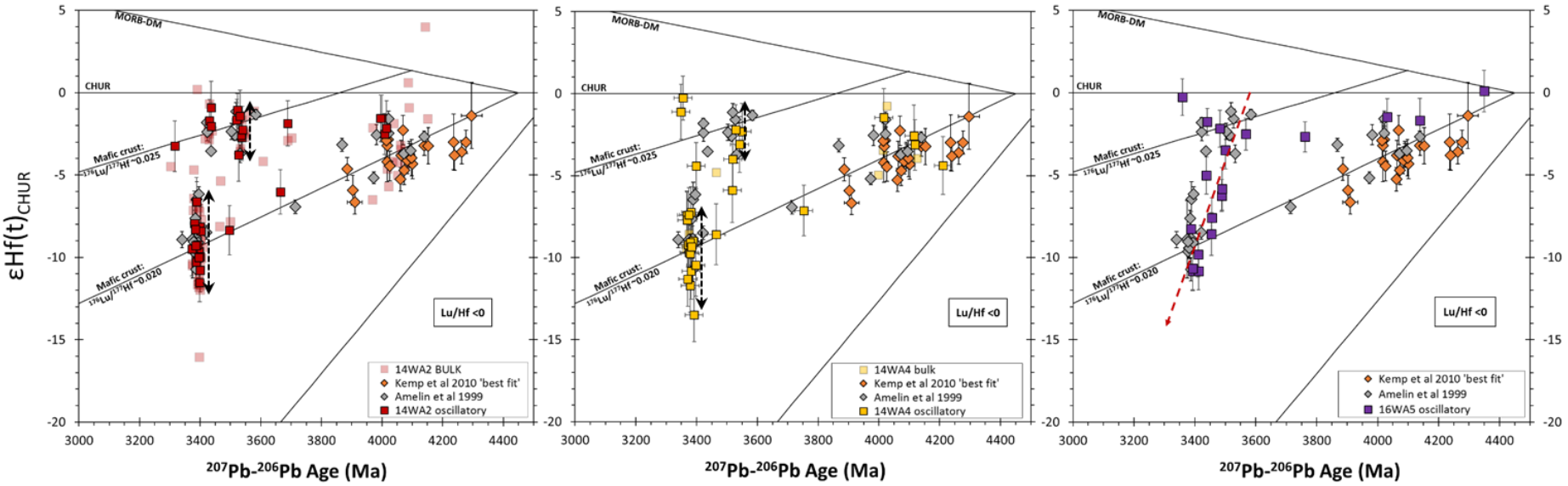

Figure 5.11: Pb-Hf data of individual samples in comparison to Amelin et al. (1999) and Kemp et al. (2010) Pb-Hf data, which has been recalculated using the ^{176}Lu decay constant of Soderlund et al. (2004) and CHUR parameters of Bouvier et al. (2008). Pb-Hf data for bulk and oscillatory zoned zircons from **A)** 14WA2, **B)** 14WA4, and **C)** oscillatory zoned grains from 16WA5. The arbitrary trend within 16WA5 shown by red dashed arrow. Potential vertical mixing arrays between 2+ sources shown by black arrows.

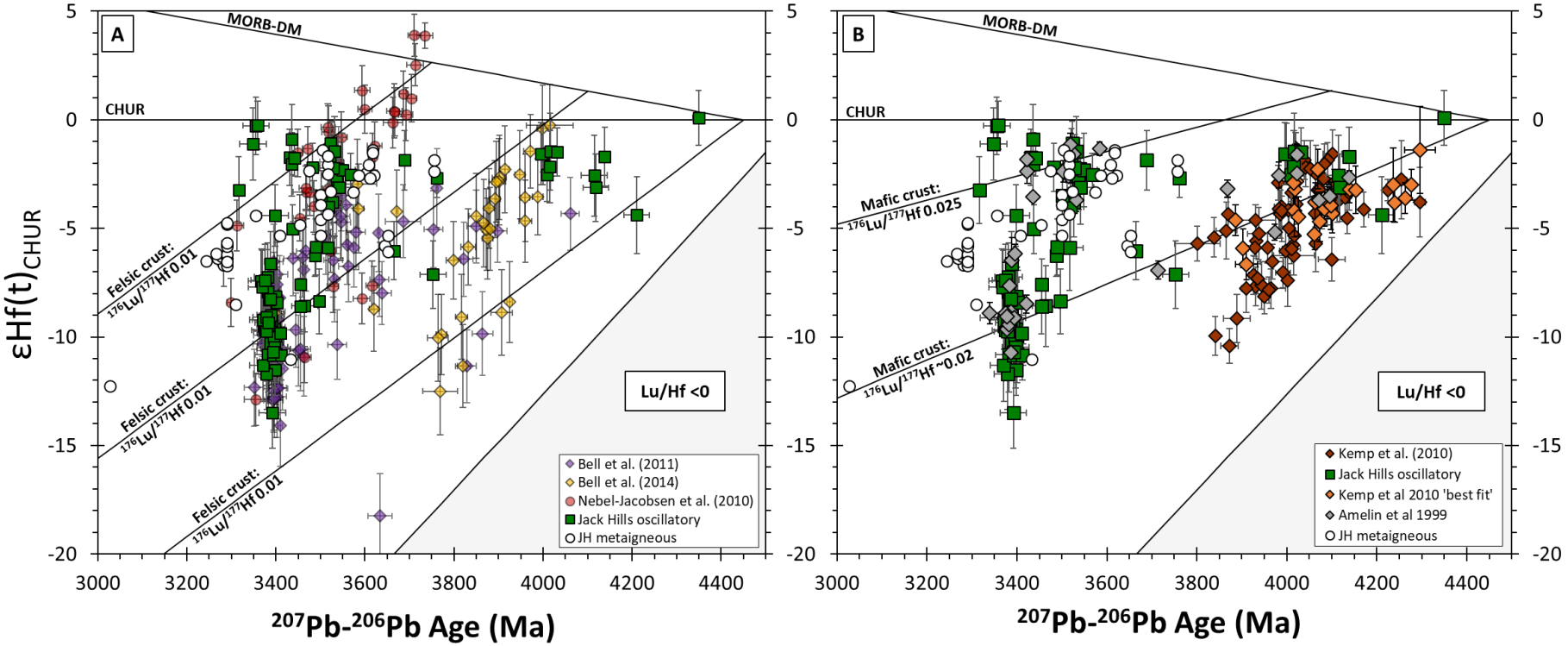

Figure 5.12: Comparison of Jack Hills oscillatory zircons analysed within this study in comparison to analyses used to testify for the two geodynamic regime inferred for Jack Hills. Only analyses with <2 2se $\varepsilon Hf(t)_{CHUR}$ uncertainties included for ease of viewing. No analyses were therefore omitted from this dataset, and that of Amelin et al. (1999) and Nebel-Jacobsen et al. (2010). Only a small number of analyses were lost from the datasets of Kemp et al. (2010) and Bell et al. (2011). However, ~25% of datapoints were omitted from Bell et al. (2014). **A)** Jack Hills oscillatory zoned zircons in comparison to data used to argue for modern-style plate tectonics, including data from Nebel-Jacobsen et al. (2010- Mount Narryer), Bell et al. (2011) and Bell et al. (2014). **B)** Jack Hills oscillatory zoned zircons in comparison to data used to argue for internal reworking within a stagnant lid regime, including data from Amelin et al. (1999) and Kemp et al. (2010). We suggest Jack Hills oscillatory data best fit internal reworking of long-lived mafic reservoirs, more applicable to graph B.

with those from 14WA2 and 14WA4, with only more intermediate compositions apparently sufficiently dissimilar (Figure 5.11c). This therefore suggests 16WA5 zircons are simply sampled from slightly different zircon-bearing sources than 14WA2 and 14WA4.

Archean 14WA2 oscillatory zoned zircon fit within uncertainty of the two mafic crustal evolution lines ($^{176}Lu/^{177}Hf$ ~0.02) defined by Kemp et al. (2010), with mantle extraction at ~4450 Ma and 4000 Ma-4100 Ma. Hadean oscillatory zoned zircon (n=3) plot within the minor shift towards more chondritic Hf compositions (Kemp et al., 2010), as do all oscillatory zoned zircon with ages between 3950 Ma and 4050 Ma in this study (Figure 5.11; Figure 5.12b). This may be an analytical artefact rather than a true representation of late Hadean zircon Hf compositions due to the low number of analyses across all samples (n=6). Of greatest interest within Archean zircon is the apparent oscillation in Hf composition between different crustal protoliths between 3600 Ma and 3350 Ma. The Kemp et al. (2010) 4400 Ma mafic crustal evolution array can account for 14WA2 zircon aged ~3660 Ma, ~3480 Ma and 3380-3400 Ma, while the Kemp et al. (2010) 4000-4100 Ma mafic crustal evolution line can account for zircon age populations at 3520 Ma, 3440 Ma and 3300 Ma. Fluctuations between these two lines (Figure 5.11a) is hard to reconcile with reworking of felsic crust (Figure 5.12a) and fits more strongly with reworking of a mafic crustal reservoir.

If this is indeed within a stagnant lid regime, this would also suggest periodic lower crustal partial melting of multiple sources for above ~200 Myr. Putatively, this may allude to a long-lived plume event, as observed in granite-greenstone and dome-and-keel terranes of similar age (e.g. Pilbara; Smithies et al., 2005), from which pulses of magmatic activity (over ~≥10 Myr for >100 Myr) induced partial melting of the lower crust to form zircon-bearing melts. Different crustal sources may represent different crustal depths of melting of a chronologically stratified crust (e.g. Kamber et al., 2005). Alternatively, refertilisation of mantle sources by dense eclogitic restites from initial plume activity may show similar features within detrital zircon (e.g. Bédard, 2006). However, it is important to note that, owing to the <300 Myr age range of Archean zircons, a regression could not be applied, and therefore formation of zircons by reworking of felsic crust not fully discounted.

It is also apparent that oscillatory grains from 14WA4 plot with good agreement to 14WA2 (Figure 5.11b). One Hadean grain falls off the Kemp et al. (2010) mafic protocrust line (Figure 5.11b), indicating either a more evolved source or ancient Pb loss. Upon closer inspection of oscillatory lamellae, this grain (14WA4-109) possesses a slight blurring of zonation, indicating the latter option may be possible. This is also potentially shown by the similar $^{176}Hf/^{177}Hf(t)$ of this grain to 16WA5-135, a ca. 4350 Ma zircon within 16WA5 (Figure 5.8; Figure 5.13). However, as this sample is represented by a single Pb-Hf analysis, it cannot be verified whether this zircon plots on a Pb-loss trajectory (Figure 5.13).

However, this grain also corresponds with compositions of zircons of this age from Kemp et al. (2010), indicating this may be a real feature of grains this age (Figure 5.11b). Another feature of interest within 14WA4 zircon are two zircons that yield near-chondritic compositions at ca. 3350 Ma. Both of these analyses were undertaken on the outer margins of finely zoned zircons with a darker CL composition (see Supplementary Material 11), and therefore higher U concentration. While it is possible these data represent mixed analyses (with younger rims? See potential cross cutting rim on 14WA4-108; Supplementary Material 11) the consistency of these points, and a third within 16WA5, suggests this is instead evidence of juvenile input at ~3350 Ma.

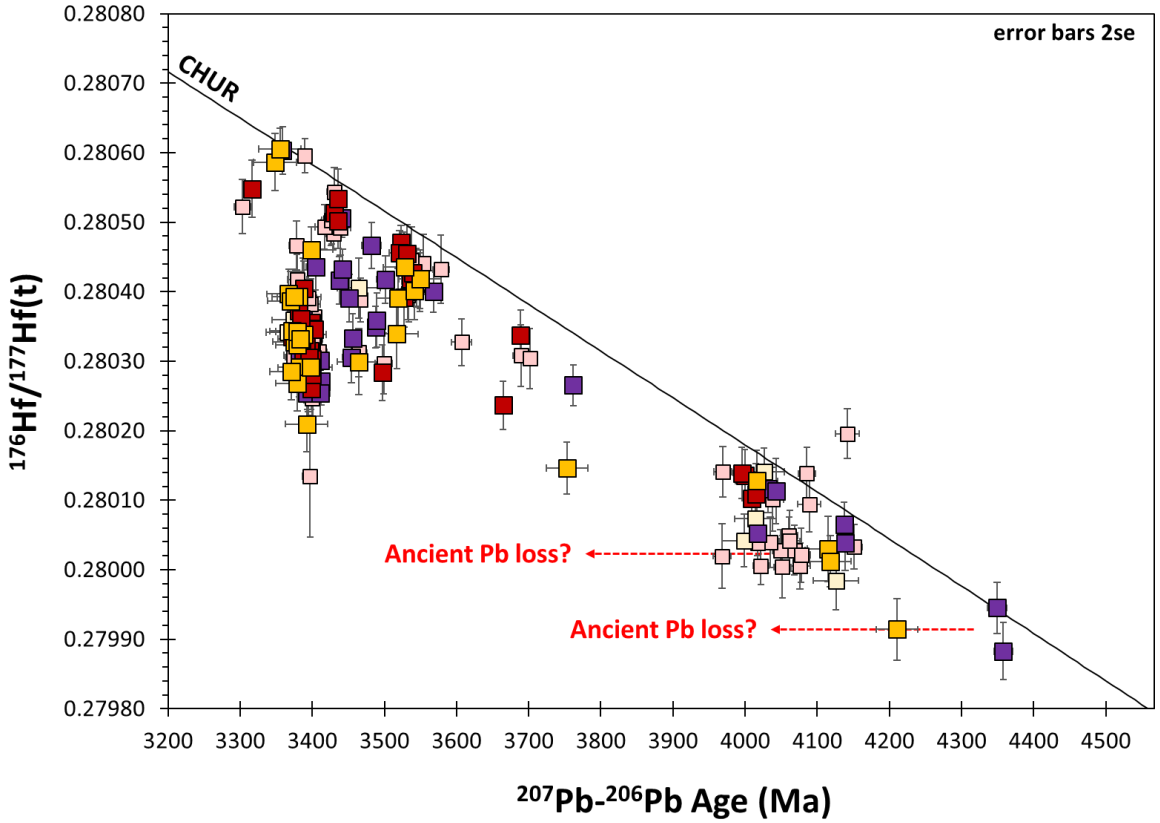

Figure 5.13: Time integrated $^{176}Hf/^{177}Hf(t)$ values of zircon measured within this study. Sample colours same as previous figures. Ancient Pb loss results in horizontal arrays in such plots (Vervoort and Kemp, 2016), and two possible examples of ancient Pb loss are shown by the black dashed arrows here. See Figure 5.10 for explanation of symbols.

As previously stated, Archean oscillatory zircons within 16WA5 arbitrarily appear to plot along an array of $^{176}Lu/^{177}Hf$ of <0, though all bar three Pb-Hf points are within uncertainty of the Amelin et al. (1999) data and the populations of 14WA2 and 14WA4. While 16WA5 grains do not show the strong relationship observed in 14WA2 and 14WA4 populations, they show similarities to the Pb-Hf compositions of Jack Hills metaigneous units (e.g. Figure 5.14) from Kemp et al. (2010). Similarities between $^{176}Lu/^{177}Hf$ and $^{176}Yb/^{177}Hf$ values for Jack Hills metaigneous and detrital zircons are also apparent in all samples, particularly at ca. 3500 Ma. Detrital zircons 16WA5-168 and 14WA2-238 also

overlap well with the Pb-Hf compositions of metaigneous zircons at ~3760 Ma and ~3665 Ma, respectively (Figure 5.14). This suggests 16WA5 data may be indicative of sampling of subtly different sources between the metasediment samples, despite the similar sampling locations of 14WA2 and 16WA5 (Figure 2.1).

Another individual grain worth discussing within 16WA5 is the most ancient zircon analysed here: 16WA5-135. The two Hf measurements undertaken on this zircon are only just within uncertainty of one another, highlighting the possibility that one analysis pit may have drilled into younger zircon to produce the apparently more radiogenic data point. However, looking at the time-resolved analysis data, both Hf analyses showed no evidence of this, with smooth ratio profiles suggesting no deviation of isotopic composition during analysis. This may be analytical: the two points are within uncertainty, overlapping on the Kemp et al. (2010) crustal evolution line. While both analyses possess amongst the highest $^{176}Yb/^{177}Hf$ ratios (0.077-0.087) recorded within this study, Yb correction at these $^{176}Yb/^{177}Hf$ ratios should be perfectly achievable. The Pb-Hf composition from the most pristine area is therefore taken as the true Hf composition of this grain, though it appears to be more radiogenic than the Hf isotopic composition of the clouded core.

To conclude, oscillatory zoned zircons from 14WA2, 14WA4 and 16WA5 produce distinctly less scattered arrays than both bulk data (Figure 5.10 and 5.11) and most previous analyses of Archean Jack Hills zircons (Bell et al., 2011; 2014; Wang and Wilde, 2018). These analyses, particularly of zircons from 14WA2 (Figure 5.11a), overlap within uncertainty of the data of Amelin et al. (1999) and the two crustal evolution lines of Kemp et al. (2010). Data arrays do not support the steeper, more evolved crustal evolution lines of Bell et al. (2011) and (2014). This study highlights the importance of filtering Jack Hills detrital zircons for magmatic features, particularly oscillatory zoning (Kemp et al., 2010; Whitehouse et al., 2017a), prior to Pb-Hf analyses. Only then can the most robust data on Hadean and Archean crustal evolution be determined.

5.4.3. Crustal reworking arrays and the problem of DM.

Coupled Pb-Hf analyses of zircons within this study fit well with the two crustal evolution arrays determined by Kemp et al. (2010), suggesting recycling of mafic crust extracted from mantle reservoirs at ~4450 Ma and ~4100 Ma. However, despite the good fit of data with the evolution of ~4100 Ma mafic crust, this event requires extraction from DM (Figure 5.11). This is at odds with numerous, more recent publications that observe little evidence of a DM reservoir prior to ca. 3500 Ma (Fisher and Vervoort, 2018; Petersson et al., 2019, and references therein). Geological evidence therefore suggests that mafic crust at ~4000 Ma to ~4100 Ma would be extracted from CHUR, rather than DM. Using the $^{176}Lu/^{177}Hf$ ratio of ~0.02 to ~0.025 determined by Kemp et al. (2010), this crustal evolution

line cannot account for the compositions of many of the <3800 Ma zircons at Jack Hills when extracted from CHUR. The shallow trend of oscillatory zoned Archean zircons also shows grains cannot be reconciled by reworking crust with a $^{176}Lu/^{177}Hf \leq 0.018$, ruling out significant quantities of felsic crust within their source (cf. Bell et al., 2011; 2014). This strongly indicates a mafic source for more radiogenic Archean detrital zircons from Jack Hills.

Two scenarios are here presented for the derivation of more juvenile Archean Jack Hills zircons at ~3520 Ma, ~3440 Ma and ~3300 Ma that plot on apparent shallow array (e.g. Figure 5.11). Due to the low number of data clusters analysed, these analyses have not been linearly regressed, and so the goodness of fit to arrays has not been statistically tested. However, both scenarios may explain both the juvenile Archean zircons from the Jack Hills detrital record and metaigneous rocks from Jack Hills (Pidgeon and Wilde, 1998; Kemp et al., 2010). Pb-Hf data collected from other cratonic domains of similar age (e.g. Reimink et al., 2016; Bauer et al., 2017; Fisher and Vervoort, 2018; Chaudhuri et al., 2018) are not included here, but discussed in the final concluding chapter.

Scenario 1- mafic crustal generation at 3730 Ma

Radiogenic Archean detrital zircon may be explained by working of mafic crust ($^{176}Lu/^{177}Hf$ ~0.02-0.022) extracted from CHUR at 3730 Ma (Figure 5.14a) coincident with the age of the Manfred Complex (Kinny et al., 1988; Fletcher et al., 1988; Kemp et al., 2019). Further analyses of WR $^{176}Lu/^{177}Hf$ from the complex may confirm this hypothesis. It should however be noted that such an interpretation would require reworking of ~3730 Ma crust just 100 Myr after it's generation, suggesting rapid recycling of crust within the early Archean. Also of importance is that while mafic crust extracted from CHUR at ca. 4050 Ma cannot justify the most radiogenic Archean zircons, it may account for some of the more subtle features observed in the Jack Hills Pb-Hf record. This crustal evolution line (line B: $^{176}Lu/^{177}Hf$ ~0.02, Figure 5.14a) fits well with many of the Jack Hills metaigneous rocks (Pidgeon and Wilde, 1998; Kemp et al., 2010), but also appears to represent the lower and upper bounds of mixing arrays at ~3520 Ma and ~3380 Ma, respectively. This could suggest that while it did not represent a significant source component of many Archean detrital zircons, it contributed directly to zircon populations during reworking events at ~3520 Ma and ~3380 Ma.

Scenario 2: a late Hadean oceanic plateau

In the second hypothesis, juvenile Archean detrital zircons may be derived from reworking of ~4050 Ma crust with a significantly higher $^{176}Lu/^{177}Hf$ of ~0.028-0.030 (Figure 5.14b). While this seems signicantly elevated in comparison to the $^{176}Lu/^{177}Hf$ of ~0.02 proposed for reworking of mafic protocrust (Kemp et al., 2010), it is worth noting that numerous modern rocks possess $^{176}Lu/^{177}Hf$

values in excess of 0.025 (e.g. Blichert-Toft and Albarede, 2008). For example, while MORB typically possesses a $^{176}Lu/^{177}Hf$ of 0.025, oceanic plateaus yield a bimodal distribution of $^{176}Lu/^{177}Hf$ ~0.021 and ~0.031, with an average of ~0.029 (Blichert-Toft and Albarede, 2008). Higher $^{176}Lu/^{177}Hf$ ratios would be produced by loss of residual garnet during partial melting, as may be expected in a hotter Hadean mantle. Such a range in $^{176}Lu/^{177}Hf$ composition could account for radiogenic Archean detrital zircon and metaigneous rocks from at and around Jack Hills (Figure 5.14b). Critically, emplacement of mafic crust in thickened oceanic plateaus has been inferred for the early Earth (Willbold et al., 2009; Reimink et al., 2014; Kemp, 2018 etc), suggesting reworking of mafic crust with elevated $^{176}Lu/^{177}Hf$ is plausible. Derivation of more radiogenic Archean zircons from reworking of Hadean crust may also account for the ^{182}W excesses observed within many of the Archean lithologies within the Narryer Terrane (D. Stubbs, pers. com.), though care should be taken when extrapolating such interpretations to detrital records.

Further Pb-Hf analyses of detrital zircons from the NW of the Jack Hills belt and from Mount Narryer, which yield older age distribution peaks, may aid in the testing of these two hypotheses. Recent work on the 3730 Ma Manfred Complex has also suggested it represents a thickened oceanic plateau (Rowe, 2016; Kemp, 2018), and so the geodynamic implications of both scenarios are not dissimilar. Overall, it can be concluded that Hadean and least radiogenic Archean zircons are likely derived from reworking of long-lived (>1 Gyr), mafic crust, while more radiogenic Archean zircons may be explained by reworking of mafic crust extracted at either ~4050 Ma, or ~4050 Ma and ~3730 Ma. It is also important to note that the absence of direct overlap of many zircons and metaigneous zircons indicates that Jack Hills metaigneous rocks cannot account for the $\varepsilon Hf(t)_{CHUR}$ compositions of all Archean zircon, requiring more distal sources.

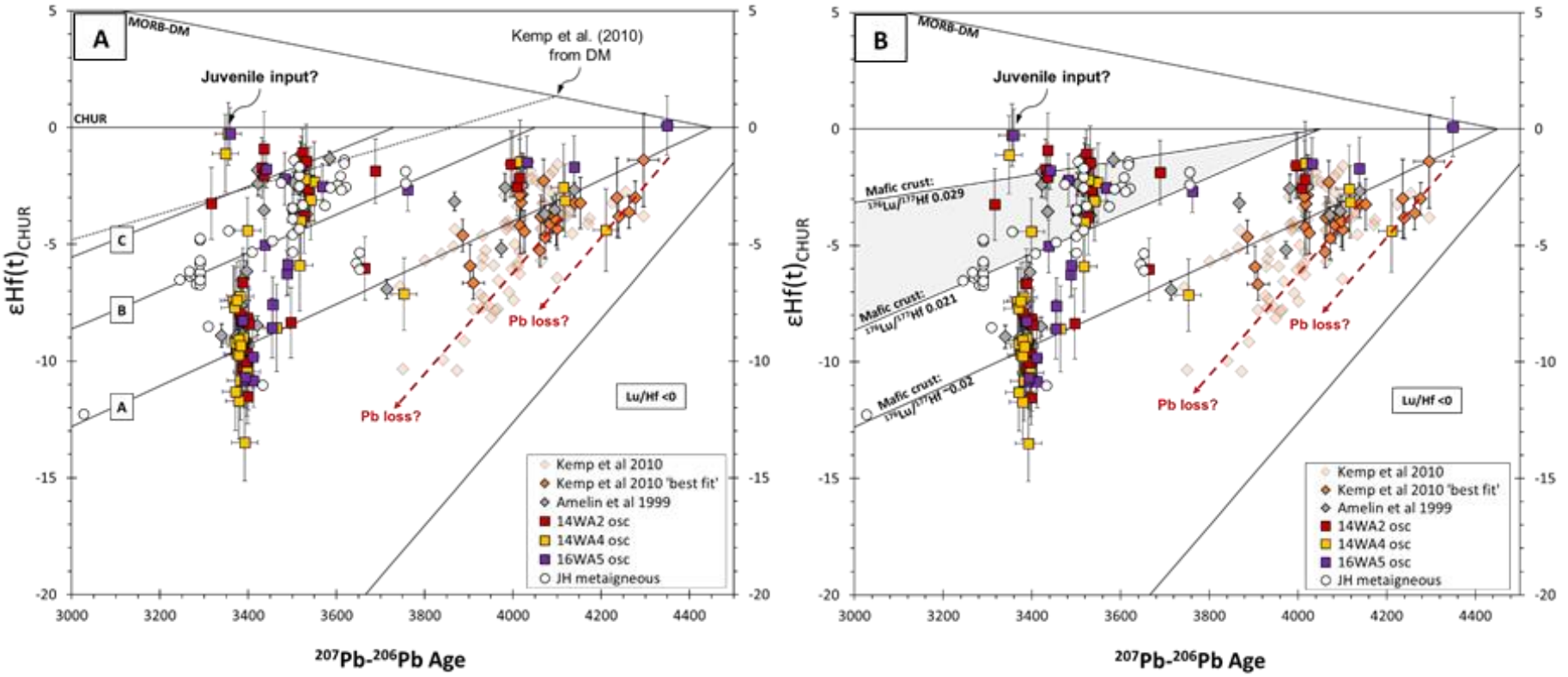

Figure 5.14: Two crustal evolution hypotheses to explain the compositions of more Archean detrital zircons from Jack Hills. **A)** Manfred Complex hypothesis: zircons derived from reworking of mafic crust ($^{176}Lu/^{177}Hf$ ~0.02) extracted from CHUR at ~4450 Ma (A), ~4050 Ma (B) and 3730 Ma (C). **B)** Oceanic plateau hypothesis: Zircons derived from reworking of mafic protocrust ($^{176}Lu/^{177}Hf$ ~0.02) and late Hadean (~4000 Ma to ~4100 Ma) mafic crust with variable $^{176}Lu/^{177}Hf$ of 0.021 to 0.029. Steep crustal arrays indicative of ancient Pb loss, rather than recycling of felsic crust. Juvenile input at ~3350 Ma also shown, as is the Kemp et al. (2010) ~4100 Ma mafic evolution line from DM. Jack Hills metaigneous data from Pidgeon and Wilde (1998) and Kemp et al. (2010).

5.5. Conclusions

Detrital zircons within metasediments at Jack Hills have been shown to predate the rock record by up to 350 Myr (Compston and Pidgeon, 1986; Wilde et al., 2001; Valley et al., 2014), though the nature of their magmatic source is intensely debated. Despite more robust Pb-Hf interpretations being derived from heavily filtered Hadean zircons (Kemp et al., 2010), few Archean zircons have been afforded the same treatment (Amelin et al., 1999; cf. Bell et al., 2011; 2014). This chapter detailed the coupled Pb-Hf composition of detrital grains from three metasediment samples (14WA2, 14WA4 and 16WA5), with both 'bulk zircons' and a subset of zircons filtered for magmatic oscillatory zoning presented. Detrital grains yield ^{207}Pb-^{206}Pb ages in good agreement with all other studies (e.g. Maas and McCulloch, 1991; Cavosie et al., 2004; Crowley et al., 2005; Holden et al., 2009 etc). This includes a dominant age distribution peak at 3380 Ma to 3400 Ma, tailing off until ~3600 Ma, and a minor age distribution peak within Hadean grains at 4000 Ma to 4100 Ma (Holden et al., 2009). While multiple spot analyses on Hadean grains show complex intra-grain age variability, only one Archean zircon analysed shows significant ^{207}Pb-^{206}Pb variability, indicating oscillatory zoned grains retain largely robust U-Pb compositions.

Bulk zircon Pb-Hf for 14WA2 results in scattered, but largely subchondritic $\varepsilon Hf(t)_{CHUR}$ values, showing derivation of Hadean and Archean grains from an enriched source with little direct input of juvenile reservoirs. When filtered for oscillatory zoning, 14WA2 zircons yield a simpler array in near perfect agreement with data derived from Amelin et al. (1999). Oscillatory zoned zircon from 14WA4 largely overlaps oscillatory zoned zircons from 14WA4, with minor juvenile input postulated by near-chondritic compositions at ~3350 Ma. 16WA5 zircons yield subtly different Pb-Hf compositions to those of 14WA2 and 14WA4, indicating some variability in source component. All zircon $\varepsilon Hf(t)_{CHUR}$ compositions can be reconciled by reworking of two or three mafic crustal reservoirs. The first of these is the Kemp et al. (2010) 4450 Ma mafic protocrust, with a $^{176}Lu/^{177}Hf$ composition of ~0.02. Reworking of this crust accounts for compositions of Hadean zircon, bar those that form the subtle shift in compositions at ~4000 Ma to ~4100 Ma, and groupings at ~3380 Ma and ~3460 Ma zircon. Reworking of either ~4050 Ma and ~3730 Ma crust with a $^{176}Lu/^{177}Hf$ of ~0.02, or ~4050 Ma crust with variable $^{176}Lu/^{177}Hf$ of 0.021-0.029 may account for the more radiogenic Archean zircon population. Juvenile input at ~3350 Ma is also inferred, though these zircon compositions may also be reconciled (within uncertainty) by reworking of mafic crust extracted from CHUR at or after ca. 3500 Ma.

While tectonic regime cannot be inferred from Pb-Hf data alone (e.g. Griffin et al., 2014), the more robust, magmatically zoned zircon record determined here enables clarification of the true Hf composition of Archean zircons at this time to facilitate further geodynamic analysis. The shallow

$\varepsilon Hf(t)_{CHUR}$ array of the most radiogenic Archean zircons precludes an origin via the recycling of felsic crust, as previously postulated (Nebel-Jacobsen et al., 2010; Bell et al., 2011; 2014). These data therefore favour recycling of long-lived mafic crust, with detrital zircons yielding very similar $\varepsilon Hf(t)_{CHUR}$ values to those derived by Amelin et al. (1999). This study therefore highlights the importance of careful pre-screening of grains for definitively magmatic features, such as oscillatory zoning and consistent ^{207}Pb-^{206}Pb ages, to deduce the most robust interpretations for crustal evolution from ancient zircons.

5.6. References

Amelin, Y., Lee, D. C., Halliday, A. N. & Pidgeon, R. T. (1999). Nature of the Earth's earliest crust from hafnium isotopes in single detrital zircons. *Nature* **399**, 252-255.

Arndt, N. T. (2013). The formation and evolution of the continental crust. *Geochemical Perspectives* **2**, 405-533.

Bauer, A. M. & Horstwood, M. S. A. (2018). Small-volume Lu-Hf and U-Pb isotope determination of complex zircons by solution and laser ablation MC-ICP-MS. *Chemical Geology* **476**, 85-99.

Bauer, A. M., Fisher, C. M., Vervoort, J. D. & Bowring, S. A. (2017). Coupled zircon Lu-Hf and U-Pb isotopic analyses of the oldest terrestrial crust, the > 4.03 Ga Acasta Gneiss Complex. *Earth and Planetary Science Letters* **458**, 37-48.

Bell, E. A., Boehnke, P., Hopkins-Wielicki, M. D. & Harrison, T. M. (2015). Distinguishing primary and secondary inclusion assemblages in Jack Hills zircons. *Lithos* **234**, 15-26.

Bell, E. A., Harrison, T. M., Kohl, I. E. & Young, E. D. (2014). Eoarchean crustal evolution of the Jack Hills zircon source and loss of Hadean crust. *Geochimica Et Cosmochimica Acta* **146**, 27-42.

Bell, E. A., Harrison, T. M., McCulloch, M. T. & Young, E. D. (2011). Early Archean crustal evolution of the Jack Hills Zircon source terrane inferred from Lu-Hf, Pb-207/Pb-206, and delta O-18 systematics of Jack Hills zircons. *Geochimica Et Cosmochimica Acta* **75**, 4816-4829.

Bellucci, J. J., Nemchin, A. A., Whitehouse, M. J., Kielman, R. B., Snape, J. F. & Pidgeon, R. T. (2018). Geochronology of Hadean zircon grains from the Jack Hills, Western Australia constrained by quantitative scanning ion imaging. *Chemical Geology* **476**, 469-480.

Blichert-Toft, J. & Albarede, F. (2008). Hafnium isotopes in Jack Hills zircons and the formation of the Hadean crust. *Earth and Planetary Science Letters* **265**, 686-702.

Blichert-Toft, J. (2008). The Hf isotopic composition of zircon reference material 91500. *Chemical Geology* **253**, 252-257.

Bouvier, A., Vervoort, J. D. & Patchett, P. J. (2008). The Lu-Hf and Sm-Nd isotopic composition of CHUR: Constraints from unequilibrated chondrites and implications for the bulk composition of terrestrial planets. *Earth and Planetary Science Letters* **273**, 48-57.

Cavosie, A. J., Valley., J. W., and Wilde., S. A. (2019). The Oldest Terrestrial Mineral Record: Thirty Years of Research on Hadean Zircon from Jack Hills, Western Australia. In: van Kranendonk, M. J., Bennett, V. C., and Hoffmann, J. E., (ed.) *Earth's Oldest Rocks*: Elsevier, 255-273.

Cavosie, A. J., Valley, J. W., Wilde, S. A. & Edinburgh Ion Microprobe, F. (2006). Correlated microanalysis of zircon: Trace element, delta O-18, and U-Th-Pb isotopic constraints on the igneous origin of complex > 3900 Ma detrital grains. *Geochimica Et Cosmochimica Acta* **70**, 5601-5616.

Cavosie, A. J., Wilde, S. A., Liu, D. Y., Weiblen, P. W. & Valley, J. W. (2004). Internal zoning and U-Th-Pb chemistry of Jack Hills detrital zircons: a mineral record of early Archean to Mesoproterozoic (4348-1576 Ma) magmatism. *Precambrian Research* **135**, 251-279.

Chaudhuri, T., Wan, Y., Mazumder, R., Ma, M. & Liu, D. (2018). Evidence of Enriched, Hadean Mantle Reservoir from 4.2-4.0 Ga zircon xenocrysts from Paleoarchean TTGs of the Singhbhum Craton, Eastern India. *Scientific Reports* **8**.

Compston, W. & Pidgeon, R. T. (1986). Jack Hills, evidence of more very old detrital zircons in Western Australia. *Nature* **321**, 766-769.

Corfu, F., Hanchar, J., Hoskin, P. & Kinny, P. (2003). Atlas of zircon textures. *Zircon* **53**, 469-500.

Crowley, J. L., Myers, J. S., Sylvester, P. J. & Cox, R. A. (2005). Detrital zircon from the Jack Hills and Mount Narryer, Western Australia: Evidence for diverse > 4.0 Ga source rocks. *Journal of Geology* **113**, 239-263.

Darling, J., Storey, C. & Hawkesworth, C. (2009). Impact melt sheet zircons and their implications for the Hadean crust. *Geology* **37**, 927-930.

Dunn, S. J., Nemchin, A. A., Cawood, P. A. & Pidgeon, R. T. (2005). Provenance record of the Jack Hills metasedimentary belt: Source of the Earth's oldest zircons. *Precambrian Research* **138**, 235-254.

Fisher, C. M. & Vervoort, J. D. (2018). Using the magmatic record to constrain the growth of continental crust-The Eoarchean zircon Hf record of Greenland. *Earth and Planetary Science Letters* **488**, 79-91.

Ge, R., Wilde, S., Nemchin, A., Whitehouse, M., Bellucci, J., Erickson, T., Frew, A. & Thern, E. (2018). A 4463 Ma apparent zircon age from the Jack Hills (Western Australia) resulting from ancient Pb mobilization. *Geology* **46**, 303-306.

Griffin, W. L., Belousova, E. A., O'Neill, C., O'Reilly, S. Y., Malkovets, V., Pearson, N. J., Spetsius, S. & Wilde, S. A. (2014). The world turns over: Hadean-Archean crust-mantle evolution. *Lithos* **189**, 2-15.

Harrison, T. M., Bell, E. A. & Boehnke, P. (2017). Hadean Zircon Petrochronology. *Petrochronology: Methods and Applications* **83**, 329.

Harrison, T. M., Schmitt, A. K., McCulloch, M. T. & Lovera, O. M. (2008). Early (>= 4.5 Ga) formation of terrestrial crust: Lu-Hf, delta O-18, and Ti thermometry results for Hadean zircons. *Earth and Planetary Science Letters* **268**, 476-486.

Harrison, T. M. & Schmitt, A. K. (2007). High sensitivity mapping of Ti distributions in Hadean zircons. *Earth and Planetary Science Letters* **261**, 9-19.

Harrison, T. M., Blichert-Toft, J., Muller, W., Albarede, F., Holden, P. & Mojzsis, S. J. (2005). Heterogeneous Hadean hafnium: Evidence of continental crust at 4.4 to 4.5 Ga. *Science* **310**, 1947-1950.

Holden, P., Lanc, P., Ireland, T. R., Harrison, T. M., Foster, J. J. & Bruce, Z. (2009). Mass-spectrometric mining of Hadean zircons by automated SHRIMP multi-collector and single-collector U/Pb zircon age dating: The first 100,000 grains. *International Journal of Mass Spectrometry* **286**, 53-63.

Hopkins, M., Harrison, T. M. & Manning, C. E. (2012). Metamorphic replacement of mineral inclusions in detrital zircon from Jack Hills, Australia: Implications for the Hadean Earth. *Geology* **40**, E281-E281.

Hopkins, M. D., Harrison, T. M. & Manning, C. E. (2010). Constraints on Hadean geodynamics from mineral inclusions in > 4 Ga zircons. *Earth and Planetary Science Letters* **298**, 367-376.

Hopkins, M., Harrison, T. M. & Manning, C. E. (2008). Low heat flow inferred from > 4 Gyr zircons suggests Hadean plate boundary interactions. *Nature* **456**, 493-496.

Horstwood, M. S. A., Kosler, J., Gehrels, G., Jackson, S. E., McLean, N. M., Paton, C., Pearson, N. J., Sircombe, K., Sylvester, P., Vermeesch, P., Bowring, J. F., Condon, D. J. & Schoene, B. (2016). Community-Derived Standards for LA-ICP-MS U-(Th-)Pb Geochronology - Uncertainty Propagation, Age Interpretation and Data Reporting. *Geostandards and Geoanalytical Research* **40**, 311-332.

Ickert, R. B. (2013). Algorithms for estimating uncertainties in initial radiogenic isotope ratios and model ages. *Chemical Geology* **340**, 131-138.

Kemp, A. I. S., Wilde, S. A., and Spaggiari, C. (2019). The Narryer Terrane, Yilgarn Craton, Western Australia: Review and Recent Developments. In: van Kranendonk, M. J., Bennett, V. C., and Hoffmann, J. E., (ed.) *Earth's Oldest Rocks*: Elsevier, 401-429.

Kemp, A. I. S. (2018). Early earth geodynamics: cross examining the geological testimony. *Philosophical Transactions of the Royal Society A* **376**.

Kemp, A., Vervoort, J., Bjorkman, K. & Iaccheri, L. (2017). Hafnium Isotope Characteristics of Palaeoarchaean Zircon OG1/OGC from the Owens Gully Diorite, Pilbara Craton, Western Australia. *Geostandards and Geoanalytical Research* **41**, 659-673.

Kemp, A. I. S., Wilde, S. A., Hawkesworth, C. J., Coath, C. D., Nemchin, A., Pidgeon, R. T., Vervoort, J. D. & DuFrane, S. A. (2010). Hadean crustal evolution revisited: New constraints from Pb-Hf isotope systematics of the Jack Hills zircons. *Earth and Planetary Science Letters* **296**, 45-56.

Kenny, G. G., Whitehouse, M. J. & Kamber, B. S. (2016). Differentiated impact melt sheets may be a potential source of Hadean detrital zircon. *Geology* **44**, 435-438.

Kinny, P. D. & Nutman, A. P. (1996). Zirconology of the Meeberrie Gneiss, Yilgarn Craton, Western Australia: An early Archaean migmatite. *Precambrian Research* **78**, 165-178.

Kinny, P. D., Williams, I. S., Froude, D. O., Ireland, T. R. & Compston, W. (1988). Early Archean zircon ages from orthogneisses and anorthosites at Mount Narryer, Western Australia. *Precambrian Research* **38**, 325-341.

Kusiak, M. A., Dunkley, D. J., Wirth, R., Whitehouse, M. J., Wilde, S. A. & Marquardt, K. (2015). Metallic lead nanospheres discovered in ancient zircons. *Proceedings of the National Academy of Sciences of the United States of America* **112**, 4958-4963.

Kusiak, M. A., Whitehouse, M. J., Wilde, S. A., Nemchin, A. A. & Clark, C. (2013). Mobilization of radiogenic Pb in zircon revealed by ion imaging: Implications for early Earth geochronology. *Geology* **41**, 291-294.

Ludwig, K.R., 2003. Isoplot/Ex: Special Publication No. 4. Berkeley Geochronology Center, Berkeley, California.

Maas, R. & McCulloch, M. T. (1991). The provenance of Archean clastic metasediments in the Narryer Gneiss Complex, Western Australia - trace-element geochemistry, Nd isotopes, and U-Pb ages for detrital zircons. *Geochimica Et Cosmochimica Acta* **55**, 1915-1932.

Myers, J. S. (1988). Early Archean Narryer Gneiss Complex, Yilgarn Craton, Western-Australia. *Precambrian Research* **38**, 297-307.

Nebel, O., Rapp, R. P. & Yaxley, G. M. (2014). The role of detrital zircons in Hadean crustal research. *Lithos* **190**, 313-327.

Nebel-Jacobsen, Y., Munker, C., Nebel, O., Gerdes, A., Mezger, K. & Nelson, D. R. (2010). Reworking of Earth's first crust: Constraints from Hf isotopes in Archean zircons from Mt. Narryer, Australia. *Precambrian Research* **182**, 175-186.

Nemchin, A. A., Pidgeon, R. T. & Whitehouse, M. J. (2006). Re-evaluation of the origin and evolution of > 4.2 Ga zircons from the Jack Hills metasedimentary rocks. *Earth and Planetary Science Letters* **244**, 218-233.

Nutman, A. P. (2006). Comment on "Zircon thermometer reveals minimum melting conditions on earliest Earth" II. *Science* **311**.

Nutman, A. P., Kinny, P. D., Compston, W. & Williams, I. S. (1991). SHRIMP U-Pb zircon geochronology of the Narryer Gneiss Complex, Western Australia. *Precambrian Research* **52**, 275-300.

O'Neil, J., Carlson, R. W., Francis, D. & Stevenson, R. K. (2008). Neodymium-142 evidence for Hadean mafic crust. *Science* **321**, 1828-1831.

Paton, C., Woodhead, J., Hellstrom, J., Hergt, J., Greig, A. & Maas, R. (2010). Improved laser ablation U-Pb zircon geochronology through robust downhole fractionation correction. *Geochemistry Geophysics Geosystems* **11**.

Petersson, A., Kemp, A. I. S., Hickman, A. H., Whitehouse, M. J., Martin, L. & Gray, C. M. (2019). A new 3.59 Ga magmatic suite and a chondritic source to the east Pilbara Craton. *Chemical Geology* **511**, 51-70.

Pidgeon, R. T. & Nemchin, A. A. (2006). High abundance of early Archaean grains and the age distribution of detrital zircons in a sillimanite-bearing quartzite from Mt Narryer, Western Australia. *Precambrian Research* **150**, 201-220.

Pidgeon, R. T. & Wilde, S. A. (1998). The interpretation of complex zircon U-Pb systems in Archaean granitoids and gneisses from the Jack Hills, Narryer gneiss Terrane, Western Australia. *Precambrian Research* **91**, 309-332.

Rasmussen, B., Fletcher, I. R., Muhling, J. R., Gregory, C. J. & Wilde, S. A. (2012). Metamorphic replacement of mineral inclusions in detrital zircon from Jack Hills, Australia: Implications for the Hadean Earth. *Geology* **40**, E282-E283.

Rasmussen, B., Fletcher, I. R., Muhling, J. R., Gregory, C. J. & Wilde,ƐƐ S. A. (2011). Metamorphic replacement of mineral inclusions in detrital zircon from Jack Hills, Australia: Implications for the Hadean Earth. *Geology* **39**, 1143-1146.

Rasmussen, B., Fletcher, I. R., Muhling, J. R. & Wilde, S. A. (2010). In situ U-Th-Pb geochronology of monazite and xenotime from the Jack Hills belt: Implications for the age of deposition and metamorphism of Hadean zircons. *Precambrian Research* **180**, 26-46.

Reimink, J. R., Davies, J., Chacko, T., Stern, R. A., Heaman, L. M., Sarkar, C., Schaltegger, U., Creaser, R. A. & Pearson, D. G. (2016). No evidence for Hadean continental crust within Earth's oldest evolved rock unit. *Nature Geoscience* **9**, 777.

Reimink, J. R., Chacko, T., Stern, R. A. & Heaman, L. M. (2014). Earth's earliest evolved crust generated in an Iceland-like setting. *Nature Geoscience* **7**, 529-533.

Rowe, M. L., 2016, Petrology and geochemistry of the Eoarchaean Manfred Complex: origin and components: Geological Survey of Western Australia, Record 2016/22, 150p.

Slama, J., Kosler, J., Condon, D., Crowley, J., Gerdes, A., Hanchar, J., Horstwood, M., Morris, G., Nasdala, L., Norberg, N., Schaltegger, U., Schoene, B., Tubrett, M. & Whitehouse, M. (2008). Plesovice zircon - A new natural reference material for U-Pb and Hf isotopic microanalysis. *Chemical Geology* **249**, 1-35.

Smithies, R., Van Kranendonk, M. & Champion, D. (2005). It started with a plume - early Archaean basaltic proto-continental crust. *Earth and Planetary Science Letters* **238**, 284-297.

Soderlund, U., Patchett, J. P., Vervoort, J. D. & Isachsen, C. E. (2004). The Lu-176 decay constant determined by Lu-Hf and U-Pb isotope systematics of Precambrian mafic intrusions. *Earth and Planetary Science Letters* **219**, 311-324.

Stern, R., Bodorkos, S., Kamo, S., Hickman, A. & Corfu, F. (2009). Measurement of SIMS Instrumental Mass Fractionation of Pb Isotopes During Zircon Dating. *Geostandards and Geoanalytical Research* **33**, 145-168.

Valley, J. W., Cavosie, A. J., Fu, B., Peck, W. H. & Wilde, S. A. (2006). Comment on "Heterogeneous hadean nafnium: Evidence of continental crust at 4.4 to 4.5 Ga". *Science* **312**.

Valley, J. W., Cavosie, A. J., Ushikubo, T., Reinhard, D. A., Lawrence, D. F., Larson, D. J., Clifton, P. H., Kelly, T. F., Wilde, S. A., Moser, D. E. & Spicuzza, M. J. (2014). Hadean age for a post-magma-ocean zircon confirmed by atom-probe tomography. *Nature Geoscience* **7**, 219-223.

Valley, J. W., Reinhard, D. A., Cavosie, A. J., Ushikubo, T., Lawrence, D. F., Larson, D. J., Kelly, T. F., Snoeyenbos, D. R. & Strickland, A. (2015). Nano- and micro-geochronology in Hadean and Archean zircons by atom-probe tomography and SIMS: New tools for old minerals. *American Mineralogist* **100**, 1355-1377.

Vermeesch, P. (2018). IsoplotR: A free and open toolbox for geochronology. *Geoscience Frontiers* **9**, 1479-1493.
Vervoort, J. D. & Kemp, A. I. S. (2016). Clarifying the zircon Hf isotope record of crust-mantle evolution. *Chemical Geology* **425**, 65-75.
Wang, Q. & Wilde, S. A. (2018). New constraints on the Hadean to Proterozoic history of the Jack Hills belt, Western Australia. *Gondwana Research* **55**, 74-91.
Watson, E. B. & Harrison, T. M. (2005). Zircon thermometer reveals minimum melting conditions on earliest Earth. *Science* **308**, 841-844.
Whitehouse, M. J., Kusiak, M. A., Wirth, R. & Kumar, G. R. R. (2017). Metallic Pb nanospheres in ultra-high temperature metamorphosed zircon from southern India. *Mineralogy and Petrology* **111**, 467-474.
Whitehouse, M. J., Nemchin, A. A. & Pidgeon, R. T. (2017). What can Hadean detrital zircon really tell us? A critical evaluation of their geochronology with implications for the interpretation of oxygen and hafnium isotopes. *Gondwana Research* **51**, 78-91.
Wilde, S. A., Valley, J. W., Peck, W. H. & Graham, C. M. (2001). Evidence from detrital zircons for the existence of continental crust and oceans on the Earth 4.4 Gyr ago. *Nature* **409**, 175-178.
Willbold, M., Hegner, E., Stracke, A. & Rocholl, A. (2009). Continental geochemical signatures in dacites from Iceland and implications for models of early Archaean crust formation. *Earth and Planetary Science Letters* **279**, 44-52.
Woodhead, J. & Hergt, J. (2005). A preliminary appraisal of seven natural zircon reference materials for in situ Hf isotope determination. *Geostandards and Geoanalytical Research* **29**, 183-195.
Wu, F., Yang, Y., Xie, L., Yang, J. & Xu, P. (2006). Hf isotopic compositions of the standard zircons and baddeleyites used in U-Pb geochronology. *Chemical Geology* **234**, 105-126.

Chapter Six:

Conclusions and the broader geodynamic picture

6.1. Introduction

This thesis focused on understanding the petrogenesis of detrital chromites and detrital zircons from fuchsitic metasediments at Jack Hills. This was undertaken to gain a greater understanding of Hadean to Archean coupled mafic-felsic crustal evolution within the Narryer Terrane. A focus away from traditional zircon-dominated detrital records is imperative due to the emerging view that the Hadean and Archean was dominated by crust with a mafic to ultramafic composition, with felsic lithologies such as TTG representing only a minor component (e.g. Dhuime et al., 2015; Kamber, 2015; Tang et al., 2016; Hawkesworth et al., 2017; Condie et al., 2018). Zircon detrital records produce information predominantly on the generation and evolution of felsic crust: as felsic crust is the volumetrically smaller component of Hadean to Archean lithosphere, this builds an incomplete picture of crustal evolution. Detrital chromites, solely derived from mafic and ultramafic crust, were largely unstudied at Jack Hills (Cavosie et al., 2002; Valley et al., 2005; Dare et al., 2016), and are only rarely used globally (e.g. Barnes and Roeder, 2001; Barkov et al., 2013). This study sought to redress that balance by use of the coupled detrital chromite-zircon record at Jack Hills, to gain additional constraints on crustal evolution and the geodynamic regime operating at the time, and clarify the debate surrounding detrital zircons from Jack Hills.

6.2. Overall conclusions

6.2.1. Detrital chromites- physical and chemical compositions

Detrital chromites are present within both the matrix and quartzite cobbles (Figure 3.4; Dare et al., 2016) of 10 metasediment samples taken from at or near the W-74 site at Jack Hills (Figure 2.1; Wilde et al., 2001). Chromites possess diverse rounding shapes, from perfectly spherical chromites to euhedral octahedra that have clearly had minimal erosional reworking (Figure 3.5). The presence of heavily rounded crystals indicates substantial sedimentary reworking of at least some grains, and therefore the likely derivation of some chromites from distal mafic or ultramafic sources. The presence of variably rounded chromites within quartzite cobbles (see also Dare et al. (2016)) suggests at least two sedimentation events. EPMA analysis of chromite major and minor elements show strong evidence of metamorphic re-equilibration, with lowered Mg# and elevated wt.% ZnO and MnO (Figure 3.7; Barnes, 2000; Colas et al., 2014). Furthermore, inclusion assemblages are dominated by quartz, muscovite (fuchsite), rutile and iron oxides, with more minor monazite, xenotime and Fe-sulphide (Figure 3.6). As chromite and quartz are not magmatically cogenetic, this also suggests recrystallisation of some grains and replacement of primary mineral assemblages. While either ZnO or Mg# are consistent within individual samples, significant inter-sample heterogeneity is present (Figure 3.7).

This is observed in metasediments sampled just meters apart, making it improbable these signatures occurred within the chromite protolith. This therefore suggests that modification of chromite major and minor elements occurred within metasediments. The variation of wt. % ZnO with the modal proportion of chromites within 14WA1 to 14WA4 is a further indication of this, likely by equilibration with metamorphic fluids (Figure 3.13), as is the replacement of mineral assemblages with those identical to metamorphic mineral assemblages within the host metasediment and the fit of highest ZnO chromites to an isopleth (Figure 3.12).

However, despite significant divalent element mobility, trivalent cations (Cr^{3+}, Al^{3+}, Fe^{3+}) appear to have undergone only localised mobility. This is discernible by the consistency of Cr# across all samples (Figure 3.8), with only a minor trend towards lowered Cr#, the absence of ferritchromit rims (Kimball, 1990), and the lack of intra-grain trivalent ion zonation profiles in most chromites (Figure 3.10). While some high Cr# domains are observed, these appear to be very localised and strongly associated with clearly altered crystals (Figure 3.11). Cr# therefore was deemed a valuable tool for petrogenetic analysis, alongside careful use of $Fe^{3+}/\Sigma R^{3+}$ and TiO_2. When applied to compositional fields of chromites and spinels from known tectonic settings (Barnes and Roeder, 2001), these signatures indicate two potential sources for chromites: layered intrusions and ophiolites (Figure 3.16 and 3.17). The variability of Cr# regardless of rounding shape is more indicative of a layered intrusive origin than ophiolitic origin, where the Cr# of chromites is controlled by melt depletion (Dick and Bullen, 1984; Barnes and Roeder, 2001) and the detrital record should possess significant heterogeneity. The apparent absence of depleted mantle prior to ca. 3000 Ma (e.g. Petersson et al., 2019; Fisher and Vervoort, 2018) also suggests that variably depleted ophiolites are unlikely to be the source of detrital chromites. A single sample of Manfred Complex metaperidotite possesses chromites that overlap compositionally with some high Cr# detrital chromites (Figure 3.19), though more chromite-bearing lithological units would be required to determine the full range of compositional variability of chromites within the Manfred Complex.

6.2.2. Detrital chromites- Re-Os model ages

Jack Hills detrital chromites yield high Os concentrations of 13 ppb to 72 ppb (Figure 4.1). Unradiogenic $^{187}Os/^{188}Os$ ratios of 0.10412-0.11443 of chromites translate to TRDs of 1849 Ma to 3323 Ma. Though recent Re mobility appears to have perturbed the Re concentration of some samples (Figure 4.2 and 4.3), five chromites possess self-consistent Re-Os TMAs that yield a weighted mean of 3528±34 Ma (Figure 4.4; 2se, MSWD 1.3). These are taken to represent the true TMAs of detrital chromites, while two grains with self-consistent Re-Os TMAs of ~3000 Ma likely represent the products of partial Re loss from this population. The broad trend of decreasing TRD with decreasing Os concentrations in all

samples bar 14WA4 implies a nugget effect (Figure 4.1), indicating that a Re-poor phase, such as discrete PGE alloys, control the Os isotopic composition of detrital chromite bulk samples. This indicates that while PGE alloys have remained largely robust, the Os isotopic composition of chromites are likely modified, producing the more radiogenic TRDs observed in lower concentration samples. The presence of three 'true' TRDs (measured Re/Os analytically indistinguishable from 0) is also of interest: two of these overlap with plausible metamorphic dates within the Narryer Terrane. One of these, at ~1850 Ma, is particularly notable as it is significantly younger than the purported ~2650 Ma to ~3000 Ma depositional age of the metasediments (Crowley et al., 2005; Rasmussen et al., 2010). This therefore strongly suggests Re mobility has occurred during metamorphism of metasediments.

Re-Os analysis of the 3730 Ma Manfred Complex (Kinny, 1988; Kemp et al., 2019) was also undertaken to assess the possibility of crustal assimilation inducing elevated γOs_i, inducing artificially younger Re-Os model ages and therefore making chromite-bearing lithologies a viable source for Jack Hills detrital chromites (Figure 4.8). WR samples of 14WA21 show clearly disturbed isotope systematics, but 13TKN80 WR samples possessed a γOs_i of +2.6 to +3.4 (Figure 4.10). While Re concentrations were erroneously high due to high blank/sample concentrations, the Re-Os TRD of the spinel separate for 13TKN80 provides a maximum γOs_i of +1±0.34. These values are very low in comparison to modern layered intrusions (Figure 4.9) and well within uncertainty of chondritic compositions, indicating a chondritic or near chondritic Re-Os composition for the Manfred Complex (Figure 4.10). This suggests the Manfred Complex is not a potential source of detrital chromites, though the variable γOs_i of Proterozoic layered intrusions (e.g. Bushveld; Schoenberg et al., 1999) indicates the Complex may possess heterogeneous γOs_i.

6.2.3. Detrital zircons- Pb-Hf composition

Detrital zircons analysed within this study yield typical Jack Hills ^{207}Pb-^{206}Pb age distribution peaks: zircons predominantly possess 3380 Ma to 3400 Ma ages, with more minor age distribution peaks at ~3440 Ma, ~3470 Ma, ~3490 Ma, ~3520 to 3540 Ma and at 4000 Ma to 4100 Ma (Figure 5.7). Most Jack Hills zircons also possess relatively low U concentrations (e.g. Crowley et al., 2005; Supplementary Material 5), a product of extensive sedimentary reworking and careful point selection away from metamict grains. Bulk zircon analyses yielded significantly more scattered Pb-Hf compositions than those with definitively magmatic zoning (Figure 5.11). The filtered subset of oscillatory zoned zircons produces Pb-Hf compositions and subsequent crustal evolution arrays in good agreement with those derived by Amelin et al. (1999) and Kemp et al. (2010) (Figure 5.11). Two scenarios are envisaged to explain the Pb-Hf compositions of Archean zircons (Figure 5.13). In the first, crust with a $^{176}Lu/^{177}Hf$ ratio of ~0.020 to 0.022 extracted from CHUR at ~4400 Ma, ~4050 Ma and at ~3730 Ma is internally

reworked to produce the compositional diversity of the Jack Hills zircons. In the second scenario, Archean zircon Pb-Hf compositions are derived from reworking of crust with a $^{176}Lu/^{177}Hf$ of ~0.02 extracted from CHUR at ~4400 Ma, and crust with $^{176}Lu/^{177}Hf$ of ~0.021 to ~0.028 extracted from CHUR at ~4050 Ma.

Critically, both hypotheses suggest reworking of crust with $^{176}Lu/^{177}Hf$ ratios of >0.02, indicative of crust with a mafic composition (Amelin et al., 1999; Blichert-Toft and Albarede, 2008). Furthermore, the highly negative ƐHf(t) composition of the ~3380 Ma population (Figure 5.14) indicates ~4400 Ma protocrust was reworked for ≥ 1 billion years (Kemp et al., 2010). The shallow arrays observed within this study are at complete odds with recycling of felsic crust, as has been previously suggested to explain the Pb-Hf compositions of Jack Hills zircons (Harrison et al., 2008; Blichert-Toft and Albarede, 2008; Bell et al., 2011; 2014), suggesting these arrays are indeed indicative of ancient Pb loss (Kemp et al., 2010). This study therefore highlights the importance of careful grain selection for the most definitively magmatic grains (e.g. Whitehouse et al., 2017): those with oscillatory zoning, optically clear crystals and <10% U-Pb discordance provide the most robust isotopic data and therefore the strongest interpretations.

6.3. Geodynamic conclusions: understanding the bigger picture

6.3.1. The importance of ophiolites

This study showed that detrital chromites within Jack Hills sediments had chemical similarities to chromites derived from ophiolites, and as such their origin within this tectonic setting could not be wholly discounted. Ophiolites, areas of oceanic lithosphere and upper mantle obducted onto continental margins (Dilek and Furnes, 2000; 2014), are a hallmark of horizontal plate tectonics. This is because subduction processes are the essential driver for ophiolite emplacement (Dilek and Furnes, 2014), and a significant portion of ophiolites formed at divergent or convergent plate margins (Dilek and Furnes, 2011). However, purported Archean ophiolites are contentious (e.g. Stern, 2005; Kamber et al., 2015); for example, suggestions of a ca. 3.8 Ga ophiolite within the Isua supracrustal belt, in SW Greenland (Furnes et al., 2007; Friend and Nutman, 2010) and a ca.2.5 Ga ophiolite within the North China Craton (Kusky et al., 2001; Santosh et al., 2016) have been met with controversy. If indeed detrital chromites represent the remnants of ophiolites, they would provide unequivocal evidence for at the very least localised subduction by the Paleoarchean. Archean layered intrusions, particularly anorthositic layered intrusions, have been postulated to originate from supra-subduction zone settings (e.g. Polat et al., 2011; Berger et al., 2013) or mantle plumes (e.g. Ernst and Buchan, 1997; Ivanic et al., 2017), with the latter favoured for mafic layered intrusions.

Ultimately, fluid-induced mobility and non-stoichiometry indicate the TiO_2 and Fe_2O_3 contents of chromites cannot be used to distinguish between the two settings. Modern ophiolitic chromites (e.g. from podiform chromitites) show Cr# variability to layered intrusions (Barnes and Roeder, 2001; González-Jiminéz et al., 2014), reflecting melt depletion but also probable fluid and melt interaction (González-Jiminéz et al., 2014; Pearce, 2014). However, while ophiolites are rare and controversial components of Archean terranes (c.f. Furnes et al., 2015), large scale layered intrusions are commonplace. Thus, given their abundance within the geological record, and the consistent range of Jack Hills chromites Cr# regardless of rounding shape, this study suggests detrital grains are not ophiolitic. Jack Hills chromites therefore do not require active Archean subduction, but may benefit from further geochemical analysis to conclusively distinguish between a layered intrusive or ophiolitic source.

6.3.2. The Jack Hills detrital record

A hypothesis was also developed for this thesis to distinguish between the two dominant geodynamic hypotheses proposed for Jack Hills zircons, stagnant lid and modern-style plate tectonics, using a dual chromite-zircon detrital record (Figure 6.1). Within a stagnant lid regime, there should be a strong temporal link between detrital zircons and detrital chromites, as significant mafic and ultramafic eruption and intrusion is required to thicken and partially melt the crust, resulting in felsic melts bearing zircons with subchondritic Hf compositions (e.g. Lu-Hf model ages > ^{207}Pb-^{206}Pb crystallisation age; Figure 6.2). Chromite major and minor elements should also reflect this, with an absence of tectonic, though not magmatic, diversity in detrital sequences. Within modern-style plate tectonics, zircon age distribution peaks largely represent preservation within orogenic belts rather than the generation of juvenile crust within arcs (e.g. Hawkesworth et al., 2009). Orogenic events are largely devoid of mantle melting, and so there should be a decoupling between the ages of detrital zircons and detrital chromites. Detrital chromite major and minor elements should also suggest tectonically diverse environments.

By careful documentation of detrital chromites from Jack Hills, this study concludes they are most likely derived from a single large-scale, potentially deep-seated, layered intrusion. Re-Os isotopic compositions indicate detrital chromites possess a Re-Os model age of 3528±34 Ma, further indicating a single population of detrital grains (Figure 4.4). A more minor, but distinct, zircon age distribution peak is observed at this time within the Jack Hills detrital record, with zircons possessing 3520 Ma to 3540 Ma ages prominent in both relative probability (Figure 5.7) and KDE plots (Supplementary Material 7). While it is important however to note that lithological units of this age are unknown within the Narryer Terrane (e.g. Kemp et al., 2019), bar a minor inherited component of the Eurada gneiss

(Nutman et al., 1991), this suggests a reworking event at this time, as zircons of this age possess subchondritic $\varepsilon Hf(t)_{CHUR}$ compositions (Figure 5.14; Amelin et al., 1999). Bar a chondritic population at ca. 3350 Ma, Jack Hills zircons consistently yield older Lu-Hf two-stage model ages than detrital chromite Re-Os TMAs (Figure 6.2). The overlap between a ^{207}Pb-^{206}Pb age distribution peak of detrital zircons that possess subchondritic Hf isotopic compositions (and therefore older Lu-Hf TMAs), and detrital chromite Re-Os model ages suggests this recycling event was contemporaneous with the intrusion (±extrusion?) of mafic and ultramafic crust. Thus, coupling of detrital chromite and detrital zircon ages (Figure 6.3), alongside the subchondritic Hf compositions of detrital zircons and the homogeneity of detrital chromite major and minor elements, is more indicative of a stagnant lid regime than modern-style plate tectonics. While it may be expected that the peak in model ages should coincide with the largest zircon U-Pb peak, the intrusive nature of these units indicates there may be a stratigraphic decoupling of chromites and zircons, so that the mafic and felsic components of the ~3530 Ma event are intruded at different crustal depths. This may also be inferred from field evidence within the Narryer Terrane: the Manfred Complex has been magmatically dismembered by intrusion of the protoliths of the Meeberrie and Dugel gneisses (Kemp et al., 2019), suggesting that within a detrital record younger zircon age distribution peaks would dominate.

Overall, detrital phases at Jack Hills more strongly support the hypothesis that at ≥3500 Ma the dominant geodynamic regime within source area of host sediments was vertical tectonics, rather than modern-style, horizontal plate tectonics. However, as has been stated previously, there is significant uncertainties surrounding the true crystallisation age of detrital chromites. Many Proterozoic and Phanerozoic layered intrusions show elevated γOs_i (Figure 4.9) and so possess non-chondritic initial Os isotopic compositions, which would induce artificially younger model ages. However, as Jack Hills chromites are detrital, the role of crustal assimilation in their petrogenesis cannot be quantified. Therefore, while it is apparent that chromite Re-Os model ages are ~3530 Ma, this does not mean this age represents true crystallisation age of detrital chromites, therefore potentially warranting previous geodynamic interpretations obsolete. If indeed chromites do represent the eroded remnants of the Manfred Complex, another complication arises: zircons of this age are under-represented within the Jack Hills detrital record (e.g. Crowley et al., 2005; Cavosie et al., 2019). As such, the Pb-Hf composition of such zircons and metaigneous rocks of comparable age are poorly constrained.

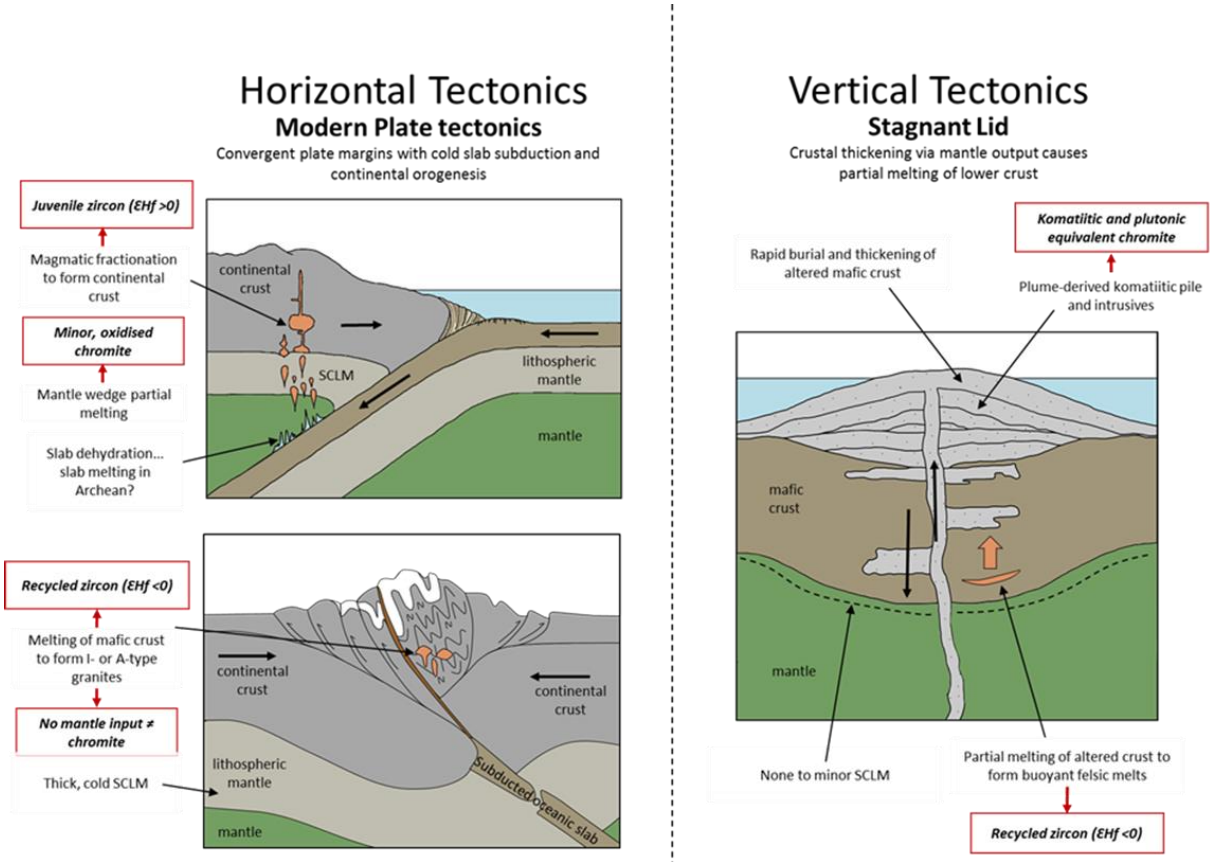

Figure 6.1: Idealised detrital zircon:chromite relationships in a modern-style plate tectonics regime vs. stagnant lid. Briefly, within a modern-style plate tectonics regime chromites represent a minor portion of a continental detrital record, and show decoupling with zircon U-Pb ages. Within a stagnant lid regime mantle melting events should be contemporaneous with the generation of felsic crust, and so there should be a strong temporal link between detrital chromites and zircons. For a more detailed explanation see chapter 1.

While Bell et al. (2014) found largely subchondritic zircon between ~3700 Ma and ~4000 Ma (Figure 5.2), the absence of focus on definitively magmatic grains suggests these interpretations may be clouded by zircons that have undergone ancient Pb loss. A single oscillatory grain from both Bell et al. (2011) and one zircon from Amelin et al. (1999) also yield subchondritic Hf compositions. Two oscillatory grains of comparable age were reported in this study (Figure 5.14). The first, 16WA5-168, overlaps with the Pb-Hf composition of zircons from ~3750 Ma metaigneous rocks presented in Kemp et al. (2010). The second, 14WA4-60, is within uncertainty of an Amelin et al. (1999) zircon and the Kemp et al. (2010) 4400 Ma mafic crustal evolution line. While clearly further work is required, this does suggest a subchondritic Hf composition for Jack Hills detrital zircons at this time, bar two points from a ~3760 Ma grain that yielded chondritic Pb-Hf, though with large uncertainties (Figure 5.2). Analysis of zircons in the NE of the belt, where a larger ~3700 Ma age distribution peak is observed (Crowley et al., 2005; Dunn et al., 2005), may provide further constraints.

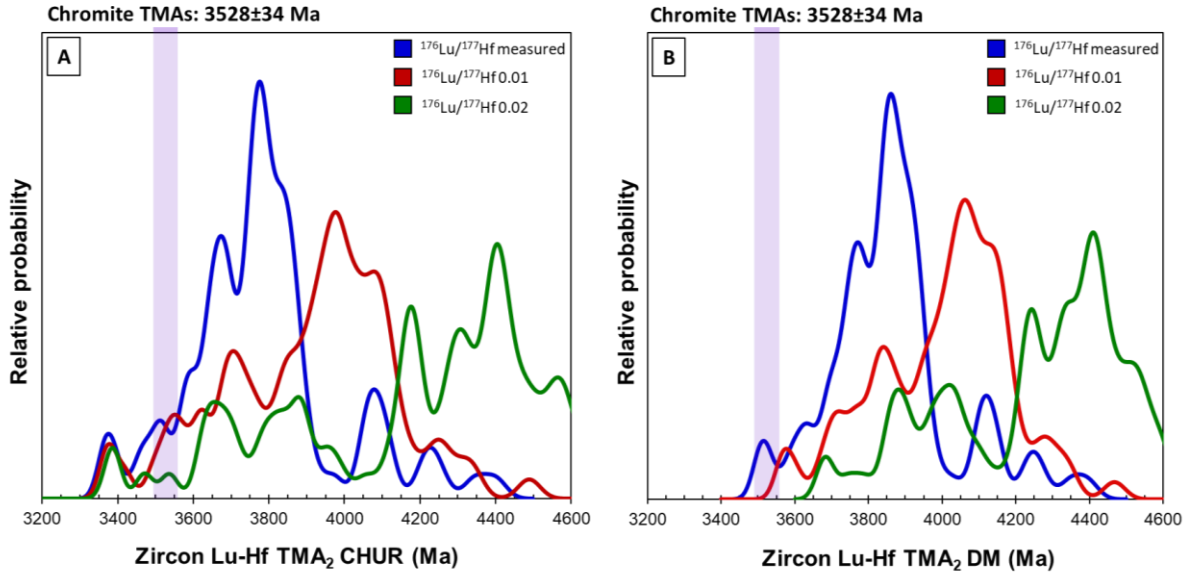

Figure 6.2: Two stage Lu-Hf model ages (TMA_2) calculated for oscillatory zoned Jack Hills zircons, showing time of extraction from **A)** CHUR and **B)** depleted mantle (DM) reservoirs, in comparison to Jack Hills chromite Re-Os TMAs. CHUR parameters for calculation: $^{176}Hf/^{177}Hf$ 0.282785 and $^{176}Lu/^{177}Hf$ 0.0336. DM parameters: $^{176}Hf/^{177}Hf$ 0.28324 (ƐHf +16) and $^{176}Lu/^{177}Hf$ 0.038965 (extraction at 4450 Ma, as per Kemp et al. (2010)). Second stage 176Lu/177Hf used were those measured within the zircons, which do not represent the $^{176}Lu/^{177}Hf$ of their protolith, 0.01, as per average continental crust, and 0.02, indicative of a more mafic reservoir. Bar the chondritic population at ~3350 Ma, Lu-Hf TMA_2 of zircon are consistently older than chromite Re-Os TMAs. Figure generated using IsoPlot (Ludwig, 2003).

However, detrital zircons with superchondritic Hf compositions at ~3730 Ma are reported at Mount Narryer (Figure 1.10a; Nebel-Jacobson et al., 2010), and used to argue for extraction of felsic crust from depleted mantle (DM) by virtue of convergent plate margins by Bell et al. (2011). This would also imply derivation of the contemporaneous Manfred Complex from a subduction zone, a strongly held, but controversial belief for the origin of anorthosites (e.g. Ashwal and Bybee, 2017). However, a DM origin is at odds with CHUR Pb-Hf compositions recently derived for zircons from anorthosites and leucogabbros within the Manfred Complex (Souders and Sylvester, 2016; T. Kemp, pers. com.), compositional trends of chromite and spinel (Rowe, 2016), and mildly subchondritic compositions of 3730 Ma Meeberrie tonalites (Hiess and Bennett, 2016). Detrital zircons from Mount Narryer are therefore apparently more juvenile than contemporaneous zircons at Jack Hills (Nebel-Jacobsen et al., 2010), though their steep Lu/Hf evolution path may be systematic of ancient Pb loss (Kemp et al., 2019), indicating discrepancies between the two supracrustal belts. An anorthositic origin of ~3730 Ma Mount Narryer detrital zircons should also not be discounted. Clearly, further work away from the W-74 site at Jack Hills is required.

In an idealised view, where chromite Re-Os TMAs represent the true crystallisation age of detrital zircons, the case for a dominantly stagnant lid regime is clear. However, given the ambiguity surrounding the true crystallisation ages of detrital chromites, conclusions as to the geodynamic regime they crystallised under should therefore be taken tentatively. The Manfred Complex appears to possess a chondritic Os initial isotopic composition: this may indicate that the ca. 3530 Ma Re-Os model ages do date chromite crystallisation, but without definitive source material sampled within the Narryer Terrane this interpretation is hypothetical. The idealised relationships between detrital

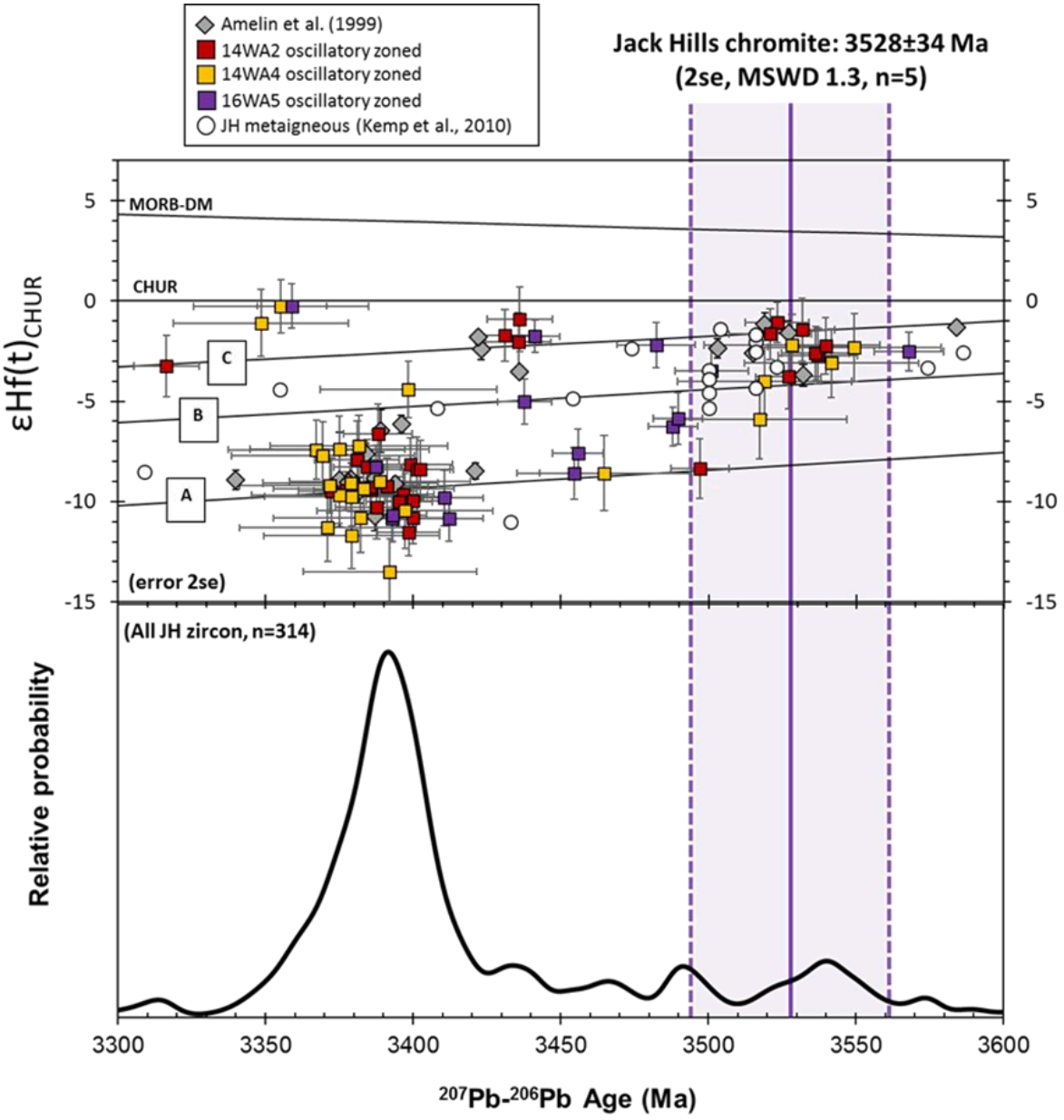

Figure 6.3: Concluding figure, showing the Pb-Hf composition of oscillatory zoned zircons, ^{207}Pb-^{206}Pb relative probability of bulk zircons, and chromite Re-Os model ages for the most robust population. All uncertainties 2se. Crustal evolution pathways from Figure 5.14a also shown. Jack Hills metaigneous zircons from Jack Hills from Kemp et al. (2010) and Jack Hills detrital zircons from Amelin et al. (1999) also shown for comparison.

chromites and zircons provided here may be best suited to detrital records that host definitively volcanic (i.e. komatiitic) chromites, which largely plot at chondritic γOs_i in the early Archean, suggesting limited assimilation of radiogenic crust (e.g. Putchel et al., 2014 and references therein).

6.3.3. Extrapolating to the Global Record

While geodynamic conclusions should be taken with caution from the dual chromite-zircon record at Jack Hills, it is important to note that many interpretations within this study have more global connotations. The recycling of long-lived, mafic crust suggested by detrital zircon Pb-Hf compositions, in agreement with Amelin et al. (1999) and Kemp et al. (2010), has been argued to be at odds with the operation of horizontal tectonics within the early Earth (Kemp et al., 2010; Nebel et al., 2014; Whitehouse et al., 2017). Evidence of reworking of Hadean mafic crust to form TTG within the Archean, and therefore in support of a more stagnant lid dominated Earth, is also suggested by zircon Pb-Hf compositions from both rock units and detrital records elsewhere (e.g. O'Neil et al., 2013; Zeh et al., 2014; Reimink et al., 2016; Bauer et al., 2017; Bohlar et al., 2017; Vezinet et al., 2018), and by the discovery of ^{142}Nd anomalies within ~2700 Ma Hudson Bay granitoids (O'Neil and Carlson, 2017). Such long-lived (>1.5 Gyr) mafic reservoirs are argued to be incompatible with destructive plate margins, therefore requiring the absence of true, modern-style subduction within the early Earth. However, examples of Eoarchean proto subduction within mafic rocks in west Greenland (Jenner et al., 2009; Polat et al., 2015) and TTG in China (Ge et al., 2018) and elsewhere (e.g. Moyen and Martin, 2012) are reported. This suggests that while the Jack Hills detrital zircons indicate the NGC was likely emplaced under a more vertical tectonic regime, such as those shown by dome and keel terranes such as the Pilbara (e.g. Smithies et al., 2005), this does not preclude the operation of subduction, or some form of proto subduction elsewhere.

The dominance of chromites within the Jack Hills detrital record (Morton and Hallsworth, 1994) and the homogeneity of detrital chromite major element compositions also indicates the source area of Jack Hills sediments had a high abundance of mafic and ultramafic crust. While this may be the result of localisation of sediment sources, numerous other lines of evidence have suggested Hadean and Archean crust was dominantly mafic in composition. These include elevated Ni/Co and Cr/Zn ratios within Archean terrigenous rocks (Tang et al., 2016; cf. Greber et al., 2017), the mafic composition of juvenile crust shown by Rb/Sr ratios (Dhuime et al., 2015) and a suggested transition from juvenile crust with a mafic composition to a more evolved composition at ~3000 Ma (Dhuime et al., 2012; 2015; Lee et al., 2016; Cawood et al., 2018), though the timing of this transition varies globally. This period also coincides with increased elevation of landmasses (Campbell and Davies, 2017; Bindeman

et al., 2018), and the first appearance of eclogitic diamonds (Shirey and Richardson, 2011) and foreland basins (Cawood et al., 2018). While preservation and localisation effects must be considered, the similar resilience of chromite and zircon to sedimentary reworking suggests the proportions of detrital chromite to zircon may provide a valuable future tool in understanding the proportions of mafic and ultramafic and evolved crust at the time of sediment deposition.

As an apparent geodynamic change at ca. 3000 Ma varies in timing globally, this also suggests some geodynamic variability across the Archean Earth. West Greenland and Eastern Canada have long been suggested to show some form of early Archean subduction (e.g. Frei et al., 2003; Jenner et al., 2009; Polat et al., 2015). It would be of interest to study more chromite-bearing detrital records, to determine if the tentative stagnant lid signature observed within the Narryer Terrane is observed in fuchsitic metasediments elsewhere. Ultimately, arguments in understanding whether vertical or horizontal tectonics operated during the Hadean and Archean are complex and contentious. However, where preserved at greenschist facies or lower (Barnes, 2000; Colas et al., 2014), both detrital chromites and those preserved in protoliths are important archives into the geodynamic regime operating at the time of their formation.

6.4. Outstanding Issues and future work

Chromite non-stoichiometry

Many detrital chromites appear be non-stoichiometric (Figure 3.9). Non-stoichiometry is a known problem within spinels (Kamperman et al., 1996; Rollinson et al., 2012), and suggests that the Fe^{3+} of chromites within this study may be underestimated by charge balance calculations. While the presence of reasonable totals suggest non-stoichiometry is not significant (Supplementary Material 2.1), it may impact petrogenetic interpretations of detrital grains. Mössbauer spectrometry may provide a viable mechanism for determining the true Fe^{3+} content of grains: traditional Mössbauer techniques would require too many chromites, which regardless possess variable compositions. Synchrotron-based micro-Mössbauer (e.g. Lenaz et al., 2013) may therefore provide additional constraints on the Fe^{3+} content and oxidisation state of chromites analysed within this study. Determination of the Fe speciation within detrital chromites may also be possible by use of micro X-ray absorption near edge structure (μ-XANES), or X-ray photoelectron spectroscopy (XPS), which has previously been used successfully in chromites (Fanlo et al., 2008).

Jack Hills metamorphic history

While metasediments at Jack Hills are arguably of global geological significance, few studies have investigated quantifying the P-T conditions reached by unit 3 of Jack Hills (Spaggiari, 2007). This is in

part due to an absence of index minerals within metasediments (Rasmussen et al., 2010; Cavosie et al., 2019), and a complex history of polyphase deformation (Spaggiari, 2007; Kemp et al., 2019). Metamorphic events are proposed to have occurred at ca.2650 Ma, 1800-1850 Ma and 800 Ma (Spaggiari, 2007; Rasmussen et al., 2010; 2011; Kemp et al., 2019). While ~2650 Ma is inferred to represent the peak metamorphic event at the W-74 site (Rasmussen et al., 2010), this interpretation has been complicated by the discovery of intercalated metasediments that host Proterozoic zircons, but are at the same apparent tectonic grade as those at the W-74 site (Cavosie et al., 2004; Dunn et a., 2005; Wang and Wilde, 2018). These sediments also host Hadean grains, suggesting they may represent reworking of the Archean (>2650 Ma) metasediments. Ar-Ar dating of muscovites (Spaggiari, 2007; 2008), U-Pb analysis of monazite and xenotime and Re-Os analysis within this study also suggest metamorphism at ~1750 Ma to ~1850 Ma, partially coincident with the Capricorn orogen. The discovery of ~1570 Ma zircons within some metasediments indicates these two events may not represent the current metamorphic signature of the belt (Cavosie et al., 2004). Clearly, further work on the depositional age and metamorphic grade of such important metasediments is required.

PGE analyses of detrital chromites

While this study favours a layered intrusive origin for detrital chromite, an ophiolitic origin cannot be ruled out. Platinum group element (PGE; Os, Ir, Ru, Pt, Pd, Re) concentrations may aid in distinguishing between these two sources. Coggon et al. (2015) showed that ophiolitic and stratiform chromites may be distinguished by plots of Os/Pt vs. Os/Ir. Within samples that have retained chromites with robust Os isotopic signatures, PGE concentrations may be a viable mechanism of distinguishing between two tectonically different sources.

Other mafic and ultramafic units within the Narryer Terrane

While the Manfred Complex represents the sole reasonably well described body of mafic and ultramafic crust within the Narryer Terrane (Kemp et al., 2019), recent analyses of mafic and ultramafic lithologies has highlighted their age diversity (Sylvester et al., 2011; Kemp et al., 2019), despite being labelled as Manfred Complex (Myers, 1997). This suggest that distinct mafic and ultramafic generation events may be further determined by continued study of these lithologies. Of particular interest is that two distinct age populations at ~3490 Ma and ~3350 Ma are present (Kemp et al., 2019), which correlate with distinct detrital zircon populations (Figure 5.13). Analyses of spinels and chromites within these samples may also highlight more potential sources for Jack Hills detrital chromites.

6.5 Final concluding remarks

This study represents the first systematic investigation of detrital chromites within Archean metasediments. Fuchsitic metasediments are commonly reported within Archean metasediments (e.g. Kerrich et al., 1987; Randive et al., 2015), yet rarely investigated for phases other than zircons. While zircons are arguably less challenging to analyse, this study has shown that despite significant metamorphic equilibration, with careful and thorough investigation, primary signatures of chromites may be observed. Detrital chromites likely represent the eroded remnants of the dominant lithology within the early Earth, and may represent a valuable tool in understanding the overall composition, evolution and destruction of this earliest crust. In contrast, detrital zircons would therefore represent a relatively minor component of Hadean and Archean lithologies, suggesting an analytical bias towards felsic crust within crustal evolution studies. Analysis of detrital chromites is therefore important to gain a more comprehensive view of crustal evolution within the early Earth. Where preserved within metasedimentary rocks that have undergone low grade metamorphism, e.g. upper greenschist facies or less, detrital chromites may therefore represent an exciting avenue of research into Archean crustal evolution. This, coupled with the geodynamic insights coupled chromite-zircon records may provide, suggests detrital chromites may be an important future phase in investigating the Earth's most ancient crustal vestiges.

6.6 References

Amelin, Y., Lee, D. C., Halliday, A. N. & Pidgeon, R. T. (1999). Nature of the Earth's earliest crust from hafnium isotopes in single detrital zircons. *Nature* **399**, 252-255.

Ashwal, L. & Bybee, G. (2017). Crustal evolution and the temporality of anorthosites. *Earth-Science Reviews* **173**, 307-330.

Barkov, A. Y., Nixon, G. T., Levson, V. M., Martin, R. F. & Fleet, M. E. (2013). Chromian spinel from PGE-bearing placer deposits, British Colombia, Canada: Mineralogical associations and provenance. *Canadian Mineralogist* **51**, 501-536.

Barnes, S. J. (2000). Chromite in komatiites, II. modification during greenschist to mid-amphibolite facies metamorphism. *Journal of Petrology* **41**, 387-409.

Barnes, S. J. & Roeder, P. L. (2001). The range of spinel compositions in terrestrial mafic and ultramafic rocks. *Journal of Petrology* **42**, 2279-2302.

Bauer, A. M., Fisher, C. M., Vervoort, J. D. & Bowring, S. A. (2017). Coupled zircon Lu-Hf and U-Pb isotopic analyses of the oldest terrestrial crust, the > 4.03 Ga Acasta Gneiss Complex. *Earth and Planetary Science Letters* **458**, 37-48.

Bell, E. A., Harrison, T. M., Kohl, I. E. & Young, E. D. (2014). Eoarchean crustal evolution of the Jack Hills zircon source and loss of Hadean crust. *Geochimica Et Cosmochimica Acta* **146**, 27-42.

Bell, E. A., Harrison, T. M., McCulloch, M. T. & Young, E. D. (2011). Early Archean crustal evolution of the Jack Hills Zircon source terrane inferred from Lu-Hf, Pb-207/Pb-206, and delta O-18 systematics of Jack Hills zircons. *Geochimica Et Cosmochimica Acta* **75**, 4816-4829.

Berger, J., Diot, H., Lo, K., Ohnenstetter, D., Femenias, O., Pivin, M., Demaiffe, D., Bernard, A. & Charlier, B. (2013). Petrogenesis of Archean PGM-bearing chromitites and associated ultramafic-mafic-anorthositic rocks from the Guelb el Azib layered complex (West African craton, Mauritania). *Precambrian Research* **224**, 612-628.

Bindeman, I., Zakharov, D., Palandri, J., Greber, N., Dauphas, N., Retallack, G., Hofmann, A., Lackey, J. & Bekker, A. (2018). Rapid emergence of subaerial landmasses and onset of a modern hydrologic cycle 2.5 billion years ago. *Nature* **557**, 545-+.

Blichert-Toft, J. & Albarede, F. (2008). Hafnium isotopes in Jack Hills zircons and the formation of the Hadean crust. *Earth and Planetary Science Letters* **265**, 686-702.

Bolhar, R., Hofmann, A., Kemp, A. I. S., Whitehouse, M. J., Wind, S. & Kamber, B. S. (2017). Juvenile crust formation in the Zimbabwe Craton deduced from the O-Hf isotopic record of 3.8-3.1 Ga detrital zircons. *Geochimica Et Cosmochimica Acta* **215**, 432-446.

Campbell, I. & Davies, D. (2017). Raising the continental crust. *Earth and Planetary Science Letters* **460**, 112-122.

Cavosie, A. J., Valley., J. W., and Wilde., S. A. (2019). The Oldest Terrestrial Mineral Record: Thirty Years of Research on Hadean Zircon from Jack Hills, Western Australia. In: van Kranendonk, M. J., Bennett, V. C., and Hoffmann, J. E., (ed.) *Earth's Oldest Rocks*: Elsevier, 255-273.

Cavosie, A. J., Wilde, S. A., Liu, D. Y., Weiblen, P. W. & Valley, J. W. (2004). Internal zoning and U-Th-Pb chemistry of Jack Hills detrital zircons: a mineral record of early Archean to Mesoproterozoic (4348-1576 Ma) magmatism. *Precambrian Research* **135**, 251-279.

Cavosie, A. J., Valley, J. W., Fournelle, J. & Wilde, S. A. (2002). Implications for sources of Jack Hills metasediments: detrital chromite. *Goldschmidt 2002*, 125.

Cawood, P., Hawkesworth, C., Pisarevsky, S., Dhuime, B., Capitanio, F. & Nebel, O. (2018). Geological archive of the onset of plate tectonics. *Philosophical Transactions of the Royal Society a-Mathematical Physical and Engineering Sciences* **376**.

Coggon, J. A., Luguet, A., Fonseca, R. O. C., Lorand, J. P., Heuser, A. & Appel, P. W. U. (2015). Understanding Re-Os systematics and model ages in metamorphosed Archean ultramafic rocks: A single mineral to whole-rock investigation. *Geochimica Et Cosmochimica Acta* **167**, 205-240.

Colas, V., Gonzalez-Jimenez, J. M., Griffin, W. L., Fanlo, I., Gervilla, F., O'Reilly, S. Y., Pearson, N. J., Kerestedjian, T. & Proenza, J. A. (2014). Fingerprints of metamorphism in chromite: New insights from minor and trace elements. *Chemical Geology* **389**, 137-152.

Condie, K., Puetz, S. & Davaille, A. (2018). Episodic crustal production before 2.7 Ga. *Precambrian Research* **312**, 16-22.

Crowley, J. L., Myers, J. S., Sylvester, P. J. & Cox, R. A. (2005). Detrital zircon from the Jack Hills and Mount Narryer, Western Australia: Evidence for diverse > 4.0 Ga source rocks. *Journal of Geology* **113**, 239-263.

Dare, M. S., Tarduno, J. A., Bono, R. K., Cottrell, R. D., Beard, J. S. & Kodama, K. P. (2016). Detrital magnetite and chromite in Jack Hills quartzite cobbles: Further evidence for the preservation of primary magnetizations and new insights into sediment provenance. *Earth and Planetary Science Letters* **451**, 298-314.

Dick, H. J. B. & Bullen, T. (1984). Chromian spinel as a petrogenetic indicator in abyssal and alpine-type peridotites and spatially associated lavas. *Contributions to Mineralogy and Petrology* **86**, 54-76.

Dhuime, B., Hawkesworth, C., Cawood, P. & Storey, C. (2012). A Change in the Geodynamics of Continental Growth 3 Billion Years Ago. *Science* **335**, 1334-1336.

Dhuime, B., Wuestefeld, A. & Hawkesworth, C. J. (2015). Emergence of modern continental crust about 3 billion years ago. *Nature Geoscience* **8**, 552-555.

Dilek, Y. & Furnes, H. (2011). Ophiolite genesis and global tectonics: Geochemical and tectonic fingerprinting of ancient oceanic lithosphere. *Geological Society of America Bulletin* **123**, 387-411.

Dilek, Y. & Furnes, H. (2014). Ophiolites and Their Origins. *Elements* **10**, 93-100.

Dunn, S. J., Nemchin, A. A., Cawood, P. A. & Pidgeon, R. T. (2005). Provenance record of the Jack Hills metasedimentary belt: Source of the Earth's oldest zircons. *Precambrian Research* **138**, 235-254.

Ernst, R. & Buchan, K. (1997). Layered mafic intrusions: a model for their feeder systems and relationship with giant dyke swarms and mantle plume centres. *South African Journal of Geology* **100**, 319-334.

Fanlo, I., Gervilla, F., Mateo, E. & Irusta, S. (2008). X-ray photoelectron spectroscopy characterization of natural chromite from Mercedita Mine (Eastern Cuba): quantification of the Fe3+/Fe2+ ratio. *European Journal of Mineralogy* **20**, 125-129.

Fisher, C. M. & Vervoort, J. D. (2018). Using the magmatic record to constrain the growth of continental crust-The Eoarchean zircon Hf record of Greenland. *Earth and Planetary Science Letters* **488**, 79-91.

Frei, R. & Jensen, B. K. (2003). Re-Os, Sm-Nd isotope- and REE systematics on ultramafic rocks and pillow basalts from the Earth's oldest oceanic crustal fragments (Isua Supracrustal Belt and Ujaragssuit nunat area, W Greenland). *Chemical Geology* **196**, 163-191.

Friend, C. & Nutman, A. (2010). Eoarchean ophiolites? New evidence for the debate on the Isua supracrustal belt, southern west Greenland. *American Journal of Science* **310**, 826-861.

Furnes, H., de Wit, M., Staudigel, H., Rosing, M. & Muehlenbachs, K. (2007). A vestige of Earth's oldest ophiolite. *Science* **315**, 1704-1707.

Furnes, H., Dilek, Y. & de Wit, M. (2015). Precambrian greenstone sequences represent different ophiolite types. *Gondwana Research* **27**, 649-685.

Ge, R., Zhu, W., Wilde, S. & Wu, H. (2018). Remnants of Eoarchean continental crust derived from a subducted proto-arc. *Science Advances* **4**.

Gonzalez-Jimenez, J., Griffin, W., Proenza, J., Gervilla, F., O'Reilly, S., Akbulut, M., Pearson, N. & Arai, S. (2014). Chromitites in ophiolites: How, where, when, why? Part II. The crystallization of chromitites. *Lithos* **189**, 140-158.

Greber, N., Dauphas, N., Bekker, A., Ptacek, M., Bindeman, I. & Hofmann, A. (2017). Titanium isotopic evidence for felsic crust and plate tectonics 3.5 billion years ago. *Science* **357**, 1271-+.

Harrison, T. M., Schmitt, A. K., McCulloch, M. T. & Lovera, O. M. (2008). Early (>= 4.5 Ga) formation of terrestrial crust: Lu-Hf, delta O-18, and Ti thermometry results for Hadean zircons. *Earth and Planetary Science Letters* **268**, 476-486.

Hawkesworth, C., Cawood, P., Dhuime, B., Kemp, T., Jeanloz, R. & Freeman, K. (2017). Earth's Continental Lithosphere Through Time. *Annual Review of Earth and Planetary Sciences, Vol 45* **45**, 169-198.

Hawkesworth, C., Cawood, P., Kemp, T., Storey, C. & Dhuime, B. (2009). Geochemistry: A Matter of Preservation. *Science* **323**, 49-50.

Hiess, J. & Bennett, V. C. (2016). Chondritic Lu/Hf in the early crust-mantle system as recorded by zircon populations from the oldest Eoarchean rocks of Yilgarn Craton, West Australia and Enderby Land, Antarctica. *Chemical Geology* **427**, 125-143.

Ivanic, T. J., Nebel, O., Brett, J., and Murdie, R. E. (2017). The Windimurra Igneous Complex: an Archean Bushveld? *The Geological Society of London, Special Publications* **453**.

Jenner, F., Bennett, V., Nutman, A., Friend, C., Norman, M. & Yaxley, G. (2009). Evidence for subduction at 3.8 Ga: Geochemistry of arc-like metabasalts from the southern edge of the Isua Supracrustal Belt. *Chemical Geology* **261**, 82-97.

Kamber, B. (2015). The evolving nature of terrestrial crust from the Hadean, through the Archaean, into the Proterozoic. *Precambrian Research* **258**, 48-82.

Kamperman, M., Danyushevsky, L. V., Taylor, W. R. & Jablonski, W. (1996). Direct oxygen measurements of Cr-rich spinel: Implications for spinel stoichiometry. *American Mineralogist* **81**, 1186-1194.

Kemp, A. I. S., Wilde, S. A., Hawkesworth, C. J., Coath, C. D., Nemchin, A., Pidgeon, R. T., Vervoort, J. D. & DuFrane, S. A. (2010). Hadean crustal evolution revisited: New constraints from Pb-Hf isotope systematics of the Jack Hills zircons. *Earth and Planetary Science Letters* **296**, 45-56.

Kemp, A. I. S., Wilde, S. A., and Spaggiari, C. (2019). The Narryer Terrane, Yilgarn Craton, Western Australia: Review and Recent Developments. In: van Kranendonk, M. J., Bennett, V. C., and Hoffmann, J. E., (ed.) *Earth's Oldest Rocks*: Elsevier, 401-429.

Kerrich, R., Fyfe, W. S., Barnett, R. L., Blair, B. B., and Willmore, L. M. (1987). Corundum, Cr-muscovite rocks at O'Briens, Zimbabwe: the conjunction of hydrothermal desilicification and LIL-element enrichment-geochemical and isotopic evidence. *Contributions to Mineralogy and Petrology* **95**, 481-498.

Kimball, K. L. (1990). Effects of hydrothermal alteration on the compositions of chromian spinels. *Contributions to Mineralogy and Petrology* **105**, 337-346.

Kinny, P. D., Williams, I. S., Froude, D. O., Ireland, T. R. & Compston, W. (1988). Early Archean zircon ages from orthogneisses and anorthosites at Mount Narryer, Western Australia. *Precambrian Research* **38**, 325-341.

Kusky, T., Li, J. & Tucker, R. (2001). The Archean Dongwanzi ophiolite complex, North China craton: 2.505-billion-year-old oceanic crust and mantle. *Science* **292**, 1142-1145.

Lee, C., Yeung, L., McKenzie, N., Yokoyama, Y., Ozaki, K. & Lenardic, A. (2016). Two-step rise of atmospheric oxygen linked to the growth of continents. *Nature Geoscience* **9**, 417-+.

Lenaz, D., Skogby, H., Logvinova, A., Sobolev, N. & Princivalle, F. (2013). A micro-Mossbauer study of chromites included in diamond and other mantle-related rocks. *Physics and Chemistry of Minerals* **40**, 671-679.

Ludwig, K.R., 2003. Isoplot/Ex: Special Publication No. 4. Berkeley Geochronology Center, Berkeley, California.

Morton, A. & Hallsworth, C. (1994). Identifying provenance-specific features of detrital heavy mineral assemblages in sandstones. *Sedimentary Geology* **90**, 241-256.

Moyen, J. F. & Martin, H. (2012). Forty years of TTG research. *Lithos* **148**, 312-336.

Nebel, O., Rapp, R. P. & Yaxley, G. M. (2014). The role of detrital zircons in Hadean crustal research. *Lithos* **190**, 313-327.

Nebel-Jacobsen, Y., Munker, C., Nebel, O., Gerdes, A., Mezger, K. & Nelson, D. R. (2010). Reworking of Earth's first crust: Constraints from Hf isotopes in Archean zircons from Mt. Narryer, Australia. *Precambrian Research* **182**, 175-186.

Nutman, A. P., Kinny, P. D., Compston, W. & Williams, I. S. (1991). SHRIMP U-Pb zircon geochronology of the Narryer Gneiss Complex, Western Australia. *Precambrian Research* **52**, 275-300.

O'Neil, J., Boyet, M., Carlson, R. W. & Paquette, J. L. (2013). Half a billion years of reworking of Hadean mafic crust to produce the Nuvvuagittuq Eoarchean felsic crust. *Earth and Planetary Science Letters* **379**, 13-25.

O'Neil, J. & Carlson, R. W. (2017). Building Archean cratons from Hadean mafic crust. *Science* **355**, 1199-1202.

Pearce, J. (2014). Immobile Element Fingerprinting of Ophiolites. *Elements* **10**, 101-108.

Petersson, A., Kemp, A. I. S., Hickman, A. H., Whitehouse, M. J., Martin, L. & Gray, C. M. (2019). A new 3.59 Ga magmatic suite and a chondritic source to the east Pilbara Craton. *Chemical Geology* **511**, 51-70.

Polat, A., Wang, L. & Appel, P. (2015). A review of structural patterns and melting processes in the Archean craton of West Greenland: Evidence for crustal growth at convergent plate margins as opposed to non-uniformitarian models. *Tectonophysics* **662**, 67-94.

Polat, A., Fryer, B., Appel, P., Kalvig, P., Kerrich, R., Dilek, Y. & Yang, Z. (2011). Geochemistry of anorthositic differentiated sills in the Archean (similar to 2970 Ma) Fiskenaesset Complex, SW Greenland: Implications for parental magma compositions, geodynamic setting, and secular heat flow in arcs. *Lithos* **123**, 50-72.

Puchtel, I. S., Walker, R. J., Touboul, M., Nisbet, E. G. & Byerly, G. R. (2014). Insights into early Earth from the Pt-Re-Os isotope and highly siderophile element abundance systematics of Barberton komatiites. *Geochimica Et Cosmochimica Acta* **125**, 394-413.

Randive, K. R., Korakoppa, M. M., Muley, S. V., Varade, A. M., Khandare, H. W., Lanjewar, S. G., Tiwari, R. R. & Aradhi, K. K. (2015). Paragenesis of Cr-rich muscovite and chlorite in green-mica quartzites of Saigaon-Palasgaon area, Western Bastar Craton, India. *Journal of Earth System Science* **124**, 213-225.

Rasmussen, B., Fletcher, I. R., Muhling, J. R., Gregory, C. J. & Wilde, S. A. (2011). Metamorphic replacement of mineral inclusions in detrital zircon from Jack Hills, Australia: Implications for the Hadean Earth. *Geology* **39**, 1143-1146.

Rasmussen, B., Fletcher, I. R., Muhling, J. R. & Wilde, S. A. (2010). In situ U-Th-Pb geochronology of monazite and xenotime from the Jack Hills belt: Implications for the age of deposition and metamorphism of Hadean zircons. *Precambrian Research* **180**, 26-46.

Reimink, J. R., Davies, J., Chacko, T., Stern, R. A., Heaman, L. M., Sarkar, C., Schaltegger, U., Creaser, R. A. & Pearson, D. G. (2016). No evidence for Hadean continental crust within Earth's oldest evolved rock unit. *Nature Geoscience* **9**, 777-+.

Rollinson, H., Adetunji, J., Yousif, A. A. & Gismelseed, A. M. (2012). New Mossbauer measurements of Fe3+/Sigma Fe in chromites from the mantle section of the Oman ophiolite: evidence for the oxidation of the sub-oceanic mantle. *Mineralogical Magazine* **76**, 579-596.

Santosh, M., Teng, X., He, X., Tang, L. & Yang, Q. (2016). Discovery of Neoarchean suprasubduction zone ophiolite suite from Yishui Complex in the North China Craton. *Gondwana Research* **38**, 1-27.

Schoenberg, R., Kruger, F. J., Nagler, T. F., Meisel, T. & Kramers, J. D. (1999). PGE enrichment in chromitite layers and the Merensky Reef of the western Bushveld Complex; a Re-Os and Rb-Sr isotope study. *Earth and Planetary Science Letters* **172**, 49-64.

Shirey, S. & Richardson, S. (2011). Start of the Wilson Cycle at 3 Ga Shown by Diamonds from Subcontinental Mantle. *Science* **333**, 434-436.

Smithies, R., Van Kranendonk, M. & Champion, D. (2005). It started with a plume - early Archaean basaltic proto-continental crust. *Earth and Planetary Science Letters* **238**, 284-297.

Souders, K., and Sylvester, P. (2016). Hf Isotope Systematics of Archean Anorthosites: Manfred Complex, Yilgarn Craton, Western Australia. *American Geophysical Union, Fall Meeting 2016*.

Spaggiari, C. V., Wartho, J. A. & Wilde, S. A. (2008). Proterozoic deformation in the northwest of the Archean Yilgarn Craton, Western Australia. *Precambrian Research* **162**, 354-384.

Spaggiari, C. V. (2007). Structural and lithological evolution of the Jack Hills greenstone belt, Narryer Terrane, Yilgarn Craton, Western Australia. *Western Australia Geological Survey* **Record 2007/3**, 49.

Stern, R. (2005). Evidence from ophiolites, blueschists, and ultrahigh-pressure metamorphic terranes that the modern episode of subduction tectonics began in Neoproterozoic time. *Geology* **33**, 557-560.

Tang, M., Chen, K. & Rudnick, R. (2016). Archean upper crust transition from mafic to felsic marks the onset of plate tectonics. *Science* **351**, 372-375.

Valley, J. W., Cavosie, A. J., Shirey, S. & Wilde, S. A. (2005). 3.2 to 3.5 Ga Re-Os Model Ages for Detrital Chromite from Jack Hills, Western Australia: Implications for Pilbara and Yilgarn Craton Evolution. *American Geophysical Union, Fall Meeting 2005, abstract #V21F-08*.

Vezinet, A., Pearson, D. G., Thomassot, E., Stern, R. A., Sarkar, C., Luo, Y. & Fisher, C. M. (2018). Hydrothermally-altered mafic crust as source for early Earth TTG: Pb/Hf/O isotope and trace element evidence in zircon from TTG of the Eoarchean Saglek Block, N. Labrador. *Earth and Planetary Science Letters* **503**, 95-107.

Wang, Q. & Wilde, S. A. (2018). New constraints on the Hadean to Proterozoic history of the Jack Hills belt, Western Australia. *Gondwana Research* **55**, 74-91.

Whitehouse, M. J., Nemchin, A. A. & Pidgeon, R. T. (2017). What can Hadean detrital zircon really tell us? A critical evaluation of their geochronology with implications for the interpretation of oxygen and hafnium isotopes. *Gondwana Research* **51**, 78-91.

Wilde, S. A., Valley, J. W., Peck, W. H. & Graham, C. M. (2001). Evidence from detrital zircons for the existence of continental crust and oceans on the Earth 4.4 Gyr ago. *Nature* **409**, 175-178.

Zeh, A., Stern, R. & Gerdes, A. (2014). The oldest zircons of Africa-Their U-Pb-Hf-O isotope and trace element systematics, and implications for Hadean to Archean crust-mantle evolution. *Precambrian Research* **241**, 203-230.

Supplementary Material One:

Jack Hills chromite EPMA data

Table S1: *EPMA data for Jack Hills detrital chromites*

Loc.	size fraction	Crystal #	Comment	SiO_2	TiO_2	Al_2O_3	Cr_2O_3	V_2O_3	Fe_2O_3	FeO	MgO	MnO	CaO	NiO	ZnO	*Total*	Cation Total	Mg#	Cr#	$Fe^{3+}/\Sigma Fe$	Fe^{3+}/R^{3+}
14WA1	CHROM	4	quite pitted	0.02	0.18	18.52	46.20	0.12	0.00	27.66	1.20	2.13	0.00	0.00	3.08	99.10	2.996	7.2	62.6	0.00	0.00
14WA1	120-50	42		0.01	0.31	20.92	41.50	0.16	1.41	26.55	2.07	1.87	0.02	0.00	3.94	98.76	3.000	11.7	57.1	0.05	1.81
14WA1	250-120	22		0.01	0.09	17.55	49.20	0.12	0.00	25.60	1.93	2.11	0.01	0.00	2.64	99.25	2.983	11.8	65.3	0.00	0.00
14WA1	250-120	27	near rim	0.02	0.14	21.96	43.08	0.14	0.13	25.51	3.23	1.74	0.01	0.01	3.64	99.61	3.000	18.4	56.8	0.00	0.17
14WA1	250-120	28		0.00	0.59	20.30	43.61	0.16	0.00	27.10	1.61	1.99	0.01	0.01	2.95	98.31	2.990	9.6	59.0	0.00	0.00
14WA1	250-120	31		0.02	0.14	16.51	48.02	0.13	0.00	26.98	1.86	1.99	0.01	0.00	2.34	98.01	2.998	10.9	66.1	0.00	0.00
14WA1	250-120	34		0.03	0.39	18.44	45.35	0.24	0.00	27.84	0.80	1.88	0.02	0.01	3.88	98.87	2.995	4.9	62.3	0.00	0.00
14WA1	250-120	37		0.03	0.43	17.93	45.91	0.16	0.26	28.91	1.33	1.93	0.01	0.02	2.40	99.30	3.000	7.5	63.2	0.01	0.34
14WA1	500-250	6		0.02	0.40	23.11	39.70	0.19	0.00	29.12	1.04	2.15	0.01	0.02	3.14	98.91	3.000	6.0	53.5	0.00	0.00
14WA1	500-250	11		0.01	0.16	20.43	44.94	0.14	0.00	24.63	2.72	2.00	0.02	0.01	3.39	98.43	2.989	16.4	59.6	0.00	0.00
14WA1	500-250	15		0.00	0.06	23.27	39.83	0.15	0.16	28.41	1.32	1.97	0.01	0.02	3.04	98.24	3.000	7.6	53.5	0.00	0.20
14WA1	500-250	16		0.03	0.17	23.27	39.74	0.11	0.38	28.03	1.37	2.29	0.01	0.00	3.37	98.77	3.000	7.9	53.4	0.01	0.48
14WA1	500-250	3	near core	0.01	0.11	24.28	41.40	0.24	0.00	24.88	1.70	1.73	0.02	0.00	3.80	98.18	2.972	10.9	53.4	0.00	0.00
14WA1	CHROM	2	Core	0.13	0.40	7.72	53.37	0.10	3.95	25.87	1.66	2.79	0.03	0.01	2.06	98.07	3.000	9.1	82.3	0.12	5.48
14WA2-PB	250-120	12		0.00	0.21	11.40	51.41	0.16	3.33	27.39	2.64	1.33	0.00	0.01	0.81	98.71	3.000	13.4	75.2	0.10	4.43
14WA2-PB	250-120	46		0.00	0.56	17.94	45.12	0.25	3.63	23.98	5.91	1.10	0.02	0.00	1.03	99.56	3.000	27.9	62.8	0.12	4.59
14WA2	TS	2		0.02	0.08	21.21	41.65	0.24	1.06	29.22	2.01	1.09	0.00	0.00	1.70	98.29	3.000	10.6	56.8	0.03	1.35
14WA2	TS	3		0.09	0.89	17.77	40.19	0.25	4.89	30.39	1.52	1.17	0.03	0.00	1.52	98.71	3.000	7.2	60.3	0.13	6.52
14WA2	TS	4		0.03	0.48	16.21	42.85	0.21	6.43	29.18	1.88	1.43	0.02	0.01	1.81	100.54	3.000	8.7	63.9	0.17	8.37
14WA2	TS	ad. 1		0.00	0.21	20.06	42.95	0.18	0.81	30.21	1.40	0.97	0.03	0.02	1.72	98.55	3.000	7.5	59.0	0.02	1.04
14WA2	TS	9		0.04	0.37	19.86	41.96	0.19	2.21	29.48	2.21	1.23	0.00	0.00	1.13	98.67	3.000	11.1	58.6	0.06	2.86
14WA2	TS	ad. 2		0.01	0.55	22.22	41.46	0.36	0.00	28.53	2.99	1.13	0.00	0.00	1.17	98.43	2.997	15.7	55.6	0.00	0.00

***Table S1 cont.**: EPMA data for Jack Hills detrital chromites*

Loc.	size fraction	Crystal #	Comment	SiO_2	TiO_2	Al_2O_3	Cr_2O_3	V_2O_3	Fe_2O_3	FeO	MgO	MnO	CaO	NiO	ZnO	*Total*	Cation Total	Mg#	Cr#	$Fe^{3+}/\Sigma fe$	Fe^{3+}/R^{3+}
14WA2	TS	ad. 4		0.05	0.15	20.92	41.25	0.36	1.65	29.83	2.08	1.02	0.00	0.02	1.10	98.43	3.000	10.6	56.9	0.05	2.13
14WA2	TS	10		0.00	0.24	17.74	48.13	0.14	0.00	27.97	2.12	1.16	0.03	0.02	1.12	98.66	2.987	11.9	64.5	0.00	0.00
14WA2	TS	ad. 5		0.07	0.33	18.63	42.06	0.21	2.67	30.50	1.36	1.16	0.00	0.02	1.08	98.08	3.000	6.9	60.2	0.07	3.51
14WA2	HF leach	1		0.03	0.20	20.08	43.37	0.30	0.68	30.06	1.86	1.24	0.00	0.00	1.04	98.87	3.000	9.7	59.2	0.02	0.88
14WA2	HF leach	2		0.02	0.12	22.19	40.01	0.31	1.82	30.98	1.72	0.83	0.00	0.01	1.00	99.00	3.000	8.6	54.7	0.05	2.31
14WA2	HF leach	3		0.10	0.21	15.13	49.60	0.22	0.00	30.33	1.25	0.90	0.00	0.02	0.85	98.61	2.996	6.9	68.7	0.00	0.00
14WA2	HF leach	5		0.12	0.17	20.40	41.22	0.30	2.16	32.32	1.11	0.56	0.00	0.02	0.79	99.17	3.000	5.5	57.5	0.06	2.79
14WA2	250-120	35		0.00	0.44	21.08	40.35	0.19	1.66	30.66	1.60	0.93	0.02	0.03	1.20	98.13	3.000	8.1	56.2	0.05	2.15
14WA2	250-120	36		0.07	0.19	13.98	51.91	0.17	0.00	28.63	1.67	0.98	0.01	0.00	0.86	98.47	2.988	9.4	71.3	0.00	0.00
14WA2	250-120	40		0.00	0.11	22.08	41.75	0.14	0.38	28.96	2.86	0.70	0.01	0.00	1.08	98.06	3.000	14.8	55.9	0.01	0.48
14WA2	500-250	24		0.01	0.16	18.48	45.05	0.15	0.56	29.69	1.82	1.04	0.02	0.00	1.04	98.01	3.000	9.7	62.1	0.02	0.73
14WA2	500-250	26		0.10	0.12	20.99	40.33	0.13	3.93	27.58	3.60	1.19	0.02	0.02	1.02	99.02	3.000	17.1	56.3	0.11	4.96
14WA2	500-250	27		0.00	0.15	21.62	41.34	0.14	1.04	29.66	1.76	1.07	0.01	0.00	1.91	98.68	3.000	9.3	56.2	0.03	1.32
14WA2	500-250	4	near rim	0.02	0.77	18.04	44.23	0.19	0.77	30.52	1.75	0.99	0.01	0.00	0.94	98.22	3.000	9.1	62.2	0.02	1.02
14WA2	500-250	5	near core	0.06	0.55	20.46	40.81	0.16	1.93	29.84	1.93	1.24	0.00	0.00	1.39	98.37	3.000	9.8	57.2	0.05	2.51
14WA2	500-250	7	near rim	0.01	0.50	21.48	41.39	0.21	0.50	29.61	2.16	1.29	0.01	0.00	1.33	98.47	3.000	11.3	56.4	0.01	0.64
14WA2	500-250	9		0.04	0.91	21.07	40.92	0.24	0.16	30.66	1.39	1.31	0.01	0.03	1.81	98.55	3.000	7.4	56.6	0.00	0.22
14WA2	500-250	13	near core	0.00	0.10	17.20	48.55	0.10	0.00	28.30	1.94	0.97	0.01	0.00	1.00	98.16	2.988	10.9	65.4	0.00	0.00
14WA2	500-250	16	slightly darker	0.00	0.60	21.01	41.25	0.22	0.88	28.23	2.33	1.36	0.01	0.00	2.41	98.29	3.000	12.5	56.8	0.03	1.14
14WA2	500-250	18		0.02	0.24	17.65	47.71	0.12	0.00	28.11	1.59	1.14	0.01	0.02	1.50	98.11	2.985	9.1	64.5	0.00	0.00

***Table S1 cont.**: EPMA data for Jack Hills detrital chromites*

Loc.	size fraction	Crystal #	Comment	SiO_2	TiO_2	Al_2O_3	Cr_2O_3	V_2O_3	Fe_2O_3	FeO	MgO	MnO	CaO	NiO	ZnO	*Total*	Cation Total	Mg#	Cr#	Fe^{3+}/Σfe	Fe^{3+}/R^{3+}
14WA2	CHROM	13	rim	0.00	0.15	18.50	45.45	0.12	0.53	29.47	2.05	1.04	0.01	0.01	1.00	98.33	3.000	10.9	62.2	0.02	0.69
14WA2	CHROM	16		0.00	0.12	17.59	47.31	0.13	0.00	28.79	1.75	1.15	0.02	0.00	1.20	98.07	2.994	9.8	64.3	0.00	0.00
14WA2 RO-1	250-120	1	A - core	0.01	0.16	18.53	46.33	0.17	0.00	29.15	1.83	1.15	0.01	0.00	1.07	98.41	2.994	10.1	62.6	0.00	0.00
14WA2 RO-1	250-120	3	A - core	0.02	0.13	21.22	44.10	0.18	0.00	28.48	1.94	1.19	0.01	0.02	1.14	98.53	2.986	10.8	58.2	0.00	0.00
14WA2 RO-1	250-120	4	A - nr core	0.00	0.21	10.55	58.14	0.12	0.00	26.40	1.11	1.23	0.01	0.03	1.43	99.28	2.967	7.0	78.7	0.00	0.00
14WA2 RO-1	250-120	5	A - core	0.00	0.10	21.03	42.27	0.19	1.09	29.29	1.94	1.24	0.01	0.00	1.33	98.54	3.000	10.2	57.4	0.03	1.39
14WA2 RO-1	250-120	6	D - nr core	0.04	0.08	20.87	45.82	0.13	0.00	26.18	3.25	0.96	0.01	0.00	1.13	98.47	2.981	18.1	59.6	0.00	0.00
14WA2 RO-1	250-120	7		0.02	0.07	21.49	42.35	0.14	0.00	29.83	1.31	1.21	0.01	0.01	1.84	98.31	2.997	7.3	56.9	0.00	0.00
14WA2 RO-1	250-120	8	A - core	0.01	0.13	17.51	48.88	0.10	0.00	26.98	2.85	1.15	0.00	0.00	1.39	99.00	2.991	15.8	65.2	0.00	0.00
14WA2 RO-1	250-120	9		0.01	0.21	18.18	42.73	0.27	3.47	29.52	1.59	1.13	0.00	0.01	1.46	98.64	3.000	8.0	61.2	0.10	4.52
14WA2 RO-1	250-120	10	A - mid	0.04	0.09	22.62	40.25	0.20	1.21	29.72	2.09	1.04	0.02	0.01	1.34	98.65	3.000	10.8	54.4	0.04	1.53
14WA2 RO-1	250-120	11	A - core	0.04	0.24	11.74	56.00	0.14	0.00	26.57	1.29	1.06	0.00	0.00	1.37	98.47	2.969	8.0	76.2	0.00	0.00
14WA2 RO-1	250-120	13	A - core	0.03	0.62	19.31	45.13	0.16	0.00	29.86	1.72	1.17	0.01	0.01	1.02	99.06	2.992	9.3	61.1	0.00	0.00
14WA2 RO-1	250-120	14	A- core	0.05	0.18	18.91	42.41	0.21	5.52	27.52	3.53	1.37	0.01	0.02	1.09	100.86	3.000	16.2	60.1	0.15	6.92
14WA2 RO-2	250-120	2	A - core	0.01	0.13	16.87	45.42	0.14	1.97	30.31	1.17	1.12	0.00	0.00	0.99	98.15	3.000	6.1	64.4	0.06	2.58
14WA2 RO-2	250-120	3	C - rim	0.02	0.09	17.56	47.52	0.14	0.00	29.38	1.78	1.11	0.00	0.01	1.11	98.77	2.997	9.7	64.5	0.00	0.00
14WA2 RO-2	250-120	4	mid	0.03	0.13	20.99	43.55	0.19	0.39	28.11	3.09	1.12	0.00	0.00	1.22	98.83	3.000	16.2	58.2	0.01	0.49
14WA2 RO-2	250-120	7	A - core	0.02	0.21	19.16	46.80	0.15	0.00	26.86	2.63	1.17	0.00	0.00	1.31	98.37	2.984	14.9	62.1	0.00	0.00
14WA2 RO-2	250-120	10	mid	0.03	0.14	20.92	41.41	0.25	2.09	28.13	3.00	1.00	0.00	0.03	1.00	98.06	3.000	15.1	57.0	0.06	2.67
14WA2 RO-2	250-120	14	A - core	0.03	0.09	19.70	43.26	0.18	1.46	28.90	2.52	1.00	0.02	0.00	0.99	98.16	3.000	13.0	59.6	0.04	1.87
14WA2 RO-2	250-120	16	mid	0.01	0.41	16.34	45.78	0.19	2.09	29.78	1.60	1.18	0.01	0.00	0.94	98.37	3.000	8.3	65.3	0.06	2.75

***Table S1 cont.**: EPMA data for Jack Hills detrital chromites*

Loc.	size fraction	Crystal #	Comment	SiO_2	TiO_2	Al_2O_3	Cr_2O_3	V_2O_3	Fe_2O_3	FeO	MgO	MnO	CaO	NiO	ZnO	*Total*	Cation Total	Mg#	Cr#	$Fe^{3+}/\Sigma fe$	Fe^{3+}/R^{3+}
14WA2 RO-2	250-120	17	A - core	0.08	0.32	11.89	51.52	0.19	3.97	28.26	2.40	1.46	0.01	0.00	0.84	101.03	3.000	11.8	74.4	0.11	5.17
14WA2 RO-2	250-120	17	B - mid	0.08	0.23	12.45	51.01	0.20	3.66	28.45	2.47	1.41	0.02	0.00	0.83	100.84	3.000	12.2	73.3	0.10	4.77
14WA2 RO-2	250-120	17	C - rim	0.09	0.14	11.96	51.21	0.16	3.67	28.42	2.34	1.40	0.01	0.00	0.79	100.21	3.000	11.6	74.2	0.10	4.81
14WA2 RO-3	250-120	1		0.02	0.07	20.72	43.70	0.15	1.21	27.97	2.88	0.98	0.00	0.01	1.72	99.50	3.000	15.0	58.6	0.04	1.52
14WA2 RO-3	250-120	2		0.04	0.14	19.15	46.05	0.14	0.00	30.16	1.64	1.09	0.01	0.01	1.12	99.59	2.997	8.8	61.7	0.00	0.00
14WA2 RO-3	250-120	3	A	0.01	0.07	18.29	46.16	0.13	0.56	29.55	1.84	1.24	0.00	0.01	1.00	98.88	3.000	9.8	62.9	0.02	0.73
14WA2 RO-3	250-120	4	A - nr core	0.00	0.10	20.54	43.33	0.15	1.00	28.61	2.33	1.08	0.01	0.01	1.57	98.79	3.000	12.4	58.6	0.03	1.27
14WA2 RO-3	250-120	6	A - core	0.04	0.25	22.17	44.16	0.15	0.00	27.33	2.34	0.88	0.00	0.00	1.53	98.90	2.977	13.3	57.2	0.00	0.00
14WA2 RO-3	250-120	7	A - core	0.02	0.21	20.28	46.14	0.14	0.00	29.48	1.36	1.09	0.00	0.02	1.12	99.87	2.982	7.6	60.4	0.00	0.00
14WA2 RO-3	250-120	9	A - core	0.01	0.23	18.62	46.45	0.13	0.00	29.48	1.66	0.85	0.02	0.00	0.90	98.39	2.989	9.1	62.6	0.00	0.00
14WA2 RO-3	250-120	10		0.01	0.08	18.27	46.77	0.11	0.31	29.17	1.93	1.34	0.00	0.01	1.33	99.36	3.000	10.4	63.2	0.01	0.40
14WA2 RO-3	250-120	11	nr rim	0.01	0.13	18.40	43.74	0.17	2.29	29.73	1.33	1.34	0.00	0.00	1.57	98.74	3.000	6.9	61.5	0.06	2.98
14WA2 RO-3	250-120	12	A - nr core	0.00	0.18	18.97	46.41	0.13	0.00	28.91	1.67	1.25	0.01	0.01	1.48	99.06	2.991	9.4	62.1	0.00	0.00
14WA2 RO-3	250-120	13		0.03	0.15	19.13	46.00	0.12	0.00	28.76	1.99	0.92	0.01	0.01	1.08	98.23	2.990	11.0	61.7	0.00	0.00
14WA2 RO-3	250-120	14		0.05	0.73	20.75	43.80	0.15	0.00	28.57	3.08	1.06	0.01	0.01	0.99	99.23	2.994	16.1	58.6	0.00	0.00
14WA2 RO-3	250-120	15		0.01	0.57	18.87	46.10	0.13	0.00	29.06	2.05	0.98	0.01	0.01	0.98	98.81	2.989	11.2	62.1	0.00	0.00
14WA2 RO-3	250-120	16	A - core	0.06	0.07	22.71	44.90	0.13	0.00	27.95	1.76	1.18	0.02	0.01	1.70	100.51	2.974	10.1	57.0	0.00	0.00
14WA2 RO-3	250-120	17	A	0.00	0.56	22.44	40.60	0.16	0.14	30.30	1.84	1.07	0.01	0.01	1.33	98.52	2.999	9.7	54.8	0.00	0.19
14WA2 RO-3	250-120	18		0.03	0.06	21.37	44.93	0.12	0.00	26.51	3.54	1.14	0.01	0.01	1.06	98.81	2.989	19.2	58.5	0.00	0.00
14WA2 RO-3	250-120	19	A	0.01	0.12	23.73	42.16	0.15	0.00	26.46	4.14	0.98	0.01	0.01	1.24	99.05	2.993	21.8	54.4	0.00	0.00
14WA2 RO-4	250-120	1	A - core	0.01	0.23	18.81	46.44	0.12	0.00	30.66	1.24	0.91	0.00	0.01	1.03	99.50	2.993	6.7	62.3	0.00	0.00

***Table S1 cont.**: EPMA data for Jack Hills detrital chromites*

Loc.	size fraction	Crystal #	Comment	SiO_2	TiO_2	Al_2O_3	Cr_2O_3	V_2O_3	Fe_2O_3	FeO	MgO	MnO	CaO	NiO	ZnO	*Total*	Cation Total	Mg#	Cr#	$Fe^{3+}/\Sigma fe$	Fe^{3+}/R^{3+}
14WA2 RO-4	250-120	2	A	0.00	0.07	18.56	47.40	0.12	0.00	28.90	1.89	1.12	0.01	0.00	1.06	99.14	2.991	10.4	63.1	0.00	0.00
14WA2 RO-4	250-120	3	A - core	0.00	0.12	17.98	48.43	0.14	0.00	28.57	1.83	0.83	0.00	0.00	1.29	99.24	2.986	10.2	64.4	0.00	0.00
14WA2 RO-4	250-120	4	A - core	0.02	0.15	14.68	52.24	0.12	0.00	28.02	1.84	1.19	0.01	0.00	0.80	99.15	2.984	10.5	70.5	0.00	0.00
14WA2 RO-4	250-120	5	nr rim	0.01	0.18	20.74	44.76	0.14	0.00	28.07	2.68	1.32	0.00	0.00	1.47	99.37	2.995	14.5	59.2	0.00	0.00
14WA2 RO-4	250-120	6	A - core	0.08	0.38	10.86	57.95	0.14	0.00	25.21	2.42	0.97	0.01	0.00	0.73	98.78	2.965	14.6	78.2	0.00	0.00
14WA2 RO-4	250-120	7	A - core	0.01	0.15	18.69	48.21	0.15	0.00	26.98	2.40	1.15	0.00	0.00	1.42	99.19	2.981	13.7	63.4	0.00	0.00
14WA2 RO-4	250-120	8		0.02	0.07	21.06	45.32	0.15	0.00	28.61	2.66	1.08	0.00	0.00	1.04	100.05	2.992	14.2	59.1	0.00	0.00
14WA2 RO-4	250-120	9	A - core	0.02	0.08	19.11	47.84	0.11	0.00	27.25	2.83	1.02	0.01	0.01	1.02	99.32	2.985	15.6	62.7	0.00	0.00
14WA2 RO-4	250-120	10		0.00	0.50	14.32	54.14	0.14	0.00	27.59	1.41	1.03	0.01	0.00	0.93	100.12	2.967	8.4	71.7	0.00	0.00
14WA2 RO-4	250-120	11	nr rim	0.00	0.28	18.79	48.43	0.13	0.00	26.97	2.63	1.07	0.01	0.01	1.03	99.39	2.979	14.8	63.4	0.00	0.00
14WA2 EO	250-120	10	A - core	0.03	0.06	19.29	46.86	0.13	0.00	28.22	2.21	1.13	0.01	0.02	1.27	99.30	2.989	12.3	62.0	0.00	0.00
14WA2 EO	250-120	12		0.02	0.09	17.58	46.73	0.14	0.39	29.18	1.77	1.01	0.01	0.01	1.37	98.35	3.000	9.7	64.1	0.01	0.51
14WA2 EO	250-120	14	A - nr core	0.00	0.11	16.48	50.30	0.12	0.00	27.29	2.71	1.19	0.01	0.00	1.03	99.29	2.990	15.1	67.2	0.00	0.00
14WA2 EO	250-120	16	A - core	0.02	0.13	18.78	48.15	0.11	0.00	27.88	2.15	1.08	0.02	0.00	1.12	99.49	2.982	12.1	63.2	0.00	0.00
14WA2 EO	250-120	17	A - core	0.02	0.07	18.41	47.09	0.14	0.00	29.03	1.61	1.17	0.00	0.01	1.06	98.64	2.990	9.0	63.2	0.00	0.00
14WA2 EO	250-120	18		0.00	0.22	17.56	47.32	0.13	0.00	29.62	1.34	1.26	0.01	0.00	1.63	99.13	2.997	7.5	64.4	0.00	0.00
14WA2 RC	250-120	3	nr rim	0.01	0.14	18.43	44.14	0.17	1.92	27.96	2.26	1.37	0.01	0.00	1.54	98.02	3.000	12.0	61.6	0.06	2.49
14WA2 RC	250-120	5	A - core	0.05	0.92	14.98	50.16	0.18	0.00	28.60	1.69	1.35	0.01	0.00	1.47	99.46	2.987	9.5	69.2	0.00	0.00
14WA2 RC	250-120	6	A	0.03	0.16	18.53	46.61	0.15	0.00	28.84	1.84	1.21	0.01	0.00	1.49	98.90	2.994	10.2	62.8	0.00	0.00
14WA2 RC	250-120	7	A - core	0.11	0.13	8.98	60.30	0.07	0.00	26.52	0.98	1.15	0.00	0.00	0.71	98.99	2.961	6.2	81.8	0.00	0.00
14WA2 RC	250-120	8	A - core	0.01	0.17	19.42	44.88	0.17	1.00	28.16	2.47	1.31	0.00	0.00	1.71	99.37	3.000	13.1	60.8	0.03	1.28

***Table S1 cont.**: EPMA data for Jack Hills detrital chromites*

Loc.	size fraction	Crystal #	Comment	SiO_2	TiO_2	Al_2O_3	Cr_2O_3	V_2O_3	Fe_2O_3	FeO	MgO	MnO	CaO	NiO	ZnO	*Total*	Cation Total	Mg#	Cr#	$Fe^{3+}/\Sigma fe$	Fe^{3+}/R^{3+}
14WA2 RC	250-120	9	A	0.02	0.20	20.30	46.33	0.11	0.00	26.68	3.03	1.20	0.01	0.02	1.17	99.09	2.984	16.8	60.5	0.00	0.00
14WA2 RC	250-120	10	nr core	0.01	0.43	18.69	47.25	0.15	0.00	28.88	1.80	1.16	0.01	0.00	1.09	99.54	2.985	10.0	62.9	0.00	0.00
14WA2 RC	250-120	11	A - nr core	0.02	0.62	22.38	43.85	0.24	0.00	27.59	2.70	0.98	0.00	0.01	1.27	99.72	2.978	14.8	56.8	0.00	0.00
14WA2 RC	250-120	13		0.00	0.11	21.53	41.13	0.22	1.58	29.86	1.80	1.29	0.00	0.00	1.20	98.75	3.000	9.3	56.2	0.05	2.01
14WA2 RC	250-120	16	A	0.02	0.64	19.07	46.40	0.14	0.00	26.97	2.81	1.38	0.01	0.00	1.68	99.19	2.988	15.7	62.0	0.00	0.00
14WA3 -P1	250-120	2		0.01	0.32	19.11	46.12	0.12	0.00	25.53	0.62	1.50	0.01	0.00	6.94	100.27	2.988	4.2	61.8	0.00	0.00
14WA3 -P1	250-120	3		0.01	0.19	19.57	43.02	0.14	1.13	26.83	0.57	1.47	0.01	0.00	6.47	99.40	3.000	3.5	59.6	0.04	1.47
14WA3 -P1	250-120	5		0.01	0.13	20.20	43.24	0.15	0.14	25.45	0.80	1.49	0.01	0.00	7.55	99.15	3.000	5.3	59.0	0.01	0.18
14WA3 -P1	250-120	6		0.01	0.41	18.88	45.36	0.12	0.00	23.72	1.01	1.89	0.01	0.00	7.68	99.09	2.990	7.1	61.7	0.00	0.00
14WA3 -P1	250-120	8	A	0.02	0.10	17.77	46.85	0.09	0.00	24.71	0.82	2.33	0.01	0.00	6.83	99.54	2.997	5.6	63.9	0.00	0.00
14WA3 -P1	250-120	9		0.02	0.31	17.91	45.71	0.12	0.40	26.91	0.54	1.33	0.00	0.00	6.63	99.88	3.000	3.4	63.1	0.01	0.53
14WA3 -P1	250-120	11		0.01	0.13	18.98	44.10	0.14	0.71	26.29	0.63	1.34	0.01	0.00	6.88	99.22	3.000	4.0	60.9	0.02	0.93
14WA3 -P1	250-120	12	A	0.01	0.07	19.40	39.96	0.13	5.60	24.23	1.13	2.42	0.01	0.01	7.44	100.41	3.000	6.5	58.0	0.17	7.18
14WA3 -P1	250-120	13		0.00	0.11	16.86	46.57	0.10	1.07	25.03	0.76	2.13	0.01	0.00	6.87	99.53	3.000	5.0	64.9	0.04	1.41
14WA3 -P1	250-120	14		0.02	0.10	17.92	46.69	0.11	1.24	23.51	2.60	1.92	0.01	0.00	6.17	100.30	3.000	15.8	63.6	0.05	1.58
14WA3 -P1	250-120	15		0.03	0.29	21.31	41.39	0.08	1.32	24.11	1.05	2.00	0.00	0.00	8.82	100.41	3.000	6.9	56.6	0.05	1.69
14WA3	CHROM	17		0.02	0.83	24.24	38.47	0.18	0.00	22.92	2.02	1.81	0.02	0.00	8.25	98.75	2.991	13.5	51.6	0.00	0.00
14WA3	CHROM	18		0.01	0.09	20.60	41.23	0.16	1.82	24.61	0.99	2.06	0.02	0.01	7.44	99.03	3.000	6.3	57.3	0.06	2.36
14WA3	CHROM	22		0.04	0.13	20.94	37.75	0.19	5.70	23.32	1.30	2.53	0.01	0.00	8.35	100.24	3.000	7.6	54.7	0.18	7.29
14WA3	120-50	44	near core	0.00	0.27	18.13	42.43	0.16	4.37	24.39	1.39	2.03	0.00	0.00	7.29	100.46	3.000	8.0	61.1	0.14	5.65
14WA3	120-50	57		0.02	0.08	16.74	45.11	0.11	3.81	25.93	1.82	1.86	0.00	0.01	4.55	100.04	3.000	9.9	64.4	0.12	4.92
14WA3	120-50	59		0.01	0.19	19.21	45.21	0.10	0.00	25.93	1.13	1.09	0.01	0.00	6.77	99.63	2.998	7.2	61.2	0.00	0.00

***Table S1 cont.**: EPMA data for Jack Hills detrital chromites*

Loc.	size fraction	Crystal #	Comment	SiO_2	TiO_2	Al_2O_3	Cr_2O_3	V_2O_3	Fe_2O_3	FeO	MgO	MnO	CaO	NiO	ZnO	*Total*	Cation Total	Mg#	Cr#	$Fe^{3+}/\Sigma fe$	Fe^{3+}/R^{3+}
14WA3	120-50	60		0.00	0.16	17.84	45.98	0.16	0.24	25.74	0.95	1.58	0.01	0.00	6.48	99.13	3.000	6.1	63.4	0.01	0.32
14WA3	250-120	21		0.11	0.10	18.45	44.14	0.15	0.35	26.62	0.57	1.41	0.06	0.01	6.09	98.05	3.000	3.6	61.6	0.01	0.46
14WA3	250-120	22		0.04	0.44	20.63	41.79	0.18	0.40	26.13	0.80	1.27	0.02	0.00	7.45	99.13	3.000	5.1	57.6	0.01	0.52
14WA3	250-120	25	core	0.12	0.15	8.69	54.51	0.07	3.33	26.75	0.49	1.94	0.01	0.01	4.96	101.02	3.000	2.8	80.8	0.10	4.48
14WA3	250-120	26	core	0.01	0.22	17.02	46.40	0.09	0.53	25.25	1.05	1.69	0.00	0.00	6.59	98.85	3.000	6.8	64.6	0.02	0.70
14WA3	250-120	28	v.pitted	0.04	0.22	18.98	45.85	0.09	0.00	24.38	1.03	1.61	0.00	0.01	7.13	99.33	2.990	7.0	61.8	0.00	0.00
14WA3	250-120	31		0.02	0.09	20.22	43.88	0.08	0.27	24.20	1.29	1.83	0.00	0.01	7.96	99.86	3.000	8.6	59.3	0.01	0.35
14WA3	250-120	32		0.08	0.11	19.40	40.70	0.09	4.40	24.89	1.69	1.73	0.01	0.00	6.40	99.50	3.000	9.5	58.5	0.14	5.68
14WA3	250-120	33		0.02	0.20	17.96	42.47	0.10	4.87	24.28	1.21	2.17	0.01	0.01	7.64	100.94	3.000	7.0	61.3	0.15	6.27
14WA3	250-120	36		0.02	0.33	17.83	46.49	0.14	0.00	25.65	0.55	1.48	0.01	0.00	6.57	99.07	2.991	3.7	63.6	0.00	0.00
14WA3	250-120	37		0.00	0.16	17.26	46.84	0.12	0.00	25.99	0.54	1.42	0.01	0.00	6.47	98.80	2.996	3.5	64.5	0.00	0.00
14WA3	250-120	38		0.11	0.25	9.63	53.35	0.13	2.78	26.51	0.74	1.70	0.02	0.01	5.05	100.28	3.000	4.3	78.8	0.09	3.76
14WA3	500-250	4		0.01	0.48	18.70	43.87	0.13	0.85	27.24	0.80	1.38	0.01	0.00	5.88	99.35	3.000	4.9	61.1	0.03	1.12
14WA3	500-250	8		0.01	0.35	19.36	40.20	0.28	4.12	27.20	0.60	1.45	0.01	0.00	6.25	99.82	3.000	3.4	58.2	0.12	5.37
14WA3	500-250	12		0.02	0.16	17.37	47.49	0.12	0.00	23.33	0.89	2.11	0.00	0.00	7.87	99.35	2.992	6.4	64.7	0.00	0.00
14WA3	500-250	14	core	0.01	0.53	21.45	40.35	0.21	1.01	24.48	1.09	1.89	0.00	0.01	8.35	99.37	3.000	7.1	55.8	0.04	1.31
14WA3	500-250	19		0.01	0.13	19.96	43.88	0.11	0.46	23.09	1.71	1.74	0.01	0.00	8.39	99.52	3.000	11.5	59.6	0.02	0.59
14WA4	CHROM	25	nr core	0.02	0.19	19.70	43.72	0.12	0.00	25.62	0.75	1.99	0.01	0.00	6.57	98.67	2.998	4.9	59.8	0.00	0.00
14WA4	CHROM	31		0.00	0.12	21.18	40.61	0.13	1.46	25.88	0.74	1.79	0.01	0.01	6.83	98.75	3.000	4.6	56.3	0.05	1.89
14WA4	CHROM	29	core	0.03	0.23	18.94	47.94	0.11	0.00	22.41	0.62	1.93	0.00	0.00	6.17	98.36	2.960	4.7	62.9	0.00	0.00
14WA4	500-250	2	nr core	0.00	0.13	17.08	46.92	0.09	0.00	25.81	0.55	2.01	0.00	0.00	5.67	98.27	2.995	3.7	64.8	0.00	0.00

***Table S1 cont.**: EPMA data for Jack Hills detrital chromites*

Loc.	size fraction	Crystal #	Comment	SiO_2	TiO_2	Al_2O_3	Cr_2O_3	V_2O_3	Fe_2O_3	FeO	MgO	MnO	CaO	NiO	ZnO	*Total*	Cation Total	Mg#	Cr#	$Fe^{3+}/\Sigma fe$	Fe^{3+}/R^{3+}
14WA4	500-250	5		0.01	0.17	18.88	44.17	0.13	0.42	25.93	0.77	1.96	0.00	0.00	6.19	98.61	3.000	4.9	61.1	0.01	0.55
14WA4	500-250	6		0.01	0.20	19.12	43.96	0.13	0.47	26.22	0.66	1.49	0.01	0.01	6.79	99.07	3.000	4.2	60.7	0.02	0.62
14WA4	500-250	11		0.08	0.17	20.18	40.33	0.17	2.94	26.42	0.64	2.07	0.01	0.00	6.24	99.25	3.000	3.8	57.3	0.09	3.82
14WA4	500-250	14		0.00	0.08	19.72	43.45	0.10	0.69	25.99	0.68	2.01	0.01	0.00	6.45	99.18	3.000	4.3	59.6	0.02	0.89
14WA4	250-120	24		0.02	0.11	18.76	44.24	0.15	0.27	26.42	0.58	2.04	0.01	0.01	5.67	98.28	3.000	3.8	61.3	0.01	0.36
14WA4	250-120	25		0.01	0.05	22.08	37.96	0.19	3.82	26.13	0.76	1.94	0.01	0.02	6.75	99.70	3.000	4.4	53.6	0.12	4.88
14WA4	250-120	29		0.04	0.09	19.83	42.54	0.13	1.04	25.67	0.74	2.10	0.00	0.02	6.50	98.71	3.000	4.7	59.0	0.04	1.36
14WA4	250-120	31		0.02	0.25	22.81	37.51	0.18	2.80	25.26	0.94	2.12	0.00	0.00	7.44	99.33	3.000	5.7	52.5	0.09	3.59
14WA4	250-120	36		0.08	0.22	9.87	55.60	0.06	0.00	25.36	0.46	2.27	0.01	0.00	4.55	98.49	2.990	3.1	79.1	0.00	0.00
14WA4	250-120	38	nr rim	0.03	0.36	17.10	44.49	0.16	1.57	27.30	0.50	1.87	0.01	0.00	5.08	98.47	3.000	3.0	63.6	0.05	2.10
14WA4	250-120	40		0.01	0.21	19.43	41.38	0.11	2.31	26.83	0.57	1.75	0.00	0.02	5.80	98.43	3.000	3.4	58.8	0.07	3.03
14WA4	120-50	43		0.09	0.16	13.91	50.71	0.15	0.00	25.61	0.84	1.33	0.01	0.00	5.23	98.05	2.991	5.5	71.0	0.00	0.00
14WA4	120-50	45		0.06	0.26	18.60	42.51	0.15	2.27	26.10	0.68	1.92	0.02	0.02	6.36	98.94	3.000	4.1	60.5	0.07	2.98
14WA4	120-50	51		0.01	0.13	19.46	42.32	0.12	2.03	26.98	0.72	1.40	0.00	0.01	5.94	99.11	3.000	4.2	59.3	0.06	2.64
14WA4	120-50	60		0.03	0.14	17.72	44.74	0.09	1.08	27.74	0.75	1.39	0.03	0.03	4.48	98.22	3.000	4.4	62.9	0.03	1.43
14WA4-P3	250-120	1		0.03	0.17	20.55	40.96	0.16	2.01	26.21	0.78	1.73	0.01	0.00	6.61	99.21	3.000	4.7	57.2	0.06	2.61
14WA4-P3	250-120	2	A	0.02	0.13	17.64	45.21	0.12	0.39	26.59	0.55	1.62	0.01	0.00	5.77	98.05	3.000	3.5	63.2	0.01	0.52
14WA4-P3	250-120	2	B	0.01	0.12	17.80	44.97	0.11	0.71	26.09	0.57	1.56	0.00	0.02	6.48	98.45	3.000	3.6	62.9	0.02	0.94
14WA4-P3	250-120	3		0.02	0.10	19.38	42.08	0.11	1.97	25.76	0.66	2.21	0.00	0.01	6.28	98.56	3.000	4.1	59.3	0.06	2.57
14WA4-P3	250-120	5		0.01	0.12	21.74	37.42	0.16	4.27	26.11	0.69	2.02	0.01	0.00	6.60	99.15	3.000	4.0	53.6	0.13	5.50
14WA4-P3	250-120	6	A	0.00	0.15	16.23	46.87	0.11	0.26	26.16	0.51	1.92	0.00	0.00	5.67	97.90	3.000	3.4	66.0	0.01	0.35

***Table S1 cont.**: EPMA data for Jack Hills detrital chromites*

Loc.	size fraction	Crystal #	Comment	SiO_2	TiO_2	Al_2O_3	Cr_2O_3	V_2O_3	Fe_2O_3	FeO	MgO	MnO	CaO	NiO	ZnO	*Total*	Cation Total	Mg#	Cr#	$Fe^{3+}/\Sigma fe$	Fe^{3+}/R^{3+}
14WA4-P3	250-120	8		0.02	0.20	19.21	40.63	0.13	3.56	26.18	0.68	2.07	0.00	0.01	6.02	98.72	3.000	3.9	58.7	0.11	4.67
14WA4-P3	250-120	9		0.03	0.18	19.55	42.49	0.12	1.01	26.40	0.70	1.88	0.01	0.01	5.90	98.28	3.000	4.4	59.3	0.03	1.33
14WA4-P3	250-120	10		0.01	0.15	17.62	45.10	0.10	0.62	25.98	0.56	2.01	0.01	0.00	6.05	98.22	3.000	3.6	63.2	0.02	0.81
14WA4-P3	250-120	12		0.01	0.31	18.38	40.03	0.19	4.96	26.23	0.75	1.53	0.01	0.01	6.41	98.81	3.000	4.1	59.4	0.15	6.55
14WA4-P3	250-120	13		0.01	0.25	17.92	42.39	0.17	3.22	26.37	0.65	2.06	0.00	0.00	5.71	98.75	3.000	3.8	61.3	0.10	4.25
14WA4-P3	250-120	14	A	0.01	0.29	18.63	44.04	0.12	0.43	26.28	0.54	1.51	0.00	0.00	6.76	98.61	3.000	3.5	61.3	0.01	0.57
14WA4-P3	250-120	15		0.00	0.13	18.80	43.46	0.15	1.63	26.22	0.86	1.95	0.00	0.00	5.76	98.97	3.000	5.3	60.8	0.05	2.12
14WA4-P3	250-120	16		0.03	0.12	16.43	46.89	0.11	0.16	25.50	0.58	1.80	0.01	0.00	6.55	98.19	3.000	3.9	65.7	0.01	0.22
14WA4-P3	250-120	18		0.03	0.70	20.03	41.37	0.15	0.87	26.16	0.85	2.00	0.00	0.00	6.52	98.68	3.000	5.3	58.1	0.03	1.15
14WA4-P3	250-120	19		0.03	0.09	20.82	38.98	0.15	3.70	25.84	0.75	2.01	0.01	0.02	6.60	99.00	3.000	4.4	55.7	0.11	4.79
14WA4-P3	250-120	20		0.01	0.07	20.09	40.50	0.13	3.22	25.42	0.82	2.03	0.00	0.01	6.79	99.09	3.000	4.9	57.5	0.10	4.16
14WA4-P3	250-120	21		0.02	0.13	17.00	43.64	0.18	3.09	25.75	0.80	1.94	0.00	0.00	5.90	98.44	3.000	4.8	63.3	0.10	4.09
14WA4-P3	250-120	22		0.02	0.29	18.35	42.93	0.11	2.12	26.56	0.99	1.98	0.01	0.00	5.06	98.42	3.000	5.8	61.1	0.07	2.80
14WA4-P3	250-120	23		0.02	0.11	20.58	39.10	0.16	3.71	25.31	0.86	2.11	0.00	0.00	6.76	98.72	3.000	5.1	56.0	0.12	4.82
14WA4-P3	250-120	24		0.02	0.20	20.13	39.62	0.22	3.41	26.40	0.67	1.85	0.01	0.00	6.22	98.75	3.000	3.9	56.9	0.10	4.45
14WA4-P3	250-120	26		0.01	0.14	14.63	47.44	0.16	1.81	25.92	0.65	2.12	0.01	0.00	5.29	98.17	3.000	4.0	68.5	0.06	2.42
14WA4-P3	250-120	27	A	0.02	0.11	16.88	42.72	0.14	4.28	26.37	0.53	2.15	0.01	0.02	5.46	98.69	3.000	3.0	62.9	0.13	5.66
14WA4-P3	250-120	28	A	0.00	0.09	18.53	44.42	0.11	0.82	26.17	0.62	1.84	0.01	0.01	6.19	98.80	3.000	4.0	61.7	0.03	1.07
14WA4-P3	250-120	29		0.10	0.21	10.00	55.23	0.08	0.00	25.30	0.48	1.91	0.00	0.00	4.36	97.67	2.986	3.2	78.7	0.00	0.00
14WA4-P3	250-120	30		0.02	0.13	17.47	45.94	0.10	0.00	26.34	0.64	1.73	0.01	0.00	5.83	98.21	3.000	4.1	63.8	0.00	0.00
14WA4-P3	250-120	31	A	0.02	0.26	17.89	44.54	0.15	0.67	26.21	0.57	1.54	0.00	0.02	6.49	98.36	3.000	3.7	62.5	0.02	0.88

***Table S1 cont.**: EPMA data for Jack Hills detrital chromites*

Loc.	size fraction	Crystal #	Comment	SiO_2	TiO_2	Al_2O_3	Cr_2O_3	V_2O_3	Fe_2O_3	FeO	MgO	MnO	CaO	NiO	ZnO	*Total*	Cation Total	Mg#	Cr#	$Fe^{3+}/\Sigma fe$	Fe^{3+}/R^{3+}
14WA4-P3	250-120	33		0.05	0.72	16.39	45.20	0.15	0.34	26.92	0.50	1.90	0.01	0.00	5.47	97.65	3.000	3.2	64.9	0.01	0.47
14WA4-P3	250-120	34	A	0.00	0.11	19.37	44.15	0.11	0.00	25.83	0.63	1.50	0.00	0.02	6.98	98.70	2.999	4.2	60.5	0.00	0.00
14WA4-P3	250-120	35		0.00	0.15	17.88	43.93	0.11	1.75	25.73	0.63	1.69	0.00	0.00	6.70	98.58	3.000	3.9	62.2	0.06	2.30
14WA4-P3	250-120	36		0.01	0.10	18.45	44.51	0.13	0.71	26.25	0.57	1.61	0.00	0.01	6.48	98.83	3.000	3.7	61.8	0.02	0.93
14WA4-P3	250-120	37		0.01	0.16	19.53	42.95	0.12	1.12	26.98	0.98	1.13	0.01	0.00	5.72	98.69	3.000	5.9	59.6	0.04	1.46
14WA4-P3	250-120	39		0.02	0.12	17.38	44.66	0.14	1.32	26.18	0.57	2.05	0.00	0.01	5.65	98.08	3.000	3.6	63.3	0.04	1.76
14WA4-P3	250-120	40		0.01	0.17	18.42	44.36	0.13	0.49	26.15	0.63	2.09	0.00	0.00	5.85	98.30	3.000	4.0	61.8	0.02	0.65
14WA4-P3	250-120	41		0.02	0.08	20.11	41.81	0.11	1.24	25.61	0.71	1.88	0.01	0.00	6.76	98.34	3.000	4.5	58.2	0.04	1.62
14WA4-P3	250-120	42		0.08	0.18	10.04	54.85	0.07	0.00	26.13	0.47	1.82	0.00	0.00	4.26	97.91	2.993	3.1	78.6	0.00	0.00
14WA4-P3	250-120	43		0.01	0.17	19.93	42.26	0.13	1.23	25.68	0.69	2.01	0.00	0.00	6.82	98.92	3.000	4.4	58.7	0.04	1.59
14WA4-P3	250-120	45		0.02	0.19	17.76	44.93	0.15	0.50	26.46	0.73	1.84	0.01	0.02	5.40	98.01	3.000	4.6	62.9	0.02	0.66
14WA4-P2	250-120	1	A	0.01	0.16	20.39	45.48	0.12	0.00	23.27	0.71	1.95	0.00	0.00	7.06	99.15	2.975	5.2	59.9	0.00	0.00
14WA4-P2	250-120	2		0.00	0.08	17.85	44.39	0.12	1.30	26.20	0.53	1.48	0.01	0.00	6.43	98.39	3.000	3.4	62.5	0.04	1.71
14WA4-P2	250-120	3		0.02	0.13	23.02	35.76	0.23	4.49	26.13	0.94	1.87	0.01	0.00	6.60	99.21	3.000	5.3	51.0	0.13	5.75
14WA4-P2	250-120	5		0.01	0.15	19.42	39.26	0.15	5.16	26.46	0.63	1.92	0.00	0.01	6.13	99.31	3.000	3.5	57.6	0.15	6.71
14WA4-P2	250-120	6		0.02	0.10	18.32	44.56	0.12	0.82	29.30	0.64	1.91	0.01	0.01	2.52	98.33	3.000	3.7	62.0	0.02	1.07
14WA4-P2	250-120	7	A	0.11	0.17	15.00	49.09	0.10	0.00	26.29	0.52	1.97	0.00	0.00	5.41	98.67	2.997	3.4	68.7	0.00	0.00
14WA4-P2	250-120	8		0.02	0.17	21.93	39.27	0.13	1.98	26.35	0.74	2.02	0.00	0.00	6.37	98.97	3.000	4.5	54.6	0.06	2.55
14WA4-P2	250-120	9		0.05	0.11	16.01	44.84	0.22	3.20	26.77	0.59	1.79	0.01	0.00	5.32	98.92	3.000	3.5	65.3	0.10	4.24
14WA4-P2	250-120	10	A	0.02	0.09	18.73	44.28	0.12	0.75	26.60	0.58	1.86	0.00	0.00	5.92	98.96	3.000	3.6	61.3	0.02	0.98
14WA4-P2	250-120	11		0.02	0.23	17.97	47.25	0.12	0.00	24.35	0.66	2.11	0.00	0.00	6.05	98.76	2.982	4.6	63.8	0.00	0.00

***Table S1 cont.**: EPMA data for Jack Hills detrital chromites*

Loc.	size fraction	Crystal #	Comment	SiO_2	TiO_2	Al_2O_3	Cr_2O_3	V_2O_3	Fe_2O_3	FeO	MgO	MnO	CaO	NiO	ZnO	*Total*	Cation Total	Mg#	Cr#	$Fe^{3+}/\Sigma fe$	Fe^{3+}/R^{3+}
14WA4-P2	250-120	12		0.00	0.17	19.90	43.13	0.13	0.52	26.57	0.63	1.82	0.01	0.01	6.17	99.05	3.000	4.0	59.2	0.02	0.67
14WA4-P2	250-120	13		0.02	0.10	19.54	43.25	0.11	0.68	26.33	0.65	1.79	0.00	0.00	6.23	98.70	3.000	4.1	59.8	0.02	0.88
14WA4-P2	250-120	14	A	0.01	0.28	19.24	43.94	0.10	0.07	26.07	0.63	2.03	0.00	0.00	6.43	98.82	3.000	4.1	60.5	0.00	0.10
14WA4-P2	250-120	15		0.01	0.30	17.67	44.69	0.11	0.83	26.31	0.65	2.02	0.00	0.02	5.71	98.32	3.000	4.1	62.9	0.03	1.10
14WA4-P2	250-120	16		0.01	0.26	20.51	41.33	0.15	1.32	25.79	0.72	1.62	0.01	0.00	7.30	99.03	3.000	4.5	57.5	0.04	1.72
14WA4-P2	250-120	17		0.01	0.14	17.18	45.64	0.12	0.87	26.44	0.49	1.66	0.00	0.00	6.14	98.69	3.000	3.1	64.1	0.03	1.15
14WA4-P2	250-120	18		0.02	0.21	16.86	44.68	0.15	2.28	26.45	0.58	2.11	0.00	0.00	5.57	98.91	3.000	3.5	64.0	0.07	3.01
14WA4-P2	250-120	20		0.02	0.09	18.39	44.93	0.10	0.16	26.04	0.58	1.57	0.00	0.01	6.63	98.52	3.000	3.8	62.1	0.01	0.21
14WA4-P2	250-120	23		0.02	0.16	18.39	39.81	0.26	5.14	26.59	0.70	1.88	0.01	0.01	5.42	98.40	3.000	3.9	59.2	0.15	6.78
14WA4-P2	250-120	24		0.02	0.11	17.39	46.06	0.08	0.47	26.17	1.01	2.07	0.00	0.00	5.03	98.43	3.000	6.4	64.0	0.02	0.62
14WA4-P2	250-120	25		0.01	0.41	16.13	42.12	0.27	5.46	26.89	0.66	2.00	0.00	0.00	5.12	99.06	3.000	3.6	63.7	0.15	7.28
16WA5	Hf leach	1		0.00	0.64	19.81	43.48	0.22	0.00	29.65	1.09	1.22	0.00	0.02	2.80	98.95	2.997	6.2	59.6	0.00	0.00
16WA5	Hf leach	2		0.02	0.22	18.13	46.85	0.21	0.00	29.19	2.00	0.74	0.00	0.00	1.49	98.86	2.995	10.9	63.4	0.00	0.00
16WA5	Hf leach	3		0.00	0.31	17.51	48.65	0.15	0.00	26.89	2.83	0.89	0.02	0.00	1.60	98.85	2.988	15.8	65.1	0.00	0.00
16WA5	Hf leach	4		0.05	0.35	13.96	49.82	0.21	0.85	30.53	1.15	0.71	0.00	0.01	1.49	99.13	3.000	6.1	70.5	0.02	1.14
16WA5	Hf leach	5	left	0.00	0.27	14.29	52.98	0.16	0.00	28.29	0.90	0.91	0.01	0.00	1.34	99.15	2.974	5.4	71.3	0.00	0.00
16WA5	<250	1	A-CORE	0.08	0.17	10.30	53.46	na	2.96	27.17	2.48	1.34	0.01	0.00	1.58	99.56	3.000	12.9	77.7	0.09	3.94
16WA5	<250	2		0.03	0.06	18.49	47.44	na	0.00	27.23	2.25	1.00	0.01	0.00	1.92	98.43	2.988	12.8	63.3	0.00	0.00
16WA5	<250	3	A	0.03	0.38	15.91	47.75	na	0.59	29.20	1.68	1.05	0.01	0.00	1.74	98.35	3.000	9.2	66.8	0.02	0.78
16WA5	<250	4		0.01	0.06	20.55	44.24	na	0.00	27.93	1.43	1.19	0.00	0.00	3.05	98.47	2.992	8.4	59.1	0.00	0.00
16WA5	<250	5		0.00	0.33	20.73	44.19	na	0.00	28.85	1.40	0.76	0.00	0.01	2.20	98.46	2.986	7.9	58.9	0.00	0.00
16WA5	<250	6		0.02	0.90	19.90	42.78	na	0.30	29.99	2.05	0.83	0.01	0.02	1.73	98.52	3.000	10.8	59.0	0.01	0.39
16WA5	<250	7		0.00	0.08	22.48	41.55	na	0.57	28.17	2.72	0.84	0.00	0.00	2.30	98.72	3.000	14.5	55.4	0.02	0.72

***Table S1 cont.**: EPMA data for Jack Hills detrital chromites*

Loc.	size fraction	Crystal #	Comment	SiO_2	TiO_2	Al_2O_3	Cr_2O_3	V_2O_3	Fe_2O_3	FeO	MgO	MnO	CaO	NiO	ZnO	*Total*	Cation Total	Mg#	Cr#	$Fe^{3+}/\Sigma fe$	Fe^{3+}/R^{3+}
16WA5	<250	10		0.02	0.09	20.46	45.45	na	0.00	27.65	2.39	0.75	0.01	0.01	2.08	98.90	2.989	13.4	59.8	0.00	0.00
16WA5	<250	11	CORE	0.01	0.09	21.37	42.95	na	0.50	27.52	3.02	0.94	0.00	0.00	2.16	98.56	3.000	16.1	57.4	0.02	0.64
16WA5	<250	12		0.01	0.08	20.50	45.27	na	0.00	26.88	2.62	1.09	0.01	0.00	2.49	98.95	2.992	14.8	59.7	0.00	0.00
16WA5	<250	14		0.01	0.09	22.85	41.82	na	0.33	27.16	3.49	0.79	0.00	0.01	2.28	98.83	3.000	18.5	55.1	0.01	0.41
16WA5	<250	15		0.03	0.94	18.01	45.60	na	0.00	28.87	1.85	0.94	0.01	0.00	1.88	98.13	2.991	10.3	62.9	0.00	0.00
16WA5	<250	16		0.01	0.12	21.83	42.00	na	0.38	29.35	1.96	0.90	0.01	0.00	2.11	98.66	3.000	10.5	56.4	0.01	0.48
16WA5	<250	17		0.01	0.19	15.31	51.71	na	0.00	26.26	1.90	0.93	0.02	0.00	2.03	98.37	2.977	11.4	69.4	0.00	0.00
16WA5	<250	18		0.01	0.14	20.82	43.69	na	0.07	26.76	3.08	1.06	0.01	0.00	2.58	98.23	3.000	17.0	58.5	0.00	0.09
16WA5	<250	19		0.01	0.12	20.28	44.18	na	0.00	28.76	2.18	0.71	0.00	0.02	2.11	98.38	2.999	11.9	59.4	0.00	0.00
16WA5	<250	20		0.11	0.16	9.53	50.12	na	7.09	28.68	1.51	1.39	0.01	0.00	1.51	100.11	3.000	7.1	77.9	0.18	9.49
16WA5	<250	21		0.00	0.07	21.47	43.17	na	0.00	27.99	2.47	0.84	0.00	0.02	2.34	98.36	2.998	13.6	57.4	0.00	0.00
16WA5	<250	22		0.01	0.08	21.70	42.90	na	0.00	28.10	1.99	1.16	0.01	0.00	2.98	98.91	2.998	11.2	57.0	0.00	0.00
16WA5	<250	23		0.02	0.16	20.40	44.98	na	0.00	27.48	2.56	0.89	0.01	0.00	2.10	98.61	2.992	14.2	59.7	0.00	0.00
16WA5	<250	24		0.02	0.74	18.13	46.81	na	0.00	28.16	1.85	0.90	0.01	0.00	1.78	98.40	2.983	10.5	63.4	0.00	0.00
16WA5	<250	25		0.02	0.08	21.09	43.89	na	0.00	27.86	2.55	0.92	0.00	0.00	2.27	98.68	2.997	14.0	58.3	0.00	0.00
16WA5	<250	26		0.00	0.05	20.89	44.45	na	0.00	27.22	2.95	0.78	0.01	0.01	1.92	98.28	2.994	16.2	58.8	0.00	0.00
16WA5	<250	27		0.01	0.11	16.27	49.39	na	0.00	26.60	2.56	1.10	0.01	0.00	2.14	98.18	2.994	14.6	67.1	0.00	0.00
16WA5	<250	28		0.01	0.20	21.95	41.65	na	0.30	28.47	1.95	0.95	0.00	0.01	3.12	98.61	3.000	10.8	56.0	0.01	0.38
16WA5	<250	29		0.00	0.24	16.86	48.27	na	0.00	28.84	1.26	0.97	0.01	0.00	1.81	98.26	2.989	7.2	65.8	0.00	0.00
16WA5	<250	30		0.01	0.56	14.07	51.89	na	0.00	28.10	1.44	0.79	0.00	0.00	1.35	98.23	2.980	8.4	71.2	0.00	0.00
16WA5	<250	31		0.00	0.28	21.64	42.82	na	0.00	28.96	1.74	0.82	0.00	0.00	2.50	98.75	2.994	9.7	57.0	0.00	0.00
16WA5	<250	32		0.00	0.19	18.45	45.41	na	2.51	28.11	2.64	1.22	0.00	0.00	2.13	100.67	3.000	13.4	62.3	0.07	3.18
16WA5	<250	33		0.00	0.08	18.02	47.54	na	0.00	27.78	1.69	0.87	0.00	0.01	2.36	98.35	2.989	9.8	63.9	0.00	0.00
16WA5	<250	34		0.03	0.10	18.82	43.78	na	1.59	28.75	1.51	1.26	0.00	0.00	2.48	98.32	3.000	8.2	60.9	0.05	2.07
16WA5	<250	36	core	0.01	0.14	16.16	45.59	na	4.73	29.14	2.09	1.01	0.00	0.00	1.63	100.49	3.000	10.0	65.4	0.13	6.07
16WA5	<250	37		0.02	0.09	23.55	40.90	na	0.07	27.34	2.90	1.07	0.00	0.00	2.92	98.86	3.000	15.9	53.8	0.00	0.09
16WA5	<250	38		0.02	0.07	22.16	42.06	na	0.10	28.54	2.24	1.01	0.00	0.00	2.43	98.63	3.000	12.3	56.0	0.00	0.13
16WA5	<250	40		0.04	0.12	20.61	46.11	na	0.00	26.36	2.92	0.85	0.01	0.01	1.80	98.82	2.982	16.5	60.0	0.00	0.00
16WA5	<250	41	bulk	0.00	0.14	20.98	41.93	na	1.34	28.32	2.29	0.97	0.01	0.00	2.34	98.31	3.000	12.1	57.3	0.04	1.71
16WA5	<250	42		0.01	0.59	18.05	45.36	na	0.54	28.41	2.52	0.96	0.00	0.00	1.81	98.26	3.000	13.5	62.8	0.02	0.71
16WA5	<250	43	bulk	0.01	0.11	18.99	47.29	na	0.00	27.78	2.02	0.79	0.00	0.00	1.73	98.73	2.984	11.5	62.6	0.00	0.00
16WA5	<250	45		0.02	0.07	15.45	50.24	na	0.00	27.46	1.49	1.30	0.00	0.00	2.09	98.12	2.989	8.8	68.6	0.00	0.00

***Table S1 cont.**: EPMA data for Jack Hills detrital chromites*

Loc.	size fraction	Crystal #	Comment	SiO_2	TiO_2	Al_2O_3	Cr_2O_3	V_2O_3	Fe_2O_3	FeO	MgO	MnO	CaO	NiO	ZnO	*Total*	Cation Total	Mg#	Cr#	$Fe^{3+}/\Sigma fe$	Fe^{3+}/R^{3+}
16WA5	<250	46		0.01	0.08	17.16	46.43	na	1.31	28.46	2.02	1.02	0.00	0.02	1.89	98.40	3.000	10.8	64.5	0.04	1.70
16WA5	<250	49		0.02	0.09	17.80	47.89	na	0.00	27.59	2.18	0.94	0.01	0.00	2.11	98.63	2.992	12.4	64.3	0.00	0.00
16WA6	<250	1		0.13	0.22	10.36	55.71	na	0.00	25.54	1.31	0.76	0.01	0.00	3.88	97.92	2.983	8.4	78.3	0.00	0.00
16WA6	<250	2	core	0.03	0.13	18.30	45.36	na	0.38	26.88	1.63	0.59	0.00	0.00	5.02	98.32	3.000	9.6	62.4	0.01	0.50
16WA6	<250	3		0.02	0.14	18.07	47.21	na	0.00	23.13	3.09	0.86	0.00	0.02	5.59	98.12	2.994	19.2	63.7	0.00	0.00
16WA6	<250	4		0.03	0.12	19.91	42.90	na	1.08	25.06	2.05	0.86	0.01	0.00	6.23	98.24	3.000	12.3	59.1	0.04	1.40
16WA6	<250	5		0.01	0.13	17.37	47.00	na	0.00	28.01	1.89	0.39	0.00	0.00	3.08	97.88	2.998	10.7	64.5	0.00	0.00
16WA6	<250	6	core	0.05	0.14	12.60	54.73	na	0.00	25.97	1.10	0.32	0.01	0.01	2.73	97.65	2.967	7.0	74.5	0.00	0.00
16WA6	<250	8		0.03	0.08	23.95	38.47	na	0.44	28.44	1.34	0.36	0.00	0.01	4.85	97.97	3.000	7.6	51.9	0.01	0.57
16WA6	<250	10		0.03	0.12	20.21	42.95	na	0.57	28.05	1.37	0.49	0.01	0.00	4.62	98.41	3.000	7.9	58.8	0.02	0.73
16WA6	<250	11		0.02	0.14	20.56	43.10	na	0.16	26.61	1.80	0.54	0.00	0.00	5.49	98.42	3.000	10.7	58.4	0.01	0.20
16WA6	<250	12		0.01	0.19	18.26	45.82	na	0.00	27.50	1.67	0.33	0.01	0.00	4.32	98.11	2.998	9.8	62.7	0.00	0.00
16WA6	<250	13		0.02	0.09	19.44	44.49	na	0.28	28.04	1.87	0.37	0.00	0.00	3.76	98.35	3.000	10.5	60.6	0.01	0.36
16WA6	<250	14	core	0.00	0.35	17.12	47.20	na	0.00	28.03	1.42	0.32	0.00	0.00	3.62	98.06	2.993	8.3	64.9	0.00	0.00
16WA6	<250	15	core	0.01	0.09	18.37	45.72	na	0.12	26.99	1.85	0.56	0.00	0.02	4.43	98.15	3.000	10.8	62.5	0.00	0.16
16WA6	<250	17		0.03	0.14	19.49	45.59	na	0.00	23.79	2.84	0.77	0.00	0.00	5.79	98.44	2.994	17.5	61.1	0.00	0.00
16WA6	<250	18		0.02	0.15	21.30	42.57	na	0.00	27.07	1.98	0.49	0.01	0.00	4.73	98.31	2.999	11.5	57.3	0.00	0.00
16WA6	<250	19		0.02	0.21	19.75	44.49	na	0.00	27.07	1.91	0.40	0.01	0.00	4.44	98.28	2.996	11.2	60.2	0.00	0.00
16WA6	<250	21		0.02	0.17	19.68	44.71	na	0.00	26.94	2.35	0.51	0.00	0.00	4.24	98.62	3.000	13.5	60.4	0.00	0.00
16WA6	<250	22		0.03	0.13	18.66	45.84	na	0.00	27.30	1.28	0.44	0.00	0.02	4.25	97.96	2.991	7.7	62.2	0.00	0.00
16WA7	<250	1		0.02	0.22	18.20	42.90	na	2.50	24.22	0.46	0.76	0.01	0.01	9.99	99.29	3.000	3.0	61.3	0.08	3.29
16WA7	<250	2	nr core	0.02	0.11	20.17	42.24	na	0.65	23.31	0.41	0.71	0.00	0.01	11.27	98.92	3.000	3.0	58.4	0.02	0.85
16WA7	<250	3	core	0.08	0.21	18.74	43.68	na	0.82	24.75	0.45	0.76	0.01	0.04	9.53	99.07	3.000	3.1	61.0	0.03	1.07
16WA7	<250	4		0.02	0.17	16.72	46.54	na	0.18	24.81	0.37	0.78	0.01	0.01	8.99	98.62	3.000	2.6	65.1	0.01	0.24
16WA7	<250	6		0.07	0.18	23.26	36.68	na	2.00	23.84	0.49	0.69	0.03	0.03	10.93	98.20	3.000	3.3	51.4	0.07	2.60
16WA7	<250	7		0.00	0.28	22.43	38.52	na	1.81	23.79	0.49	0.73	0.01	0.00	11.24	99.31	3.000	3.3	53.5	0.06	2.34
16WA7	<250	8		0.01	0.21	25.49	34.75	na	2.24	22.75	0.55	0.66	0.00	0.00	12.91	99.57	3.000	3.8	47.8	0.08	2.84
16WA7	<250	10	core	0.00	0.23	20.73	41.20	na	1.10	23.85	0.43	0.77	0.00	0.00	10.87	99.20	3.000	3.0	57.1	0.04	1.43
16WA7	<250	11		0.02	0.21	21.60	36.26	na	5.23	24.53	0.47	0.74	0.00	0.02	10.17	99.25	3.000	2.8	53.0	0.16	6.77
16WA7	<250	12		0.05	0.19	17.48	44.40	na	1.43	23.71	0.41	0.81	0.01	0.00	10.34	98.83	3.000	2.8	63.0	0.05	1.89
16WA7	<250	13		0.01	0.17	18.06	44.53	na	1.25	23.33	0.49	0.79	0.01	0.00	10.91	99.53	3.000	3.5	62.3	0.05	1.63
16WA7	<250	14		0.03	0.18	19.11	43.91	na	0.11	23.77	0.42	0.75	0.01	0.03	10.58	98.91	3.000	3.1	60.6	0.00	0.14

***Table S1 cont.**: EPMA data for Jack Hills detrital chromites*

Loc.	size fraction	Crystal #	Comment	SiO_2	TiO_2	Al_2O_3	Cr_2O_3	V_2O_3	Fe_2O_3	FeO	MgO	MnO	CaO	NiO	ZnO	*Total*	Cation Total	Mg#	Cr#	$Fe^{3+}/\Sigma fe$	Fe^{3+}/R^{3+}
16WA7	<250	15	core	0.00	0.10	18.56	45.17	na	0.00	23.52	0.41	0.76	0.00	0.00	10.36	98.88	2.997	3.0	62.0	0.00	0.00
16WA7	<250	16		0.01	0.15	18.07	44.91	na	0.37	23.94	0.41	0.75	0.01	0.00	10.18	98.81	3.000	2.9	62.5	0.01	0.49
16WA7	<250	17		0.00	0.16	18.09	44.82	na	0.92	23.94	0.36	0.79	0.02	0.00	10.48	99.58	3.000	2.5	62.4	0.03	1.21
16WA7	<250	18		0.03	0.56	16.96	44.85	na	0.60	24.69	0.31	0.76	0.01	0.04	9.56	98.37	3.000	2.2	63.9	0.02	0.81
16WA7	<250	19	core	0.03	0.48	20.71	43.90	na	0.00	21.55	0.52	0.76	0.01	0.01	11.95	99.92	2.982	4.1	58.7	0.00	0.00
16WA7	<250	20		0.02	0.18	18.80	43.37	na	1.12	24.07	0.43	0.76	0.00	0.03	10.16	98.96	3.000	3.0	60.7	0.04	1.48
16WA8	<250	1		0.01	0.27	18.03	45.66	na	0.00	28.60	0.76	0.92	0.01	0.00	4.01	98.25	2.997	4.5	62.9	0.00	0.00
16WA8	<250	2	core	0.02	0.08	17.94	45.08	na	0.92	27.99	0.97	0.93	0.00	0.02	4.40	98.35	3.000	5.6	62.8	0.03	1.20
16WA8	<250	3		0.00	0.06	19.78	43.66	na	0.08	28.75	0.78	0.91	0.01	0.01	4.12	98.17	3.000	4.6	59.7	0.00	0.10
16WA8	<250	4		0.01	0.14	17.59	46.03	na	0.00	28.93	0.73	0.98	0.00	0.00	3.65	98.07	3.000	4.3	63.7	0.00	0.00
16WA8	<250	5	core	0.01	0.08	19.02	44.69	na	0.05	28.63	0.91	0.95	0.00	0.01	3.95	98.31	3.000	5.4	61.2	0.00	0.06
16WA8	<250	6		0.02	0.09	17.29	46.99	na	0.00	27.83	0.83	0.94	0.01	0.01	4.41	98.40	2.997	5.0	64.6	0.00	0.00
16WA8	<250	7		0.03	0.15	17.58	47.10	na	0.00	27.37	0.76	0.91	0.00	0.00	4.44	98.36	2.990	4.7	64.2	0.00	0.00
16WA8	<250	8		0.02	0.11	18.25	45.45	na	0.00	28.69	0.74	0.95	0.01	0.00	3.84	98.06	2.998	4.4	62.6	0.00	0.00
16WA8	<250	9	core	0.02	0.14	17.70	45.71	na	0.17	28.04	0.86	0.91	0.00	0.00	4.47	98.02	3.000	5.1	63.4	0.01	0.22
16WA8	<250	10		0.01	0.08	18.04	44.98	na	0.73	28.00	0.87	0.92	0.00	0.02	4.50	98.14	3.000	5.1	62.6	0.02	0.96
16WA8	<250	11		0.02	0.08	22.58	39.45	0.17	1.34	28.51	0.85	0.87	0.01	0.00	5.10	98.96	3.000	4.8	54.0	0.04	1.71
16WA8	<250	12	A	0.02	0.08	17.69	46.35	0.13	0.00	27.57	1.03	0.99	0.01	0.00	4.42	98.29	2.998	6.3	63.7	0.00	0.00
16WA8	<250	13		0.00	0.25	19.48	43.64	0.12	0.19	29.17	0.76	0.95	0.00	0.01	3.93	98.51	3.000	4.4	60.0	0.01	0.25
16WA8	<250	14		0.01	0.07	19.39	42.83	0.16	1.23	28.83	0.81	0.95	0.00	0.00	3.89	98.18	3.000	4.6	59.7	0.04	1.60
16WA8	<250	15		0.01	0.10	18.37	45.98	0.12	0.00	27.33	0.78	0.92	0.01	0.00	4.54	98.15	2.991	4.9	62.7	0.00	0.00
16WA8	<250	17		0.00	0.11	19.58	43.91	0.12	0.00	28.61	0.82	0.93	0.00	0.00	4.24	98.32	3.000	4.9	60.1	0.00	0.00
16WA8	<250	18	A	0.00	0.38	18.15	46.42	0.11	0.00	27.45	0.68	0.91	0.01	0.00	4.53	98.66	2.987	4.3	63.2	0.00	0.00
16WA8	<250	19		0.00	0.07	20.20	43.02	0.12	0.29	28.71	0.72	0.92	0.01	0.00	4.45	98.50	3.000	4.2	58.8	0.01	0.37
16WA8	<250	20		0.06	0.08	20.04	41.89	0.17	1.42	29.49	0.75	1.00	0.01	0.00	3.47	98.38	3.000	4.2	58.4	0.04	1.84
16WA8	<250	21		0.00	0.08	19.00	44.58	0.14	0.11	28.82	0.77	0.97	0.01	0.00	4.02	98.49	3.000	4.5	61.1	0.00	0.14
16WA8	<250	23	B	0.01	0.09	18.84	45.79	0.11	0.00	27.30	1.06	0.98	0.01	0.01	4.17	98.36	2.991	6.5	62.0	0.00	0.00
16WA8	<250	25		0.01	0.27	19.31	43.93	0.13	0.00	28.72	0.72	0.88	0.00	0.03	4.56	98.57	3.000	4.3	60.4	0.00	0.00
16WA8	<250	29	A	0.01	0.61	18.86	44.11	0.12	0.00	29.16	0.71	0.95	0.00	0.01	3.82	98.36	2.996	4.2	61.1	0.00	0.00
16WA8	<250	30		0.00	0.12	17.37	47.11	0.10	0.00	28.54	0.77	0.94	0.00	0.01	3.55	98.51	2.994	4.6	64.5	0.00	0.00
16WA9	<250	2		0.03	0.22	19.48	45.26	0.14	0.00	29.19	0.76	1.80	0.00	0.00	1.39	98.27	2.985	4.4	60.9	0.00	0.00
16WA9	<250	6		0.03	0.64	22.51	40.24	0.21	0.00	30.27	0.78	1.78	0.01	0.00	1.57	98.03	2.990	4.4	54.5	0.00	0.00

***Table S1 cont.**: EPMA data for Jack Hills detrital chromites*

Loc.	size fraction	Crystal #	Comment	SiO_2	TiO_2	Al_2O_3	Cr_2O_3	V_2O_3	Fe_2O_3	FeO	MgO	MnO	CaO	NiO	ZnO	*Total*	Cation Total	Mg#	Cr#	$Fe^{3+}/\Sigma fe$	Fe^{3+}/R^{3+}
16WA9	<250	7		0.03	0.27	21.34	43.34	0.12	0.00	28.61	0.82	1.77	0.00	0.01	1.55	97.87	2.979	4.9	57.7	0.00	0.00
16WA9	<250	8	B	0.04	0.04	20.84	43.70	0.13	0.00	28.74	0.90	1.78	0.01	0.00	1.50	97.69	2.985	5.3	58.5	0.00	0.00
16WA9	<250	9		0.01	0.10	20.12	44.97	0.14	0.00	28.02	0.83	1.81	0.00	0.00	1.94	97.95	2.981	5.0	60.0	0.00	0.00
16WA9	<250	13	B	0.03	0.03	24.10	40.67	0.11	0.00	29.54	0.89	1.73	0.00	0.00	1.14	98.26	2.983	5.1	53.1	0.00	0.00
16WA9	<250	14		0.02	0.32	18.41	46.07	0.16	0.00	28.55	0.81	1.86	0.01	0.00	1.33	97.56	2.983	4.8	62.7	0.00	0.00
16WA9	<250	21	NR RIM	0.02	0.20	18.47	46.78	0.21	0.00	27.78	0.65	1.79	0.00	0.00	1.66	97.55	2.975	4.0	63.0	0.00	0.00
16WA9	<250	27		0.00	0.15	18.95	46.10	0.14	0.00	28.39	0.74	1.80	0.02	0.00	1.21	97.51	2.979	4.4	62.0	0.00	0.00
16WA9	<250	31		0.01	0.06	17.30	46.74	0.11	0.00	29.84	0.70	1.80	0.00	0.03	1.27	97.87	2.997	4.0	64.4	0.00	0.00
16WA10	<250	2		0.02	0.37	19.03	44.83	0.12	0.00	26.67	0.44	1.37	0.01	0.00	4.79	97.64	2.983	2.9	61.2	0.00	0.00
16WA10	<250	4		0.01	0.81	19.26	41.58	0.13	0.31	26.97	0.31	1.13	0.01	0.00	7.04	97.57	3.000	2.0	59.2	0.01	0.41
16WA10	<250	8		0.01	0.11	22.57	41.71	0.15	0.00	25.89	0.48	1.19	0.01	0.00	5.94	98.06	2.981	3.2	55.3	0.00	0.00
16WA10	<250	13	B	0.00	0.22	19.08	45.10	0.13	0.00	25.51	0.44	1.23	0.01	0.01	6.21	97.96	2.984	3.0	61.3	0.00	0.00
16WA10	<250	15		0.00	0.02	15.48	50.31	0.11	0.00	27.77	0.32	1.60	0.01	0.00	3.18	98.80	2.985	2.0	68.5	0.00	0.00
16WA10	<250	17		0.02	0.39	20.16	43.53	0.15	0.00	25.69	0.49	1.24	0.00	0.00	6.08	97.76	2.983	3.3	59.2	0.00	0.00
16WA10	<250	18		0.05	0.79	20.31	43.44	0.20	0.00	23.85	0.46	1.23	0.00	0.01	8.11	98.46	2.976	3.3	58.9	0.00	0.00
16WA10	<250	19		0.01	0.14	21.31	42.83	0.12	0.00	27.17	0.53	1.28	0.00	0.00	4.62	98.02	2.985	3.4	57.4	0.00	0.00
16WA10	<250	20		0.03	0.04	20.35	44.11	0.13	0.00	26.65	0.42	1.28	0.00	0.00	5.50	98.52	2.987	2.8	59.2	0.00	0.00
16WA10	<250	21		0.02	0.05	20.19	43.27	0.13	0.00	27.36	0.47	1.13	0.00	0.00	5.23	97.85	2.993	2.9	59.0	0.00	0.00
16WA10	<250	24		0.03	0.02	19.98	43.65	0.11	0.00	25.90	0.47	1.31	0.00	0.00	6.65	98.13	2.993	3.1	59.4	0.00	0.00
16WA10	<250	26		0.02	0.08	18.94	44.39	0.13	0.00	26.95	0.45	1.32	0.00	0.02	5.84	98.13	2.998	2.9	61.1	0.00	0.00
16WA10	<250	27	A	0.01	0.23	17.05	46.51	0.11	0.00	26.06	0.39	1.18	0.00	0.00	6.09	97.61	2.991	2.6	64.7	0.00	0.00
16WA10	<250	27	B	0.03	0.05	17.08	46.25	0.10	0.00	26.07	0.41	1.21	0.01	0.00	6.44	97.64	2.997	2.7	64.5	0.00	0.00
16WA10	<250	29		0.01	0.05	19.72	44.12	0.12	0.00	27.81	0.51	1.35	0.00	0.00	4.04	97.73	2.991	3.2	60.0	0.00	0.00

Supplementary Material Two:

Chromite physical and chemical compositions

S2.1- EPMA totals plotted against cation totals (normalised to 4 anions) prior to charge balance to calculate Fe_2O_3 contents of chromite. Clear absence of relationship between low totals and non-stoichiometric compositions. This suggests analytical error is not the cause of non-stoichiometry and that both low totals and non-stoichiometry is an inherent feature of some grains. Some analytical points with high totals and non-stoichiometric compositions may represent overlap with another phase.

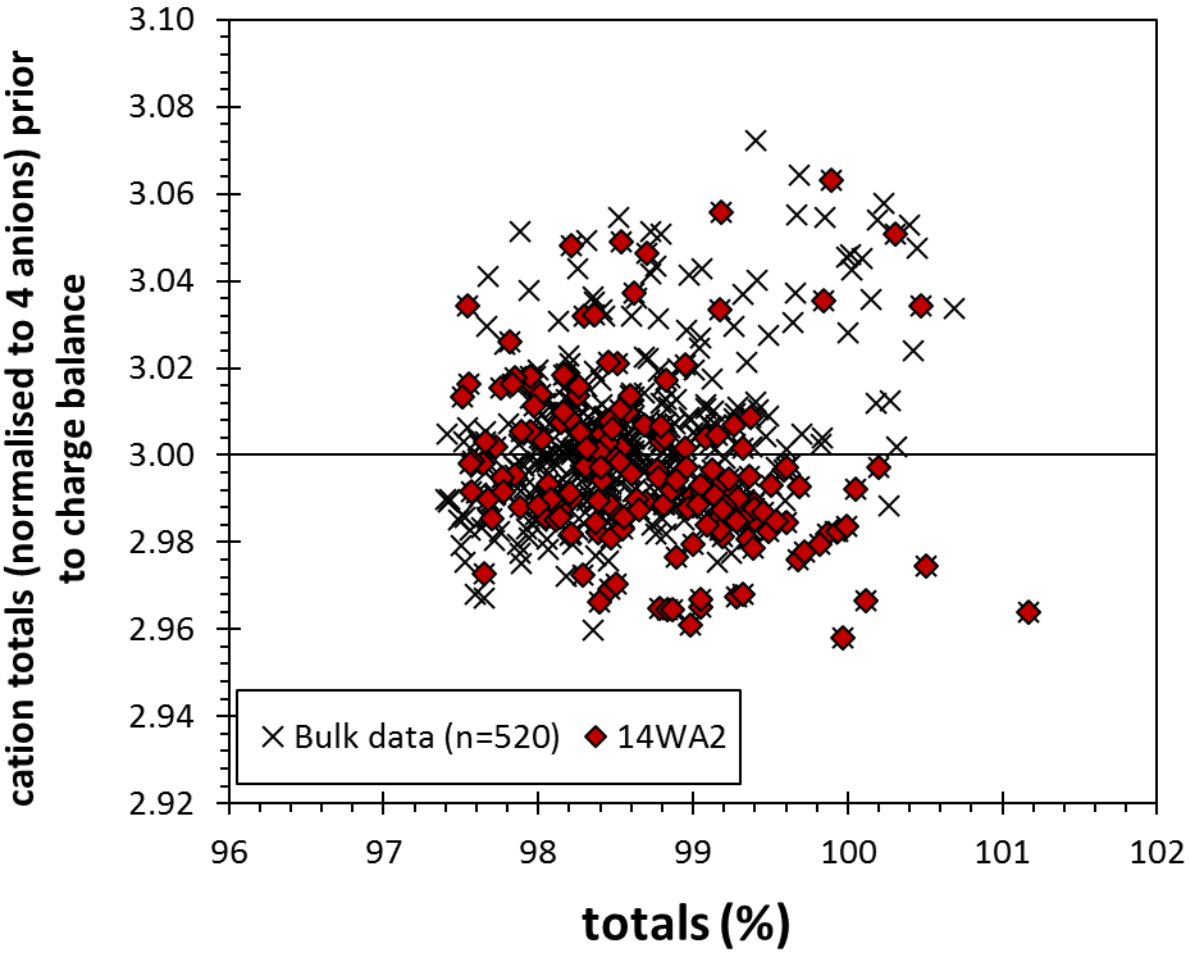

S2.2 - Divalent and Trivalent plot showing the absence of variable mineral chemistry with rounding shape. Each point represents a single-grain analysis. This figure shows bulk samples (excluding 14WA1) split into rounded chromite (RC), rounded octahedra (RO) and euhedral octahedra (EO), as per the main publication. A potential indication that EO yield slightly lowered wt. % TiO_2 in comparison to RC and RO.

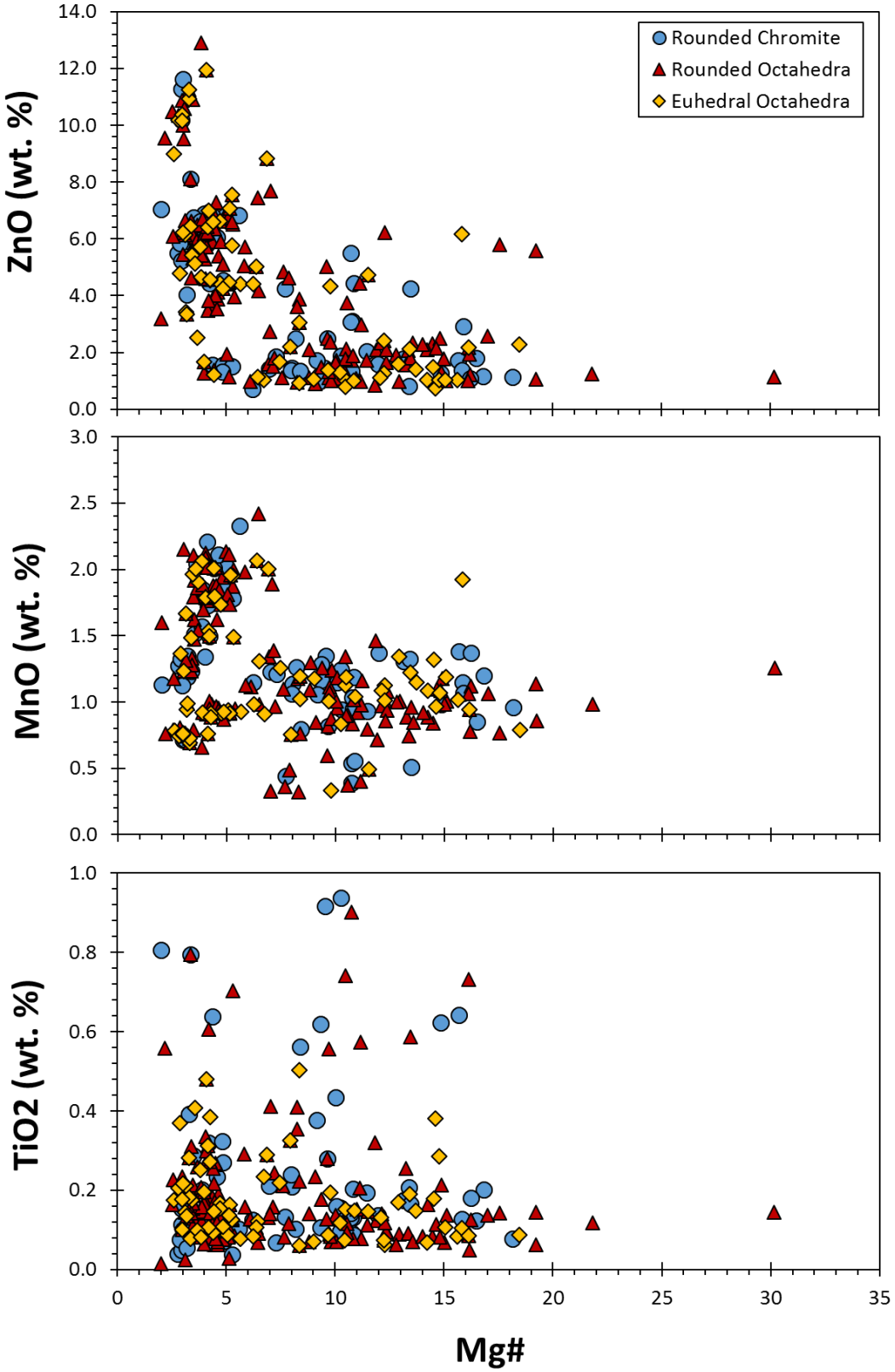

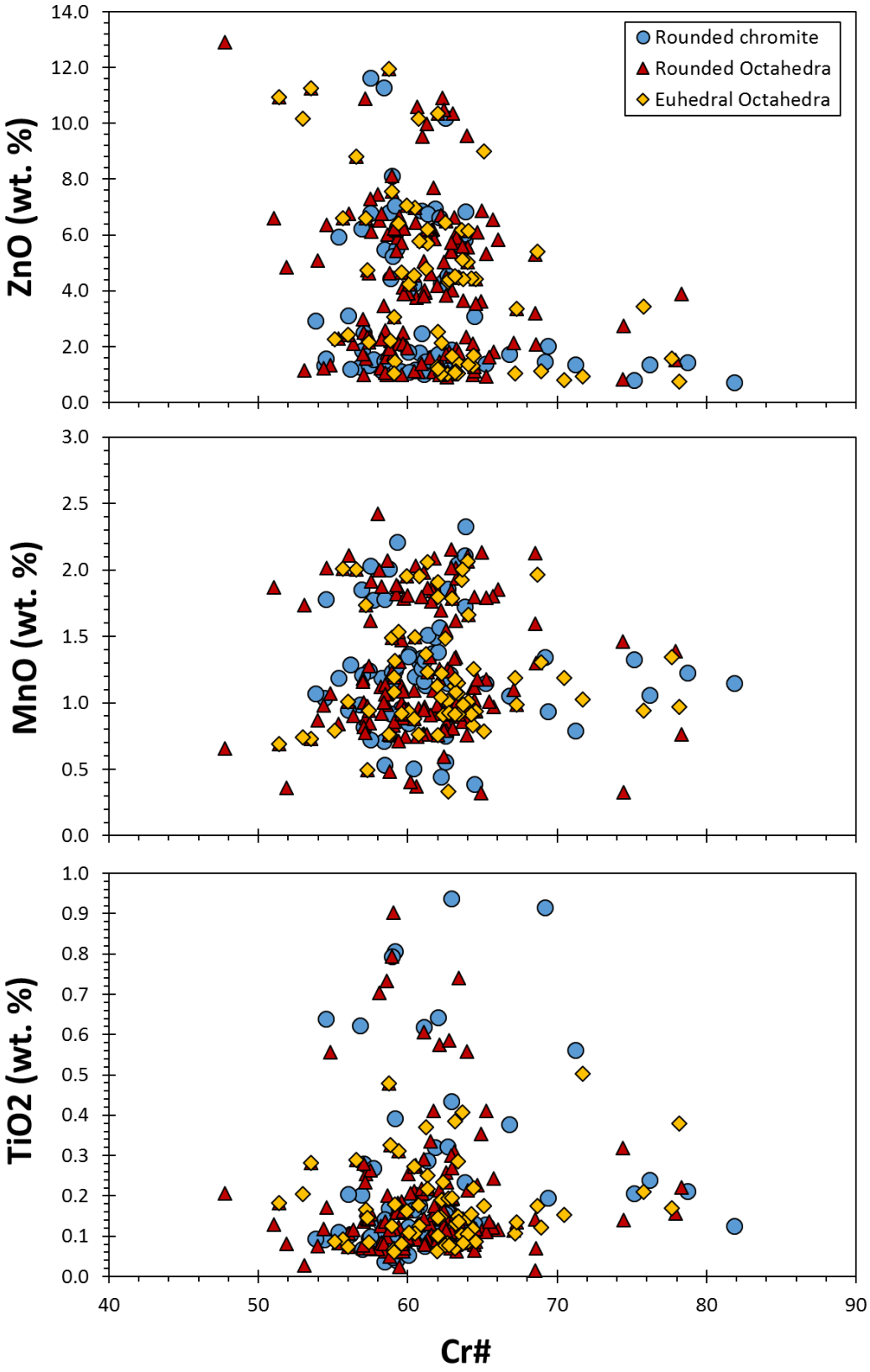
Rounded chromite
Rounded Octahedra
Euhedral Octahedra
ZnO (wt. %)
MnO (wt. %)
TiO2 (wt. %)
Cr#
14.0
12.0
10.0
8.0
6.0
4.0
2.0
0.0
3.0
2.5
2.0
1.5
1.0
0.5
0.0
1.0
0.9
0.8
0.7
0.6
0.5
0.4
0.3
0.2
0.1
0.0
40
50
60
70
80
90

S2.3 - Divalent and Trivalent plot showing the absence of variable mineral chemistry with rounding shape for 14WA2 chromites. Each point represents a single-grain analysis. This figure again shows the absence of mineral chemistry variation with rounding shape, but this time for the most heavily analysed 14WA2. Here, 14WA2 has been split into six difference rounding shapes, RC, EO, and four subcategories of RO, with RO-1 representing the most rounded, and RO-4 the most euhedral.

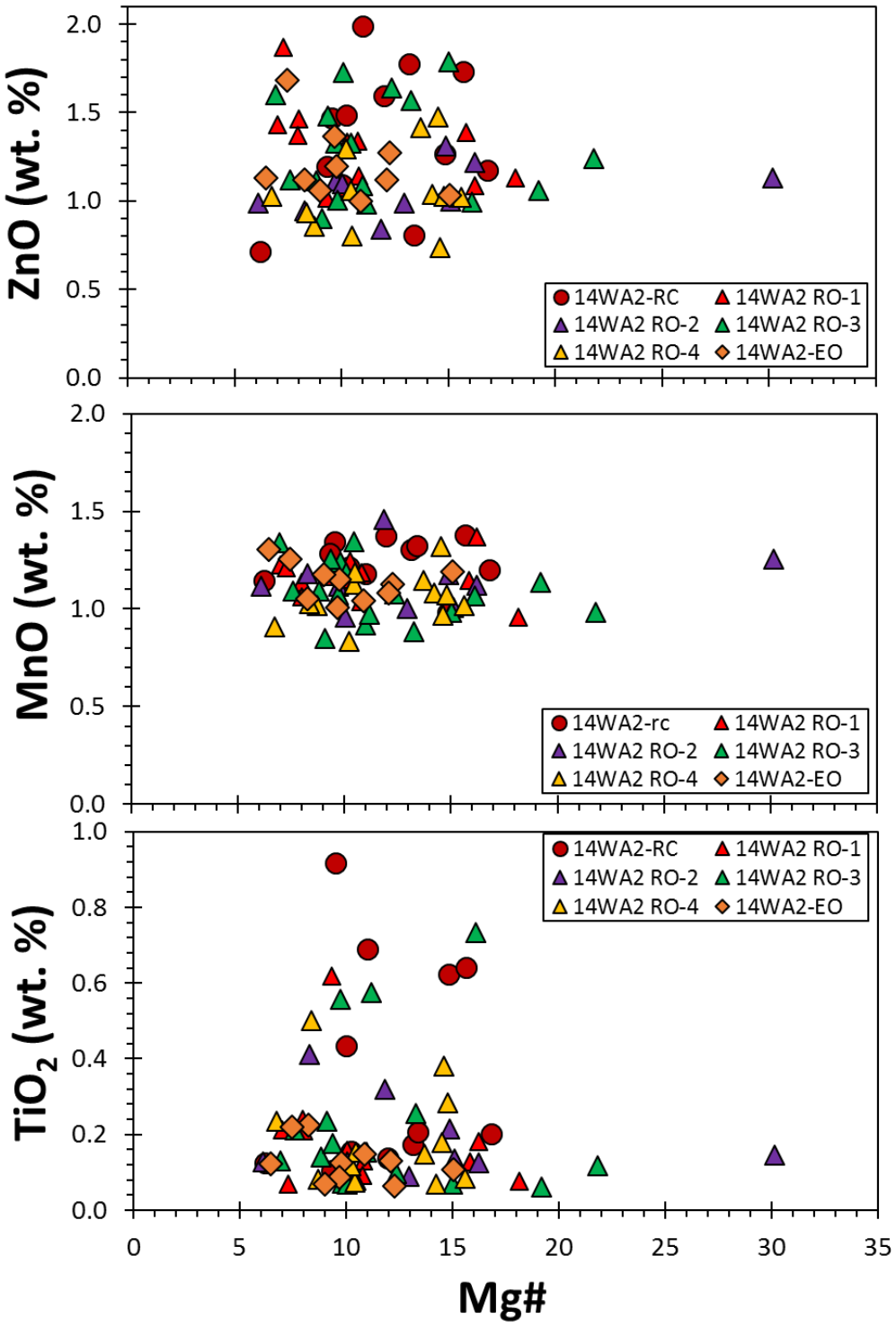

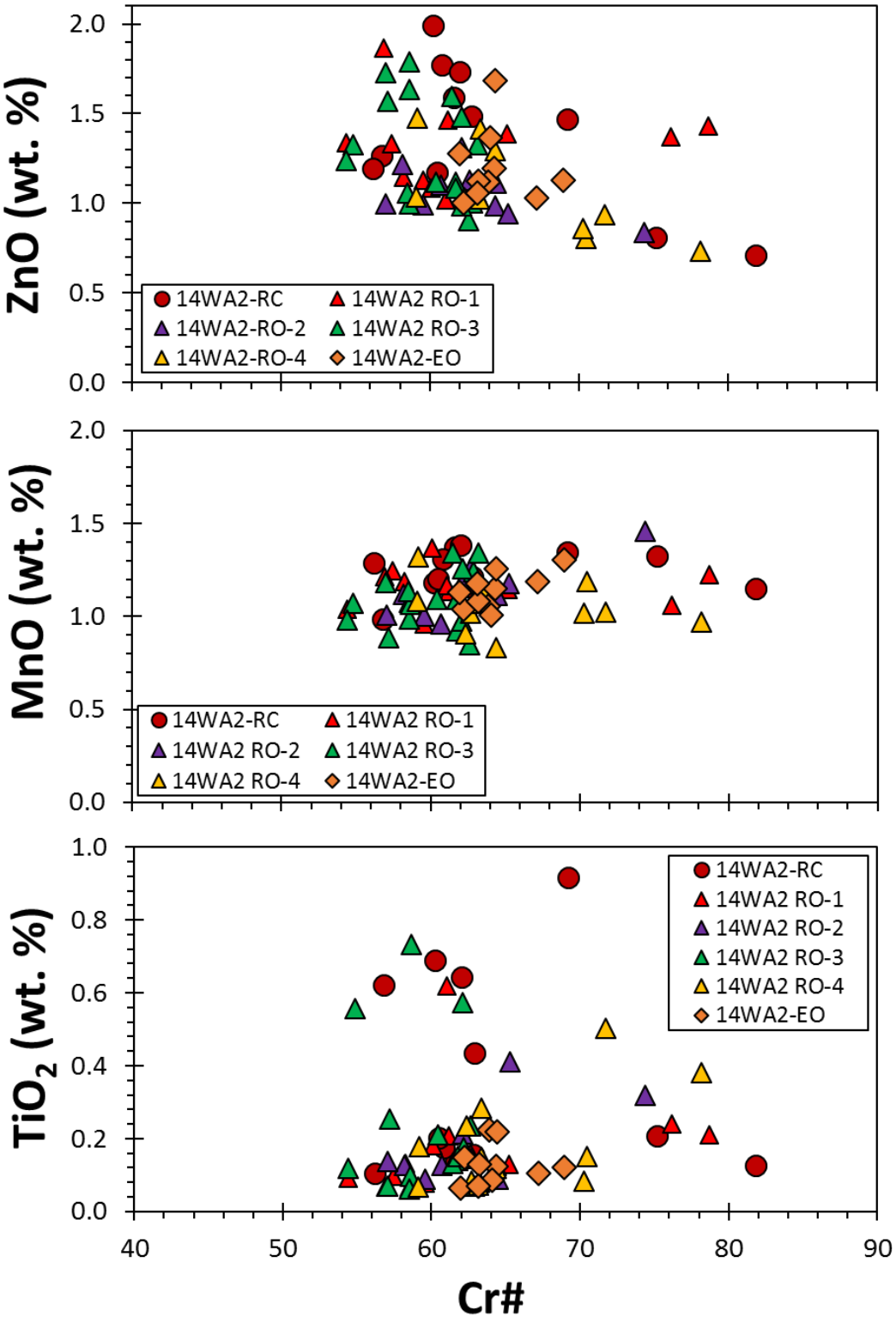
ZnO (wt. %)
2.0
1.5
1.0
0.5
0.0
14WA2-RC
14WA2 RO-1
14WA2-RO-2
14WA2 RO-3
14WA2-RO-4
14WA2-EO
MnO (wt. %)
2.0
1.5
1.0
0.5
0.0
14WA2-RC
14WA2 RO-1
14WA2 RO-2
14WA2 RO-3
14WA2 RO-4
14WA2-EO
TiO2 (wt. %)
1.0
0.8
0.6
0.4
0.2
0.0
14WA2-RC
14WA2 RO-1
14WA2 RO-2
14WA2 RO-3
14WA2 RO-4
14WA2-EO
40
50
60
70
80
90
Cr#

S2.4- Figure showing wt. % NiO vs Mg#. Each individual point represents a single chromite grain, split by sample location. Most NiO below detection limit of ~300 ppm (0.03 wt.%), with only a few high ZnO grains yielding NiO above detection limits.

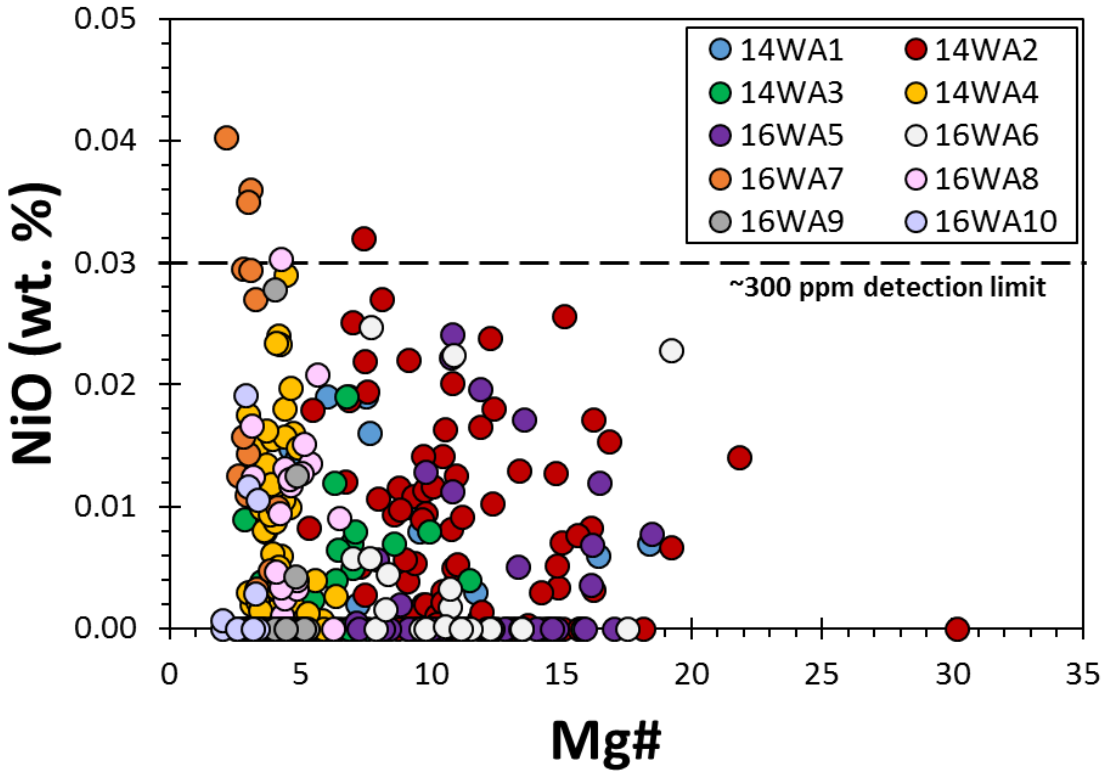

S2.5- A) Figure showing wt. % V_2O_3 vs Cr#. V_2O_3 is shown to be generally higher in lower Cr# samples. There is perhaps hints of two trends: a 'high' V_2O_3 trend, and a lower V_2O_3 with more restricted Cr# variation of Cr# 50 to 68. The source of these possible trends is unknown but may be systematic of the TiO_2 content of grains. **Figure S2.5 B)** shows wt.% V_2O_3 vs wt. % TiO_2 for all chromites in which V_2O_3 was measured, coloured for Cr# of grains. The first trend, marked as *trend A*, shows a small subset of samples typically with Cr# < 65 which yield elevated V_2O_3 with only a minor increase in TiO_2 contents. *Trend B* shows a broad correlation of increasing V_2O_3 and TiO_2. Correlations between V_2O_3 and TiO_2 contents within chromites are expected, and both trend A and B have been reported elsewhere (e.g. Barnes, 1998). While the mobility of V_2O_3 during metamorphism is not as well constrained as major elements, it is typically thought V_2O_3 is lost during amphibolite facies metamorphism (Colás et a., 2014). Therefore, the correlations observed here may have a primary, magmatic origin, with high Cr# grains yielding low wt. % TiO_2 and V_2O_3.

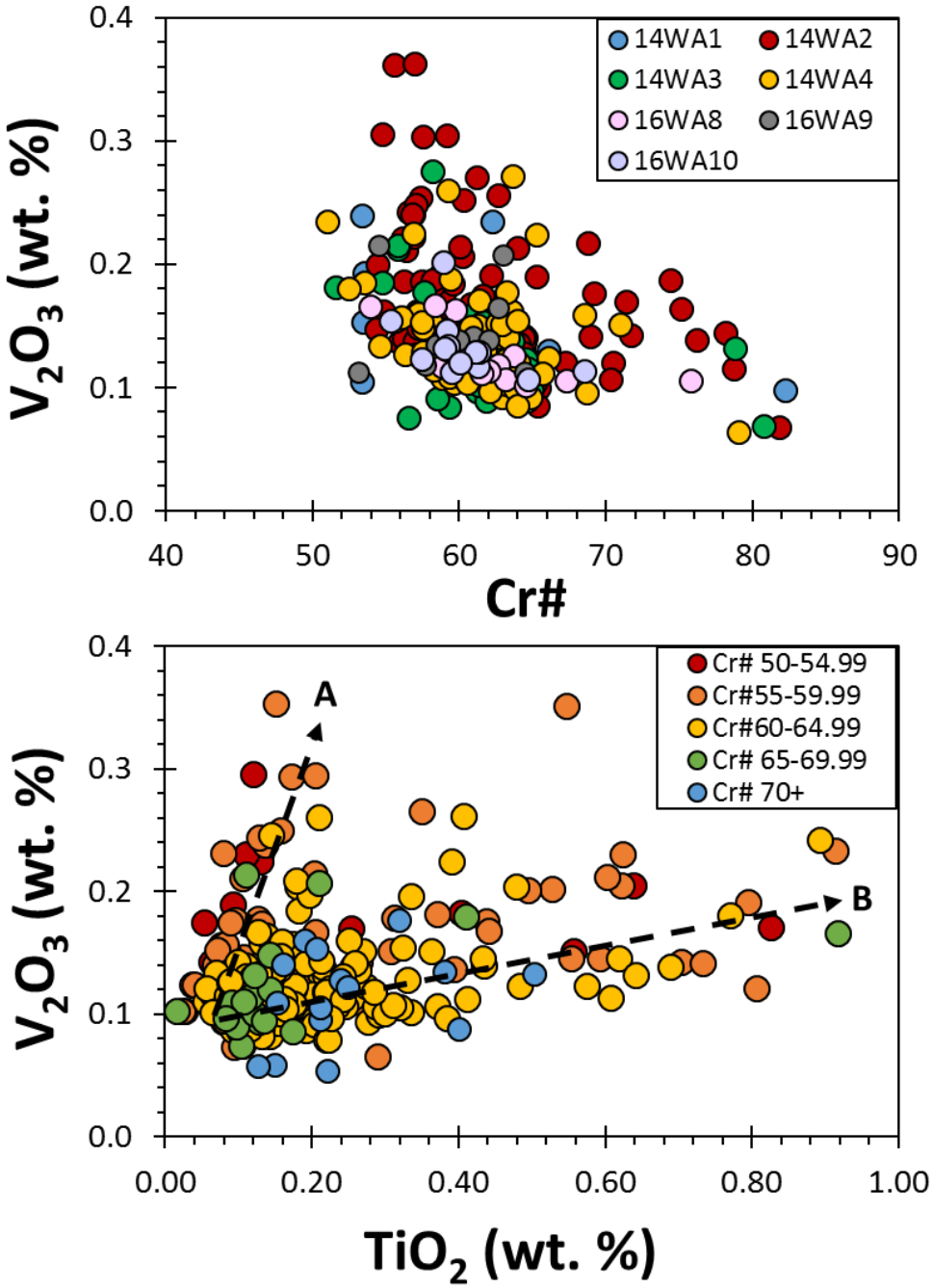

S2.6-Extra line scan material: **A)** 16WA5-41: points every 5 µm showing variations from core, through high Cr# domain, and into fuchsite. Points with <97.5% within chromite and <90% removed, generally correlating with highly fractured, less polished areas. Note the strong drop in wt.% V_2O_3 within the high Cr# domain. **B)** 14WA1-FS-4. Grain heavily equilibrated with surrounding fuchsite. Again, some loss of points within fuchsite due to low (<90%) totals. Mg# shows a nice equilibration, bell curve within this example.

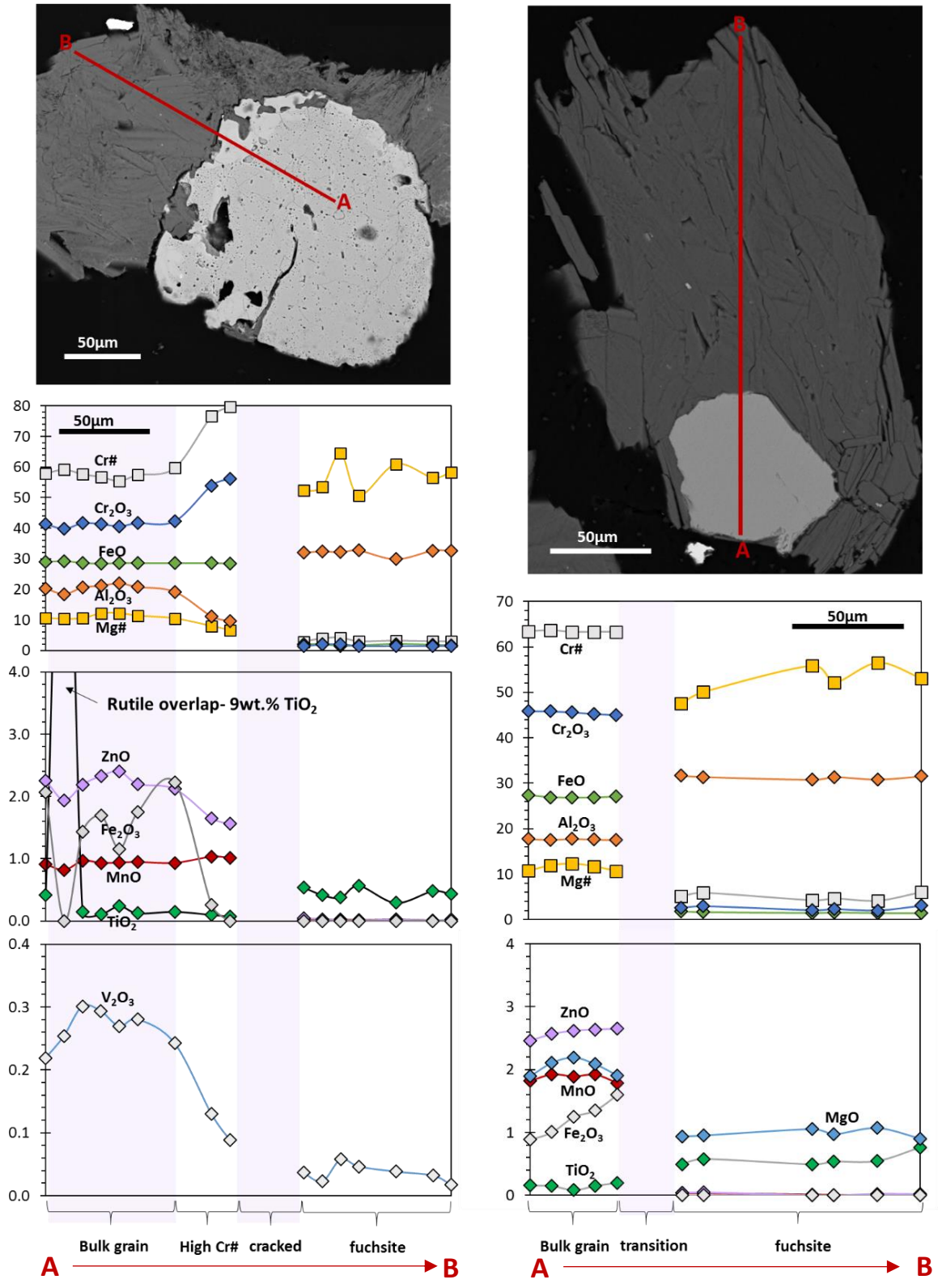

S2.7- BSE images of high and low Cr# domains. A) Diffuse high Cr# domains, paths potentially determined by deformational stress? Closely associated with pitted domains. **B)** A low Cr# domain (darker in BSE) surrounding secondary quartz (**qtz**) inclusion rimmed by iron oxide (**FeOx**). Note radiating cracks from inclusions likely coincident with replacement of primary inclusion assemblage. **C)** High Cr# domains at the edge of chromite and associated with annealed fractures. Polygonal fracturing at 120° junctions lost near high Cr# domain in top right. **D)** High Cr# domains within heavily altered crystal. Large fracture filled with quartz, fuchsite and iron oxide.

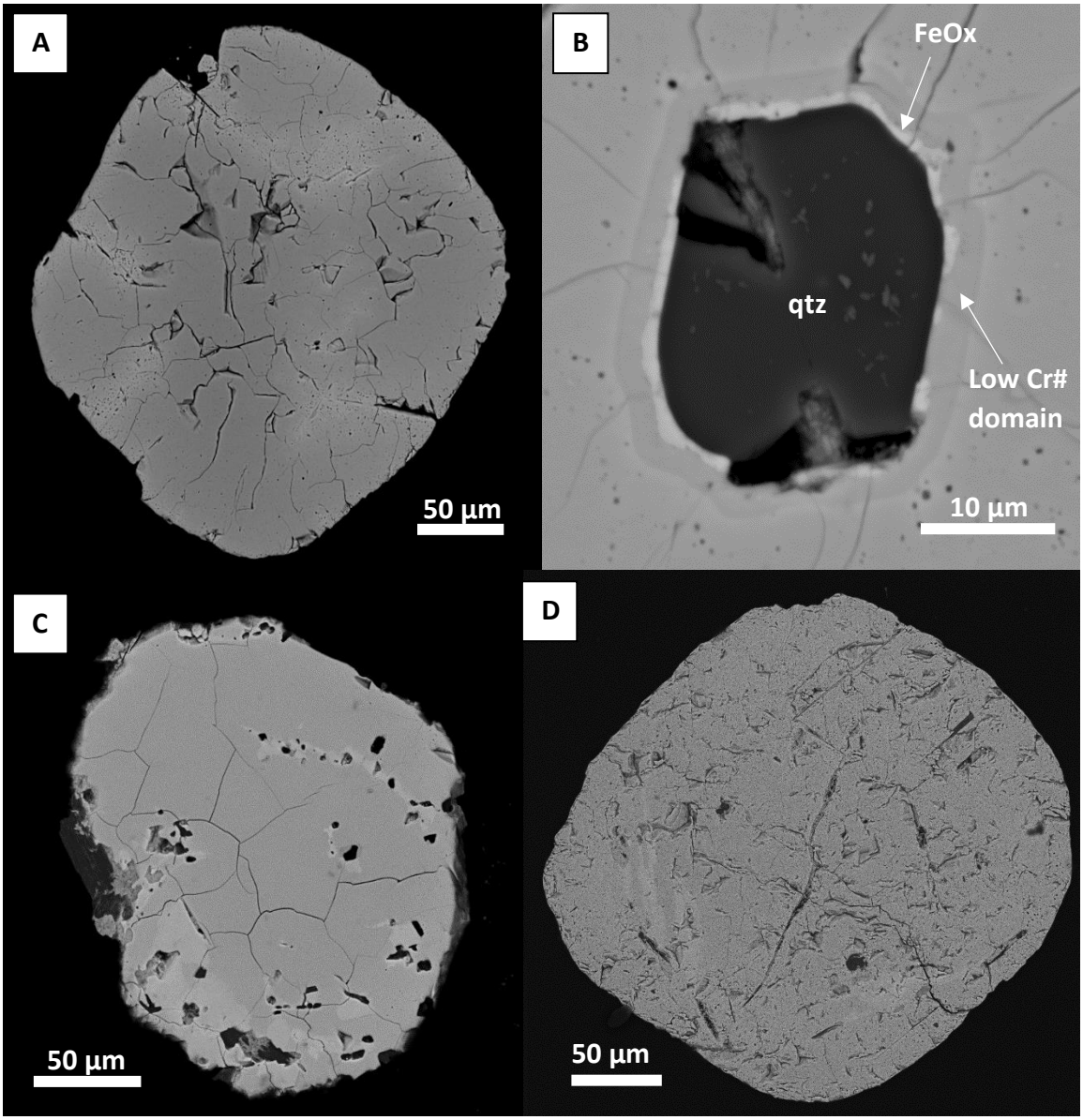

S2.8- Further secondary inclusion assemblages. A) Fuchsite (**fuch**) and rutile (**rut**) with associated fine grained, pitted domain. Note the ragged, clearly disequilibriated boundary between fuchsite and chromite. **B)** Spherical quartz, fuchsite and monazite within chromite. Spherical shape of the assemblage suggests possible replacement of a melt inclusion. Radial cracks, as observed in Figure S2.7b, likely indicate replacement of a higher-pressure phase and subsequent volume expansion. **C)** Unusual pair of elongate inclusions associated with a pitted domain. Brightest phase shown by Raman spectroscopy to be sulphide, though the darker phase could not be detected by either Raman or EDS. It's dark colouration within BSE suggests it may be graphite, though this is speculative. **D)** Porous chromite showing almost complete replacement of grain by iron oxide (**FeOx**) and quartz (**qtz**).

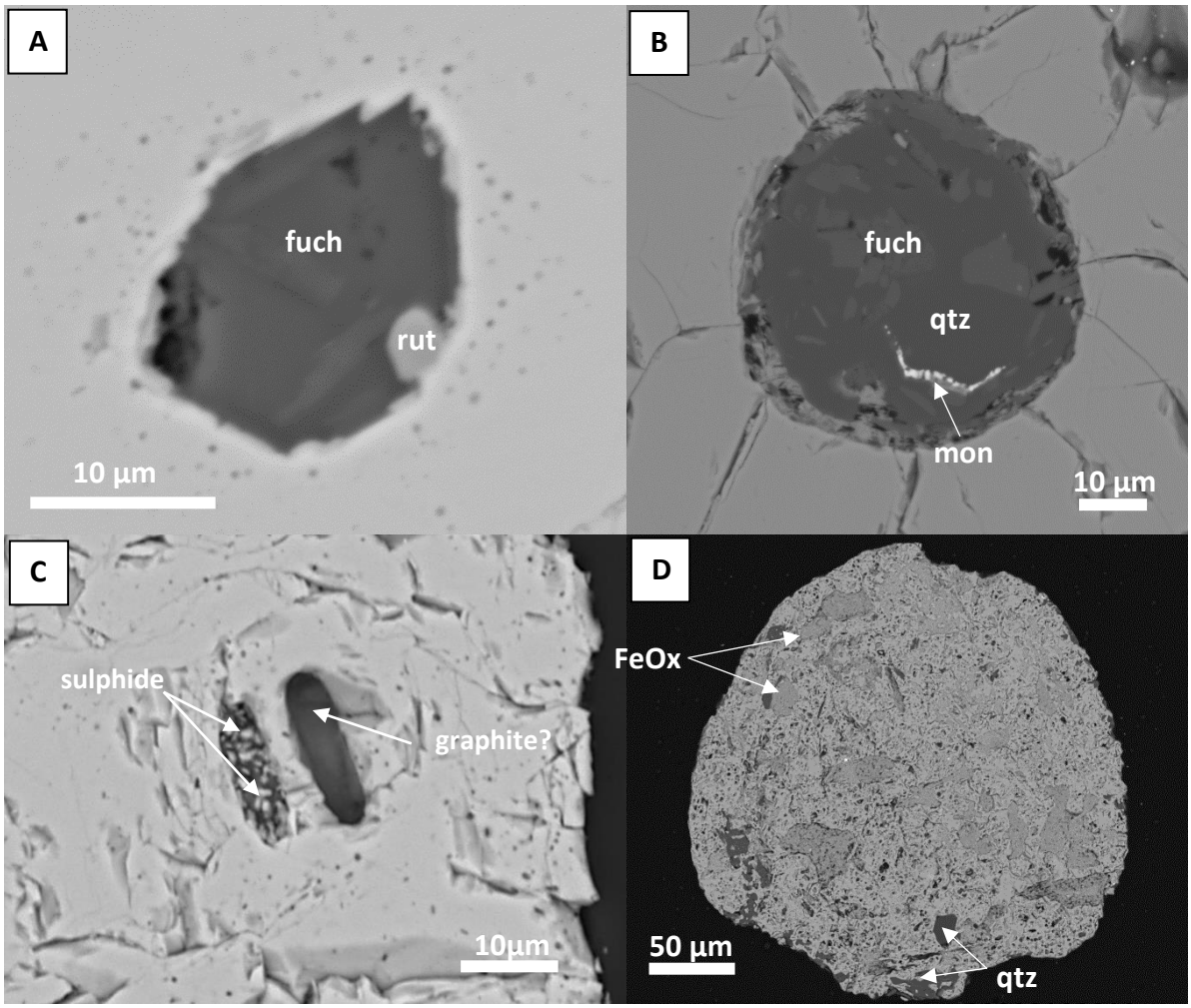

S2.9- A) Reflected light image of sulphides within 14WA1 banded cobble. Fe-sulphide (pyrrhotite and pyrite- typically deep gold and light gold in reflected light, respectively). Boundary between sulphide-rich and sulphide-poor clast marked by dashed line- the space between the two clasts is also marked by matrix fuchsite. Darker areas likely represent the presence of iron oxides lost during creation of thin section, suggesting original quartz-iron oxide banding of this clast, perhaps akin to unit 1 metasediments at Jack Hills (Spaggiari et al., 2007). **B) Reflected light higher-magnification image of sulphides.** Potential multiphase crystal indicated by arrow, similar to isolated sulphides observed within quartzite cobbles by Dare et al. (2016) and in this study, which are shown in **C)** and **D). C) BSE image of isolated sulphide within 16WA5 quartzite cobble.** Pyrrhotite (pyrr) and pyrite labelled for reference. Brightest phase unknown. **D) BSE image of a sulphide within 16WA5 quartzite cobble.** Grain has a pyrite **(pyr)** core and a pyrrhotite **(pyrr)** outer edge**.** The brightest phase between pyrite and pyrrhotite is too small to determine through EDS, but may represent pentlandite or chalcopyrite, which have also been observed within Jack Hills quatzite cobbles (Figure 3.6; Dare et al., 2016). Scale bars for both images are 10 µm.

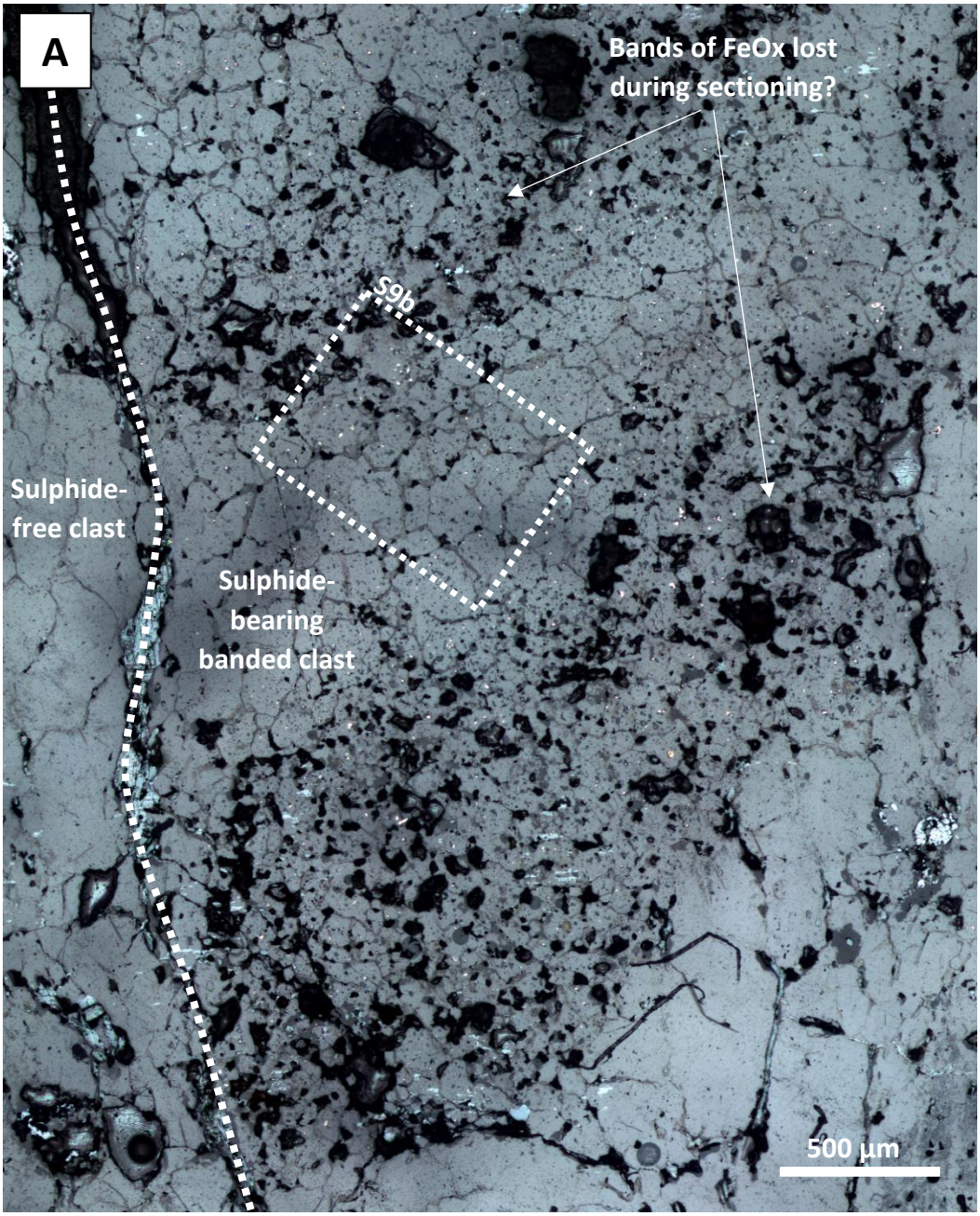

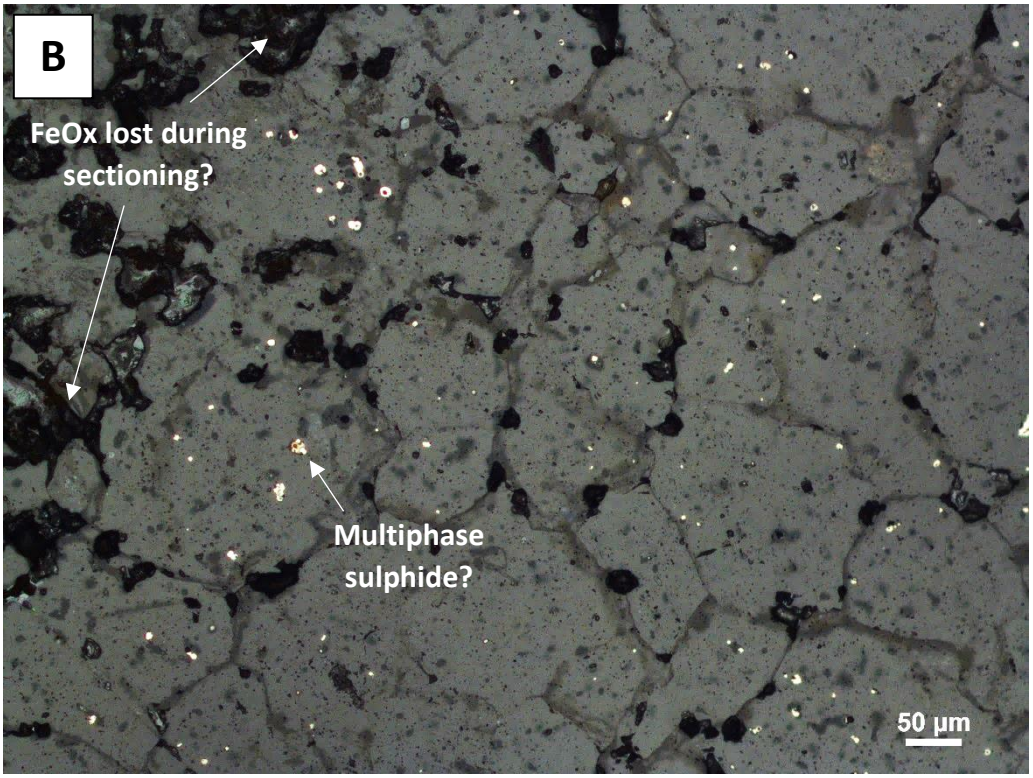

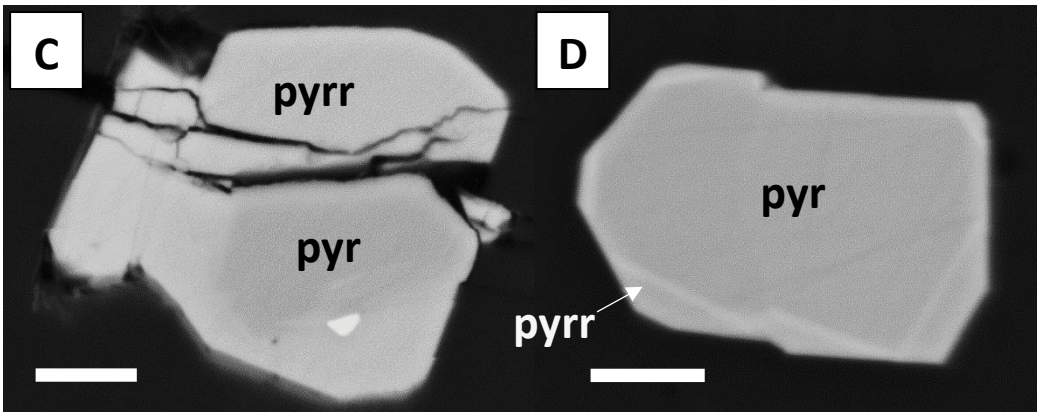

S2.10- Jack Hills fuchsite

Analysis of the mineral fuchsite was also undertaken using line scans and spot analyses, to determine the effect of its crystallisation on the mineral chemistry of chromites. Analytical sites were chosen where the transition from chromite to fuchsite is preserved, and where minimal cracks and other contaminating phases, such as quartz and iron oxide, were present.

S10.2- Images of fuchsite. A) PPL image of 14WA2 thin section, with chromite, fuchsite and zircon concentrated in matrix of the metasediments. **B)** BSE image of inset. Upper chromite mechanically disaggregated by fuchsite, quartz and iron oxide, while the bottom chromite remains intact but heavily cracked. Despite this, there is very limited evidence for strong fluid infiltration: pitted domains restricted to the outer edges of the both chromites. **C)** BSE image of more heavily modified chromite, with grains mechanical disaggregated and highly fractured. Fluid infiltration is also obvious from the high abundance of pitted domains within chromite fragments. **Chr**= chromite, **fch**= fuchsite, **zrc**= zircon, **rut**= rutile, and **FeOx**= iron oxide, likely magnetite.

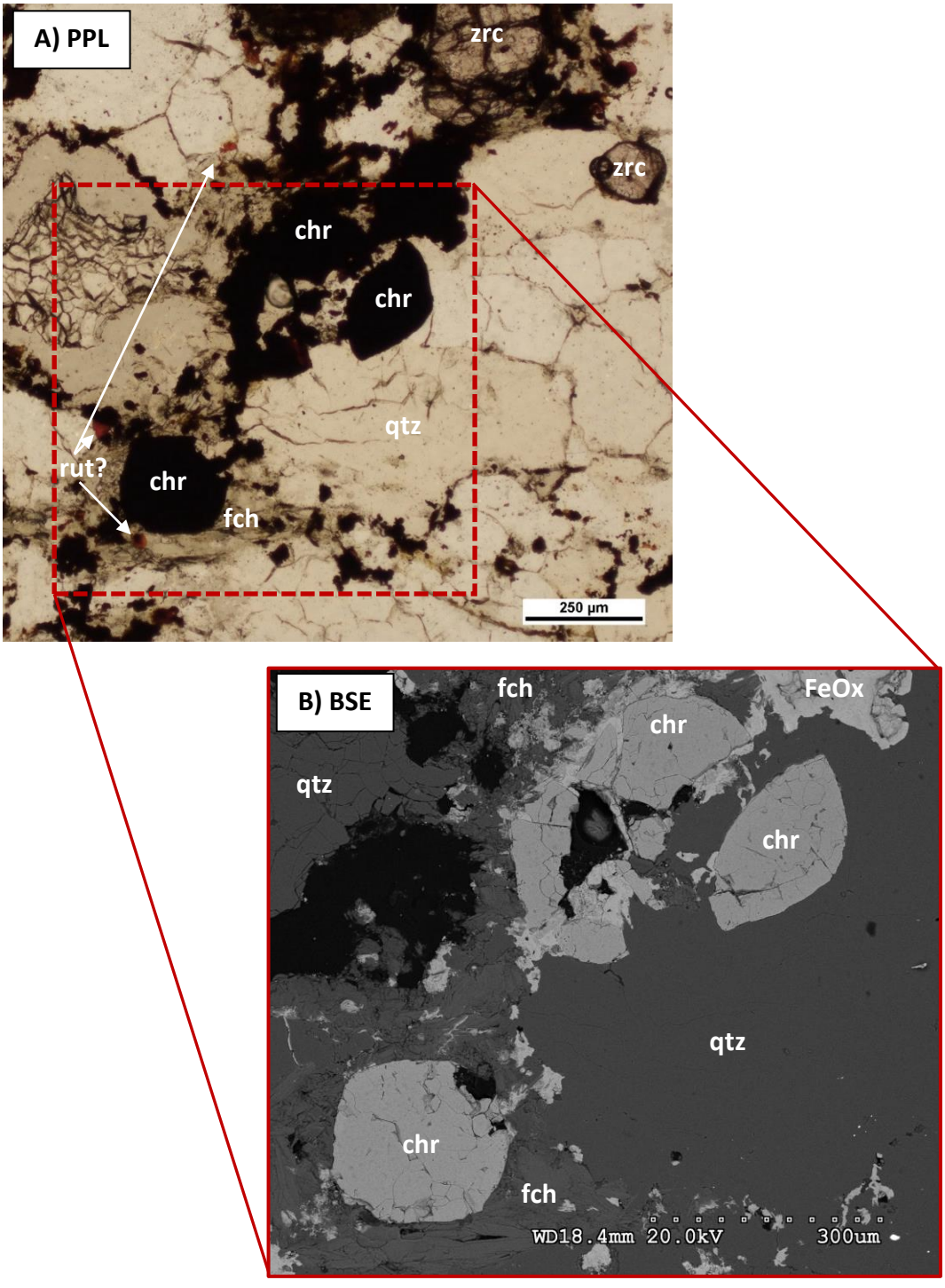

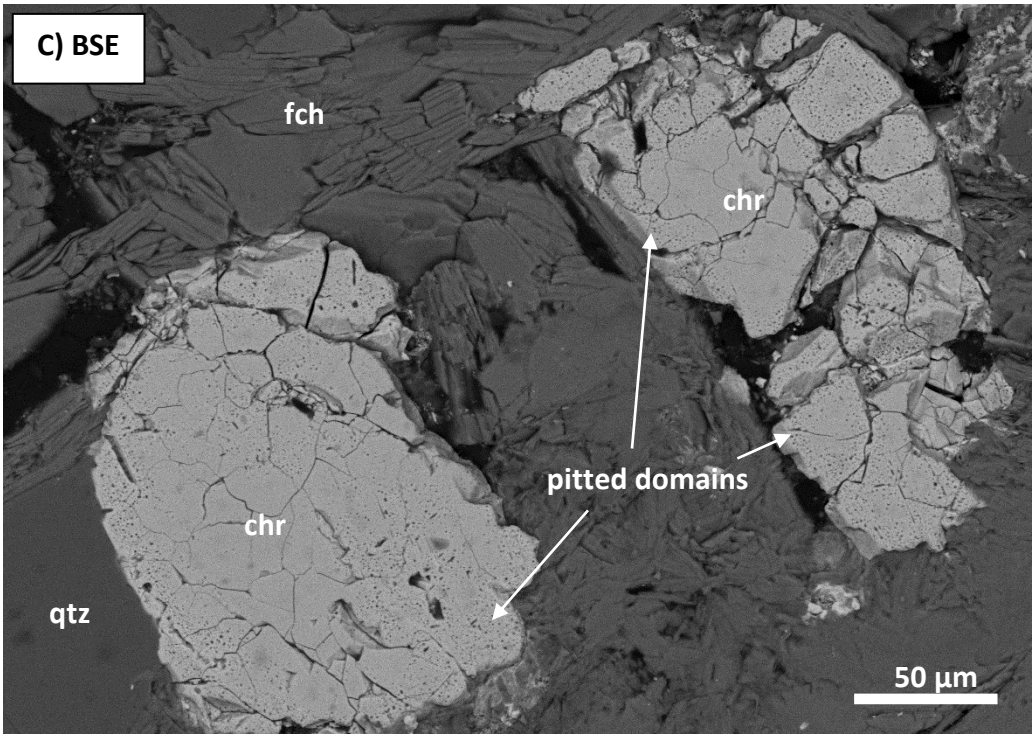
C) BSE
fch
chr
pitted domains
chr
qtz
50 µm

S2.10: Table 1- EPMA data of fuchsite from Jack Hills from samples 14WA1, 14WA2 and 16WA5. TS = thin section. FeO* represents total iron, representative proportions of Fe^{3+} and Fe^{2+} not determined.

Sample location	14WA1	14WA1	14WA1	16WA5	16WA5	14WA1	14WA1	14WA2	14WA2	14WA2	14WA2	14WA2
Size fraction	250-120	250-120	250-120	250-120	250-120	250-120	250-120	TS	TS	TS	TS	TS
Grain # associated of chromite	FS-3	FS-3	FS-3	41	41	FS-4	FS-4	TS-1	TS-1	TS-1	TS-6	TS-6
Distance from chromite (μm)	30	110	200	18	86	20	100	30	150	300	20	60
SiO_2	46.19	45.43	47.21	43.92	45.71	45.68	46.94	46.81	44.52	45.38	46.08	46.27
TiO_2	0.55	0.55	0.52	0.54	0.48	0.58	0.54	0.50	0.41	0.53	0.29	0.62
Al_2O_3	32.50	32.33	32.21	31.95	32.69	31.39	30.85	32.30	30.08	32.18	31.71	32.84
Cr_2O_3	1.90	2.42	1.41	1.41	1.48	2.94	2.00	1.87	1.60	2.00	1.76	1.35
V_2O_3	0.05	0.03	0.07	0.04	0.03	0.05	0.07	0.05	0.04	0.05	0.05	0.09
FeO*	1.91	1.68	2.03	1.99	1.85	1.70	1.47	2.49	1.72	1.81	1.53	1.88
MgO	0.98	1.02	1.09	1.22	1.35	0.95	1.07	1.08	0.87	0.93	1.36	1.16
MnO	0.00	0.02	0.02	0.02	0.01	0.03	0.01	0.01	0.01	0.00	0.02	0.00
K_2O	10.27	10.40	10.01	10.47	10.26	10.06	10.21	10.35	9.67	10.55	10.57	10.82
CaO	0.02	0.03	0.01	0.03	0.02	0.04	0.01	0.11	0.00	0.00	0.00	0.00
Na_2O	0.48	0.42	0.35	0.34	0.29	0.33	0.35	0.25	0.22	0.31	0.26	0.32
NiO	0.00	0.00	0.00	0.02	0.01	0.01	0.01	0.00	0.00	0.00	0.00	0.00
ZnO	0.03	0.03	0.02	0.04	0.01	0.05	0.03	0.02	0.00	0.00	0.01	0.02
Total	***94.86***	***94.35***	***94.95***	***91.98***	***94.20***	***93.81***	***93.56***	***95.82***	***89.14***	***93.72***	***93.61***	***95.39***
Mg#	47.76	51.92	48.80	52.28	56.54	50.05	56.52	43.48	47.58	47.90	61.28	52.41
Cr#	3.77	4.79	2.85	2.87	2.95	5.92	4.18	3.74	3.45	4.01	3.59	2.69

S2.11- chromite-fuchsite Cr# mass balance

Mass balance of Cr between chromite and fuchsite was challenging owing to the absence of distinct zonation profiles, and the observation that, where present, areas that have undergone Cr exchange appear to have lost Al preferentially. First order mass balance calculation based solely on Cr# and proportions of fuchsite use the following calculation:

Previous Cr# chromite = (current Cr# - (fuchsite Cr# x (1-f)))/f

Where f is the proportion of chromite, and 1-f is the proportion of fuchsite. Using Cr# observed (~3-4 for fuchsite and average 62 for chromite) shows that if chromite loses Cr at the observed fuchsite Cr#, this rapidly results in impossibly high Cr# within chromites (Figure S2.11.1). As the observed proportion of chromite to fuchsite is approximately 1:1, this would result in an impossible Cr# of >120 if Cr was lost at fuchsite Cr# of 3-5. Similarly, simple exchange of Cr for Fe^{3+} (i.e. at Cr#100) would result in very low Cr#s: domains of which are only very rarely observed (see Figure S.7b). Figure S11.1 therefore suggests that to produce the secondary, high Cr# domains observed, exchange of both Cr and Al occurred with surrounding fuchsite must have occurred at Cr#50-60.

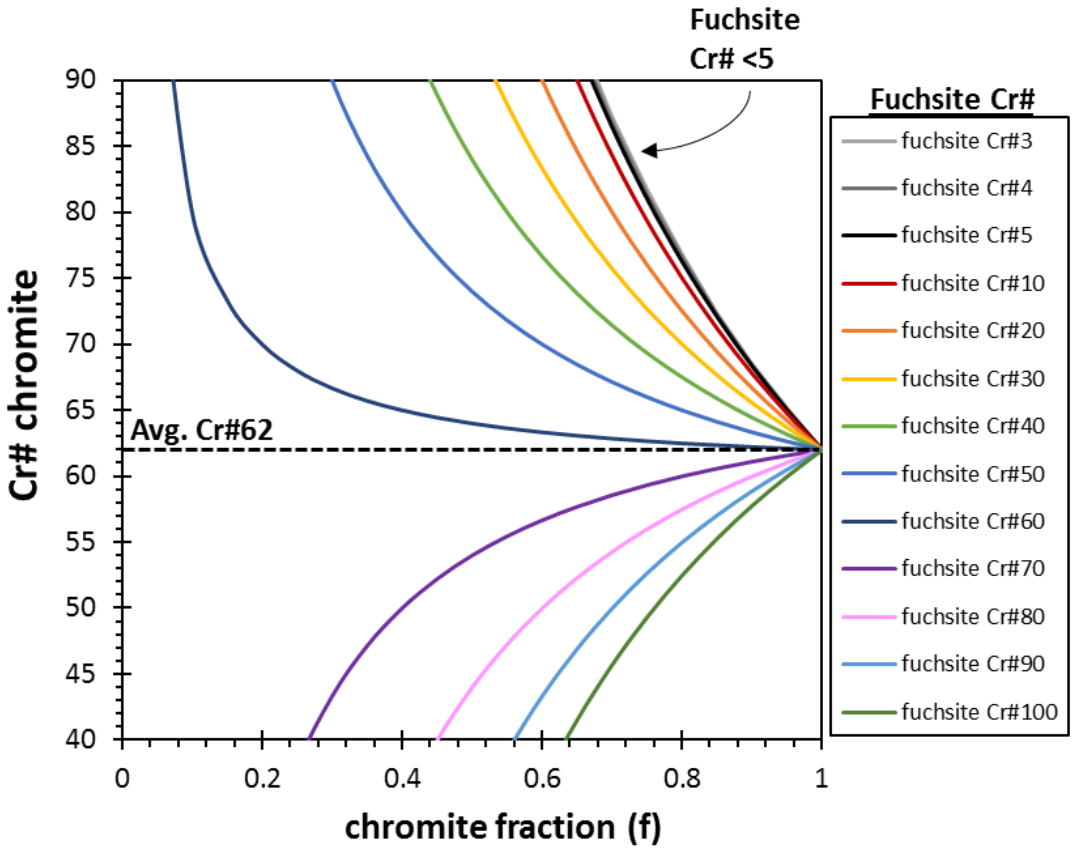

Figure S2.11.1 (previous page): Mass balance calculation of the previous Cr# of chromite prior to Cr loss to fuchsite, assuming closed system behaviour. Loss of Cr from chromite modelled at numerous Cr# to simulate different equilibration scenarios. Cr clearly not lost from chromite at current fuchsite Cr#, which quickly yield impossibly high Cr# at chromite: fuchsite proportions not observed.

However, this does not consider the finer, more localised portions of chromite that exchanged with fuchsite to form high Cr# domains. While the localised nature of these domains would also decrease the proportion of fuchsite available to exchange (i.e. fuchsite on the opposite side of a chromite grain is unlikely to directly exchange), it is likely these domains represent chromite fractions considerably lower than the bulk assemblage. This suggests Cr# exchange far nearer the Cr# of the bulk crystal. For example, Figure S11.1 indicates that a high Cr# domain of Cr# ~75 could be reconciled by a domain proportion of ~0.1 exchanging with fuchsite at Cr#60, which is very close to the bulk crystal value of Cr#62.

Another way to look at Cr# mass balance is to use the same methodology that was applied for mass balance of Mg in the main text (Figure 14). If you assume closed system behaviour and simple exchange of Cr for Al or Fe^{3+}, the 'previous Cr#' of chromite can be back calculated from the assumption that all Cr in fuchsite is derived from chromite (Figure S11.2). Back calculating from a current Cr# of 58, based on 16WA5-41 shown in S6a, equates to a previous Cr# of ~75 if Cr is lost in exchange for Fe^{3+} (Figure S11.2a). However, back calculated mass balance for the previous Cr# of chromite where Cr has been lost in direct exchange for Al, rapidly results in impossible Cr# (Figure S11.2b). While this methodology works for simple Mg exchange, it indicates changes in Cr# are not the product of direct exchange (i.e. loss at Cr#100) between chromite and fuchsite. Back modelling also has implications for the presence of high Cr# domains, showing that unless high Cr# domains are highly non-stoichiometric, straight exchange of Cr for Al or Fe^{3+} cannot account their presence within detrital chromites. This instead suggests equilibration with fuchsite at a lower Cr#, with preferential loss of Al, in all but a few rare examples (S2.7b).

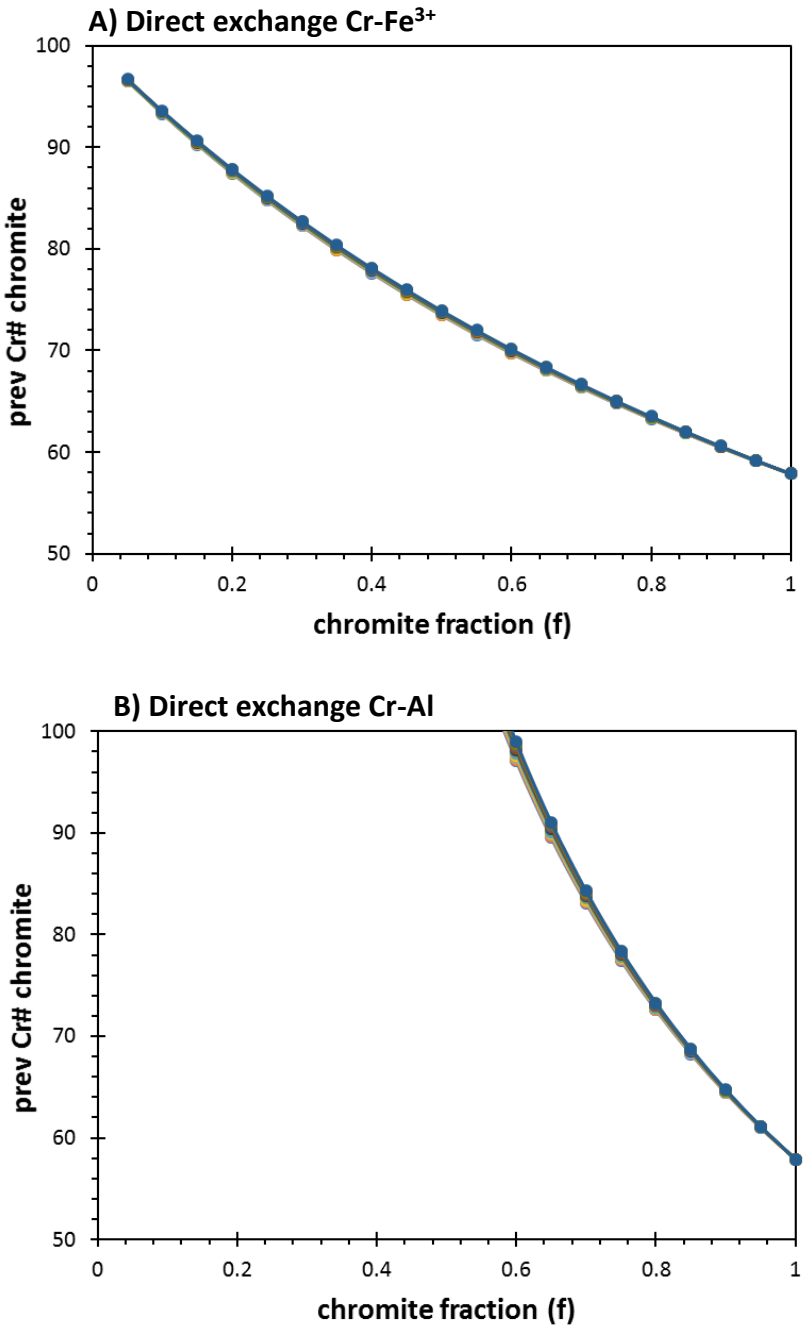

Figure S11.2: Back calculated previous chromite Cr# from a current Cr# of 58. **A)** Assumed loss of Cr to fuchsite in exchange for Fe^{3+}, so 11.2a calculates the Cr# of the grain prior to this exchange. F represents chromite: fuchsite proportions: at the observed ~1:1 proportion the previous chromite is calculated to be approximately 75. However, as there is no linear relationship between Cr and Fe^{3+} observed and Fe^{3+} is not observed within many grains, it is likely this scenario is obsolete. **B)** Assumed loss of Cr to fuchsite in exchange for Al, so 11.2b calculates the Cr# of the grain prior to this exchange. This quickly results in elevated Cr#, and impossible Cr# at the ~1:1 observed proportion of chromite: fuchsite. This situation is therefore implausible, and direct exchange of Cr-Al cannot account for the formation of fuchsite.

S2.12- Provenance plots from Kamenetsky et al. (2001). A) Detrital chromite compositions compared to fields of primitive spinel (within olivine) from different tectonic settings, including; large igneous provinces (LIP), ocean island basalts (OIB), mid ocean ridge basalt (MORB) and arcs. Plume derived W. Greenland picrites also shown, which display very similar Cr# to grains, but at higher TiO_2 contents. B) Detrital chromite compositions compared to fields of mantle spinels. As shown within the main text, Jack Hills chromites yield TiO_2 comparable to mantle spinels, but at far more variable Cr# than expected from derivation from a single mantle source.

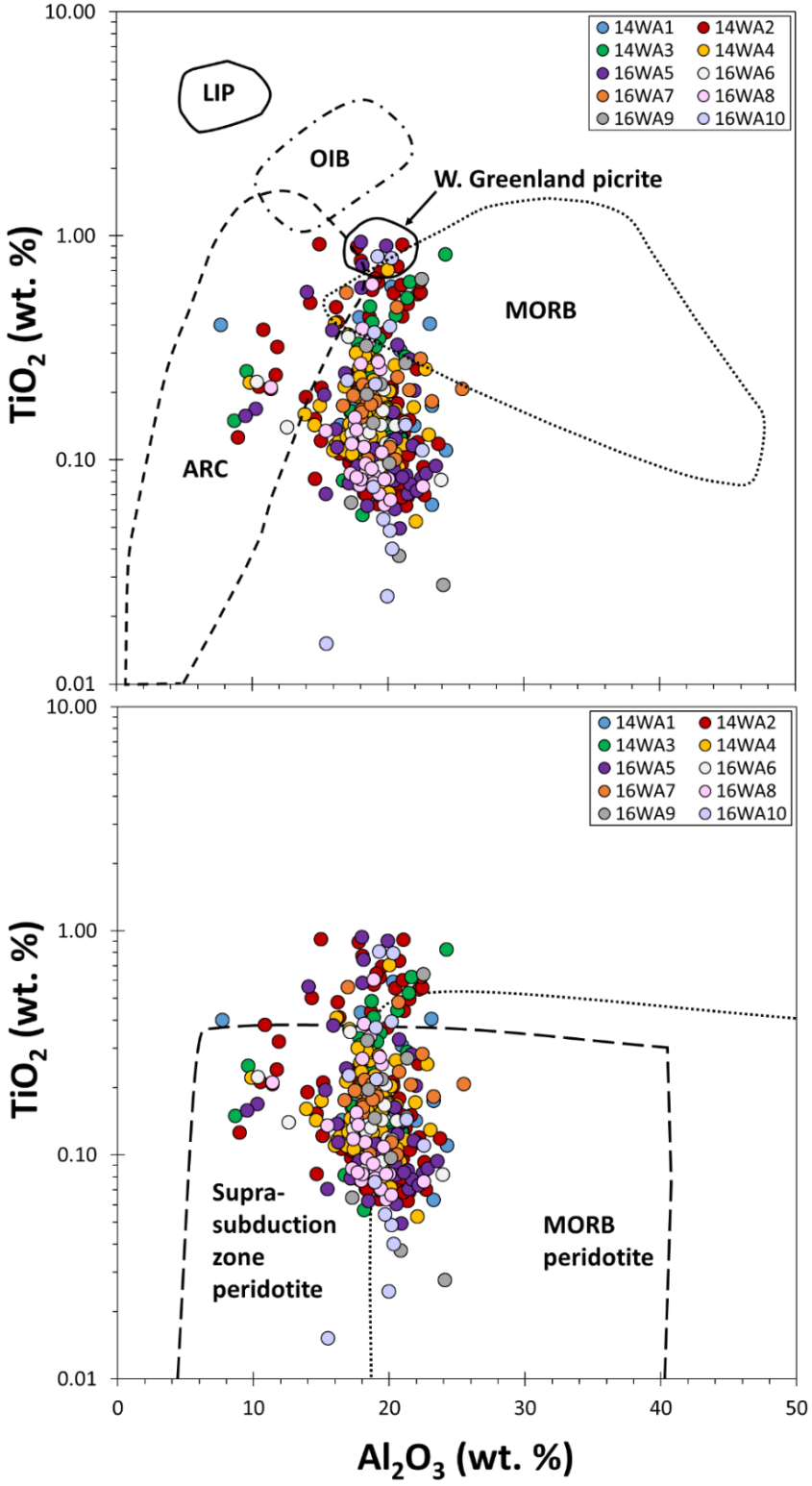

Supplementary material references

Barnes, S. J. (1998). Chromite in komatiites, 1. Magmatic controls on crystallization and composition. *Journal of Petrology* **39**, 1689-1720.

Colas, V., Gonzalez-Jimenez, J. M., Griffin, W. L., Fanlo, I., Gervilla, F., O'Reilly, S. Y., Pearson, N. J., Kerestedjian, T. & Proenza, J. A. (2014). Fingerprints of metamorphism in chromite: New insights from minor and trace elements. *Chemical Geology* **389**, 137-152.

Dare, M. S., Tarduno, J. A., Bono, R. K., Cottrell, R. D., Beard, J. S. & Kodama, K. P. (2016). Detrital magnetite and chromite in Jack Hills quartzite cobbles: Further evidence for the preservation of primary magnetizations and new insights into sediment provenance. *Earth and Planetary Science Letters* **451**, 298-314.

Hopkins, M. D., Harrison, T. M. & Manning, C. E. (2010). Constraints on Hadean geodynamics from mineral inclusions in > 4 Ga zircons. *Earth and Planetary Science Letters* **298**, 367-376.

Kamenetsky, V. S., Crawford, A. J. & Meffre, S. (2001). Factors controlling chemistry of magmatic spinel: An empirical study of associated olivine, Cr-spinel and melt inclusions from primitive rocks. *Journal of Petrology* **42**, 655-671.

Rasmussen, B., Fletcher, I. R., Muhling, J. R., Gregory, C. J. & Wilde, S. A. (2011). Metamorphic replacement of mineral inclusions in detrital zircon from Jack Hills, Australia: Implications for the Hadean Earth. *Geology* **39**, 1143-1146.

Spaggiari, C. V., Pidgeon, R. T. & Wilde, S. A. (2007b). The Jack Hills greenstone belt, Western Australia - Part 2: Lithological relationships and implications for the deposition of > 4.0 Ga detrital zircons. *Precambrian Research* **155**, 261-286.

Zane, A. & Rizzo, G. (1999). The compositional space of muscovite in granitic rocks. *Canadian Mineralogist* **37**, 1229-1238.

Supplementary Material Three:

Standards Os isotopic composition

Session	Sample	$^{184}Os/^{188}Os$	2se	$^{187}Re/^{188}Os$	2se	$^{186}Os/^{188}Os$	2se	$^{187}Os/^{188}Os$ corr.	2se	$^{189}Os/^{188}Os$	2se	$^{190}Os/^{188}Os$	2se
1	DROsS	0.001312	0.000009	0.000002	0.0000004	0.120176	0.000173	0.161043	0.000171	1.220104	0.000648	1.984130	0.001148
2	DTM	0.001317	0.000009	0.000003	0.0000005	0.119801	0.000196	0.173846	0.000226	1.219906	0.000881	1.985292	0.001730
3	DTM	0.001329	0.000007	0.000006	0.0000005	0.120019	0.000216	0.174239	0.000201	1.220624	0.000852	1.985383	0.001333
4	DTM	0.001323	0.000013	0.000040	0.0000018	0.120728	0.000261	0.174284	0.000294	1.219209	0.001233	1.984473	0.001926
4	DTM	0.001301	0.000021	0.000016	0.0000021	0.120149	0.000748	0.174208	0.000391	1.219981	0.001488	1.987582	0.003519
5	DTM	0.001394	0.000009	0.000013	0.0000008	0.120151	0.000098	0.174028	0.000101	1.219679	0.000438	1.984024	0.000531
5	DTM	0.001541	0.000024	0.000016	0.0000016	0.120293	0.000253	0.173995	0.000352	1.220995	0.001729	1.982462	0.002433
5	DTM	0.001474	0.000013	0.000029	0.0000014	0.120151	0.000357	0.173785	0.000289	1.219169	0.001158	1.980948	0.001990
5	DTM	0.002149	0.000016	0.000126	0.0000034	0.120537	0.000151	0.173795	0.000206	1.219974	0.000933	1.983595	0.000863
6	DTM	0.001394	0.000009	0.000013	0.0000008	0.120151	0.000098	0.174028	0.000101	1.219679	0.000438	1.984024	0.000531
6	DTM	0.001394	0.000012	0.000037	0.0000020	0.120116	0.000195	0.173807	0.000189	1.219909	0.000897	1.982232	0.001105
6	DTM	0.001394	0.000012	0.000037	0.0000020	0.120116	0.000195	0.173807	0.000189	1.219909	0.000897	1.982232	0.001105
6	DTM	0.001357	0.000014	0.000131	0.0000040	0.120005	0.000174	0.174219	0.000202	1.219084	0.000650	1.981519	0.001099
6	DTM	0.001351	0.000012	0.000102	0.0000025	0.120020	0.000138	0.173924	0.000149	1.219752	0.000648	1.976774	0.000938
	Avg.	**0.001434**		**0.000044**		**0.120150**		**0.173997**		**1.219738**		**1.982646**	
	2sd	0.000393		0.000084		0.000422		0.000360		0.001025		0.006345	

Table S3.1: Os isotopic compositions of DROsS and DTM standards analysed during this study. Generally, a standard was run at the beginning of each analytical session prior to analysis of unknowns. Extra standard analyses reported in session 6 due to unusual tuning parameters of extraction lenses. DTM standards were analysed exclusively after the first analytical session, generally for 100 pg loads.

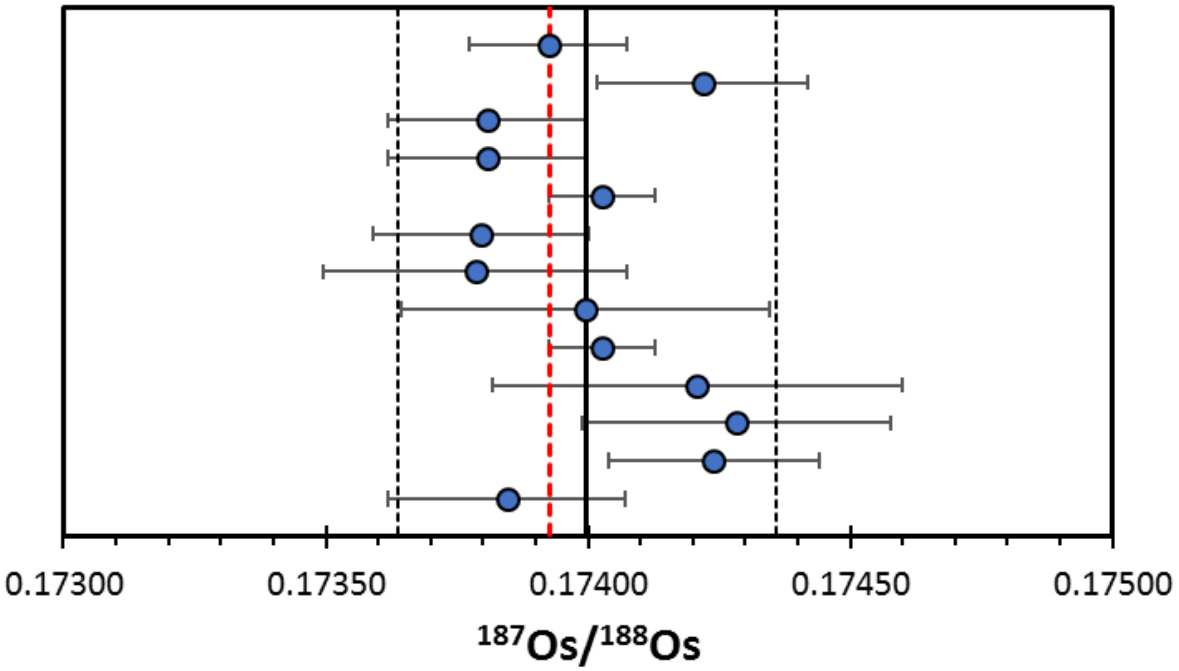

Figure S3.2: $^{187}Os/^{188}Os$ compositions of DTM standards (n=15) throughout analytical sessions. Uncertainties are 2se. Standards produced a long-term $^{187}Os/^{188}Os$ average of 0.173997±0.000360 (2sd), well within uncertainty of values provided by Luguet et al. (2008) (dashed red line).

Supplementary Material Four:

U-Pb zircon standards

Table S4.1: Table of PRM GJ1 from September 2017 to October 2018. Systematic age uncertainties propagated using excess variance derived from Plesovice. Values of this propagation stated in Chapter 2- methods and materials.

Table S4.2: Table of PRM GJ1 in May 2017. No systematic propagation required for ages: the poorer analytical uncertainties in these measurements capture long term variation.

Table S4.3: VRM 91500 from September 2017 to October 2018. Includes systematic uncertainty propagation.

Table S4.4: VRM 91500 from May 2017. Required no systematic uncertainty propagation.

Table S4.5: VRM Plesovice from September 2017 to October 2018. Includes systematic uncertainty propagation.

Table S4.6: VRM Plesovice from May 2017. Required no systematic uncertainty propagation.

Table S4.7: VRM OG1 from September 2017 to October 2018. Includes systematic uncertainty propagation. This standard was not run during May 2017. analysis session, and so none from this time are reported.

***Table S4.1**: PRM GJ1*

Sample		Conc[a]		For Tera-Wasserberg plot				For Wetherill Plot					Ages									Conc[b]
Date	sample	^{206}Pb (mV)	U ppm	$^{238}U/^{206}Pb$	1s%	$^{207}Pb/^{206}Pb$	1s%	$^{207}Pb/^{235}U$	1s%	$^{206}Pb/^{238}U$	1s%	Rho	^{207}Pb-^{206}Pb Age	2s abs	$2s_{sys}$ abs	^{207}Pb-^{235}U Age	2s abs	$2s_{sys}$ abs	^{206}Pb-^{238}U Age	2s abs	$2s_{sys}$ abs	Disc %
12/10/2017	GJ1	2.27	286	10.28	1.28	0.06	0.50	0.80	1.38	0.10	1.28	0.93	594	22	25	598	12	12	599	15	16	-0.8
12/10/2017	GJ1	2.33	292	10.24	1.74	0.06	0.45	0.81	1.80	0.10	1.74	0.97	609	20	23	603	16	14	601	20	21	1.4
12/10/2017	GJ1	2.33	289	10.17	1.58	0.06	0.42	0.82	1.63	0.10	1.58	0.97	615	19	22	607	15	13	604	18	20	1.7
12/10/2017	GJ1	2.31	284	10.18	1.48	0.06	0.45	0.81	1.54	0.10	1.48	0.96	602	20	23	604	14	13	604	17	19	-0.3
12/10/2017	GJ1	2.31	283	10.21	1.07	0.06	0.39	0.81	1.14	0.10	1.07	0.94	608	18	21	603	10	12	602	12	15	0.9
12/10/2017	GJ1	2.29	279	10.21	1.63	0.06	0.46	0.81	1.70	0.10	1.63	0.96	612	20	24	604	15	13	602	19	20	1.6
12/10/2017	GJ1	2.44	293	10.20	1.28	0.06	0.39	0.82	1.33	0.10	1.28	0.96	621	17	21	607	12	12	603	15	16	3.0
12/10/2017	GJ1	2.39	288	10.21	1.43	0.06	0.44	0.81	1.50	0.10	1.43	0.96	594	20	23	600	14	13	602	16	18	-1.3
12/10/2017	GJ1	2.41	289	10.24	1.48	0.06	0.53	0.81	1.58	0.10	1.48	0.94	613	23	26	603	14	13	601	17	19	2.0
12/10/2017	GJ1	2.37	281	10.10	1.36	0.06	0.51	0.82	1.46	0.10	1.36	0.94	610	23	26	609	13	13	609	16	18	0.3
12/10/2017	GJ1	2.42	288	10.33	1.39	0.06	0.48	0.80	1.48	0.10	1.39	0.95	606	21	24	598	13	13	596	16	18	1.7
12/10/2017	GJ1	2.43	288	10.26	1.49	0.06	0.48	0.81	1.56	0.10	1.49	0.95	599	21	25	600	14	13	600	17	19	-0.1
13/10/2017	GJ1	3.97	291	10.32	0.52	0.06	0.55	0.81	0.76	0.10	0.52	0.68	619	24	27	601	7	10	596	6	9	3.6
13/10/2017	GJ1	4.00	287	10.33	0.67	0.06	0.54	0.81	0.86	0.10	0.67	0.78	623	24	26	601	8	11	596	8	11	4.3
13/10/2017	GJ1	4.03	280	10.26	0.77	0.06	0.52	0.81	0.93	0.10	0.77	0.83	609	23	26	602	8	11	600	9	12	1.5
13/10/2017	GJ1	5.06	291	10.17	0.81	0.06	0.49	0.81	0.95	0.10	0.81	0.86	604	22	25	604	9	11	604	9	12	-0.1
13/10/2017	GJ1	5.14	289	10.14	0.91	0.06	0.45	0.82	1.02	0.10	0.91	0.90	617	20	23	608	9	11	606	11	13	1.7
13/10/2017	GJ1	5.12	287	10.15	0.91	0.06	0.42	0.82	1.00	0.10	0.91	0.91	607	19	22	606	9	11	606	11	13	0.3
13/10/2017	GJ1	4.51	278	10.19	1.07	0.06	0.51	0.81	1.18	0.10	1.07	0.90	605	22	26	604	11	12	603	12	15	0.3
13/10/2017	GJ1	4.60	289	10.13	1.32	0.06	0.45	0.81	1.39	0.10	1.32	0.95	594	20	24	604	13	12	607	15	17	-2.1
13/10/2017	GJ1	4.63	299	10.16	1.02	0.06	0.55	0.82	1.15	0.10	1.02	0.88	608	24	27	606	11	12	605	12	14	0.5
13/10/2017	GJ1	4.09	282	10.24	0.56	0.06	0.59	0.81	0.82	0.10	0.56	0.69	605	26	28	602	7	11	601	6	10	0.7
13/10/2017	GJ1	4.11	289	10.21	0.72	0.06	0.54	0.81	0.90	0.10	0.72	0.80	615	24	26	605	8	11	602	8	11	2.1
13/10/2017	GJ1	4.12	291	10.30	0.51	0.06	0.49	0.81	0.71	0.10	0.51	0.72	611	22	25	600	6	10	597	6	9	2.3
13/10/2017	GJ1	4.14	288	10.24	0.61	0.06	0.50	0.81	0.79	0.10	0.61	0.78	613	22	25	604	7	11	601	7	11	2.0
13/10/2017	GJ1	4.22	288	10.17	0.56	0.06	0.48	0.82	0.74	0.10	0.56	0.76	611	21	24	606	7	10	604	6	10	1.0
13/10/2017	GJ1	4.22	282	10.19	0.51	0.06	0.48	0.82	0.70	0.10	0.51	0.73	615	21	24	606	6	10	603	6	9	1.9
13/10/2017	GJ1	5.21	290	10.14	0.71	0.06	0.47	0.82	0.85	0.10	0.71	0.84	609	21	24	607	8	11	606	8	11	0.4
13/10/2017	GJ1	5.26	288	10.07	1.01	0.06	0.49	0.83	1.12	0.10	1.01	0.90	615	22	25	611	10	12	610	12	14	0.8
13/10/2017	GJ1	5.27	288	10.08	0.66	0.06	0.51	0.82	0.83	0.10	0.66	0.79	611	23	26	610	8	11	610	8	11	0.1
13/10/2017	GJ1	4.43	276	10.20	1.12	0.06	0.52	0.82	1.24	0.10	1.12	0.91	616	23	26	605	11	12	603	13	15	2.1

***Table S4.1 cont.**: PRM GJ1*

Date	sample	^{206}Pb (mV)	U ppm	^{238}U/ ^{206}Pb	1s%	^{207}Pb/ ^{206}Pb	1s%	^{207}Pb/ ^{235}U	1s%	^{206}Pb /^{238}U	1s%	Rho	^{207}Pb-^{206}Pb Age	2s abs	2s $_{sys}$ abs	^{207}Pb -^{235}U Age	2s abs	2s $_{sys}$ abs	^{206}Pb -^{238}U Age	2s abs	2s $_{sys}$ abs	Disc %
13/10/2017	GJ1	4.59	289	10.05	1.41	0.06	0.51	0.83	1.50	0.10	1.41	0.94	610	22	25	611	14	13	611	16	18	-0.3
13/10/2017	GJ1	4.68	301	10.05	1.36	0.06	0.48	0.81	1.44	0.10	1.36	0.94	577	21	25	604	13	13	611	16	18	-5.9
13/10/2017	GJ1	4.04	280	10.27	0.48	0.06	0.48	0.80	0.67	0.10	0.48	0.71	593	21	24	598	6	10	599	6	9	-1.1
13/10/2017	GJ1	4.04	285	10.22	0.51	0.06	0.48	0.81	0.70	0.10	0.51	0.73	602	21	25	602	6	10	602	6	9	0.1
13/10/2017	GJ1	4.05	292	10.25	0.82	0.06	0.47	0.81	0.94	0.10	0.82	0.87	605	21	24	601	9	11	600	9	12	0.8
13/10/2017	GJ1	3.76	286	10.22	0.61	0.06	0.53	0.81	0.81	0.10	0.61	0.76	607	23	26	603	7	11	602	7	11	0.9
13/10/2017	GJ1	3.81	285	10.20	0.66	0.06	0.51	0.82	0.84	0.10	0.66	0.79	617	23	26	606	8	11	603	8	11	2.3
13/10/2017	GJ1	4.00	294	10.20	0.71	0.06	0.46	0.81	0.85	0.10	0.71	0.84	595	20	24	601	8	11	603	8	11	-1.3
13/10/2017	GJ1	3.84	285	10.24	0.72	0.06	0.56	0.81	0.91	0.10	0.72	0.79	610	25	28	603	8	11	601	8	11	1.5
13/10/2017	GJ1	3.89	288	10.22	0.72	0.06	0.51	0.81	0.88	0.10	0.72	0.82	609	22	26	603	8	11	602	8	11	1.2
13/10/2017	GJ1	3.96	292	10.18	0.76	0.06	0.48	0.82	0.90	0.10	0.76	0.85	616	21	24	606	8	11	604	9	12	2.0
13/10/2017	GJ1	3.74	281	10.26	0.87	0.06	0.46	0.80	0.99	0.10	0.87	0.88	591	21	24	598	9	11	600	10	12	-1.4
13/10/2017	GJ1	3.88	285	10.24	0.72	0.06	0.58	0.82	0.92	0.10	0.72	0.78	624	25	28	606	8	11	601	8	11	3.7
13/10/2017	GJ1	4.10	298	10.30	0.98	0.06	0.52	0.81	1.11	0.10	0.98	0.88	624	23	26	603	10	12	597	11	14	4.3
13/10/2017	GJ1	3.66	284	10.24	0.46	0.06	0.42	0.81	0.62	0.10	0.46	0.74	621	19	22	605	6	10	600	5	9	3.3
13/10/2017	GJ1	3.72	285	10.18	0.48	0.06	0.38	0.81	0.61	0.10	0.48	0.79	598	17	21	603	6	10	604	6	9	-1.0
13/10/2017	GJ1	3.82	297	10.22	0.56	0.06	0.35	0.81	0.66	0.10	0.56	0.85	606	16	20	603	6	10	602	6	10	0.7
13/10/2017	GJ1	3.58	278	10.29	0.57	0.06	0.38	0.80	0.68	0.10	0.57	0.83	602	17	21	599	6	10	598	6	10	0.7
13/10/2017	GJ1	3.79	291	10.18	0.50	0.06	0.28	0.82	0.58	0.10	0.50	0.87	612	13	18	606	5	10	604	6	9	1.2
13/10/2017	GJ1	3.87	295	10.21	0.48	0.06	0.37	0.81	0.61	0.10	0.48	0.80	608	16	20	604	6	10	603	6	9	0.9
13/10/2017	GJ1	3.97	290	10.26	0.48	0.06	0.34	0.81	0.59	0.10	0.48	0.81	609	15	19	601	5	10	599	6	9	1.7
13/10/2017	GJ1	4.01	289	10.22	0.51	0.06	0.33	0.81	0.61	0.10	0.51	0.84	608	15	19	603	6	10	602	6	9	1.1
13/10/2017	GJ1	4.09	289	10.16	0.50	0.06	0.39	0.81	0.64	0.10	0.50	0.79	603	18	21	605	6	10	605	6	9	-0.3
13/10/2017	GJ1	5.15	281	10.21	0.51	0.06	0.46	0.81	0.69	0.10	0.51	0.75	609	20	24	604	6	10	602	6	9	1.1
13/10/2017	GJ1	5.22	288	10.22	0.77	0.06	0.49	0.81	0.91	0.10	0.77	0.84	611	22	25	604	8	11	602	9	12	1.6
13/10/2017	GJ1	5.26	291	10.22	0.82	0.06	0.48	0.81	0.95	0.10	0.82	0.86	594	21	24	600	9	11	602	9	12	-1.2
13/10/2017	GJ1	5.18	283	10.22	0.77	0.06	0.43	0.81	0.88	0.10	0.77	0.87	614	19	23	604	8	11	602	9	12	2.1
13/10/2017	GJ1	5.28	288	10.17	0.86	0.06	0.46	0.82	0.98	0.10	0.86	0.88	611	21	24	606	9	11	604	10	12	1.1
13/10/2017	GJ1	5.35	294	10.21	0.66	0.06	0.45	0.81	0.80	0.10	0.66	0.83	616	20	23	605	7	11	602	8	11	2.2
13/10/2017	GJ1	5.17	282	10.22	0.77	0.06	0.47	0.81	0.90	0.10	0.77	0.85	613	21	24	604	8	11	602	9	12	1.9
13/10/2017	GJ1	5.20	284	10.20	0.92	0.06	0.46	0.81	1.03	0.10	0.92	0.90	606	20	24	603	9	11	603	11	13	0.5
13/10/2017	GJ1	5.34	291	10.25	0.72	0.06	0.41	0.80	0.83	0.10	0.72	0.87	596	18	22	600	8	11	600	8	11	-0.6

***Table S4.1 cont.**: PRM GJ1*

Date	sample	^{206}Pb (mV)	U ppm	^{238}U/ ^{206}Pb	1s%	^{207}Pb/ ^{206}Pb	1s%	^{207}Pb/ ^{235}U	1s%	^{206}Pb /^{238}U	1s%	Rho	^{207}Pb-^{206}Pb Age	2s abs	2s $_{sys}$ abs	^{207}Pb -^{235}U Age	2s abs	2s $_{sys}$ abs	^{206}Pb -^{238}U Age	2s abs	2s $_{sys}$ abs	Disc %
16/10/2017	GJ1	3.69	297	10.24	0.77	0.06	0.38	0.81	0.86	0.10	0.77	0.90	613	17	21	603	8	11	601	9	12	2.0
16/10/2017	GJ1	3.74	299	10.18	0.71	0.06	0.45	0.82	0.84	0.10	0.71	0.85	613	20	23	606	8	11	604	8	11	1.4
16/10/2017	GJ1	3.80	304	10.15	0.76	0.06	0.46	0.81	0.89	0.10	0.76	0.86	603	20	24	605	8	11	606	9	12	-0.5
16/10/2017	GJ1	3.70	298	10.20	0.82	0.06	0.33	0.81	0.88	0.10	0.82	0.93	600	15	19	602	8	11	603	9	12	-0.4
16/10/2017	GJ1	3.77	303	10.18	1.07	0.06	0.47	0.82	1.17	0.10	1.07	0.91	615	21	24	606	11	12	604	12	15	1.8
16/10/2017	GJ1	3.71	297	10.22	0.87	0.06	0.38	0.81	0.95	0.10	0.87	0.92	606	17	21	602	9	11	602	10	12	0.7
16/10/2017	GJ1	3.60	293	10.29	0.98	0.06	0.37	0.81	1.05	0.10	0.98	0.93	617	17	21	602	10	11	598	11	14	3.1
16/10/2017	GJ1	3.58	290	10.27	0.98	0.06	0.37	0.81	1.04	0.10	0.98	0.93	605	17	21	600	10	11	599	11	14	1.0
16/10/2017	GJ1	3.56	288	10.26	0.92	0.06	0.31	0.81	0.97	0.10	0.92	0.95	610	14	18	602	9	11	600	11	13	1.7
16/10/2017	GJ1	3.33	278	10.24	0.82	0.06	0.37	0.81	0.90	0.10	0.82	0.91	611	16	20	603	8	11	601	9	12	1.6
16/10/2017	GJ1	3.36	281	10.22	0.77	0.06	0.37	0.81	0.85	0.10	0.77	0.90	615	17	21	605	8	11	602	9	12	2.2
16/10/2017	GJ1	3.41	283	10.17	0.71	0.06	0.39	0.81	0.81	0.10	0.71	0.88	588	17	21	601	7	11	605	8	11	-2.9
16/10/2017	GJ1	3.42	287	10.25	1.08	0.06	0.37	0.81	1.14	0.10	1.08	0.94	615	17	21	603	10	12	600	12	15	2.4
16/10/2017	GJ1	3.39	285	10.16	1.07	0.06	0.39	0.82	1.14	0.10	1.07	0.94	613	17	21	607	10	12	605	12	15	1.4
16/10/2017	GJ1	3.36	282	10.22	0.97	0.06	0.36	0.81	1.04	0.10	0.97	0.94	599	16	20	601	9	11	602	11	14	-0.4
16/10/2017	GJ1	3.35	284	10.25	1.08	0.06	0.41	0.81	1.15	0.10	1.08	0.93	604	18	22	601	10	12	600	12	15	0.6
16/10/2017	GJ1	3.36	284	10.20	0.77	0.06	0.46	0.81	0.90	0.10	0.77	0.85	611	21	24	604	8	11	603	9	12	1.3
16/10/2017	GJ1	3.42	290	10.20	0.87	0.06	0.45	0.81	0.98	0.10	0.87	0.89	605	20	23	603	9	11	603	10	12	0.4
16/10/2017	GJ1	3.07	272	10.34	0.78	0.06	0.39	0.80	0.87	0.10	0.78	0.89	617	17	21	600	8	11	595	9	12	3.6
16/10/2017	GJ1	3.09	273	10.26	1.03	0.06	0.38	0.81	1.09	0.10	1.03	0.94	606	17	21	601	10	11	600	12	14	1.0
16/10/2017	GJ1	3.18	281	10.28	0.77	0.06	0.45	0.80	0.89	0.10	0.77	0.86	604	20	23	600	8	11	598	9	12	1.0
16/10/2017	GJ1	3.20	282	10.17	1.12	0.06	0.43	0.82	1.20	0.10	1.12	0.93	614	19	23	606	11	12	604	13	15	1.5
16/10/2017	GJ1	3.19	283	10.22	1.07	0.06	0.43	0.81	1.16	0.10	1.07	0.93	610	19	23	603	11	12	602	12	15	1.4
16/10/2017	GJ1	3.08	273	10.24	1.13	0.06	0.31	0.80	1.17	0.10	1.13	0.96	590	14	19	599	11	12	601	13	15	-1.9
16/10/2017	GJ1	3.09	275	10.20	0.97	0.06	0.43	0.81	1.06	0.10	0.97	0.91	602	19	23	603	10	11	603	11	14	-0.1
16/10/2017	GJ1	3.14	278	10.15	1.12	0.06	0.37	0.82	1.18	0.10	1.12	0.95	610	16	20	607	11	12	606	13	15	0.7
16/10/2017	GJ1	3.27	290	10.16	1.02	0.06	0.41	0.82	1.10	0.10	1.02	0.93	613	19	22	607	10	12	605	12	14	1.2
16/10/2017	GJ1	2.92	277	10.42	0.94	0.06	0.37	0.80	1.01	0.10	0.94	0.93	616	17	21	596	9	11	591	11	13	4.1
16/10/2017	GJ1	3.05	286	10.28	0.98	0.06	0.55	0.81	1.12	0.10	0.98	0.87	604	24	27	600	10	12	599	11	14	0.9
16/10/2017	GJ1	2.92	277	10.42	0.78	0.06	0.38	0.79	0.87	0.10	0.78	0.90	605	17	21	594	8	11	591	9	12	2.4
16/10/2017	GJ1	2.88	272	10.35	0.98	0.06	0.41	0.80	1.06	0.10	0.98	0.92	602	18	22	596	10	11	594	11	14	1.3
16/10/2017	GJ1	2.90	274	10.45	0.89	0.06	0.37	0.79	0.96	0.10	0.89	0.92	607	16	21	593	9	11	589	10	12	2.9

***Table S4.1 cont.**: PRM GJ1*

Date	sample	^{206}Pb (mV)	U ppm	^{238}U/ ^{206}Pb	1s%	^{207}Pb/ ^{206}Pb	1s%	^{207}Pb/ ^{235}U	1s%	^{206}Pb /^{238}U	1s%	Rho	^{207}Pb-^{206}Pb Age	2s abs	2s $_{sys}$ abs	^{207}Pb -^{235}U Age	2s abs	2s $_{sys}$ abs	^{206}Pb -^{238}U Age	2s abs	2s $_{sys}$ abs	Disc %
16/10/2017	GJ1	3.04	285	10.16	0.81	0.06	0.38	0.81	0.90	0.10	0.81	0.90	597	17	21	603	8	11	605	9	12	-1.3
16/10/2017	GJ1	3.08	287	10.15	0.91	0.06	0.40	0.82	1.00	0.10	0.91	0.92	622	18	21	609	9	11	606	11	13	2.6
16/10/2017	GJ1	3.11	290	10.11	0.86	0.06	0.41	0.82	0.95	0.10	0.86	0.90	621	18	22	611	9	11	608	10	12	2.0
16/10/2017	GJ1	3.33	311	10.07	0.86	0.06	0.45	0.82	0.97	0.10	0.86	0.88	600	20	23	608	9	11	610	10	12	-1.8
16/10/2017	GJ1	3.39	314	10.04	0.85	0.06	0.45	0.83	0.97	0.10	0.85	0.88	618	20	24	613	9	11	612	10	12	1.0
16/10/2017	GJ1	3.33	310	10.07	0.81	0.06	0.37	0.82	0.89	0.10	0.81	0.91	602	17	21	609	8	11	610	9	12	-1.4
16/10/2017	GJ1	3.01	297	10.27	0.77	0.06	0.34	0.81	0.84	0.10	0.77	0.92	619	15	20	603	8	11	599	9	12	3.3
16/10/2017	GJ1	3.09	304	10.18	0.76	0.06	0.39	0.81	0.86	0.10	0.76	0.89	604	18	21	604	8	11	604	9	12	0.1
16/10/2017	GJ1	3.16	311	10.24	0.87	0.06	0.38	0.81	0.95	0.10	0.87	0.92	615	17	21	604	9	11	601	10	12	2.3
16/10/2017	GJ1	2.89	287	10.22	1.02	0.06	0.42	0.81	1.11	0.10	1.02	0.92	606	19	22	602	10	12	602	12	14	0.8
16/10/2017	GJ1	2.96	293	10.19	0.87	0.06	0.38	0.81	0.95	0.10	0.87	0.91	603	17	21	603	9	11	603	10	12	-0.1
16/10/2017	GJ1	2.92	290	10.18	0.97	0.06	0.44	0.81	1.06	0.10	0.97	0.91	610	20	23	605	10	11	604	11	14	1.0
16/10/2017	GJ1	2.96	295	10.21	1.02	0.06	0.35	0.81	1.08	0.10	1.02	0.95	595	16	20	601	10	11	602	12	14	-1.3
16/10/2017	GJ1	2.94	292	10.16	0.91	0.06	0.33	0.82	0.97	0.10	0.91	0.94	611	15	19	606	9	11	605	11	13	1.0
16/10/2017	GJ1	2.93	291	10.17	0.92	0.06	0.39	0.81	1.00	0.10	0.92	0.92	607	18	21	605	9	11	604	11	13	0.4
17/10/2017	GJ1	4.69	288	10.30	0.82	0.06	0.40	0.81	0.92	0.10	0.82	0.90	611	18	22	600	8	11	597	9	12	2.3
17/10/2017	GJ1	4.68	286	10.21	0.82	0.06	0.42	0.81	0.92	0.10	0.82	0.89	606	19	22	603	8	11	602	9	12	0.6
17/10/2017	GJ1	4.65	285	10.29	0.72	0.06	0.43	0.80	0.84	0.10	0.72	0.86	597	19	23	598	8	11	598	8	11	-0.2
17/10/2017	GJ1	4.54	283	10.24	0.82	0.06	0.43	0.81	0.92	0.10	0.82	0.89	620	19	22	605	8	11	601	9	12	3.1
17/10/2017	GJ1	4.68	289	10.14	0.71	0.06	0.43	0.82	0.83	0.10	0.71	0.86	617	19	23	608	8	11	606	8	11	1.7
17/10/2017	GJ1	4.58	285	10.17	0.71	0.06	0.42	0.82	0.82	0.10	0.71	0.86	609	19	22	605	8	11	604	8	11	0.8
17/10/2017	GJ1	4.59	289	10.20	0.61	0.06	0.42	0.81	0.74	0.10	0.61	0.83	611	19	22	604	7	10	603	7	11	1.4
17/10/2017	GJ1	4.59	289	10.25	0.67	0.06	0.44	0.81	0.80	0.10	0.67	0.83	613	20	23	603	7	11	600	8	11	2.1
17/10/2017	GJ1	4.62	291	10.18	0.66	0.06	0.38	0.81	0.76	0.10	0.66	0.87	606	17	21	604	7	10	604	8	11	0.4
17/10/2017	GJ1	4.04	286	10.35	0.78	0.06	0.47	0.81	0.91	0.10	0.78	0.86	623	21	24	600	8	11	594	9	12	4.6
17/10/2017	GJ1	4.06	284	10.27	0.62	0.06	0.44	0.81	0.76	0.10	0.62	0.81	611	20	23	602	7	10	599	7	10	2.0
17/10/2017	GJ1	4.04	284	10.31	0.52	0.06	0.43	0.80	0.67	0.10	0.52	0.77	609	19	23	599	6	10	597	6	9	2.1
17/10/2017	GJ1	4.12	285	10.17	0.66	0.06	0.41	0.81	0.78	0.10	0.66	0.85	599	18	22	603	7	10	604	8	11	-0.9
17/10/2017	GJ1	4.10	282	10.20	0.87	0.06	0.48	0.81	0.99	0.10	0.87	0.87	603	21	25	603	9	11	603	10	12	0.1
17/10/2017	GJ1	4.08	281	10.16	0.56	0.06	0.42	0.81	0.70	0.10	0.56	0.80	592	19	22	602	6	10	605	6	10	-2.2
17/10/2017	GJ1	4.34	300	10.25	0.61	0.06	0.41	0.81	0.74	0.10	0.61	0.83	601	18	22	600	7	10	600	7	11	0.1
17/10/2017	GJ1	4.42	302	10.14	0.66	0.06	0.56	0.82	0.87	0.10	0.66	0.76	614	25	28	608	8	11	606	8	11	1.3

***Table S4.1 cont.**: PRM GJ1*

Date	sample	^{206}Pb (mV)	U ppm	^{238}U/ ^{206}Pb	1s%	^{207}Pb/ ^{206}Pb	1s%	^{207}Pb/ ^{235}U	1s%	^{206}Pb /^{238}U	1s%	Rho	^{207}Pb-^{206}Pb Age	2s abs	2s $_{sys}$ abs	^{207}Pb -^{235}U Age	2s abs	2s $_{sys}$ abs	^{206}Pb -^{238}U Age	2s abs	2s $_{sys}$ abs	Disc %
17/10/2017	GJ1	4.42	302	10.16	0.76	0.06	0.41	0.81	0.87	0.10	0.76	0.88	597	18	22	603	8	11	605	9	12	-1.4
17/10/2017	GJ1	4.34	297	10.27	0.82	0.06	0.45	0.81	0.94	0.10	0.82	0.88	612	20	23	602	9	11	599	9	12	2.0
17/10/2017	GJ1	4.35	296	10.20	0.77	0.06	0.45	0.82	0.89	0.10	0.77	0.86	621	20	24	607	8	11	603	9	12	2.9
17/10/2017	GJ1	4.35	294	10.09	0.96	0.06	0.47	0.82	1.07	0.10	0.96	0.90	596	21	24	606	10	12	609	11	13	-2.2
17/10/2017	GJ1	4.04	281	10.15	0.86	0.06	0.47	0.82	0.98	0.10	0.86	0.88	605	21	24	606	9	11	606	10	12	0.0
17/10/2017	GJ1	4.04	285	10.24	1.02	0.06	0.55	0.81	1.16	0.10	1.02	0.88	621	24	27	605	11	12	601	12	14	3.2
17/10/2017	GJ1	4.03	283	10.15	0.91	0.06	0.43	0.81	1.01	0.10	0.91	0.90	595	19	23	603	9	11	606	11	13	-1.8
17/10/2017	GJ1	3.84	289	10.27	0.45	0.06	0.42	0.81	0.61	0.10	0.45	0.73	606	19	22	600	6	10	599	5	9	1.2
17/10/2017	GJ1	3.82	283	10.19	0.66	0.06	0.49	0.81	0.82	0.10	0.66	0.80	609	22	25	604	8	11	603	8	11	0.9
17/10/2017	GJ1	3.83	283	10.19	0.61	0.06	0.41	0.81	0.74	0.10	0.61	0.83	612	19	22	605	7	10	603	7	11	1.4
17/10/2017	GJ1	3.85	284	10.13	0.49	0.06	0.47	0.82	0.68	0.10	0.49	0.72	625	21	24	611	6	10	607	6	9	2.9
17/10/2017	GJ1	3.86	290	10.26	0.51	0.06	0.56	0.81	0.76	0.10	0.51	0.68	606	25	27	601	7	10	600	6	9	1.1
17/10/2017	GJ1	3.89	288	10.16	0.61	0.06	0.51	0.81	0.80	0.10	0.61	0.77	585	23	26	601	7	10	605	7	11	-3.5
17/10/2017	GJ1	3.84	285	10.18	0.48	0.06	0.47	0.81	0.67	0.10	0.48	0.71	607	21	24	605	6	10	604	6	9	0.5
17/10/2017	GJ1	3.94	289	10.31	1.08	0.06	0.45	0.80	1.17	0.10	1.08	0.92	606	20	23	599	11	12	597	12	15	1.5
17/10/2017	GJ1	3.92	287	10.29	1.13	0.06	0.39	0.81	1.20	0.10	1.13	0.95	615	17	21	602	11	12	598	13	15	2.7
17/10/2017	GJ1	3.88	282	10.20	1.02	0.06	0.41	0.81	1.10	0.10	1.02	0.93	591	18	22	600	10	11	603	12	14	-2.0
17/10/2017	GJ1	3.92	284	10.28	0.77	0.06	0.45	0.81	0.89	0.10	0.77	0.86	607	20	23	600	8	11	599	9	12	1.3
17/10/2017	GJ1	4.08	295	10.20	1.02	0.06	0.49	0.81	1.13	0.10	1.02	0.90	606	22	25	603	10	12	603	12	14	0.5
17/10/2017	GJ1	4.13	298	10.16	1.12	0.06	0.41	0.82	1.19	0.10	1.12	0.94	613	18	22	607	11	12	605	13	15	1.3
17/10/2017	GJ1	4.05	290	10.32	0.98	0.06	0.44	0.81	1.07	0.10	0.98	0.91	619	19	23	601	10	11	596	11	14	3.6
17/10/2017	GJ1	4.03	287	10.22	0.87	0.06	0.42	0.81	0.96	0.10	0.87	0.90	608	19	22	603	9	11	602	10	12	1.1
17/10/2017	GJ1	3.99	285	10.34	0.72	0.06	0.49	0.80	0.87	0.10	0.72	0.83	614	22	25	599	8	11	595	8	11	3.2
18/10/2017	GJ1	4.97	289	10.21	0.82	0.06	0.38	0.82	0.90	0.10	0.82	0.91	620	17	21	606	8	11	602	9	12	2.9
18/10/2017	GJ1	4.96	284	10.16	0.81	0.06	0.48	0.82	0.95	0.10	0.81	0.86	606	21	24	605	9	11	605	9	12	0.2
18/10/2017	GJ1	4.94	284	10.13	0.81	0.06	0.41	0.81	0.91	0.10	0.81	0.89	596	18	22	605	8	11	607	9	12	-1.7
18/10/2017	GJ1	5.04	291	10.27	1.90	0.06	0.37	0.81	1.93	0.10	1.90	0.98	603	17	21	600	18	14	599	22	23	0.6
18/10/2017	GJ1	5.06	290	10.19	1.99	0.06	0.33	0.81	2.02	0.10	1.99	0.99	600	15	20	603	18	15	603	23	24	-0.5
18/10/2017	GJ1	5.07	292	10.19	2.04	0.06	0.35	0.81	2.07	0.10	2.04	0.99	596	16	20	602	19	15	603	23	25	-1.1
18/10/2017	GJ1	5.04	289	10.26	2.00	0.06	0.36	0.81	2.03	0.10	2.00	0.98	612	16	20	602	18	15	600	23	24	1.9
18/10/2017	GJ1	4.99	284	10.22	2.25	0.06	0.35	0.81	2.28	0.10	2.25	0.99	596	16	20	600	21	15	602	26	27	-0.9
18/10/2017	GJ1	4.96	284	10.24	1.33	0.06	0.39	0.81	1.39	0.10	1.33	0.96	602	18	21	601	13	12	601	15	17	0.2

***Table S4.1 cont.**: PRM GJ1*

Date	sample	^{206}Pb (mV)	U ppm	$^{238}U/^{206}Pb$	1s%	$^{207}Pb/^{206}Pb$	1s%	$^{207}Pb/^{235}U$	1s%	$^{206}Pb/^{238}U$	1s%	Rho	^{207}Pb-^{206}Pb Age	2s abs	2s $_{sys}$ abs	^{207}Pb-^{235}U Age	2s abs	2s $_{sys}$ abs	^{206}Pb-^{238}U Age	2s abs	2s $_{sys}$ abs	Disc %
18/10/2017	GJ1	4.86	284	10.32	0.57	0.06	0.42	0.81	0.71	0.10	0.57	0.80	619	19	22	601	6	10	596	6	10	3.6
18/10/2017	GJ1	4.97	288	10.22	0.72	0.06	0.38	0.81	0.81	0.10	0.72	0.88	616	17	21	605	7	11	602	8	11	2.4
18/10/2017	GJ1	4.95	284	10.24	0.61	0.06	0.39	0.81	0.73	0.10	0.61	0.84	615	17	21	604	7	10	601	7	11	2.3
18/10/2017	GJ1	5.05	289	10.22	0.61	0.06	0.41	0.81	0.74	0.10	0.61	0.83	615	18	22	604	7	10	602	7	11	2.2
18/10/2017	GJ1	5.04	287	10.14	0.66	0.06	0.39	0.81	0.77	0.10	0.66	0.86	599	18	21	605	7	10	606	8	11	-1.1
18/10/2017	GJ1	5.08	289	10.27	0.62	0.06	0.44	0.81	0.76	0.10	0.62	0.81	615	20	23	602	7	10	599	7	10	2.7
18/10/2017	GJ1	5.09	289	10.25	0.51	0.06	0.37	0.81	0.63	0.10	0.51	0.81	612	16	20	602	6	10	600	6	9	2.0
18/10/2017	GJ1	5.07	287	10.18	0.56	0.06	0.35	0.82	0.66	0.10	0.56	0.85	617	16	20	606	6	10	604	6	10	2.1
18/10/2017	GJ1	5.03	284	10.14	0.56	0.06	0.34	0.82	0.65	0.10	0.56	0.85	611	15	19	607	6	10	606	6	10	0.8
18/10/2017	GJ1	5.09	288	10.37	1.09	0.06	0.32	0.80	1.14	0.10	1.09	0.96	620	15	19	599	10	12	593	12	14	4.3
18/10/2017	GJ1	5.07	284	10.41	1.30	0.06	0.38	0.80	1.36	0.10	1.30	0.96	613	17	21	596	12	12	592	15	16	3.5
18/10/2017	GJ1	5.08	283	10.28	0.67	0.06	0.36	0.81	0.76	0.10	0.67	0.88	611	16	20	601	7	10	599	8	11	2.1
18/10/2017	GJ1	4.86	281	10.37	1.04	0.06	0.37	0.80	1.10	0.10	1.04	0.94	616	17	21	598	10	11	593	12	14	3.6
18/10/2017	GJ1	4.90	283	10.32	1.34	0.06	0.42	0.80	1.40	0.10	1.34	0.96	611	19	22	599	13	12	596	15	17	2.3
18/10/2017	GJ1	4.92	285	10.38	1.04	0.06	0.35	0.79	1.10	0.10	1.04	0.95	599	16	20	594	10	11	593	12	14	1.0
18/10/2017	GJ1	4.89	293	10.18	1.53	0.06	0.48	0.82	1.60	0.10	1.53	0.95	614	21	24	606	15	13	604	18	19	1.7
18/10/2017	GJ1	4.90	297	10.32	1.81	0.06	0.35	0.80	1.84	0.10	1.81	0.98	610	16	20	599	17	14	596	21	22	2.3
18/10/2017	GJ1	5.00	308	10.34	1.40	0.06	0.36	0.80	1.44	0.10	1.40	0.97	614	16	20	599	13	12	595	16	18	3.2
18/10/2017	GJ1	2.89	277	10.18	0.81	0.06	0.43	0.81	0.92	0.10	0.81	0.88	596	19	23	602	8	11	604	9	12	-1.4
18/10/2017	GJ1	2.86	276	10.14	0.86	0.06	0.43	0.81	0.96	0.10	0.86	0.89	601	19	23	605	9	11	606	10	12	-0.8
18/10/2017	GJ1	2.88	284	9.99	1.05	0.06	0.54	0.83	1.18	0.10	1.05	0.89	596	24	27	611	11	12	615	12	15	-3.2
18/10/2017	GJ1	2.84	283	10.08	1.16	0.06	0.53	0.83	1.27	0.10	1.16	0.91	616	23	26	611	12	12	610	14	15	1.0
18/10/2017	GJ1	2.90	293	10.13	1.01	0.06	0.53	0.81	1.14	0.10	1.01	0.89	589	23	26	603	10	12	607	12	14	-3.0
18/10/2017	GJ1	2.93	296	10.01	1.15	0.06	0.39	0.83	1.22	0.10	1.15	0.95	605	18	21	612	11	12	614	13	15	-1.4
18/10/2017	GJ1	2.92	288	10.20	0.66	0.06	0.53	0.81	0.85	0.10	0.66	0.78	610	23	26	604	8	11	603	8	11	1.2
18/10/2017	GJ1	2.92	288	10.22	0.72	0.06	0.39	0.81	0.82	0.10	0.72	0.88	600	18	21	601	7	11	602	8	11	-0.2
18/10/2017	GJ1	2.85	290	10.25	0.87	0.06	0.52	0.81	1.01	0.10	0.87	0.86	606	23	26	602	9	11	600	10	12	1.0
18/10/2017	GJ1	2.81	286	10.21	0.87	0.06	0.51	0.81	1.01	0.10	0.87	0.86	594	23	26	600	9	11	602	10	12	-1.4
18/10/2017	GJ1	2.79	285	10.27	0.77	0.06	0.50	0.81	0.92	0.10	0.77	0.84	605	22	25	600	8	11	599	9	12	0.9
18/10/2017	GJ1	2.80	287	10.19	0.82	0.06	0.49	0.81	0.95	0.10	0.82	0.86	591	22	25	601	9	11	603	9	12	-2.1
18/09/2018	GJ1	4.49	289	10.32	0.52	0.06	0.44	0.81	0.68	0.10	0.52	0.76	618	19	23	601	6	10	596	6	9	3.6
18/09/2018	GJ1	4.44	283	10.26	0.56	0.06	0.42	0.81	0.71	0.10	0.56	0.80	604	19	22	601	6	10	600	6	10	0.8

***Table S4.1 cont.**: PRM GJ1*

Date	sample	^{206}Pb (mV)	U ppm	^{238}U/ ^{206}Pb	1s%	^{207}Pb/ ^{206}Pb	1s%	^{207}Pb/ ^{235}U	1s%	^{206}Pb /^{238}U	1s%	Rho	^{207}Pb-^{206}Pb Age	2s abs	2s $_{sys}$ abs	^{207}Pb -^{235}U Age	2s abs	2s $_{sys}$ abs	^{206}Pb -^{238}U Age	2s abs	2s $_{sys}$ abs	Disc %
18/09/2018	GJ1	4.43	282	10.22	0.51	0.06	0.38	0.81	0.64	0.10	0.51	0.81	593	17	21	600	6	10	602	6	9	-1.5
18/09/2018	GJ1	4.44	285	10.24	0.56	0.06	0.32	0.81	0.65	0.10	0.56	0.87	612	15	19	603	6	10	601	6	10	1.7
18/09/2018	GJ1	4.51	289	10.19	0.61	0.06	0.37	0.81	0.71	0.10	0.61	0.86	602	17	21	603	7	10	603	7	11	-0.3
18/09/2018	GJ1	4.57	293	10.19	0.61	0.06	0.28	0.81	0.67	0.10	0.61	0.91	608	13	18	604	6	10	603	7	11	0.8
18/09/2018	GJ1	4.42	287	10.27	0.47	0.06	0.38	0.81	0.60	0.10	0.47	0.77	611	17	21	602	6	10	599	5	9	1.9
18/09/2018	GJ1	4.46	290	10.25	0.56	0.06	0.29	0.81	0.63	0.10	0.56	0.89	605	13	18	601	6	10	600	6	10	0.9
18/09/2018	GJ1	4.51	291	10.21	0.61	0.06	0.36	0.82	0.71	0.10	0.61	0.86	618	16	20	606	7	10	602	7	11	2.6
18/09/2018	GJ1	3.95	276	10.25	0.45	0.06	0.44	0.81	0.63	0.10	0.45	0.71	619	19	23	604	6	10	600	5	9	3.0
18/09/2018	GJ1	4.04	281	10.22	0.48	0.06	0.43	0.81	0.64	0.10	0.48	0.74	617	19	23	605	6	10	602	5	9	2.5
18/09/2018	GJ1	4.17	288	10.15	0.38	0.06	0.40	0.82	0.55	0.10	0.38	0.69	613	18	21	607	5	9	606	4	9	1.2
18/09/2018	GJ1	4.26	291	10.10	0.47	0.06	0.38	0.82	0.60	0.10	0.47	0.78	616	17	21	610	6	9	608	5	9	1.2
18/09/2018	GJ1	4.26	292	10.20	0.37	0.06	0.37	0.81	0.52	0.10	0.37	0.71	612	16	20	605	5	10	603	4	9	1.4
18/09/2018	GJ1	4.26	292	10.22	0.42	0.06	0.39	0.81	0.58	0.10	0.42	0.73	600	18	21	602	5	10	602	5	9	-0.2
18/09/2018	GJ1	4.20	287	10.22	0.45	0.06	0.51	0.81	0.68	0.10	0.45	0.66	604	22	26	602	6	10	602	5	9	0.5
18/09/2018	GJ1	4.23	289	10.25	0.42	0.06	0.45	0.81	0.61	0.10	0.42	0.68	601	20	23	600	6	10	600	5	9	0.1
18/09/2018	GJ1	4.23	287	10.16	0.42	0.06	0.34	0.82	0.54	0.10	0.42	0.77	605	15	19	605	5	10	605	5	9	-0.1
18/09/2018	GJ1	3.98	286	10.31	0.72	0.06	0.34	0.81	0.80	0.10	0.72	0.91	624	15	20	602	7	11	597	8	11	4.3
18/09/2018	GJ1	3.99	285	10.20	0.56	0.06	0.44	0.82	0.71	0.10	0.56	0.79	619	19	23	606	7	10	603	6	10	2.7
18/09/2018	GJ1	4.01	288	10.29	0.67	0.06	0.43	0.80	0.79	0.10	0.67	0.84	598	19	22	598	7	10	598	8	11	0.0
18/09/2018	GJ1	4.00	283	10.21	0.56	0.06	0.39	0.81	0.68	0.10	0.56	0.82	610	18	21	604	6	10	602	6	10	1.3
18/09/2018	GJ1	4.00	283	10.22	0.49	0.06	0.44	0.81	0.66	0.10	0.49	0.74	611	20	23	604	6	10	602	6	9	1.6
18/09/2018	GJ1	4.11	290	10.22	0.66	0.06	0.40	0.81	0.77	0.10	0.66	0.86	613	18	21	604	7	10	602	8	11	1.9
18/09/2018	GJ1	4.13	291	10.26	0.56	0.06	0.39	0.81	0.69	0.10	0.56	0.82	610	18	21	602	6	10	600	6	10	1.7
18/09/2018	GJ1	4.11	290	10.26	0.67	0.06	0.38	0.80	0.77	0.10	0.67	0.87	598	17	21	599	7	10	600	8	11	-0.2
18/09/2018	GJ1	4.16	291	10.18	0.66	0.06	0.45	0.82	0.80	0.10	0.66	0.83	611	20	23	605	7	11	604	8	11	1.1
18/09/2018	GJ1	3.89	284	10.21	0.87	0.06	0.40	0.82	0.96	0.10	0.87	0.91	624	18	22	607	9	11	602	10	12	3.5
18/09/2018	GJ1	3.97	290	10.20	0.71	0.06	0.37	0.81	0.80	0.10	0.71	0.89	604	17	21	603	7	11	603	8	11	0.2
18/09/2018	GJ1	3.98	290	10.26	0.77	0.06	0.33	0.81	0.84	0.10	0.77	0.92	600	15	19	600	8	11	600	9	12	0.0
18/09/2018	GJ1	3.82	281	10.21	0.82	0.06	0.46	0.81	0.94	0.10	0.82	0.87	611	20	24	604	9	11	602	9	12	1.5
20/09/2018	GJ1	3.97	285	10.28	0.87	0.06	0.48	0.81	1.00	0.10	0.87	0.88	605	21	24	600	9	11	599	10	12	1.1
20/09/2018	GJ1	4.02	290	10.28	0.98	0.06	0.49	0.81	1.09	0.10	0.98	0.89	629	22	25	605	10	12	599	11	14	4.8
20/09/2018	GJ1	3.97	283	10.19	0.97	0.06	0.45	0.81	1.07	0.10	0.97	0.91	611	20	23	605	10	11	603	11	14	1.2

***Table S4.1 cont.**: PRM GJ1*

Date	sample	^{206}Pb (mV)	U ppm	^{238}U/ ^{206}Pb	1s%	^{207}Pb/ ^{206}Pb	1s%	^{207}Pb/ ^{235}U	1s%	^{206}Pb /^{238}U	1s%	Rho	^{207}Pb- ^{206}Pb Age	2s abs	2s $_{sys}$ abs	^{207}Pb -^{235}U Age	2s abs	2s $_{sys}$ abs	^{206}Pb -^{238}U Age	2s abs	2s $_{sys}$ abs	Disc %
20/09/2018	GJ1	4.09	288	10.32	0.98	0.06	0.44	0.80	1.08	0.10	0.98	0.91	600	20	23	597	10	11	596	11	14	0.7
20/09/2018	GJ1	4.15	291	10.26	0.92	0.06	0.49	0.80	1.04	0.10	0.92	0.88	592	22	25	598	9	11	600	11	13	-1.4
20/09/2018	GJ1	4.13	290	10.31	0.88	0.06	0.45	0.80	0.99	0.10	0.88	0.89	602	20	23	598	9	11	597	10	12	0.8
20/09/2018	GJ1	4.02	285	10.31	0.82	0.06	0.47	0.80	0.95	0.10	0.82	0.87	607	21	24	599	9	11	597	9	12	1.6
20/09/2018	GJ1	4.10	285	10.05	1.01	0.06	0.49	0.83	1.12	0.10	1.01	0.90	617	22	25	613	10	12	611	12	14	0.9
20/09/2018	GJ1	4.08	287	10.12	1.01	0.06	0.51	0.82	1.14	0.10	1.01	0.89	615	23	26	609	10	12	607	12	14	1.3
20/09/2018	GJ1	4.01	288	10.18	0.87	0.06	0.55	0.82	1.03	0.10	0.87	0.84	630	24	27	610	9	11	604	10	12	4.2
20/09/2018	GJ1	4.00	290	10.26	0.92	0.06	0.49	0.81	1.04	0.10	0.92	0.88	616	22	25	603	10	11	600	11	13	2.6
20/09/2018	GJ1	4.05	291	10.15	0.96	0.06	0.59	0.82	1.13	0.10	0.96	0.85	619	26	29	608	10	12	606	11	14	2.1
20/09/2018	GJ1	2.08	279	10.11	1.01	0.06	0.55	0.82	1.15	0.10	1.01	0.88	616	24	27	610	11	12	608	12	14	1.3
20/09/2018	GJ1	2.10	284	10.20	0.87	0.06	0.57	0.81	1.04	0.10	0.87	0.83	612	25	28	605	10	11	603	10	12	1.5
20/09/2018	GJ1	2.18	292	10.05	0.90	0.06	0.59	0.82	1.08	0.10	0.90	0.84	602	26	29	609	10	12	611	11	13	-1.7
20/09/2018	GJ1	2.12	286	10.03	1.00	0.06	0.53	0.82	1.13	0.10	1.00	0.89	598	23	26	610	10	12	613	12	14	-2.4
20/09/2018	GJ1	2.11	288	10.20	0.92	0.06	0.64	0.81	1.12	0.10	0.92	0.82	604	28	31	603	10	12	603	11	13	0.2
20/09/2018	GJ1	2.12	286	10.07	0.96	0.06	0.66	0.81	1.16	0.10	0.96	0.82	582	29	32	604	11	12	610	11	13	-4.8
20/09/2018	GJ1	2.16	293	10.16	0.91	0.06	0.56	0.82	1.07	0.10	0.91	0.85	613	24	27	607	10	12	605	11	13	1.3
20/09/2018	GJ1	2.13	289	10.22	0.87	0.06	0.54	0.81	1.02	0.10	0.87	0.85	601	24	27	602	9	11	602	10	12	-0.1
20/09/2018	GJ1	2.10	285	10.20	0.82	0.06	0.60	0.81	1.01	0.10	0.82	0.80	592	27	29	600	9	11	603	9	12	-1.9
20/09/2018	GJ1	2.01	281	10.17	0.92	0.06	0.57	0.82	1.08	0.10	0.92	0.85	611	25	28	606	10	12	604	11	13	1.1
20/09/2018	GJ1	2.02	288	10.34	0.93	0.06	0.62	0.80	1.12	0.10	0.93	0.83	609	27	30	598	10	11	595	11	13	2.4
20/09/2018	GJ1	2.05	290	10.29	1.08	0.06	0.55	0.81	1.21	0.10	1.08	0.89	614	24	27	601	11	12	598	12	15	2.6
20/09/2018	GJ1	2.08	293	10.34	0.93	0.06	0.64	0.80	1.13	0.10	0.93	0.82	595	28	56	595	10	26	595	11	29	0.0
20/09/2018	GJ1	2.08	291	10.33	0.88	0.06	0.61	0.80	1.07	0.10	0.88	0.82	605	27	49	597	10	19	595	10	20	1.5
20/09/2018	GJ1	2.10	292	10.21	1.02	0.06	0.61	0.81	1.19	0.10	1.02	0.86	599	27	56	601	11	17	602	12	16	-0.5
20/09/2018	GJ1	2.06	284	10.11	1.01	0.06	0.65	0.82	1.20	0.10	1.01	0.84	615	29	51	609	11	19	608	12	20	1.2
20/09/2018	GJ1	2.04	282	10.17	0.92	0.06	0.54	0.82	1.06	0.10	0.92	0.86	628	24	57	609	10	19	604	11	19	3.8
20/09/2018	GJ1	2.05	285	10.20	0.97	0.06	0.62	0.81	1.15	0.10	0.97	0.84	606	27	52	603	10	17	603	11	16	0.5
20/09/2018	GJ1	2.14	289	10.30	0.93	0.06	0.56	0.81	1.08	0.10	0.93	0.86	624	25	56	603	10	26	597	11	29	4.3
20/09/2018	GJ1	2.16	290	10.30	0.93	0.06	0.55	0.80	1.08	0.10	0.93	0.86	605	24	53	599	10	25	597	11	29	1.3
20/09/2018	GJ1	2.13	284	10.19	0.97	0.06	0.57	0.81	1.13	0.10	0.97	0.86	606	25	50	604	10	26	603	11	30	0.4
21/09/2018	GJ1	3.68	265	10.21	1.94	0.06	0.39	0.81	1.98	0.10	1.94	0.98	613	17	49	604	18	25	602	22	29	1.7
21/09/2018	GJ1	3.74	267	10.09	2.12	0.06	0.43	0.82	2.16	0.10	2.12	0.98	607	19	52	609	20	20	609	25	22	-0.4

***Table S4.1 cont.**: PRM GJ1*

Date	sample	^{206}Pb (mV)	U ppm	^{238}U/ ^{206}Pb	1s%	^{207}Pb/ ^{206}Pb	1s%	^{207}Pb/ ^{235}U	1s%	^{206}Pb /^{238}U	1s%	Rho	^{207}Pb-^{206}Pb Age	2s abs	2s $_{sys}$ abs	^{207}Pb -^{235}U Age	2s abs	2s $_{sys}$ abs	^{206}Pb -^{238}U Age	2s abs	2s $_{sys}$ abs	Disc %
21/09/2018	GJ1	3.80	272	10.18	1.78	0.06	0.46	0.81	1.84	0.10	1.78	0.97	608	20	55	605	17	24	604	21	26	0.7
21/09/2018	GJ1	3.87	278	10.09	1.31	0.06	0.36	0.82	1.36	0.10	1.31	0.96	605	16	56	608	12	21	609	15	22	-0.7
21/09/2018	GJ1	3.84	275	10.12	1.47	0.06	0.42	0.82	1.53	0.10	1.47	0.96	608	19	53	608	14	20	607	17	21	0.2
21/09/2018	GJ1	3.89	277	10.14	1.37	0.06	0.39	0.81	1.42	0.10	1.37	0.96	599	18	50	605	13	20	606	16	22	-1.3
21/09/2018	GJ1	4.04	300	10.27	1.28	0.06	0.39	0.81	1.34	0.10	1.28	0.96	614	17	59	602	12	22	599	15	22	2.4
21/09/2018	GJ1	4.07	302	10.26	1.18	0.06	0.46	0.81	1.27	0.10	1.18	0.93	615	21	50	603	12	21	600	14	22	2.5
21/09/2018	GJ1	4.04	298	10.14	1.12	0.06	0.40	0.81	1.19	0.10	1.12	0.94	587	18	52	602	11	22	606	13	24	-3.3
21/09/2018	GJ1	4.02	302	10.29	1.08	0.06	0.41	0.81	1.16	0.10	1.08	0.93	612	19	55	601	11	20	598	12	21	2.3
21/09/2018	GJ1	3.30	240	9.85	1.13	0.06	0.46	0.84	1.22	0.10	1.13	0.93	615	20	52	621	11	29	623	13	33	-1.4
21/09/2018	GJ1	4.04	302	10.25	1.08	0.06	0.41	0.81	1.15	0.10	1.08	0.94	618	18	49	604	11	35	600	12	42	2.9
21/09/2018	GJ1	4.05	302	10.16	1.12	0.06	0.36	0.81	1.17	0.10	1.12	0.95	604	16	53	605	11	25	605	13	27	-0.2
21/09/2018	GJ1	4.08	309	10.33	1.03	0.06	0.50	0.81	1.15	0.10	1.03	0.90	616	22	49	600	10	26	596	12	30	3.2
21/09/2018	GJ1	4.15	311	10.20	0.71	0.06	0.36	0.82	0.80	0.10	0.71	0.89	617	16	52	606	7	27	603	8	31	2.3
21/09/2018	GJ1	4.15	310	10.15	1.02	0.06	0.37	0.82	1.08	0.10	1.02	0.94	611	16	52	607	10	29	606	12	35	0.9
21/09/2018	GJ1	3.51	279	10.37	0.99	0.06	0.50	0.80	1.11	0.10	0.99	0.89	621	22	52	599	10	34	593	11	40	4.4
21/09/2018	GJ1	3.62	284	10.26	0.82	0.06	0.41	0.81	0.92	0.10	0.82	0.89	623	18	49	605	8	28	600	9	33	3.7
21/09/2018	GJ1	3.62	287	10.28	0.72	0.06	0.44	0.81	0.84	0.10	0.72	0.85	608	20	52	601	8	36	599	8	44	1.6
21/09/2018	GJ1	3.66	292	10.21	0.92	0.06	0.43	0.81	1.02	0.10	0.92	0.90	608	19	48	603	9	20	602	11	21	0.9
21/09/2018	GJ1	3.66	291	10.19	0.82	0.06	0.44	0.81	0.92	0.10	0.82	0.88	592	19	52	601	8	27	603	9	31	-1.9
21/09/2018	GJ1	3.74	299	10.30	0.62	0.06	0.41	0.80	0.74	0.10	0.62	0.83	608	18	55	600	7	39	597	7	46	1.7
21/09/2018	GJ1	3.62	295	10.36	0.83	0.06	0.43	0.80	0.94	0.10	0.83	0.89	607	19	59	597	8	29	594	9	34	2.1
21/09/2018	GJ1	3.69	297	10.30	0.88	0.06	0.43	0.81	0.98	0.10	0.88	0.90	615	19	55	601	9	23	597	10	25	2.9
21/09/2018	GJ1	3.70	295	10.22	0.82	0.06	0.37	0.81	0.90	0.10	0.82	0.91	612	16	49	604	8	31	602	9	36	1.8
21/09/2018	GJ1	3.41	283	10.29	1.34	0.06	0.46	0.81	1.41	0.10	1.34	0.95	611	20	53	601	13	21	598	15	23	2.1
21/09/2018	GJ1	3.46	286	10.24	0.87	0.06	0.44	0.81	0.98	0.10	0.87	0.89	600	20	60	601	9	31	601	10	35	-0.1
21/09/2018	GJ1	3.46	287	10.25	1.18	0.06	0.47	0.81	1.27	0.10	1.18	0.93	598	21	50	600	12	26	600	14	31	-0.4
21/09/2018	GJ1	3.50	292	10.17	1.42	0.06	0.48	0.81	1.50	0.10	1.42	0.95	597	21	60	603	14	28	604	16	32	-1.3
21/09/2018	GJ1	3.47	290	10.16	1.73	0.06	0.55	0.81	1.81	0.10	1.73	0.95	603	24	56	605	17	41	605	20	49	-0.3
21/09/2018	GJ1	3.48	288	10.15	1.57	0.06	0.42	0.82	1.63	0.10	1.57	0.97	609	19	53	606	15	25	606	18	28	0.6
21/09/2018	GJ1	3.53	297	10.20	1.48	0.06	0.44	0.81	1.54	0.10	1.48	0.96	610	20	32	604	14	24	603	17	29	1.2
21/09/2018	GJ1	3.50	297	10.33	1.96	0.06	0.43	0.81	2.01	0.10	1.96	0.98	621	19	36	601	18	50	596	22	65	4.1
21/09/2018	GJ1	3.54	296	10.13	1.47	0.06	0.44	0.81	1.53	0.10	1.47	0.96	594	20	42	604	14	56	607	17	71	-2.2

***Table S4.1 cont.**: PRM GJ1*

Date	sample	^{206}Pb (mV)	U ppm	$^{238}U/^{206}Pb$	1s%	$^{207}Pb/^{206}Pb$	1s%	$^{207}Pb/^{235}U$	1s%	$^{206}Pb/^{238}U$	1s%	Rho	^{207}Pb-^{206}Pb Age	2s abs	2s $_{sys}$ abs	^{207}Pb-^{235}U Age	2s abs	2s $_{sys}$ abs	^{206}Pb-^{238}U Age	2s abs	2s $_{sys}$ abs	Disc %
21/09/2018	GJ1	3.22	276	10.26	0.77	0.06	0.38	0.81	0.86	0.10	0.77	0.90	616	17	36	603	8	26	600	9	32	2.7
21/09/2018	GJ1	3.29	281	10.21	0.92	0.06	0.45	0.82	1.02	0.10	0.92	0.90	627	20	49	607	9	29	602	11	35	3.9
21/09/2018	GJ1	3.26	277	10.09	1.01	0.06	0.41	0.82	1.09	0.10	1.01	0.93	606	18	36	609	10	35	609	12	43	-0.5
21/09/2018	GJ1	3.34	284	10.11	1.47	0.06	0.39	0.82	1.52	0.10	1.47	0.97	608	18	45	608	14	30	608	17	36	0.0
21/09/2018	GJ1	3.34	285	10.10	1.31	0.06	0.41	0.81	1.38	0.10	1.31	0.95	593	18	39	605	13	47	609	15	59	-2.7
21/09/2018	GJ1	3.24	279	10.16	1.63	0.06	0.48	0.82	1.70	0.10	1.63	0.96	618	21	41	608	16	44	605	19	53	2.0
21/09/2018	GJ1	3.23	274	10.04	1.61	0.06	0.43	0.82	1.66	0.10	1.61	0.97	603	19	32	610	15	37	612	19	46	-1.4
21/09/2018	GJ1	3.25	278	10.04	2.21	0.06	0.45	0.83	2.25	0.10	2.21	0.98	612	20	36	612	21	34	612	26	42	-0.1
21/09/2018	GJ1	3.22	276	10.07	1.71	0.06	0.44	0.82	1.77	0.10	1.71	0.97	612	20	20	611	16	34	610	20	43	0.2

Table S4.2 *PRM GJ1*

Sample		Conc[a]		For Tera-Wasserberg plot				For Wetherill Plot					Ages									Conc[b]
Date	sample	^{206}Pb (mV)	U ppm	$^{238}U/^{206}Pb$	1s%	$^{207}Pb/^{206}Pb$	1s%	$^{207}Pb/^{235}U$	1s%	$^{206}Pb/^{238}U$	1s%	Rho	^{207}Pb-^{206}Pb Age	2s abs	2s sys abs	^{207}Pb-^{235}U Age	2s abs	2s sys abs	^{206}Pb-^{238}U Age	2s abs	2s sys abs	Disc%
22/05/2017	GJ1	1.85	na	10.41	2.45	0.06	1.26	0.79	2.75	0.10	2.45	0.89	579	55	55	589	25	25	592	28	28	-2.2
22/05/2017	GJ1	1.95	na	10.40	1.66	0.06	1.08	0.80	1.99	0.10	1.66	0.84	602	47	47	594	18	18	592	19	19	1.6
22/05/2017	GJ1	1.91	na	10.41	1.25	0.06	1.26	0.79	1.78	0.10	1.25	0.70	581	55	55	589	16	16	592	14	14	-1.8
22/05/2017	GJ1	1.96	293	10.31	1.55	0.06	1.28	0.78	2.01	0.10	1.55	0.77	555	56	56	588	18	18	597	18	18	-7.5
22/05/2017	GJ1	2.07	303	10.26	1.28	0.06	1.17	0.80	1.74	0.10	1.28	0.74	593	51	51	598	16	16	600	15	15	-1.1
22/05/2017	GJ1	2.19	214	10.30	2.47	0.06	1.26	0.80	2.77	0.10	2.47	0.89	584	55	55	595	25	25	597	28	28	-2.2
22/05/2017	GJ1	2.09	218	10.31	2.42	0.06	1.19	0.79	2.70	0.10	2.42	0.90	563	52	52	590	24	24	597	28	28	-6.0
22/05/2017	GJ1	2.22	na	10.33	2.48	0.06	1.09	0.79	2.71	0.10	2.48	0.92	583	48	48	593	24	24	596	28	28	-2.2
22/05/2017	GJ1	2.19	na	10.41	1.82	0.06	1.17	0.80	2.16	0.10	1.82	0.84	605	51	51	594	19	19	592	21	21	2.3
22/05/2017	GJ1	2.04	na	10.34	2.22	0.06	1.24	0.80	2.55	0.10	2.22	0.87	613	54	54	599	23	23	595	25	25	3.0
22/05/2017	GJ1	2.10	na	10.37	1.87	0.06	1.25	0.79	2.25	0.10	1.87	0.83	595	55	55	594	20	20	593	21	21	0.4
22/05/2017	GJ1	2.01	na	10.31	1.75	0.06	1.18	0.79	2.12	0.10	1.75	0.83	570	52	52	591	19	19	597	20	20	-4.7
22/05/2017	GJ1	2.23	na	10.36	1.81	0.06	1.10	0.79	2.12	0.10	1.81	0.86	575	48	48	590	19	19	594	21	21	-3.4
22/05/2017	GJ1	1.97	na	10.45	1.88	0.06	1.33	0.79	2.31	0.10	1.88	0.82	603	58	58	592	21	21	589	21	21	2.2
22/05/2017	GJ1	1.89	na	10.43	1.82	0.06	1.14	0.81	2.15	0.10	1.82	0.85	660	49	49	605	20	20	590	21	21	10.5
22/05/2017	GJ1	1.94	na	10.43	1.98	0.06	1.17	0.79	2.30	0.10	1.98	0.86	603	51	51	593	21	21	590	22	22	2.1
22/05/2017	GJ1	2.25	na	10.29	1.70	0.06	1.24	0.81	2.10	0.10	1.70	0.81	612	54	54	601	19	19	598	19	19	2.3
22/05/2017	GJ1	2.31	na	10.24	2.87	0.06	1.17	0.81	3.09	0.10	2.87	0.93	602	51	51	601	28	28	601	33	33	0.2
22/05/2017	GJ1	2.13	279	10.25	3.64	0.06	1.09	0.80	3.80	0.10	3.64	0.96	582	48	48	596	34	34	600	42	42	-3.2
22/05/2017	GJ1	2.11	266	10.37	2.28	0.06	1.21	0.82	2.58	0.10	2.28	0.88	671	52	52	610	24	24	593	26	26	11.6
22/05/2017	GJ1	2.00	400	10.50	2.57	0.06	1.08	0.79	2.79	0.10	2.57	0.92	600	47	47	589	25	25	586	29	29	2.4
22/05/2017	GJ1	2.09	393	10.42	2.60	0.06	1.16	0.80	2.85	0.10	2.60	0.91	613	50	50	596	26	26	591	29	29	3.6
22/05/2017	GJ1	2.22	415	10.33	3.00	0.06	1.17	0.80	3.22	0.10	3.00	0.93	588	51	51	594	29	29	596	34	34	-1.2

Table S4.2 cont. *PRM GJ1*

Date	sample	^{206}Pb (mV)	U ppm	$^{238}U/^{206}Pb$	1s%	$^{207}Pb/^{206}Pb$	1s%	$^{207}Pb/^{235}U$	1s%	$^{206}Pb/^{238}U$	1s%	Rho	^{207}Pb-^{206}Pb Age	2s abs	2s sys abs	^{207}Pb-^{235}U Age	2s abs	2s sys abs	^{206}Pb-^{238}U Age	2s abs	2s sys abs	Disc%
22/05/2017	GJ1	2.17	395	10.30	3.45	0.06	1.17	0.80	3.64	0.10	3.45	0.95	600	51	51	598	33	33	597	39	39	0.4
22/05/2017	GJ1	2.20	291	10.46	2.88	0.06	1.08	0.79	3.07	0.10	2.88	0.94	604	47	47	592	28	28	589	32	32	2.6
22/05/2017	GJ1	2.16	269	10.43	3.81	0.06	1.17	0.79	3.98	0.10	3.81	0.96	603	51	51	593	36	36	590	43	43	2.2
22/05/2017	GJ1	2.17	386	10.44	1.77	0.06	1.07	0.80	2.07	0.10	1.77	0.86	629	46	46	598	19	19	590	20	20	6.3
22/05/2017	GJ1	2.09	390	10.53	2.74	0.06	1.17	0.79	2.98	0.10	2.74	0.92	602	51	51	589	27	27	585	31	31	2.8
22/05/2017	GJ1	2.13	na	10.42	4.06	0.06	1.24	0.80	4.25	0.10	4.06	0.96	624	54	54	598	38	38	591	46	46	5.3
22/05/2017	GJ1	2.24	na	10.44	2.92	0.06	1.34	0.79	3.21	0.10	2.92	0.91	599	58	58	592	29	29	590	33	33	1.5
22/05/2017	GJ1	2.06	299	10.42	2.08	0.06	1.23	0.80	2.42	0.10	2.08	0.86	631	53	53	599	22	22	591	24	24	6.3
22/05/2017	GJ1	2.05	259	10.63	3.19	0.06	1.08	0.78	3.37	0.09	3.19	0.95	604	47	47	585	30	30	580	35	35	4.0
22/05/2017	GJ1	2.09	468	10.63	1.97	0.06	1.19	0.76	2.30	0.09	1.97	0.86	563	52	52	576	20	20	580	22	22	-2.9
22/05/2017	GJ1	2.05	456	10.50	3.10	0.06	1.34	0.78	3.38	0.10	3.10	0.92	588	58	58	587	30	30	586	35	35	0.3
22/05/2017	GJ1	1.95	307	10.44	2.66	0.06	1.10	0.78	2.88	0.10	2.66	0.92	569	48	48	586	26	26	590	30	30	-3.6
22/05/2017	GJ1	2.05	326	10.40	2.81	0.06	1.34	0.79	3.11	0.10	2.81	0.90	584	59	59	591	28	28	592	32	32	-1.3
22/05/2017	GJ1	2.02	388	10.52	4.36	0.06	1.25	0.78	4.54	0.10	4.36	0.96	595	55	55	588	41	41	586	49	49	1.6
22/05/2017	GJ1	2.11	418	10.55	2.43	0.06	1.18	0.78	2.70	0.09	2.43	0.90	580	51	51	583	24	24	584	27	27	-0.6
24/05/2017	GJ1	2.05	306	10.44	2.51	0.06	0.68	0.79	2.60	0.10	2.51	0.96	608	30	30	594	23	23	590	28	28	3.1
24/05/2017	GJ1	1.95	287	9.52	5.24	0.06	0.78	0.87	5.30	0.11	5.24	0.99	613	34	34	637	50	50	644	64	64	-5.0
24/05/2017	GJ1	1.93	284	10.00	6.00	0.06	0.91	0.83	6.07	0.10	6.00	0.99	610	40	40	613	56	56	614	70	70	-0.8
24/05/2017	GJ1	1.88	295	10.19	2.65	0.06	0.76	0.81	2.76	0.10	2.65	0.96	591	33	33	601	25	25	603	31	31	-2.0
24/05/2017	GJ1	1.78	277	10.17	2.95	0.06	1.08	0.81	3.14	0.10	2.95	0.94	606	47	47	605	29	29	604	34	34	0.3
24/05/2017	GJ1	1.69	260	10.10	3.69	0.06	0.78	0.83	3.77	0.10	3.69	0.98	619	34	34	611	35	35	609	43	43	1.8
24/05/2017	GJ1	1.89	306	10.31	3.09	0.06	1.00	0.80	3.25	0.10	3.09	0.95	610	43	43	600	29	29	597	35	35	2.1
24/05/2017	GJ1	1.73	279	10.20	5.10	0.06	0.84	0.80	5.17	0.10	5.10	0.99	587	37	37	599	47	47	603	59	59	-2.6
24/05/2017	GJ1	1.63	264	10.31	4.59	0.06	0.90	0.82	4.67	0.10	4.59	0.98	649	39	39	608	43	43	597	52	52	8.0
24/05/2017	GJ1	1.71	269	10.29	4.01	0.06	0.68	0.80	4.07	0.10	4.01	0.99	594	30	30	597	37	37	598	46	46	-0.7
24/05/2017	GJ1	1.66	267	10.43	3.65	0.06	0.77	0.79	3.73	0.10	3.65	0.98	595	34	34	591	33	33	590	41	41	0.8
24/05/2017	GJ1	1.82	298	10.11	3.64	0.06	0.36	0.82	3.66	0.10	3.64	1.00	614	16	16	609	34	34	608	42	42	1.1
24/05/2017	GJ1	1.80	284	10.00	6.50	0.06	0.82	0.83	6.55	0.10	6.50	0.99	599	36	36	611	60	60	614	76	76	-2.6
24/05/2017	GJ1	1.93	313	10.04	4.22	0.06	0.61	0.83	4.26	0.10	4.22	0.99	610	27	27	612	39	39	612	49	49	-0.4
24/05/2017	GJ1	1.87	301	10.36	4.04	0.06	1.24	0.80	4.23	0.10	4.04	0.96	617	54	54	599	38	38	594	46	46	3.7
24/05/2017	GJ1	1.81	298	10.50	5.20	0.06	0.80	0.80	5.26	0.10	5.20	0.99	627	35	35	595	47	47	586	58	58	6.5
24/05/2017	GJ1	1.85	300	10.10	5.56	0.06	0.83	0.81	5.62	0.10	5.56	0.99	578	36	36	602	51	51	609	65	65	-5.3

Table S4.2 cont. *PRM GJ1*

Date	sample	^{206}Pb (mV)	U ppm	$^{238}U/^{206}Pb$	1s%	$^{207}Pb/^{206}Pb$	1s%	$^{207}Pb/^{235}U$	1s%	$^{206}Pb/^{238}U$	1s%	Rho	^{207}Pb-^{206}Pb Age	2s abs	2s $_{sys}$ abs	^{207}Pb-^{235}U Age	2s abs	2s $_{sys}$ abs	^{206}Pb-^{238}U Age	2s abs	2s $_{sys}$ abs	Disc%
24/05/2017	GJ1	1.81	296	10.49	4.20	0.06	1.00	0.79	4.31	0.10	4.20	0.97	610	43	43	592	39	39	587	47	47	3.8
24/05/2017	GJ1	1.77	291	9.43	5.66	0.06	0.83	0.88	5.72	0.11	5.66	0.99	601	36	36	639	54	54	649	70	70	-8.1
24/05/2017	GJ1	1.81	296	10.53	5.11	0.06	0.90	0.80	5.18	0.10	5.11	0.98	635	39	39	595	47	47	585	57	57	7.8
24/05/2017	GJ1	1.84	291	9.43	6.60	0.06	0.83	0.88	6.66	0.11	6.60	0.99	603	36	36	639	63	63	649	82	82	-7.8

Table S4.3.: *VRM 91500*

Sample		Conc[a]		For Tera-Wasserberg plot				For Wetherill Plot					Ages									Conc[b]
Date	sample	^{206}Pb (mV)	U ppm	$^{238}U/^{206}Pb$	1s%	$^{207}Pb/^{206}Pb$	1s%	$^{207}Pb/^{235}U$	1s%	$^{206}Pb/^{238}U$	1s%	Rho	^{207}Pb-^{206}Pb Age	2s abs	2s $_{sys}$ abs	^{207}Pb-^{235}U Age	2s abs	2s $_{sys}$ abs	^{206}Pb-^{238}U Age	2s abs	2s $_{sys}$ abs	Disc%
18/09/2018	91500	2.34	81	5.56	0.56	0.07	0.46	1.85	0.72	0.18	0.56	0.77	1055	22	22	1062	10	13	1065	11	17	-0.9
18/09/2018	91500	2.36	83	5.58	0.70	0.07	0.41	1.84	0.81	0.18	0.70	0.86	1060	20	20	1061	11	14	1062	14	19	-0.2
18/09/2018	91500	2.35	82	5.58	0.81	0.07	0.46	1.84	0.93	0.18	0.81	0.87	1055	22	22	1060	12	15	1062	16	20	-0.6
18/09/2018	91500	2.30	81	5.56	0.75	0.07	0.51	1.84	0.90	0.18	0.75	0.83	1045	24	24	1059	12	15	1066	15	20	-2.1
18/09/2018	91500	2.43	85	5.50	1.07	0.07	0.44	1.87	1.16	0.18	1.07	0.93	1058	21	21	1071	15	18	1077	21	25	-1.7
18/09/2018	91500	2.26	79	5.52	0.97	0.07	0.41	1.85	1.05	0.18	0.97	0.92	1048	20	20	1064	14	17	1072	19	23	-2.3
18/09/2018	91500	2.00	76	5.55	0.55	0.08	0.47	1.86	0.72	0.18	0.55	0.77	1068	22	22	1068	10	13	1069	11	17	0.0
18/09/2018	91500	1.96	74	5.57	0.47	0.07	0.46	1.85	0.66	0.18	0.47	0.72	1059	22	22	1063	9	13	1065	9	16	-0.5
18/09/2018	91500	1.96	74	5.56	0.47	0.07	0.46	1.85	0.66	0.18	0.47	0.71	1054	22	22	1062	9	13	1066	9	16	-1.1
18/09/2018	91500	2.20	83	5.61	0.45	0.08	0.43	1.84	0.62	0.18	0.45	0.72	1069	21	21	1061	8	13	1057	9	15	1.2
18/09/2018	91500	2.22	83	5.61	0.50	0.08	0.58	1.86	0.77	0.18	0.50	0.65	1083	26	26	1066	10	14	1058	10	16	2.3
18/09/2018	91500	1.98	74	5.54	0.66	0.07	0.46	1.85	0.81	0.18	0.66	0.82	1056	22	22	1065	11	14	1070	13	19	-1.3
18/09/2018	91500	1.78	69	5.56	0.72	0.07	0.64	1.85	0.97	0.18	0.72	0.75	1056	29	29	1062	13	16	1065	14	19	-0.9
18/09/2018	91500	1.71	67	5.63	0.59	0.07	0.47	1.83	0.76	0.18	0.59	0.78	1065	23	23	1058	10	14	1054	12	17	1.0
18/09/2018	91500	1.72	67	5.60	0.62	0.07	0.54	1.83	0.82	0.18	0.62	0.75	1051	25	25	1057	11	14	1060	12	18	-0.8
18/09/2018	91500	1.95	76	5.61	1.07	0.07	0.42	1.82	1.15	0.18	1.07	0.93	1044	21	21	1053	15	18	1057	21	25	-1.2
18/09/2018	91500	2.01	77	5.58	0.59	0.07	0.56	1.85	0.81	0.18	0.59	0.73	1061	25	25	1062	11	14	1063	12	17	-0.2
18/09/2018	91500	2.00	78	5.57	1.00	0.07	0.49	1.85	1.12	0.18	1.00	0.90	1066	23	23	1064	15	17	1064	20	24	0.2
20/09/2018	91500	2.31	91	5.62	1.04	0.07	0.54	1.83	1.17	0.18	1.04	0.89	1059	25	25	1056	15	18	1055	20	24	0.4
20/09/2018	91500	2.36	92	5.62	0.87	0.07	0.53	1.82	1.02	0.18	0.87	0.86	1047	24	24	1052	13	16	1055	17	21	-0.8
20/09/2018	91500	2.37	92	5.59	0.95	0.07	0.47	1.84	1.06	0.18	0.95	0.90	1061	22	22	1061	14	17	1062	19	22	-0.1
20/09/2018	91500	1.87	73	5.59	0.95	0.07	0.52	1.84	1.09	0.18	0.95	0.88	1054	24	24	1058	14	17	1060	19	22	-0.6
20/09/2018	91500	1.97	75	5.49	1.04	0.07	0.59	1.86	1.20	0.18	1.04	0.87	1045	27	27	1067	16	18	1078	21	25	-3.2
20/09/2018	91500	1.98	77	5.58	1.09	0.08	0.50	1.86	1.20	0.18	1.09	0.91	1077	23	23	1067	16	18	1062	21	25	1.4

Table S4.4.: *VRM 91500*

Sample		Conc[a]		For Tera-Wasserberg plot				For Wetherill Plot					Ages									Conc[b]
Date	sample	^{206}Pb (mV)	U ppm	$^{238}U/^{206}Pb$	1s%	$^{207}Pb/^{206}Pb$	1s%	$^{207}Pb/^{235}U$	1s%	$^{206}Pb/^{238}U$	1s%	Rho	^{207}Pb-^{206}Pb Age	2s abs	2s sys abs	^{207}Pb-^{235}U Age	2s abs	2s sys abs	^{206}Pb-^{238}U Age	2s abs	2s sys abs	Disc%
22/05/2017	91500	0.81	na	5.73	2.41	0.07	1.70	1.76	2.95	0.17	2.41	0.82	1024	70	70	1032	38	38	1036	46	46	-1.2
22/05/2017	91500	0.87	173	5.71	2.20	0.07	1.36	1.77	2.59	0.18	2.20	0.85	1024	57	57	1035	34	34	1041	42	42	-1.6
22/05/2017	91500	0.88	82	5.74	2.70	0.07	1.85	1.75	3.27	0.17	2.70	0.83	1016	76	76	1029	42	42	1035	52	52	-1.9
22/05/2017	91500	0.93	78	5.64	2.57	0.07	1.44	1.78	2.94	0.18	2.57	0.87	1013	59	59	1040	38	38	1052	50	50	-3.9
22/05/2017	91500	0.94	84	5.70	1.97	0.07	1.30	1.77	2.36	0.18	1.97	0.84	1021	54	54	1035	31	31	1042	38	38	-2.0
22/05/2017	91500	1.00	95	5.64	2.14	0.07	1.15	1.81	2.43	0.18	2.14	0.88	1041	48	48	1048	32	32	1052	42	42	-1.1
22/05/2017	91500	0.90	63	5.70	2.11	0.07	1.55	1.80	2.62	0.18	2.11	0.81	1049	63	63	1044	34	34	1041	41	41	0.7
22/05/2017	91500	0.93	73	5.65	3.95	0.07	1.62	1.81	4.27	0.18	3.95	0.93	1041	67	67	1047	56	56	1051	77	77	-1.0
22/05/2017	91500	0.99	95	5.69	1.73	0.07	1.42	1.79	2.24	0.18	1.73	0.77	1041	59	59	1043	29	29	1045	33	33	-0.4
22/05/2017	91500	1.01	86	5.75	2.50	0.07	1.55	1.77	2.94	0.17	2.50	0.85	1041	64	64	1036	38	38	1034	48	48	0.6
22/05/2017	91500	1.02	85	5.56	3.61	0.07	1.54	1.85	3.93	0.18	3.61	0.92	1060	63	63	1065	52	52	1067	71	71	-0.7
22/05/2017	91500	1.03	91	5.70	2.45	0.07	1.41	1.80	2.83	0.18	2.45	0.87	1054	58	58	1046	37	37	1042	47	47	1.2
22/05/2017	91500	0.97	103	5.65	2.68	0.08	1.67	1.83	3.16	0.18	2.68	0.85	1068	68	68	1056	42	42	1051	52	52	1.6
22/05/2017	91500	0.96	101	5.69	2.53	0.08	1.39	1.82	2.89	0.18	2.53	0.88	1076	57	57	1054	38	38	1043	49	49	3.0
22/05/2017	91500	1.00	105	5.69	2.79	0.07	1.41	1.81	3.12	0.18	2.79	0.89	1057	58	58	1049	41	41	1045	54	54	1.2
22/05/2017	91500	1.11	103	5.67	2.38	0.08	1.06	1.84	2.60	0.18	2.38	0.91	1087	44	44	1060	34	34	1047	46	46	3.7
22/05/2017	91500	1.06	93	5.68	2.53	0.08	1.39	1.84	2.88	0.18	2.53	0.88	1084	57	57	1058	38	38	1046	49	49	3.5
22/05/2017	91500	0.97	92	5.59	4.19	0.08	1.05	1.89	4.32	0.18	4.19	0.97	1109	43	43	1077	57	57	1062	82	82	4.2
22/05/2017	91500	1.07	97	5.62	3.65	0.08	1.52	1.85	3.96	0.18	3.65	0.92	1084	62	62	1065	52	52	1056	71	71	2.5
22/05/2017	91500	1.08	102	5.56	6.39	0.07	1.34	1.85	6.53	0.18	6.39	0.98	1057	55	55	1064	86	86	1067	126	126	-1.0
22/05/2017	91500	1.17	103	5.46	5.74	0.07	1.22	1.85	5.87	0.18	5.74	0.98	1027	51	51	1065	77	77	1083	114	114	-5.5
22/05/2017	91500	1.09	115	5.65	4.52	0.08	1.37	1.86	4.72	0.18	4.52	0.96	1105	56	56	1068	62	62	1051	88	88	4.9
22/05/2017	91500	1.15	124	5.78	4.91	0.07	1.27	1.79	5.07	0.17	4.91	0.97	1065	52	52	1040	66	66	1029	93	93	3.4
22/05/2017	91500	1.11	215	5.59	4.75	0.07	1.15	1.82	4.89	0.18	4.75	0.97	1038	48	48	1054	64	64	1062	93	93	-2.3
22/05/2017	91500	1.17	174	5.59	3.63	0.08	1.33	1.86	3.87	0.18	3.63	0.94	1073	55	55	1065	51	51	1062	71	71	1.1
22/05/2017	91500	1.19	143	5.71	3.14	0.08	1.39	1.82	3.44	0.18	3.14	0.91	1076	57	57	1051	45	45	1040	60	60	3.3
22/05/2017	91500	1.13	132	5.68	3.13	0.07	1.28	1.80	3.38	0.18	3.13	0.93	1046	53	53	1045	44	44	1045	60	60	0.1
22/05/2017	91500	1.15	104	5.75	3.74	0.07	1.69	1.77	4.10	0.17	3.74	0.91	1038	69	69	1035	53	53	1034	71	71	0.4
22/05/2017	91500	1.17	107	5.66	2.69	0.08	1.32	1.85	2.99	0.18	2.69	0.90	1092	54	54	1063	39	39	1049	52	52	3.9
24/05/2017	91500	1.07	87	5.41	4.86	0.07	1.07	1.90	4.98	0.19	4.86	0.98	1060	45	45	1083	66	66	1094	98	98	-3.3

Table S4.4 cont.: *VRM 91500*

24/05/2017	91500	1.03	85	5.62	6.18	0.08	1.32	1.85	6.32	0.18	6.18	0.98	1084	54	54	1065	83	83	1056	120	120	2.5
24/05/2017	91500	1.07	87	5.41	5.68	0.08	0.93	1.91	5.75	0.19	5.68	0.99	1070	39	39	1086	77	77	1094	114	114	-2.2
24/05/2017	91500	0.98	84	5.65	3.11	0.08	0.99	1.84	3.26	0.18	3.11	0.95	1078	42	42	1060	43	43	1051	60	60	2.6
24/05/2017	91500	1.02	86	5.46	3.01	0.08	0.92	1.91	3.14	0.18	3.01	0.96	1092	39	39	1086	42	42	1083	60	60	0.8
24/05/2017	91500	0.98	84	5.70	2.48	0.08	1.12	1.83	2.72	0.18	2.48	0.91	1089	47	47	1057	36	36	1041	48	48	4.4
24/05/2017	91500	0.92	81	5.65	3.95	0.08	0.93	1.84	4.06	0.18	3.95	0.97	1081	39	39	1060	53	53	1051	77	77	2.8
24/05/2017	91500	0.94	81	5.35	4.28	0.07	0.87	1.92	4.37	0.19	4.28	0.98	1057	37	37	1089	58	58	1105	87	87	-4.6
24/05/2017	91500	0.94	81	5.32	3.99	0.07	0.87	1.94	4.08	0.19	3.99	0.98	1065	37	37	1095	55	55	1111	81	81	-4.3
24/05/2017	91500	0.87	79	5.75	6.90	0.07	0.95	1.76	6.96	0.17	6.90	0.99	1021	41	41	1030	90	90	1034	132	132	-1.2
24/05/2017	91500	0.99	84	5.18	4.92	0.07	1.01	1.97	5.03	0.19	4.92	0.98	1043	42	42	1106	68	68	1138	103	103	-9.0
24/05/2017	91500	0.98	84	5.32	5.32	0.08	0.98	1.98	5.41	0.19	5.32	0.98	1105	41	41	1109	73	73	1111	109	109	-0.5
24/05/2017	91500	0.91	79	5.29	6.88	0.07	1.14	1.94	6.97	0.19	6.88	0.99	1049	48	48	1093	93	93	1116	141	141	-6.4
24/05/2017	91500	1.00	86	5.38	5.38	0.07	0.95	1.90	5.46	0.19	5.38	0.98	1041	40	40	1080	73	73	1100	109	109	-5.7
24/05/2017	91500	0.98	87	5.75	4.60	0.07	0.95	1.77	4.69	0.17	4.60	0.98	1038	40	40	1035	61	61	1034	88	88	0.4
24/05/2017	91500	0.95	86	5.71	4.57	0.08	0.92	1.83	4.66	0.18	4.57	0.98	1086	39	39	1055	61	61	1040	88	88	4.3
24/05/2017	91500	1.08	90	5.26	6.05	0.08	1.04	2.01	6.14	0.19	6.05	0.99	1113	43	43	1118	83	83	1121	125	125	-0.8
24/05/2017	91500	1.02	90	5.52	4.97	0.07	0.87	1.86	5.05	0.18	4.97	0.98	1054	37	37	1066	67	67	1072	98	98	-1.7

***Table S4.5.**: VRM Plesovice*

Sample		Conc[a]		For Tera-Wasserberg plot				For Wetherill Plot					Ages									Conc[b]
Date	sample	^{206}Pb (mV)	U ppm	^{238}U/^{206}Pb	1s%	^{207}Pb/^{206}Pb	1s%	^{207}Pb/^{235}U	1s%	^{206}Pb/^{238}U	1s%	Rho	^{207}Pb-^{206}Pb Age	2s abs	2s $_{sys}$ abs	^{207}Pb-^{235}U Age	2s abs	2s $_{sys}$ abs	^{206}Pb-^{238}U Age	2s abs	2s $_{sys}$ abs	Disc %
12/10/2017	Ples	4.33	966	18.59	2.14	0.05	0.37	0.40	2.17	0.05	2.14	0.99	352	17	22	340	13	13	338	14	13	4.0
12/10/2017	Ples	4.37	986	18.48	2.40	0.05	0.40	0.40	2.43	0.05	2.40	0.99	343	19	22	340	14	15	340	16	15	0.9
12/10/2017	Ples	4.37	985	18.52	1.94	0.05	0.38	0.40	1.99	0.05	1.94	0.98	347	18	22	340	11	12	339	13	12	2.4
12/10/2017	Ples	4.48	961	18.35	1.74	0.05	0.41	0.41	1.79	0.05	1.74	0.97	374	19	23	346	11	12	342	12	12	8.6
12/10/2017	Ples	4.57	987	18.52	1.76	0.05	0.34	0.40	1.80	0.05	1.76	0.98	357	16	21	341	10	11	339	12	11	5.0
12/10/2017	Ples	4.53	984	18.66	1.59	0.05	0.35	0.40	1.62	0.05	1.59	0.98	368	16	21	341	9	10	337	10	10	8.4
13/10/2017	Ples	5.85	711	18.63	0.46	0.05	0.46	0.40	0.65	0.05	0.46	0.71	345	21	25	338	4	6	337	3	6	2.4
13/10/2017	Ples	5.76	667	18.53	0.58	0.05	0.45	0.40	0.74	0.05	0.58	0.79	352	21	24	341	4	6	339	4	6	3.8
13/10/2017	Ples	5.68	631	18.49	0.48	0.05	0.41	0.40	0.63	0.05	0.48	0.76	337	19	23	339	4	6	340	3	6	-0.8
13/10/2017	Ples	2.49	249	18.27	0.74	0.05	0.66	0.40	0.99	0.05	0.74	0.75	338	30	33	343	6	7	343	5	7	-1.5
13/10/2017	Ples	3.69	375	18.20	0.86	0.05	0.56	0.41	1.03	0.05	0.86	0.84	368	25	28	348	6	7	345	6	7	6.2
13/10/2017	Ples	4.10	428	18.18	1.00	0.05	0.48	0.40	1.11	0.06	1.00	0.90	334	22	26	344	6	8	345	7	8	-3.4
13/10/2017	Ples	4.91	578	18.47	0.54	0.05	0.51	0.40	0.74	0.05	0.54	0.73	344	23	27	340	4	6	340	4	6	1.2
13/10/2017	Ples	4.78	532	18.24	0.55	0.05	0.57	0.40	0.79	0.05	0.55	0.69	324	26	29	341	5	6	344	4	6	-6.2
13/10/2017	Ples	4.98	537	18.45	0.56	0.05	0.47	0.40	0.73	0.05	0.56	0.77	345	22	25	341	4	6	340	4	6	1.3
13/10/2017	Ples	4.07	407	18.16	0.86	0.05	0.51	0.41	1.00	0.06	0.86	0.86	345	24	27	345	6	7	346	6	7	-0.1
13/10/2017	Ples	4.30	443	18.39	0.80	0.05	0.48	0.40	0.93	0.05	0.80	0.86	329	22	26	340	5	7	341	5	7	-3.7
13/10/2017	Ples	4.36	452	18.09	0.87	0.05	0.50	0.40	1.00	0.06	0.87	0.87	328	23	27	344	6	7	347	6	7	-5.8
13/10/2017	Ples	6.80	898	18.68	0.48	0.05	0.40	0.40	0.62	0.05	0.48	0.76	351	19	23	338	4	5	336	3	5	4.3
13/10/2017	Ples	6.54	856	18.59	0.35	0.05	0.40	0.40	0.54	0.05	0.35	0.66	341	19	23	338	3	5	338	2	5	1.0
13/10/2017	Ples	6.06	790	18.58	0.63	0.05	0.49	0.40	0.80	0.05	0.63	0.79	341	23	26	338	5	6	338	4	6	0.8
13/10/2017	Ples	6.94	930	18.51	0.79	0.05	0.42	0.40	0.89	0.05	0.79	0.88	346	20	23	340	5	7	339	5	7	1.9
13/10/2017	Ples	6.97	941	18.58	0.86	0.05	0.42	0.40	0.96	0.05	0.86	0.90	364	19	23	341	6	7	338	6	7	7.1
13/10/2017	Ples	6.89	938	18.61	0.86	0.05	0.41	0.40	0.95	0.05	0.86	0.90	360	19	23	340	6	7	337	6	7	6.3
13/10/2017	Ples	3.88	547	18.48	0.51	0.05	0.39	0.40	0.64	0.05	0.51	0.80	329	18	22	338	4	6	340	3	6	-3.1
13/10/2017	Ples	3.75	527	18.46	0.48	0.05	0.43	0.40	0.65	0.05	0.48	0.74	333	20	24	339	4	6	340	3	6	-2.1
13/10/2017	Ples	3.89	552	18.45	0.47	0.05	0.34	0.40	0.58	0.05	0.47	0.81	328	16	21	339	3	5	340	3	5	-3.7
13/10/2017	Ples	4.15	574	18.90	0.51	0.05	0.43	0.39	0.67	0.05	0.51	0.77	357	20	24	335	4	6	332	3	6	6.9
13/10/2017	Ples	3.88	525	18.63	0.49	0.05	0.39	0.39	0.63	0.05	0.49	0.79	335	18	22	337	4	5	337	3	5	-0.6

Table S4.5. cont.: *VRM Plesovice*

Date	sample	^{206}Pb (mV)	U ppm	^{238}U/^{206}Pb	1s%	^{207}Pb/^{206}Pb	1s%	^{207}Pb/^{235}U	1s%	^{206}Pb/^{238}U	1s%	Rho	^{207}Pb-^{206}Pb Age	2s abs	2s $_{sys}$ abs	^{207}Pb-^{235}U Age	2s abs	2s $_{sys}$ abs	^{206}Pb-^{238}U Age	2s abs	2s $_{sys}$ abs	Disc %
13/10/2017	Ples	5.41	538	18.49	0.48	0.05	0.45	0.40	0.66	0.05	0.48	0.73	342	21	25	340	4	6	340	3	6	0.7
13/10/2017	Ples	7.74	771	18.49	0.42	0.05	0.40	0.40	0.58	0.05	0.42	0.72	344	19	22	340	3	5	340	3	5	1.4
13/10/2017	Ples	8.72	867	18.45	0.50	0.05	0.42	0.40	0.65	0.05	0.50	0.76	348	20	23	341	4	6	340	3	6	2.3
13/10/2017	Ples	6.62	648	18.27	0.40	0.05	0.46	0.40	0.61	0.05	0.40	0.66	343	21	25	343	4	6	343	3	6	-0.2
13/10/2017	Ples	9.01	885	18.40	0.45	0.05	0.40	0.40	0.61	0.05	0.45	0.75	347	19	22	342	4	5	341	3	5	1.7
16/10/2017	Ples	6.07	887	18.57	0.80	0.05	0.27	0.40	0.84	0.05	0.80	0.95	354	13	18	340	5	7	338	5	7	4.4
16/10/2017	Ples	6.10	887	18.49	0.85	0.05	0.30	0.40	0.90	0.05	0.85	0.94	334	14	19	339	5	7	339	6	7	-1.6
16/10/2017	Ples	6.22	901	18.45	0.76	0.05	0.35	0.40	0.83	0.05	0.76	0.91	367	16	21	344	5	7	340	5	7	7.3
16/10/2017	Ples	6.19	909	18.70	0.93	0.05	0.24	0.39	0.97	0.05	0.93	0.97	352	12	17	338	6	7	336	6	7	4.6
16/10/2017	Ples	6.19	897	18.50	1.02	0.05	0.36	0.40	1.08	0.05	1.02	0.94	347	17	21	340	6	7	339	7	7	2.3
16/10/2017	Ples	6.23	911	18.52	0.93	0.05	0.34	0.40	0.99	0.05	0.93	0.94	343	16	20	339	6	7	339	6	7	1.1
16/10/2017	Ples	5.56	844	18.52	0.72	0.05	0.26	0.40	0.77	0.05	0.72	0.94	334	13	18	338	4	6	339	5	6	-1.4
16/10/2017	Ples	5.62	848	18.45	0.78	0.05	0.27	0.40	0.83	0.05	0.78	0.94	340	13	18	340	5	7	340	5	7	-0.2
16/10/2017	Ples	5.74	868	18.44	0.75	0.05	0.24	0.40	0.79	0.05	0.75	0.95	342	12	17	341	5	6	341	5	6	0.4
16/10/2017	Ples	5.38	829	18.78	0.94	0.05	0.33	0.39	0.99	0.05	0.94	0.94	356	15	20	337	6	7	335	6	7	6.0
16/10/2017	Ples	5.41	827	18.48	0.90	0.05	0.37	0.40	0.97	0.05	0.90	0.93	340	17	21	340	6	7	340	6	7	0.0
16/10/2017	Ples	5.43	837	18.60	1.02	0.05	0.36	0.39	1.08	0.05	1.02	0.94	320	17	21	335	6	7	338	7	7	-5.5
16/10/2017	Ples	4.82	775	18.59	1.02	0.05	0.37	0.40	1.09	0.05	1.02	0.94	346	17	21	339	6	7	338	7	7	2.3
16/10/2017	Ples	4.79	764	18.57	0.88	0.05	0.40	0.39	0.97	0.05	0.88	0.91	332	18	23	337	6	7	338	6	7	-1.8
16/10/2017	Ples	4.99	795	18.50	0.77	0.05	0.35	0.40	0.84	0.05	0.77	0.91	352	16	21	341	5	7	339	5	7	3.7
16/10/2017	Ples	4.89	798	18.83	1.13	0.05	0.38	0.39	1.19	0.05	1.13	0.95	341	18	22	335	7	8	334	7	8	2.3
16/10/2017	Ples	4.88	791	18.70	0.87	0.05	0.35	0.39	0.94	0.05	0.87	0.93	329	16	21	335	5	7	336	6	7	-2.1
16/10/2017	Ples	4.93	793	18.55	0.87	0.05	0.26	0.40	0.91	0.05	0.87	0.96	352	13	18	340	5	7	338	6	7	4.0
16/10/2017	Ples	4.68	801	18.89	0.93	0.05	0.29	0.39	0.98	0.05	0.93	0.95	340	14	19	333	6	7	333	6	7	2.1
16/10/2017	Ples	4.77	812	18.64	0.93	0.05	0.34	0.39	0.99	0.05	0.93	0.94	340	16	20	337	6	7	337	6	7	0.9
16/10/2017	Ples	4.75	812	18.70	0.79	0.05	0.44	0.39	0.91	0.05	0.79	0.87	321	21	25	334	5	7	336	5	7	-4.7
16/10/2017	Ples	5.02	854	18.44	0.90	0.05	0.37	0.40	0.98	0.05	0.90	0.93	339	17	21	340	6	7	340	6	7	-0.3
16/10/2017	Ples	4.99	842	18.46	0.92	0.05	0.27	0.40	0.96	0.05	0.92	0.96	352	13	18	342	6	7	340	6	7	3.3
16/10/2017	Ples	4.80	802	18.34	0.86	0.05	0.50	0.41	1.00	0.05	0.86	0.87	378	23	26	347	6	7	342	6	7	9.5
16/10/2017	Ples	4.77	855	18.48	0.92	0.05	0.35	0.40	0.99	0.05	0.92	0.94	348	16	21	341	6	7	340	6	7	2.4
16/10/2017	Ples	4.89	868	18.33	0.86	0.05	0.35	0.40	0.93	0.05	0.86	0.93	324	16	21	340	5	7	342	6	7	-5.7
16/10/2017	Ples	4.98	881	18.25	0.80	0.05	0.34	0.40	0.87	0.05	0.80	0.92	325	16	21	341	5	7	344	5	7	-5.7

Table S4.5. cont.: *VRM Plesovice*

Date	sample	^{206}Pb (mV)	U ppm	^{238}U/^{206}Pb	1s%	^{207}Pb/^{206}Pb	1s%	^{207}Pb/^{235}U	1s%	^{206}Pb/^{238}U	1s%	Rho	^{207}Pb-^{206}Pb Age	2s abs	2s $_{sys}$ abs	^{207}Pb-^{235}U Age	2s abs	2s $_{sys}$ abs	^{206}Pb-^{238}U Age	2s abs	2s $_{sys}$ abs	Disc %
16/10/2017	Ples	4.73	849	18.50	0.85	0.05	0.32	0.40	0.91	0.05	0.85	0.94	349	15	20	340	5	7	339	6	7	2.7
16/10/2017	Ples	4.84	869	18.37	0.77	0.05	0.30	0.40	0.83	0.05	0.77	0.93	329	14	19	340	5	7	342	5	7	-3.7
17/10/2017	Ples	7.34	816	18.53	0.52	0.05	0.37	0.40	0.64	0.05	0.52	0.81	350	17	22	340	4	6	339	3	6	3.3
17/10/2017	Ples	7.31	810	18.44	0.38	0.05	0.37	0.40	0.53	0.05	0.38	0.72	333	17	21	340	3	5	340	3	5	-2.1
17/10/2017	Ples	7.38	823	18.52	0.57	0.05	0.39	0.40	0.70	0.05	0.57	0.82	338	18	23	339	4	6	339	4	6	-0.4
17/10/2017	Ples	7.29	831	18.59	0.66	0.05	0.39	0.39	0.77	0.05	0.66	0.86	339	18	23	338	4	6	338	4	6	0.5
17/10/2017	Ples	7.40	841	18.62	0.63	0.05	0.37	0.39	0.73	0.05	0.63	0.87	342	17	21	338	4	6	337	4	6	1.3
17/10/2017	Ples	7.45	845	18.54	0.54	0.05	0.41	0.40	0.68	0.05	0.54	0.79	338	19	23	339	4	6	339	4	6	-0.3
17/10/2017	Ples	6.80	858	18.54	0.70	0.05	0.40	0.40	0.81	0.05	0.70	0.87	364	19	23	342	5	7	339	5	7	7.0
17/10/2017	Ples	7.05	895	18.61	0.55	0.05	0.38	0.40	0.67	0.05	0.55	0.82	365	18	22	341	4	6	337	4	6	7.5
17/10/2017	Ples	7.02	894	18.58	0.48	0.05	0.37	0.40	0.61	0.05	0.48	0.79	344	18	22	339	4	5	338	3	5	1.8
17/10/2017	Ples	7.12	896	18.67	0.57	0.05	0.37	0.39	0.68	0.05	0.57	0.84	340	17	21	337	4	6	336	4	6	1.1
17/10/2017	Ples	7.16	896	18.63	0.62	0.05	0.37	0.39	0.72	0.05	0.62	0.86	342	17	21	338	4	6	337	4	6	1.4
17/10/2017	Ples	7.22	912	18.73	0.58	0.05	0.36	0.39	0.68	0.05	0.58	0.85	341	17	21	336	4	6	335	4	6	1.8
17/10/2017	Ples	7.24	898	18.61	0.56	0.05	0.37	0.40	0.67	0.05	0.56	0.84	346	17	21	338	4	6	337	4	6	2.4
17/10/2017	Ples	7.30	910	18.59	0.93	0.05	0.37	0.40	1.00	0.05	0.93	0.93	348	17	22	339	6	7	338	6	7	2.9
17/10/2017	Ples	7.34	906	18.54	0.77	0.05	0.42	0.40	0.88	0.05	0.77	0.88	347	20	23	340	5	7	339	5	7	2.4
17/10/2017	Ples	7.37	931	18.52	0.92	0.05	0.35	0.40	0.98	0.05	0.92	0.94	351	16	21	341	6	7	339	6	7	3.3
17/10/2017	Ples	7.36	929	18.41	0.80	0.05	0.36	0.40	0.88	0.05	0.80	0.91	343	17	21	341	5	7	341	5	7	0.5
17/10/2017	Ples	7.29	930	18.58	0.76	0.05	0.37	0.40	0.85	0.05	0.76	0.90	357	17	21	340	5	7	338	5	7	5.4
17/10/2017	Ples	6.03	824	18.92	0.80	0.05	0.40	0.39	0.90	0.05	0.80	0.90	334	18	23	332	5	7	332	5	7	0.7
17/10/2017	Ples	7.00	958	18.71	0.76	0.05	0.41	0.39	0.86	0.05	0.76	0.88	338	19	23	336	5	7	336	5	7	0.8
17/10/2017	Ples	7.44	1014	18.73	0.68	0.05	0.41	0.39	0.80	0.05	0.68	0.86	340	19	23	336	5	6	335	4	6	1.4
17/10/2017	Ples	3.61	484	18.80	1.41	0.05	0.50	0.39	1.50	0.05	1.41	0.94	332	23	26	334	9	10	334	9	10	-0.6
17/10/2017	Ples	3.65	483	18.69	1.03	0.05	0.48	0.39	1.13	0.05	1.03	0.91	339	22	26	336	7	8	336	7	8	0.9
17/10/2017	Ples	3.80	499	18.69	1.21	0.05	0.52	0.39	1.32	0.05	1.21	0.92	332	24	27	335	8	9	336	8	9	-1.2
17/10/2017	Ples	3.57	467	18.80	0.43	0.05	0.52	0.39	0.68	0.05	0.43	0.64	343	24	27	335	4	6	334	3	6	2.6
17/10/2017	Ples	3.59	469	18.73	1.22	0.05	0.52	0.39	1.33	0.05	1.22	0.92	345	24	27	337	8	9	335	8	9	2.9
17/10/2017	Ples	3.44	448	18.66	1.12	0.05	0.51	0.39	1.23	0.05	1.12	0.91	347	23	27	338	7	8	337	7	8	3.1
18/10/2017	Ples	6.39	682	18.80	2.07	0.05	0.35	0.39	2.10	0.05	2.07	0.99	338	16	21	335	12	12	334	13	12	1.1
18/10/2017	Ples	7.48	802	18.73	2.53	0.05	0.34	0.39	2.55	0.05	2.53	0.99	327	16	21	334	15	15	335	17	15	-2.4
18/10/2017	Ples	8.44	907	18.94	1.99	0.05	0.34	0.39	2.02	0.05	1.99	0.99	337	16	20	332	11	12	332	13	12	1.6

Table S4.5. cont.: *VRM Plesovice*

Date	sample	^{206}Pb (mV)	U ppm	^{238}U/^{206}Pb	1s%	^{207}Pb/^{206}Pb	1s%	^{207}Pb/^{235}U	1s%	^{206}Pb/^{238}U	1s%	Rho	^{207}Pb-^{206}Pb Age	2s abs	2s $_{sys}$ abs	^{207}Pb-^{235}U Age	2s abs	2s $_{sys}$ abs	^{206}Pb-^{238}U Age	2s abs	2s $_{sys}$ abs	Disc %
18/10/2017	Ples	4.43	466	18.76	1.88	0.05	0.38	0.39	1.91	0.05	1.88	0.98	357	18	22	338	11	12	335	12	12	6.2
18/10/2017	Ples	4.50	472	18.73	1.59	0.05	0.48	0.39	1.66	0.05	1.59	0.96	334	22	26	335	10	10	335	10	10	-0.4
18/10/2017	Ples	4.52	476	18.83	1.98	0.05	0.38	0.39	2.01	0.05	1.98	0.98	324	18	22	332	11	12	334	13	12	-3.0
18/10/2017	Ples	4.43	461	18.44	0.58	0.05	0.36	0.40	0.68	0.05	0.58	0.85	347	17	21	341	4	6	340	4	6	1.8
18/10/2017	Ples	4.67	482	18.40	0.79	0.05	0.43	0.40	0.90	0.05	0.79	0.88	337	20	24	341	5	7	341	5	7	-1.3
18/10/2017	Ples	4.29	443	18.58	0.59	0.05	0.43	0.40	0.73	0.05	0.59	0.81	347	20	24	339	4	6	338	4	6	2.6
18/10/2017	Ples	4.47	460	18.46	0.57	0.05	0.44	0.40	0.72	0.05	0.57	0.79	343	20	24	340	4	6	340	4	6	0.8
18/10/2017	Ples	4.53	469	18.44	0.68	0.05	0.42	0.40	0.80	0.05	0.68	0.85	340	20	23	340	5	7	340	5	7	-0.2
18/10/2017	Ples	4.54	468	18.44	0.55	0.05	0.33	0.40	0.64	0.05	0.55	0.86	331	16	20	339	4	6	340	4	6	-2.9
18/10/2017	Ples	4.63	471	18.59	1.12	0.05	0.37	0.39	1.17	0.05	1.12	0.95	318	17	22	335	7	8	338	7	8	-6.3
18/10/2017	Ples	5.17	523	18.45	1.48	0.05	0.37	0.40	1.52	0.05	1.48	0.97	333	17	21	339	9	9	340	10	9	-2.1
18/10/2017	Ples	5.81	588	18.66	1.40	0.05	0.38	0.39	1.45	0.05	1.40	0.97	340	18	22	337	8	9	337	9	9	0.9
18/10/2017	Ples	8.99	954	18.80	1.03	0.05	0.37	0.39	1.10	0.05	1.03	0.94	348	17	22	336	6	7	334	7	7	4.0
18/10/2017	Ples	8.95	944	18.80	1.22	0.05	0.37	0.39	1.28	0.05	1.22	0.96	346	18	22	336	7	8	334	8	8	3.3
18/10/2017	Ples	9.03	962	18.73	1.12	0.05	0.32	0.40	1.17	0.05	1.12	0.96	365	15	20	339	7	8	335	7	8	8.2
18/10/2017	Ples	4.28	752	18.29	0.86	0.05	0.45	0.40	0.97	0.05	0.86	0.89	333	21	24	342	6	7	343	6	7	-3.1
18/10/2017	Ples	4.28	748	18.25	1.00	0.05	0.36	0.40	1.06	0.05	1.00	0.94	346	17	21	344	6	7	344	7	7	0.6
18/10/2017	Ples	4.28	780	18.42	0.70	0.05	0.39	0.40	0.80	0.05	0.70	0.87	340	18	23	341	5	7	341	5	7	-0.2
18/10/2017	Ples	4.28	775	18.20	0.90	0.05	0.44	0.40	1.00	0.05	0.90	0.90	347	20	24	345	6	7	345	6	7	0.6
18/10/2017	Ples	2.45	437	18.35	0.61	0.05	0.51	0.40	0.79	0.05	0.61	0.77	343	23	27	342	5	7	342	4	7	0.3
18/10/2017	Ples	2.44	443	18.63	0.92	0.05	0.60	0.39	1.10	0.05	0.92	0.84	328	28	30	336	6	7	337	6	7	-2.9
18/10/2017	Ples	2.51	457	18.48	0.90	0.05	0.47	0.40	1.01	0.05	0.90	0.88	363	22	25	343	6	7	340	6	7	6.5
18/10/2017	Ples	2.47	455	18.49	0.78	0.05	0.42	0.39	0.88	0.05	0.78	0.88	317	19	23	337	5	7	340	5	7	-7.3
18/09/2018	Ples	6.74	782	18.52	0.66	0.05	0.29	0.40	0.72	0.05	0.66	0.92	348	14	19	340	4	6	339	4	6	2.6
18/09/2018	Ples	6.76	779	18.41	0.74	0.05	0.35	0.40	0.81	0.05	0.74	0.91	352	16	21	342	5	7	341	5	7	3.0
18/09/2018	Ples	6.77	777	18.29	0.59	0.05	0.32	0.40	0.68	0.05	0.59	0.88	335	15	20	342	4	6	343	4	6	-2.4
18/09/2018	Ples	6.72	792	18.71	0.52	0.05	0.35	0.39	0.63	0.05	0.52	0.83	355	17	21	338	4	6	336	3	6	5.3
18/09/2018	Ples	6.78	791	18.42	0.66	0.05	0.29	0.40	0.72	0.05	0.66	0.92	340	14	19	341	4	6	341	4	6	-0.2
18/09/2018	Ples	6.71	779	18.42	0.72	0.05	0.35	0.40	0.80	0.05	0.72	0.90	345	16	21	341	5	7	341	5	7	1.2
18/09/2018	Ples	6.63	829	18.36	0.33	0.05	0.30	0.40	0.45	0.05	0.33	0.74	341	14	19	342	3	5	342	2	5	-0.4
18/09/2018	Ples	6.81	845	18.20	0.33	0.05	0.28	0.40	0.43	0.05	0.33	0.76	339	14	19	344	3	5	345	2	5	-1.6
18/09/2018	Ples	6.96	870	18.36	0.33	0.05	0.36	0.40	0.49	0.05	0.33	0.68	337	17	21	341	3	5	342	2	5	-1.4

Table S4.5. cont.: *VRM Plesovice*

Date	sample	^{206}Pb (mV)	U ppm	^{238}U/^{206}Pb	1s%	^{207}Pb/^{206}Pb	1s%	^{207}Pb/^{235}U	1s%	^{206}Pb/^{238}U	1s%	Rho	^{207}Pb-^{206}Pb Age	2s abs	2s $_{sys}$ abs	^{207}Pb-^{235}U Age	2s abs	2s $_{sys}$ abs	^{206}Pb-^{238}U Age	2s abs	2s $_{sys}$ abs	Disc %
18/09/2018	Ples	6.82	844	18.42	0.36	0.05	0.28	0.40	0.46	0.05	0.36	0.79	343	13	19	341	3	5	341	2	5	0.7
18/09/2018	Ples	6.43	790	18.29	0.34	0.05	0.36	0.40	0.49	0.05	0.34	0.69	331	17	21	341	3	5	343	2	5	-3.7
18/09/2018	Ples	6.56	804	18.30	0.36	0.05	0.37	0.40	0.52	0.05	0.36	0.69	349	17	22	344	3	5	343	2	5	1.7
18/09/2018	Ples	6.38	828	18.59	0.49	0.05	0.26	0.40	0.56	0.05	0.49	0.88	360	13	18	341	3	5	338	3	5	6.1
18/09/2018	Ples	6.34	820	18.58	0.62	0.05	0.43	0.40	0.76	0.05	0.62	0.82	340	20	24	338	4	6	338	4	6	0.5
18/09/2018	Ples	6.13	797	18.62	0.55	0.05	0.32	0.39	0.64	0.05	0.55	0.86	335	15	20	337	4	6	337	4	6	-0.5
18/09/2018	Ples	5.33	675	18.47	0.50	0.05	0.34	0.40	0.60	0.05	0.50	0.83	344	16	20	341	4	5	340	3	5	1.3
18/09/2018	Ples	5.49	691	18.27	0.41	0.05	0.43	0.40	0.60	0.05	0.41	0.69	337	20	24	343	4	5	344	3	5	-1.9
18/09/2018	Ples	5.44	685	18.32	0.48	0.05	0.40	0.40	0.62	0.05	0.48	0.77	333	18	23	341	4	6	343	3	6	-2.9
18/09/2018	Ples	2.96	394	18.63	0.52	0.05	0.43	0.39	0.68	0.05	0.52	0.77	339	20	24	337	4	6	337	3	6	0.6
18/09/2018	Ples	3.55	469	18.45	0.62	0.05	0.43	0.40	0.75	0.05	0.62	0.82	345	20	24	341	4	6	340	4	6	1.3
18/09/2018	Ples	5.27	696	18.42	0.48	0.05	0.37	0.40	0.61	0.05	0.48	0.79	343	18	22	341	4	5	341	3	5	0.6
18/09/2018	Ples	5.49	718	18.20	0.50	0.05	0.35	0.40	0.61	0.05	0.50	0.82	341	16	21	344	4	6	345	3	6	-1.0
18/09/2018	Ples	5.97	783	18.24	0.61	0.05	0.33	0.40	0.69	0.05	0.61	0.88	338	16	20	343	4	6	344	4	6	-1.7
18/09/2018	Ples	3.65	473	18.07	0.45	0.05	0.40	0.40	0.60	0.06	0.45	0.75	325	19	22	344	4	6	347	3	6	-6.8
20/09/2018	Ples	3.87	504	18.83	1.32	0.05	0.54	0.39	1.43	0.05	1.32	0.92	338	25	28	334	8	9	334	9	9	1.2
20/09/2018	Ples	3.97	509	18.69	1.03	0.05	0.47	0.39	1.13	0.05	1.03	0.91	335	22	25	336	6	7	336	7	7	-0.3
20/09/2018	Ples	4.39	561	18.52	1.39	0.05	0.49	0.39	1.47	0.05	1.39	0.94	329	23	26	338	8	9	339	9	9	-3.0
20/09/2018	Ples	3.77	502	19.01	1.33	0.05	0.51	0.39	1.42	0.05	1.33	0.93	337	23	27	331	8	9	330	9	9	2.0
20/09/2018	Ples	4.00	535	19.08	1.62	0.05	0.50	0.38	1.70	0.05	1.62	0.96	341	23	26	331	10	10	329	10	10	3.4
20/09/2018	Ples	4.26	570	19.08	1.62	0.05	0.50	0.38	1.70	0.05	1.62	0.96	330	23	27	329	10	10	329	10	10	0.2
20/09/2018	Ples	2.28	568	18.56	1.11	0.05	0.59	0.40	1.26	0.05	1.11	0.88	347	27	30	339	7	8	338	7	8	2.5
20/09/2018	Ples	2.64	650	18.48	1.20	0.05	0.52	0.40	1.31	0.05	1.20	0.92	347	24	27	341	8	9	340	8	9	2.2
20/09/2018	Ples	1.71	421	18.67	0.90	0.05	0.67	0.39	1.12	0.05	0.90	0.80	342	30	33	337	6	7	336	6	7	1.7
20/09/2018	Ples	2.50	624	18.64	0.90	0.05	0.55	0.40	1.06	0.05	0.90	0.85	357	25	28	339	6	7	337	6	7	5.6
20/09/2018	Ples	2.69	665	18.42	1.11	0.05	0.48	0.40	1.21	0.05	1.11	0.92	361	22	26	343	7	8	341	7	8	5.7
20/09/2018	Ples	2.40	602	18.73	0.86	0.05	0.71	0.39	1.12	0.05	0.86	0.77	341	33	35	336	6	7	335	6	7	1.7
20/09/2018	Ples	2.41	624	18.69	1.21	0.05	0.52	0.40	1.32	0.05	1.21	0.92	354	24	27	338	8	9	336	8	9	5.1
20/09/2018	Ples	1.40	361	18.71	1.12	0.05	0.66	0.39	1.30	0.05	1.12	0.86	321	30	33	334	7	9	336	7	9	-4.5
20/09/2018	Ples	1.45	372	18.66	1.21	0.05	0.68	0.39	1.39	0.05	1.21	0.87	330	31	34	336	8	9	337	8	9	-1.9
20/09/2018	Ples	1.25	321	18.73	1.22	0.05	1.03	0.39	1.59	0.05	1.22	0.76	349	47	49	337	9	10	335	8	10	3.9
20/09/2018	Ples	1.25	323	18.95	0.93	0.05	0.75	0.39	1.20	0.05	0.93	0.78	357	34	37	335	7	8	332	6	8	7.3

Table S4.5. cont.: *VRM Plesovice*

Date	sample	^{206}Pb (mV)	U ppm	^{238}U/^{206}Pb	1s%	^{207}Pb/^{206}Pb	1s%	^{207}Pb/^{235}U	1s%	^{206}Pb/^{238}U	1s%	Rho	^{207}Pb-^{206}Pb Age	2s abs	2s $_{sys}$ abs	^{207}Pb-^{235}U Age	2s abs	2s $_{sys}$ abs	^{206}Pb-^{238}U Age	2s abs	2s $_{sys}$ abs	Disc %
20/09/2018	Ples	1.56	399	18.86	0.91	0.05	0.61	0.39	1.10	0.05	0.91	0.83	363	28	31	337	6	7	333	6	7	8.3
20/09/2018	Ples	1.64	403	18.89	0.84	0.05	0.67	0.39	1.07	0.05	0.84	0.78	338	31	33	333	6	7	333	5	7	1.7
20/09/2018	Ples	1.66	408	18.92	0.88	0.05	0.62	0.39	1.08	0.05	0.88	0.82	328	29	31	332	6	7	332	6	7	-1.3
21/09/2018	Ples	3.48	459	18.66	2.05	0.05	0.45	0.40	2.10	0.05	2.05	0.98	353	21	24	339	12	13	337	13	13	4.6
21/09/2018	Ples	3.36	437	18.38	2.30	0.05	0.42	0.40	2.34	0.05	2.30	0.98	319	19	23	339	13	14	341	15	14	-7.0
21/09/2018	Ples	3.45	448	18.38	2.11	0.05	0.48	0.40	2.17	0.05	2.11	0.98	326	22	26	339	13	13	341	14	13	-4.9
21/09/2018	Ples	3.38	457	18.69	1.50	0.05	0.54	0.39	1.59	0.05	1.50	0.94	338	25	28	336	9	10	336	10	10	0.6
21/09/2018	Ples	3.32	446	18.52	1.39	0.05	0.43	0.40	1.45	0.05	1.39	0.96	349	20	24	340	8	9	339	9	9	3.0
21/09/2018	Ples	3.37	451	18.52	1.57	0.05	0.46	0.40	1.64	0.05	1.57	0.96	345	21	25	340	9	10	339	10	10	1.7
21/09/2018	Ples	3.22	437	18.52	1.11	0.05	0.46	0.40	1.20	0.05	1.11	0.92	349	21	25	340	7	8	339	7	8	2.8
21/09/2018	Ples	3.31	449	18.48	1.94	0.05	0.45	0.40	1.99	0.05	1.94	0.97	328	21	24	338	11	12	340	13	12	-3.5
21/09/2018	Ples	3.55	480	18.42	1.38	0.05	0.46	0.40	1.46	0.05	1.38	0.95	351	21	24	342	8	9	341	9	9	2.9
21/09/2018	Ples	2.91	411	18.26	0.80	0.05	0.45	0.40	0.92	0.05	0.80	0.87	340	21	25	343	5	7	344	5	7	-1.0
21/09/2018	Ples	2.93	411	18.25	1.09	0.05	0.44	0.40	1.18	0.05	1.09	0.93	349	20	24	345	7	8	344	7	8	1.5
21/09/2018	Ples	2.96	418	18.39	0.86	0.05	0.44	0.40	0.96	0.05	0.86	0.89	353	20	24	343	6	7	341	6	7	3.3
21/09/2018	Ples	3.13	443	18.12	1.09	0.05	0.43	0.40	1.17	0.06	1.09	0.93	336	20	24	345	7	8	346	7	8	-3.0
21/09/2018	Ples	3.07	437	18.25	1.28	0.05	0.50	0.40	1.37	0.05	1.28	0.93	333	23	26	343	8	9	344	9	9	-3.2
21/09/2018	Ples	3.11	440	18.18	1.18	0.05	0.45	0.40	1.27	0.06	1.18	0.93	332	21	24	343	7	9	345	8	9	-4.1
21/09/2018	Ples	3.20	480	18.59	1.21	0.05	0.48	0.39	1.30	0.05	1.21	0.93	339	22	26	338	7	9	338	8	9	0.3
21/09/2018	Ples	3.18	481	18.69	1.03	0.05	0.51	0.39	1.15	0.05	1.03	0.89	314	24	27	333	7	8	336	7	8	-7.1
21/09/2018	Ples	3.19	477	18.37	0.87	0.05	0.47	0.40	0.99	0.05	0.87	0.88	341	22	25	342	6	7	342	6	7	-0.1
21/09/2018	Ples	3.19	487	18.52	1.30	0.05	0.42	0.40	1.36	0.05	1.30	0.95	346	20	23	340	8	9	339	9	9	1.9
21/09/2018	Ples	3.20	486	18.48	1.66	0.05	0.46	0.40	1.73	0.05	1.66	0.96	348	21	25	341	10	11	340	11	11	2.5
21/09/2018	Ples	3.27	495	18.42	1.75	0.05	0.48	0.40	1.81	0.05	1.75	0.96	338	22	26	341	11	12	341	12	12	-0.8
21/09/2018	Ples	3.23	501	18.59	0.71	0.05	0.51	0.40	0.87	0.05	0.71	0.81	347	23	27	339	5	7	338	5	7	2.6
21/09/2018	Ples	3.26	504	18.59	0.93	0.05	0.43	0.39	1.02	0.05	0.93	0.91	339	20	24	338	6	7	338	6	7	0.3
21/09/2018	Ples	3.26	505	18.62	1.12	0.05	0.44	0.39	1.20	0.05	1.12	0.93	333	21	24	337	7	8	337	7	8	-1.2
21/09/2018	Ples	3.28	516	18.50	0.67	0.05	0.39	0.39	0.77	0.05	0.67	0.86	324	18	22	337	4	6	339	4	6	-4.7
21/09/2018	Ples	3.32	524	18.67	0.75	0.05	0.36	0.40	0.83	0.05	0.75	0.90	352	17	21	338	5	7	336	5	7	4.4
21/09/2018	Ples	3.23	507	18.63	0.74	0.05	0.40	0.39	0.84	0.05	0.74	0.88	341	19	23	338	5	7	337	5	7	1.0

Table S4.6.: *VRM Plesovice*

Sample		Conc[a]		For Tera-Wasserberg plot				For Wetherill Plot					Ages									Conc[b]
Date	sample	^{206}Pb (mV)	U ppm	^{238}U/^{206}Pb	1s%	^{207}Pb/^{206}Pb	1s%	^{207}Pb/^{235}U	1s%	^{206}Pb/^{238}U	1s%	Rho	^{207}Pb-^{206}Pb Age	2s abs	2s $_{sys}$ abs	^{207}Pb-^{235}U Age	2s abs	2s $_{sys}$ abs	^{206}Pb-^{238}U Age	2s abs	2s $_{sys}$ abs	Disc %
22/05/2017	Ples	2.05	795	18.90	1.80	0.05	1.24	0.39	2.14	0.05	1.80	0.82	295	57	57	328	12	12	332	12	12	-12.5
22/05/2017	Ples	1.33	672	18.25	2.10	0.05	1.33	0.41	2.44	0.05	2.10	0.84	315	61	61	340	14	14	344	14	14	-9.2
22/05/2017	Ples	2.19	823	18.35	1.56	0.05	1.13	0.41	1.88	0.05	1.56	0.81	328	52	52	340	11	11	342	10	10	-4.4
22/05/2017	Ples	2.28	749	18.48	1.48	0.05	1.34	0.40	1.96	0.05	1.48	0.74	297	61	61	334	11	11	340	10	10	-14.3
22/05/2017	Ples	2.33	756	18.38	2.02	0.05	1.22	0.41	2.32	0.05	2.02	0.86	331	56	56	340	14	14	341	13	13	-3.1
22/05/2017	Ples	2.42	757	18.48	1.76	0.05	1.32	0.41	2.15	0.05	1.76	0.80	336	60	60	339	13	13	340	12	12	-1.0
22/05/2017	Ples	1.94	817	18.62	2.23	0.05	1.13	0.40	2.45	0.05	2.23	0.89	334	51	51	337	14	14	337	15	15	-1.0
22/05/2017	Ples	1.23	676	18.66	2.05	0.05	1.51	0.40	2.49	0.05	2.05	0.81	332	68	68	336	15	15	337	13	13	-1.4
22/05/2017	Ples	1.90	857	18.52	2.78	0.05	1.37	0.41	3.05	0.05	2.78	0.90	403	61	61	347	18	18	339	18	18	15.9
22/05/2017	Ples	2.32	734	18.55	1.76	0.05	1.23	0.40	2.10	0.05	1.76	0.82	328	56	56	337	12	12	338	12	12	-3.1
22/05/2017	Ples	2.12	811	18.80	2.16	0.05	1.12	0.40	2.38	0.05	2.16	0.89	355	51	51	337	14	14	334	14	14	5.8
22/05/2017	Ples	1.22	738	18.66	2.61	0.05	1.30	0.41	2.85	0.05	2.61	0.90	362	59	59	340	17	17	337	17	17	6.9
22/05/2017	Ples	2.18	760	18.83	1.32	0.05	1.13	0.40	1.70	0.05	1.32	0.76	335	51	51	334	10	10	334	9	9	0.6
22/05/2017	Ples	2.13	749	18.90	1.51	0.05	1.04	0.40	1.79	0.05	1.51	0.82	331	47	47	332	10	10	332	10	10	-0.5
22/05/2017	Ples	2.20	759	18.80	1.88	0.05	1.13	0.40	2.15	0.05	1.88	0.86	332	51	51	334	12	12	334	12	12	-0.8
22/05/2017	Ples	2.78	752	18.76	2.06	0.05	1.22	0.40	2.33	0.05	2.06	0.86	343	55	55	336	14	14	335	13	13	2.3
22/05/2017	Ples	2.98	757	18.73	2.34	0.05	1.11	0.41	2.53	0.05	2.34	0.90	368	50	50	339	15	15	335	15	15	8.8
22/05/2017	Ples	2.64	752	19.01	2.38	0.05	1.21	0.40	2.60	0.05	2.38	0.89	366	55	55	335	15	15	330	15	15	9.8
22/05/2017	Ples	2.85	758	18.87	1.98	0.05	1.12	0.40	2.22	0.05	1.98	0.87	346	51	51	335	13	13	333	13	13	3.8
22/05/2017	Ples	2.84	746	18.59	2.88	0.05	1.11	0.42	2.97	0.05	2.88	0.93	368	50	50	342	18	18	338	19	19	8.3
22/05/2017	Ples	3.07	763	18.15	3.72	0.05	1.13	0.41	3.79	0.06	3.72	0.96	338	51	51	345	23	23	346	25	25	-2.2
22/05/2017	Ples	2.08	753	17.89	3.22	0.05	1.19	0.43	3.35	0.06	3.22	0.94	389	54	54	356	21	21	351	22	22	9.9
22/05/2017	Ples	1.98	758	18.15	4.08	0.05	1.21	0.42	4.14	0.06	4.08	0.96	366	55	55	348	25	25	346	27	27	5.6
22/05/2017	Ples	1.94	743	18.42	5.25	0.05	1.24	0.40	5.25	0.05	5.25	0.97	308	57	57	337	31	31	341	35	35	-10.8
22/05/2017	Ples	2.47	769	18.45	3.78	0.05	1.14	0.40	3.85	0.05	3.78	0.96	303	52	52	336	23	23	340	25	25	-12.4
22/05/2017	Ples	2.01	753	18.73	3.37	0.05	1.12	0.41	3.42	0.05	3.37	0.95	351	51	51	337	20	20	335	22	22	4.4
22/05/2017	Ples	2.11	757	18.18	3.00	0.05	1.52	0.41	3.28	0.06	3.00	0.89	311	69	69	341	19	19	345	20	20	-11.1
22/05/2017	Ples	2.40	759	18.62	4.93	0.05	1.14	0.40	4.91	0.05	4.93	0.97	308	52	52	334	29	29	337	32	32	-9.5
22/05/2017	Ples	2.28	751	18.66	4.48	0.05	1.34	0.39	4.56	0.05	4.48	0.96	293	61	61	331	26	26	337	29	29	-14.8
24/05/2017	Ples	2.01	533	17.61	5.99	0.05	0.80	0.42	6.04	0.06	5.99	0.99	360	36	36	357	36	36	356	41	41	1.1
24/05/2017	Ples	1.84	496	17.45	8.12	0.05	0.76	0.42	8.15	0.06	8.12	1.00	323	35	35	354	49	49	359	57	57	-11.0

Table S4.6. cont.: *VRM Plesovice*

24/05/2017	Ples	1.88	505	18.35	6.33	0.05	0.85	0.41	6.39	0.05	6.33	0.99	374	39	39	346	37	37	342	42	42	8.5
24/05/2017	Ples	2.30	640	18.52	4.81	0.05	0.82	0.40	4.88	0.05	4.81	0.99	335	37	37	338	28	28	339	32	32	-1.3
24/05/2017	Ples	2.49	681	18.02	3.33	0.05	0.77	0.41	3.42	0.06	3.33	0.97	355	35	35	349	20	20	348	23	23	1.8
24/05/2017	Ples	2.64	741	18.18	3.18	0.05	0.75	0.41	3.27	0.06	3.18	0.97	356	34	34	347	19	19	345	21	21	3.1
24/05/2017	Ples	2.66	765	17.24	8.62	0.05	0.77	0.43	8.66	0.06	8.62	1.00	355	35	35	362	53	53	363	61	61	-2.5
24/05/2017	Ples	2.67	736	17.04	5.96	0.05	0.76	0.43	6.01	0.06	5.96	0.99	355	35	35	366	37	37	368	43	43	-3.7
24/05/2017	Ples	2.46	716	18.59	6.60	0.05	0.66	0.40	6.63	0.05	6.60	0.99	348	30	30	339	38	38	338	43	43	3.0
24/05/2017	Ples	1.88	551	18.08	7.96	0.05	0.84	0.40	8.00	0.06	7.96	0.99	316	39	39	343	47	47	347	54	54	-9.9
24/05/2017	Ples	2.10	593	18.48	4.99	0.05	0.56	0.40	5.02	0.05	4.99	0.99	334	26	26	339	29	29	340	33	33	-1.8
24/05/2017	Ples	2.09	598	17.04	6.90	0.05	0.91	0.43	6.96	0.06	6.90	0.99	355	42	42	366	43	43	368	49	49	-3.6
24/05/2017	Ples	2.36	669	17.39	7.04	0.05	0.77	0.42	7.09	0.06	7.04	0.99	327	35	35	356	43	43	360	49	49	-10.1
24/05/2017	Ples	1.74	502	17.67	5.92	0.05	1.04	0.41	6.01	0.06	5.92	0.98	328	47	47	351	36	36	355	41	41	-8.3
24/05/2017	Ples	2.64	759	17.61	7.22	0.05	0.70	0.42	7.25	0.06	7.22	1.00	353	32	32	356	44	44	356	50	50	-0.8
24/05/2017	Ples	2.55	724	17.42	7.23	0.05	0.83	0.42	7.28	0.06	7.23	0.99	338	38	38	357	44	44	360	51	51	-6.3
24/05/2017	Ples	2.98	877	17.76	5.77	0.05	0.49	0.41	5.79	0.06	5.77	1.00	312	23	23	348	34	34	353	40	40	-13.1
24/05/2017	Ples	3.00	842	16.92	6.43	0.05	0.70	0.43	6.47	0.06	6.43	0.99	326	32	32	364	40	40	370	46	46	-13.4
22/05/2017	Ples	2.05	795	18.90	1.80	0.05	1.24	0.39	2.14	0.05	1.80	0.82	295	57	57	328	12	12	332	12	12	-12.5
22/05/2017	Ples	1.33	672	18.25	2.10	0.05	1.33	0.41	2.44	0.05	2.10	0.84	315	61	61	340	14	14	344	14	14	-9.2
22/05/2017	Ples	2.19	823	18.35	1.56	0.05	1.13	0.41	1.88	0.05	1.56	0.81	328	52	52	340	11	11	342	10	10	-4.4
22/05/2017	Ples	2.28	749	18.48	1.48	0.05	1.34	0.40	1.96	0.05	1.48	0.74	297	61	61	334	11	11	340	10	10	-14.3
22/05/2017	Ples	2.33	756	18.38	2.02	0.05	1.22	0.41	2.32	0.05	2.02	0.86	331	56	56	340	14	14	341	13	13	-3.1
22/05/2017	Ples	2.42	757	18.48	1.76	0.05	1.32	0.41	2.15	0.05	1.76	0.80	336	60	60	339	13	13	340	12	12	-1.0
22/05/2017	Ples	1.94	817	18.62	2.23	0.05	1.13	0.40	2.45	0.05	2.23	0.89	334	51	51	337	14	14	337	15	15	-1.0
22/05/2017	Ples	1.23	676	18.66	2.05	0.05	1.51	0.40	2.49	0.05	2.05	0.81	332	68	68	336	15	15	337	13	13	-1.4
22/05/2017	Ples	1.90	857	18.52	2.78	0.05	1.37	0.41	3.05	0.05	2.78	0.90	403	61	61	347	18	18	339	18	18	15.9
22/05/2017	Ples	2.32	734	18.55	1.76	0.05	1.23	0.40	2.10	0.05	1.76	0.82	328	56	56	337	12	12	338	12	12	-3.1
22/05/2017	Ples	2.12	811	18.80	2.16	0.05	1.12	0.40	2.38	0.05	2.16	0.89	355	51	51	337	14	14	334	14	14	5.8
22/05/2017	Ples	1.22	738	18.66	2.61	0.05	1.30	0.41	2.85	0.05	2.61	0.90	362	59	59	340	17	17	337	17	17	6.9
22/05/2017	Ples	2.18	760	18.83	1.32	0.05	1.13	0.40	1.70	0.05	1.32	0.76	335	51	51	334	10	10	334	9	9	0.6
22/05/2017	Ples	2.13	749	18.90	1.51	0.05	1.04	0.40	1.79	0.05	1.51	0.82	331	47	47	332	10	10	332	10	10	-0.5
22/05/2017	Ples	2.20	759	18.80	1.88	0.05	1.13	0.40	2.15	0.05	1.88	0.86	332	51	51	334	12	12	334	12	12	-0.8

Table S4.7.: *VRM OG1*

Sample		Conc[a]		For Tera-Wasserberg plot				For Wetherill Plot					Ages									Conc[b]
Date	sample	^{206}Pb (mV)	U ppm	^{238}U/^{206}Pb	1s%	^{207}Pb/^{206}Pb	1s%	^{207}Pb/^{235}U	1s%	^{206}Pb/^{238}U	1s%	Rho	^{207}Pb-^{206}Pb Age	2s abs	2s $_{sys}$ abs	^{207}Pb-^{235}U Age	2s abs	2s $_{sys}$ abs	^{206}Pb-^{238}U Age	2s abs	2s $_{sys}$ abs	Disc %
16/10/2017	OG1	14.41	158	1.39	0.84	0.30	0.11	29.74	0.84	0.72	0.84	0.99	3471	9	10	3478	17	22	3490	45	57	-0.5
16/10/2017	OG1	14.53	158	1.38	0.97	0.30	0.10	29.99	0.97	0.72	0.97	0.99	3472	8	10	3487	20	24	3511	52	63	-1.1
16/10/2017	OG1	6.91	75	1.38	0.90	0.30	0.16	30.00	0.91	0.73	0.90	0.99	3471	9	10	3487	19	23	3515	49	60	-1.3
16/10/2017	OG1	15.15	167	1.39	1.05	0.30	0.10	29.73	1.05	0.72	1.05	1.00	3474	8	10	3478	21	25	3485	56	66	-0.3
16/10/2017	OG1	17.20	188	1.38	1.04	0.30	0.10	30.04	1.04	0.72	1.04	1.00	3477	8	10	3488	21	25	3507	56	66	-0.9
16/10/2017	OG1	13.08	143	1.38	0.90	0.30	0.13	29.97	0.91	0.72	0.90	0.99	3472	9	10	3486	18	23	3510	49	60	-1.1
16/10/2017	OG1	7.97	90	1.38	0.69	0.30	0.11	29.95	0.70	0.73	0.69	0.99	3464	8	10	3485	14	20	3522	38	52	-1.7
16/10/2017	OG1	11.20	127	1.38	0.76	0.30	0.11	29.73	0.77	0.72	0.76	0.99	3459	8	10	3478	16	21	3511	41	54	-1.5
16/10/2017	OG1	9.56	108	1.38	0.69	0.30	0.13	29.70	0.70	0.72	0.69	0.98	3457	9	10	3477	15	20	3513	38	52	-1.6
16/10/2017	OG1	7.20	80	1.35	1.08	0.30	0.15	30.64	1.09	0.74	1.08	0.99	3465	9	10	3508	22	26	3582	59	69	-3.4
16/10/2017	OG1	11.82	133	1.36	0.88	0.31	0.13	31.26	0.89	0.73	0.88	0.99	3514	9	10	3527	18	23	3550	48	60	-1.0
16/10/2017	OG1	17.10	194	1.37	0.96	0.30	0.10	30.18	0.97	0.73	0.96	0.99	3472	8	10	3493	20	24	3530	52	63	-1.7
16/10/2017	OG1	16.14	194	1.39	0.97	0.30	0.11	29.63	0.98	0.72	0.97	0.99	3467	9	10	3475	20	24	3489	53	63	-0.6
16/10/2017	OG1	14.77	175	1.38	0.96	0.30	0.10	29.96	0.97	0.73	0.96	0.99	3466	8	10	3485	20	24	3518	52	63	-1.5
16/10/2017	OG1	16.67	199	1.39	0.97	0.30	0.11	29.80	0.98	0.72	0.97	0.99	3469	8	10	3480	20	24	3500	53	63	-0.9
16/10/2017	OG1	15.15	183	1.39	1.04	0.30	0.13	29.74	1.05	0.72	1.04	0.99	3468	9	10	3478	21	25	3496	56	66	-0.8
16/10/2017	OG1	16.47	200	1.40	0.98	0.30	0.12	29.66	0.99	0.72	0.98	0.99	3472	9	10	3476	20	24	3481	53	63	-0.3
16/10/2017	OG1	15.26	183	1.38	0.83	0.30	0.10	29.87	0.84	0.72	0.83	0.99	3467	8	10	3482	17	22	3509	45	57	-1.2
16/10/2017	OG1	12.69	162	1.40	0.91	0.30	0.13	29.45	0.92	0.71	0.91	0.99	3468	9	10	3469	19	23	3470	49	60	-0.1
16/10/2017	OG1	10.67	136	1.39	0.84	0.30	0.13	29.57	0.85	0.72	0.84	0.99	3464	9	10	3473	17	22	3488	45	57	-0.7
16/10/2017	OG1	11.11	141	1.39	0.83	0.30	0.11	29.69	0.84	0.72	0.83	0.99	3464	8	10	3477	17	22	3499	45	57	-1.0
16/10/2017	OG1	10.08	128	1.37	0.89	0.30	0.14	30.14	0.90	0.73	0.89	0.99	3467	9	10	3491	18	23	3533	49	60	-1.9
16/10/2017	OG1	10.00	126	1.37	0.82	0.30	0.11	30.22	0.83	0.73	0.82	0.99	3468	9	10	3494	17	21	3539	45	57	-2.1
16/10/2017	OG1	10.30	129	1.35	0.94	0.30	0.12	30.68	0.95	0.74	0.94	0.99	3468	9	10	3509	19	23	3582	52	63	-3.3
16/10/2017	OG1	10.35	138	1.38	0.90	0.30	0.13	29.84	0.90	0.73	0.90	0.99	3461	9	10	3482	18	23	3518	49	60	-1.6
16/10/2017	OG1	9.55	126	1.37	0.82	0.30	0.11	29.94	0.83	0.73	0.82	0.99	3459	9	10	3485	17	22	3530	45	57	-2.1
16/10/2017	OG1	10.63	141	1.37	0.82	0.30	0.12	30.10	0.83	0.73	0.82	0.99	3464	9	10	3490	17	22	3536	45	57	-2.1
16/10/2017	OG1	9.57	128	1.38	0.83	0.30	0.11	29.91	0.83	0.73	0.83	0.99	3466	9	10	3484	17	22	3516	45	57	-1.4
16/10/2017	OG1	10.46	140	1.38	0.96	0.30	0.10	29.97	0.97	0.73	0.96	0.99	3465	8	10	3486	20	24	3522	52	63	-1.7
16/10/2017	OG1	11.15	150	1.37	0.89	0.30	0.13	29.95	0.90	0.73	0.89	0.99	3463	9	10	3485	18	23	3524	49	60	-1.8
17/10/2017	OG1	22.90	198	1.42	0.47	0.30	0.30	29.15	0.56	0.70	0.47	0.84	3473	12	13	3458	12	18	3434	25	43	1.1

Table S4.7. cont.: *VRM OG1*

Date	sample	^{206}Pb (mV)	U ppm	^{238}U/^{206}Pb	1s%	^{207}Pb/^{206}Pb	1s%	^{207}Pb/^{235}U	1s%	^{206}Pb/^{238}U	1s%	Rho	^{207}Pb-^{206}Pb Age	2s abs	2s $_{sys}$ abs	^{207}Pb-^{235}U Age	2s abs	2s $_{sys}$ abs	^{206}Pb-^{238}U Age	2s abs	2s $_{sys}$ abs	Disc %
17/10/2017	OG1	13.66	115	1.39	0.41	0.30	0.30	29.73	0.51	0.72	0.41	0.81	3467	12	13	3478	11	17	3496	22	42	-0.8
17/10/2017	OG1	16.08	138	1.42	0.40	0.30	0.28	29.13	0.49	0.71	0.40	0.81	3468	12	13	3458	11	17	3440	21	41	0.8
17/10/2017	OG1	12.17	103	1.40	0.47	0.30	0.28	29.35	0.55	0.71	0.47	0.85	3461	12	13	3465	12	18	3473	25	43	-0.3
17/10/2017	OG1	13.14	112	1.38	0.46	0.30	0.28	29.82	0.54	0.72	0.46	0.85	3466	12	13	3481	12	18	3507	25	43	-1.2
17/10/2017	OG1	13.57	115	1.39	0.46	0.30	0.28	29.73	0.54	0.72	0.46	0.85	3467	12	13	3478	12	18	3496	25	43	-0.8
17/10/2017	OG1	11.96	102	1.39	0.48	0.30	0.28	29.73	0.56	0.72	0.48	0.86	3467	12	13	3478	12	18	3498	26	44	-0.9
17/10/2017	OG1	14.62	139	1.39	0.44	0.30	0.28	29.72	0.52	0.72	0.44	0.84	3467	12	13	3478	11	17	3497	24	42	-0.9
17/10/2017	OG1	19.27	186	1.41	0.54	0.30	0.27	29.26	0.60	0.71	0.54	0.90	3471	11	12	3462	13	18	3447	29	45	0.7
17/10/2017	OG1	20.87	199	1.40	0.46	0.30	0.28	29.52	0.54	0.71	0.46	0.85	3471	12	13	3471	12	18	3471	25	43	0.0
17/10/2017	OG1	20.01	189	1.40	0.47	0.30	0.28	29.61	0.55	0.71	0.47	0.86	3472	12	13	3474	12	18	3477	25	43	-0.1
17/10/2017	OG1	20.34	192	1.40	0.64	0.30	0.28	29.56	0.70	0.71	0.64	0.91	3472	12	13	3472	14	20	3473	34	49	0.0
17/10/2017	OG1	19.56	184	1.40	0.47	0.30	0.28	29.65	0.55	0.72	0.47	0.86	3471	12	13	3475	12	18	3483	25	43	-0.3
17/10/2017	OG1	26.14	249	1.42	0.38	0.30	0.28	29.09	0.48	0.70	0.38	0.81	3473	12	13	3457	10	17	3428	21	40	1.3
17/10/2017	OG1	24.56	234	1.42	0.78	0.30	0.27	29.22	0.83	0.70	0.78	0.95	3476	11	12	3461	17	21	3436	42	54	1.1
17/10/2017	OG1	25.37	243	1.43	0.70	0.30	0.28	28.96	0.75	0.70	0.70	0.93	3476	12	13	3452	15	20	3412	37	51	1.8
17/10/2017	OG1	23.48	226	1.42	0.65	0.30	0.27	29.32	0.70	0.71	0.65	0.93	3476	11	12	3464	15	20	3444	35	49	0.9
17/10/2017	OG1	20.73	200	1.41	0.77	0.30	0.27	29.41	0.82	0.71	0.77	0.95	3473	11	12	3467	17	21	3458	42	54	0.4
17/10/2017	OG1	21.70	211	1.42	0.71	0.30	0.27	29.18	0.76	0.70	0.71	0.94	3473	11	12	3459	16	20	3436	38	51	1.1
17/10/2017	OG1	20.78	214	1.41	0.49	0.30	0.27	29.32	0.56	0.71	0.49	0.88	3473	11	12	3464	12	18	3449	27	44	0.7
17/10/2017	OG1	21.08	217	1.42	0.48	0.30	0.28	29.18	0.55	0.70	0.48	0.86	3475	12	13	3460	12	18	3433	26	43	1.2
17/10/2017	OG1	19.05	196	1.42	0.55	0.30	0.27	29.15	0.61	0.70	0.55	0.90	3472	11	12	3459	13	18	3436	30	46	1.0
17/10/2017	OG1	20.63	206	1.42	1.07	0.30	0.28	29.19	1.10	0.70	1.07	0.97	3474	12	13	3460	22	26	3436	57	67	1.1
17/10/2017	OG1	20.13	201	1.42	1.14	0.30	0.28	29.21	1.17	0.70	1.14	0.97	3475	12	13	3461	23	27	3436	61	70	1.1
17/10/2017	OG1	20.37	205	1.42	1.13	0.30	0.28	29.31	1.17	0.71	1.13	0.97	3478	12	13	3464	23	27	3440	61	70	1.1
17/10/2017	OG1	19.33	191	1.41	1.13	0.30	0.28	29.37	1.17	0.71	1.13	0.97	3477	12	13	3466	23	27	3447	61	70	0.9
17/10/2017	OG1	19.30	189	1.41	1.06	0.30	0.28	29.33	1.10	0.71	1.06	0.97	3475	12	13	3465	22	26	3447	57	66	0.8
17/10/2017	OG1	18.53	181	1.40	1.12	0.30	0.27	29.69	1.15	0.72	1.12	0.97	3476	11	12	3476	23	27	3477	60	70	0.0
18/10/2017	OG1	18.32	151	1.44	0.67	0.30	0.23	28.68	0.71	0.69	0.67	0.94	3472	11	12	3443	15	20	3392	36	50	2.3
18/10/2017	OG1	19.61	160	1.43	0.78	0.30	0.22	29.02	0.81	0.70	0.78	0.96	3470	10	11	3454	17	21	3427	42	54	1.2
18/10/2017	OG1	20.03	162	1.41	0.78	0.30	0.23	29.27	0.81	0.71	0.78	0.96	3472	11	12	3463	17	21	3447	42	54	0.7
18/10/2017	OG1	19.86	160	1.42	0.70	0.30	0.23	29.14	0.74	0.70	0.70	0.95	3470	11	12	3458	15	20	3437	38	51	1.0
18/10/2017	OG1	16.24	130	1.40	0.77	0.30	0.22	29.45	0.80	0.71	0.77	0.96	3469	10	11	3468	16	21	3467	42	54	0.0

Table S4.7. cont.: *VRM OG1*

Date	sample	^{206}Pb (mV)	U ppm	^{238}U/^{206}Pb	1s%	^{207}Pb/^{206}Pb	1s%	^{207}Pb/^{235}U	1s%	^{206}Pb/^{238}U	1s%	Rho	^{207}Pb-^{206}Pb Age	2s abs	2s $_{sys}$ abs	^{207}Pb-^{235}U Age	2s abs	2s $_{sys}$ abs	^{206}Pb-^{238}U Age	2s abs	2s $_{sys}$ abs	Disc %
18/10/2017	OG1	14.36	114	1.40	0.42	0.30	0.22	29.65	0.47	0.72	0.42	0.89	3472	10	11	3475	10	17	3481	23	42	-0.2
18/10/2017	OG1	13.79	109	1.39	0.44	0.30	0.22	29.82	0.49	0.72	0.44	0.90	3469	10	11	3481	11	17	3502	24	43	-0.9
18/10/2017	OG1	17.07	135	1.41	0.41	0.30	0.22	29.43	0.46	0.71	0.41	0.88	3474	10	11	3468	10	17	3458	22	41	0.5
18/10/2017	OG1	19.74	156	1.41	0.39	0.30	0.22	29.48	0.45	0.71	0.39	0.88	3478	10	11	3469	10	17	3454	21	41	0.7
18/10/2017	OG1	19.03	150	1.42	0.44	0.30	0.22	29.30	0.49	0.71	0.44	0.90	3475	10	11	3463	11	17	3444	24	42	0.9
18/10/2017	OG1	14.23	111	1.40	0.50	0.30	0.23	29.65	0.55	0.72	0.50	0.91	3471	11	12	3475	12	18	3483	27	44	-0.4
18/10/2017	OG1	16.43	129	1.43	1.07	0.30	0.22	28.88	1.10	0.70	1.07	0.98	3471	10	11	3450	22	26	3413	57	67	1.7
18/10/2017	OG1	23.85	186	1.43	0.86	0.30	0.22	29.03	0.89	0.70	0.86	0.97	3476	10	11	3454	18	22	3417	46	57	1.7
18/10/2017	OG1	24.25	190	1.43	1.15	0.30	0.22	28.95	1.17	0.70	1.15	0.98	3476	10	11	3452	23	27	3409	61	70	1.9
18/10/2017	OG1	14.64	120	1.42	0.71	0.30	0.23	29.08	0.75	0.70	0.71	0.95	3467	11	12	3456	15	20	3438	38	51	0.8
18/10/2017	OG1	12.90	105	1.42	0.63	0.30	0.23	29.09	0.67	0.70	0.63	0.94	3469	11	12	3456	14	19	3435	33	48	1.0
18/10/2017	OG1	18.59	152	1.41	0.57	0.30	0.22	29.31	0.61	0.71	0.57	0.94	3471	10	11	3464	13	18	3452	31	46	0.5
18/10/2017	OG1	9.43	125	1.36	1.09	0.30	0.23	30.26	1.11	0.73	1.09	0.98	3465	11	12	3495	22	26	3548	60	69	-2.4
18/10/2017	OG1	15.15	203	1.38	0.83	0.30	0.22	29.91	0.86	0.72	0.83	0.97	3468	10	11	3484	17	22	3511	45	57	-1.2
18/10/2017	OG1	9.41	128	1.37	0.96	0.30	0.23	30.12	0.98	0.73	0.96	0.97	3462	11	12	3491	20	24	3541	52	63	-2.3
18/10/2017	OG1	15.22	211	1.39	1.18	0.30	0.22	29.84	1.20	0.72	1.18	0.98	3469	10	11	3482	24	27	3504	64	73	-1.0
18/10/2017	OG1	14.74	206	1.42	1.14	0.30	0.22	29.04	1.16	0.70	1.14	0.98	3470	10	11	3455	23	27	3428	61	70	1.2
18/10/2017	OG1	10.20	137	1.38	1.17	0.30	0.22	30.00	1.19	0.73	1.17	0.98	3467	10	11	3487	24	27	3522	64	73	-1.6
18/10/2017	OG1	14.54	206	1.42	0.99	0.30	0.22	29.03	1.02	0.70	0.99	0.98	3465	10	11	3455	21	24	3436	53	63	0.9
18/10/2017	OG1	9.82	137	1.38	1.03	0.30	0.22	29.81	1.06	0.73	1.03	0.98	3461	10	11	3480	21	25	3515	56	66	-1.6
18/09/2018	OG1	20.11	181	1.44	0.86	0.30	0.20	29.02	0.88	0.70	0.86	0.97	3482	10	11	3454	18	22	3405	46	57	2.2
18/09/2018	OG1	19.41	175	1.43	0.93	0.30	0.18	29.11	0.95	0.70	0.93	0.98	3483	10	11	3457	19	23	3413	49	60	2.0
18/09/2018	OG1	19.47	174	1.42	1.13	0.30	0.18	29.39	1.15	0.71	1.13	0.99	3482	10	11	3467	23	27	3440	61	70	1.2
18/09/2018	OG1	13.79	124	1.42	0.85	0.29	0.20	28.67	0.87	0.71	0.85	0.97	3442	10	11	3442	18	22	3443	45	57	0.0
18/09/2018	OG1	22.17	198	1.41	0.55	0.30	0.18	29.51	0.58	0.71	0.55	0.95	3483	10	11	3471	12	18	3450	30	46	0.9
18/09/2018	OG1	11.68	103	1.39	0.76	0.30	0.18	29.79	0.79	0.72	0.76	0.97	3471	10	11	3480	16	21	3496	41	54	-0.7
18/09/2018	OG1	13.06	125	1.41	0.32	0.30	0.18	29.36	0.37	0.71	0.32	0.87	3474	10	11	3466	9	16	3451	17	39	0.7
18/09/2018	OG1	14.38	137	1.41	0.34	0.30	0.18	29.49	0.39	0.71	0.34	0.88	3475	10	11	3470	9	16	3461	19	40	0.4
18/09/2018	OG1	12.74	122	1.41	0.42	0.30	0.18	29.35	0.45	0.71	0.42	0.92	3473	10	11	3465	10	17	3451	23	42	0.6
18/09/2018	OG1	16.63	160	1.43	0.32	0.30	0.20	29.14	0.37	0.70	0.32	0.85	3485	10	11	3458	9	16	3412	17	38	2.1
18/09/2018	OG1	13.37	127	1.41	0.53	0.30	0.18	29.45	0.56	0.71	0.53	0.95	3478	10	11	3469	12	18	3452	29	45	0.7
18/09/2018	OG1	9.90	94	1.41	0.38	0.30	0.20	29.32	0.43	0.71	0.38	0.89	3474	10	11	3464	10	16	3448	21	40	0.7

Table S4.7. cont.: *VRM OG1*

Date	sample	^{206}Pb (mV)	U ppm	^{238}U/^{206}Pb	1s%	^{207}Pb/^{206}Pb	1s%	^{207}Pb/^{235}U	1s%	^{206}Pb/^{238}U	1s%	Rho	^{207}Pb-^{206}Pb Age	2s abs	2s $_{sys}$ abs	^{207}Pb-^{235}U Age	2s abs	2s $_{sys}$ abs	^{206}Pb-^{238}U Age	2s abs	2s $_{sys}$ abs	Disc %
18/09/2018	OG1	17.17	163	1.42	0.33	0.30	0.18	29.38	0.37	0.70	0.33	0.87	3484	10	11	3466	9	16	3436	18	39	1.4
18/09/2018	OG1	17.10	164	1.43	0.34	0.30	0.18	29.20	0.38	0.70	0.34	0.88	3484	10	11	3460	9	16	3420	18	39	1.8
18/09/2018	OG1	14.88	147	1.42	0.61	0.30	0.20	29.19	0.64	0.71	0.61	0.95	3472	10	11	3460	13	19	3440	33	48	0.9
18/09/2018	OG1	10.31	102	1.42	0.45	0.30	0.20	29.19	0.49	0.71	0.45	0.91	3469	10	11	3460	11	17	3445	24	42	0.7
18/09/2018	OG1	13.88	138	1.43	0.51	0.30	0.20	29.03	0.55	0.70	0.51	0.93	3472	10	11	3454	12	18	3425	28	44	1.3
18/09/2018	OG1	13.74	135	1.43	0.39	0.30	0.18	29.00	0.43	0.70	0.39	0.91	3471	10	11	3453	10	16	3423	21	41	1.4
18/09/2018	OG1	12.35	121	1.43	0.56	0.30	0.20	28.96	0.60	0.70	0.56	0.94	3472	10	11	3452	13	18	3418	30	46	1.5
18/09/2018	OG1	13.37	130	1.42	0.52	0.30	0.20	29.22	0.55	0.71	0.52	0.93	3471	10	11	3461	12	18	3443	28	45	0.8
18/09/2018	OG1	17.24	177	1.43	0.52	0.30	0.18	29.13	0.55	0.70	0.52	0.94	3481	10	11	3458	12	18	3418	28	44	1.8
18/09/2018	OG1	16.46	167	1.42	0.58	0.30	0.18	29.26	0.60	0.70	0.58	0.95	3480	10	11	3462	13	18	3432	31	46	1.4
18/09/2018	OG1	16.46	166	1.41	0.51	0.30	0.18	29.53	0.55	0.71	0.51	0.94	3478	10	11	3471	12	18	3459	28	44	0.6
18/09/2018	OG1	15.94	161	1.41	0.48	0.30	0.18	29.59	0.51	0.71	0.48	0.93	3481	10	11	3473	11	17	3459	26	43	0.6
18/09/2018	OG1	14.58	148	1.42	0.51	0.30	0.18	29.35	0.54	0.71	0.51	0.94	3480	10	11	3465	12	18	3441	27	44	1.1
18/09/2018	OG1	13.53	138	1.42	0.55	0.30	0.18	29.33	0.58	0.71	0.55	0.95	3478	10	11	3465	12	18	3441	30	46	1.1
20/09/2018	OG1	11.06	106	1.39	0.91	0.30	0.35	29.75	0.97	0.72	0.91	0.93	3473	13	14	3479	20	24	3489	49	60	-0.4
20/09/2018	OG1	11.18	108	1.41	0.77	0.30	0.35	29.46	0.85	0.71	0.77	0.91	3475	13	14	3469	17	22	3458	42	54	0.5
20/09/2018	OG1	7.09	134	1.41	0.84	0.30	0.35	29.37	0.91	0.71	0.84	0.92	3467	13	14	3466	19	23	3464	45	57	0.1
20/09/2018	OG1	7.24	136	1.40	0.84	0.30	0.35	29.63	0.91	0.72	0.84	0.92	3470	13	14	3475	18	23	3482	45	57	-0.3
20/09/2018	OG1	7.25	137	1.39	0.91	0.30	0.37	29.62	0.98	0.72	0.91	0.93	3468	14	15	3474	20	24	3485	49	60	-0.5
20/09/2018	OG1	7.53	142	1.42	0.85	0.30	0.35	29.18	0.92	0.71	0.85	0.92	3469	13	14	3460	19	23	3444	45	57	0.7
20/09/2018	OG1	8.95	168	1.40	0.91	0.30	0.37	29.56	0.98	0.71	0.91	0.93	3472	14	15	3472	20	24	3473	49	60	0.0
20/09/2018	OG1	9.78	190	1.42	0.92	0.30	0.35	29.23	0.99	0.70	0.92	0.94	3474	13	14	3461	20	24	3439	49	60	1.0
20/09/2018	OG1	8.74	167	1.40	0.84	0.30	0.37	29.63	0.92	0.71	0.84	0.92	3474	14	15	3475	19	23	3475	45	57	0.0
20/09/2018	OG1	8.70	160	1.42	0.85	0.30	0.36	29.37	0.93	0.71	0.85	0.92	3481	14	15	3466	19	23	3441	46	57	1.1
20/09/2018	OG1	8.48	155	1.40	1.05	0.30	0.36	29.67	1.11	0.71	1.05	0.94	3480	14	15	3476	22	26	3470	57	67	0.3
20/09/2018	OG1	10.19	189	1.43	0.93	0.30	0.36	29.12	1.00	0.70	0.93	0.93	3479	14	15	3457	20	24	3421	49	60	1.7
20/09/2018	OG1	20.53	344	1.43	0.86	0.30	0.35	29.13	0.93	0.70	0.86	0.93	3482	13	14	3458	19	23	3415	46	57	1.9
20/09/2018	OG1	19.57	328	1.47	0.81	0.30	0.35	28.44	0.88	0.68	0.81	0.92	3485	13	14	3434	18	22	3347	42	54	4.0
20/09/2018	OG1	19.58	324	1.46	0.80	0.30	0.35	28.42	0.88	0.68	0.80	0.92	3479	13	14	3434	18	22	3357	42	54	3.5
21/09/2018	OG1	10.38	102	1.40	0.77	0.30	0.27	29.35	0.81	0.72	0.77	0.94	3458	11	12	3465	17	21	3477	42	54	-0.5
21/09/2018	OG1	10.10	97	1.37	0.75	0.30	0.29	29.95	0.80	0.73	0.75	0.93	3453	12	13	3485	16	21	3541	41	54	-2.5
21/09/2018	OG1	16.27	159	1.39	0.64	0.30	0.25	29.66	0.69	0.72	0.64	0.93	3461	11	12	3476	14	19	3501	35	49	-1.2

Table S4.7. cont.: *VRM OG1*

Date	sample	^{206}Pb (mV)	U ppm	^{238}U/^{206}Pb	1s%	^{207}Pb/^{206}Pb	1s%	^{207}Pb/^{235}U	1s%	^{206}Pb/^{238}U	1s%	Rho	^{207}Pb-^{206}Pb Age	2s abs	2s $_{sys}$ abs	^{207}Pb-^{235}U Age	2s abs	2s $_{sys}$ abs	^{206}Pb-^{238}U Age	2s abs	2s $_{sys}$ abs	Disc %
21/09/2018	OG1	10.35	105	1.39	0.63	0.30	0.27	29.53	0.68	0.72	0.63	0.92	3464	11	12	3471	14	19	3485	34	49	-0.6
21/09/2018	OG1	10.61	107	1.39	0.69	0.30	0.25	29.80	0.74	0.72	0.69	0.94	3469	11	12	3480	15	20	3500	38	51	-0.9
21/09/2018	OG1	8.24	83	1.38	0.59	0.30	0.27	29.99	0.65	0.73	0.59	0.91	3469	11	12	3487	14	19	3517	32	48	-1.4
21/09/2018	OG1	20.63	213	1.41	0.46	0.30	0.25	29.56	0.52	0.71	0.46	0.88	3478	11	12	3472	11	17	3462	25	43	0.5
21/09/2018	OG1	18.72	190	1.39	0.69	0.30	0.25	29.96	0.73	0.72	0.69	0.94	3478	11	12	3486	15	20	3499	37	51	-0.6
21/09/2018	OG1	17.22	183	1.38	0.51	0.30	0.25	30.00	0.57	0.72	0.51	0.90	3475	11	12	3487	12	18	3508	28	45	-1.0
21/09/2018	OG1	15.42	164	1.38	0.61	0.30	0.27	29.97	0.66	0.72	0.61	0.92	3472	11	12	3486	14	19	3510	33	48	-1.1
21/09/2018	OG1	11.73	128	1.41	0.68	0.30	0.27	29.29	0.73	0.71	0.68	0.93	3466	11	12	3463	15	20	3459	36	50	0.2
21/09/2018	OG1	14.75	160	1.39	0.39	0.30	0.25	29.78	0.46	0.72	0.39	0.84	3473	11	12	3479	10	17	3490	21	41	-0.5
21/09/2018	OG1	14.06	151	1.38	0.52	0.30	0.25	30.04	0.57	0.73	0.52	0.90	3472	11	12	3488	12	18	3517	28	45	-1.3
21/09/2018	OG1	14.48	156	1.38	0.59	0.30	0.27	30.03	0.65	0.72	0.59	0.91	3475	11	12	3488	14	19	3511	32	48	-1.0
21/09/2018	OG1	14.81	168	1.40	0.98	0.30	0.25	29.59	1.01	0.71	0.98	0.97	3473	11	12	3473	20	24	3474	53	63	0.0
21/09/2018	OG1	11.51	127	1.36	0.95	0.30	0.25	30.35	0.99	0.73	0.95	0.97	3470	11	12	3498	20	24	3548	52	63	-2.3
21/09/2018	OG1	15.86	175	1.37	1.09	0.30	0.25	30.30	1.12	0.73	1.09	0.98	3473	11	12	3497	23	26	3537	60	69	-1.8
21/09/2018	OG1	13.75	153	1.36	1.02	0.30	0.27	30.51	1.05	0.74	1.02	0.97	3471	11	12	3503	21	25	3559	56	66	-2.5
21/09/2018	OG1	18.49	211	1.39	1.25	0.30	0.25	29.86	1.28	0.72	1.25	0.98	3477	11	12	3482	26	29	3492	68	76	-0.5
21/09/2018	OG1	15.86	185	1.42	1.07	0.30	0.25	29.15	1.09	0.70	1.07	0.97	3472	11	12	3458	22	26	3436	57	67	1.0
21/09/2018	OG1	16.67	193	1.38	0.76	0.30	0.25	29.91	0.80	0.73	0.76	0.95	3464	11	12	3484	16	21	3518	41	54	-1.6
21/09/2018	OG1	16.91	199	1.40	0.51	0.30	0.25	29.54	0.57	0.71	0.51	0.90	3471	11	12	3472	12	18	3472	28	44	0.0
21/09/2018	OG1	18.41	213	1.38	0.66	0.30	0.25	30.04	0.71	0.72	0.66	0.94	3474	11	12	3488	15	20	3513	36	50	-1.1
21/09/2018	OG1	18.68	221	1.40	0.70	0.30	0.25	29.66	0.74	0.72	0.70	0.94	3472	11	12	3476	15	20	3481	38	51	-0.2
21/09/2018	OG1	12.79	152	1.40	0.51	0.30	0.27	29.51	0.58	0.71	0.51	0.89	3470	11	12	3471	12	18	3471	28	44	0.0
21/09/2018	OG1	18.09	210	1.37	0.63	0.30	0.25	30.27	0.68	0.73	0.63	0.93	3471	11	12	3496	14	19	3539	34	50	-1.9

Supplementary Material Five:

Zircon Standards U-Pb II

	May 2017				October 2017 to September 2018			
Standard	**^{207}Pb-^{206}Pb Age (Ma)**	**2σ**	**^{206}Pb-^{238}U Age (Ma)**	**2σ**	**^{207}Pb-^{206}Pb Age (Ma)**	**2σ**	**^{206}Pb-^{238}U Age (Ma)**	**2σ**
GJ1	602.4	5.7	593.9	3.25	608.1	1.1	601.9	0.5
91500	1063	7.6	1051	9.0	1058.1	4.6	1063.1	3.8
Plesovice	339.2	6.5	338.3	2.6	342.1	1.6	339.2	0.5
OG1	na	na	na	na	3471.6	0.9	3469.4	5.8

Supplementary Material 5.1: Weighted averages generated for ^{207}Pb-^{206}Pb ages and ^{206}Pb-^{238}U ages of PRM (GJ1) and VRMs (91500, Plesovice, OG1). For full plots see the remainder of this supplementary material.

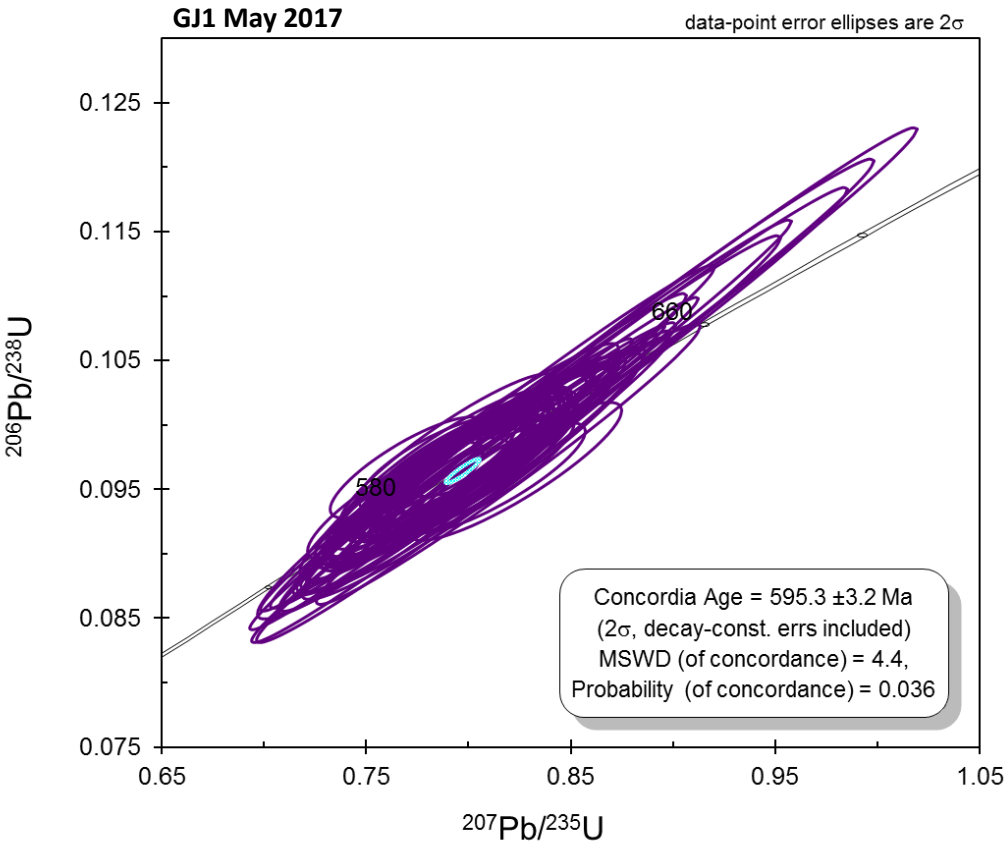
GJ1 May 2017
data-point error ellipses are 2σ
0.125
0.115
0.105
0.095
0.085
0.075
206Pb/238U
660
580
Concordia Age = 595.3 ±3.2 Ma
(2σ, decay-const. errs included)
MSWD (of concordance) = 4.4,
Probability (of concordance) = 0.036
0.65
0.75
0.85
0.95
1.05
207Pb/235U

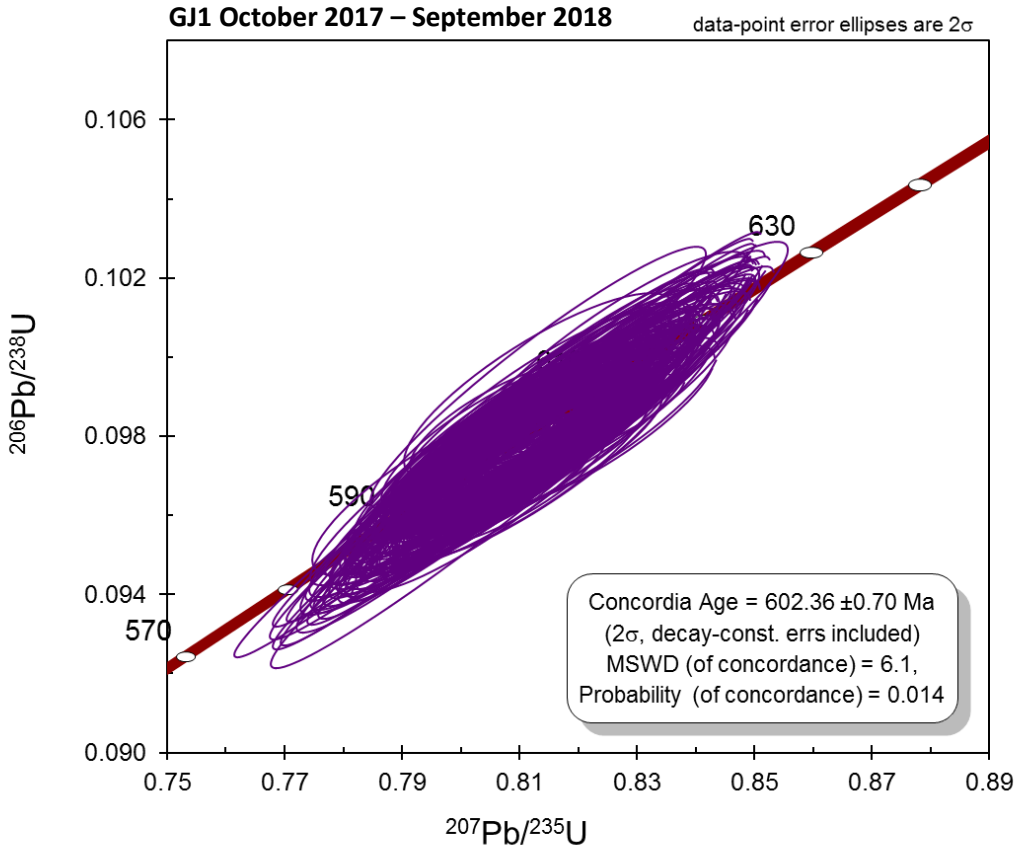
GJ1 October 2017 – September 2018
data-point error ellipses are 2σ
0.106
0.102
0.098
0.094
0.090
206Pb/238U
630
590
570
Concordia Age = 602.36 ±0.70 Ma
(2σ, decay-const. errs included)
MSWD (of concordance) = 6.1,
Probability (of concordance) = 0.014
0.75
0.77
0.79
0.81
0.83
0.85
0.87
0.89
207Pb/235U

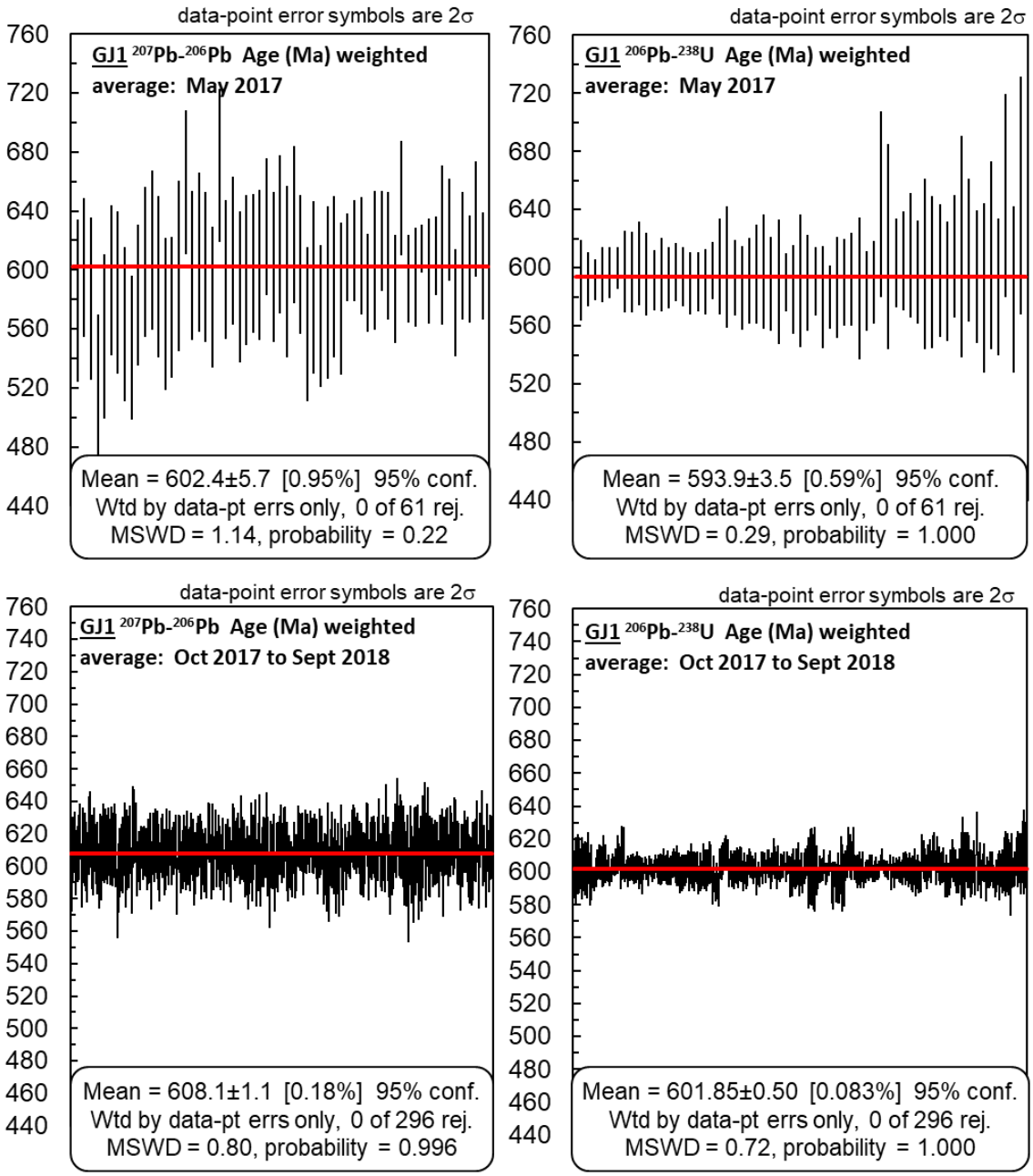

Supplementary Material 5.2: Concordia plots and weighted averages of ^{207}Pb-^{206}Pb ages and ^{206}Pb-^{238}U ages (Ma) of PRM GJ1. Data separated by session: lower uncertainties during October 2017 to September 2018 analytical sessions are clearly apparent, which translate into lower analytical uncertainties for sample unknowns. GJ1 ^{207}Pb-^{206}Pb ages and ^{206}Pb-^{238}U ages (Ma) are 607.7±0.7 and 601.9±0.4 (Horstwood et al., 2016), all data bar ^{206}Pb-^{238}U ages within May 2017 weighted average are within uncertainty. The ~1.5% lower ^{206}Pb-^{238}U ages within May 2017 weighted average indicates slight underestimation of PRM, which appears to have translated into lower ^{206}Pb-^{238}U weighted average ages of 91500. This has not been replicated within Plesovice: most grains within 14WA4 are slightly discordant, but generally masked by larger ^{206}Pb-^{238}U uncertainties in comparison to October 2017 to September 2018 data. Concordia ages are slightly younger than previously determined values in both analytical sessions.

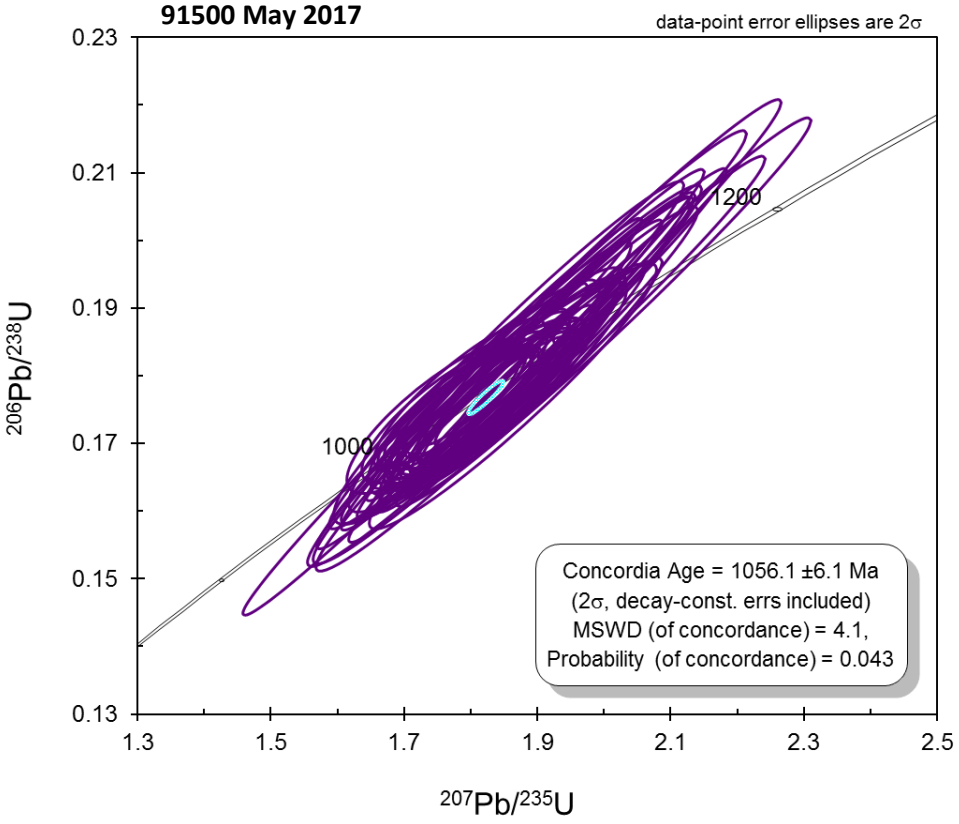
91500 May 2017
data-point error ellipses are 2σ
0.23
0.21
0.19
0.17
0.15
0.13
1.3
1.5
1.7
1.9
2.1
2.3
2.5
206Pb/238U
207Pb/235U
1200
1000
Concordia Age = 1056.1 ±6.1 Ma
(2σ, decay-const. errs included)
MSWD (of concordance) = 4.1,
Probability (of concordance) = 0.043

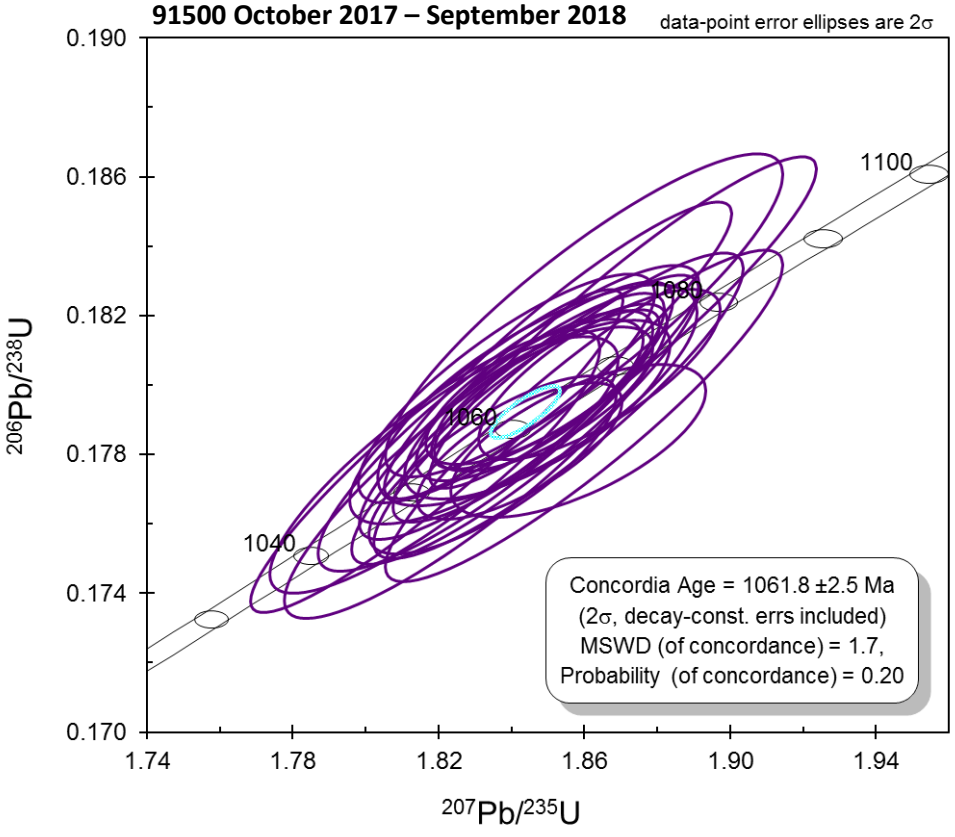
91500 October 2017 – September 2018
data-point error ellipses are 2σ
0.190
0.186
0.182
0.178
0.174
0.170
1.74
1.78
1.82
1.86
1.90
1.94
206Pb/238U
207Pb/235U
1100
1080
1060
1040
Concordia Age = 1061.8 ±2.5 Ma
(2σ, decay-const. errs included)
MSWD (of concordance) = 1.7,
Probability (of concordance) = 0.20

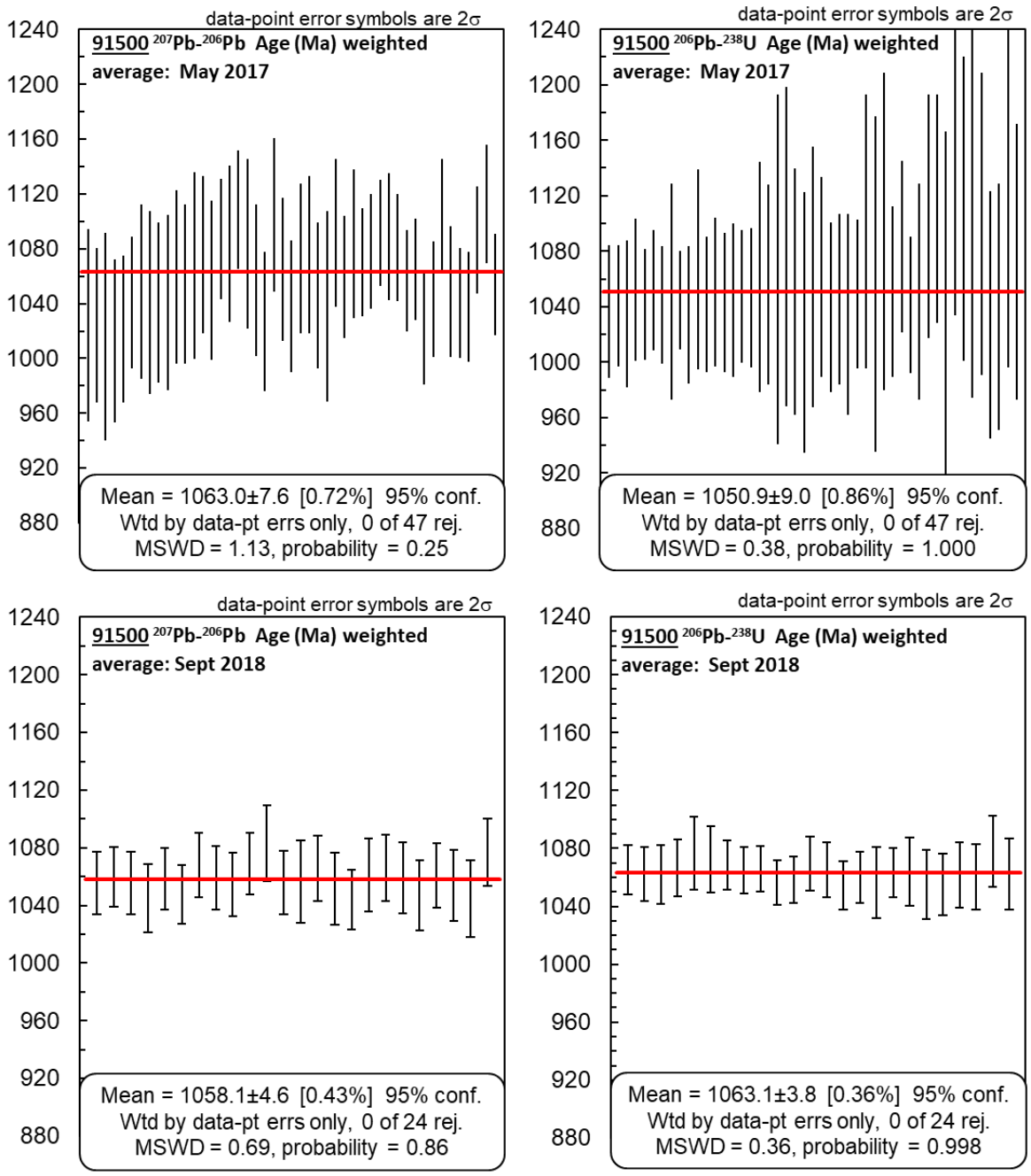

Supplementary Material 5.3: Concordia plots and weighted averages of ^{207}Pb-^{206}Pb ages and ^{206}Pb-^{238}U ages (Ma) of VRM 91500 using propagated age uncertainties. Data separated by session: lower uncertainties during October 2017 to September 2018 analytical sessions are again apparent. 91500 was not used as heavily within the September 2018 session, and was omitted entirely in October 2017, owing to the introduction of the OG1 VRM. Low MSWDs indicate over propagation of ^{206}Pb-^{238}U ages within this VRM. 91500 ^{207}Pb-^{206}Pb ages and ^{206}Pb-^{238}U ages (Ma) are 1066±0.6 and 1063.5±0.4 (Horstwood et al., 2016). Concordia ages are moderately younger than expected, resulting in concordia ages ~1% and ~0.4% younger than previously determined ^{207}Pb-^{206}Pb ages. ^{207}Pb-^{206}Pb are a little underestimated, but ^{206}Pb-^{238}U ages within the September 2018 are analytically indistinguishable from previous data.

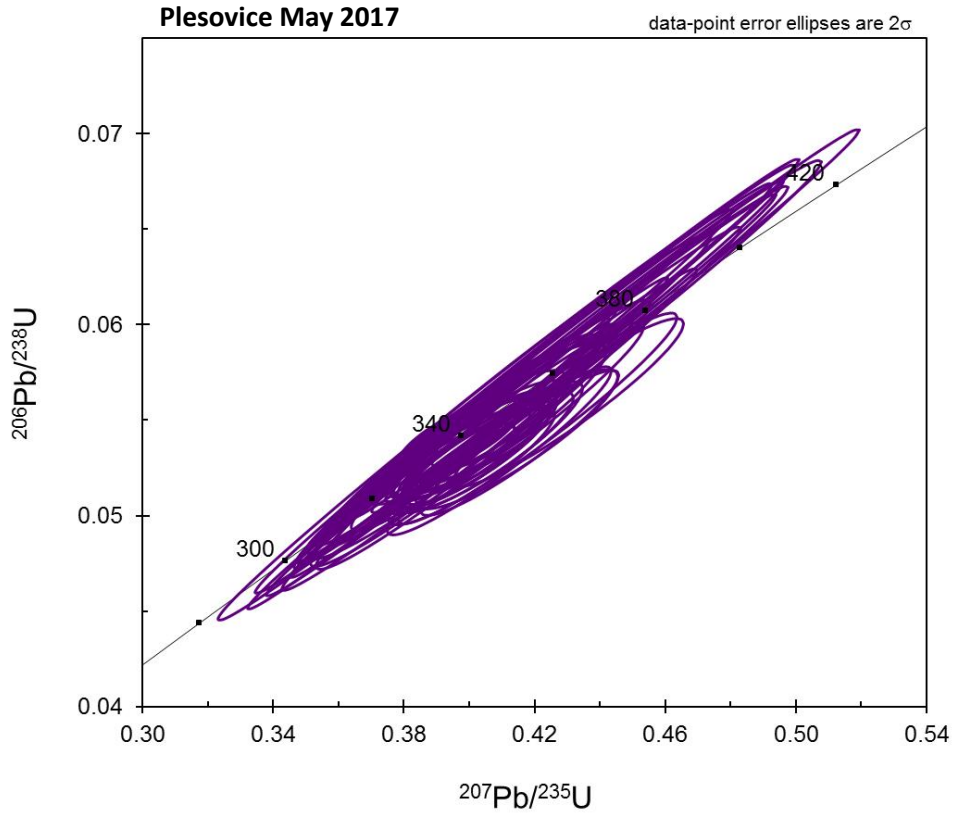
Plesovice May 2017
data-point error ellipses are 2σ
0.07
0.06
0.05
0.04
206Pb/238U
300
340
380
420
0.30
0.34
0.38
0.42
0.46
0.50
0.54
207Pb/235U

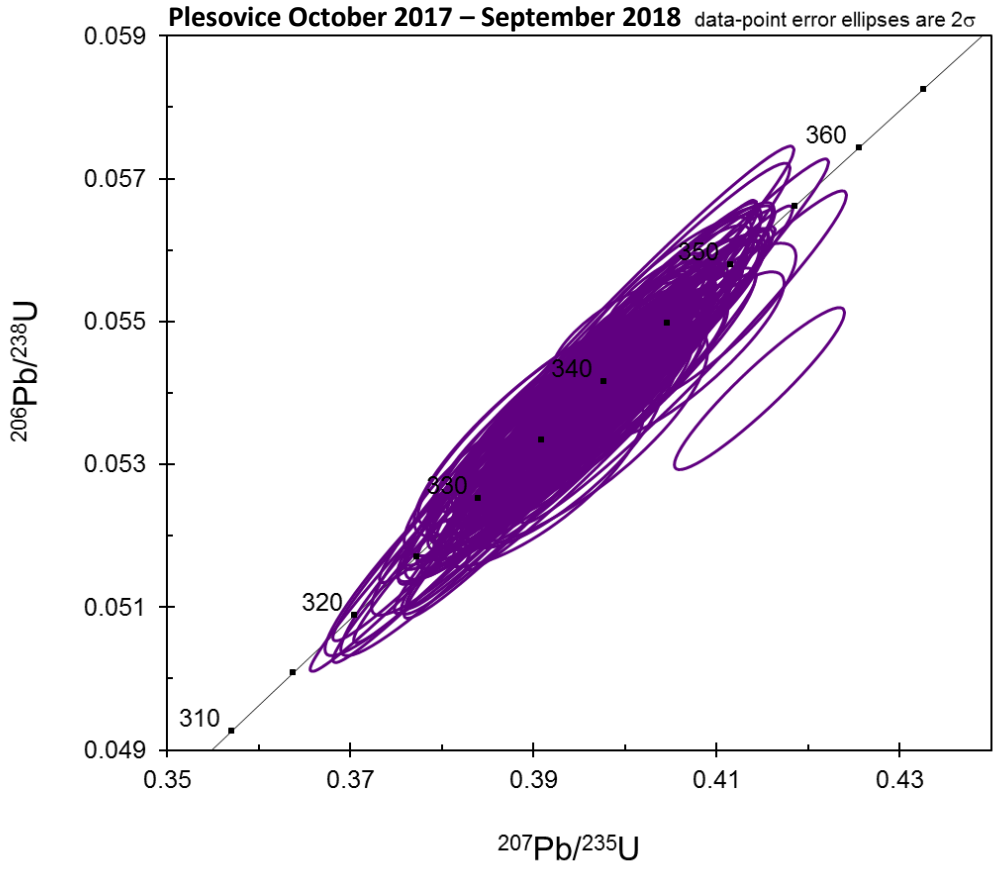
Plesovice October 2017 – September 2018
data-point error ellipses are 2σ
0.059
0.057
0.055
0.053
0.051
0.049
206Pb/238U
310
320
330
340
350
360
0.35
0.37
0.39
0.41
0.43
207Pb/235U

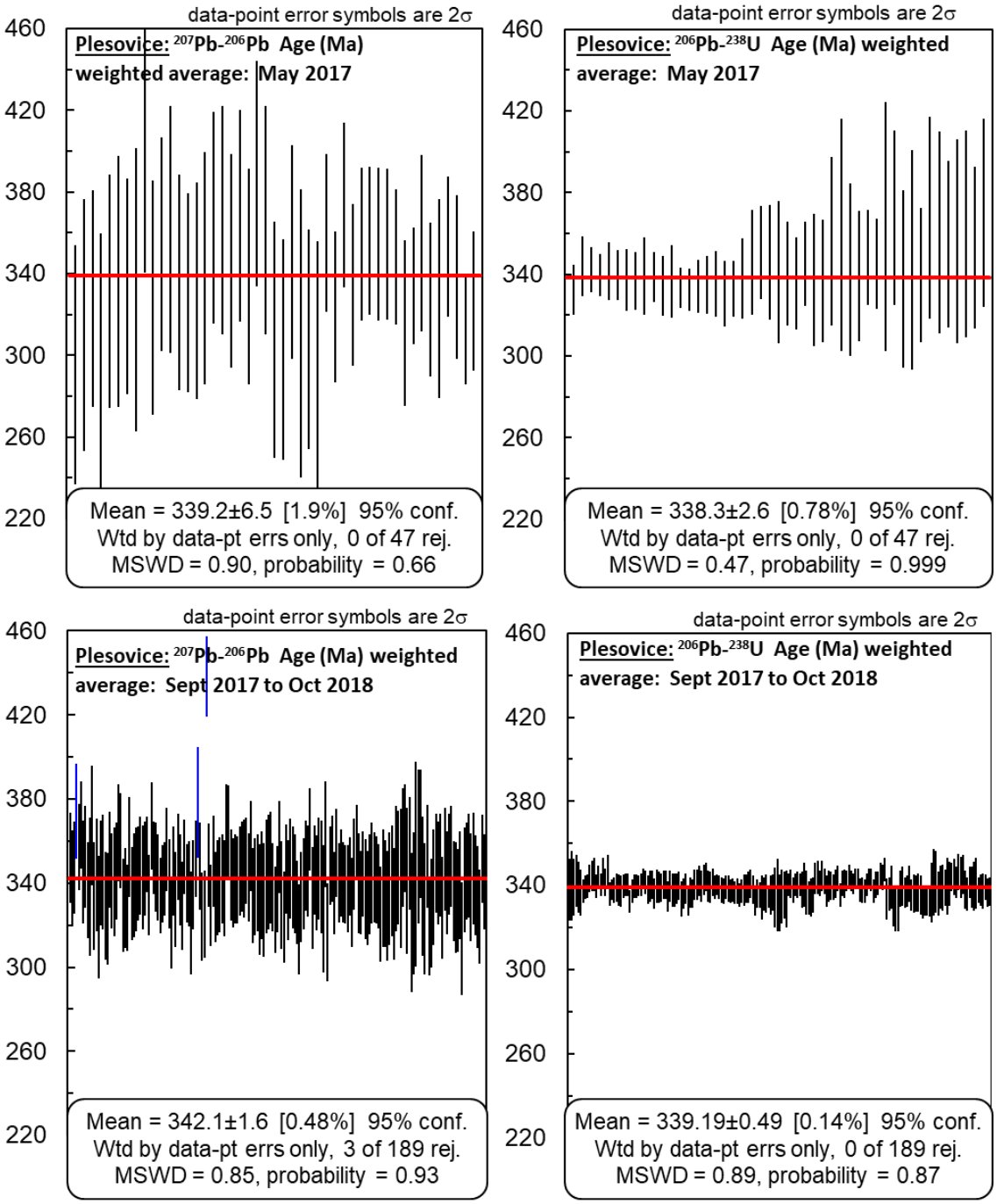

Supplementary Material 5.4: Concordia plots and weighted averages of ^{207}Pb-^{206}Pb ages and ^{206}Pb-^{238}U ages (Ma) of VRM Plesovice using propagated age uncertainties. Data separated by session: lower uncertainties during October 2017 to September 2018 analytical sessions are again apparent. Good MSWDs suggest uncertainties are well characterised within this VRM. Plesovice ^{207}Pb-^{206}Pb ages and ^{206}Pb-^{238}U ages (Ma) are 338±0.6 and 337.3±0.2 (Horstwood et al., 2016). Concordia ages could not be calculated via Isoplot (Ludwig, 2003). Weighted averages are well within error: while reference material ages were calculated by TIMS for this standard, it has been commonly found to possess slight older ^{207}Pb-^{206}Pb ages during LA-ICP-MS (M. Horstwood, pers. com) of ~341 Ma. As such, values determined here are in good agreement with previous analyses.

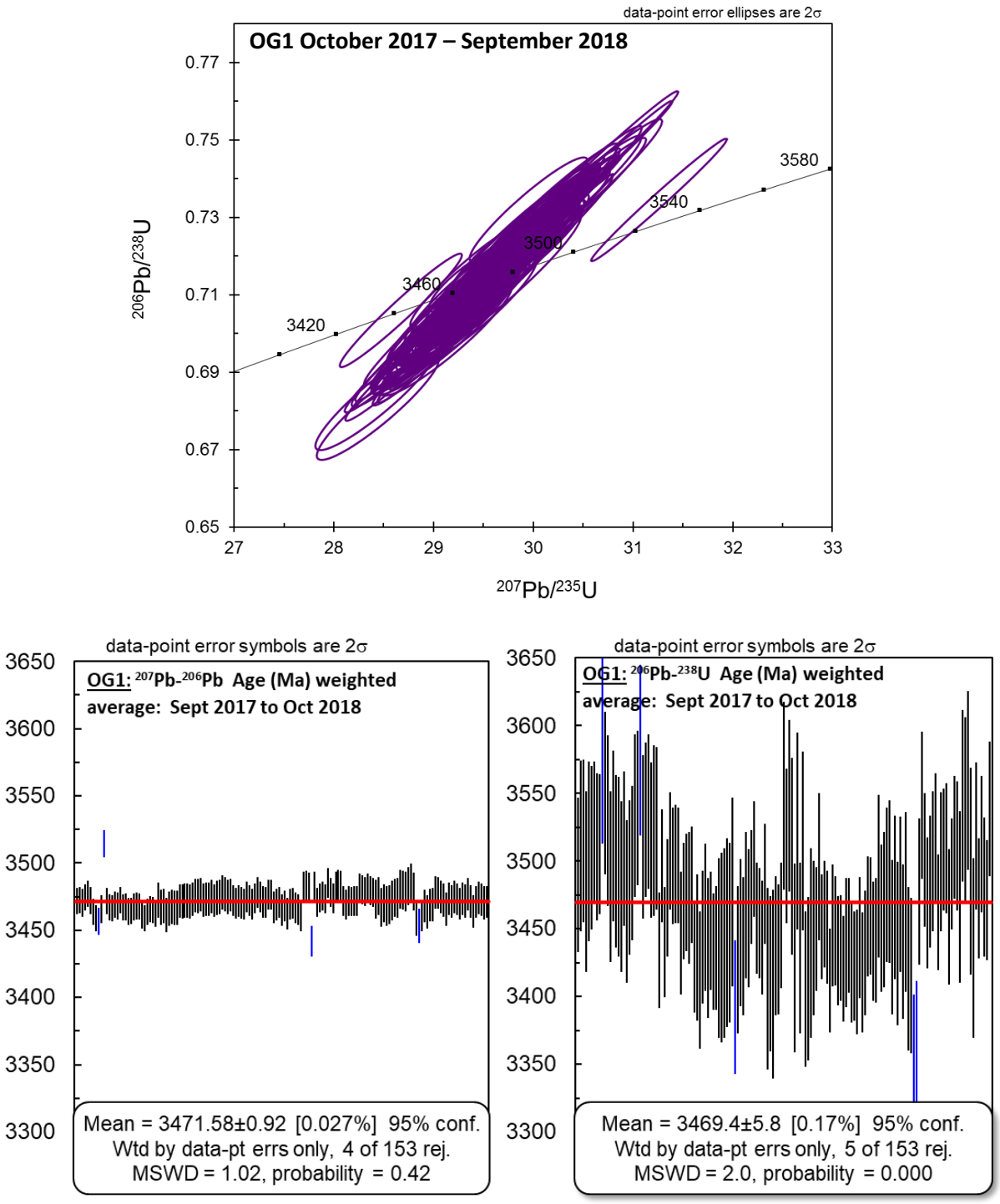

Supplementary Material 5.5: Concordia plots and weighted averages of ^{207}Pb-^{206}Pb ages and ^{206}Pb-^{238}U ages (Ma) of VRM OG1 using propagated age uncertainties. OG1 ^{207}Pb-^{206}Pb ages and ^{206}Pb-^{238}U ages (Ma) are 3465±0.6 and 3440.7±3.2 (Stern et al., 2009). As with Plesovice, concordia ages could not be calculated via Isoplot (Ludwig, 2003). ^{207}Pb-^{206}Pb ages are slightly older (~0.2%) than previously determined values. ^{206}Pb-^{238}U ages appear to be far more heterogeneous than other samples, with clear analytical drift both during and between sessions. As such, the resultant higher MSWD suggests propagated uncertainties for ^{206}Pb-^{238}U ages are underestimated for OG1. Some apparent intra-sample heterogeneity was observed during September 2018, with individual crystals yielding distinct ^{207}Pb-^{206}Pb ages: this may be of interest for further analyses.

Supplementary Material Six:

Jack Hills zircons U-Pb

Table S6.1.: *Jack Hills zircons analysed October 2017-September 2018.*

Sample		Concentration		For Tera-Wasserberg plot				For Wetherill Plot					Ages									Conc
Sam-ple	zircon #	^{206}Pb (mV)	U ppm	^{238}U/ ^{206}Pb	1s%	^{207}Pb/ ^{206}Pb	1s%	^{207}Pb/ ^{235}U	1s%	^{206}Pb/ ^{238}U	1s%	Rho	^{207}Pb-^{206}Pb Age	2s abs	2s $_{sys}$ abs	^{207}Pb-^{235}U Age	2s abs	2s $_{sys}$ abs	^{206}Pb-^{238}U Age	2s abs	2s $_{sys}$ abs	Disc%
14WA2	2[a]	11.0	112	1.46	0.61	0.29	0.19	27.32	0.64	0.69	0.61	0.95	3411	10	11	3395	13	19	3368	32	47	1.3
14WA2	5	17.6	178	1.45	0.80	0.29	0.19	27.49	0.82	0.69	0.80	0.97	3417	10	11	3401	17	21	3375	42	54	1.2
14WA2	5	6.4	65	1.41	1.84	0.29	0.38	28.20	1.88	0.71	1.84	0.98	3412	14	15	3426	37	39	3451	98	104	-1.2
14WA2	5	6.3	62	1.43	0.69	0.29	0.19	27.55	0.71	0.70	0.69	0.96	3399	10	11	3403	15	20	3411	37	50	-0.4
14WA2	7	8.3	84	1.46	0.61	0.29	0.21	26.93	0.65	0.68	0.61	0.95	3394	10	11	3381	14	19	3360	32	47	1.0
14WA2	9	9.1	92	1.46	0.60	0.29	0.21	27.13	0.63	0.68	0.60	0.94	3403	10	11	3388	13	19	3363	32	46	1.2
14WA2	11	7.0	70	1.43	0.64	0.28	0.19	27.16	0.67	0.70	0.64	0.96	3377	10	11	3389	14	19	3410	34	48	-1.0
14WA2	13	6.6	52	1.15	0.55	0.44	0.24	52.77	0.60	0.87	0.55	0.92	4049	11	11	4046	13	19	4040	33	51	0.2
14WA2	13	6.2	49	1.14	0.63	0.44	0.27	53.59	0.68	0.88	0.63	0.92	4061	12	12	4061	15	20	4063	38	55	0.0
14WA2	15	4.8	47	1.42	0.71	0.29	0.25	27.65	0.75	0.70	0.71	0.95	3392	11	12	3407	15	20	3432	38	51	-1.2
14WA2	19*	10.0	100	1.45	0.57	0.28	0.19	27.00	0.60	0.69	0.57	0.95	3386	10	11	3383	13	18	3379	30	45	0.2
14WA2	20*	7.5	75	1.45	0.67	0.29	0.23	27.24	0.71	0.69	0.67	0.95	3397	10	12	3392	15	20	3385	36	50	0.4
14WA2	21*	16.6	150	1.30	0.58	0.35	0.19	36.59	0.61	0.77	0.58	0.95	3689	10	11	3682	13	19	3671	33	49	0.5
14WA2	22	6.3	51	1.16	1.10	0.43	0.24	51.32	1.13	0.86	1.10	0.98	4022	11	11	4018	23	27	4011	66	76	0.3
14WA2	22	4.7	37	1.10	0.72	0.47	0.24	58.96	0.76	0.91	0.72	0.95	4151	11	11	4157	16	21	4168	44	59	-0.4
14WA2	24	12.8	127	1.44	0.79	0.28	0.21	27.05	0.82	0.69	0.79	0.97	3378	10	11	3385	17	21	3398	42	54	-0.6
14WA2	25	9.0	90	1.40	0.53	0.31	0.24	30.55	0.58	0.71	0.53	0.91	3523	11	12	3505	12	18	3472	28	45	1.5
14WA2	25*	8.0	80	1.39	0.84	0.31	0.22	30.81	0.87	0.72	0.84	0.97	3527	10	12	3513	18	22	3489	45	57	1.1
14WA2	26*	6.7	71	1.46	0.59	0.29	0.23	27.00	0.63	0.68	0.59	0.93	3398	10	12	3383	13	19	3358	31	46	1.2
14WA2	28*	9.2	95	1.45	0.59	0.29	0.21	27.78	0.62	0.69	0.59	0.94	3429	10	11	3411	13	19	3381	31	46	1.4
14WA2	28*	10.4	106	1.42	0.55	0.29	0.19	28.37	0.58	0.70	0.55	0.95	3431	10	11	3432	12	18	3434	29	45	-0.1
14WA2	29	10.6	112	1.47	0.48	0.29	0.21	26.83	0.53	0.68	0.48	0.92	3391	10	11	3377	11	17	3354	26	43	1.1
14WA2	30	14.5	151	1.45	0.71	0.29	0.19	27.79	0.73	0.69	0.71	0.97	3429	10	11	3412	15	20	3382	38	51	1.4
14WA2	32	11.8	142	1.64	0.79	0.27	0.28	22.48	0.84	0.61	0.79	0.94	3295	12	13	3205	17	21	3062	39	50	7.1
14WA2	32*	10.4	108	1.47	0.65	0.28	0.25	26.59	0.70	0.68	0.65	0.93	3377	11	12	3369	14	20	3354	34	48	0.7
14WA2	32*	14.3	152	1.48	0.52	0.29	0.19	26.61	0.55	0.68	0.52	0.94	3392	10	11	3369	12	18	3330	27	43	1.8
14WA2	33	6.0	62	1.44	0.50	0.29	0.22	27.96	0.54	0.69	0.50	0.91	3431	10	12	3418	12	18	3396	27	43	1.0
14WA2	36	11.3	116	1.43	0.93	0.30	0.20	28.93	0.95	0.70	0.93	0.98	3467	10	11	3451	19	23	3424	49	60	1.2
14WA2	39*	10.2	109	1.47	0.81	0.29	0.19	26.96	0.83	0.68	0.81	0.97	3400	10	11	3382	17	21	3352	42	54	1.4
14WA2	42	10.9	108	1.38	0.68	0.32	0.21	31.54	0.71	0.73	0.68	0.96	3545	10	11	3536	15	20	3520	37	51	0.7
14WA2	47*	12.5	126	1.40	0.62	0.31	0.20	30.08	0.65	0.71	0.62	0.95	3497	10	11	3490	14	19	3477	34	48	0.6
14WA2	48	16.0	170	1.46	0.70	0.28	0.18	26.83	0.72	0.68	0.70	0.97	3390	9	11	3377	15	20	3356	37	50	1.0
14WA2	50	21.2	209	1.38	0.76	0.32	0.21	31.66	0.79	0.73	0.76	0.97	3554	10	11	3540	16	21	3515	41	54	1.1
14WA2	51	6.3	66	1.44	0.87	0.28	0.19	27.18	0.89	0.69	0.87	0.98	3387	10	11	3390	18	22	3394	46	57	-0.2
14WA2	53	6.6	70	1.46	0.87	0.29	0.21	27.08	0.90	0.69	0.87	0.97	3398	10	11	3386	18	22	3367	46	57	0.9

Table S6.1. cont.: *Jack Hills zircons analysed October 2017-September 2018.*

Sam-ple	zircon #	^{206}Pb (mV)	U ppm	^{238}U/ ^{206}Pb	1s%	^{207}Pb/ ^{206}Pb	1s%	^{207}Pb/ ^{235}U	1s%	^{206}Pb/ ^{238}U	1s%	Rho	^{207}Pb-^{206}Pb Age	2s abs	2s $_{sys}$ abs	^{207}Pb-^{235}U Age	2s abs	2s $_{sys}$ abs	^{206}Pb-^{238}U Age	2s abs	2s $_{sys}$ abs	Disc%
14WA2	57	4.6	72	1.16	0.98	0.45	0.39	52.94	1.06	0.86	0.98	0.93	4068	15	15	4049	22	25	4011	59	71	1.4
14WA2	57	2.8	44	1.17	1.05	0.44	0.44	51.46	1.14	0.86	1.05	0.92	4035	16	16	4021	23	27	3994	63	74	1.0
14WA2	58	4.3	86	1.47	1.03	0.28	0.37	26.51	1.10	0.68	1.03	0.94	3381	14	15	3365	22	26	3340	54	64	1.2
14WA2	61	5.0	98	1.44	0.94	0.29	0.37	27.20	1.01	0.69	0.94	0.93	3391	14	15	3391	20	24	3391	50	60	0.0
14WA2	62*	4.2	67	1.17	0.99	0.43	0.36	50.53	1.06	0.86	0.99	0.94	4009	14	14	4003	22	25	3990	59	71	0.5
14WA2	64*	4.2	78	1.38	0.90	0.31	0.37	31.01	0.97	0.73	0.90	0.92	3521	14	15	3519	20	24	3517	49	60	0.1
14WA2	65	4.6	88	1.42	0.93	0.29	0.36	28.24	0.99	0.70	0.93	0.93	3426	14	15	3428	20	24	3431	49	60	-0.2
14WA2	66	5.9	116	1.46	0.95	0.28	0.37	26.82	1.02	0.68	0.95	0.93	3389	14	15	3377	20	24	3357	50	61	0.9
14WA2	67	2.5	50	1.47	0.95	0.28	0.39	26.78	1.03	0.68	0.95	0.93	3389	14	15	3376	21	24	3352	50	61	1.1
14WA2	71	5.2	104	1.48	0.82	0.28	0.35	26.27	0.89	0.67	0.82	0.92	3379	13	14	3357	18	22	3319	43	54	1.8
14WA2	72	3.3	65	1.46	1.02	0.29	0.39	27.03	1.09	0.69	1.02	0.94	3393	14	15	3385	22	26	3371	54	63	0.6
14WA2	79	6.4	126	1.46	0.95	0.29	0.35	26.98	1.01	0.68	0.95	0.94	3398	13	14	3383	20	24	3357	50	61	1.2
14WA2	80	10.0	198	1.47	0.96	0.29	0.34	27.19	1.02	0.68	0.96	0.94	3417	13	14	3390	20	24	3346	50	60	2.1
14WA2	83	6.9	108	1.16	0.93	0.45	0.47	53.68	1.04	0.86	0.93	0.89	4089	16	16	4063	21	25	4011	56	68	1.9
14WA2	85*	5.0	96	1.40	1.12	0.31	0.35	30.92	1.17	0.72	1.12	0.95	3537	13	14	3517	24	27	3481	60	69	1.6
14WA2	90	5.7	92	1.17	0.94	0.44	0.40	51.34	1.02	0.85	0.94	0.92	4038	15	15	4019	21	25	3980	56	68	1.4
14WA2	92[a]	5.0	102	1.48	0.96	0.28	0.37	26.52	1.03	0.68	0.96	0.93	3387	14	15	3366	21	25	3331	50	60	1.7
14WA2	93	3.2	63	1.45	1.02	0.28	0.41	26.84	1.10	0.69	1.02	0.93	3379	15	16	3378	22	26	3375	54	63	0.1
14WA2	95	2.2	33	1.11	1.34	0.47	0.47	57.82	1.42	0.90	1.34	0.94	4142	16	16	4137	29	32	4127	82	91	0.3
14WA2	96*	3.8	75	1.45	0.94	0.29	0.38	27.20	1.02	0.69	0.94	0.93	3399	14	15	3391	20	24	3377	50	60	0.7
14WA2	100	3.5	67	1.40	0.91	0.31	0.40	30.92	0.99	0.71	0.91	0.92	3544	15	15	3517	20	24	3468	49	60	2.2
14WA2	102	4.0	80	1.45	1.02	0.28	0.37	26.84	1.08	0.69	1.02	0.94	3379	14	15	3377	22	25	3375	54	63	0.1
14WA2	104*	5.0	101	1.48	0.96	0.29	0.37	26.59	1.03	0.68	0.96	0.93	3391	14	15	3368	21	25	3330	50	60	1.8
14WA2	113	3.5	56	1.17	1.06	0.45	0.38	52.53	1.12	0.85	1.06	0.94	4076	14	14	4042	23	27	3973	63	74	2.5
14WA2	113	2.8	44	1.18	1.12	0.44	0.38	51.92	1.18	0.85	1.12	0.95	4062	14	14	4030	24	27	3966	66	77	2.4
14WA2	117	2.8	58	1.49	1.12	0.29	0.40	26.40	1.19	0.67	1.12	0.94	3395	15	16	3361	24	27	3306	58	67	2.6
14WA2	119*	4.5	92	1.50	1.05	0.28	0.37	26.20	1.11	0.67	1.05	0.94	3388	14	15	3354	22	26	3298	54	64	2.6
14WA2	119*	3.4	69	1.50	1.12	0.28	0.37	25.98	1.18	0.67	1.12	0.95	3374	14	15	3346	24	27	3298	58	67	2.3
14WA2	122	4.0	81	1.49	1.04	0.29	0.37	26.51	1.10	0.67	1.04	0.94	3396	14	15	3365	22	26	3314	54	64	2.4
14WA2	124	7.7	158	1.50	0.90	0.29	0.35	26.35	0.96	0.67	0.90	0.93	3395	13	14	3360	19	23	3301	46	57	2.8
14WA2	125*	3.7	75	1.49	0.97	0.28	0.39	26.13	1.05	0.67	0.97	0.93	3381	14	15	3352	21	25	3302	50	61	2.3
14WA2	126	4.2	84	1.47	0.96	0.29	0.36	27.28	1.02	0.68	0.96	0.94	3427	14	14	3393	21	24	3337	50	60	2.6
14WA2	127	7.1	134	1.38	0.83	0.33	0.37	32.74	0.91	0.72	0.83	0.91	3607	14	14	3573	18	23	3512	45	57	2.6
14WA2	131	3.3	64	1.42	0.99	0.29	0.37	28.52	1.06	0.70	0.99	0.94	3439	14	15	3437	21	25	3434	53	63	0.1
14WA2	132*	7.9	83	1.45	1.16	0.29	0.26	27.20	1.19	0.69	1.16	0.98	3395	11	12	3391	24	27	3383	61	70	0.4
14WA2	134	13.0	136	1.44	2.30	0.29	0.26	27.41	2.32	0.70	2.30	0.99	3396	11	12	3398	46	47	3402	122	127	-0.2
14WA2	134	7.6	81	1.47	1.55	0.28	0.26	26.64	1.57	0.68	1.55	0.99	3388	11	12	3370	31	34	3341	81	88	1.4

Table S6.1. cont.: *Jack Hills zircons analysed October 2017-September 2018.*

Sample	zircon #	^{206}Pb (mV)	U ppm	^{238}U/^{206}Pb	1s%	^{207}Pb/^{206}Pb	1s%	^{207}Pb/^{235}U	1s%	^{206}Pb/^{238}U	1s%	Rho	^{207}Pb-^{206}Pb Age	2s abs	2s $_{sys}$ abs	^{207}Pb-^{235}U Age	2s abs	2s $_{sys}$ abs	^{206}Pb-^{238}U Age	2s abs	2s $_{sys}$ abs	Disc%
14WA2	135*	3.5	37	1.47	1.03	0.29	0.30	26.79	1.07	0.68	1.03	0.96	3390	12	13	3376	21	25	3352	54	64	1.1
14WA2	135*	6.9	72	1.43	1.43	0.29	0.28	27.68	1.46	0.70	1.43	0.98	3400	12	13	3408	29	32	3421	76	83	-0.6
14WA2	137*	5.6	60	1.49	0.63	0.28	0.27	26.11	0.69	0.67	0.63	0.92	3372	11	12	3351	14	19	3314	33	47	1.7
14WA2	139	12.8	127	1.37	1.37	0.32	0.25	31.69	1.40	0.73	1.37	0.98	3549	11	12	3541	28	31	3526	75	82	0.7
14WA2	143	14.1	149	1.42	2.07	0.30	0.25	28.93	2.08	0.70	2.07	0.99	3464	11	12	3451	41	43	3428	110	115	1.0
14WA2	146*	13.3	139	1.42	2.70	0.29	0.26	28.48	2.71	0.70	2.70	1.00	3436	11	12	3436	53	55	3436	144	148	0.0
14WA2	149*	6.1	69	1.57	1.33	0.27	0.28	23.67	1.36	0.64	1.33	0.98	3303	12	13	3255	27	30	3177	67	74	3.8
14WA2	149*	15.8	177	1.54	1.08	0.27	0.26	24.36	1.11	0.65	1.08	0.97	3316	11	12	3283	22	26	3228	55	64	2.7
14WA2	150[a]	10.4	105	1.38	1.59	0.31	0.27	31.32	1.61	0.73	1.59	0.99	3537	11	12	3529	32	35	3515	86	93	0.6
14WA2	151	13.0	110	1.15	1.67	0.45	0.32	53.52	1.70	0.87	1.67	0.98	4078	13	13	4060	34	37	4025	100	107	1.3
14WA2	151	10.6	89	1.15	1.91	0.44	0.30	52.54	1.93	0.87	1.91	0.99	4052	12	13	4042	39	41	4021	114	121	0.8
14WA2	151	6.7	57	1.14	2.80	0.42	0.31	50.19	2.82	0.88	2.80	0.99	3968	13	13	3996	56	58	4052	169	173	-2.1
14WA2	152	7.2	77	1.46	1.68	0.29	0.26	26.92	1.70	0.68	1.68	0.99	3393	11	12	3381	34	36	3360	88	95	1.0
14WA2	153	8.2	86	1.43	2.43	0.29	0.28	27.83	2.44	0.70	2.43	0.99	3409	12	13	3413	48	50	3421	129	133	-0.3
14WA2	155	7.4	68	1.18	1.06	0.43	0.26	50.15	1.09	0.85	1.06	0.97	4017	11	12	3995	22	26	3952	63	74	1.6
14WA2	160*	7.0	65	1.20	0.72	0.43	0.26	48.91	0.76	0.84	0.72	0.94	3999	11	12	3970	16	21	3913	42	57	2.2
14WA2	161	10.3	133	1.66	1.33	0.28	0.27	23.37	1.36	0.60	1.33	0.98	3374	11	12	3243	27	30	3034	65	72	10.1
14WA2	161	6.3	71	1.46	1.46	0.29	0.28	27.12	1.48	0.69	1.46	0.98	3397	12	13	3388	29	32	3371	77	84	0.8
14WA2	169*	6.6	70	1.38	1.38	0.31	0.26	31.16	1.40	0.72	1.38	0.98	3532	11	12	3524	28	31	3511	75	83	0.6
14WA2	171*	14.1	130	1.19	1.31	0.42	0.26	49.01	1.34	0.84	1.31	0.98	3995	11	12	3972	27	30	3927	77	86	1.7
14WA2	171*	8.8	82	1.21	0.78	0.42	0.29	47.59	0.84	0.83	0.78	0.94	3969	12	12	3943	17	22	3892	46	60	1.9
14WA2	173	6.8	76	1.45	0.72	0.29	0.26	27.32	0.77	0.69	0.72	0.94	3400	11	12	3395	16	21	3386	38	51	0.4
14WA2	174*	14.4	163	1.47	1.25	0.29	0.26	26.94	1.28	0.68	1.25	0.98	3401	11	12	3381	25	29	3348	65	74	1.6
14WA2	175	9.9	111	1.46	0.61	0.29	0.26	27.10	0.66	0.68	0.61	0.92	3403	11	12	3387	14	19	3360	32	47	1.2
14WA2	181	9.2	104	1.46	1.39	0.29	0.26	26.98	1.41	0.69	1.39	0.98	3394	11	12	3383	28	31	3364	73	80	0.9
14WA2	184*	6.9	63	1.16	1.10	0.43	0.28	50.97	1.14	0.86	1.10	0.97	4015	12	12	4011	23	27	4004	66	77	0.3
14WA2	186	6.2	69	1.45	0.87	0.29	0.28	27.35	0.91	0.69	0.87	0.95	3399	12	13	3396	18	23	3390	46	57	0.3
14WA2	187	5.7	63	1.43	0.86	0.29	0.28	27.49	0.90	0.70	0.86	0.95	3394	12	13	3401	18	23	3413	46	57	-0.6
14WA2	188*	10.1	108	1.38	1.24	0.31	0.26	31.03	1.27	0.72	1.24	0.98	3527	11	12	3520	25	29	3507	67	76	0.6
14WA2	188	8.2	86	1.36	1.22	0.32	0.26	32.70	1.25	0.74	1.22	0.98	3578	11	12	3571	25	28	3559	67	76	0.5
14WA2	189*	10.6	118	1.44	1.51	0.29	0.26	27.56	1.53	0.70	1.51	0.99	3402	11	12	3404	30	33	3405	80	87	-0.1
14WA2	190	8.1	93	1.48	0.74	0.28	0.26	26.52	0.78	0.68	0.74	0.94	3386	11	12	3366	16	21	3333	39	51	1.6
14WA2	191	10.2	115	1.45	1.16	0.29	0.26	27.37	1.19	0.69	1.16	0.98	3405	11	12	3397	24	27	3383	61	70	0.7
14WA2	191	7.1	81	1.46	0.70	0.29	0.26	27.14	0.75	0.69	0.70	0.94	3400	11	12	3389	15	20	3369	37	50	0.9
14WA2	195	9.8	118	1.48	0.96	0.29	0.26	26.60	1.00	0.68	0.96	0.96	3395	11	12	3369	20	24	3325	50	60	2.1
14WA2	196*	10.4	118	1.39	0.90	0.31	0.27	31.04	0.94	0.72	0.90	0.96	3536	11	12	3520	19	23	3492	49	60	1.2
14WA2	196*	7.4	83	1.39	1.19	0.31	0.27	30.87	1.22	0.72	1.19	0.97	3532	11	12	3515	24	28	3485	64	73	1.3

Table S6.1. cont.: *Jack Hills zircons analysed October 2017-September 2018.*

Sample	zircon #	^{206}Pb (mV)	U ppm	^{238}U/^{206}Pb	1s%	^{207}Pb/^{206}Pb	1s%	^{207}Pb/^{235}U	1s%	^{206}Pb/^{238}U	1s%	Rho	^{207}Pb-^{206}Pb Age	2s abs	2s $_{sys}$ abs	^{207}Pb-^{235}U Age	2s abs	2s $_{sys}$ abs	^{206}Pb-^{238}U Age	2s abs	2s $_{sys}$ abs	Disc%
14WA2	196*	9.3	104	1.37	1.23	0.31	0.26	31.50	1.26	0.73	1.23	0.98	3534	11	12	3535	25	28	3537	67	76	-0.1
14WA2	197*	11.3	127	1.37	1.58	0.31	0.27	31.50	1.60	0.73	1.58	0.99	3540	11	12	3535	32	35	3526	86	93	0.4
14WA2	197*	9.3	105	1.39	0.97	0.31	0.27	31.16	1.01	0.72	0.97	0.96	3536	11	12	3524	20	24	3504	53	63	0.9
14WA2	198*	5.1	60	1.45	1.59	0.28	0.28	27.11	1.62	0.69	1.59	0.98	3388	12	13	3387	32	35	3386	84	91	0.0
14WA2	199*	7.3	87	1.46	1.83	0.28	0.26	26.73	1.85	0.68	1.83	0.99	3384	11	12	3374	36	39	3356	96	102	0.8
14WA2	200	10.9	129	1.45	2.24	0.29	0.26	27.15	2.26	0.69	2.24	0.99	3390	11	12	3389	44	46	3386	118	123	0.1
14WA2	201	15.5	148	1.16	2.15	0.45	0.26	53.44	2.16	0.86	2.15	0.99	4086	11	12	4059	43	45	4004	128	134	2.0
14WA2	202	9.6	114	1.47	2.13	0.29	0.26	26.98	2.14	0.68	2.13	0.99	3401	11	12	3383	42	44	3352	111	116	1.4
14WA2	206[a]	13.0	152	1.43	1.79	0.30	0.27	28.89	1.81	0.70	1.79	0.99	3473	11	12	3450	36	38	3409	95	101	1.8
14WA2	208	17.3	189	1.34	1.01	0.35	0.26	35.48	1.04	0.74	1.01	0.97	3689	11	12	3652	21	25	3585	56	66	2.8
14WA2	208	22.0	241	1.34	0.94	0.35	0.24	35.77	0.97	0.74	0.94	0.97	3701	11	12	3660	20	24	3585	52	63	3.1
14WA2	218[a]	4.5	54	1.45	1.09	0.29	0.30	27.32	1.13	0.69	1.09	0.97	3407	12	13	3395	23	26	3375	57	67	0.9
14WA2	219	17.6	218	1.51	1.74	0.29	0.26	26.18	1.76	0.66	1.74	0.99	3403	11	12	3353	35	37	3271	89	95	3.9
14WA2	219	7.4	87	1.45	1.45	0.29	0.26	27.07	1.48	0.69	1.45	0.98	3392	11	12	3386	29	32	3375	76	84	0.5
14WA2	221[a]	18.3	223	1.48	1.33	0.29	0.26	26.89	1.35	0.68	1.33	0.98	3407	11	12	3379	27	30	3333	69	77	2.2
14WA2	225	11.0	133	1.48	2.14	0.28	0.26	26.54	2.16	0.68	2.14	0.99	3387	11	12	3367	42	44	3333	112	116	1.6
14WA2	228[a]	8.9	106	1.46	1.17	0.28	0.26	26.86	1.20	0.68	1.17	0.98	3390	11	12	3379	24	27	3360	61	70	0.9
14WA2	229*	8.9	106	1.46	1.31	0.28	0.26	26.87	1.34	0.69	1.31	0.98	3386	11	12	3379	27	30	3367	69	77	0.5
14WA2	237*	13.6	161	1.43	2.30	0.29	0.26	28.20	2.31	0.70	2.30	0.99	3436	11	12	3426	46	47	3409	122	126	0.8
14WA2	238*	14.9	165	1.36	1.49	0.34	0.25	34.54	1.52	0.74	1.49	0.99	3665	11	12	3626	30	33	3556	82	89	3.0
14WA2	246	11.7	146	1.48	1.26	0.28	0.26	26.38	1.29	0.68	1.26	0.98	3382	11	12	3361	26	29	3325	66	74	1.7
14WA2	247	2.9	36	1.46	1.24	0.29	0.31	27.07	1.28	0.69	1.24	0.97	3399	12	13	3386	25	29	3364	65	73	1.0
14WA2	249[a]	12.6	157	1.49	1.26	0.29	0.26	26.48	1.29	0.67	1.26	0.98	3395	11	12	3364	26	29	3314	66	74	2.4
14WA2	251[a]	10.8	134	1.46	1.24	0.29	0.26	26.88	1.27	0.68	1.24	0.98	3393	11	12	3379	25	29	3356	65	74	1.1
14WA2	251[a]	11.1	138	1.48	1.26	0.29	0.26	26.63	1.28	0.68	1.26	0.98	3392	11	12	3370	26	29	3333	65	74	1.7
14WA2	251[a]	8.9	109	1.47	1.54	0.28	0.28	26.75	1.57	0.68	1.54	0.98	3388	12	13	3374	31	34	3352	81	87	1.0
14WA2	256[a]	7.1	84	1.39	1.39	0.31	0.29	30.34	1.42	0.72	1.39	0.98	3499	12	13	3498	28	31	3496	75	83	0.1
14WA2	258[a]	7.6	98	1.53	1.07	0.27	0.26	24.43	1.10	0.66	1.07	0.97	3309	11	12	3286	22	26	3248	55	64	1.8
14WA2	259[a]	8.1	101	1.47	1.99	0.29	0.26	26.86	2.01	0.68	1.99	0.99	3401	11	12	3378	40	42	3341	104	109	1.8
14WA2	259[a]	6.9	85	1.46	1.82	0.29	0.26	27.10	1.84	0.69	1.82	0.99	3399	11	12	3387	36	39	3367	96	102	0.9
14WA2	260[a]	6.1	74	1.44	1.65	0.29	0.27	28.01	1.68	0.70	1.65	0.99	3430	11	13	3419	33	36	3402	88	94	0.8
14WA2	260[a]	8.1	100	1.45	1.96	0.29	0.26	27.89	1.97	0.69	1.96	0.99	3434	11	12	3415	39	41	3383	103	109	1.5
14WA3	46	2.7	61	1.43	4.56	0.28	0.35	27.25	4.58	0.70	4.56	1.00	3374	13	14	3393	90	91	3424	243	246	-1.5
14WA3	47	6.0	103	1.09	3.98	0.47	0.26	59.75	3.99	0.92	3.98	1.00	4158	12	12	4170	80	81	4195	246	248	-0.9
14WA3	48	8.7	253	1.88	3.48	0.29	0.25	21.58	3.49	0.53	3.48	1.00	3440	11	12	3165	68	69	2750	156	158	20.1
14WA3	49	6.5	147	1.48	4.90	0.28	0.30	26.35	4.91	0.67	4.90	1.00	3383	12	13	3360	96	97	3321	254	256	1.8
14WA3	53	4.2	77	1.14	4.34	0.43	0.28	51.53	4.35	0.88	4.34	1.00	4007	12	12	4022	87	88	4052	261	264	-1.1

Table S6.1. cont.: *Jack Hills zircons analysed October 2017-September 2018.*

Sam-ple	zircon #	^{206}Pb (mV)	U ppm	^{238}U/ ^{206}Pb	1s%	^{207}Pb/ ^{206}Pb	1s%	^{207}Pb/ ^{235}U	1s%	^{206}Pb/ ^{238}U	1s%	Rho	^{207}Pb-^{206}Pb Age	2s abs	2s $_{sys}$ abs	^{207}Pb-^{235}U Age	2s abs	2s $_{sys}$ abs	^{206}Pb-^{238}U Age	2s abs	2s $_{sys}$ abs	Disc%
14WA3	53	4.6	83	1.16	3.43	0.43	0.29	50.85	3.44	0.86	3.43	1.00	4013	12	12	4009	69	70	4000	205	208	0.3
14WA3	61[a]	7.5	162	1.43	3.08	0.31	0.32	30.20	3.09	0.70	3.08	0.99	3538	13	13	3493	61	62	3417	163	167	3.4
14WA3	62	13.4	298	1.39	4.11	0.29	0.26	28.26	4.12	0.72	4.11	1.00	3393	11	12	3428	81	82	3489	221	224	-2.8
14WA3	64	10.8	295	1.73	3.71	0.31	0.28	24.49	3.72	0.58	3.71	1.00	3505	12	13	3288	73	74	2945	176	178	16.0
14WA3	64	8.7	216	1.61	4.26	0.31	0.27	26.92	4.27	0.62	4.26	1.00	3540	11	12	3380	84	85	3118	211	214	11.9
14WA3	66	3.0	68	1.43	3.72	0.28	0.32	27.08	3.73	0.70	3.72	1.00	3368	13	14	3386	73	74	3417	197	200	-1.4
14WA3	70	3.6	89	1.54	6.31	0.29	0.33	25.61	6.32	0.65	6.31	1.00	3395	13	14	3332	124	124	3228	320	322	4.9
14WA3	71	4.0	92	1.46	3.73	0.28	0.34	26.72	3.74	0.68	3.73	1.00	3382	13	14	3373	73	75	3360	195	198	0.6
14WA3	71	2.7	60	1.38	3.59	0.28	0.41	28.00	3.61	0.72	3.59	0.99	3366	15	16	3419	71	72	3511	194	198	-4.3
14WA3	73	2.1	54	1.56	3.76	0.23	0.39	20.48	3.78	0.64	3.76	0.99	3069	14	16	3114	73	74	3185	189	192	-3.8
14WA3	80	19.8	421	1.36	3.54	0.32	0.27	32.12	3.55	0.73	3.54	1.00	3557	11	12	3554	70	71	3548	193	197	0.2
14WA3	81[a]	11.6	270	1.52	3.19	0.28	0.25	25.63	3.20	0.66	3.19	1.00	3374	11	12	3332	63	64	3263	163	167	3.3
14WA3	83[a]	5.8	101	1.11	3.66	0.45	0.29	55.52	3.67	0.90	3.66	1.00	4075	12	12	4097	74	75	4141	224	228	-1.6
14WA3	83[a]	7.9	140	1.09	4.92	0.44	0.30	55.92	4.93	0.91	4.92	1.00	4064	12	13	4104	99	99	4185	303	306	-3.0
14WA3	85	5.8	129	1.37	2.05	0.30	0.30	30.33	2.07	0.73	2.05	0.99	3473	12	13	3497	41	43	3541	112	117	-2.0
16WA5	3*	25.3	249	1.14	0.86	0.47	0.09	56.41	0.86	0.88	0.86	0.99	4139	9	9	4112	18	22	4059	52	65	1.9
16WA5	3*	19.4	189		0.90	0.47	0.09	57.18	0.90	0.89	0.90	1.00	4137	9	9	4126	19	23	4104	55	68	0.8
16WA5	4	5.4	73	1.45	0.94	0.28	0.14	26.99	0.96	0.69	0.94	0.99	3388	9	10	3383	19	23	3375	50	60	0.4
16WA5	4	7.2	96	1.45	0.95	0.28	0.15	26.90	0.96	0.69	0.95	0.99	3384	9	10	3380	19	23	3373	50	60	0.3
16WA5	5	11.6	124	1.17	0.76	0.43	0.11	50.62	0.77	0.85	0.76	0.99	4017	9	9	4005	16	21	3980	45	59	0.9
16WA5	7	17.9	226	1.39	1.25	0.42	0.14	41.28	1.26	0.72	1.25	0.99	3965	9	10	3802	25	29	3500	68	76	11.7
16WA5	8	15.6	807	5.29	3.44	0.29	0.14	7.57	3.44	0.19	3.44	1.00	3421	9	10	2182	62	63	1116	70	72	67.4
16WA5	9	11.2	149	1.45	0.94	0.29	0.12	27.33	0.95	0.69	0.94	0.99	3400	8	10	3395	19	23	3386	50	60	0.4
16WA5	10	12.8	173	1.47	1.03	0.29	0.14	26.98	1.04	0.68	1.03	0.99	3405	9	10	3383	21	25	3344	54	64	1.8
16WA5	11*	9.1	120	1.45	0.80	0.29	0.13	27.20	0.81	0.69	0.80	0.99	3393	9	10	3391	16	21	3386	42	54	0.2
16WA5	11*	7.9	106	1.47	0.88	0.29	0.13	26.84	0.89	0.68	0.88	0.99	3393	9	10	3378	18	22	3352	46	57	1.2
16WA5	12	18.4	249	1.47	0.81	0.29	0.12	27.07	0.82	0.68	0.81	0.99	3413	8	10	3386	17	21	3342	42	54	2.1
16WA5	13	5.2	56	1.16	1.05	0.41	0.19	48.63	1.07	0.86	1.05	0.98	3948	10	11	3965	22	26	3997	63	74	-1.2
16WA5	13	30.7	750	2.61	2.09	0.46	0.12	24.08	2.09	0.38	2.09	1.00	4105	9	10	3271	41	43	2090	75	78	49.1
16WA5	16	9.0	125	1.51	1.21	0.28	0.14	25.94	1.22	0.66	1.21	0.99	3386	9	10	3344	24	28	3275	62	71	3.3
16WA5	16	7.8	104	1.44	1.01	0.28	0.14	27.12	1.02	0.69	1.01	0.99	3382	9	10	3388	20	24	3398	53	64	-0.5
16WA5	17*	7.1	95	1.45	1.08	0.28	0.14	27.14	1.09	0.69	1.08	0.99	3387	9	10	3389	22	26	3390	57	67	-0.1
16WA5	18*	8.0	104	1.41	0.92	0.30	0.16	29.00	0.93	0.71	0.92	0.99	3452	9	10	3454	19	23	3457	49	60	-0.2
16WA5	18*	11.7	161	1.42	0.85	0.30	0.12	28.81	0.86	0.70	0.85	0.99	3456	9	10	3447	18	22	3432	46	57	0.7
16WA5	19	10.0	140	1.45	0.72	0.29	0.12	27.15	0.73	0.69	0.72	0.99	3390	9	10	3389	15	20	3387	38	51	0.1
16WA5	20*	7.5	134	1.46	2.78	0.29	0.19	27.76	2.79	0.68	2.78	1.00	3443	10	11	3411	55	56	3356	146	149	2.5
16WA5	20*	13.1	133	1.46	0.63	0.30	0.34	28.03	0.72	0.69	0.63	0.88	3449	13	14	3420	15	20	3372	33	48	2.2

Table S6.1. cont.: *Jack Hills zircons analysed October 2017-September 2018.*

Sample	zircon #	^{206}Pb (mV)	U ppm	^{238}U/^{206}Pb	1s%	^{207}Pb/^{206}Pb	1s%	^{207}Pb/^{235}U	1s%	^{206}Pb/^{238}U	1s%	Rho	^{207}Pb-^{206}Pb Age	2s abs	2s $_{sys}$ abs	^{207}Pb-^{235}U Age	2s abs	2s $_{sys}$ abs	^{206}Pb-^{238}U Age	2s abs	2s $_{sys}$ abs	Disc%
16WA5	20*	9.1	126	1.42	0.78	0.29	0.15	28.49	0.80	0.70	0.78	0.98	3438	9	10	3436	16	21	3434	42	54	0.1
16WA5	20*	9.4	129	1.41	0.85	0.29	0.13	28.78	0.86	0.71	0.85	0.99	3442	9	10	3446	17	22	3453	45	57	-0.3
16WA5	23	25.1	362	1.47	0.95	0.29	0.13	27.26	0.96	0.68	0.95	0.99	3419	9	10	3393	19	23	3348	50	60	2.1
16WA5	25	6.0	82	1.41	0.85	0.29	0.19	28.64	0.87	0.71	0.85	0.98	3437	10	11	3441	18	22	3449	45	57	-0.3
16WA5	26*	20.5	287	1.45	0.80	0.29	0.10	28.07	0.80	0.69	0.80	0.99	3441	8	10	3422	16	21	3388	42	54	1.5
16WA5	27	23.2	309	1.39	0.83	0.31	0.12	31.14	0.84	0.72	0.83	0.99	3540	9	10	3523	17	22	3495	45	57	1.2
16WA5	28	29.2	430	1.52	0.91	0.34	0.28	30.42	0.95	0.66	0.91	0.96	3642	12	13	3500	19	23	3259	47	58	10.5
16WA5	29	21.1	301	1.47	0.81	0.29	0.11	26.99	0.82	0.68	0.81	0.99	3410	8	10	3383	17	21	3338	42	54	2.1
16WA5	29	19.2	193	1.48	1.26	0.29	0.28	27.02	1.29	0.68	1.26	0.98	3414	12	13	3384	26	29	3333	65	74	2.4
16WA5	30	24.7	199	1.18	1.35	0.43	0.28	50.94	1.38	0.85	1.35	0.98	4032	12	12	4011	28	31	3969	80	89	1.5
16WA5	31*	13.4	127	1.40	0.63	0.31	0.31	30.12	0.70	0.71	0.63	0.90	3501	12	13	3491	15	20	3472	34	49	0.8
16WA5	34*	21.8	213	1.44	1.37	0.29	0.28	27.65	1.40	0.69	1.37	0.98	3412	12	13	3407	28	31	3398	72	80	0.4
16WA5	37[a]	24.5	267	1.61	1.85	0.29	0.27	24.98	1.87	0.62	1.85	0.99	3422	12	13	3308	37	39	3122	91	97	8.8
16WA5	40*	9.6	93	1.45	1.52	0.28	0.29	26.61	1.55	0.69	1.52	0.98	3359	12	13	3369	31	33	3386	80	87	-0.8
16WA5	41	7.3	71	1.46	0.63	0.29	0.30	27.03	0.69	0.69	0.63	0.90	3396	12	13	3385	14	19	3365	33	47	0.9
16WA5	42	14.3	144	1.48	0.67	0.28	0.28	26.43	0.72	0.67	0.67	0.92	3388	12	13	3363	15	20	3320	35	49	2.0
16WA5	43[a]	10.7	102	1.42	0.59	0.29	0.28	27.85	0.66	0.71	0.59	0.90	3396	12	13	3414	14	19	3444	32	47	-1.4
16WA5	45*	6.1	108	1.47	2.87	0.29	0.19	26.71	2.88	0.68	2.87	1.00	3392	10	11	3373	57	58	3341	150	154	1.5
16WA5	45*	6.3	64	1.44	0.79	0.28	0.35	27.23	0.87	0.70	0.79	0.91	3386	13	14	3392	18	22	3402	42	54	-0.5
16WA5	45*	10.3	100	1.47	0.88	0.29	0.28	26.80	0.92	0.68	0.88	0.95	3393	12	13	3376	19	23	3348	46	57	1.3
16WA5	47	27.1	322	1.78	0.65	0.24	0.30	18.28	0.72	0.56	0.65	0.91	3096	12	13	3005	14	19	2870	30	43	7.3
16WA5	48	6.2	49	1.18	1.00	0.41	0.32	47.91	1.05	0.85	1.00	0.95	3949	13	13	3950	22	25	3952	60	71	-0.1
16WA5	50	4.6	82	1.44	3.16	0.29	0.23	27.43	3.17	0.70	3.16	1.00	3395	10	12	3399	62	64	3405	167	171	-0.3
16WA5	50	7.7	79	1.44	0.67	0.29	0.35	27.27	0.76	0.69	0.67	0.89	3392	13	14	3393	16	20	3395	36	49	-0.1
16WA5	50	10.2	99	1.45	0.94	0.29	0.28	27.16	0.98	0.69	0.94	0.96	3393	12	13	3389	20	24	3383	50	60	0.3
16WA5	52	22.2	882	5.94	2.08	0.29	0.31	6.81	2.10	0.17	2.08	0.99	3437	12	13	2088	37	39	1003	39	40	70.8
16WA5	53	14.6	164	1.67	0.76	0.23	0.28	19.35	0.81	0.60	0.76	0.94	3083	11	13	3059	16	21	3024	37	48	1.9
16WA5	55	4.2	41	1.45	0.87	0.29	0.33	27.17	0.93	0.69	0.87	0.93	3391	13	14	3390	19	23	3386	46	57	0.1
16WA5	56[a]	22.7	210	1.37	0.96	0.33	0.29	33.58	1.00	0.73	0.96	0.96	3630	12	13	3598	20	24	3541	52	63	2.4
16WA5	58	4.9	86	1.45	2.61	0.29	0.23	27.17	2.62	0.69	2.61	1.00	3396	10	12	3390	52	53	3379	137	142	0.5
16WA5	58	8.1	83	1.44	0.79	0.29	0.35	27.42	0.87	0.69	0.79	0.92	3399	13	14	3399	18	22	3398	42	54	0.0
16WA5	58	6.6	65	1.45	0.87	0.29	0.30	27.25	0.92	0.69	0.87	0.95	3394	12	13	3392	19	23	3390	46	57	0.1
16WA5	60[a]	6.3	62	1.45	0.94	0.28	0.30	27.06	0.99	0.69	0.94	0.95	3388	12	13	3386	20	24	3383	50	60	0.1
16WA5	62	16.5	170	1.52	0.99	0.27	0.28	24.07	1.03	0.66	0.99	0.96	3276	12	13	3271	20	24	3263	51	61	0.4
16WA5	63[a]	15.7	151	1.43	1.08	0.29	0.28	27.62	1.11	0.70	1.08	0.97	3403	12	13	3406	22	26	3409	57	66	-0.2
16WA5	64[a]	9.7	91	1.39	0.90	0.30	0.28	30.24	0.94	0.72	0.90	0.96	3492	12	13	3495	19	23	3500	49	60	-0.2
16WA5	66	7.4	131	1.50	2.26	0.28	0.19	25.95	2.26	0.67	2.26	1.00	3379	10	11	3345	45	46	3287	116	121	2.7

Table S6.1. cont.: *Jack Hills zircons analysed October 2017-September 2018.*

Sample	zircon #	^{206}Pb (mV)	U ppm	^{238}U/^{206}Pb	1s%	^{207}Pb/^{206}Pb	1s%	^{207}Pb/^{235}U	1s%	^{206}Pb/^{238}U	1s%	Rho	^{207}Pb-^{206}Pb Age	2s abs	2s $_{sys}$ abs	^{207}Pb-^{235}U Age	2s abs	2s $_{sys}$ abs	^{206}Pb-^{238}U Age	2s abs	2s $_{sys}$ abs	Disc%
16WA5	66	13.7	145	1.47	0.51	0.28	0.34	26.45	0.61	0.68	0.51	0.83	3377	13	14	3363	13	18	3340	27	43	1.1
16WA5	66	9.4	130	2.00	1.80	0.28	0.28	19.66	1.82	0.50	1.80	0.99	3388	12	13	3075	35	38	2618	77	82	22.7
16WA5	69	10.3	99	1.41	1.13	0.30	0.30	29.18	1.17	0.71	1.13	0.97	3458	12	13	3460	23	27	3462	60	70	-0.1
16WA5	70[a]	25.7	249	1.43	1.00	0.31	0.28	29.42	1.04	0.70	1.00	0.96	3499	12	13	3468	21	25	3413	53	63	2.5
16WA5	76[a]	5.2	54	1.43	1.43	0.30	0.30	28.81	1.46	0.70	1.43	0.98	3465	12	13	3447	29	32	3417	76	83	1.4
16WA5	79	10.7	97	1.23	1.98	0.39	0.32	43.50	2.00	0.81	1.98	0.99	3869	13	13	3854	40	42	3825	114	120	1.1
16WA5	81*	13.7	231	1.41	2.82	0.32	0.17	31.13	2.82	0.71	2.82	1.00	3560	10	11	3523	56	57	3458	151	155	2.9
16WA5	81*	21.8	240	1.50	1.05	0.31	0.34	28.40	1.11	0.67	1.05	0.95	3519	13	14	3433	22	26	3287	54	64	6.6
16WA5	81*	23.3	233	1.39	0.58	0.32	0.28	31.70	0.65	0.72	0.58	0.90	3568	12	13	3541	14	19	3494	32	47	2.1
16WA5	84	12.3	129	1.47	0.81	0.28	0.28	26.48	0.86	0.68	0.81	0.94	3381	12	13	3365	17	22	3337	42	54	1.3
16WA5	86*	6.8	115	1.41	3.24	0.30	0.20	29.03	3.25	0.71	3.24	1.00	3452	10	11	3455	64	65	3458	173	177	-0.2
16WA5	86*	11.4	118	1.42	0.52	0.30	0.34	28.76	0.62	0.70	0.52	0.84	3454	13	14	3445	13	19	3430	28	44	0.7
16WA5	86*	10.4	106	1.43	0.57	0.30	0.29	28.71	0.64	0.70	0.57	0.89	3455	12	13	3444	13	19	3425	31	46	0.8
16WA5	87	9.2	97	1.46	0.80	0.29	0.30	27.06	0.86	0.69	0.80	0.94	3399	12	13	3386	17	22	3364	42	54	1.0
16WA5	88[a]	17.5	188	1.49	0.66	0.28	0.28	26.29	0.71	0.67	0.66	0.92	3388	12	13	3357	15	20	3306	34	48	2.4
16WA5	92[a]	8.0	83	1.44	0.58	0.29	0.28	27.50	0.65	0.70	0.58	0.90	3399	12	13	3401	13	19	3405	31	46	-0.2
16WA5	99	7.1	73	1.45	0.80	0.28	0.30	27.01	0.85	0.69	0.80	0.94	3389	12	13	3384	17	22	3375	42	54	0.4
16WA5	100	21.7	368	2.40	1.32	0.27	0.28	15.66	1.35	0.42	1.32	0.98	3320	11	13	2856	26	29	2247	50	56	32.3
16WA5	103[a]	21.1	218	1.45	0.79	0.29	0.29	27.65	0.85	0.69	0.79	0.94	3417	12	13	3407	17	22	3390	42	54	0.8
16WA5	104	21.4	225	1.47	0.67	0.29	0.28	27.04	0.72	0.68	0.67	0.92	3406	12	13	3385	15	20	3349	35	49	1.7
16WA5	109	8.5	86	1.41	1.27	0.30	0.28	29.76	1.30	0.71	1.27	0.98	3493	12	13	3479	26	29	3455	68	76	1.1
16WA5	110[a]	17.0	160	1.34	0.80	0.33	0.29	34.24	0.85	0.75	0.80	0.94	3624	12	13	3617	17	22	3604	44	57	0.6
16WA5	112	10.2	83	1.14	0.97	0.45	0.28	53.90	1.01	0.88	0.97	0.96	4071	12	12	4067	21	25	4059	59	70	0.3
16WA5	115	3.1	35	1.58	1.58	0.27	0.33	23.54	1.62	0.63	1.58	0.98	3307	13	14	3250	32	34	3157	79	85	4.5
16WA5	118	9.8	101	1.45	1.30	0.28	0.28	27.08	1.33	0.69	1.30	0.98	3388	12	13	3386	27	30	3383	69	77	0.2
16WA5	120	14.5	147	1.45	0.94	0.29	0.28	27.36	0.98	0.69	0.94	0.96	3409	12	13	3396	20	24	3375	50	60	1.0
16WA5	121[a]	9.5	167	1.48	1.41	0.29	0.19	26.83	1.42	0.67	1.41	0.99	3411	10	11	3377	28	31	3321	73	80	2.6
16WA5	121[a]	14.1	149	1.44	0.72	0.29	0.33	27.56	0.79	0.70	0.72	0.91	3404	13	14	3403	16	21	3402	38	51	0.1
16WA5	121[a]	18.3	185	1.44	0.37	0.29	0.28	27.62	0.46	0.70	0.37	0.80	3408	12	13	3406	10	17	3402	20	40	0.2
16WA5	122*	11.2	100	1.16	0.57	0.43	0.09	51.58	0.58	0.86	0.57	0.99	4032	9	9	4023	13	18	4006	34	52	0.6
16WA5	122*	10.1	89	1.14	0.53	0.44	0.09	52.70	0.53	0.87	0.53	0.99	4043	9	9	4045	12	18	4049	32	51	-0.2
16WA5	123*	10.1	110	1.42	0.62	0.30	0.10	29.52	0.63	0.71	0.62	0.99	3488	8	10	3471	13	19	3442	33	48	1.3
16WA5	125	19.5	206	1.37	0.59	0.31	0.09	31.61	0.60	0.73	0.59	0.99	3542	8	10	3538	13	18	3531	32	48	0.3
16WA5	126	35.3	1510	5.41	2.97	0.28	0.34	7.06	2.99	0.19	2.97	0.99	3345	13	14	2119	53	55	1094	60	61	67.3
16WA5	127[a]	18.3	208	1.46	0.52	0.29	0.09	27.06	0.53	0.68	0.52	0.99	3401	8	10	3385	11	17	3359	27	44	1.2
16WA5	127[a]	18.8	214	1.47	0.70	0.29	0.09	27.04	0.70	0.68	0.70	0.99	3407	8	10	3385	15	20	3348	37	50	1.7
16WA5	128	20.1	213	1.37	0.47	0.32	0.08	32.20	0.47	0.73	0.47	0.99	3573	8	9	3557	11	17	3527	26	44	1.3

Table S6.1. cont.: *Jack Hills zircons analysed October 2017-September 2018.*

Sample	zircon #	^{206}Pb (mV)	U ppm	^{238}U/^{206}Pb	1s%	^{207}Pb/^{206}Pb	1s%	^{207}Pb/^{235}U	1s%	^{206}Pb/^{238}U	1s%	Rho	^{207}Pb-^{206}Pb Age	2s abs	2s $_{sys}$ abs	^{207}Pb-^{235}U Age	2s abs	2s $_{sys}$ abs	^{206}Pb-^{238}U Age	2s abs	2s $_{sys}$ abs	Disc%
16WA5	129	23.5	349	1.89	1.23	0.28	0.10	20.50	1.23	0.53	1.23	1.00	3369	8	10	3115	24	28	2737	55	62	18.8
16WA5	130*	9.1	96	1.37	0.62	0.30	0.10	30.57	0.62	0.73	0.62	0.99	3490	8	10	3505	13	19	3533	34	49	-1.2
16WA5	131*	22.6	181	1.49	1.05	0.29	0.35	26.63	1.10	0.67	1.05	0.95	3411	13	14	3370	22	26	3302	54	64	3.2
16WA5	131*	23.5	182	1.46	1.24	0.29	0.35	27.31	1.29	0.69	1.24	0.96	3411	13	14	3395	26	29	3367	65	73	1.3
16WA5	133	15.7	121	1.45	1.01	0.28	0.35	27.07	1.07	0.69	1.01	0.94	3386	13	14	3386	22	25	3386	53	64	0.0
16WA5	135*	26.8	150	1.06	0.69	0.54	0.34	70.19	0.77	0.95	0.69	0.89	4349	13	13	4331	16	21	4292	43	59	1.3
16WA5	135*	19.3	117	1.14	0.97	0.51	0.36	61.39	1.03	0.88	0.97	0.94	4259	14	14	4197	21	25	4069	58	70	4.4
16WA5	135*	5.6	46	1.13	0.90	0.46	0.65	56.05	1.11	0.89	0.90	0.81	4114	21	21	4106	23	26	4090	55	67	0.6
16WA5	135*	8.7	63	1.07	0.54	0.54	0.30	69.49	0.61	0.93	0.54	0.88	4358	12	12	4321	14	19	4242	34	52	2.7
16WA5	135*	12.7	97	1.05	1.05	0.54	0.37	70.40	1.12	0.95	1.05	0.94	4347	14	14	4334	23	27	4305	66	78	1.0
16WA5	135*	13.7	102	1.07	0.86	0.52	0.30	67.42	0.91	0.93	0.86	0.95	4309	12	12	4291	19	23	4252	54	67	1.3
16WA5	135*	13.6	99	1.07	0.59	0.53	0.28	67.78	0.66	0.93	0.59	0.90	4320	12	12	4296	14	19	4245	37	55	1.7
16WA5	137	6.9	52	1.42	1.14	0.29	0.37	27.66	1.19	0.70	1.14	0.95	3390	14	15	3407	24	27	3436	61	70	-1.3
16WA5	137	9.1	70	1.46	0.80	0.29	0.35	27.00	0.87	0.69	0.80	0.92	3391	13	14	3383	18	22	3371	42	54	0.6
16WA5	139	19.5	141	1.37	1.03	0.33	0.35	33.33	1.09	0.73	1.03	0.95	3626	13	14	3590	22	26	3526	56	66	2.8
16WA5	141	21.7	164	1.42	0.85	0.30	0.35	29.15	0.92	0.71	0.85	0.92	3468	13	14	3459	19	23	3443	45	57	0.7
16WA5	144*	11.9	87	1.39	1.46	0.30	0.35	29.89	1.51	0.72	1.46	0.97	3482	13	14	3483	30	33	3485	79	86	-0.1
16WA5	145	32.1	382	1.42	1.13	0.32	0.10	31.24	1.14	0.71	1.13	1.00	3576	9	10	3527	23	26	3440	61	70	3.8
16WA5	146[a]	7.7	87	1.37	1.85	0.30	0.15	30.52	1.86	0.73	1.85	1.00	3491	9	10	3504	37	39	3526	101	107	-1.0
16WA5	147	7.1	87	1.49	1.19	0.28	0.15	25.90	1.20	0.67	1.19	0.99	3360	9	10	3343	24	27	3314	62	70	1.4
16WA5	150	19.4	228	1.43	1.00	0.29	0.10	27.65	1.01	0.70	1.00	0.99	3401	8	10	3407	20	24	3417	53	63	-0.5
16WA5	154	28.3	368	1.57	1.02	0.29	0.10	25.19	1.03	0.64	1.02	1.00	3405	8	10	3316	21	24	3169	51	61	6.9
16WA5	156[a]	6.0	71	1.43	1.07	0.28	0.17	27.14	1.09	0.70	1.07	0.99	3374	9	11	3388	22	25	3413	57	67	-1.2
16WA5	157	24.0	327	1.65	1.24	0.24	0.10	19.69	1.24	0.61	1.24	1.00	3088	8	10	3076	24	28	3058	60	68	1.0
16WA5	163	5.5	65	1.42	1.07	0.28	0.13	27.52	1.08	0.70	1.07	0.99	3387	9	10	3402	22	25	3428	57	67	-1.2
16WA5	163[a]	4.4	52	1.45	1.45	0.28	0.21	27.07	1.46	0.69	1.45	0.99	3386	10	11	3386	29	32	3386	76	83	0.0
16WA5	164[a]	14.6	145	1.20	1.38	0.39	0.10	45.20	1.38	0.83	1.38	1.00	3883	9	9	3892	28	31	3910	81	89	-0.7
16WA5	165	14.9	186	1.44	1.44	0.29	0.13	27.63	1.44	0.70	1.44	1.00	3406	9	10	3406	29	32	3405	76	84	0.0
16WA5	168*	26.1	288	1.25	2.80	0.37	0.45	40.70	2.84	0.80	2.80	0.99	3782	16	16	3788	56	58	3800	161	165	-0.5
16WA5	168*	15.2	165	1.26	1.33	0.36	0.10	39.57	1.33	0.79	1.33	1.00	3762	9	10	3760	27	30	3757	76	84	0.1
16WA5	170	25.4	292	1.33	1.07	0.32	0.23	33.56	1.09	0.75	1.07	0.98	3589	11	12	3597	22	26	3611	59	69	-0.6
16WA5	173[a]	16.0	208	1.50	0.90	0.27	0.12	24.96	0.91	0.67	0.90	0.99	3315	8	10	3307	18	23	3293	47	57	0.7
16WA5	174	17.9	212	1.37	0.89	0.32	0.10	31.75	0.90	0.73	0.89	0.99	3549	8	10	3543	18	23	3530	49	60	0.5
16WA5	175[a]	8.3	103	1.44	0.79	0.29	0.13	27.31	0.80	0.70	0.79	0.99	3390	9	10	3395	16	21	3402	42	54	-0.4
16WA6	4	15.7	159	1.86	1.02	0.28	0.22	20.48	1.04	0.54	1.02	0.98	3338	10	12	3114	21	24	2779	46	55	16.7
16WA6	6[a]	18.2	144	1.43	0.79	0.31	0.24	29.45	0.83	0.70	0.79	0.96	3503	11	12	3469	17	21	3409	42	54	2.7
16WA6	6[a]	12.8	100	1.41	0.92	0.30	0.21	29.73	0.94	0.71	0.92	0.97	3494	10	11	3478	19	23	3451	49	60	1.2

Table S6.1. cont.: *Jack Hills zircons analysed October 2017-September 2018.*

Sample	zircon #	^{206}Pb (mV)	U ppm	^{238}U/^{206}Pb	1s%	^{207}Pb/^{206}Pb	1s%	^{207}Pb/^{235}U	1s%	^{206}Pb/^{238}U	1s%	Rho	^{207}Pb-^{206}Pb Age	2s abs	2s $_{sys}$ abs	^{207}Pb-^{235}U Age	2s abs	2s $_{sys}$ abs	^{206}Pb-^{238}U Age	2s abs	2s $_{sys}$ abs	Disc%
16WA6	9[a]	22.4	184	1.48	0.74	0.29	0.22	26.99	0.77	0.68	0.74	0.96	3415	10	12	3383	16	21	3329	39	51	2.5
16WA6	12	14.1	172	2.19	1.31	0.30	0.21	19.05	1.33	0.46	1.31	0.99	3482	10	11	3044	26	29	2426	53	59	30.3
16WA6	13	12.7	104	1.47	1.10	0.29	0.23	26.69	1.13	0.68	1.10	0.98	3391	10	12	3372	23	26	3341	58	67	1.5
16WA6	13	4.0	55	1.43	0.93	0.28	0.25	27.15	0.96	0.70	0.93	0.97	3377	11	12	3389	19	24	3409	50	60	-1.0
16WA6	15[a]	8.5	116	1.39	1.04	0.29	0.23	28.49	1.06	0.72	1.04	0.98	3397	10	12	3436	21	25	3504	56	66	-3.1
16WA6	16[a]	4.7	67	1.45	0.94	0.28	0.25	26.95	0.97	0.69	0.94	0.97	3377	11	12	3382	20	24	3390	50	60	-0.4
16WA6	16[a]	4.9	70	1.44	1.01	0.28	0.25	27.03	1.04	0.69	1.01	0.97	3379	11	12	3385	21	25	3394	53	64	-0.4
16WA6	17[a]	5.8	81	1.45	0.80	0.29	0.25	27.19	0.83	0.69	0.80	0.96	3392	11	12	3390	17	21	3387	42	54	0.2
16WA6	17[a]	4.0	58	1.45	0.80	0.28	0.26	27.00	0.84	0.69	0.80	0.95	3386	11	12	3383	17	22	3379	42	54	0.2
16WA6	18[a]	22.5	328	1.48	1.19	0.28	0.31	25.79	1.23	0.67	1.19	0.97	3349	12	13	3338	24	28	3321	62	70	0.8
16WA6	20[a]	7.6	103	1.38	0.90	0.30	0.23	30.36	0.93	0.73	0.90	0.97	3489	11	12	3499	19	23	3515	49	60	-0.7
16WA6	22	8.0	115	1.45	0.80	0.29	0.23	27.24	0.83	0.69	0.80	0.96	3398	10	12	3392	17	21	3383	42	54	0.4
16WA6	23[a]	12.0	173	1.47	0.95	0.28	0.23	26.37	0.98	0.68	0.95	0.97	3365	11	12	3360	20	24	3352	50	61	0.4

Table S6.1: U-Pb analysis of 14WA2, 14WA3, 16WA5 and 16WA6. These data required additional systematic uncertainty propagation into final age uncertainties owing to excess variance of VRM Plesovice. Values included in this propagation are given in Chapter 2. Disc%= % discordance of ^{206}Pb-^{238}U age and ^{207}Pb-^{206}Pb age. Uncertainties presented as "s", which is standard error. *Zircons with oscillatory zoning in the Pb-Hf subset of Chapter 5. [a] zircon included in oscillatory zoned grains (n=135) in Figure 5.7 but not the Pb-Hf subset, as they were not analysed for Hf.

Table S6.2 : *Jack Hills zircons analysed May 2017*

Sample		Concentration		For Tera-Wasserberg plot				For Wetherill Plot					Ages									Conc
Sam-ple	zircon #	^{206}Pb (mV)	U ppm	^{238}U/^{206}Pb	1s%	^{207}Pb/^{206}Pb	1s%	^{207}Pb/^{235}U	1s%	^{206}Pb/^{238}U	1s%	Rho	^{207}Pb-^{206}Pb Age	2s abs	2s $_{sys}$ abs	^{207}Pb-^{235}U Age	2s abs	2s $_{sys}$ abs	^{206}Pb-^{238}U Age	2s abs	2s $_{sys}$ abs	Disc%
14WA4	2	5.2	116	1.43	1.43	0.28	0.94	27.16	1.71	0.70	1.43	0.84	3373	30	30	3389	34	34	3417	76	76	-1.3
14WA4	4	10.6	233	1.47	1.77	0.28	0.93	26.56	2.00	0.68	1.77	0.88	3383	30	30	3367	39	39	3341	92	92	1.3
14WA4	5*	11.6	246	1.51	1.89	0.28	0.92	25.91	2.10	0.66	1.89	0.90	3382	30	30	3343	41	41	3279	97	97	3.1
14WA4	9	3.0	58	1.47	2.79	0.28	0.94	26.33	2.95	0.68	2.79	0.95	3368	30	30	3359	58	58	3344	146	146	0.7
14WA4	11*	4.7	92	1.57	1.57	0.30	0.92	26.25	1.82	0.64	1.57	0.86	3465	30	30	3356	36	36	3177	79	79	8.3
14WA4	12	4.3	74	1.44	4.02	0.28	0.97	26.79	4.14	0.70	4.02	0.97	3358	31	31	3376	81	81	3405	213	213	-1.4
14WA4	15*	4.9	63	1.15	2.48	0.43	0.93	51.30	2.65	0.87	2.48	0.94	4016	29	29	4018	53	53	4021	149	149	-0.1
14WA4	18*	11.7	167	1.34	2.75	0.31	0.92	31.80	2.90	0.75	2.75	0.95	3519	29	29	3544	57	57	3589	152	152	-2.0
14WA4	20*	6.4	74	1.13	1.58	0.46	0.93	56.15	1.83	0.89	1.58	0.86	4115	29	29	4108	37	37	4093	96	96	0.5
14WA4	21	12.8	178	1.43	2.92	0.28	0.91	27.16	3.06	0.70	2.92	0.96	3369	29	29	3389	60	60	3424	155	155	-1.7
14WA4	22	3.7	51	1.46	2.33	0.28	0.95	26.42	2.52	0.69	2.33	0.93	3359	31	31	3362	49	49	3367	122	122	-0.3
14WA4	23	3.1	33	1.18	2.89	0.42	0.95	49.31	3.04	0.85	2.89	0.95	3990	30	30	3978	61	61	3955	171	171	0.9
14WA4	24	6.4	82	1.44	2.51	0.29	0.94	28.11	2.68	0.70	2.51	0.94	3433	30	30	3423	53	53	3405	133	133	0.8
14WA4	28	4.0	50	1.44	2.30	0.28	0.93	26.86	2.48	0.70	2.30	0.93	3364	30	30	3378	49	49	3402	122	122	-1.1
14WA4	29	4.7	58	1.44	2.74	0.28	0.92	26.94	2.89	0.69	2.74	0.95	3372	30	30	3381	57	57	3398	145	145	-0.8
14WA4	30	7.0	75	1.27	2.22	0.36	0.96	39.18	2.41	0.79	2.22	0.92	3749	30	30	3750	48	48	3753	126	126	-0.1
14WA4	33	11.9	142	1.45	2.61	0.28	0.91	26.65	2.77	0.69	2.61	0.94	3366	29	29	3371	54	54	3379	137	137	-0.4
14WA4	37[a]	4.7	58	1.45	2.60	0.28	0.93	26.77	2.76	0.69	2.60	0.94	3366	30	30	3375	54	54	3390	137	137	-0.7
14WA4	38	11.2	143	1.51	4.46	0.28	0.92	25.72	4.56	0.66	4.46	0.98	3375	30	30	3336	89	89	3271	229	229	3.1
14WA4	40	7.6	180	1.35	1.48	0.31	0.93	31.83	1.75	0.74	1.48	0.85	3529	30	30	3545	35	35	3574	82	82	-1.3
14WA4	41*	5.5	135	1.38	2.00	0.31	0.92	30.91	2.20	0.73	2.00	0.91	3517	29	29	3516	44	44	3515	108	108	0.1
14WA4	42*	12.0	155	1.45	2.46	0.28	0.92	26.96	2.63	0.69	2.46	0.94	3379	30	30	3382	52	52	3386	130	130	-0.2
14WA4	43	3.7	92	1.43	2.22	0.28	0.93	26.86	2.41	0.70	2.22	0.92	3358	30	30	3378	47	47	3413	118	118	-1.6
14WA4	44	13.7	351	1.46	1.46	0.28	0.92	26.57	1.73	0.68	1.46	0.85	3375	30	30	3368	34	34	3356	77	77	0.6
14WA4	44	5.4	137	1.44	1.80	0.28	0.94	26.87	2.03	0.69	1.80	0.89	3367	30	30	3379	40	40	3398	95	95	-0.9
14WA4	46	13.3	276	1.17	2.63	0.43	0.91	50.99	2.79	0.86	2.63	0.94	4026	29	29	4012	56	56	3983	156	156	1.1
14WA4	49*	5.2	135	1.46	1.53	0.28	0.93	26.52	1.79	0.69	1.53	0.86	3367	30	30	3366	35	35	3364	80	80	0.1
14WA4	51*	3.3	87	1.45	2.62	0.28	0.92	26.70	2.77	0.69	2.62	0.94	3371	30	30	3373	55	55	3375	138	138	-0.1
14WA4	51*	10.0	267	1.45	2.39	0.28	0.91	26.70	2.56	0.69	2.39	0.93	3366	29	29	3372	50	50	3383	126	126	-0.5
14WA4	54[a]	7.9	217	1.46	2.41	0.28	0.92	26.81	2.58	0.69	2.41	0.93	3384	30	30	3376	51	51	3364	126	126	0.6
14WA4	54	6.9	186	1.42	2.28	0.28	0.93	27.47	2.46	0.70	2.28	0.93	3384	30	30	3400	48	48	3428	121	121	-1.3
14WA4	55*	4.3	122	1.47	3.09	0.28	0.96	26.32	3.24	0.68	3.09	0.96	3369	31	31	3359	64	64	3341	161	161	0.9
14WA4	55*	6.5	185	1.46	3.00	0.28	0.94	26.56	3.14	0.68	3.00	0.95	3374	30	30	3368	62	62	3356	157	157	0.6
14WA4	58	4.5	133	1.49	1.87	0.28	0.94	25.93	2.09	0.67	1.87	0.89	3367	30	30	3344	41	41	3306	97	97	1.8
14WA4	60*	15.5	387	1.27	2.60	0.36	0.91	39.24	2.75	0.79	2.60	0.94	3753	29	29	3752	55	55	3750	148	148	0.1
14WA4	64	7.1	209	1.48	1.56	0.28	0.93	26.14	1.81	0.68	1.56	0.86	3368	30	30	3352	36	36	3325	81	81	1.3
14WA4	65	17.3	502	1.48	1.63	0.29	0.91	26.57	1.87	0.68	1.63	0.87	3391	29	29	3368	37	37	3329	85	85	1.8
14WA4	65	13.1	370	1.46	1.97	0.28	0.91	26.90	2.17	0.69	1.97	0.91	3387	29	29	3380	43	43	3367	103	103	0.6
14WA4	66	14.3	393	1.43	3.57	0.30	0.93	28.56	3.69	0.70	3.57	0.97	3447	30	30	3438	72	72	3424	190	190	0.6

Table S6.2. cont.: *Jack Hills zircons analysed May 2017*

Sample	zircon #	^{206}Pb (mV)	U ppm	^{238}U/^{206}Pb	1s%	^{207}Pb/^{206}Pb	1s%	^{207}Pb/^{235}U	1s%	^{206}Pb/^{238}U	1s%	Rho	^{207}Pb-^{206}Pb Age	2s abs	2s $_{sys}$ abs	^{207}Pb-^{235}U Age	2s abs	2s $_{sys}$ abs	^{206}Pb-^{238}U Age	2s abs	2s $_{sys}$ abs	Disc%
14WA4	67*	14.1	384	1.50	4.12	0.28	0.92	25.51	4.22	0.67	4.12	0.98	3348	30	30	3328	83	83	3294	213	213	1.6
14WA4	68	9.9	153	1.16	1.85	0.43	0.92	50.67	2.07	0.86	1.85	0.90	4001	29	29	4005	42	42	4014	111	111	-0.3
14WA4	72	1.8	35	1.45	6.17	0.28	1.01	26.92	6.25	0.69	6.17	0.99	3382	32	32	3381	122	122	3379	324	324	0.1
14WA4	73*	6.5	123	1.47	3.10	0.28	0.92	26.38	3.23	0.68	3.10	0.96	3375	30	30	3361	63	63	3337	161	161	1.1
14WA4	75*	9.3	175	1.48	3.55	0.28	0.93	26.41	3.67	0.68	3.55	0.97	3382	30	30	3362	72	72	3329	185	185	1.6
14WA4	76	3.8	71	1.46	2.92	0.28	0.97	26.83	3.08	0.69	2.92	0.95	3385	31	31	3377	60	60	3364	153	153	0.6
14WA4	77	9.5	184	1.50	2.99	0.28	0.91	26.20	3.13	0.67	2.99	0.96	3387	29	29	3354	61	61	3298	155	155	2.6
14WA4	77	3.9	77	1.50	2.18	0.28	0.94	26.00	2.37	0.67	2.18	0.92	3381	30	30	3347	47	47	3290	112	112	2.7
14WA4	79	7.0	137	1.52	5.16	0.29	0.93	25.94	5.24	0.66	5.16	0.98	3393	30	30	3344	103	103	3263	264	264	3.8
14WA4	80	2.8	56	1.43	5.36	0.28	0.96	27.19	5.45	0.70	5.36	0.98	3374	31	31	3390	107	107	3417	285	285	-1.3
14WA4	83	7.4	148	1.40	3.44	0.31	0.92	30.52	3.56	0.71	3.44	0.97	3525	29	29	3504	70	70	3466	185	185	1.7
14WA4	84	3.6	78	1.45	3.70	0.28	0.95	26.98	3.82	0.69	3.70	0.97	3383	31	31	3383	75	75	3383	195	195	0.0
14WA4	85*	4.5	101	1.46	4.39	0.28	0.94	26.56	4.49	0.68	4.39	0.98	3372	30	30	3367	88	88	3360	230	230	0.4
14WA4	86*	9.3	218	1.47	1.91	0.29	0.92	26.86	2.12	0.68	1.91	0.90	3398	30	30	3378	42	42	3344	100	100	1.6
14WA4	88*	17.4	428	1.47	3.68	0.29	0.91	26.71	3.79	0.68	3.68	0.97	3392	29	29	3373	74	74	3341	192	192	1.5
14WA4	89*	6.9	135	1.14	3.12	0.46	0.92	55.89	3.26	0.88	3.12	0.96	4118	29	29	4103	65	65	4073	189	189	1.1
14WA4	89	3.1	61	1.11	4.28	0.46	1.02	57.39	4.40	0.90	4.28	0.97	4126	31	31	4130	88	88	4138	261	261	-0.3
14WA4	91	5.9	156	1.46	4.16	0.28	0.92	26.74	4.26	0.69	4.16	0.98	3380	30	30	3374	84	84	3364	218	218	0.5
14WA4	92	6.2	174	1.51	6.81	0.28	0.92	25.74	6.87	0.66	6.81	0.99	3376	30	30	3337	134	134	3271	349	349	3.1
14WA4	93	6.9	186	1.46	3.35	0.28	0.94	26.73	3.48	0.69	3.35	0.96	3377	30	30	3374	68	68	3367	176	176	0.3
14WA4	93	3.9	na	1.49	2.17	0.28	0.92	26.14	2.35	0.67	2.17	0.92	3382	30	30	3352	46	46	3302	112	112	2.4
14WA4	94[a]	3.2	na	1.46	2.48	0.28	0.93	26.81	2.65	0.69	2.48	0.94	3382	30	30	3377	52	52	3367	130	130	0.4
14WA4	95[a]	6.5	na	1.50	2.78	0.28	0.93	25.99	2.93	0.67	2.78	0.95	3382	30	30	3346	58	58	3287	143	143	2.8
14WA4	97*	16.3	na	1.42	4.05	0.31	0.92	30.45	4.16	0.70	4.05	0.98	3542	30	30	3502	82	82	3432	216	216	3.1
14WA4	98*	6.8	na	1.50	3.01	0.28	0.92	25.94	3.14	0.67	3.01	0.96	3379	30	30	3344	62	62	3287	155	155	2.7
14WA4	99	4.0	na	1.47	3.02	0.28	0.92	26.48	3.16	0.68	3.02	0.96	3379	30	30	3364	62	62	3341	157	157	1.1
14WA4	101	10.5	na	1.44	4.54	0.30	0.91	28.37	4.63	0.69	4.54	0.98	3452	29	29	3432	91	91	3398	240	240	1.6
14WA4	101	7.6	na	1.44	3.45	0.30	0.93	28.37	3.57	0.70	3.45	0.97	3448	30	30	3432	70	70	3405	182	182	1.2
14WA4	105	4.8	na	1.45	4.93	0.29	0.93	27.12	5.02	0.69	4.93	0.98	3393	30	30	3388	98	98	3379	260	260	0.4
14WA4	105	2.3	na	1.50	5.02	0.28	0.94	25.96	5.11	0.67	5.02	0.98	3376	30	30	3345	100	100	3294	259	259	2.4
14WA4	106	5.7	na	1.50	2.93	0.29	0.93	26.17	3.07	0.67	2.93	0.95	3390	30	30	3353	60	60	3290	151	151	2.9
14WA4	107*	4.0	na	1.49	3.73	0.28	0.95	26.34	3.84	0.67	3.73	0.97	3389	31	31	3359	75	75	3310	193	193	2.3
14WA4	108*	12.1	na	1.53	3.60	0.28	0.91	25.05	3.72	0.65	3.60	0.97	3355	30	30	3310	73	73	3236	183	183	3.6
14WA4	109*	9.7	na	1.14	2.90	0.49	0.92	59.36	3.04	0.88	2.90	0.95	4211	28	28	4163	61	61	4066	175	175	3.4
14WA4	109*	4.9	na	1.14	3.19	0.42	0.97	51.46	3.33	0.88	3.19	0.96	3999	30	30	4021	67	67	4066	192	192	-1.7
14WA4	110	10.1	na	1.44	3.67	0.30	0.93	28.28	3.79	0.69	3.67	0.97	3447	30	30	3429	74	74	3398	194	194	1.4
14WA4	114*	7.5	na	1.50	4.57	0.28	0.92	26.05	4.66	0.67	4.57	0.98	3379	30	30	3349	91	91	3298	236	236	2.4
14WA4	114*	1.9	na	1.48	3.34	0.28	0.94	26.19	3.47	0.67	3.34	0.96	3373	30	30	3354	68	68	3321	173	173	1.5
14WA4	114*	3.2	na	1.47	2.86	0.28	0.94	26.38	3.01	0.68	2.86	0.95	3366	30	30	3361	59	59	3352	150	150	0.4
14WA4	115	1.8	315	1.49	3.36	0.28	0.96	26.04	3.49	0.67	3.36	0.96	3373	31	31	3348	68	68	3306	174	174	2.0
14WA4	118	3.5	95	1.46	3.14	0.30	0.95	28.38	3.28	0.69	3.14	0.96	3473	30	30	3432	64	64	3364	165	165	3.1
14WA4	119	6.6	179	1.47	3.98	0.28	0.93	26.63	4.08	0.68	3.98	0.97	3388	30	30	3370	80	80	3341	207	207	1.4
14WA4	120*	9.9	245	1.38	2.77	0.32	0.92	31.48	2.91	0.72	2.77	0.95	3549	29	29	3534	58	58	3507	150	150	1.2

Table S6.2. cont.: *Jack Hills zircons analysed May 2017*

Sam-ple	zirco n #	^{206}Pb (mV)	U ppm	^{238}U/^{206} Pb	1s%	^{207}Pb/ ^{206}Pb	1s%	^{207}Pb /^{235}U	1s%	^{206}Pb /^{238}U	1s%	Rho	^{207}Pb-^{206}Pb Age	2s abs	2s $_{sys}$ abs	^{207}Pb-^{235}U Age	2s abs	2s $_{sys}$ abs	^{206}Pb-^{238}U Age	2s abs	2s $_{sys}$ abs	Disc%
14WA4	122*	3.6	91	1.44	6.04	0.28	0.94	27.04	6.12	0.70	6.04	0.99	3375	30	30	3385	120	120	3402	319	319	-0.8
14WA4	123[a]	3.1	79	1.46	3.37	0.29	0.93	26.90	3.49	0.68	3.37	0.96	3394	30	30	3380	69	69	3356	176	176	1.1
14WA4	124*	10.2	239	1.41	2.47	0.31	0.93	30.40	2.64	0.71	2.47	0.94	3528	30	30	3500	52	52	3451	132	132	2.2
14WA4	124*	6.2	145	1.44	2.66	0.30	0.92	28.64	2.82	0.70	2.66	0.95	3464	30	30	3441	55	55	3402	141	141	1.8
14WA4	125	9.0	211	1.47	3.39	0.29	0.91	26.67	3.51	0.68	3.39	0.97	3392	29	29	3372	69	69	3337	177	177	1.6
14WA4	126	18.4	398	1.39	3.26	0.33	0.92	32.30	3.39	0.72	3.26	0.96	3596	29	29	3560	67	67	3496	176	176	2.8
14WA4	128	4.1	111	1.77	3.63	0.28	0.94	21.54	3.75	0.57	3.63	0.97	3343	30	30	3163	73	73	2887	169	169	13.6
14WA4	130	5.9	133	1.49	2.69	0.28	0.93	26.26	2.84	0.67	2.69	0.94	3387	30	30	3356	56	56	3306	139	139	2.4
14WA4	131[a]	5.3	96	1.21	3.33	0.43	0.92	48.86	3.45	0.83	3.33	0.96	4014	29	29	3969	69	69	3882	194	194	3.3
14WA4	132*	5.0	111	1.50	3.45	0.28	0.95	26.09	3.58	0.67	3.45	0.96	3383	31	31	3350	70	70	3294	178	178	2.6
14WA4	134	16.7	289	1.18	3.02	0.44	0.91	51.56	3.16	0.84	3.02	0.96	4062	29	29	4023	63	63	3945	178	178	2.9
14WA4	136	13.2	287	1.50	2.77	0.29	0.91	26.28	2.92	0.67	2.77	0.95	3392	29	29	3357	57	57	3298	143	143	2.8
14WA4	138	4.6	98	1.49	3.13	0.28	0.93	26.26	3.27	0.67	3.13	0.96	3384	30	30	3356	64	64	3310	162	162	2.2
14WA4	139	8.9	183	1.42	2.77	0.32	0.92	30.99	2.92	0.70	2.77	0.95	3566	29	29	3519	58	58	3436	148	148	3.7
14WA4	144	7.2	123	1.22	3.10	0.44	0.92	50.34	3.23	0.82	3.10	0.96	4064	29	29	3999	65	65	3871	180	180	4.7
14WA4	145	11.3	235	1.42	2.35	0.32	0.92	30.65	2.52	0.70	2.35	0.93	3552	29	29	3508	50	50	3432	125	125	3.4
14WA4	146*	11.5	254	1.50	2.77	0.29	0.93	26.36	2.92	0.67	2.77	0.95	3397	30	30	3360	57	57	3298	143	143	2.9

Table S6.2: U-Pb analysis of 14WA4. These data required no additional systematic uncertainty propagation into final age uncertainties. Disc%= % discordance of ^{206}Pb-^{238}U age and ^{207}Pb-^{206}Pb age. Uncertainties presented as "s", which is standard error. *Zircons with oscillatory zoning in the Pb-Hf subset of Chapter 5. [a] zircon included in oscillatory zoned grains (n=135) in Figure 5.7 but not the Pb-Hf subset, owing in many cases to fainter zonation

.

Supplementary Material Seven:

Jack Hills zircons KDE plot

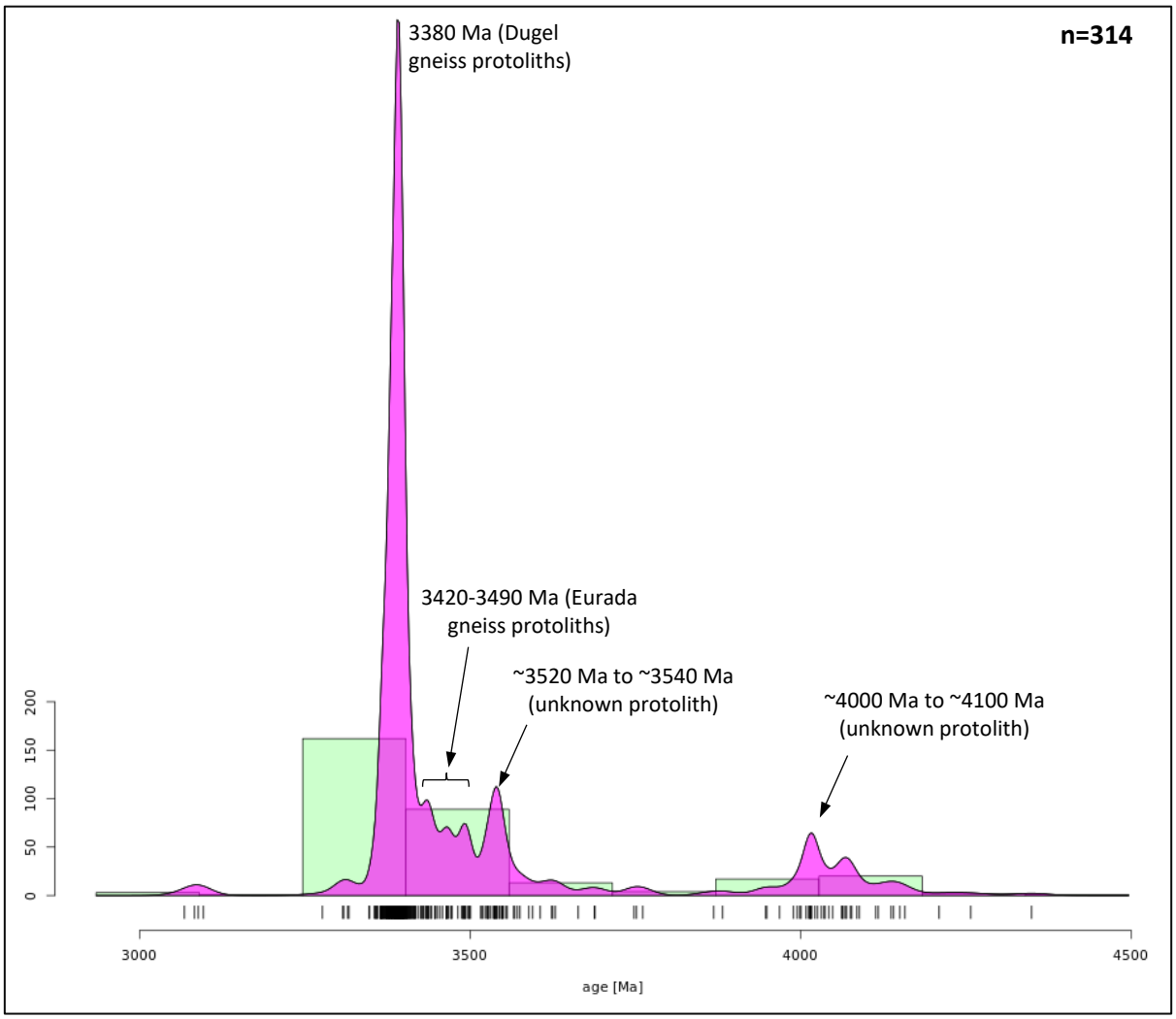

Supplementary S7.1: Kernel distribution estimate (KDE) plot of detrital zircon ^{207}Pb-^{206}Pb age distributions. This plot yields zircon age distribution peaks in good agreement with the ages in relative probability plots (Figure 5.7). Slight changes in the probability of minor zircon age peaks are present, with ~3520 Ma to ~3540 Ma becoming the most dominant age distribution peak after the ~3380 Ma peak. Peaks at ~3420 Ma, ~3440 Ma and ~3490 Ma are less pronounced from background zircon ages within this plot. Generated using IsoplotR (Vermeesch, 2018).

Supplementary Material Eight:

Zircon Standards Lu-Hf

Standard	$^{176}Yb/^{177}Hf$	2se	$^{176}Lu/^{177}Hf$	2se	2se prop	$^{176}Hf/^{177}Hf$	2se	2se prop
91500	0.013600	0.000130	0.0003113	0.0000005	0.0000082	0.282303	0.000029	0.000029
91500	0.013670	0.000130	0.0003106	0.0000004	0.0000080	0.282299	0.000029	0.000029
91500	0.013590	0.000130	0.0003111	0.0000002	0.0000078	0.282318	0.000034	0.000034
91500	0.013491	0.000078	0.0003111	0.0000003	0.0000083	0.282293	0.000037	0.000037
91500	0.013556	0.000087	0.0003107	0.0000003	0.0000080	0.282297	0.000028	0.000028
91500	0.013656	0.000077	0.0003113	0.0000004	0.0000082	0.282324	0.000042	0.000042
91500	0.013519	0.000050	0.0003110	0.0000003	0.0000090	0.282328	0.000040	0.000040
91500	0.013387	0.000062	0.0003109	0.0000003	0.0000082	0.282317	0.000036	0.000036
91500	0.013399	0.000050	0.0003110	0.0000003	0.0000083	0.282303	0.000032	0.000032
91500	0.013580	0.000096	0.0003111	0.0000004	0.0000110	0.282307	0.000033	0.000033
91500	0.013177	0.000079	0.0003110	0.0000004	0.0000120	0.282292	0.000045	0.000045
91500	0.012924	0.000066	0.0003110	0.0000005	0.0000087	0.282288	0.000044	0.000044
91500	0.012996	0.000073	0.0003110	0.0000005	0.0000090	0.282307	0.000051	0.000051
91500	0.013562	0.000066	0.0003137	0.0000019	0.0000089	0.282324	0.000042	0.000042
91500	0.013223	0.000090	0.0003108	0.0000006	0.0000089	0.282334	0.000039	0.000039
91500	0.016180	0.000110	0.0003111	0.0000005	0.0000098	0.282297	0.000038	0.000038
91500	0.015860	0.000100	0.0003109	0.0000007	0.0000100	0.282297	0.000033	0.000033
91500	0.015290	0.000120	0.0003103	0.0000003	0.0000065	0.282306	0.000034	0.000034
91500	0.015800	0.000160	0.0003118	0.0000003	0.0000069	0.282319	0.000035	0.000035
91500	0.015260	0.000100	0.0003108	0.0000004	0.0000086	0.282266	0.000044	0.000044
91500	0.015410	0.000140	0.0003112	0.0000004	0.0000088	0.282267	0.000037	0.000037
91500	0.013450	0.000110	0.0003110	0.0000004	0.0000090	0.282323	0.000040	0.000040
91500	0.013420	0.000130	0.0003109	0.0000006	0.0000092	0.282321	0.000037	0.000037
91500	0.014080	0.000130	0.0003108	0.0000005	0.0000100	0.282318	0.000034	0.000034
91500	0.013756	0.000086	0.0003113	0.0000006	0.0000110	0.282325	0.000033	0.000033
91500	0.012750	0.000140	0.0003106	0.0000003	0.0000091	0.282302	0.000035	0.000035
91500	0.013450	0.000160	0.0003125	0.0000003	0.0000045	0.282295	0.000029	0.000029
91500	0.015210	0.000290	0.0002944	0.0000007	0.0000200	0.282289	0.000034	0.000041
91500	0.014960	0.000230	0.0002942	0.0000007	0.0000200	0.282309	0.000035	0.000042
91500	0.014990	0.000190	0.0002962	0.0000010	0.0000200	0.282312	0.000048	0.000053
91500	0.014630	0.000160	0.0002941	0.0000005	0.0000190	0.282305	0.000029	0.000037
91500	0.014660	0.000140	0.0002935	0.0000007	0.0000190	0.282288	0.000034	0.000041
91500	0.016610	0.000100	0.0003362	0.0000008	0.0000220	0.282303	0.000043	0.000048
91500	0.016250	0.000160	0.0003314	0.0000007	0.0000220	0.282332	0.000039	0.000045
91500	0.016253	0.000081	0.0003319	0.0000007	0.0000220	0.282341	0.000039	0.000045
91500	0.016466	0.000075	0.0003351	0.0000006	0.0000220	0.282332	0.000043	0.000049
91500	0.016157	0.000078	0.0003315	0.0000007	0.0000220	0.282293	0.000032	0.000039
91500	0.016520	0.000130	0.0003374	0.0000007	0.0000220	0.282298	0.000043	0.000048
91500	0.016130	0.000100	0.0003350	0.0000006	0.0000220	0.282329	0.000043	0.000049
91500	0.015300	0.000130	0.0003140	0.0000005	0.0000210	0.282284	0.000033	0.000040
91500	0.016600	0.000130	0.0003397	0.0000008	0.0000230	0.282316	0.000039	0.000045
91500	0.013560	0.000220	0.0002948	0.0000009	0.0000200	0.282333	0.000040	0.000046
91500	0.013380	0.000150	0.0002926	0.0000008	0.0000190	0.282316	0.000023	0.000032
91500	0.013342	0.000068	0.0002943	0.0000006	0.0000200	0.282295	0.000037	0.000044
91500	0.013920	0.000360	0.0002971	0.0000009	0.0000200	0.282314	0.000034	0.000041

Standard	$^{176}Yb/^{177}Hf$	2se	$^{176}Lu/^{177}Hf$	2se	2se prop	$^{176}Hf/^{177}Hf$	2se	2se prop
91500	0.013450	0.000180	0.0002953	0.0000006	0.0000200	0.282298	0.000036	0.000042
91500	0.013510	0.000140	0.0002975	0.0000007	0.0000200	0.282274	0.000026	0.000035
91500	0.013540	0.000190	0.0003015	0.0000008	0.0000200	0.282297	0.000040	0.000046
91500	0.013540	0.000160	0.0003001	0.0000009	0.0000200	0.282346	0.000033	0.000040
91500	0.013640	0.000180	0.0003000	0.0000008	0.0000200	0.282269	0.000033	0.000040
91500	0.014350	0.000180	0.0003057	0.0000007	0.0000200	0.282319	0.000031	0.000038
91500	0.014094	0.000097	0.0003089	0.0000005	0.0000210	0.282294	0.000041	0.000047
91500	0.014130	0.000140	0.0003084	0.0000009	0.0000200	0.282311	0.000036	0.000043
91500	0.013314	0.000073	0.0003033	0.0000008	0.0000200	0.282301	0.000035	0.000042
91500	0.013460	0.000110	0.0003064	0.0000005	0.0000200	0.282319	0.000037	0.000044
91500	0.013240	0.000120	0.0003043	0.0000007	0.0000200	0.282266	0.000038	0.000045
91500	0.013950	0.000110	0.0003055	0.0000007	0.0000200	0.282300	0.000031	0.000039
91500	0.013790	0.000110	0.0003100	0.0000008	0.0000210	0.282318	0.000032	0.000039
91500	0.013273	0.000076	0.0003069	0.0000004	0.0000200	0.282281	0.000039	0.000045
91500	0.013110	0.000170	0.0003084	0.0000008	0.0000200	0.282338	0.000039	0.000045
91500	0.013110	0.000110	0.0003090	0.0000010	0.0000210	0.282328	0.000037	0.000043
91500	0.012980	0.000110	0.0003079	0.0000008	0.0000200	0.282314	0.000041	0.000047
91500	0.013283	0.000072	0.0003135	0.0000004	0.0000210	0.282331	0.000034	0.000041
91500	0.013065	0.000081	0.0003109	0.0000006	0.0000210	0.282318	0.000049	0.000054
91500	0.013320	0.000120	0.0003152	0.0000008	0.0000210	0.282324	0.000036	0.000042
91500	0.012980	0.000110	0.0003134	0.0000007	0.0000210	0.282320	0.000041	0.000047
91500	0.012980	0.000130	0.0003141	0.0000005	0.0000210	0.282284	0.000034	0.000041
91500	0.013050	0.000170	0.0003138	0.0000009	0.0000210	0.282296	0.000034	0.000041
91500	0.012870	0.000100	0.0003160	0.0000006	0.0000210	0.282312	0.000028	0.000036
91500	0.012990	0.000150	0.0003167	0.0000006	0.0000210	0.282303	0.000045	0.000050
91500	0.013430	0.000150	0.0003182	0.0000007	0.0000210	0.282273	0.000031	0.000039
91500	0.013400	0.000120	0.0003184	0.0000008	0.0000210	0.282309	0.000045	0.000051
91500	0.014330	0.000340	0.0003102	0.0000009	0.0000120	0.282325	0.000042	0.000046
91500	0.014510	0.000330	0.0003135	0.0000013	0.0000140	0.282350	0.000037	0.000042
91500	0.014040	0.000290	0.0003106	0.0000009	0.0000150	0.282316	0.000043	0.000047
91500	0.013800	0.000250	0.0003108	0.0000006	0.0000120	0.282289	0.000030	0.000035
91500	0.013910	0.000220	0.0003112	0.0000007	0.0000120	0.282322	0.000054	0.000057
91500	0.014330	0.000260	0.0003111	0.0000007	0.0000130	0.282330	0.000044	0.000047
91500	0.013740	0.000220	0.0003101	0.0000007	0.0000110	0.282293	0.000040	0.000044
91500	0.014140	0.000270	0.0003121	0.0000006	0.0000120	0.282311	0.000045	0.000048
91500	0.014470	0.000360	0.0003101	0.0000010	0.0000140	0.282290	0.000039	0.000043
91500	0.013930	0.000190	0.0003110	0.0000007	0.0000130	0.282300	0.000036	0.000040
91500	0.013780	0.000150	0.0003110	0.0000004	0.0000130	0.282325	0.000037	0.000041
91500	0.013990	0.000200	0.0003112	0.0000004	0.0000110	0.282279	0.000032	0.000037
91500	0.013520	0.000160	0.0003107	0.0000004	0.0000110	0.282266	0.000036	0.000040
91500	0.013900	0.000200	0.0003114	0.0000004	0.0000130	0.282301	0.000034	0.000038
91500	0.013940	0.000230	0.0003107	0.0000006	0.0000140	0.282285	0.000047	0.000051
91500	0.013650	0.000170	0.0003107	0.0000005	0.0000130	0.282334	0.000034	0.000039
91500	0.013610	0.000140	0.0003114	0.0000004	0.0000140	0.282314	0.000044	0.000047
91500	0.013690	0.000180	0.0003106	0.0000007	0.0000160	0.282293	0.000033	0.000038

Standard	$^{176}Yb/^{177}Hf$	2se	$^{176}Lu/^{177}Hf$	2se	2se prop	$^{176}Hf/^{177}Hf$	2se	2se prop
91500	0.013190	0.000190	0.0003099	0.0000008	0.0000130	0.282296	0.000041	0.000045
91500	0.013140	0.000160	0.0003128	0.0000008	0.0000160	0.282343	0.000039	0.000043
91500	0.012860	0.000140	0.0003102	0.0000010	0.0000200	0.282329	0.000040	0.000044
91500	0.012980	0.000150	0.0003101	0.0000006	0.0000120	0.282280	0.000043	0.000047
91500	0.013120	0.000100	0.0003132	0.0000008	0.0000170	0.282295	0.000044	0.000047
91500	0.012640	0.000130	0.0003102	0.0000009	0.0000240	0.282284	0.000041	0.000045
91500	0.013120	0.000170	0.0003112	0.0000005	0.0000120	0.282316	0.000034	0.000039
91500	0.013140	0.000160	0.0003108	0.0000003	0.0000120	0.282283	0.000045	0.000049
91500	0.013470	0.000210	0.0003112	0.0000005	0.0000110	0.282303	0.000046	0.000049
91500	0.013370	0.000180	0.0003110	0.0000008	0.0000140	0.282334	0.000040	0.000044
91500	0.013420	0.000200	0.0003108	0.0000007	0.0000170	0.282319	0.000036	0.000041
91500	0.013430	0.000160	0.0003110	0.0000005	0.0000130	0.282311	0.000030	0.000035
91500	0.013600	0.000220	0.0003110	0.0000005	0.0000130	0.282324	0.000037	0.000042
91500	0.013840	0.000210	0.0003110	0.0000008	0.0000140	0.282295	0.000037	0.000041
91500	0.013780	0.000210	0.0003110	0.0000005	0.0000140	0.282303	0.000041	0.000045
91500	0.012750	0.000220	0.0003110	0.0000005	0.0000140	0.282301	0.000038	0.000042
91500	0.012680	0.000170	0.0003110	0.0000006	0.0000140	0.282310	0.000046	0.000049
91500	0.012820	0.000220	0.0003110	0.0000007	0.0000130	0.282304	0.000035	0.000040
91500	0.012580	0.000150	0.0003111	0.0000007	0.0000160	0.282269	0.000033	0.000038
91500	0.012510	0.000150	0.0003109	0.0000009	0.0000160	0.282285	0.000033	0.000038
91500	0.012630	0.000190	0.0003110	0.0000004	0.0000079	0.282305	0.000041	0.000045
91500	0.013040	0.000240	0.0003111	0.0000004	0.0000078	0.282316	0.000040	0.000044
91500	0.012550	0.000110	0.0003109	0.0000003	0.0000110	0.282294	0.000042	0.000046
91500	0.013050	0.000220	0.0003112	0.0000005	0.0000160	0.282334	0.000035	0.000039
91500	0.012640	0.000170	0.0003108	0.0000007	0.0000140	0.282318	0.000038	0.000042
91500	0.012800	0.000150	0.0003111	0.0000006	0.0000130	0.282316	0.000043	0.000047
MT	0.004409	0.000020	0.0000832	0.0000002	0.0000023	0.282538	0.000026	0.000026
MT	0.004122	0.000021	0.0000775	0.0000002	0.0000021	0.282547	0.000031	0.000031
MT	0.004043	0.000012	0.0000758	0.0000002	0.0000021	0.282517	0.000034	0.000034
MT	0.004517	0.000015	0.0000850	0.0000002	0.0000022	0.282535	0.000032	0.000032
MT	0.004373	0.000014	0.0000822	0.0000002	0.0000022	0.282532	0.000036	0.000036
MT	0.004437	0.000011	0.0000826	0.0000002	0.0000022	0.282541	0.000035	0.000035
MT	0.004244	0.000016	0.0000858	0.0000002	0.0000023	0.282542	0.000031	0.000031
MT	0.004300	0.000018	0.0000888	0.0000003	0.0000027	0.282541	0.000036	0.000036
MT	0.004061	0.000016	0.0000800	0.0000002	0.0000022	0.282545	0.000034	0.000034
MT	0.003920	0.000013	0.0000763	0.0000002	0.0000021	0.282509	0.000029	0.000029
MT	0.003882	0.000012	0.0000642	0.0000002	0.0000019	0.282506	0.000031	0.000031
MT	0.003856	0.000020	0.0000650	0.0000002	0.0000018	0.282495	0.000036	0.000036
MT	0.004045	0.000020	0.0000641	0.0000001	0.0000017	0.282519	0.000038	0.000038
MT	0.004001	0.000024	0.0000630	0.0000002	0.0000017	0.282534	0.000030	0.000030
MT	0.006860	0.000110	0.0001155	0.0000005	0.0000032	0.282517	0.000037	0.000037
MT	0.006594	0.000067	0.0001139	0.0000003	0.0000032	0.282475	0.000032	0.000032
MT	0.004134	0.000021	0.0000780	0.0000001	0.0000023	0.282521	0.000027	0.000027
MT	0.004111	0.000013	0.0000802	0.0000002	0.0000021	0.282530	0.000026	0.000026

Standard	$^{176}Yb/^{177}Hf$	2se	$^{176}Lu/^{177}Hf$	2se	2se prop	$^{176}Hf/^{177}Hf$	2se	2se prop
MT	0.004572	0.000021	0.0000753	0.0000002	0.000005	0.282509	0.000028	0.000036
MT	0.004598	0.000039	0.0000758	0.0000002	0.000005	0.282548	0.000033	0.000040
MT	0.004604	0.000033	0.0000756	0.0000003	0.000005	0.282542	0.000027	0.000035
MT	0.004522	0.000029	0.0000754	0.0000003	0.000005	0.282517	0.000034	0.000041
MT	0.004585	0.000036	0.0000760	0.0000002	0.000005	0.282500	0.000033	0.000040
MT	0.004627	0.000041	0.0000766	0.0000003	0.0000051	0.282514	0.000029	0.000037
MT	0.004760	0.000057	0.0000772	0.0000003	0.0000051	0.282533	0.000020	0.000031
MT	0.004669	0.000044	0.0000769	0.0000003	0.0000051	0.282528	0.000029	0.000037
MT	0.004632	0.000051	0.0000759	0.0000002	0.000005	0.282524	0.000030	0.000037
MT	0.004678	0.000027	0.0000769	0.0000002	0.0000051	0.282517	0.000027	0.000035
MT	0.004771	0.000029	0.0000788	0.0000003	0.0000052	0.282529	0.000023	0.000033
MT	0.004722	0.000042	0.0000787	0.0000002	0.0000052	0.282511	0.000026	0.000035
MT	0.004694	0.000028	0.0000785	0.0000002	0.0000052	0.282537	0.000031	0.000039
MT	0.004768	0.000048	0.0000791	0.0000002	0.0000052	0.282535	0.000024	0.000033
MT	0.004740	0.000034	0.0000790	0.0000002	0.0000052	0.282509	0.000026	0.000035
MT	0.004768	0.000027	0.0000796	0.0000002	0.0000053	0.282519	0.000032	0.000039
MT	0.004826	0.000021	0.0000809	0.0000002	0.0000054	0.282547	0.000019	0.000030
MT	0.004708	0.000035	0.0000808	0.0000002	0.0000054	0.282505	0.000026	0.000034
MT	0.004753	0.000021	0.0000812	0.0000002	0.0000054	0.282547	0.000023	0.000032
MT	0.004686	0.000029	0.0000818	0.0000003	0.0000054	0.282527	0.000024	0.000033
MT	0.004448	0.000020	0.0000785	0.0000002	0.0000052	0.282509	0.000031	0.000038
MT	0.004472	0.000026	0.0000792	0.0000002	0.0000052	0.282509	0.000032	0.000039
MT	0.004625	0.000029	0.0000834	0.0000003	0.0000055	0.282531	0.000039	0.000045
MT	0.004562	0.000031	0.0000831	0.0000003	0.0000055	0.282552	0.000028	0.000036
MT	0.004557	0.000065	0.0000822	0.0000003	0.0000055	0.282516	0.000026	0.000034
MT	0.004507	0.000037	0.0000815	0.0000003	0.0000054	0.282540	0.000033	0.000040
MT	0.004748	0.000037	0.0000871	0.0000003	0.0000058	0.282541	0.000035	0.000042
MT	0.004731	0.000030	0.0000868	0.0000003	0.0000058	0.282517	0.000026	0.000034
MT	0.004612	0.000033	0.0000861	0.0000003	0.0000057	0.282563	0.000034	0.000041
MT	0.004514	0.000036	0.0000832	0.0000003	0.0000055	0.282514	0.000031	0.000038
MT	0.004332	0.000030	0.0000825	0.0000002	0.0000055	0.282509	0.000043	0.000049
MT	0.004366	0.000021	0.0000835	0.0000003	0.0000055	0.282524	0.000032	0.000040
MT	0.004669	0.000026	0.0000899	0.0000002	0.000006	0.282486	0.000027	0.000035
MT	0.004598	0.000030	0.0000884	0.0000003	0.0000059	0.282525	0.000023	0.000032
MT	0.004828	0.000022	0.0000908	0.0000003	0.000006	0.282507	0.000031	0.000038
MT	0.004777	0.000028	0.0000904	0.0000003	0.000006	0.282520	0.000042	0.000048
MT	0.003991	0.000045	0.0000751	0.0000002	0.0000034	0.282505	0.000042	0.000045
MT	0.004069	0.000061	0.0000779	0.0000002	0.0000033	0.282528	0.000032	0.000037
MT	0.004003	0.000030	0.0000766	0.0000003	0.0000035	0.282484	0.000038	0.000042
MT	0.004269	0.000046	0.0000768	0.0000003	0.0000034	0.282479	0.000027	0.000032
MT	0.004050	0.000043	0.0000739	0.0000002	0.0000034	0.282516	0.000034	0.000039
MT	0.004219	0.000048	0.0000771	0.0000002	0.0000035	0.282491	0.000029	0.000034
MT	0.004336	0.000062	0.0000779	0.0000002	0.0000035	0.282538	0.000037	0.000041
MT	0.004291	0.000063	0.0000770	0.0000002	0.0000034	0.282516	0.000034	0.000039
MT	0.004041	0.000043	0.0000755	0.0000002	0.0000034	0.282547	0.000032	0.000037

Standard	$^{176}Yb/^{177}Hf$	2se	$^{176}Lu/^{177}Hf$	2se	2se prop	$^{176}Hf/^{177}Hf$	2se	2se prop
MT	0.004020	0.000035	0.0000764	0.0000002	0.0000034	0.282505	0.000030	0.000035
MT	0.003851	0.000046	0.0000806	0.0000002	0.0000042	0.282533	0.000029	0.000034
MT	0.003332	0.000057	0.0000758	0.0000003	0.0000028	0.282509	0.000031	0.000036
MT	0.003992	0.000055	0.0000844	0.0000002	0.000004	0.282530	0.000027	0.000033
MT	0.003971	0.000039	0.0000862	0.0000002	0.0000039	0.282534	0.000030	0.000035
MT	0.003578	0.000075	0.0000674	0.0000002	0.000003	0.282502	0.000029	0.000034
MT	0.003626	0.000064	0.0000685	0.0000003	0.0000031	0.282508	0.000034	0.000039
MT	0.003134	0.000047	0.0000591	0.0000002	0.0000026	0.282518	0.000026	0.000032
MT	0.003184	0.000046	0.0000601	0.0000002	0.0000027	0.282528	0.000034	0.000039
MT	0.005487	0.000073	0.0000912	0.0000011	0.0000042	0.282479	0.000034	0.000039
MT	0.005667	0.000089	0.0000951	0.0000012	0.0000044	0.282478	0.000031	0.000036
MT	0.003528	0.000021	0.0000731	0.0000002	0.0000032	0.282503	0.000033	0.000038
MT	0.003856	0.000014	0.0000787	0.0000002	0.0000035	0.282524	0.000036	0.000041
MT	0.003924	0.000023	0.0000742	0.0000002	0.0000028	0.282529	0.000030	0.000035
MT	0.003846	0.000019	0.0000709	0.0000002	0.0000032	0.282500	0.000028	0.000034
MT	0.003864	0.000034	0.0000744	0.0000002	0.0000032	0.282531	0.000027	0.000032
MT	0.004078	0.000038	0.0000782	0.0000002	0.0000035	0.282498	0.000031	0.000036
Ples	0.003206	0.000082	0.0000521	0.0000004	0.0000015	0.282490	0.000035	0.000035
Ples	0.002895	0.000076	0.0000470	0.0000002	0.0000013	0.282485	0.000029	0.000029
Ples	0.002836	0.000070	0.0000456	0.0000003	0.0000013	0.282487	0.000028	0.000028
Ples	0.004236	0.000065	0.0000669	0.0000002	0.0000018	0.282488	0.000024	0.000024
Ples	0.003629	0.000046	0.0000572	0.0000003	0.0000016	0.282495	0.000027	0.000027
Ples	0.004807	0.000041	0.0000759	0.0000003	0.0000021	0.282511	0.000033	0.000033
Ples	0.004347	0.000044	0.0000797	0.0000003	0.0000023	0.282502	0.000022	0.000022
Ples	0.004480	0.000065	0.0000828	0.0000002	0.0000024	0.282475	0.000017	0.000017
Ples	0.004460	0.000100	0.0000732	0.0000003	0.0000020	0.282482	0.000028	0.000028
Ples	0.008780	0.000180	0.0001441	0.0000006	0.0000039	0.282487	0.000027	0.000027
Ples	0.006333	0.000042	0.0000948	0.0000012	0.0000029	0.282490	0.000023	0.000023
Ples	0.006406	0.000052	0.0000984	0.0000010	0.0000030	0.282475	0.000029	0.000029
Ples	0.008791	0.000099	0.0001187	0.0000008	0.0000034	0.282504	0.000032	0.000032
Ples	0.008980	0.000270	0.0001192	0.0000006	0.0000032	0.282496	0.000040	0.000040
Ples	0.006870	0.000110	0.0001155	0.0000005	0.0000032	0.282515	0.000038	0.000038
Ples	0.006690	0.000120	0.0001138	0.0000003	0.0000032	0.282471	0.000031	0.000031
Ples	0.007431	0.000061	0.0001342	0.0000004	0.0000041	0.282493	0.000027	0.000027
Ples	0.007542	0.000081	0.0001388	0.0000004	0.0000043	0.282475	0.000024	0.000024
Ples	0.004078	0.000029	0.0000578	0.0000005	0.0000039	0.282495	0.000021	0.000031
Ples	0.004656	0.000020	0.0000662	0.0000005	0.0000044	0.282457	0.000024	0.000033
Ples	0.004855	0.000041	0.0000699	0.0000004	0.0000047	0.282454	0.000032	0.000039
Ples	0.004220	0.000120	0.0000644	0.0000021	0.0000047	0.282473	0.000024	0.000033
Ples	0.004386	0.000078	0.0000643	0.0000015	0.0000045	0.282491	0.000022	0.000032
Ples	0.008586	0.000080	0.0001222	0.0000005	0.0000081	0.282459	0.000023	0.000032
Ples	0.008954	0.000041	0.0001274	0.0000003	0.0000084	0.282479	0.000026	0.000034
Ples	0.008985	0.000051	0.0001279	0.0000003	0.0000085	0.282494	0.000017	0.000028
Ples	0.009262	0.000050	0.0001321	0.0000002	0.0000088	0.282483	0.000023	0.000033

Standard	$^{176}Yb/^{177}Hf$	2se	$^{176}Lu/^{177}Hf$	2se	2se prop	$^{176}Hf/^{177}Hf$	2se	2se prop
Ples	0.009748	0.000037	0.0001377	0.0000003	0.0000091	0.282488	0.000023	0.000032
Ples	0.010782	0.000063	0.0001497	0.0000004	0.0000099	0.282498	0.000024	0.000033
Ples	0.011332	0.000061	0.0001591	0.0000002	0.0000110	0.282458	0.000024	0.000033
Ples	0.004540	0.000160	0.0000583	0.0000003	0.0000039	0.282494	0.000028	0.000036
Ples	0.011045	0.000083	0.0001607	0.0000012	0.0000110	0.282467	0.000024	0.000033
Ples	0.003490	0.000120	0.0000503	0.0000009	0.0000034	0.282471	0.000025	0.000034
Ples	0.005223	0.000034	0.0000757	0.0000003	0.0000050	0.282478	0.000019	0.000030
Ples	0.006877	0.000089	0.0000922	0.0000005	0.0000061	0.282472	0.000021	0.000031
Ples	0.006866	0.000065	0.0000917	0.0000005	0.0000061	0.282449	0.000029	0.000037
Ples	0.006830	0.000073	0.0000918	0.0000007	0.0000061	0.282469	0.000032	0.000039
Ples	0.006876	0.000083	0.0000934	0.0000008	0.0000062	0.282503	0.000020	0.000030
Ples	0.006870	0.000100	0.0000939	0.0000010	0.0000063	0.282491	0.000036	0.000043
Ples	0.006810	0.000150	0.0000932	0.0000005	0.0000062	0.282458	0.000029	0.000037
Ples	0.006780	0.000110	0.0000941	0.0000007	0.0000063	0.282495	0.000030	0.000037
Ples	0.006840	0.000090	0.0000959	0.0000007	0.0000064	0.282475	0.000027	0.000035
Ples	0.003430	0.000110	0.0000552	0.0000009	0.0000038	0.282451	0.000034	0.000041
Ples	0.004610	0.000036	0.0000759	0.0000006	0.0000051	0.282499	0.000019	0.000030
Ples	0.003746	0.000083	0.0000620	0.0000008	0.0000042	0.282506	0.000033	0.000040
Ples	0.003820	0.000100	0.0000647	0.0000007	0.0000043	0.282484	0.000037	0.000043
Ples	0.004872	0.000060	0.0000826	0.0000010	0.0000056	0.282478	0.000028	0.000036
Ples	0.003868	0.000046	0.0000655	0.0000005	0.0000044	0.282484	0.000034	0.000041
Ples	0.004403	0.000054	0.0000746	0.0000005	0.0000050	0.282494	0.000032	0.000040
Ples	0.004980	0.000140	0.0000811	0.0000025	0.0000059	0.282477	0.000033	0.000040
Ples	0.004730	0.000140	0.0000764	0.0000025	0.0000056	0.282488	0.000014	0.000026
Ples	0.006220	0.000200	0.0000943	0.0000013	0.0000044	0.282476	0.000028	0.000034
Ples	0.006110	0.000150	0.0000936	0.0000012	0.0000043	0.282478	0.000038	0.000043
Ples	0.006150	0.000140	0.0000955	0.0000015	0.0000045	0.282462	0.000031	0.000036
Ples	0.006010	0.000120	0.0000908	0.0000015	0.0000043	0.282500	0.000022	0.000028
Ples	0.005980	0.000100	0.0000908	0.0000014	0.0000043	0.282484	0.000027	0.000033
Ples	0.005998	0.000065	0.0000945	0.0000011	0.0000043	0.282434	0.000035	0.000040
Ples	0.005950	0.000220	0.0000900	0.0000004	0.0000040	0.282460	0.000030	0.000035
Ples	0.009478	0.000090	0.0001514	0.0000006	0.0000068	0.282483	0.000033	0.000037
Ples	0.005660	0.000120	0.0000928	0.0000011	0.0000042	0.282498	0.000024	0.000030
Ples	0.008388	0.000043	0.0001367	0.0000014	0.0000063	0.282464	0.000027	0.000033
Ples	0.006405	0.000057	0.0001172	0.0000003	0.0000064	0.282477	0.000021	0.000028
Ples	0.006426	0.000058	0.0001211	0.0000002	0.0000062	0.282506	0.000028	0.000034
Ples	0.006581	0.000044	0.0001158	0.0000002	0.0000051	0.282456	0.000021	0.000028
Ples	0.006154	0.000041	0.0001067	0.0000002	0.0000051	0.282493	0.000025	0.000031
Ples	0.005828	0.000036	0.0000941	0.0000002	0.0000042	0.282496	0.000031	0.000036
Ples	0.006070	0.000036	0.0000983	0.0000002	0.0000044	0.282497	0.000029	0.000034
Ples	0.005880	0.000071	0.0000906	0.0000002	0.0000041	0.282474	0.000026	0.000032
Ples	0.006330	0.000053	0.0000987	0.0000002	0.0000044	0.282468	0.000024	0.000030
Ples	0.005466	0.000061	0.0000914	0.0000010	0.0000042	0.282483	0.000034	0.000039
Ples	0.005661	0.000092	0.0000949	0.0000011	0.0000044	0.282476	0.000032	0.000037
Ples	0.004740	0.000045	0.0000807	0.0000006	0.0000036	0.282487	0.000027	0.000033

Standard	$^{176}Yb/^{177}Hf$	2se	$^{176}Lu/^{177}Hf$	2se	2se prop	$^{176}Hf/^{177}Hf$	2se	2se prop
Ples	0.004818	0.000070	0.0000820	0.0000007	0.0000037	0.282500	0.000031	0.000036
Ples	0.005773	0.000068	0.0000845	0.0000004	0.0000033	0.282464	0.000039	0.000043
Ples	0.006072	0.000061	0.0000878	0.0000004	0.0000034	0.282501	0.000031	0.000036
Ples	0.006412	0.000058	0.0001039	0.0000003	0.0000050	0.282482	0.000031	0.000036
Ples	0.006476	0.000065	0.0001054	0.0000003	0.0000053	0.282494	0.000031	0.000036
OG1	0.024900	0.001100	0.0005900	0.0000150	0.0000220	0.280626	0.000028	0.000028
OG1	0.023320	0.000670	0.0005847	0.0000098	0.0000190	0.280591	0.000022	0.000022
OG1	0.036600	0.001700	0.0008680	0.0000330	0.0000410	0.280646	0.000036	0.000036
OG1	0.078100	0.001600	0.0017670	0.0000120	0.0000490	0.280694	0.000032	0.000032
OG1	0.094050	0.000940	0.0021560	0.0000160	0.0000610	0.280749	0.000033	0.000033
OG1	0.098200	0.001500	0.0022520	0.0000170	0.0000630	0.280738	0.000033	0.000033
OG1	0.022650	0.000150	0.0006968	0.0000096	0.0000220	0.280591	0.000030	0.000030
OG1	0.040500	0.001100	0.0012050	0.0000270	0.0000420	0.280625	0.000020	0.000020
OG1	0.026580	0.000250	0.0007494	0.0000039	0.0000210	0.280613	0.000028	0.000028
OG1	0.049000	0.006100	0.0011600	0.0001300	0.0001300	0.280651	0.000036	0.000036
OG1	0.043210	0.000410	0.0009700	0.0000120	0.0000300	0.280589	0.000020	0.000020
OG1	0.039560	0.000260	0.0009184	0.0000068	0.0000270	0.280655	0.000025	0.000025
OG1	0.045450	0.000710	0.0009510	0.0000210	0.0000330	0.280634	0.000028	0.000028
OG1	0.042030	0.000720	0.0008920	0.0000170	0.0000300	0.280663	0.000032	0.000032
OG1	0.038800	0.001600	0.0009870	0.0000470	0.0000540	0.280624	0.000024	0.000024
OG1	0.073400	0.004100	0.0018100	0.0001100	0.0001200	0.280688	0.000033	0.000033
OG1	0.059900	0.003000	0.0015770	0.0000820	0.0000930	0.280658	0.000028	0.000028
OG1	0.030290	0.000870	0.0008480	0.0000180	0.0000290	0.280584	0.000027	0.000027
OG1	0.064600	0.004500	0.0013320	0.0000920	0.0001300	0.280647	0.000029	0.000037
OG1	0.059600	0.004100	0.0012320	0.0000850	0.0001200	0.280659	0.000033	0.000040
OG1	0.030900	0.001000	0.0006910	0.0000190	0.0000500	0.280633	0.000033	0.000040
OG1	0.037700	0.001200	0.0008280	0.0000270	0.0000610	0.280650	0.000025	0.000034
OG1	0.040980	0.000830	0.0009080	0.0000200	0.0000640	0.280661	0.000028	0.000036
OG1	0.035700	0.001500	0.0007930	0.0000260	0.0000590	0.280645	0.000025	0.000034
OG1	0.037310	0.000880	0.0007902	0.0000080	0.0000530	0.280646	0.000026	0.000034
OG1	0.048800	0.001000	0.0010180	0.0000180	0.0000700	0.280638	0.000024	0.000033
OG1	0.055740	0.000830	0.0011530	0.0000200	0.0000790	0.280671	0.000023	0.000032
OG1	0.049900	0.002500	0.0010440	0.0000550	0.0000890	0.280648	0.000024	0.000033
OG1	0.053480	0.000940	0.0010765	0.0000048	0.0000710	0.280624	0.000025	0.000034
OG1	0.049080	0.000540	0.0010310	0.0000200	0.0000710	0.280668	0.000028	0.000036
OG1	0.046960	0.000830	0.0010110	0.0000110	0.0000680	0.280674	0.000028	0.000036
OG1	0.044950	0.000220	0.0009892	0.0000072	0.0000660	0.280661	0.000021	0.000031
OG1	0.036440	0.000380	0.0008605	0.0000042	0.0000570	0.280614	0.000022	0.000031
OG1	0.048800	0.001700	0.0010630	0.0000290	0.0000760	0.280654	0.000021	0.000031
OG1	0.038400	0.001400	0.0008620	0.0000290	0.0000640	0.280611	0.000012	0.000025
OG1	0.061800	0.001500	0.0013460	0.0000300	0.0000940	0.280664	0.000026	0.000034
OG1	0.048750	0.000860	0.0010600	0.0000140	0.0000720	0.280669	0.000025	0.000034
OG1	0.042690	0.000650	0.0009630	0.0000140	0.0000650	0.280624	0.000023	0.000032
OG1	0.055600	0.001700	0.0012890	0.0000400	0.0000940	0.280639	0.000030	0.000037

Standard	$^{176}Yb/^{177}Hf$	2se	$^{176}Lu/^{177}Hf$	2se	2se prop	$^{176}Hf/^{177}Hf$	2se	2se prop
OG1	0.052700	0.007300	0.0011700	0.0001500	0.0001700	0.280626	0.000033	0.000040
OG1	0.055800	0.001700	0.0012480	0.0000460	0.0000950	0.280669	0.000029	0.000036
OG1	0.047900	0.006300	0.0010800	0.0001300	0.0001500	0.280636	0.000030	0.000037
OG1	0.038550	0.000610	0.0009460	0.0000210	0.0000660	0.280638	0.000031	0.000038
OG1	0.079500	0.003000	0.0018060	0.0000410	0.0001300	0.280701	0.000030	0.000037
OG1	0.009590	0.000150	0.0002690	0.0000060	0.0000190	0.280596	0.000022	0.000032
OG1	0.062030	0.000520	0.0014090	0.0000180	0.0000950	0.280673	0.000036	0.000042
OG1	0.017410	0.000870	0.0005048	0.0000064	0.0000340	0.280610	0.000026	0.000034
OG1	0.056100	0.001100	0.0014090	0.0000200	0.0000950	0.280639	0.000029	0.000037
OG1	0.050400	0.002000	0.0011920	0.0000400	0.0000880	0.280676	0.000023	0.000032
OG1	0.056320	0.000440	0.0013620	0.0000140	0.0000910	0.280647	0.000018	0.000029
GJ1	0.011270	0.000210	0.0002528	0.0000010	0.0000110	0.282017	0.000042	0.000046
GJ1	0.011230	0.000250	0.0002520	0.0000009	0.0000110	0.282010	0.000035	0.000040
GJ1	0.011170	0.000250	0.0002501	0.0000009	0.0000100	0.282002	0.000044	0.000047
GJ1	0.011180	0.000220	0.0002528	0.0000010	0.0000120	0.281998	0.000045	0.000049
GJ1	0.011220	0.000250	0.0002528	0.0000009	0.0000110	0.282059	0.000039	0.000043
GJ1	0.011300	0.000290	0.0002512	0.0000008	0.0000110	0.281990	0.000055	0.000058
GJ1	0.010800	0.000210	0.0002392	0.0000005	0.0000110	0.281989	0.000035	0.000040
GJ1	0.010810	0.000180	0.0002401	0.0000007	0.0000110	0.282015	0.000035	0.000039
GJ1	0.010600	0.000150	0.0002436	0.0000005	0.0000110	0.281997	0.000026	0.000032
GJ1	0.010570	0.000150	0.0002430	0.0000006	0.0000100	0.282013	0.000028	0.000034
GJ1	0.010530	0.000180	0.0002955	0.0000010	0.0000160	0.282011	0.000037	0.000042
GJ1	0.010510	0.000200	0.0003014	0.0000010	0.0000170	0.282009	0.000034	0.000039
GJ1	0.010500	0.000190	0.0002613	0.0000004	0.0000088	0.282008	0.000028	0.000033
GJ1	0.010580	0.000250	0.0002552	0.0000006	0.0000093	0.282011	0.000033	0.000038
GJ1	0.010390	0.000160	0.0002490	0.0000006	0.0000110	0.282031	0.000030	0.000035
GJ1	0.010430	0.000170	0.0002495	0.0000005	0.0000110	0.282015	0.000029	0.000034
GJ1	0.010530	0.000210	0.0002400	0.0000005	0.0000100	0.282031	0.000035	0.000040
GJ1	0.010320	0.000130	0.0002404	0.0000005	0.0000100	0.282030	0.000037	0.000041
GJ1	0.010380	0.000190	0.0002554	0.0000005	0.0000120	0.282016	0.000034	0.000038
GJ1	0.010420	0.000210	0.0002567	0.0000006	0.0000120	0.281961	0.000033	0.000038
GJ1	0.010380	0.000160	0.0002183	0.0000003	0.0000077	0.282036	0.000031	0.000036
GJ1	0.010290	0.000160	0.0002151	0.0000003	0.0000077	0.282037	0.000035	0.000040
GJ1	0.010400	0.000210	0.0002531	0.0000007	0.0000130	0.282044	0.000028	0.000033
GJ1	0.010260	0.000170	0.0002563	0.0000005	0.0000130	0.282072	0.000026	0.000032

Supplementary Table S8: Lu-Hf compositions of standards during analysis in October 2018. Propagated $^{176}Lu/^{177}Hf$ and $^{176}Hf/^{177}Hf$ ratio uncertainties incorporate the excess variance of the PRM, which is 91500, into SRMs (MT- mudtank, ples- plesovice, OG1 and GJ1).

Supplementary Material Nine:

Zircon standard Lu-Hf II

Weighted avergaes of isotope ratios for Lu-Hf PRM and VRMs						
Ref. Material	**$^{176}Hf/^{177}Hf$**	**2se**	**$^{176}Lu/^{177}Hf$**	**2se**	**$^{176}Yb/^{177}Hf$**	**2se**
91500	0.2823062	37	0.0003109	11	0.01336	11
Mud Tank*	0.2825208	42	0.0000770	60	0.00427	8
Plesovice*	0.2824829	36	0.0000758	58	0.00576	38
OG1*	0.2806413	82	0.0008440	740	0.03570	350
GJ1	0.2820177	81	0.0002496	32	0.01058	130

Table S9.1: $^{176}Hf/^{177}Hf$, $^{176}Lu/^{177}Hf$ and $^{176}Yb/^{177}Hf$ ratios of PRM 91500 and VRMs**.** Uncertainties have been propagated for excess variance of PRM for $^{176}Hf/^{177}Hf$ and $^{176}Lu/^{177}Hf$, but not $^{176}Yb/^{177}Hf$. *Lu/Hf and Yb/Hf of Mud Tank, Plesovice and OG1 are known to be variable (e.g. Woodhead and Hergt, 2005; Slama et al., 2009; Kemp et al., 2017), but weighted averages here fall well within accepted values. For previously determined isotopic ratios of PRM 91500 and VRMs Mud Tank, Plesovice and OG1 see Table 2.3.

Figure S9.1: 91500 $^{176}Hf/^{177}Hf$

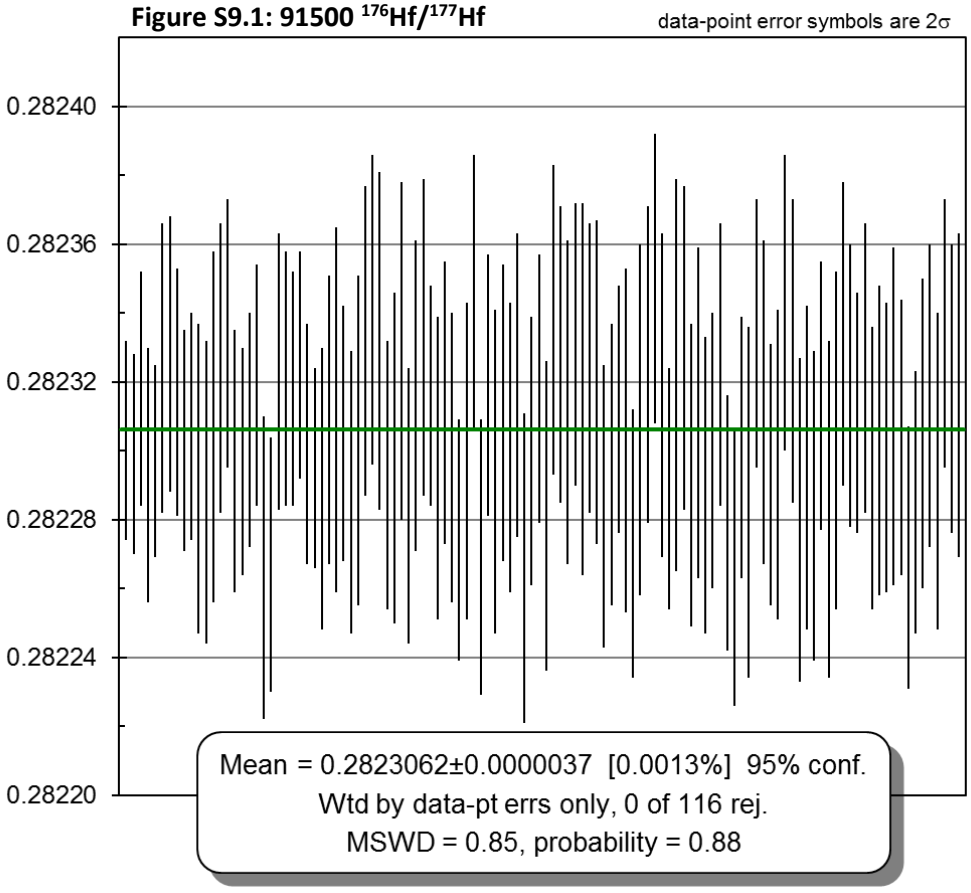

Figure S9.2: 91500 $^{176}Lu/^{177}Hf$

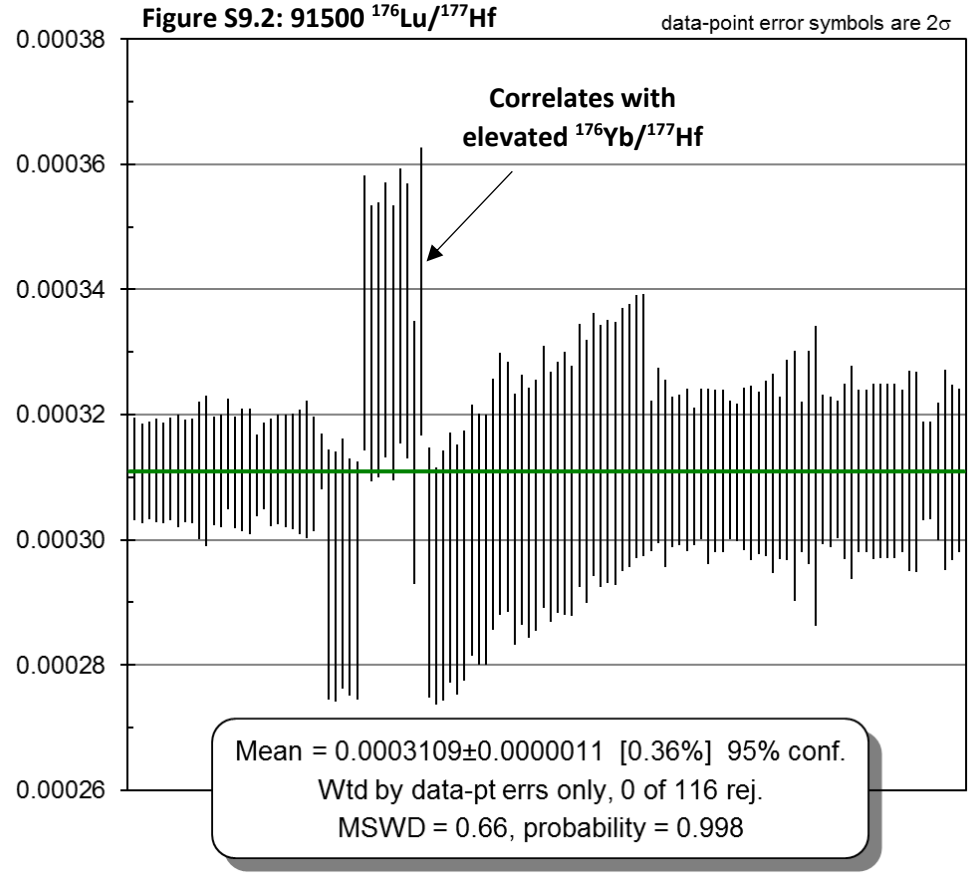

Figure S9.3: MudTank $^{176}Hf/^{177}Hf$

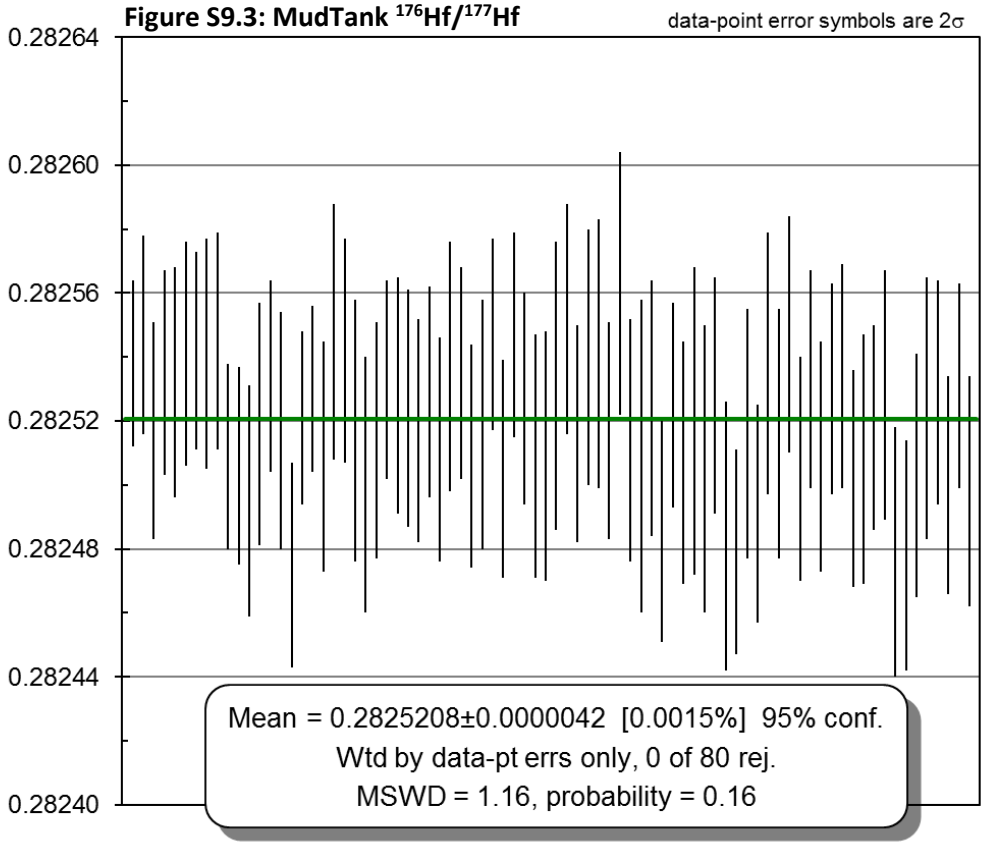

Figure S9.4: MudTank $^{176}Lu/^{177}Hf$

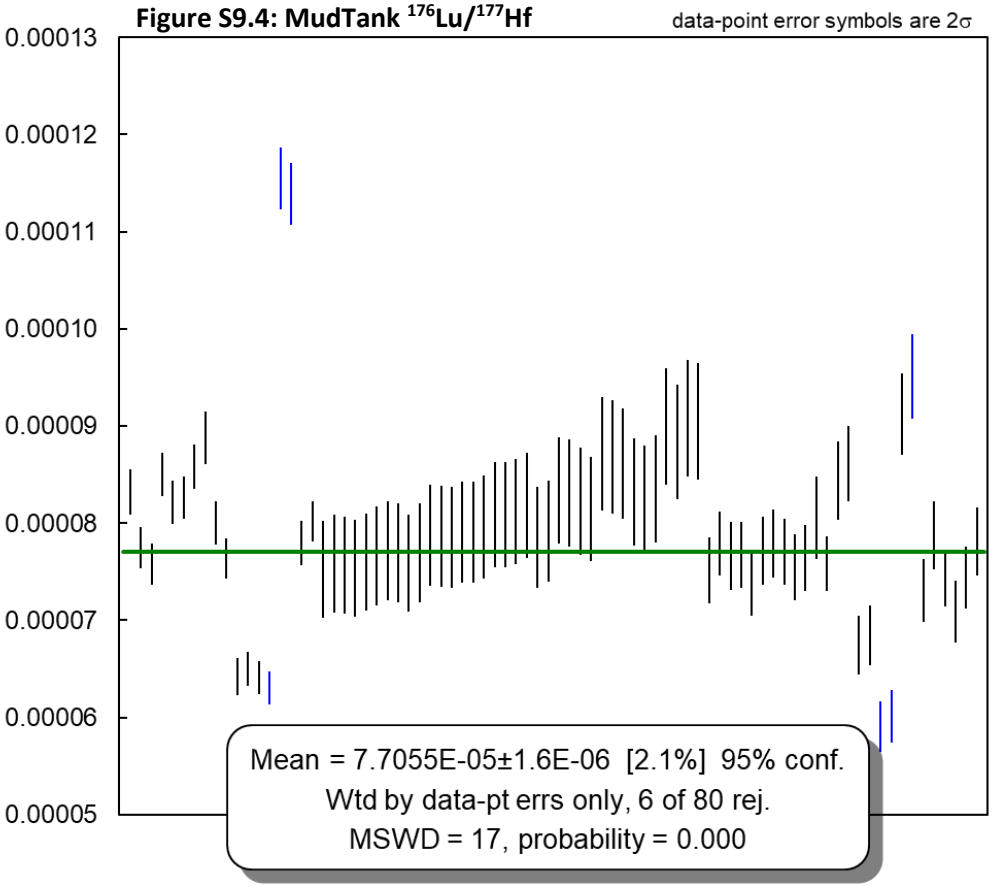

Figure S9.5: Plesovice $^{176}Hf/^{177}Hf$

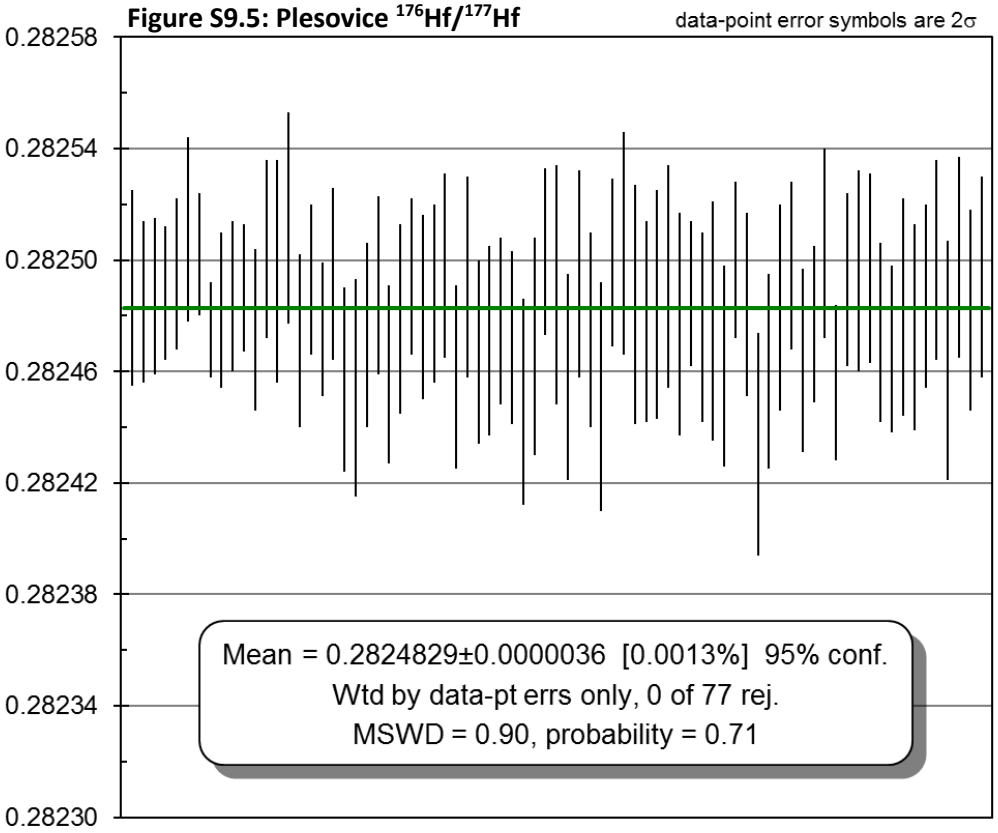

Figure S9.6: Plesovice $^{176}Lu/^{177}Hf$ (variable Lu and Yb)

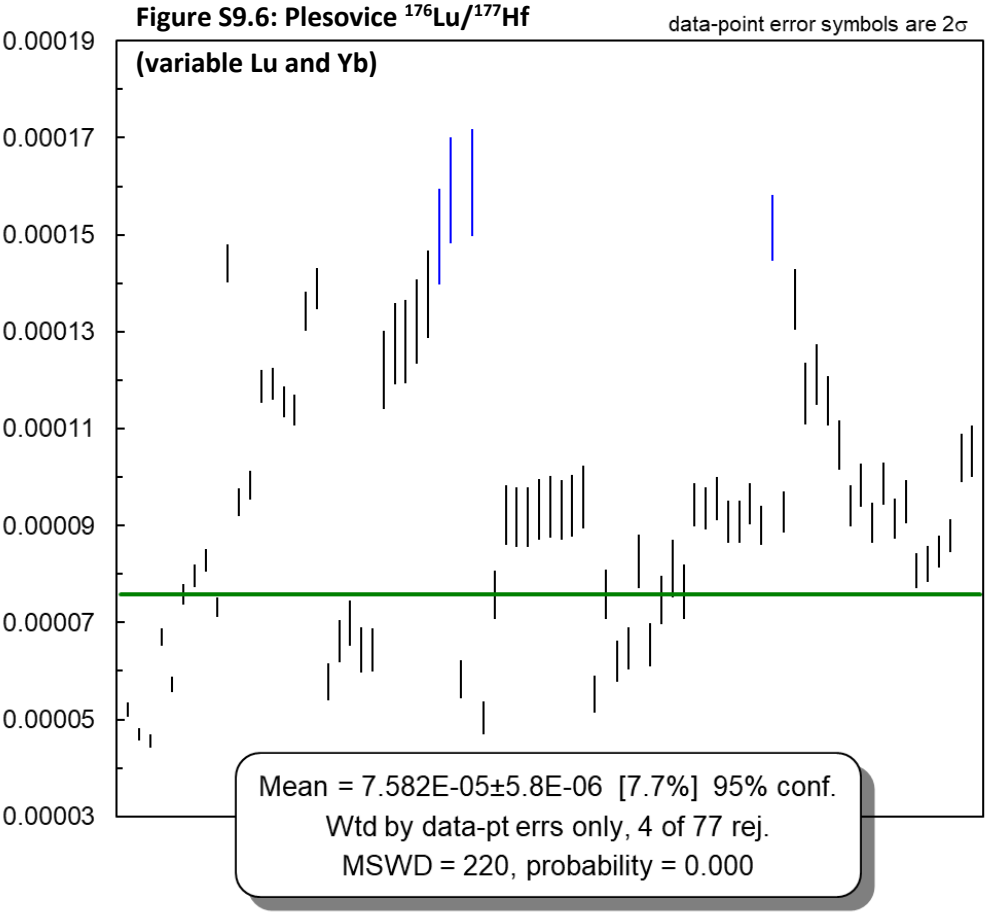

Figure S9.7: OG1 $^{176}Hf/^{177}Hf$

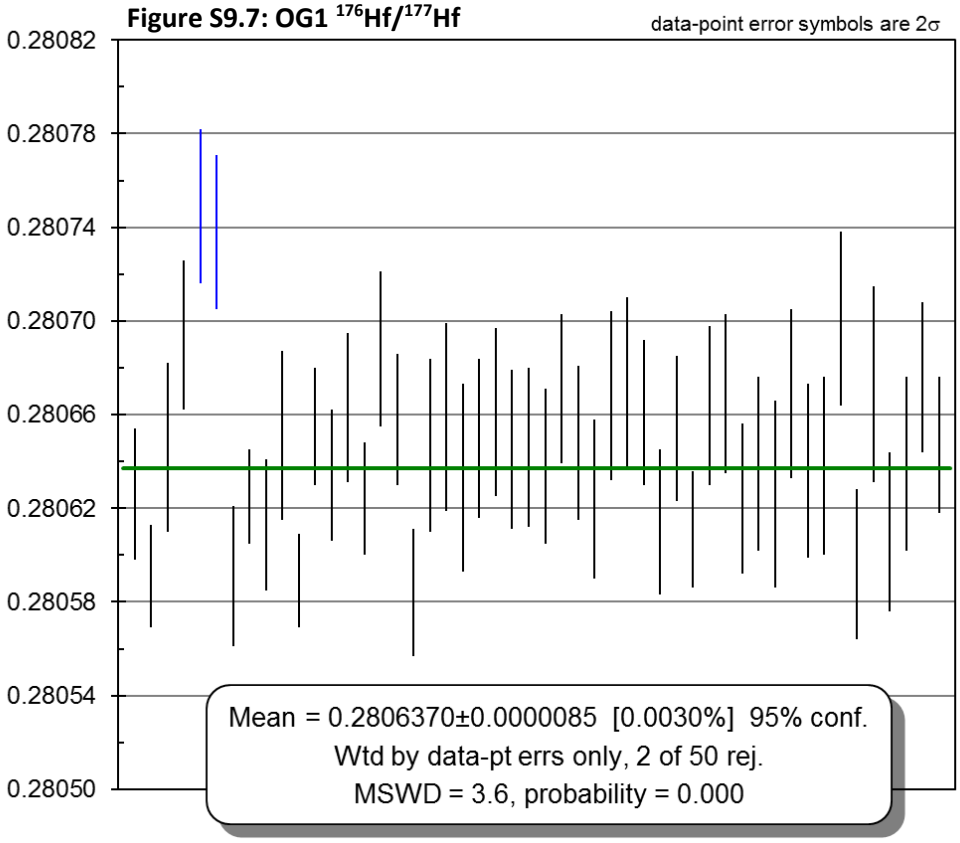

Figure S9.8: OG1 $^{176}Lu/^{177}Hf$ (variable Lu and Yb)

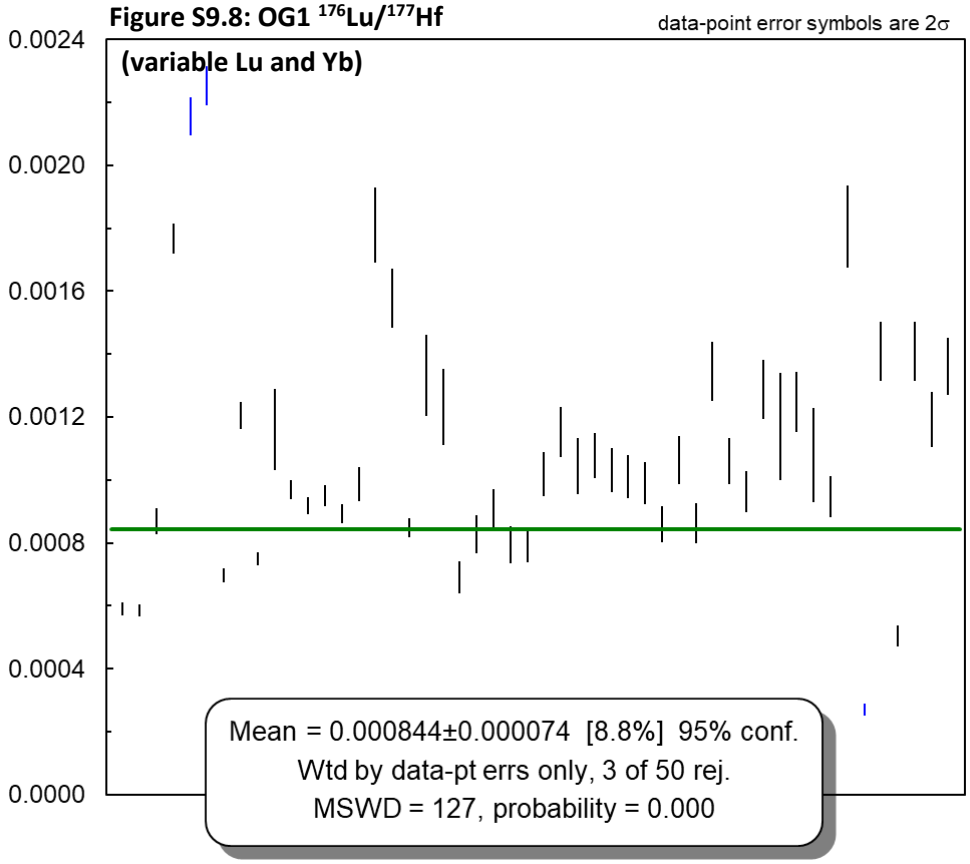

Figure S9.9: GJ1 $^{176}Hf/^{177}Hf$

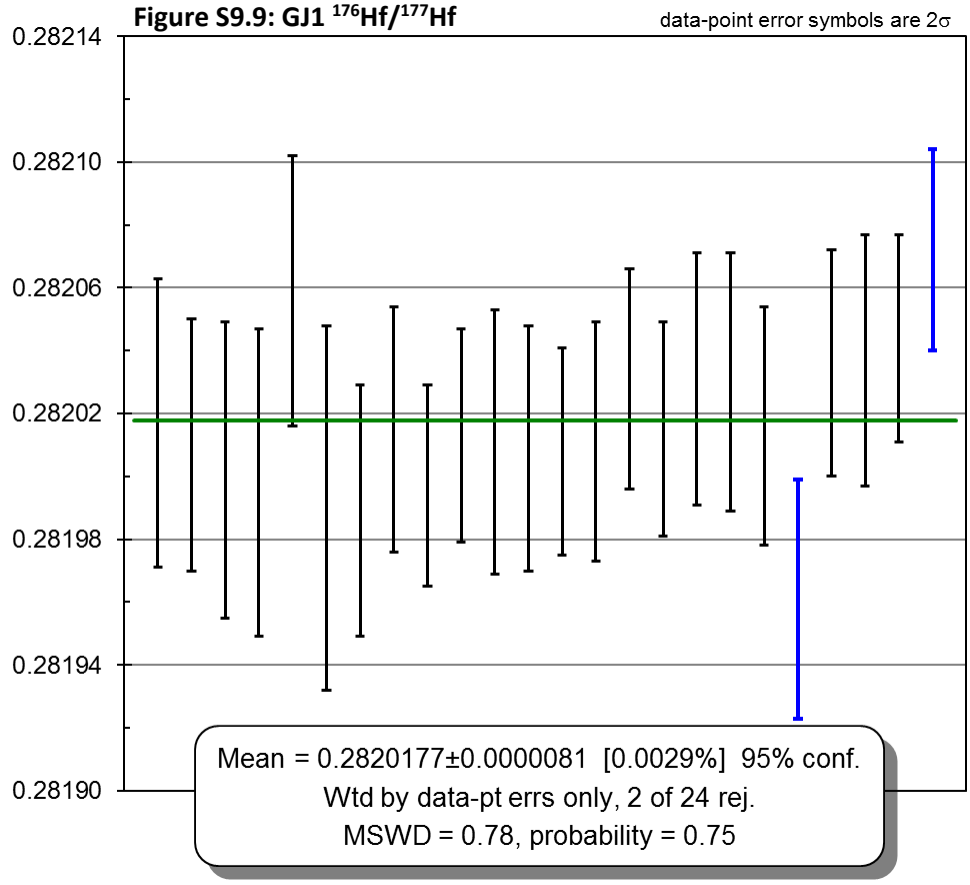

Figure S9.10: GJ1 $^{176}Lu/^{177}Hf$

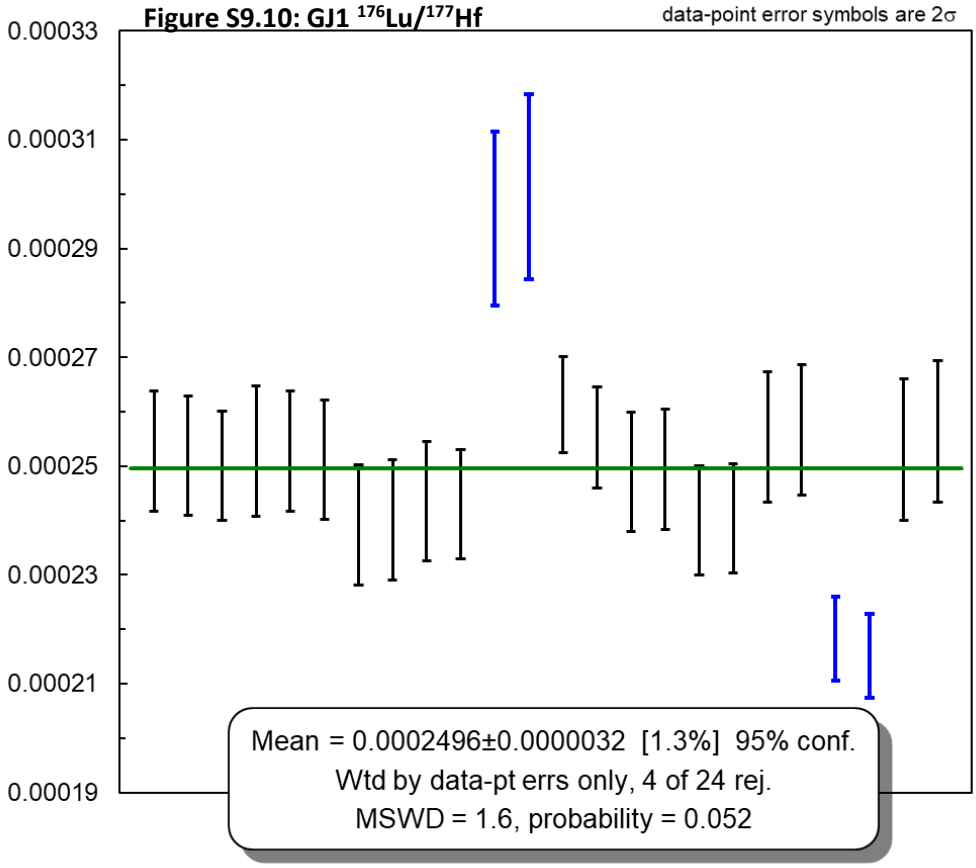

Supplementary Material Ten:

Jack Hills zircons Lu-Hf

Table S10.1: *Jack Hills zircon Lu-Hf compositions*

Sample		Standard corrected ratios						Ages				Time integrated Hf		$\varepsilon Hf(t)_{CHUR}$		
Sample	Zirco-n #	$^{176}Yb/^{177}Hf$	2se	$^{176}Lu/^{177}Hf$	2se	$^{176}Hf/^{177}Hf$	2se prop	Disc %	^{207}Pb-^{206}Pb Age	2se	2se prop	$^{176}Hf/^{177}Hf(t)_{SAMP}$	$^{176}Hf/^{177}Hf(t)_{CHUR}$	$\varepsilon Hf(t)_{CHUR}$	2se	2se sys
14WA2	9	0.022170	0.000070	0.000621	0.000017	0.280405	0.000026	1.19	3403	10	11	0.280364	0.280581	-7.72	1.04	1.04
14WA2	11	0.022260	0.000190	0.000625	0.000018	0.280439	0.000032	-0.97	3377	10	11	0.280398	0.280598	-7.13	1.23	1.24
14WA2	13	0.028430	0.000670	0.000796	0.000033	0.280090	0.000030	0.23	4049	11	11	0.280027	0.280147	-4.25	1.19	1.20
14WA2	13	0.018098	0.000063	0.000506	0.000014	0.280089	0.000027	-0.04	4061	12	12	0.280049	0.280139	-3.19	1.10	1.10
14WA2	15	0.026080	0.000260	0.000693	0.000018	0.280307	0.000022	-1.18	3392	11	12	0.280262	0.280588	-11.64	0.92	0.92
14WA2	19	0.042220	0.000330	0.001171	0.000033	0.280405	0.000035	0.20	3386	10	11	0.280329	0.280592	-9.40	1.33	1.33
14WA2	20	0.031410	0.000190	0.000798	0.000022	0.280367	0.000033	0.35	3397	10	12	0.280315	0.280585	-9.64	1.27	1.27
14WA2	20	0.031080	0.000100	0.000802	0.000021	0.280187	0.000088	0.35	3397	10	12	0.280134	0.280585	-16.06	3.17	3.17
14WA2	21	0.015730	0.000290	0.000406	0.000014	0.280366	0.000036	0.48	3689	10	11	0.280337	0.280389	-1.87	1.37	1.38
14WA2	22	0.013745	0.000093	0.000352	0.000010	0.280033	0.000027	0.28	4022	11	11	0.280006	0.280165	-5.68	1.10	1.10
14WA2	22	0.008385	0.000047	0.000238	0.000007	0.280052	0.000032	-0.41	4151	11	11	0.280033	0.280077	-1.60	1.26	1.26
14WA2	24	0.012860	0.000240	0.000331	0.000010	0.280488	0.000035	-0.59	3378	10	11	0.280466	0.280598	-4.67	1.33	1.34
14WA2	25	0.026790	0.000480	0.000699	0.000019	0.280518	0.000025	1.45	3523	11	12	0.280470	0.280501	-1.07	1.01	1.02
14WA2	25	0.017050	0.000230	0.000435	0.000012	0.280484	0.000031	1.08	3527	10	12	0.280454	0.280498	-1.56	1.20	1.21
14WA2	26	0.026040	0.000330	0.000644	0.000017	0.280303	0.000030	1.19	3398	10	12	0.280261	0.280584	-11.52	1.17	1.17
14WA2	28	0.009821	0.000098	0.000262	0.000007	0.280501	0.000024	1.40	3429	10	11	0.280484	0.280564	-2.85	0.98	0.98
14WA2	28	0.016250	0.000120	0.000469	0.000013	0.280545	0.000034	-0.08	3431	10	11	0.280514	0.280562	-1.72	1.30	1.30
14WA2	29	0.022304	0.000065	0.000606	0.000017	0.280388	0.000020	1.10	3391	10	11	0.280348	0.280589	-8.57	0.85	0.86
14WA2	30	0.025453	0.000066	0.000706	0.000019	0.280540	0.000020	1.38	3429	10	11	0.280493	0.280563	-2.50	0.85	0.86
14WA2	32	0.022450	0.000300	0.000617	0.000017	0.280373	0.000023	0.69	3377	11	12	0.280333	0.280598	-9.46	0.95	0.95
14WA2	32	0.030960	0.000190	0.000867	0.000024	0.280381	0.000035	1.83	3392	10	11	0.280324	0.280588	-9.40	1.33	1.33
14WA2	33	0.011210	0.000130	0.000264	0.000007	0.280561	0.000035	1.02	3431	10	12	0.280544	0.280562	-0.67	1.33	1.34
14WA2	36	0.030270	0.000900	0.000598	0.000031	0.280428	0.000032	1.23	3467	10	11	0.280388	0.280538	-5.35	1.23	1.24
14WA2	39	0.018080	0.000890	0.000359	0.000010	0.280327	0.000023	1.41	3400	10	11	0.280303	0.280583	-9.96	0.94	0.95
14WA2	42	0.024100	0.000510	0.000481	0.000014	0.280443	0.000031	0.71	3545	10	11	0.280410	0.280486	-2.70	1.20	1.21
14WA2	57	0.016070	0.000260	0.000330	0.000010	0.280054	0.000036	1.41	4068	15	15	0.280028	0.280134	-3.77	1.41	1.41
14WA2	47	0.021320	0.000780	0.000392	0.000011	0.280310	0.000040	0.59	3497	10	11	0.280284	0.280518	-8.36	1.50	1.51
14WA2	48	0.076760	0.000720	0.001443	0.000039	0.280690	0.000025	0.99	3390	9	11	0.280596	0.280590	0.21	1.00	1.01
14WA2	50	0.020800	0.000600	0.000396	0.000011	0.280468	0.000042	1.11	3554	10	11	0.280441	0.280480	-1.39	1.57	1.58
14WA2	51	0.037400	0.001000	0.000718	0.000021	0.280382	0.000022	-0.20	3387	10	11	0.280335	0.280591	-9.14	0.91	0.92
14WA2	53	0.031850	0.000720	0.000598	0.000017	0.280321	0.000033	0.89	3398	10	11	0.280282	0.280585	-10.79	1.26	1.27
14WA2	57	0.010450	0.000110	0.000212	0.000014	0.280056	0.000036	1.02	4035	16	16	0.280039	0.280156	-4.17	1.41	1.42
14WA2	58	0.022750	0.000500	0.000453	0.000030	0.280357	0.000033	1.21	3381	14	15	0.280328	0.280596	-9.56	1.29	1.29
14WA2	61	0.024200	0.000180	0.000485	0.000032	0.280387	0.000033	0.00	3391	14	15	0.280355	0.280589	-8.34	1.29	1.29

Table S10.1 cont.: *Jack Hills zircon Lu-Hf compositions*

Sample	Zirco -n #	$^{176}Yb/^{177}Hf$	2se	$^{176}Lu/^{177}Hf$	2se	$^{176}Hf/^{177}Hf$	2se prop	Disc %	$^{207}Pb-^{206}Pb$ Age	2se	2se prop	$^{176}Hf/^{177}Hf(t)_{SAMP}$	$^{176}Hf/^{177}Hf(t)_{CHUR}$	$\varepsilon Hf(t)_{CHUR}$	2se	2se sys
14WA2	62	0.038950	0.000170	0.000722	0.000048	0.280159	0.000031	0.47	4009	14	14	0.280103	0.280174	-2.52	1.24	1.25
14WA2	64	0.034010	0.000580	0.000638	0.000044	0.280499	0.000032	0.11	3521	14	15	0.280456	0.280502	-1.66	1.26	1.26
14WA2	65	0.014260	0.000250	0.000287	0.000019	0.280519	0.000034	-0.15	3426	14	15	0.280500	0.280566	-2.34	1.32	1.32
14WA2	66	0.031730	0.000330	0.000620	0.000041	0.280351	0.000039	0.95	3389	14	15	0.280310	0.280591	-9.98	1.48	1.49
14WA2	67	0.035040	0.000230	0.000690	0.000046	0.280333	0.000037	1.09	3389	14	15	0.280288	0.280590	-10.77	1.42	1.43
14WA2	71	0.033940	0.000700	0.000703	0.000047	0.280463	0.000036	1.76	3379	13	14	0.280417	0.280597	-6.41	1.38	1.39
14WA2	79	0.030800	0.001400	0.000623	0.000043	0.280423	0.000036	1.18	3398	13	14	0.280382	0.280585	-7.21	1.38	1.39
14WA2	80	0.050600	0.001700	0.000939	0.000063	0.280555	0.000032	2.09	3417	13	14	0.280493	0.280572	-2.80	1.25	1.26
14WA2	83	0.018170	0.000240	0.000452	0.000032	0.280130	0.000040	1.91	4089	16	16	0.280094	0.280120	-0.91	1.55	1.55
14WA2	85	0.014970	0.000590	0.000298	0.000020	0.280435	0.000036	1.58	3537	13	14	0.280415	0.280491	-2.73	1.39	1.39
14WA2	90	0.009630	0.000320	0.000201	0.000013	0.280117	0.000046	1.45	4038	15	15	0.280101	0.280154	-1.88	1.74	1.74
14WA2	92	0.028350	0.000890	0.000574	0.000038	0.280347	0.000035	1.67	3387	14	15	0.280310	0.280592	-10.06	1.35	1.36
14WA2	93	0.017490	0.000270	0.000364	0.000025	0.280366	0.000039	0.13	3379	15	16	0.280342	0.280597	-9.07	1.49	1.49
14WA2	95	0.017030	0.000280	0.000364	0.000027	0.280225	0.000036	0.35	4142	16	16	0.280196	0.280084	4.00	1.42	1.42
14WA2	96	0.024100	0.000220	0.000486	0.000032	0.280387	0.000034	0.66	3399	14	15	0.280355	0.280584	-8.14	1.32	1.33
14WA2	100	0.025900	0.001300	0.000545	0.000047	0.280457	0.000042	2.16	3544	15	15	0.280420	0.280486	-2.38	1.59	1.60
14WA2	104	0.027830	0.000590	0.000555	0.000037	0.280366	0.000036	1.80	3391	14	15	0.280330	0.280589	-9.24	1.38	1.39
14WA2	113	0.022330	0.000390	0.000447	0.000030	0.280041	0.000033	2.53	4076	14	14	0.280006	0.280128	-4.38	1.31	1.31
14WA2	113	0.025470	0.000540	0.000517	0.000034	0.280082	0.000044	2.37	4062	14	14	0.280041	0.280138	-3.45	1.67	1.67
14WA2	117	0.019270	0.000270	0.000394	0.000027	0.280281	0.000039	2.62	3395	15	16	0.280255	0.280586	-11.81	1.49	1.49
14WA2	119	0.014680	0.000680	0.000315	0.000021	0.280323	0.000041	2.64	3388	14	15	0.280302	0.280591	-10.29	1.55	1.56
14WA2	119	0.012510	0.000350	0.000271	0.000018	0.280326	0.000041	2.25	3374	14	15	0.280308	0.280600	-10.40	1.55	1.56
14WA2	124	0.015170	0.000250	0.000380	0.000026	0.280290	0.000038	2.75	3395	13	14	0.280265	0.280586	-11.45	1.45	1.45
14WA2	125	0.026510	0.000900	0.000537	0.000036	0.280408	0.000053	2.33	3381	14	15	0.280373	0.280596	-7.93	1.96	1.97
14WA2	126	0.015830	0.000350	0.000362	0.000024	0.280527	0.000035	2.62	3427	14	14	0.280503	0.280565	-2.20	1.35	1.36
14WA2	127	0.018280	0.000480	0.000414	0.000027	0.280356	0.000034	2.63	3607	14	14	0.280327	0.280444	-4.18	1.32	1.33
14WA2	131	0.019480	0.000580	0.000423	0.000028	0.280520	0.000039	0.13	3439	14	15	0.280492	0.280557	-2.32	1.49	1.49
14WA2	132	0.048500	0.001500	0.000975	0.000068	0.280369	0.000032	0.37	3395	11	12	0.280305	0.280586	-10.01	1.24	1.25
14WA2	134	0.025870	0.000650	0.000567	0.000039	0.280358	0.000032	-0.16	3396	11	12	0.280321	0.280586	-9.43	1.24	1.25
14WA2	135	0.028300	0.003700	0.000603	0.000088	0.280331	0.000031	1.12	3390	12	13	0.280292	0.280590	-10.63	1.23	1.23
14WA2	135	0.038200	0.000490	0.000821	0.000055	0.280334	0.000034	-0.61	3400	12	13	0.280280	0.280583	-10.79	1.31	1.32
14WA2	137	0.041740	0.000510	0.000933	0.000064	0.280396	0.000044	1.72	3372	11	12	0.280335	0.280601	-9.48	1.64	1.65
14WA2	139	0.011790	0.000200	0.000242	0.000016	0.280430	0.000042	0.65	3549	11	12	0.280413	0.280483	-2.48	1.58	1.58
14WA2	143	0.041400	0.000610	0.000907	0.000060	0.280373	0.000035	1.04	3464	11	12	0.280312	0.280540	-8.11	1.34	1.35
14WA2	146	0.020090	0.000270	0.000474	0.000031	0.280533	0.000039	-0.01	3436	11	12	0.280502	0.280559	-2.05	1.47	1.48

Table S10.1 cont.: *Jack Hills zircon Lu-Hf compositions*

Sample	Zirco -n #	$^{176}Yb/^{177}Hf$	2se	$^{176}Lu/^{177}Hf$	2se	$^{176}Hf/^{177}Hf$	2se prop	Disc %	$^{207}Pb-^{206}Pb$ Age	2se	2se prop	$^{176}Hf/^{177}Hf(t)_{SAMP}$	$^{176}Hf/^{177}Hf(t)_{CHUR}$	$\varepsilon Hf(t)_{CHUR}$	2se	2se sys
14WA2	149	0.012760	0.000670	0.000282	0.000024	0.280540	0.000039	3.81	3303	12	13	0.280522	0.280648	-4.47	1.47	1.48
14WA2	149	0.025430	0.000720	0.000584	0.000040	0.280585	0.000041	2.66	3316	11	12	0.280548	0.280639	-3.24	1.54	1.54
14WA2	150	0.024880	0.000470	0.000548	0.000037	0.280482	0.000049	0.64	3537	11	12	0.280445	0.280491	-1.66	1.82	1.82
14WA2	151	0.040700	0.001800	0.000858	0.000062	0.280089	0.000039	1.30	4078	13	13	0.280021	0.280127	-3.79	1.51	1.51
14WA2	151	0.026250	0.000180	0.000574	0.000039	0.280049	0.000045	0.75	4052	12	13	0.280004	0.280145	-5.03	1.70	1.70
14WA2	151	0.013930	0.000180	0.000304	0.000021	0.280043	0.000046	-2.12	3968	13	13	0.280020	0.280201	-6.48	1.73	1.73
14WA2	153	0.026580	0.000550	0.000585	0.000039	0.280352	0.000033	-0.35	3409	12	13	0.280314	0.280577	-9.39	1.27	1.28
14WA2	155	0.025820	0.000880	0.000549	0.000037	0.280081	0.000042	1.63	4017	11	12	0.280038	0.280168	-4.63	1.59	1.59
14WA2	160	0.026610	0.000490	0.000581	0.000041	0.280181	0.000037	2.15	3999	11	12	0.280136	0.280180	-1.57	1.43	1.43
14WA2	161	0.032530	0.000440	0.000701	0.000046	0.280324	0.000039	0.77	3397	12	13	0.280278	0.280585	-10.93	1.47	1.48
14WA2	169	0.027840	0.000410	0.000639	0.000044	0.280498	0.000042	0.58	3532	11	12	0.280454	0.280495	-1.44	1.58	1.58
14WA2	171	0.008830	0.000190	0.000168	0.000011	0.280152	0.000037	1.70	3995	11	12	0.280139	0.280183	-1.56	1.42	1.42
14WA2	171	0.005812	0.000071	0.000108	0.000007	0.280149	0.000036	1.94	3969	12	12	0.280141	0.280201	-2.14	1.39	1.39
14WA2	173	0.031970	0.000840	0.000627	0.000042	0.280288	0.000048	0.40	3400	11	12	0.280247	0.280583	-11.98	1.78	1.78
14WA2	174	0.037300	0.002400	0.000802	0.000063	0.280399	0.000043	1.56	3401	11	12	0.280346	0.280582	-8.40	1.61	1.62
14WA2	175	0.032990	0.000370	0.000662	0.000046	0.280377	0.000044	1.25	3403	11	12	0.280334	0.280581	-8.82	1.64	1.65
14WA2	181	0.033920	0.000750	0.000739	0.000049	0.280439	0.000041	0.91	3394	11	12	0.280391	0.280587	-6.99	1.54	1.55
14WA2	184	0.053300	0.001000	0.001118	0.000075	0.280196	0.000044	0.28	4015	12	12	0.280109	0.280170	-2.16	1.67	1.67
14WA2	186	0.017120	0.000360	0.000375	0.000025	0.280314	0.000044	0.27	3399	12	13	0.280289	0.280583	-10.48	1.64	1.65
14WA2	187	0.021200	0.000500	0.000465	0.000031	0.280296	0.000035	-0.57	3394	12	13	0.280266	0.280587	-11.46	1.34	1.35
14WA2	188	0.015550	0.000160	0.000340	0.000023	0.280415	0.000043	0.56	3527	11	12	0.280392	0.280498	-3.78	1.61	1.61
14WA2	188	0.007780	0.000250	0.000172	0.000012	0.280444	0.000049	0.53	3578	11	12	0.280432	0.280464	-1.12	1.82	1.82
14WA2	189	0.047700	0.001300	0.001060	0.000070	0.280415	0.000039	-0.09	3402	11	12	0.280345	0.280581	-8.41	1.48	1.48
14WA2	190	0.025470	0.000570	0.000555	0.000037	0.280363	0.000041	1.56	3386	11	12	0.280327	0.280593	-9.48	1.54	1.54
14WA2	191	0.066200	0.001400	0.001352	0.000090	0.280387	0.000037	0.67	3405	11	12	0.280298	0.280579	-10.02	1.42	1.42
14WA2	191	0.033450	0.000540	0.000704	0.000047	0.280301	0.000044	0.93	3400	11	12	0.280255	0.280583	-11.69	1.64	1.65
14WA2	195	0.020000	0.001200	0.000443	0.000033	0.280336	0.000051	2.05	3395	11	12	0.280307	0.280586	-9.96	1.88	1.89
14WA2	196	0.021260	0.000240	0.000485	0.000032	0.280452	0.000035	1.24	3536	11	12	0.280419	0.280492	-2.60	1.34	1.35
14WA2	196	0.014610	0.000110	0.000330	0.000022	0.280417	0.000035	1.33	3532	11	12	0.280395	0.280495	-3.57	1.34	1.35
14WA2	196	0.015190	0.000110	0.000351	0.000023	0.280422	0.000041	-0.10	3534	11	12	0.280398	0.280494	-3.40	1.54	1.55
14WA2	197	0.018370	0.000500	0.000416	0.000028	0.280455	0.000037	0.38	3540	11	12	0.280427	0.280490	-2.25	1.41	1.41
14WA2	197	0.010240	0.000180	0.000229	0.000015	0.280439	0.000038	0.92	3536	11	12	0.280423	0.280492	-2.44	1.44	1.45
14WA2	198	0.018340	0.000180	0.000430	0.000029	0.280433	0.000039	0.05	3388	12	13	0.280405	0.280591	-6.63	1.47	1.48
14WA2	199	0.029590	0.000620	0.000694	0.000046	0.280406	0.000036	0.85	3384	11	12	0.280361	0.280593	-8.29	1.37	1.38
14WA2	200	0.038120	0.000460	0.000884	0.000059	0.280395	0.000048	0.11	3390	11	12	0.280337	0.280589	-8.99	1.78	1.78

Table S10.1 cont.: *Jack Hills zircon Lu-Hf compositions*

Sample	Zirco -n #	$^{176}Yb/^{177}Hf$	2se	$^{176}Lu/^{177}Hf$	2se	$^{176}Hf/^{177}Hf$	2se prop	Disc %	^{207}Pb-^{206}Pb Age	2se	2se prop	$^{176}Hf/^{177}Hf(t)_{SAMP}$	$^{176}Hf/^{177}Hf(t)_{CHUR}$	$\varepsilon Hf(t)_{CHUR}$	2se	2se sys
14WA2	201	0.010630	0.000110	0.000246	0.000016	0.280158	0.000038	2.00	4086	11	12	0.280138	0.280122	0.60	1.46	1.46
14WA2	202	0.051080	0.000470	0.001083	0.000073	0.280402	0.000039	1.44	3401	11	12	0.280331	0.280582	-8.96	1.48	1.48
14WA2	208	0.024690	0.000550	0.000545	0.000037	0.280347	0.000044	2.81	3689	11	12	0.280308	0.280389	-2.89	1.65	1.65
14WA2	208	0.033640	0.000900	0.000744	0.000055	0.280357	0.000043	3.13	3701	11	12	0.280304	0.280381	-2.75	1.62	1.62
14WA2	225	0.022630	0.000340	0.000583	0.000039	0.280444	0.000042	1.60	3387	11	12	0.280406	0.280592	-6.62	1.57	1.58
14WA2	229	0.038700	0.001000	0.000853	0.000057	0.280388	0.000043	0.54	3386	11	12	0.280332	0.280593	-9.28	1.61	1.61
14WA2	237	0.021620	0.000280	0.000510	0.000034	0.280567	0.000043	0.78	3436	11	12	0.280533	0.280559	-0.91	1.61	1.61
14WA2	238	0.008996	0.000090	0.000204	0.000014	0.280251	0.000035	2.97	3665	11	12	0.280237	0.280406	-6.03	1.34	1.35
14WA2	251	0.033010	0.000930	0.000726	0.000048	0.280397	0.000031	1.09	3393	11	12	0.280350	0.280588	-8.49	1.21	1.21
14WA2	256	0.046600	0.002500	0.001011	0.000087	0.280365	0.000044	0.09	3499	12	13	0.280297	0.280517	-7.84	1.66	1.66
14WA4	5	0.021920	0.000270	0.000521	0.000026	0.280325	0.000042	3.06	3382	30	30	0.280291	0.280595	-10.83	1.70	1.70
14WA4	11	0.026180	0.000770	0.000583	0.000027	0.280338	0.000047	8.30	3465	30	30	0.280299	0.280540	-8.58	1.86	1.86
14WA4	15	0.027880	0.000430	0.000683	0.000031	0.280181	0.000044	-0.13	4016	29	29	0.280128	0.280169	-1.46	1.77	1.77
14WA4	18	0.021900	0.001300	0.000500	0.000023	0.280425	0.000042	-1.99	3519	29	29	0.280391	0.280503	-4.01	1.70	1.70
14WA4	20	0.052490	0.000750	0.001302	0.000073	0.280134	0.000047	0.52	4115	29	29	0.280030	0.280102	-2.57	1.87	1.87
14WA4	41	0.021190	0.000410	0.000469	0.000023	0.280371	0.000050	0.07	3517	29	29	0.280339	0.280505	-5.90	1.96	1.96
14WA4	42	0.033700	0.001000	0.000841	0.000038	0.280323	0.000040	-0.21	3379	30	30	0.280268	0.280597	-11.71	1.63	1.63
14WA4	46	0.026600	0.001800	0.000632	0.000033	0.280190	0.000034	1.07	4026	29	29	0.280141	0.280162	-0.76	1.46	1.46
14WA4	49	0.045600	0.001800	0.001081	0.000049	0.280467	0.000035	0.11	3367	30	30	0.280397	0.280605	-7.41	1.48	1.48
14WA4	51	0.034200	0.001000	0.000753	0.000033	0.280334	0.000041	-0.11	3371	30	30	0.280285	0.280602	-11.31	1.67	1.67
14WA4	55	0.041150	0.000390	0.000956	0.000051	0.280449	0.000042	0.86	3369	31	31	0.280387	0.280603	-7.71	1.71	1.71
14WA4	55	0.025790	0.000510	0.000608	0.000026	0.280399	0.000031	0.55	3374	30	30	0.280359	0.280600	-8.57	1.37	1.37
14WA4	60	0.030760	0.000470	0.000905	0.000040	0.280212	0.000037	0.09	3753	29	29	0.280146	0.280346	-7.13	1.54	1.55
14WA4	67	0.022500	0.001700	0.000725	0.000050	0.280633	0.000041	1.62	3348	30	30	0.280586	0.280617	-1.11	1.67	1.67
14WA4	73	0.027020	0.000230	0.000832	0.000036	0.280382	0.000033	1.14	3375	30	30	0.280328	0.280600	-9.69	1.42	1.42
14WA4	75	0.025490	0.000450	0.000792	0.000034	0.280444	0.000037	1.56	3382	30	30	0.280392	0.280595	-7.23	1.54	1.55
14WA4	85	0.022120	0.000600	0.000686	0.000033	0.280388	0.000030	0.36	3372	30	30	0.280343	0.280602	-9.21	1.34	1.34
14WA4	86	0.057920	0.000420	0.001613	0.000073	0.280566	0.000033	1.59	3398	30	30	0.280460	0.280584	-4.41	1.41	1.42
14WA4	88	0.031160	0.000960	0.000953	0.000040	0.280272	0.000040	1.52	3392	29	29	0.280210	0.280588	-13.49	1.63	1.63
14WA4	89	0.042900	0.000990	0.001126	0.000041	0.280102	0.000037	1.10	4118	29	29	0.280012	0.280100	-3.13	1.55	1.55
14WA4	89	0.019990	0.000360	0.000522	0.000025	0.280026	0.000042	-0.29	4126	31	31	0.279984	0.280094	-3.94	1.74	1.74
14WA4	97	0.030640	0.000610	0.000815	0.000036	0.280457	0.000042	3.09	3542	30	30	0.280401	0.280488	-3.10	1.70	1.70
14WA4	98	0.022710	0.000810	0.000563	0.000022	0.280360	0.000035	2.74	3379	30	30	0.280323	0.280597	-9.75	1.48	1.48
14WA4	107	0.026850	0.000960	0.000638	0.000027	0.280380	0.000037	2.33	3389	31	31	0.280338	0.280591	-8.99	1.55	1.55

Table S10.1 cont.: *Jack Hills zircon Lu-Hf compositions*

Sample	Zirco -n #	$^{176}Yb/^{177}Hf$	2se	$^{176}Lu/^{177}Hf$	2se	$^{176}Hf/^{177}Hf$	2se prop	Disc %	^{207}Pb-^{206}Pb Age	2se	2se prop	$^{176}Hf/^{177}Hf(t)_{SAMP}$	$^{176}Hf/^{177}Hf(t)_{CHUR}$	$\varepsilon Hf(t)_{CHUR}$	2se	2se sys
14WA4	108	0.031990	0.000430	0.000848	0.000039	0.280660	0.000030	3.55	3355	30	30	0.280605	0.280613	-0.27	1.33	1.33
14WA4	109	0.076500	0.001000	0.001576	0.000081	0.280043	0.000044	3.44	4211	28	28	0.279914	0.280037	-4.39	1.77	1.78
14WA4	109	0.009610	0.000140	0.000248	0.000011	0.280061	0.000038	-1.69	3999	30	30	0.280042	0.280181	-4.95	1.60	1.60
14WA4	114	0.031400	0.001100	0.000714	0.000032	0.280389	0.000033	2.39	3379	30	30	0.280342	0.280597	-9.07	1.42	1.42
14WA4	114	0.028170	0.000650	0.000639	0.000030	0.280383	0.000046	0.42	3366	30	30	0.280342	0.280606	-9.41	1.83	1.83
14WA4	120	0.029500	0.001100	0.000668	0.000031	0.280464	0.000042	1.18	3549	29	29	0.280418	0.280483	-2.31	1.70	1.70
14WA4	122	0.020580	0.000590	0.000471	0.000028	0.280423	0.000040	-0.79	3375	30	30	0.280392	0.280600	-7.39	1.64	1.64
14WA4	124	0.031360	0.000920	0.000701	0.000032	0.280483	0.000036	2.19	3528	30	30	0.280435	0.280497	-2.21	1.52	1.52
14WA4	124	0.007170	0.000120	0.000175	0.000008	0.280417	0.000043	1.81	3464	30	30	0.280405	0.280540	-4.80	1.73	1.73
14WA4	131	0.032730	0.000540	0.000717	0.000032	0.280129	0.000045	3.30	4014	29	29	0.280073	0.280170	-3.46	1.80	1.80
14WA4	132	0.026470	0.000430	0.000600	0.000027	0.280371	0.000035	2.63	3383	31	31	0.280332	0.280594	-9.35	1.49	1.49
14WA4	146	0.029830	0.000810	0.000686	0.000031	0.280336	0.000048	2.92	3397	30	30	0.280291	0.280585	-10.47	1.89	1.89
16WA5	3	0.050500	0.001000	0.001117	0.000054	0.280128	0.000039	1.92	4139	9	9	0.280038	0.280086	-1.70	1.49	1.49
16WA5	3	0.038850	0.000730	0.000885	0.000044	0.280136	0.000032	0.81	4137	9	9	0.280065	0.280087	-0.78	1.26	1.26
16WA5	4	0.024400	0.000590	0.000575	0.000026	0.280349	0.000038	0.39	3388	9	10	0.280311	0.280591	-9.96	1.43	1.43
16WA5	5	0.019420	0.000310	0.000487	0.000023	0.280090	0.000032	0.92	4017	9	9	0.280052	0.280168	-4.15	1.25	1.25
16WA5	11	0.037020	0.000740	0.000844	0.000038	0.280339	0.000036	0.19	3393	9	10	0.280284	0.280588	-10.83	1.36	1.37
16WA5	11	0.027710	0.000280	0.000640	0.000029	0.280296	0.000037	1.21	3393	9	10	0.280254	0.280588	-11.88	1.39	1.40
16WA5	16	0.037820	0.000530	0.000896	0.000043	0.280368	0.000039	-0.47	3382	9	10	0.280310	0.280595	-10.17	1.46	1.47
16WA5	17	0.017020	0.000660	0.000439	0.000020	0.280388	0.000033	-0.08	3387	9	10	0.280359	0.280591	-8.27	1.26	1.27
16WA5	18	0.014190	0.000420	0.000331	0.000015	0.280413	0.000034	-0.17	3452	9	10	0.280391	0.280549	-5.61	1.30	1.30
16WA5	18	0.021860	0.000480	0.000515	0.000023	0.280367	0.000036	0.69	3456	9	10	0.280333	0.280546	-7.59	1.36	1.37
16WA5	20	0.037200	0.000510	0.000880	0.000040	0.280475	0.000034	0.12	3438	9	10	0.280417	0.280558	-5.03	1.30	1.30
16WA5	20	0.033300	0.001100	0.000779	0.000035	0.280484	0.000029	-0.31	3442	9	10	0.280432	0.280555	-4.37	1.13	1.14
16WA5	26	0.035770	0.000280	0.000924	0.000042	0.280567	0.000027	1.55	3441	8	10	0.280506	0.280555	-1.77	1.06	1.07
16WA5	31	0.011570	0.000086	0.000287	0.000013	0.280437	0.000034	0.82	3501	12	13	0.280418	0.280515	-3.49	1.31	1.32
16WA5	34	0.024990	0.000290	0.000609	0.000030	0.280311	0.000034	0.42	3412	12	13	0.280271	0.280575	-10.83	1.31	1.31
16WA5	40	0.012830	0.000350	0.000337	0.000015	0.280625	0.000034	-0.82	3359	12	13	0.280603	0.280610	-0.26	1.31	1.31
16WA5	45	0.029050	0.000320	0.000598	0.000029	0.280327	0.000038	-0.46	3386	13	13	0.280288	0.280592	-10.84	1.45	1.44
16WA5	58	0.023780	0.000470	0.000477	0.000023	0.280340	0.000035	0.04	3399	13	13	0.280309	0.280584	-9.80	1.35	1.35
16WA5	81	0.032610	0.000470	0.000757	0.000030	0.280452	0.000030	2.06	3568	12	13	0.280400	0.280471	-2.52	1.18	1.19
16WA5	86	0.020570	0.000170	0.000471	0.000024	0.280337	0.000037	0.70	3454	13	13	0.280306	0.280547	-8.59	1.41	1.41
16WA5	121	0.028900	0.001800	0.000656	0.000037	0.280479	0.000034	0.08	3404	13	13	0.280436	0.280580	-5.13	1.31	1.31
16WA5	122	0.032400	0.001200	0.000709	0.000033	0.280172	0.000034	0.63	4032	9	9	0.280117	0.280158	-1.48	1.31	1.32

Table S10.1 cont.: *Jack Hills zircon Lu-Hf compositions*

Sample	Zirco -n #	$^{176}Yb/^{177}Hf$	2se	$^{176}Lu/^{177}Hf$	2se	$^{176}Hf/^{177}Hf$	2se	Disc %	^{207}Pb-^{206}Pb Age	2se	2se prop	$^{176}Hf/^{177}Hf(t)_{SAMP}$	$^{176}Hf/^{177}Hf(t)_{CHUR}$	$\varepsilon Hf(t)_{CHUR}$	2se	2se sys
16WA5	122	0.032490	0.000220	0.000813	0.000039	0.280177	0.000047	-0.15	4043	9	9	0.280113	0.280151	-1.34	1.75	1.75
16WA5	123	0.033260	0.000480	0.000776	0.000040	0.280401	0.000030	1.32	3488	8	10	0.280349	0.280524	-6.25	1.16	1.17
16WA5	130	0.051800	0.001100	0.001162	0.000056	0.280437	0.000039	-1.24	3490	8	10	0.280359	0.280523	-5.85	1.47	1.47
16WA5	131	0.049200	0.001400	0.001224	0.000054	0.280381	0.000041	3.18	3411	13	14	0.280301	0.280576	-9.82	1.55	1.55
16WA5	131	0.030200	0.001000	0.000807	0.000053	0.280307	0.000033	1.27	3411	13	14	0.280254	0.280576	-11.47	1.29	1.29
16WA5	135	0.087000	0.001300	0.002209	0.000098	0.280132	0.000037	1.32	4349	13	13	0.279945	0.279943	0.08	1.46	1.46
16WA5	135	0.077200	0.002000	0.001868	0.000093	0.280041	0.000041	1.32	4358	12	12	0.279883	0.279937	-1.94	1.59	1.59
16WA5	144	0.025040	0.000440	0.000677	0.000030	0.280512	0.000033	-0.07	3482	13	14	0.280467	0.280528	-2.19	1.28	1.29
16WA5	168	0.042400	0.000270	0.001068	0.000050	0.280343	0.000029	0.13	3762	9	10	0.280265	0.280340	-2.68	1.14	1.15

Supplementary S10.1: Compositions of sample unknowns analysed during a Lu-Hf session in October 2018. Disc%= % discordance of ^{206}Pb-^{238}U age and ^{207}Pb-^{206}Pb age. 2se $\varepsilon Hf(t)_{CHUR}$ uncertainties calculated using the method of Ickert (2013), which incorporate analytical uncertainties of the $^{176}Lu/^{177}Hf$ ratio, $^{176}Hf/^{177}Hf$ ratio, ^{207}Pb-^{206}Pb age 2se, uncertainties surrounding chondritic compositions and 176Lu decay constant uncertainties. 2se sys (systematic propagation) uses the systematic uncertainty of the ^{207}Pb-^{206}Pb measurement, rather than the analytical measurement.

Supplementary Material Eleven:

Jack Hills zircons imaging and spot selection

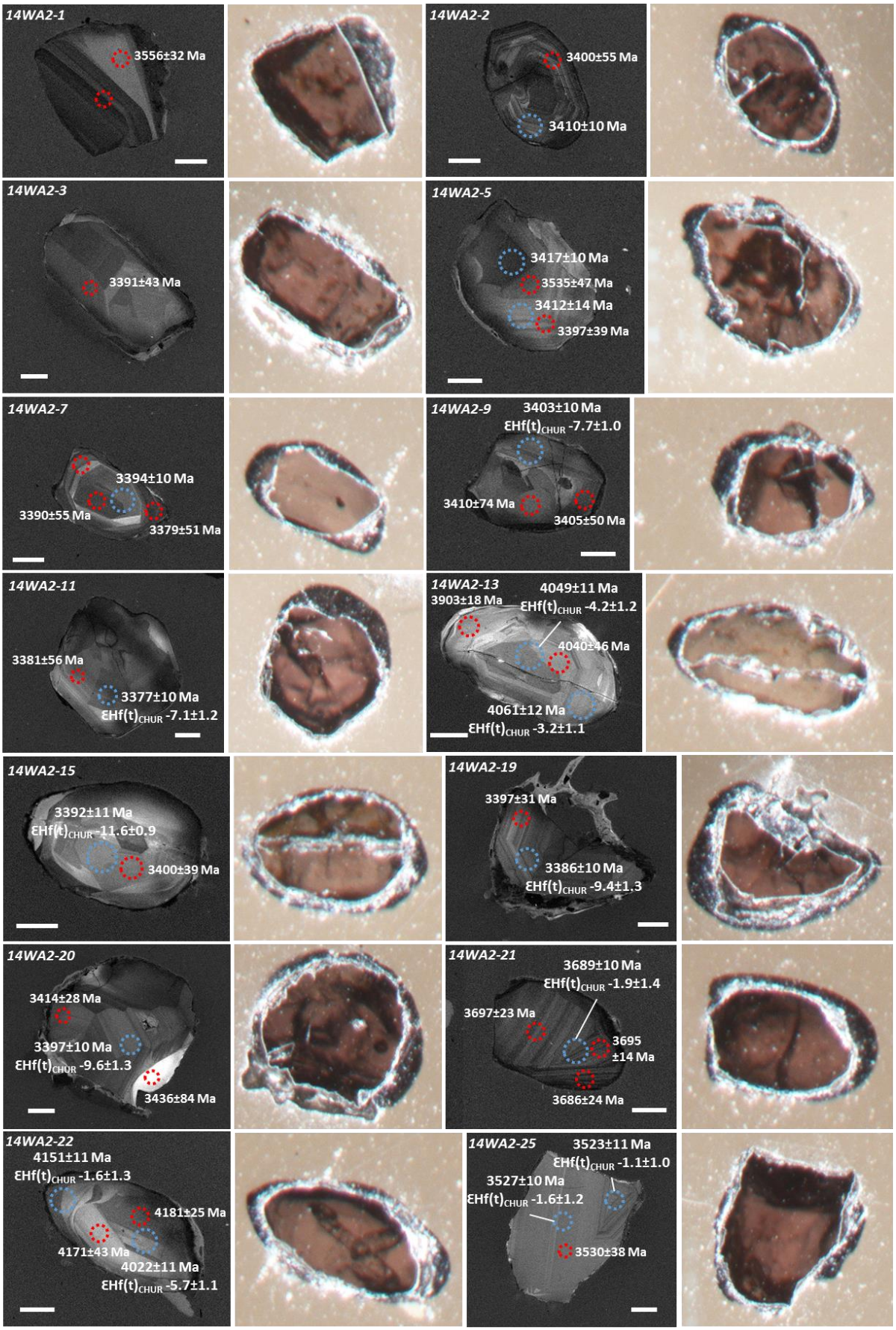
14WA2-1
3556±32 Ma
14WA2-2
3400±55 Ma
3410±10 Ma
14WA2-3
3391±43 Ma
14WA2-5
3417±10 Ma
3535±47 Ma
3412±14 Ma
3397±39 Ma
14WA2-7
3394±10 Ma
3390±55 Ma
3379±51 Ma
14WA2-9
3403±10 Ma
εHf(t)CHUR -7.7±1.0
3410±74 Ma
3405±50 Ma
14WA2-11
3381±56 Ma
3377±10 Ma
εHf(t)CHUR -7.1±1.2
14WA2-13
4049±11 Ma
3903±18 Ma
εHf(t)CHUR -4.2±1.2
4040±46 Ma
4061±12 Ma
εHf(t)CHUR -3.2±1.1
14WA2-15
3392±11 Ma
εHf(t)CHUR -11.6±0.9
3400±39 Ma
14WA2-19
3397±31 Ma
3386±10 Ma
εHf(t)CHUR -9.4±1.3
14WA2-20
3414±28 Ma
3397±10 Ma
εHf(t)CHUR -9.6±1.3
3436±84 Ma
14WA2-21
3689±10 Ma
εHf(t)CHUR -1.9±1.4
3697±23 Ma
3695
±14 Ma
3686±24 Ma
14WA2-22
4151±11 Ma
εHf(t)CHUR -1.6±1.3
4181±25 Ma
4171±43 Ma
4022±11 Ma
εHf(t)CHUR -5.7±1.1
14WA2-25
3523±11 Ma
εHf(t)CHUR -1.1±1.0
3527±10 Ma
εHf(t)CHUR -1.6±1.2
3530±38 Ma

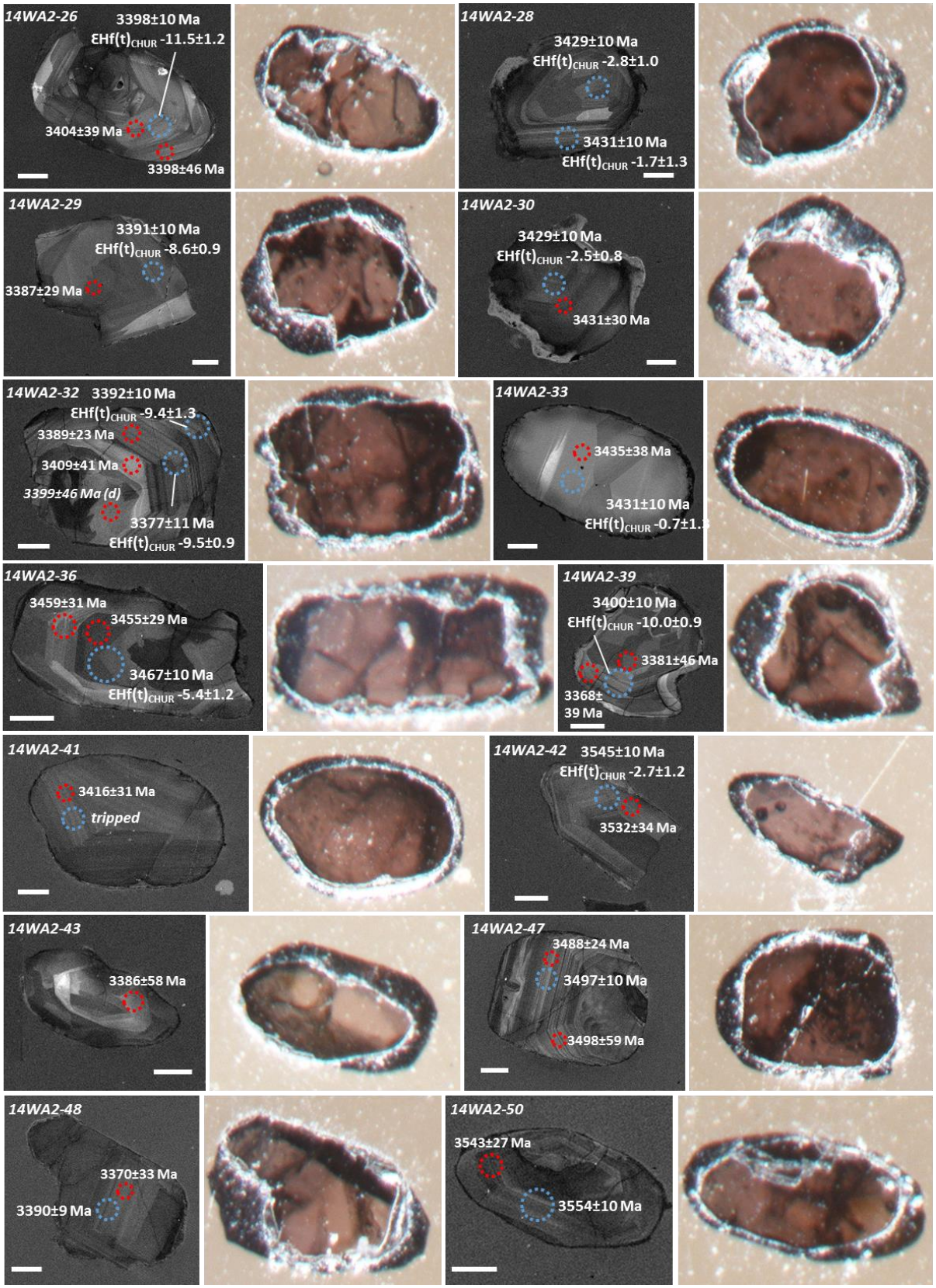
14WA2-26
3398±10 Ma
εHf(t)CHUR -11.5±1.2
3404±39 Ma
3398±46 Ma
14WA2-28
3429±10 Ma
εHf(t)CHUR -2.8±1.0
3431±10 Ma
εHf(t)CHUR -1.7±1.3
14WA2-29
3391±10 Ma
εHf(t)CHUR -8.6±0.9
3387±29 Ma
14WA2-30
3429±10 Ma
εHf(t)CHUR -2.5±0.8
3431±30 Ma
14WA2-32
3392±10 Ma
εHf(t)CHUR -9.4±1.3
3389±23 Ma
3409±41 Ma
3399±46 Ma (d)
3377±11 Ma
εHf(t)CHUR -9.5±0.9
14WA2-33
3435±38 Ma
3431±10 Ma
εHf(t)CHUR -0.7±1.
14WA2-36
3459±31 Ma
3455±29 Ma
3467±10 Ma
εHf(t)CHUR -5.4±1.2
14WA2-39
3400±10 Ma
εHf(t)CHUR -10.0±0.9
3381±46 Ma
3368±
39 Ma
14WA2-41
3416±31 Ma
tripped
14WA2-42
3545±10 Ma
εHf(t)CHUR -2.7±1.2
3532±34 Ma
14WA2-43
3386±58 Ma
14WA2-47
3488±24 Ma
3497±10 Ma
3498±59 Ma
14WA2-48
3370±33 Ma
3390±9 Ma
14WA2-50
3543±27 Ma
3554±10 Ma

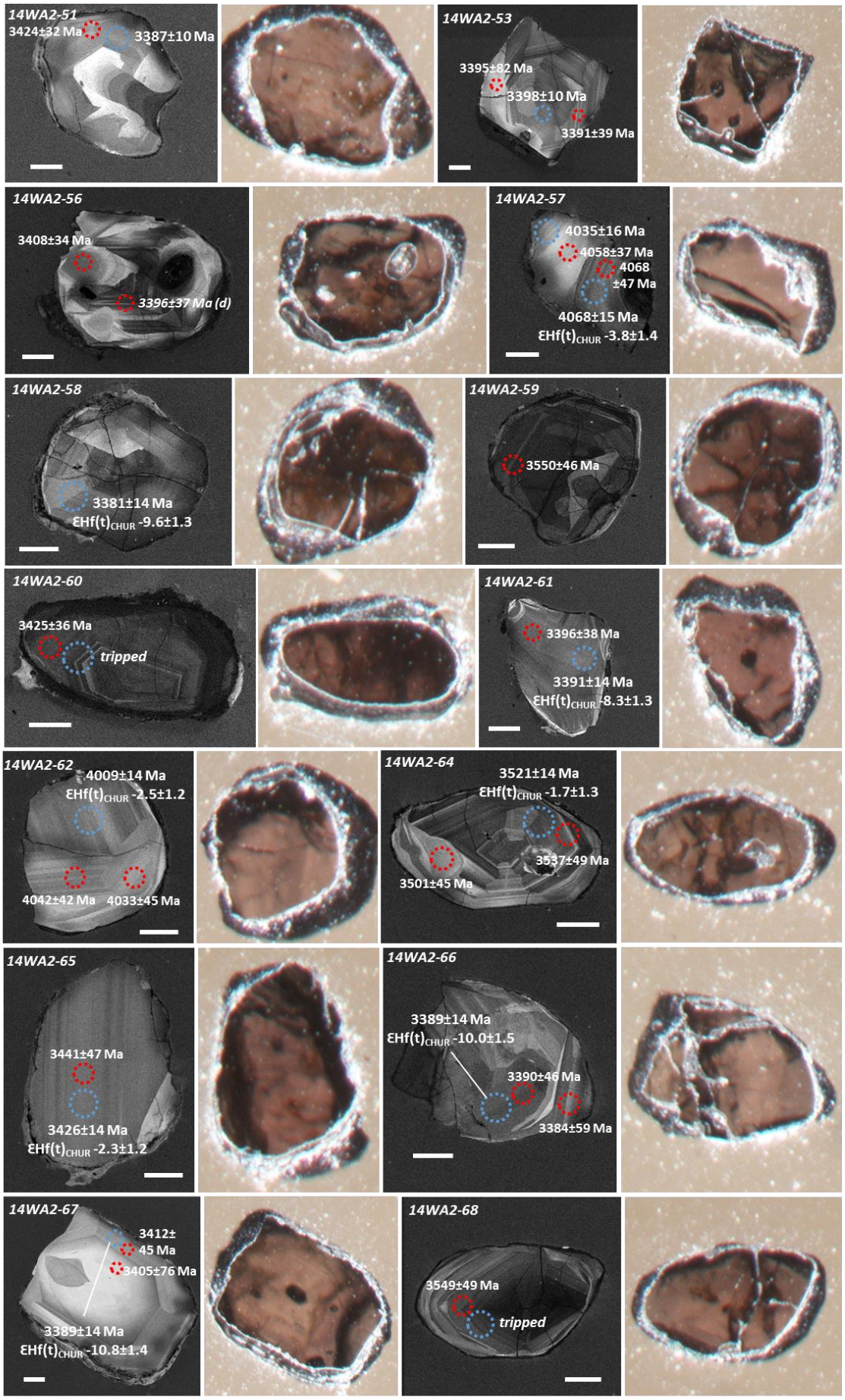
14WA2-51
3424±32 Ma
3387±10 Ma
14WA2-53
3395±82 Ma
3398±10 Ma
3391±39 Ma
14WA2-56
3408±34 Ma
3396±37 Ma (d)
14WA2-57
4035±16 Ma
4058±37 Ma
4068
±47 Ma
4068±15 Ma
εHf(t)CHUR -3.8±1.4
14WA2-58
3381±14 Ma
εHf(t)CHUR -9.6±1.3
14WA2-59
3550±46 Ma
14WA2-60
3425±36 Ma
tripped
14WA2-61
3396±38 Ma
3391±14 Ma
εHf(t)CHUR -8.3±1.3
14WA2-62
4009±14 Ma
εHf(t)CHUR -2.5±1.2
4042±42 Ma
4033±45 Ma
14WA2-64
3521±14 Ma
εHf(t)CHUR -1.7±1.3
3537±49 Ma
3501±45 Ma
14WA2-65
3441±47 Ma
3426±14 Ma
εHf(t)CHUR -2.3±1.2
14WA2-66
3389±14 Ma
εHf(t)CHUR -10.0±1.5
3390±46 Ma
3384±59 Ma
14WA2-67
3412±
45 Ma
3405±76 Ma
3389±14 Ma
εHf(t)CHUR -10.8±1.4
14WA2-68
3549±49 Ma
tripped

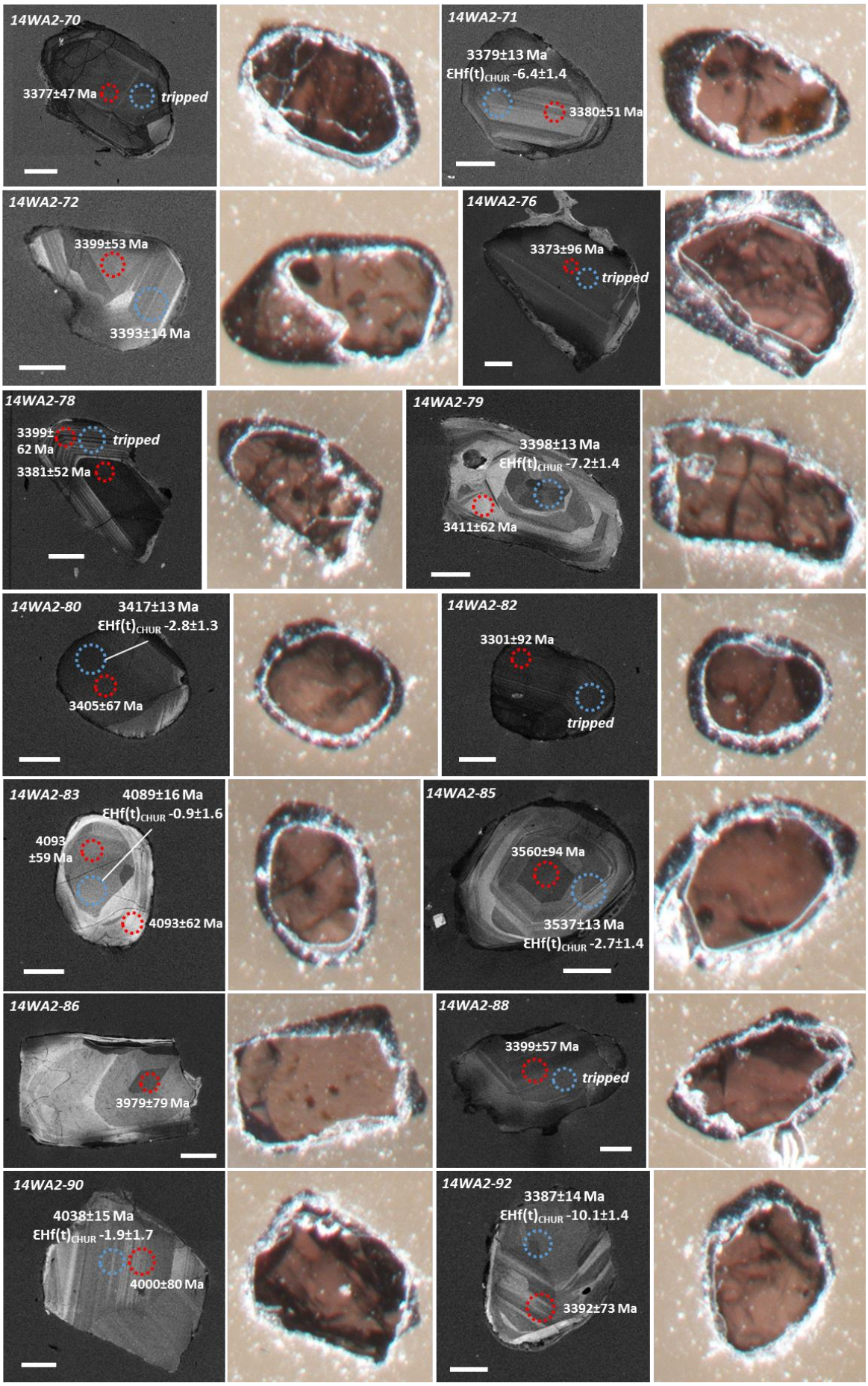
14WA2-70
3377±47 Ma
tripped
14WA2-71
3379±13 Ma
εHf(t)CHUR -6.4±1.4
3380±51 Ma
14WA2-72
3399±53 Ma
3393±14 Ma
14WA2-76
3373±96 Ma
tripped
14WA2-78
3399±
62 Ma
tripped
3381±52 Ma
14WA2-79
3398±13 Ma
εHf(t)CHUR -7.2±1.4
3411±62 Ma
14WA2-80
3417±13 Ma
εHf(t)CHUR -2.8±1.3
3405±67 Ma
14WA2-82
3301±92 Ma
tripped
14WA2-83
4089±16 Ma
εHf(t)CHUR -0.9±1.6
4093
±59 Ma
4093±62 Ma
14WA2-85
3560±94 Ma
3537±13 Ma
εHf(t)CHUR -2.7±1.4
14WA2-86
3979±79 Ma
14WA2-88
3399±57 Ma
tripped
14WA2-90
4038±15 Ma
εHf(t)CHUR -1.9±1.7
4000±80 Ma
14WA2-92
3387±14 Ma
εHf(t)CHUR -10.1±1.4
3392±73 Ma

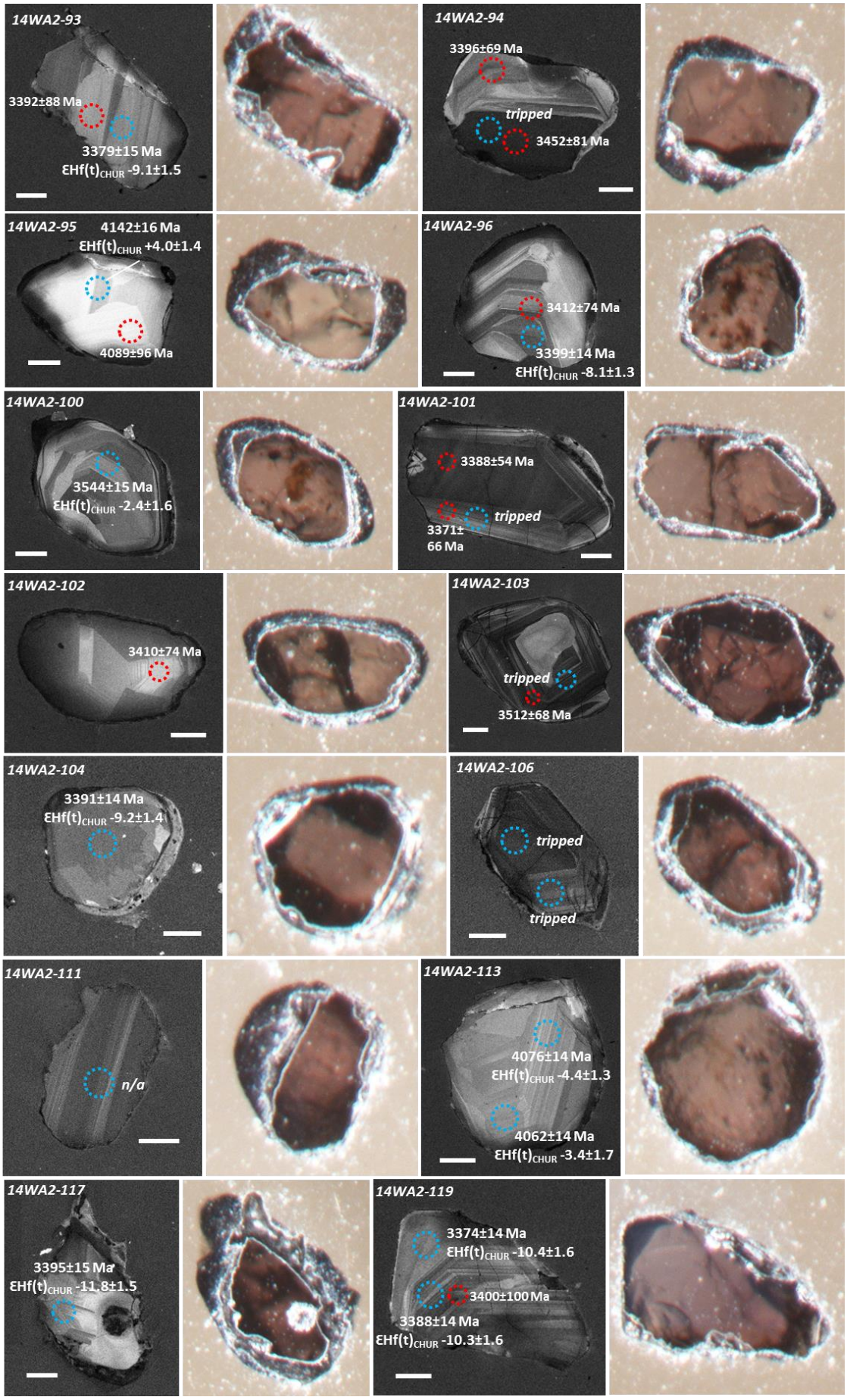
14WA2-93
3392±88 Ma
3379±15 Ma
εHf(t)CHUR -9.1±1.5
14WA2-94
3396±69 Ma
tripped
3452±81 Ma
14WA2-95
4142±16 Ma
εHf(t)CHUR +4.0±1.4
4089±96 Ma
14WA2-96
3412±74 Ma
3399±14 Ma
εHf(t)CHUR -8.1±1.3
14WA2-100
3544±15 Ma
εHf(t)CHUR -2.4±1.6
14WA2-101
3388±54 Ma
tripped
3371±
66 Ma
14WA2-102
3410±74 Ma
14WA2-103
tripped
3512±68 Ma
14WA2-104
3391±14 Ma
εHf(t)CHUR -9.2±1.4
14WA2-106
tripped
tripped
14WA2-111
n/a
14WA2-113
4076±14 Ma
εHf(t)CHUR -4.4±1.3
4062±14 Ma
εHf(t)CHUR -3.4±1.7
14WA2-117
3395±15 Ma
εHf(t)CHUR -11.8±1.5
14WA2-119
3374±14 Ma
εHf(t)CHUR -10.4±1.6
3400±100 Ma
3388±14 Ma
εHf(t)CHUR -10.3±1.6

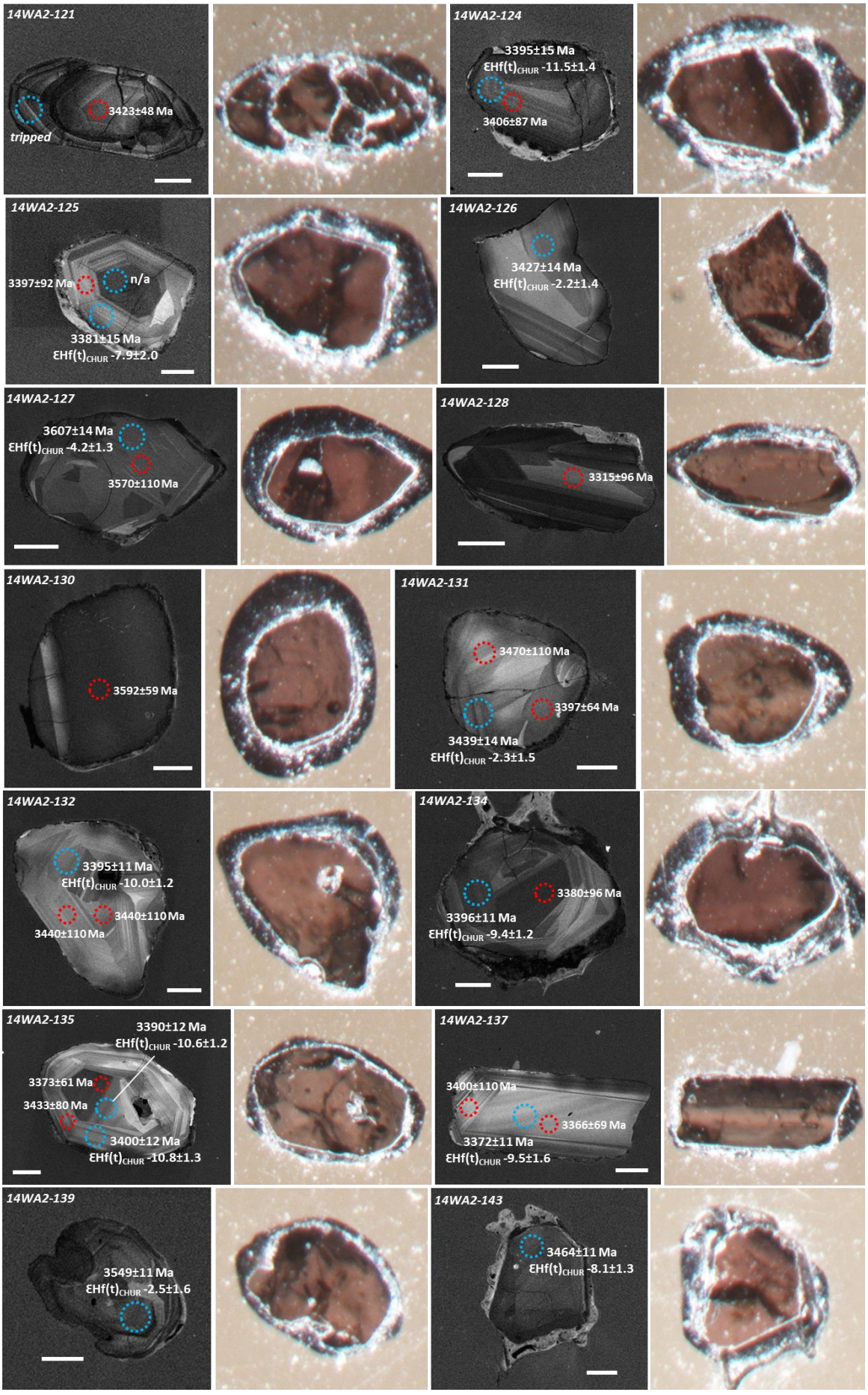
14WA2-121
3423±48 Ma
tripped
14WA2-124
3395±15 Ma
εHf(t)CHUR -11.5±1.4
3406±87 Ma
14WA2-125
3397±92 Ma
n/a
3381±15 Ma
εHf(t)CHUR -7.9±2.0
14WA2-126
3427±14 Ma
εHf(t)CHUR -2.2±1.4
14WA2-127
3607±14 Ma
εHf(t)CHUR -4.2±1.3
3570±110 Ma
14WA2-128
3315±96 Ma
14WA2-130
3592±59 Ma
14WA2-131
3470±110 Ma
3397±64 Ma
3439±14 Ma
εHf(t)CHUR -2.3±1.5
14WA2-132
3395±11 Ma
εHf(t)CHUR -10.0±1.2
3440±110 Ma
3440±110 Ma
14WA2-134
3380±96 Ma
3396±11 Ma
εHf(t)CHUR -9.4±1.2
14WA2-135
3390±12 Ma
εHf(t)CHUR -10.6±1.2
3373±61 Ma
3433±80 Ma
3400±12 Ma
εHf(t)CHUR -10.8±1.3
14WA2-137
3400±110 Ma
3366±69 Ma
3372±11 Ma
εHf(t)CHUR -9.5±1.6
14WA2-139
3549±11 Ma
εHf(t)CHUR -2.5±1.6
14WA2-143
3464±11 Ma
εHf(t)CHUR -8.1±1.3

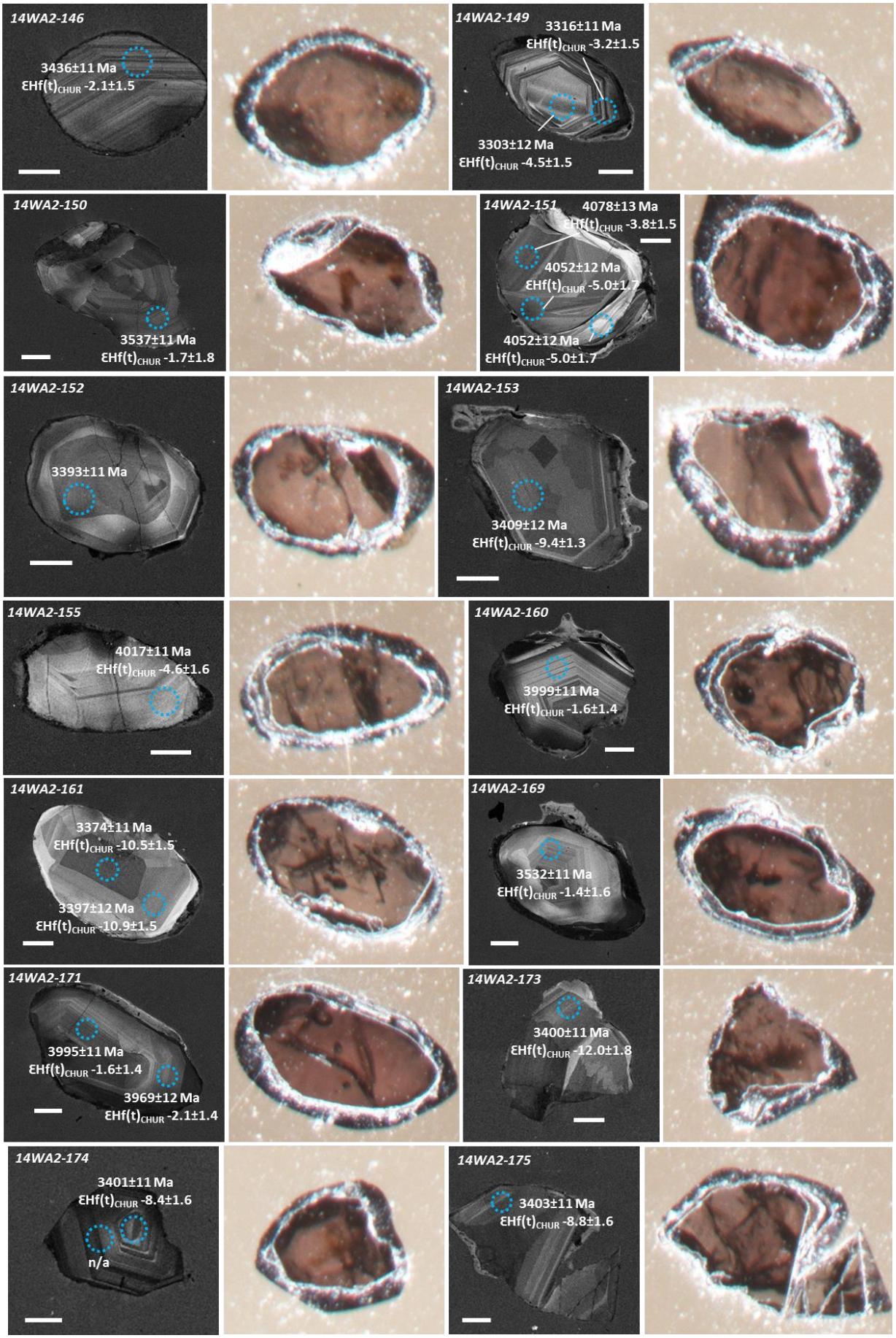
14WA2-146
3436±11 Ma
εHf(t)CHUR -2.1±1.5
14WA2-149
3316±11 Ma
εHf(t)CHUR -3.2±1.5
3303±12 Ma
εHf(t)CHUR -4.5±1.5
14WA2-150
3537±11 Ma
εHf(t)CHUR -1.7±1.8
14WA2-151
4078±13 Ma
εHf(t)CHUR -3.8±1.5
4052±12 Ma
εHf(t)CHUR -5.0±1.7
4052±12 Ma
εHf(t)CHUR -5.0±1.7
14WA2-152
3393±11 Ma
14WA2-153
3409±12 Ma
εHf(t)CHUR -9.4±1.3
14WA2-155
4017±11 Ma
εHf(t)CHUR -4.6±1.6
14WA2-160
3999±11 Ma
εHf(t)CHUR -1.6±1.4
14WA2-161
3374±11 Ma
εHf(t)CHUR -10.5±1.5
3397±12 Ma
εHf(t)CHUR -10.9±1.5
14WA2-169
3532±11 Ma
εHf(t)CHUR -1.4±1.6
14WA2-171
3995±11 Ma
εHf(t)CHUR -1.6±1.4
3969±12 Ma
εHf(t)CHUR -2.1±1.4
14WA2-173
3400±11 Ma
εHf(t)CHUR -12.0±1.8
14WA2-174
3401±11 Ma
εHf(t)CHUR -8.4±1.6
n/a
14WA2-175
3403±11 Ma
εHf(t)CHUR -8.8±1.6

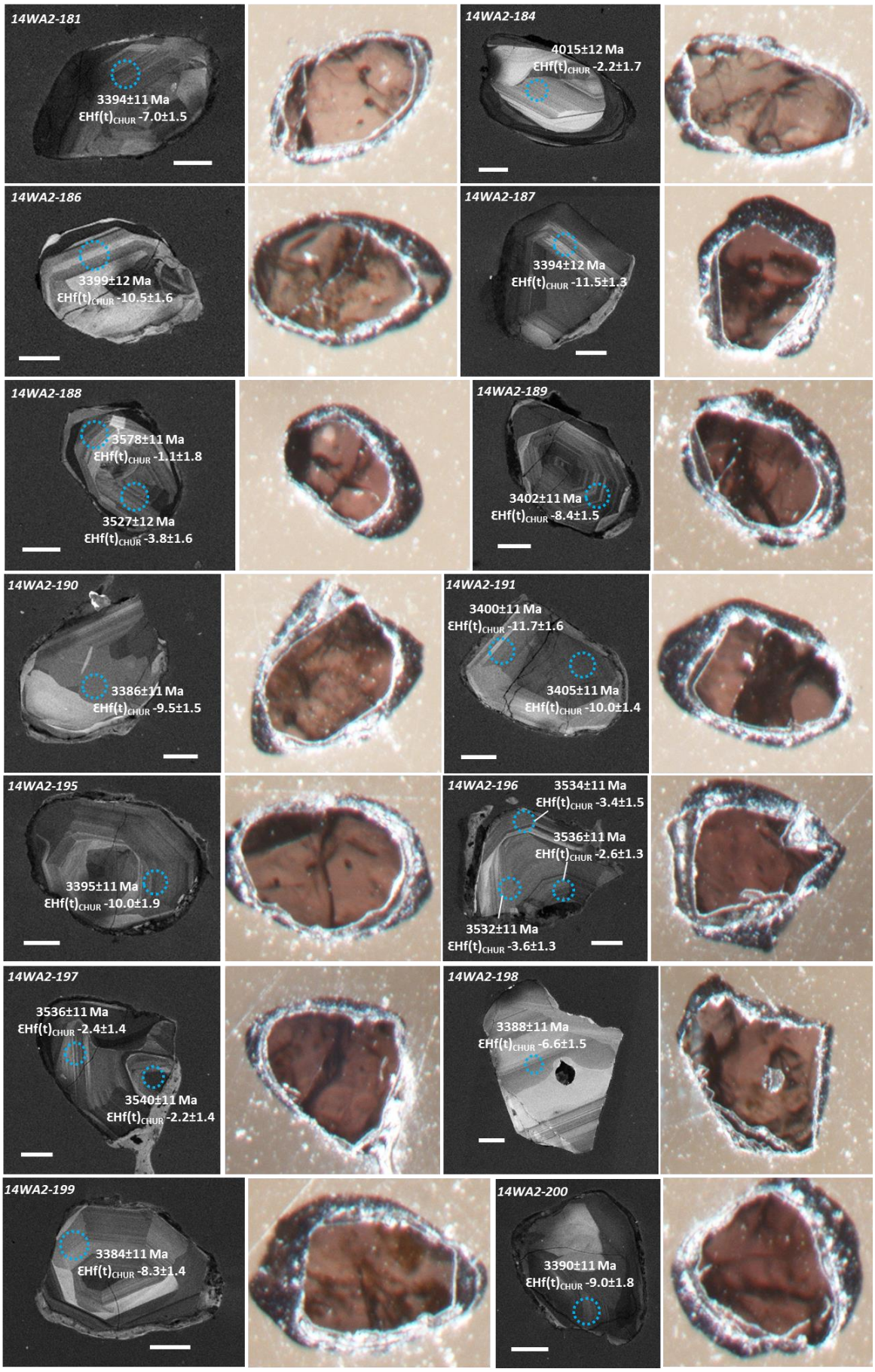
14WA2-181
3394±11 Ma
εHf(t)CHUR -7.0±1.5
14WA2-184
4015±12 Ma
εHf(t)CHUR -2.2±1.7
14WA2-186
3399±12 Ma
εHf(t)CHUR -10.5±1.6
14WA2-187
3394±12 Ma
εHf(t)CHUR -11.5±1.3
14WA2-188
3578±11 Ma
εHf(t)CHUR -1.1±1.8
3527±12 Ma
εHf(t)CHUR -3.8±1.6
14WA2-189
3402±11 Ma
εHf(t)CHUR -8.4±1.5
14WA2-190
3386±11 Ma
εHf(t)CHUR -9.5±1.5
14WA2-191
3400±11 Ma
εHf(t)CHUR -11.7±1.6
3405±11 Ma
εHf(t)CHUR -10.0±1.4
14WA2-195
3395±11 Ma
εHf(t)CHUR -10.0±1.9
14WA2-196
3534±11 Ma
εHf(t)CHUR -3.4±1.5
3536±11 Ma
εHf(t)CHUR -2.6±1.3
3532±11 Ma
εHf(t)CHUR -3.6±1.3
14WA2-197
3536±11 Ma
εHf(t)CHUR -2.4±1.4
3540±11 Ma
εHf(t)CHUR -2.2±1.4
14WA2-198
3388±11 Ma
εHf(t)CHUR -6.6±1.5
14WA2-199
3384±11 Ma
εHf(t)CHUR -8.3±1.4
14WA2-200
3390±11 Ma
εHf(t)CHUR -9.0±1.8

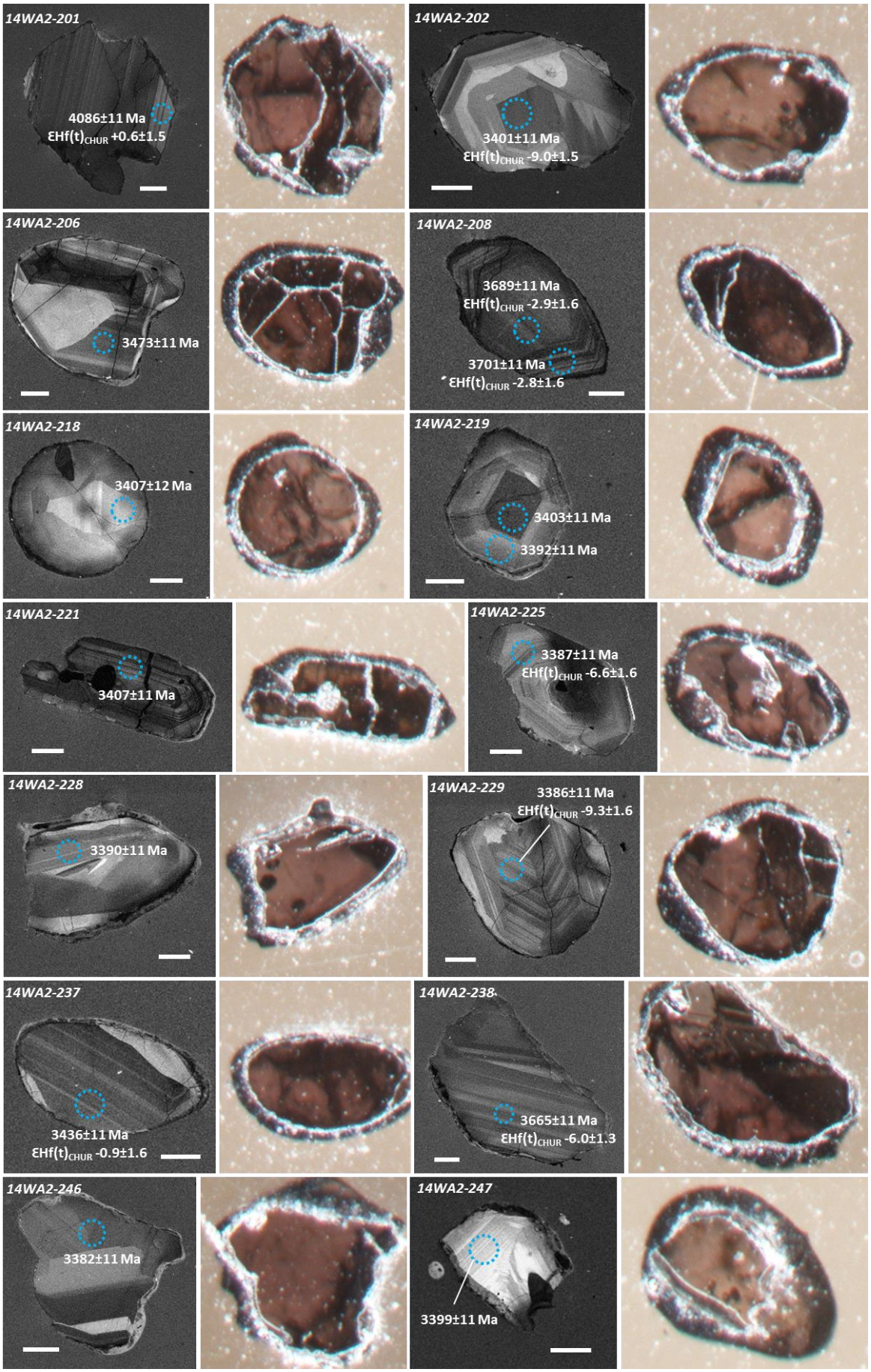
14WA2-201
4086±11 Ma
εHf(t)CHUR +0.6±1.5
14WA2-202
3401±11 Ma
εHf(t)CHUR -9.0±1.5
14WA2-206
3473±11 Ma
14WA2-208
3689±11 Ma
εHf(t)CHUR -2.9±1.6
3701±11 Ma
εHf(t)CHUR -2.8±1.6
14WA2-218
3407±12 Ma
14WA2-219
3403±11 Ma
3392±11 Ma
14WA2-221
3407±11 Ma
14WA2-225
3387±11 Ma
εHf(t)CHUR -6.6±1.6
14WA2-228
3390±11 Ma
14WA2-229
3386±11 Ma
εHf(t)CHUR -9.3±1.6
14WA2-237
3436±11 Ma
εHf(t)CHUR -0.9±1.6
14WA2-238
3665±11 Ma
εHf(t)CHUR -6.0±1.3
14WA2-246
3382±11 Ma
14WA2-247
3399±11 Ma

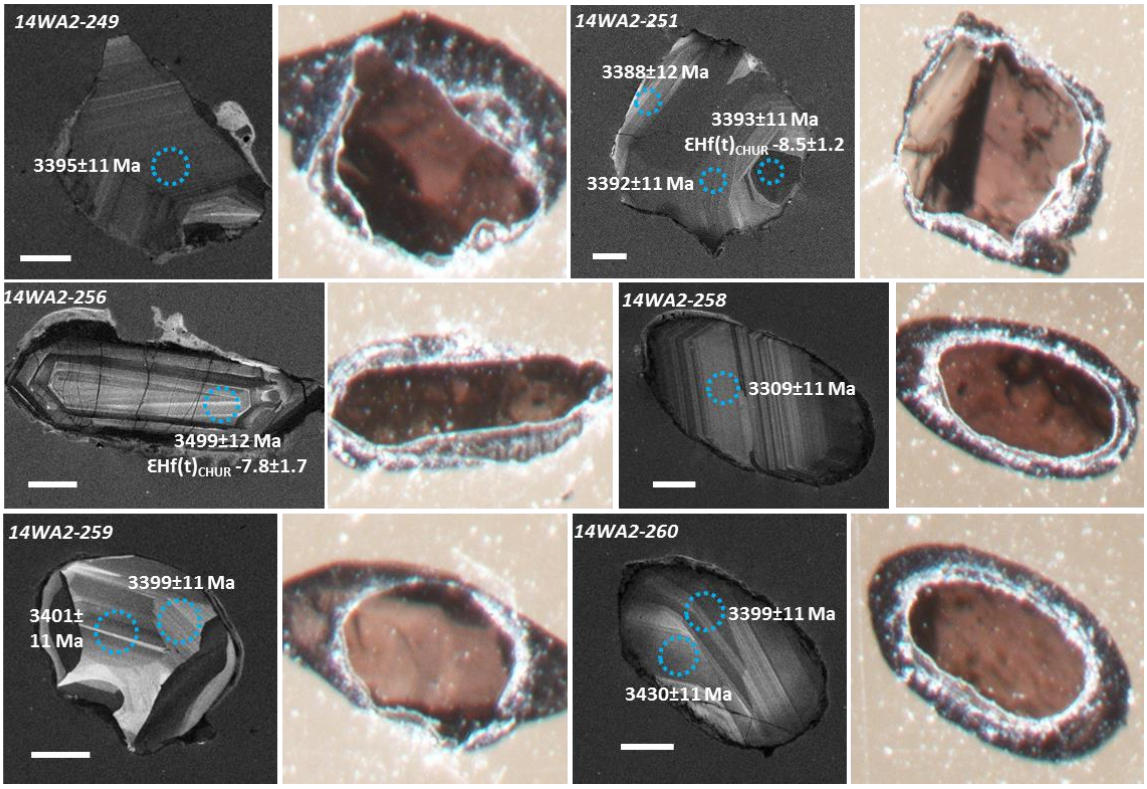

Figure S11.1: CL and transmitted light images of 14WA2 Jack Hills zircons analysed within this study. Spots are 35 µm, the size of the Hf spot used within this study. Where only a U-Pb ablation was performed (20 µm) this was placed in the centre of 35 µm spots. Red circles denote preliminary U-Pb analyses, blue circles represent the data presented in this thesis. Both U-Pb and εHf(t) uncertainties are the analytical uncertainties.

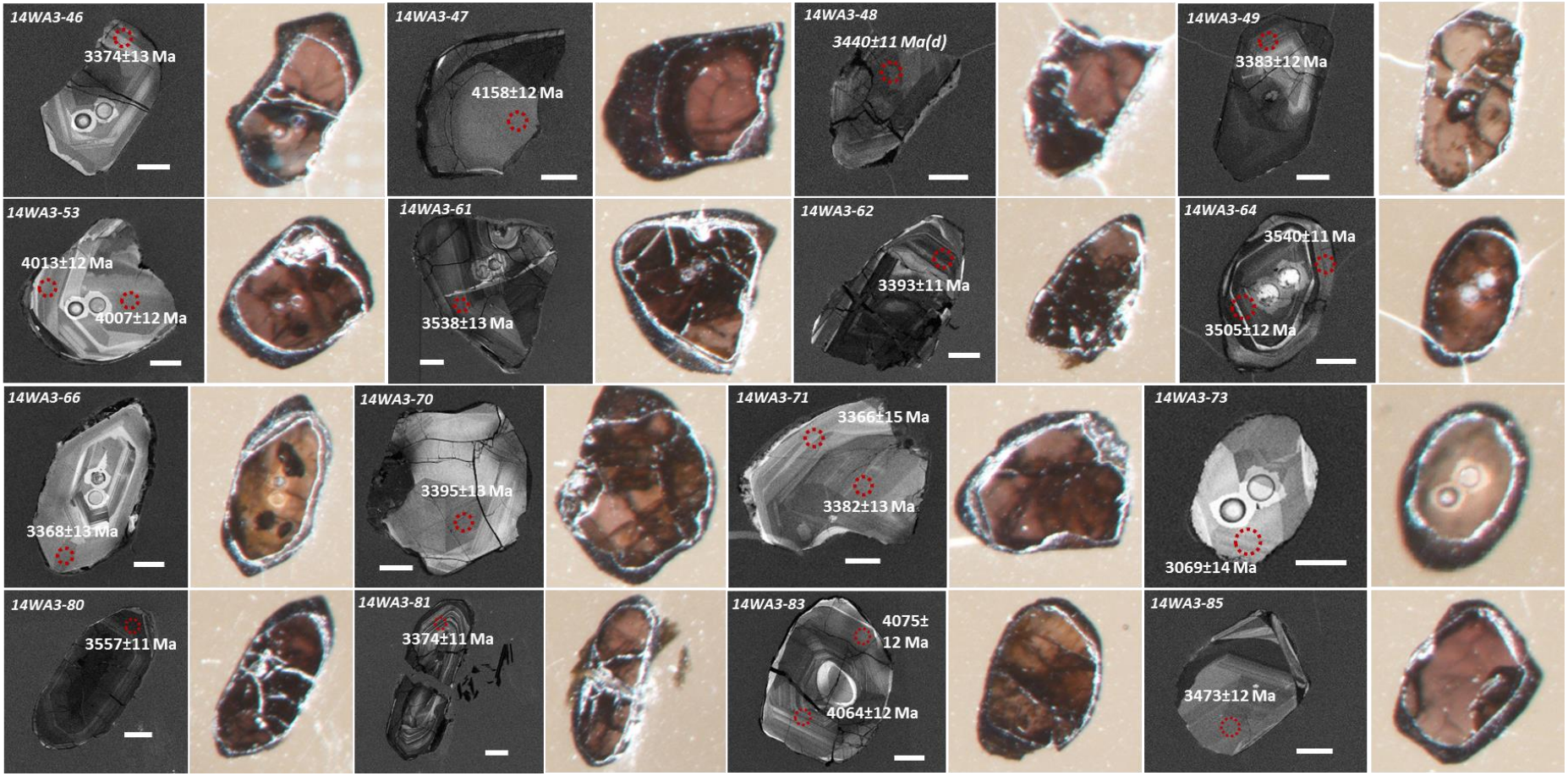

Figure S11.2: CL and transmitted light images of 14WA3 Jack Hills zircons analysed within this study. Spots are 35 µm, the size of the Hf spot used within this study. Where only a U-Pb ablation was performed (20 µm) this was placed in the centre of 35 µm spots. Previous ablation pits are U-Pb and REE analyses undertaken by Bruno Dhuime and Ben Brennan.

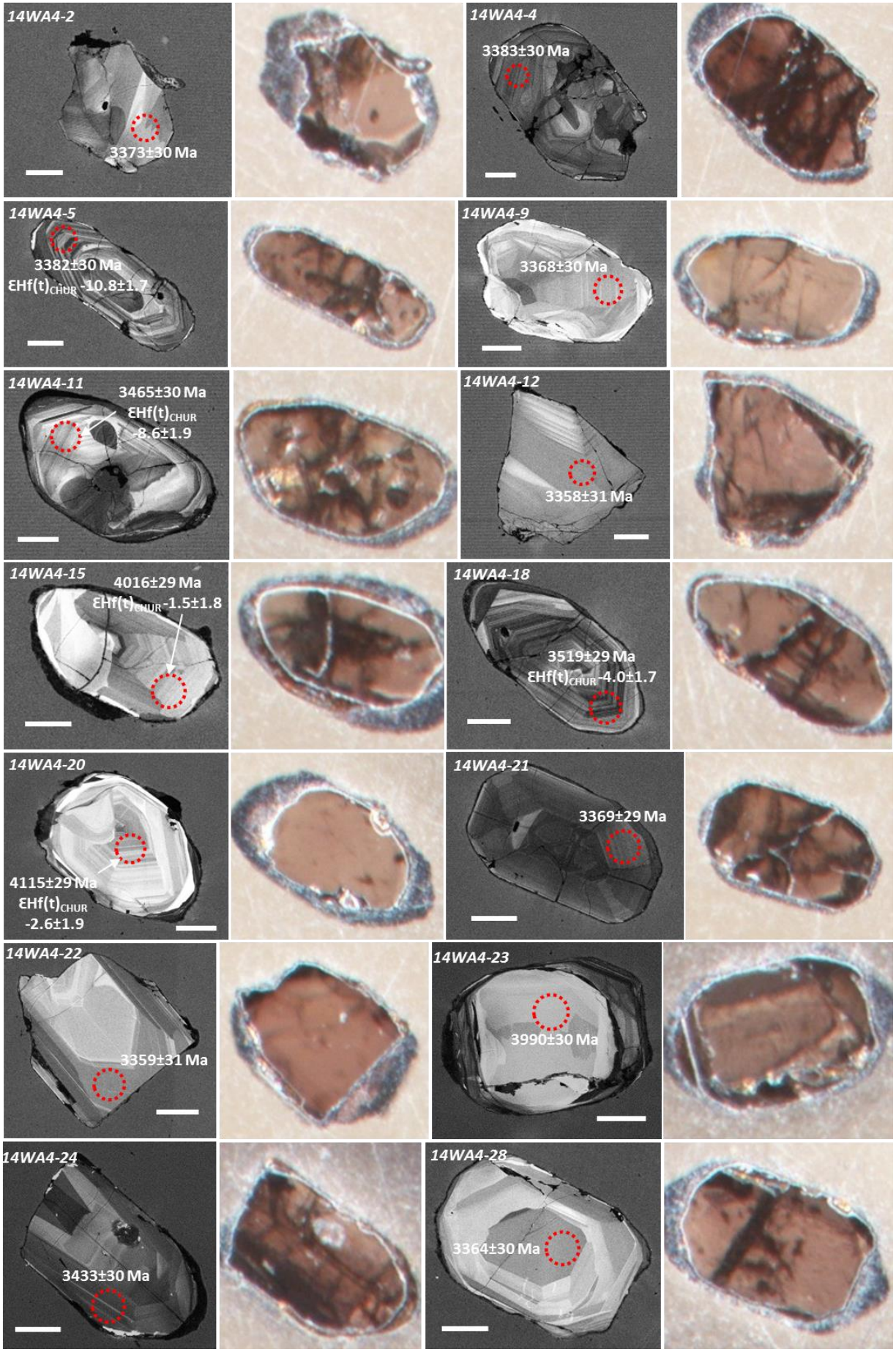
14WA4-2
3373±30 Ma
14WA4-4
3383±30 Ma
14WA4-5
3382±30 Ma
εHf(t)CHUR -10.8±1.7
14WA4-9
3368±30 Ma
14WA4-11
3465±30 Ma
εHf(t)CHUR
-8.6±1.9
14WA4-12
3358±31 Ma
14WA4-15
4016±29 Ma
εHf(t)CHUR -1.5±1.8
14WA4-18
3519±29 Ma
εHf(t)CHUR -4.0±1.7
14WA4-20
4115±29 Ma
εHf(t)CHUR
-2.6±1.9
14WA4-21
3369±29 Ma
14WA4-22
3359±31 Ma
14WA4-23
3990±30 Ma
14WA4-24
3433±30 Ma
14WA4-28
3364±30 Ma

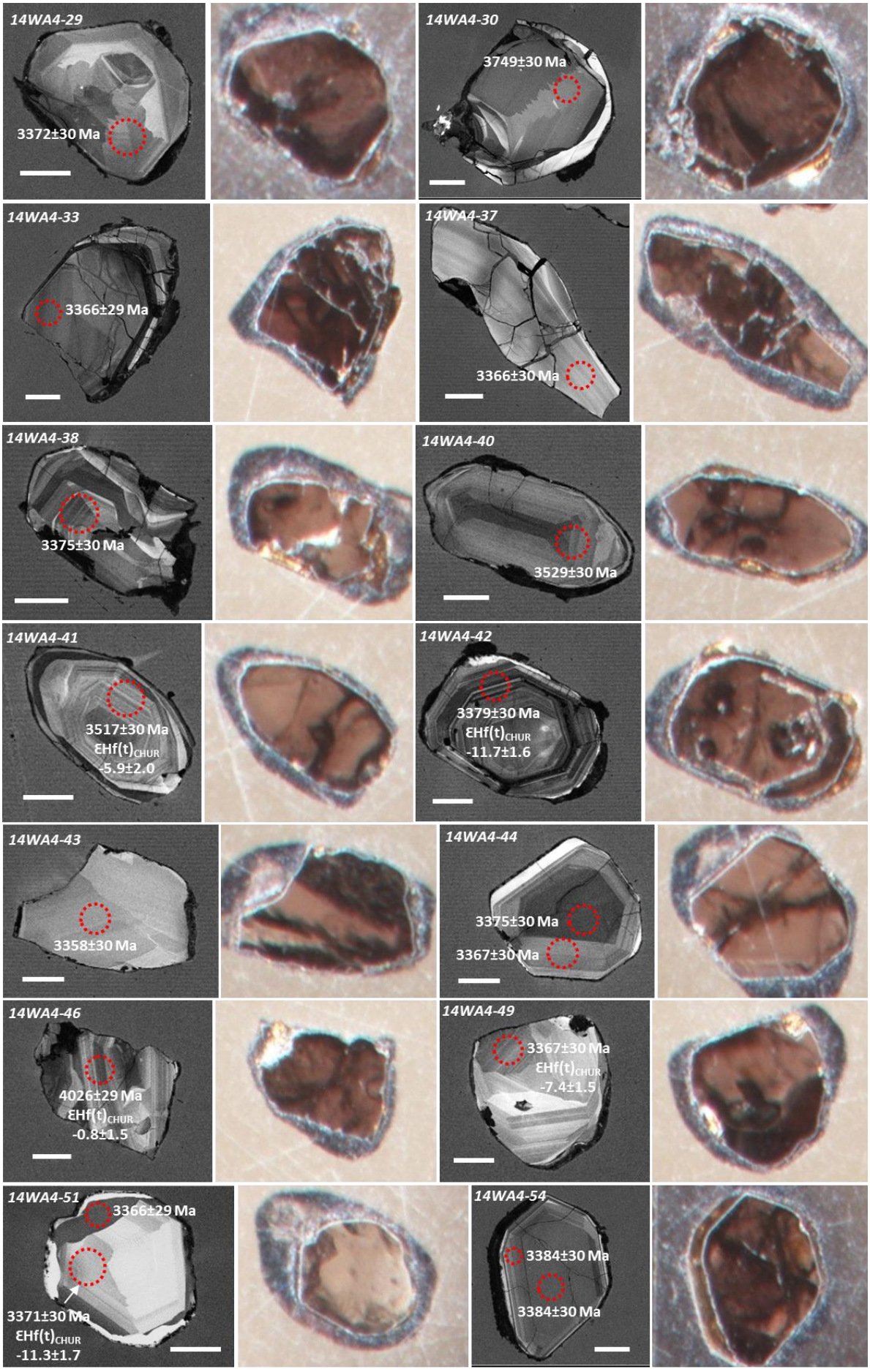
14WA4-29
3372±30 Ma
14WA4-30
3749±30 Ma
14WA4-33
3366±29 Ma
14WA4-37
3366±30 Ma
14WA4-38
3375±30 Ma
14WA4-40
3529±30 Ma
14WA4-41
3517±30 Ma
εHf(t)CHUR
-5.9±2.0
14WA4-42
3379±30 Ma
εHf(t)CHUR
-11.7±1.6
14WA4-43
3358±30 Ma
14WA4-44
3375±30 Ma
3367±30 Ma
14WA4-46
4026±29 Ma
εHf(t)CHUR
-0.8±1.5
14WA4-49
3367±30 Ma
εHf(t)CHUR
-7.4±1.5
14WA4-51
3366±29 Ma
3371±30 Ma
εHf(t)CHUR
-11.3±1.7
14WA4-54
3384±30 Ma
3384±30 Ma

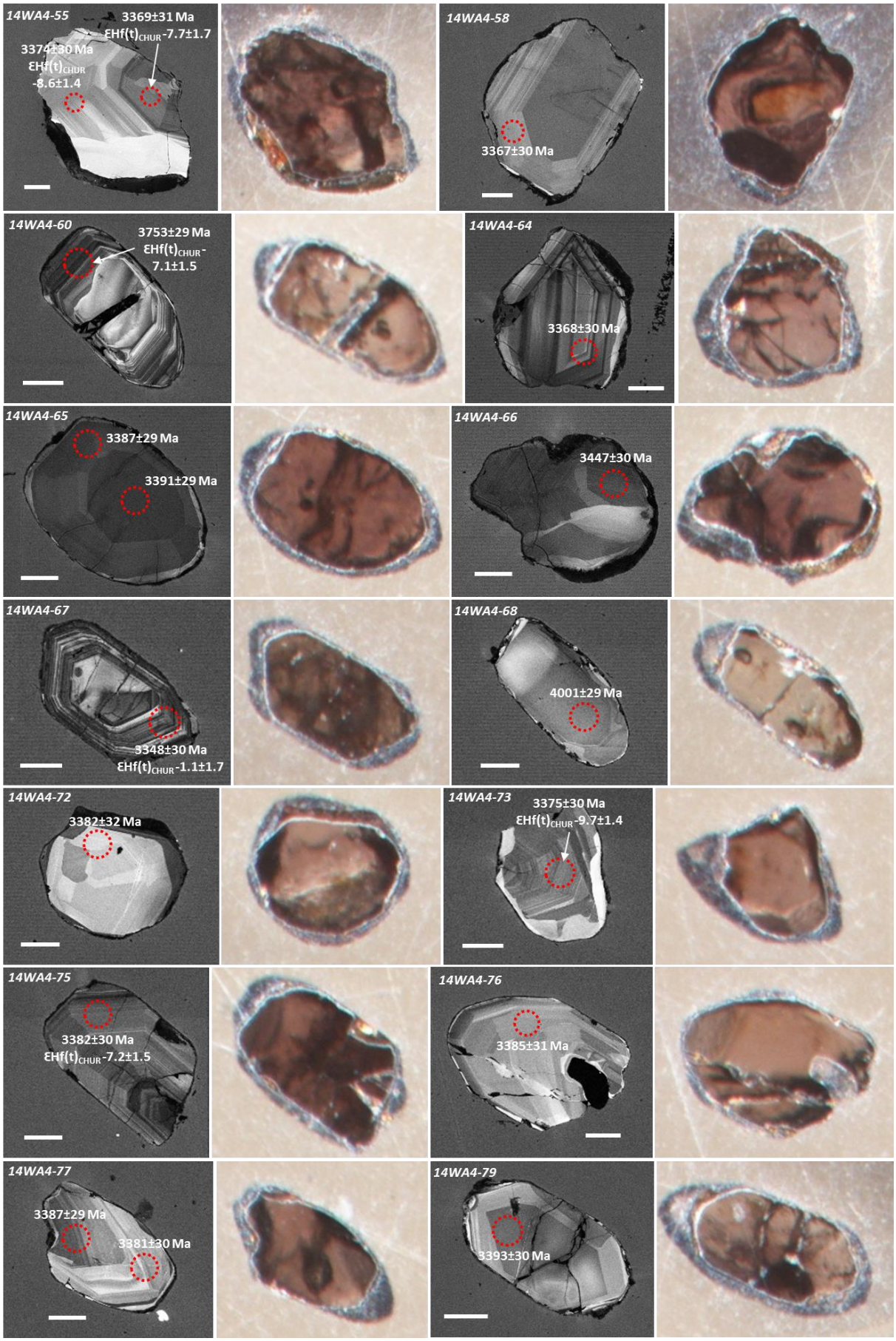
14WA4-55
3369±31 Ma
εHf(t)CHUR -7.7±1.7
3374±30 Ma
εHf(t)CHUR -8.6±1.4
14WA4-58
3367±30 Ma
14WA4-60
3753±29 Ma
εHf(t)CHUR -7.1±1.5
14WA4-64
3368±30 Ma
14WA4-65
3387±29 Ma
3391±29 Ma
14WA4-66
3447±30 Ma
14WA4-67
3348±30 Ma
εHf(t)CHUR -1.1±1.7
14WA4-68
4001±29 Ma
14WA4-72
3382±32 Ma
14WA4-73
3375±30 Ma
εHf(t)CHUR -9.7±1.4
14WA4-75
3382±30 Ma
εHf(t)CHUR -7.2±1.5
14WA4-76
3385±31 Ma
14WA4-77
3387±29 Ma
3381±30 Ma
14WA4-79
3393±30 Ma

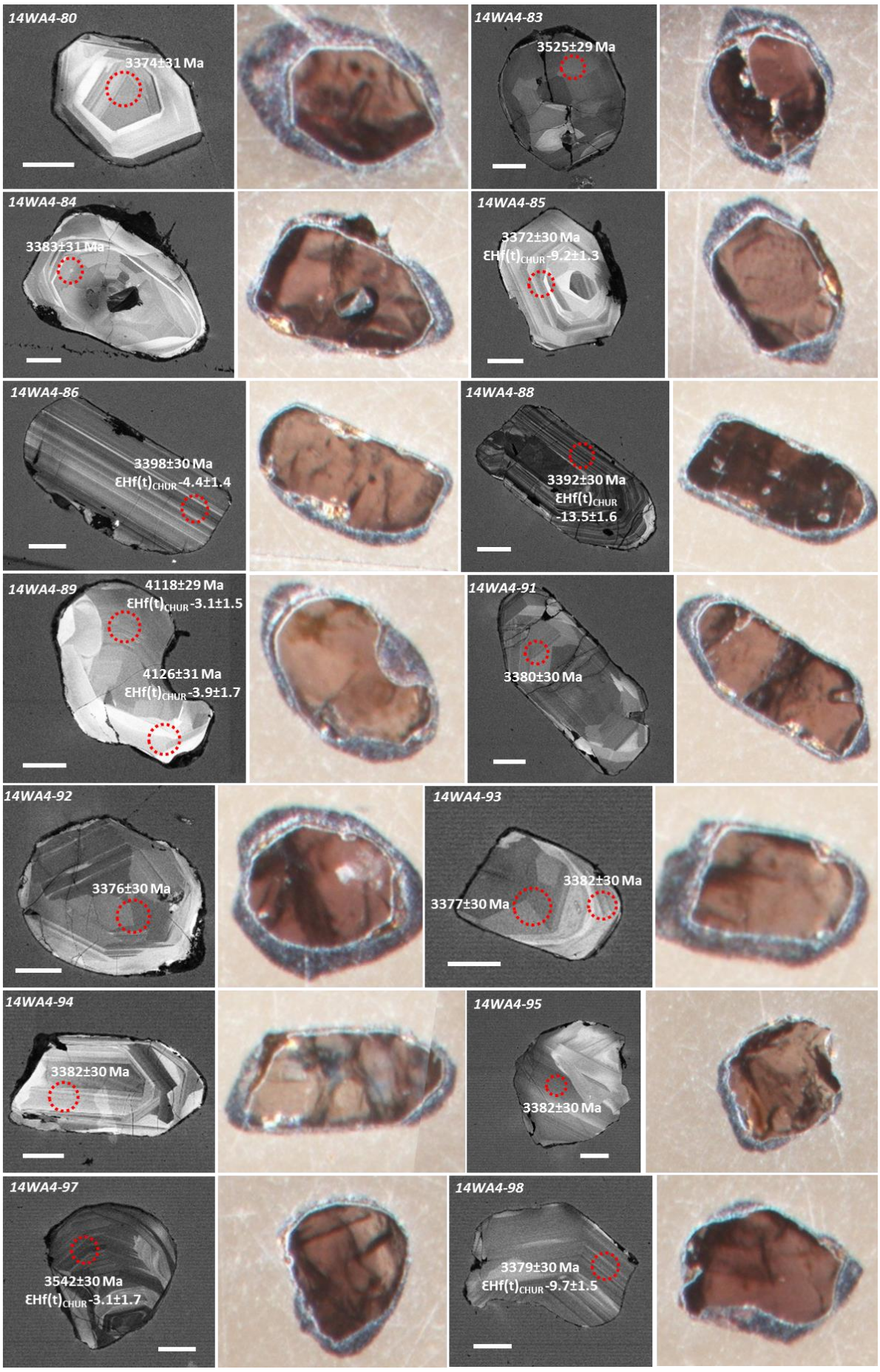
14WA4-80
3374±31 Ma
14WA4-83
3525±29 Ma
14WA4-84
3383±31 Ma
14WA4-85
3372±30 Ma
εHf(t)CHUR -9.2±1.3
14WA4-86
3398±30 Ma
εHf(t)CHUR -4.4±1.4
14WA4-88
3392±30 Ma
εHf(t)CHUR
-13.5±1.6
14WA4-89
4118±29 Ma
εHf(t)CHUR -3.1±1.5
4126±31 Ma
εHf(t)CHUR -3.9±1.7
14WA4-91
3380±30 Ma
14WA4-92
3376±30 Ma
14WA4-93
3382±30 Ma
3377±30 Ma
14WA4-94
3382±30 Ma
14WA4-95
3382±30 Ma
14WA4-97
3542±30 Ma
εHf(t)CHUR -3.1±1.7
14WA4-98
3379±30 Ma
εHf(t)CHUR -9.7±1.5

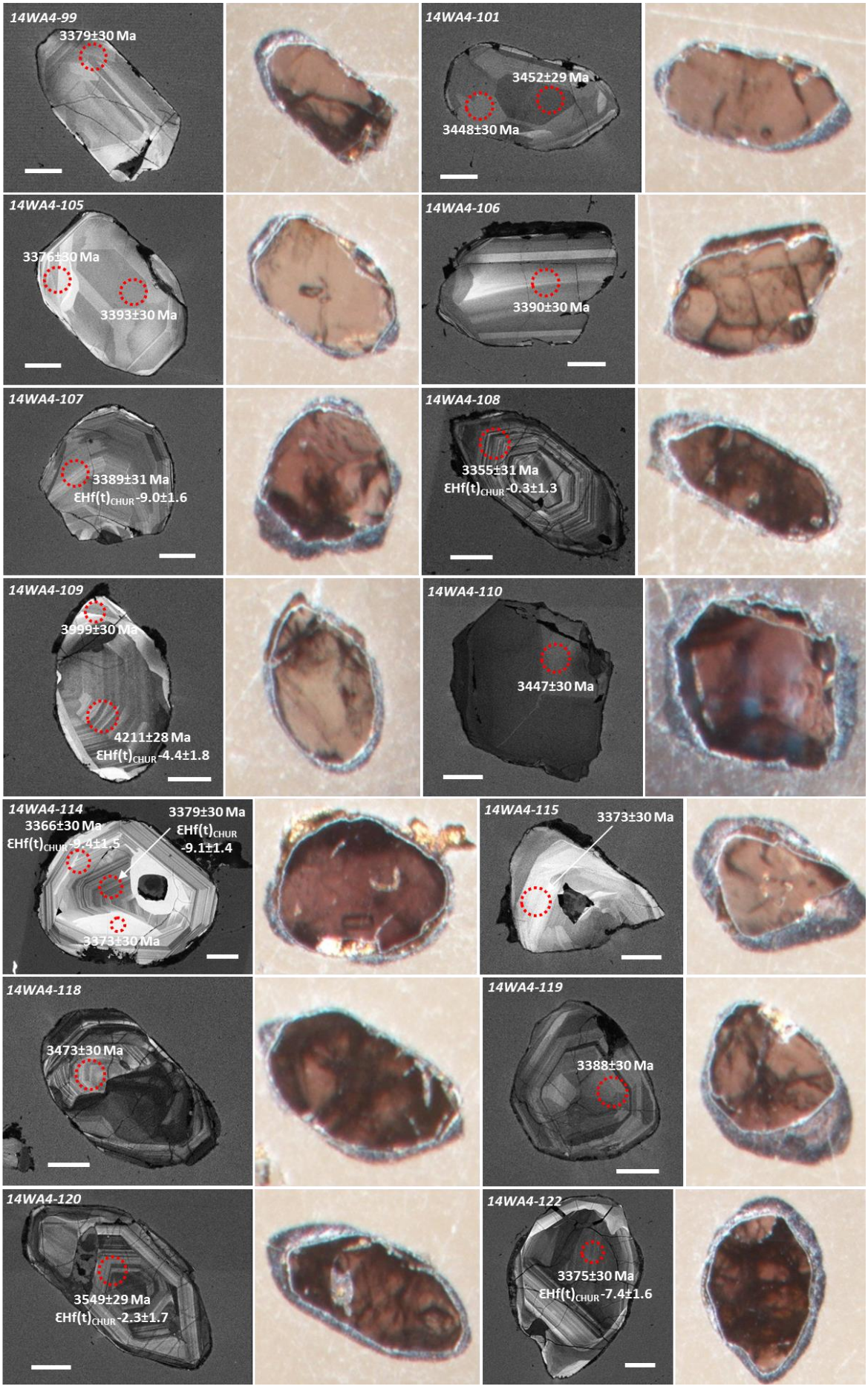
14WA4-99
3379±30 Ma
14WA4-101
3452±29 Ma
3448±30 Ma
14WA4-105
3376±30 Ma
3393±30 Ma
14WA4-106
3390±30 Ma
14WA4-107
3389±31 Ma
εHf(t)CHUR -9.0±1.6
14WA4-108
3355±31 Ma
εHf(t)CHUR -0.3±1.3
14WA4-109
3999±30 Ma
4211±28 Ma
εHf(t)CHUR -4.4±1.8
14WA4-110
3447±30 Ma
14WA4-114
3366±30 Ma
εHf(t)CHUR -9.4±1.5
3379±30 Ma
εHf(t)CHUR -9.1±1.4
3373±30 Ma
14WA4-115
3373±30 Ma
14WA4-118
3473±30 Ma
14WA4-119
3388±30 Ma
14WA4-120
3549±29 Ma
εHf(t)CHUR -2.3±1.7
14WA4-122
3375±30 Ma
εHf(t)CHUR -7.4±1.6

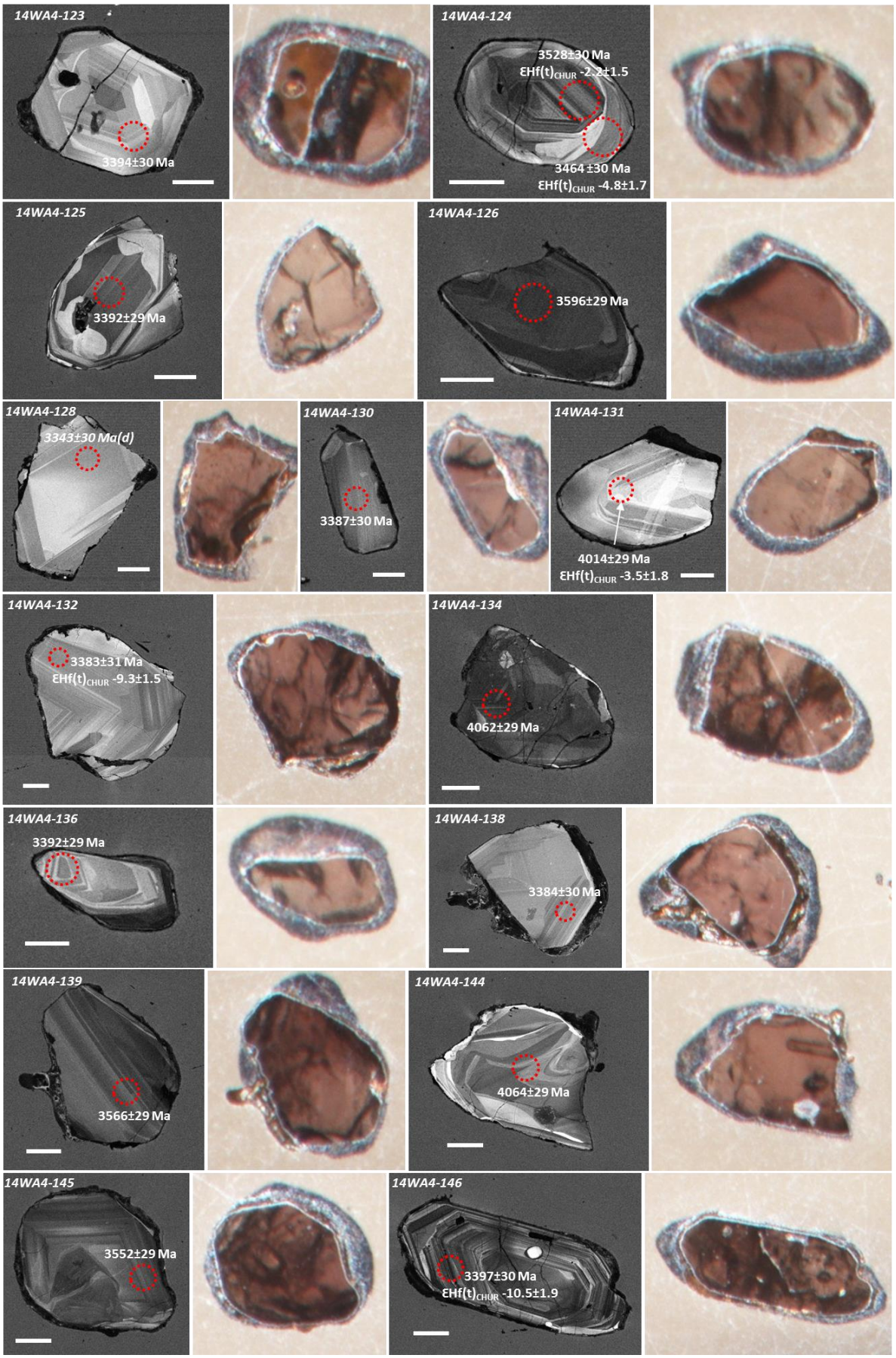
14WA4-123
3394±30 Ma
14WA4-124
3528±30 Ma
εHf(t)CHUR -2.2±1.5
3464 ±30 Ma
εHf(t)CHUR -4.8±1.7
14WA4-125
3392±29 Ma
14WA4-126
3596±29 Ma
14WA4-128
3343±30 Ma(d)
14WA4-130
3387±30 Ma
14WA4-131
4014±29 Ma
εHf(t)CHUR -3.5±1.8
14WA4-132
3383±31 Ma
εHf(t)CHUR -9.3±1.5
14WA4-134
4062±29 Ma
14WA4-136
3392±29 Ma
14WA4-138
3384±30 Ma
14WA4-139
3566±29 Ma
14WA4-144
4064±29 Ma
14WA4-145
3552±29 Ma
14WA4-146
3397±30 Ma
εHf(t)CHUR -10.5±1.9

Figure S11.3 (previous pages): CL and transmitted light images of 14WA4 Jack Hills zircons analysed within this study. Spots are 35 µm, the size of the Hf spot used within this study. Where only a U-Pb ablation was performed (20 µm) this was placed in the centre of 35 µm spots. Both U-Pb and ƐHf(t) uncertainties are the analytical uncertainties.

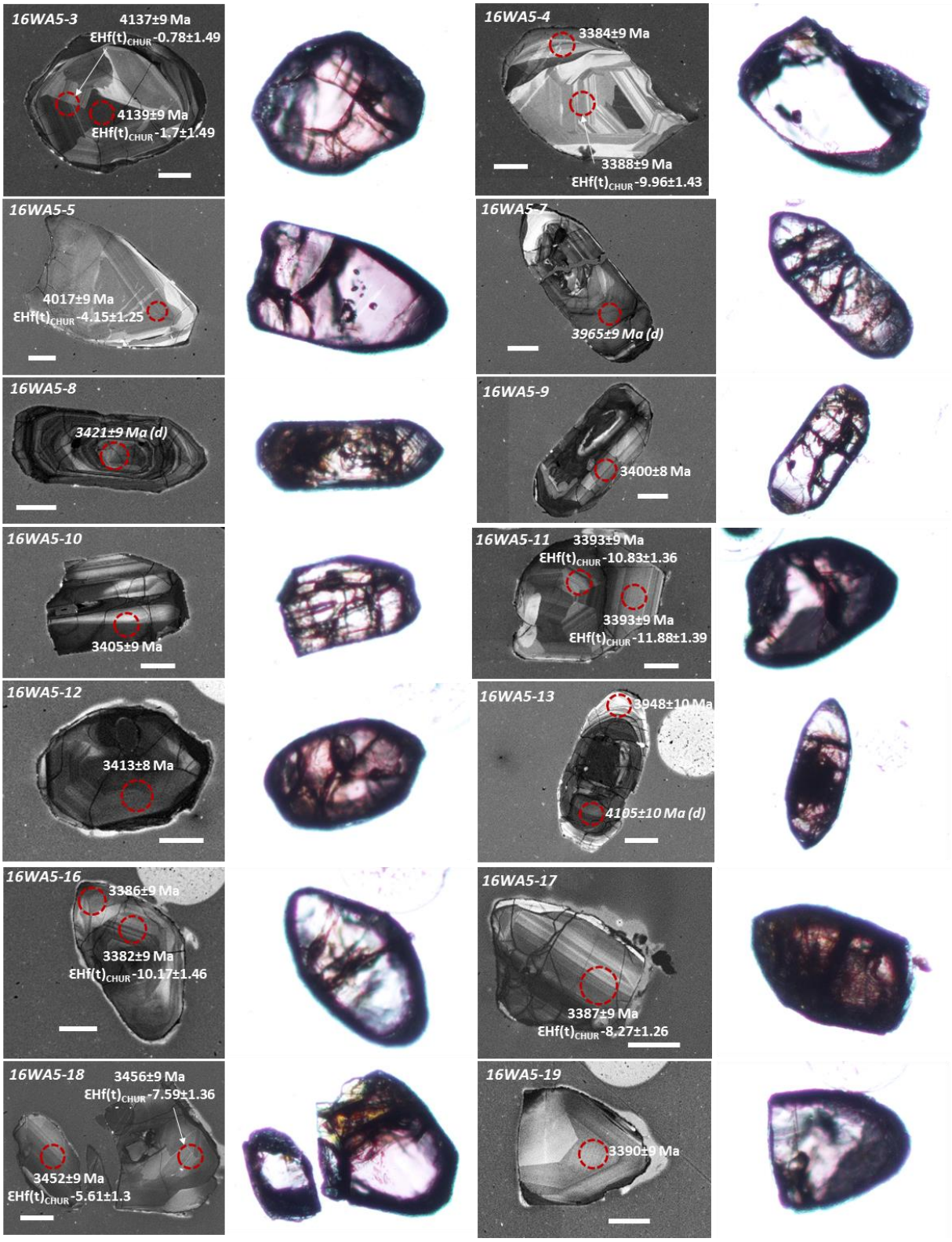
16WA5-3
4137±9 Ma
εHf(t)CHUR -0.78±1.49
4139±9 Ma
εHf(t)CHUR -1.7±1.49
16WA5-4
3384±9 Ma
3388±9 Ma
εHf(t)CHUR -9.96±1.43
16WA5-5
4017±9 Ma
εHf(t)CHUR -4.15±1.25
16WA5-7
3965±9 Ma (d)
16WA5-8
3421±9 Ma (d)
16WA5-9
3400±8 Ma
16WA5-10
3405±9 Ma
16WA5-11
3393±9 Ma
εHf(t)CHUR -10.83±1.36
3393±9 Ma
εHf(t)CHUR -11.88±1.39
16WA5-12
3413±8 Ma
16WA5-13
3948±10 Ma
4105±10 Ma (d)
16WA5-16
3386±9 Ma
3382±9 Ma
εHf(t)CHUR -10.17±1.46
16WA5-17
3387±9 Ma
εHf(t)CHUR -8.27±1.26
16WA5-18
3456±9 Ma
εHf(t)CHUR -7.59±1.36
3452±9 Ma
εHf(t)CHUR -5.61±1.3
16WA5-19
3390±9 Ma

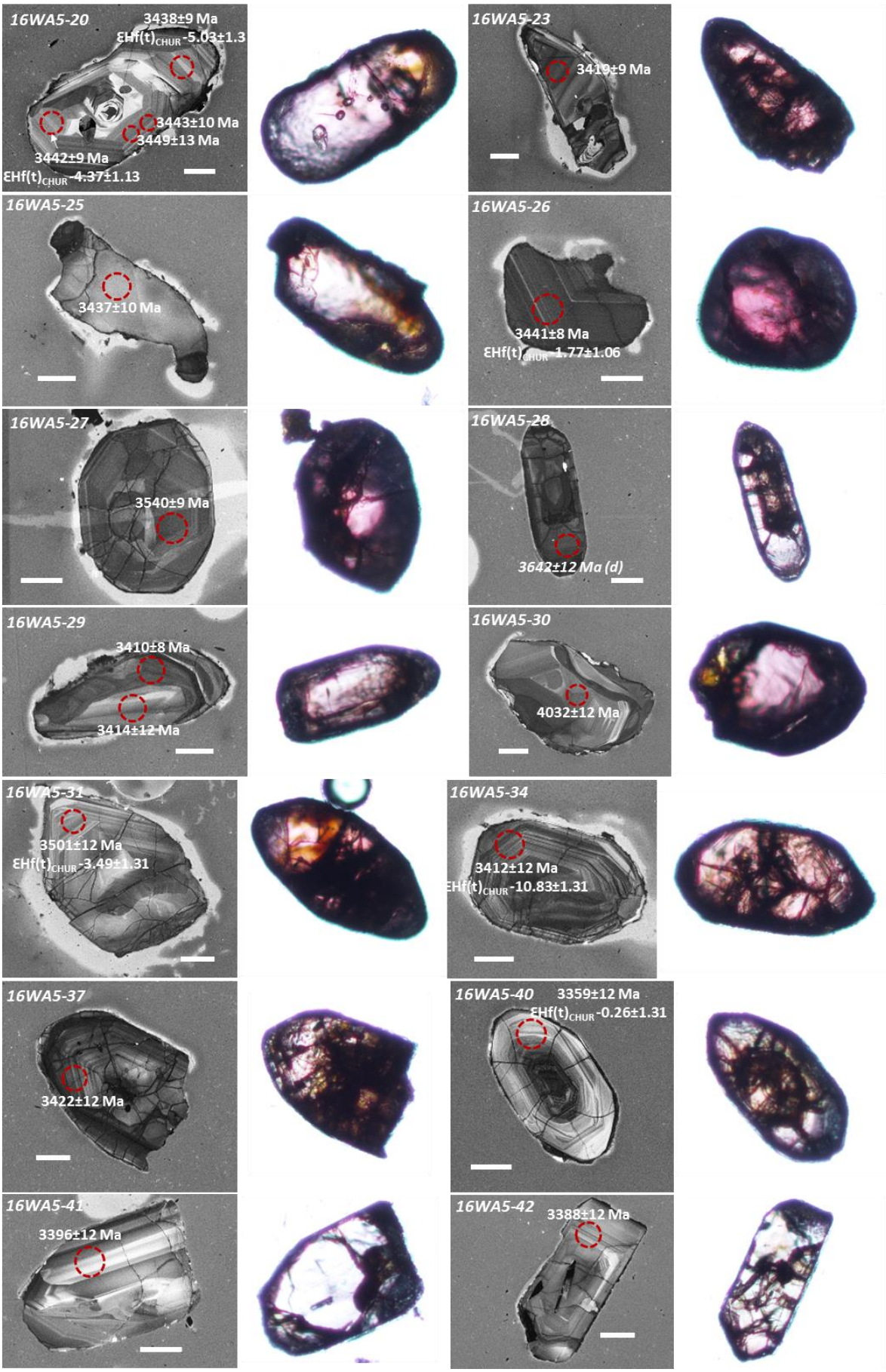
16WA5-20
3438±9 Ma
εHf(t)CHUR -5.03±1.3
3443±10 Ma
3449±13 Ma
3442±9 Ma
εHf(t)CHUR -4.37±1.13
16WA5-23
3419±9 Ma
16WA5-25
3437±10 Ma
16WA5-26
3441±8 Ma
εHf(t)CHUR 1.77±1.06
16WA5-27
3540±9 Ma
16WA5-28
3642±12 Ma (d)
16WA5-29
3410±8 Ma
3414±12 Ma
16WA5-30
4032±12 Ma
16WA5-31
3501±12 Ma
εHf(t)CHUR -3.49±1.31
16WA5-34
3412±12 Ma
εHf(t)CHUR -10.83±1.31
16WA5-37
3422±12 Ma
16WA5-40
3359±12 Ma
εHf(t)CHUR -0.26±1.31
16WA5-41
3396±12 Ma
16WA5-42
3388±12 Ma

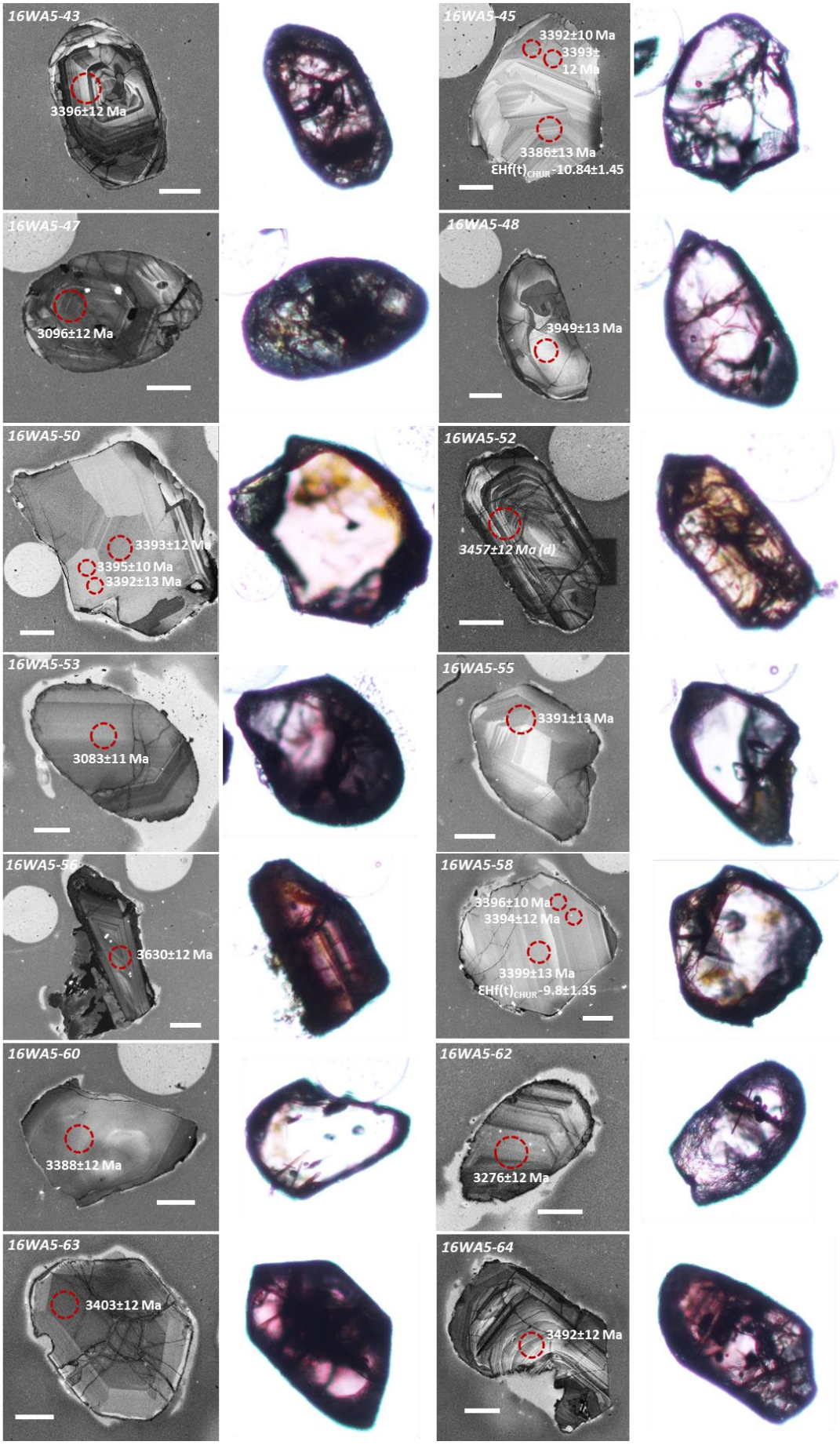
16WA5-43
3396±12 Ma
16WA5-45
3392±10 Ma
3393±
12 Ma
3386±13 Ma
εHf(t)CHUR -10.84±1.45
16WA5-47
3096±12 Ma
16WA5-48
3949±13 Ma
16WA5-50
3393±12 Ma
3395±10 Ma
3392±13 Ma
16WA5-52
3457±12 Ma (d)
16WA5-53
3083±11 Ma
16WA5-55
3391±13 Ma
16WA5-56
3630±12 Ma
16WA5-58
3396±10 Ma
3394±12 Ma
3399±13 Ma
εHf(t)CHUR -9.8±1.35
16WA5-60
3388±12 Ma
16WA5-62
3276±12 Ma
16WA5-63
3403±12 Ma
16WA5-64
3492±12 Ma


16WA5-66
3388±12 Ma (d)
3379±10 Ma
3377±13 Ma
16WA5-69
3458±12 Ma
16WA5-70
3499±12 Ma
16WA5-79
3869±13 Ma
16WA5-81
3560±10 Ma
3519±
13 Ma
3568±12 Ma
εHf(t)CHUR -2.52±1.18
16WA5-84
3381±10 Ma
16WA5-86
3454±13 Ma
εHf(t)CHUR -8.59±1.41
3452±10 Ma
3455±12 Ma
16WA5-87
3399±12 Ma
16WA5-88
3388±12 Ma
16WA5-92
3399±12 Ma
16WA5-99
3389±12 Ma
16WA5-100
3320±11 Ma (d)
16WA5-103
3417±12 Ma
16WA5-104
3406±12 Ma

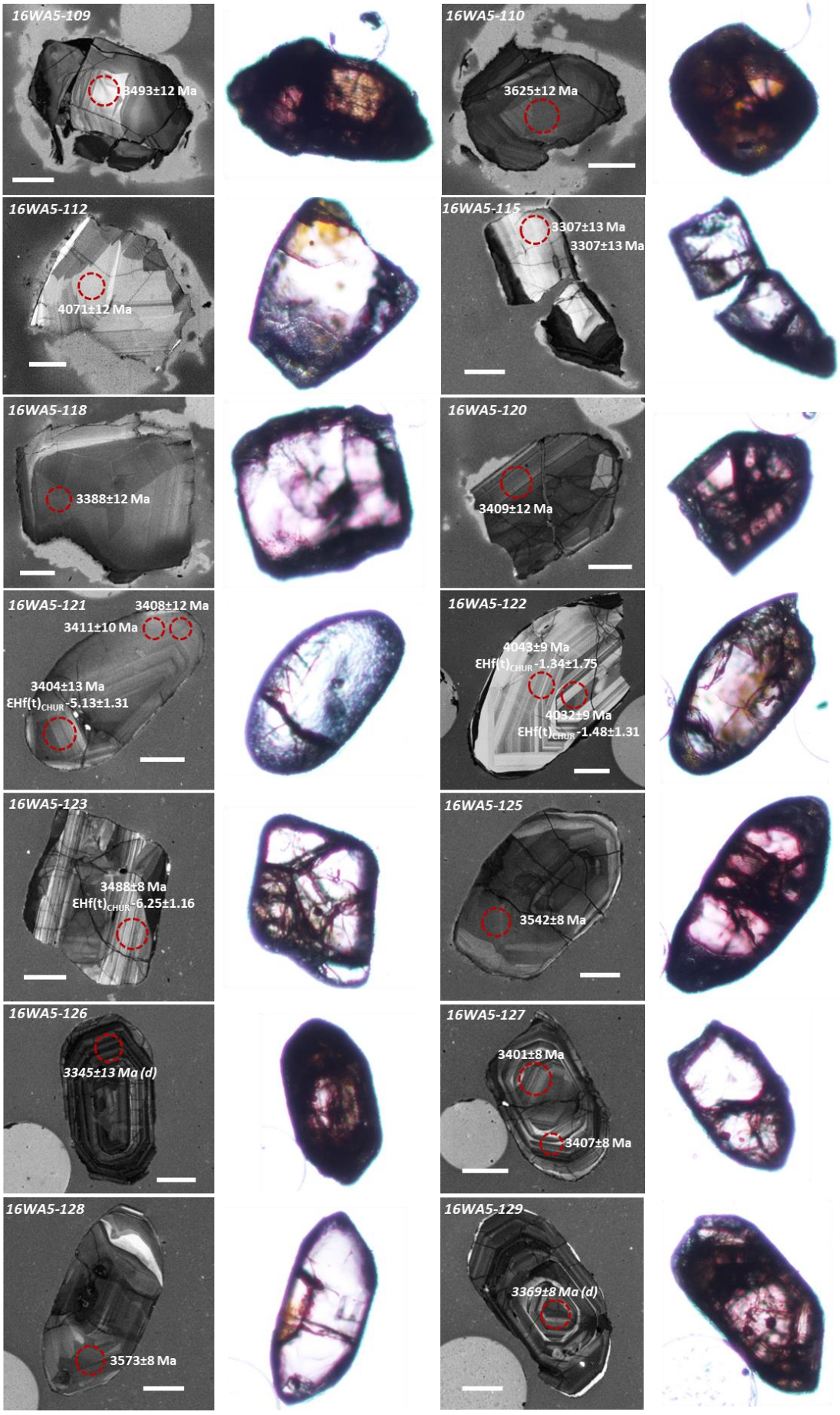
16WA5-109
3493±12 Ma
16WA5-110
3625±12 Ma
16WA5-112
4071±12 Ma
16WA5-115
3307±13 Ma
3307±13 Ma
16WA5-118
3388±12 Ma
16WA5-120
3409±12 Ma
16WA5-121
3408±12 Ma
3411±10 Ma
3404±13 Ma
εHf(t)CHUR -5.13±1.31
16WA5-122
4043±9 Ma
εHf(t)CHUR -1.34±1.75
4032±9 Ma
εHf(t)CHUR -1.48±1.31
16WA5-123
3488±8 Ma
εHf(t)CHUR -6.25±1.16
16WA5-125
3542±8 Ma
16WA5-126
3345±13 Ma (d)
16WA5-127
3401±8 Ma
3407±8 Ma
16WA5-128
3573±8 Ma
16WA5-129
3369±8 Ma (d)

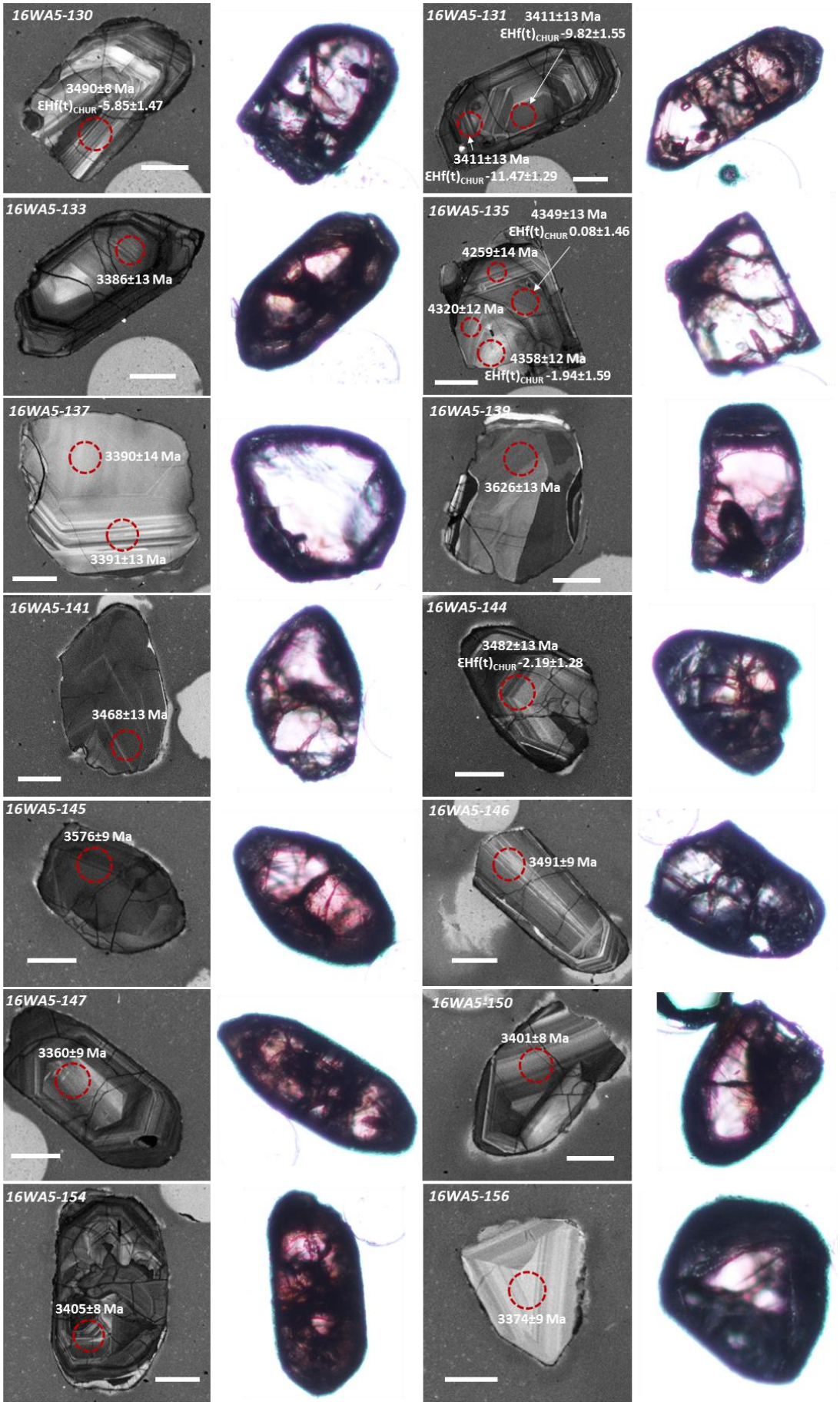
16WA5-130
3490±8 Ma
εHf(t)CHUR -5.85±1.47
16WA5-131
3411±13 Ma
εHf(t)CHUR -9.82±1.55
3411±13 Ma
εHf(t)CHUR -11.47±1.29
16WA5-133
3386±13 Ma
16WA5-135
4349±13 Ma
εHf(t)CHUR 0.08±1.46
4259±14 Ma
4320±12 Ma
4358±12 Ma
εHf(t)CHUR -1.94±1.59
16WA5-137
3390±14 Ma
3391±13 Ma
16WA5-139
3626±13 Ma
16WA5-141
3468±13 Ma
16WA5-144
3482±13 Ma
εHf(t)CHUR -2.19±1.28
16WA5-145
3576±9 Ma
16WA5-146
3491±9 Ma
16WA5-147
3360±9 Ma
16WA5-150
3401±8 Ma
16WA5-154
3405±8 Ma
16WA5-156
3374±9 Ma

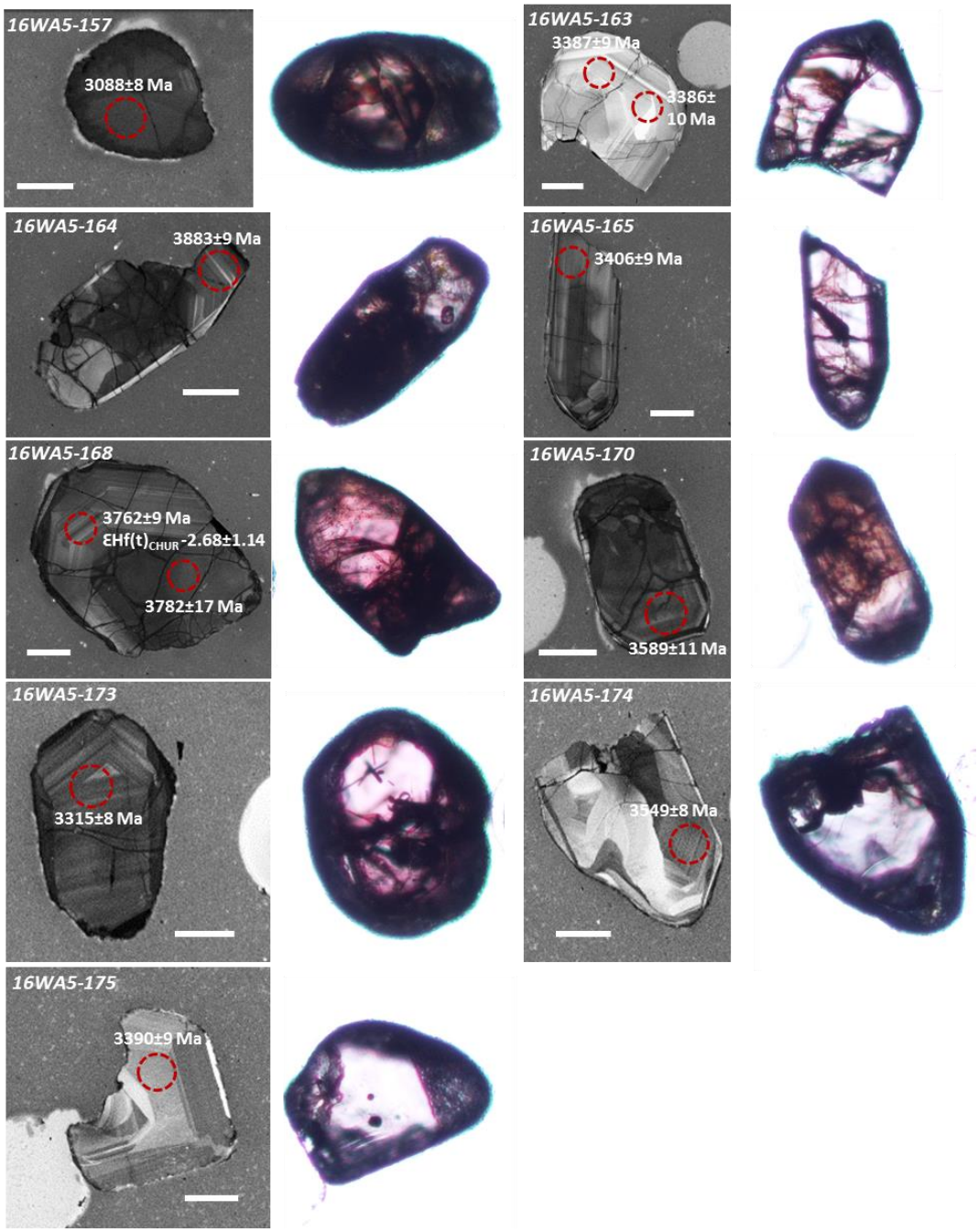

Figure S11.4: CL and transmitted light images of 16WA5 Jack Hills zircons analysed within this study. Spots are 35 µm, the size of the Hf spot used within this study. Where only a U-Pb ablation was performed (20 µm) this was placed in the centre of 35 µm spots. Both U-Pb and εHf(t) uncertainties are the analytical uncertainties. Lighter epoxy is due to secondary infilling of bubbles with newer epoxy resin.

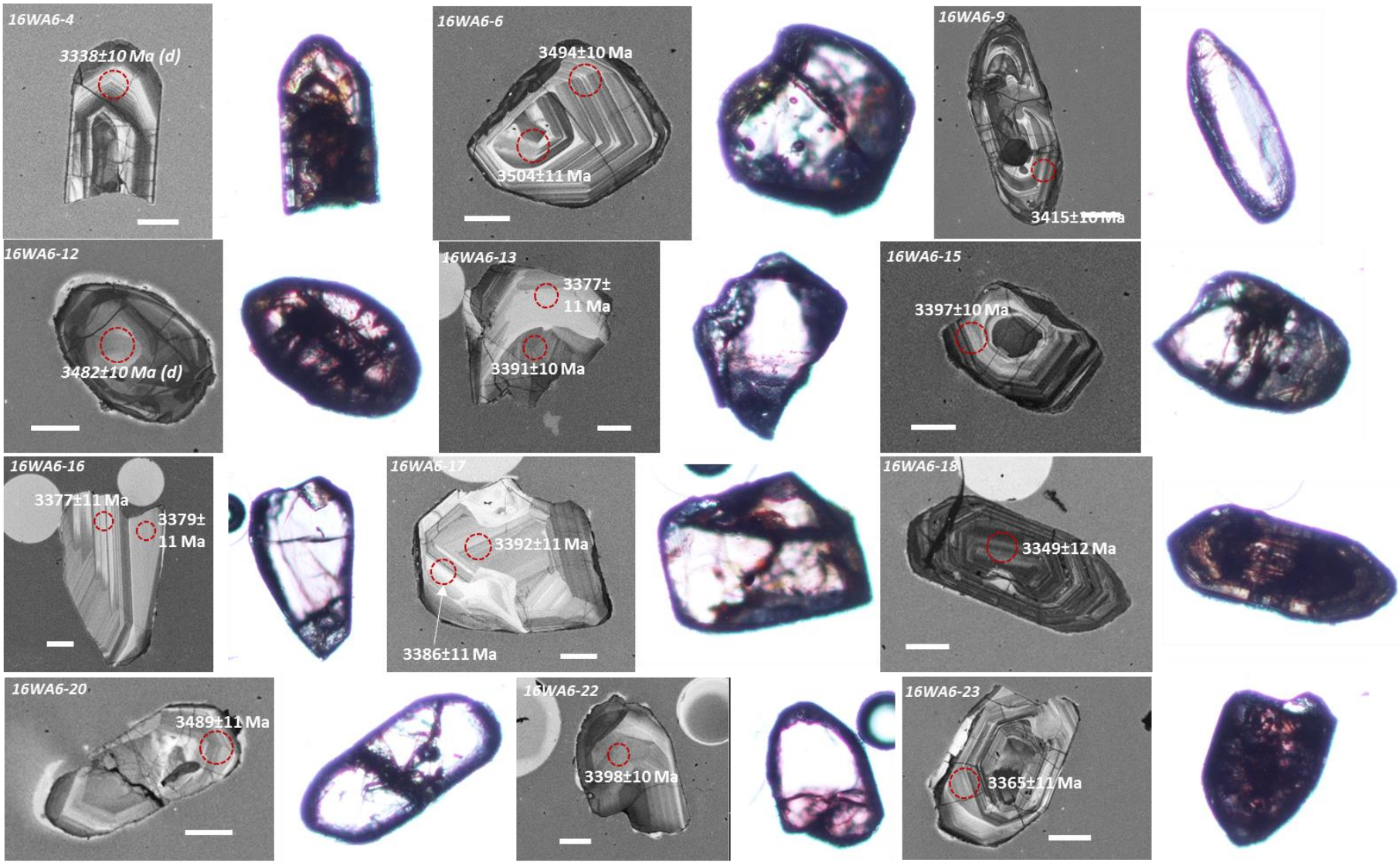
16WA6-4
3338±10 Ma (d)
16WA6-6
3494±10 Ma
3504±11 Ma
16WA6-9
3415±10 Ma
16WA6-12
3482±10 Ma (d)
16WA6-13
3377±
11 Ma
3391±10 Ma
16WA6-15
3397±10 Ma
16WA6-16
3377±11 Ma
3379±
11 Ma
16WA6-17
3392±11 Ma
3386±11 Ma
16WA6-18
3349±12 Ma
16WA6-20
3489±11 Ma
16WA6-22
3398±10 Ma
16WA6-23
3365±11 Ma

Figure S11.5 (previous page): CL and transmitted light images of 16WA6 Jack Hills zircons analysed within this study. Spots are 35 µm, the size of the Hf spot used within this study. Where only a U-Pb ablation was performed (20 µm) this was placed in the centre of 35 µm spots. Both U-Pb uncertainties are the analytical uncertainties.